UNIVERSITY OF SOUTHAMPTON

NON-FERROUS COMPOSITELY REINFORCED CONCRETE COLUMNS

by

Duncan Lillistone, BEng

This thesis was submitted for the award of
Doctor of Philosophy

FACULTY OF ENGINEERING AND APPLIED SCIENCE
CIVIL AND ENVIRONMENTAL ENGINEERING

February 2000

UNIVERSITY OF SOUTHAMPTON

ABSTRACT

FACULTY OF ENGINEERING AND APPLIED SCIENCE

CIVIL AND ENVIRONMENTAL ENGINEERING

Doctor of Philosophy

NON-FERROUS COMPOSITELY REINFORCED CONCRETE COLUMNS

by Duncan Lillistone

This research investigates the structural behaviour of concrete-filled FRP-composite columns under short-term monotonic loading, and describes a methodology for the analysis of concrete-filled FRP-composite columns. The proposed reinforcing system for concrete columns uses prefabricated FRP-composite filament wound tubes as the primary structural reinforcement for the column.

The efficient design of concrete structures requires the stress-strain response to be fully characterised. To determine the short-term behaviour of concrete confined by FRP-composites, 26 stub columns confined by E-glass/epoxy composites were tested to failure in monotonic uniaxial compression and their results are reported in this thesis. An equivalent uniaxial stress-strain confinement model has been developed for concrete confined by E-glass FRP-composite tubes, the mathematics of which is capable of reproducing all the characteristics observed in experimental stress-strain curves.

The experimental programme investigated the behaviour of 81 stocky concrete-filled E-glass FRP-composite columns subject to a nominal eccentric load. The main parameters investigated were concrete strength, orientation of confining fibres, column slenderness and type of longitudinal FRP reinforcement. The experimental study found the greatest enhancement in load capacity was achieved using FRP-composites with fibres orientated in the hoop direction.

The failure mode of the columns was governed by the type of longitudinal FRP reinforcement. Failure of columns reinforced with additional carbon FRP bars were initiated by the failure of the FRP. Additional E-glass FRP-composite bars as longitudinal reinforcement were found to increase the post-crushing stiffness and the ultimate load capacity of the column. The compressive failure strain of the E-glass reinforcement with triaxial confinement was comparable to the tensile failure strain.

Second-order effects were found to be more significant at lower slenderness ratios in concrete-filled FRP-composite columns than for conventional R.C. columns. Furthermore, the benefits of FRP-confinement are negligible if the column slenderness ratio is greater than 12.

The proposed design method for concrete-filled FRP-composite columns uses the CONFINE computer model developed as part of this research. The deflected profile of the column is assumed to be approximated by a part sinusoidal waveform. The CONFINE model gives good correlation with the experimental data for concrete-filled E-glass FRP-composite columns subjected to small eccentricities of load. The mathematics of the model enables predictions of the deflections, curvature and strains in the columns over the entire load history with a high degree of confidence.

Limited additional experimental work on concrete confined by carbon FRP-composites is also reported in this thesis.

LIST OF CONTENTS

CHAPTER 2

CHAPTER 3

CHAPTER 4

LIST OF TABLES

LIST OF FIGURES

LIST OF PLATES

ACKNOWLEDGEMENTS

I would like to acknowledge the help, guidance and supervision of Dr C. K. Jolly, whose knowledge and advice has proven invaluable. I would like to thank the Department of Civil and Environmental Engineering, University of Southampton for providing the facilities for this research, the Engineering and Physical Science Research Council for their financial support and Prof. J. L. Clarke of the Concrete Society for his interest in this work.

I would also like to thank the Building Research Establishment for their help on the collaborative experimental work testing the large diameter columns and the Eurocrete project for donating the FRP reinforcing bars used in this research.

My thanks also to all the technical staff and postgraduates, past and present in the Civil Engineering Department but especially Messrs R. Waterhouse and M. Foster for their help in carrying out the experimental investigation and Dr M. Gou.

I would also like to thank my wife, Helen, for all her support and patience.

NOTATION

A_c	cross-sectional area of concrete
A_r	cross-sectional area of longitudinal reinforcement
A_s	cross-sectional area of steel
A_t	cross-sectional area of composite tube
D	diameter of concrete core
e	initial eccentricity
E_{ci}	initial tangent modulus of concrete
E_{c1}	secant modulus of unconfined concrete
E_{cr}	initial radial tangent modulus of concrete
E_f	modulus of elasticity of a fibre
E_m	modulus of elasticity of the matrix
E_r	modulus of elasticity of longitudinal reinforcement
E_s	modulus of elasticity of steel
E_{sec}	secant modulus of elasticity of confined concrete
$E_{\theta\theta}$	elastic hoop modulus of an FRP-composite tube
$\overline{E}_{\theta\theta}$	effective elastic hoop modulus of an FRP-composite tube
E_x	modulus of elasticity in the axial direction
E_{xx}	axial elastic modulus of an FRP-composite tube
E_{11}, E_{22}	modulus of elasticity of a FRP-composite laminate in the principal fibre directions
E_{pr}	radial post-crushing tangent modulus of confined concrete
E_{px}	axial post-crushing tangent modulus of confined concrete
E_{1r}	$= E_{cr} - E_{pr}$
E_{1x}	$= E_{ci} - E_{px}$
f_c	concrete compressive stress
f_{cc}	compressive strength of confined concrete
f_{ccd}	design compressive strength of confined concrete
f_{ck}	characteristic compressive strength of unconfined concrete
f_{co}	compressive strength of unconfined concrete
f_{cu}	concrete cube strength
f_{or}	radial plastic stress

f_{ox}	axial plastic stress
f_r	radial stress
f_{rk}	stress in longitudinal reinforcing bar k
f_{sr}	radial stress component in steel
f_{sx}	axial stress component in steel
f_{sy}	yield strength of steel
$f_{s\theta}$	circumferential stress component in steel
f_t	axial stress in composite tube
f_θ	circumferential stress
G_f	fibre shear modulus
G_m	matrix shear modulus
$G_{x\theta}$	axial shear modulus of an FRP-composite tube
G_{12}	shear modulus of a FRP-composite laminate
h	laminate thickness
I	second moment of area
I_c	second moment of area of concrete
I_r	second moment of longitudinal reinforcement
I_s	second moment of area of steel
k	concrete strength coefficient
k_c	initial column stiffness
L	column length
L_{crit}	length of column for which its Euler load equals its squash load
L_e	effective column length
t	thickness of composite wall
M	moment
M_u	ultimate moment
$\overline{M}$	normalised moment
M^{ext}	external moment
M^{int}	internal moment
M^r	moment residual
m	number of FRP-composite strip elements
N	axial load
N_{crit}	Euler buckling load

N_{exp}	experimental axial load
N_T	theoretical axial load
N_u	ultimate axial load
N_{uz}	ultimate axial load in the absence of any moment on cross-section
$N_{(\varepsilon=3500)}$	axial load at $3500\mu\varepsilon$
$\overline{N}$	$= \dfrac{N_u}{f_{co}A_c + f_y A_s}$ normalised ultimate axial load
N^{ext}	external axial force
N^{int}	internal axial force
N_{max}	maximum axial load
n	shape parameter, number of concrete strip elements
u	axial displacement
V	volume
ΔV	net volume change
V_f	fibre volume fraction
w	total lateral deflection
w''	curvature
w_o	total lateral deflection at mid-height of column
X_c	longitudinal compressive failure strength of FRP-composite
X_t	longitudinal tensile failure strength of FRP-composite
Y_o	position of the neutral axis from centroidal axis
Y_1, Y_2	internal end point position of the neutral axis
y	distance of neutral axis from extreme compressive concrete fibre
$\overline{y}_i$	$= y_i - Y_o$
$\overline{y}_j$	$= y_j - Y_o$
$\overline{y}_k$	$= y_k - Y_o$
α	enhancement factor for the triaxial strength of concrete
β	ratio of circumferential stress to axial stress
$\overline{\beta}$	reduction factor of the biaxial strength of steel
δ	lateral column deflection
δ_o	lateral column deflection at mid-height of column
δ_u	column deflection at failure
γ_{mc}	material partial factor of safety

γ_{me}	modulus of elasticity partial factor of safety
ε_c	axial strain in concrete
ε_{cc}	strain corresponding to peak stress of confined concrete
ε_{co}	strain corresponding to peak stress of unconfined concrete
ε_{cu}	ultimate failure strain of unconfined concrete
ε_{mu}	matrix ultimate failure strain
ε_r	radial strain
ε_v	volumetric strain
ε_x	axial strain
ε_θ	circumferential strain
ε_1	strain at extreme concave concrete fibre
ε_{1u}	ultimate strain at extreme concave concrete fibre
ε_2	strain at extreme convex concrete fibre
η_1	coefficient used to estimate the reduced strength of steel and the enhanced concrete strength
η_2	coefficient used to estimate the reduced strength of steel
λ	sinusoidal buckling wavelength
$\overline{\lambda}$	non-dimensional slenderness ratio
ν_a	apparent Poisson's ratio of concrete
ν_c	Poisson's ratio of concrete
ν_f	Poisson's ratio of the fibre
ν_m	Poisson's ratio of the matrix
ν_s	Poisson's ratio of steel
$\nu_{x\theta}$	axial Poisson's ratio of a FRP-composite tube
$\nu_{\theta x}$	transverse Poisson's ratio of a FRP-composite tube
ν_{12}	axial Poisson's ratio of a FRP-composite laminate
ν_{21}	transverse Poisson's ratio of a FRP-composite laminate
ξ	fibre packing factor coefficient
σ_x	axial stress
σ^c	compressive failure stress
σ_{11}^c	compressive failure stress in longitudinal direction
σ^t	tensile failure stress
σ_{11}^t	tensile failure stress in longitudinal direction

σ_f	failure stress of fibre
σ_m	failure stress of matrix
ϕ	angle of fibre orientation
χ	curvature
χ_o	curvature at mid-height of column
$[A]$	extensional stiffness matrix
$[B]$	coupling stiffness matrix
$[D]$	bending stiffness matrix
$\{M\}$	moment per unit length
$\{N\}$	in-plane force per unit length
$[Q]$	reduced stiffness matrix for a laminate
$[\overline{Q}]$	transformed reduced stiffness matrix for a laminate
$[T_1]$	stress transformation matrix
$[T_2]$	strain transformation matrix – engineering shear
$\{\varepsilon\}_{1,2}$	strain in principal fibre directions
$\{\varepsilon\}_{x,\theta}$	strain in global co-ordinate system
$\{\sigma\}_{1,2}$	stress in principal fibre directions
$\{\sigma\}_{x,\theta}$	stress in global co-ordinate system

CHAPTER 1

INTRODUCTION

1.1 BACKGROUND

Durability is one of the greatest limitations of conventional reinforced concrete, particularly in aggressive environments. Instances of premature deterioration of concrete structures due to steel reinforcement corrosion are increasing. This increase is primarily due to the extensive use of de-icing salts applied to roads and bridges, although exposure to marine environments and atmospheric gases also accelerates the corrosion process. The annual repair cost for concrete structures damaged by steel corrosion in the United Kingdom has been estimated to be £500 million [1].

The increasing cost of maintaining concrete structures damaged by corrosion has resulted in the development of alternative non-ferrous reinforcement, such as advanced fibre-reinforced plastic (FRP) composites. These materials consist of high-strength and high-modulus continuous fibres embedded in a resin matrix. FRP-composites have the rigidity necessary for ease of fabrication and construction combined with an inherent resistance to the corrosion and environmentally induced degradation observed in steel reinforced concrete structures. Short, chopped fibres used for fibre reinforced concrete are beyond the scope of this study, and are not considered.

Concrete can be reinforced with FRP-composite bars similar to conventional steel reinforcement [2-5], FRP-prestressing tendons [6-7], or two- or three-dimensional FRP-composite grids [8]. Alternatively, concrete structures may be repaired or strengthened with resin bonded FRP-composite plates [9-10]. One of the advantages of FRP-composites compared to steel, is the ability to tailor their properties to suit a particular requirement by varying the amount of fibre in a given direction. Therefore, FRP-composites offer the potential for the development of new structural concepts that combine the superior mechanical properties of the fibres with the dominant characteristics of conventional materials, such as concrete.

FRP-composites have been used in North America [11-14] to retrofit concrete bridge columns for seismic strengthening. This process involves wrapping continuous FRP-composite prepreg tow around the column to provide a confining jacket. Experimental research on concrete confined using FRP-composite wraps has demonstrated that enhancements in strength of up to four times the unconfined compressive strength and up to forty times the ductility can be achieved [15-24]. In 1998, three columns on the 'Bible Christian Overbridge' on the A30 in Cornwall were strengthened with FRP-composite wraps

to improve the vehicle impact resistance of the columns [25]. The strengthened columns, shown in Plate 1.1, were finished with a cosmetic grey polyurethane coating which also protects the composite against ultra-violet degradation.

This research investigates the performance of an innovative reinforcing system for concrete columns, which uses prefabricated filament wound FRP-composite tubes as both permanent formwork and structural reinforcement. The proposed reinforcing system is illustrated in Figure 1.1. The fibres around the periphery of the column act in circumferential tension, providing triaxial confinement to the concrete core. When concrete is subjected to a state of triaxial confinement, significant increases in both strength and ductility are achieved. The FRP-composite tubes may be used in isolation to replace conventional steel reinforcement or in conjunction with FRP-composite or steel reinforcing bars. Since the FRP-composite tube isolates the concrete from the external environment, any reinforcing steel is protected from salt, acid or gas induced corrosion.

1.2 FIBRE-REINFORCED PLASTIC COMPOSITES

There are three basic families of fibres suitable for the reinforcement of concrete, namely glass, carbon and aramid. Within each of these families, the fibres have a variety of mechanical properties. The tensile strengths of the fibres range from about 2,400 N/mm^2 to over 3,000 N/mm^2, with elastic moduli ranging from approximately 70 kN/mm^2 for glass to over 200 kN/mm^2 for carbon. The fibres have a linear elastic response up to ultimate load, as shown in Figure 1.2, and exhibit no yield or plasticity.

In addition to their high strength and modulus, the specific density of the fibres is very low. A comparison of the specific strength and specific stiffness of the various fibres with steel is given in Figure 1.3. The specific strength of a glass fibre is 16 times that of steel, with a comparable specific stiffness. However, the specific strength of a carbon fibre is 35 times that of steel, whilst the specific stiffness is 5 times that of steel. Thus, FRP-composites offer the potential for large weight savings.

The type of resin used to form FRP-composites depends on the required durability, the manufacturing process and the cost. Generally, thermosetting resins are used to produce FRP-composites for reinforcing concrete structures, although thermoplastic resins are in development.

1.3 CORROSION OF STEEL REINFORCEMENT

Steel reinforcement is normally protected from corrosion by the alkaline environment of concrete. The hydrated cement components in concrete produce alkaline compounds, which result in the concrete matrix having a pH ranging from approximately 12.6 to 13.5 [26]. Within this pH range, steel is normally protected from corrosion by the passivating alkaline environment. Furthermore, a barrier to the ingress of moisture and oxygen is provided by the cement matrix, thus giving both chemical and physical protection to the steel reinforcement. How long this protection remains effective depends on a number of factors, including the retention of a high pH and the physical integrity of the cover. If the passivity of the steel is upset by external agents present in the environment, corrosion of the steel may be initiated.

Corrosion of the steel reinforcement results in a reduction in the mechanical strength of the parent material. However, the more critical effect of corrosion is the formation of hydrated ferrous oxide $Fe_2O_3 . xH_2O$ (common rust). Where x represents the number of water molecules in the hydrated ferrous oxide. The volume per unit mass of common rust is about three times greater than the parent metal [27]. This volumetric expansion induces internal tensile stresses in the cover concrete which causes cracking and eventually spalling and delamination. Corrosion also results in a reduction of the cross-sectional area of sound steel, decreasing the load-carrying capacity of the structure.

1.3.1 Causes of reinforcement corrosion

The causes of reinforcement corrosion can be classified as either chemical or physical. The most important substances which depassivate steel in concrete are chloride salts and carbon dioxide [27]. Chloride ions are the most common and damaging cause of corrosion of steel reinforcement in concrete. The presence of chloride ions may originate from the use of de-icing salts on roads and bridges or, in the case of structures located in marine environments, the chloride ions are present in the seawater.

The alkalinity of the concrete may also be reduced by carbon dioxide or sulphur dioxide in the atmosphere. These acidic gases react with the alkaline hydroxides in the cement matrix to produce carbonates and sulphates which lower the concrete pH, enabling corrosion to occur [28]. The carbonation slowly penetrates the concrete from the exposed surface, and eventually depassivates the steel in the concrete affected.

The physical factors that increase the likelihood of corrosion of reinforcement are porous concrete and low depth of concrete cover. These facilitate access of chlorides and

atmospheric gases to the reinforcement.

1.4 CONFINED CONCRETE

Triaxial confinement of concrete is an established technique for improving the compressive strength and ductility of the concrete. The enhancement in strength and ductility is a function of the magnitude and method of application of the confining pressure. The compressive strength of triaxially confined concrete was first quantified by Richart *et al.* [29]. Based on experimental data for cylindrical concrete specimens subjected to a constant uniform hydrostatic pressure (active confinement), they proposed that the augmented strength of the concrete was directly proportional to the lateral pressure.

$$\frac{f_{cc}}{f_{co}} = 1 + 4.1\frac{f_r}{f_{co}} \qquad (1.1)$$

Several other failure strength criteria for active confinement of concrete have been proposed by various researchers [30-32] and are summarised in Table 1.1. All of the equations define the failure strength as a function of the applied lateral pressure. At low confining pressures all the equations predict similar failure strengths. The maximum variation in the predicted failure strengths of the four equations is 8 percent provided the ratio f_r/f_{co} is less than unity. The power functions in the equations account for the reduction in strength enhancement observed in concrete specimens subjected to high triaxial confinement pressures [30].

The confinement in real concrete members is defined as passive. When concrete is subjected to an axial compressive strain, lateral deformations occur due to Poisson's effect. The stresses developed in the lateral reinforcement, due to the lateral expansion of the concrete, induce a confining stress to the concrete core. Thus, passive confinement is due to lateral reinforcement, and is neither uniform nor constant. The confining pressure acting on the core can be determined from the free body diagram shown in Figure 1.4.

$$f_r = \frac{2t}{D} f_{s\theta} \qquad (1.2)$$

The derivation of equation 1.2 is given in Appendix A. Therefore, the enhancement in compressive strength and ductility is a function of the applied axial strain, the Poisson's ratio of the concrete core and the mechanical properties of the lateral reinforcement.

1.4.1 Concrete-filled steel tubes

In the United Kingdom, the augmented strength of concrete due to confinement is utilised in the design of concrete-filled steel tubes. In general, the resistance of a concrete-filled steel

column to compression is increased by 15% due to the effects of triaxial confinement [33]. The steel tube confines the concrete core, enhancing its compressive strength and ductility as well as providing increased shear strength to the core. Conversely, the concrete core prevents premature buckling of the steel tube. Mechanical interlock and chemical interaction between the steel and concrete also results in a degree of composite action that enhances the flexural strength of the column. The ultimate load capacity of concentrically loaded concrete-filled circular hollow sections is:

$$N = A_s f_{sx} + A_c f_{co}\left(1 + \alpha \frac{2t}{D}\frac{f_{s\theta}}{f_{co}}\right) \qquad \textbf{(1.3)}$$

The augmented strength of concrete under confinement from the steel shell is given by:

$$\frac{f_{cc}}{f_{co}} = 1 + \alpha \frac{f_{sr}}{f_{co}} = 1 + \alpha \frac{2t}{D}\frac{f_{s\theta}}{f_{co}} \qquad \textbf{(1.4)}$$

The coefficient α determines the triaxial concrete strength for a given column slenderness. The effects of triaxial confinement are found to diminish as the column slenderness increases. The non-dimensional slenderness ratio at which triaxial effects become negligible is approximately $\bar{\lambda} = 1.0$ [34]. The non-dimensional slenderness ratio is the ratio of the column length L to a unit critical length of column L_{crit}, which is defined as the length of the column for which its Euler load equals its squash load. Thus:

$$\bar{\lambda} = \frac{L}{L_{crit}} = \frac{L}{\pi}\sqrt{\frac{A_c f_{co} + A_s f_{sy}}{E_{ci} I_c + E_s I_s}} \qquad \textbf{(1.5)}$$

The reduction in triaxial enhancement as the column slenderness increases is illustrated in Figure 1.5, which compares the experimental failure loads of concrete-filled steel tubes [35-39] with the non-dimensional slenderness ratio. The buckling curve in Figure 1.5 gives the theoretical strength of the composite column, ignoring the triaxial effects.

When the concrete-filled steel tube is subjected to an axial compressive load, the steel tube is subjected to stresses in the axial, circumferential and radial directions, as shown in Figure 1.4(d). However, for thin shells the stress in the radial direction is small relative to the axial and circumferential stresses and can be neglected [40]. Therefore, the steel tube is in a state of biaxial stress and the onset of plastic behaviour is defined by a yield criterion such as Von Mises. Assuming the steel has yielded biaxially, the stresses in the axial and circumferential directions must satisfy:

$$f_{sx}^2 + f_{s\theta}^2 - f_{sx} f_{s\theta} = f_{sy}^2 \qquad (1.6)$$

In order to satisfy equation 1.6 for the loading condition of circumferential tension and axial compression, both f_{sx} and $f_{s\theta}$ must be less than the yield stress of the steel. If the ratio of the circumferential stress to the axial stress in the steel tube is given by:

$$\beta = \frac{f_{s\theta}}{f_{sx}} \qquad (1.7)$$

By substitution of equation 1.7 into equation 1.6 and rearrangement thereof, the axial and circumferential stresses in the steel are given by:

$$f_{sx} = \frac{f_{sy}}{\sqrt{1-\beta+\beta^2}} = \frac{f_{sy}}{\bar{\beta}}$$

$$f_{s\theta} = \frac{\beta}{\bar{\beta}} f_{sy} \qquad (1.8)$$

Therefore, the axial load capacity of a concrete-filled steel tube in terms of the yield strength of the steel is:

$$N = A_s \frac{f_{sy}}{\bar{\beta}} + A_c f_{co}\left(1 + \frac{\alpha\beta}{\bar{\beta}} \frac{2t}{D} \frac{f_{sy}}{f_{co}}\right) \qquad (1.9)$$

The European design code for concrete-filled circular columns [41] simplifies equation 1.9 by expressing the enhancement in concrete strength and reduction in the yield strength as two separate functions, η_1 and η_2 respectively:

$$N = A_s \eta_2 f_{sy} + A_c f_{co}\left(1 + \eta_1 \frac{t}{D} \frac{f_{sy}}{f_{co}}\right) \qquad (1.10)$$

The basic values of η_1 and η_2 depend on the non-dimensional slenderness and are defined as follows:

$$\eta_1 = 4.9 - 18.5\bar{\lambda} + 17\bar{\lambda}^2 \qquad \eta_1 \geq 0$$

$$\eta_2 = 0.25\left(3 + 2\bar{\lambda}\right) \qquad \eta_2 \leq 1.0 \qquad (1.11)$$

A comparison of the experimental failure loads of 86 columns [35-39] versus the predicted failure loads using equation 1.10 is shown in Figure 1.6. The average value of the ratio of the experimental ultimate load to the predicted ultimate load is 1.028 with a standard deviation of 13.4 percent.

There are a number of disadvantages of using a circular steel tube as a confinement system for concrete:

1. The steel is not protected from the environment and is therefore more susceptible to corrosion than embedded steel reinforcement.
2. The high modulus of elasticity of steel compared to concrete results in significant axial stresses in the steel, thus reducing the maximum confining stress of the steel, as illustrated by equation 1.8.
3. In the initial stages of loading, the Poisson's ratio of concrete ($\nu_c \approx 0.20$) is smaller than the Poisson's ratio of steel ($\nu_s \approx 0.30$) Therefore, the lateral expansion of the steel is greater than that of the concrete. This results in a partial separation of the steel concrete interface, delaying the development of a circumferential confining pressure.

1.4.2 Concrete confined by lateral steel ties

An alternative form of providing triaxial confinement to concrete reinforcement is achieved using closely spaced hoop reinforcement or spiral reinforcement, as shown in Figure 1.7(a-b). This form of construction is frequently used in the seismic design of reinforced concrete columns, where increased ductility is required to ensure that the shaking from large earthquakes does not cause collapse. Adequate ductility of concrete members is also necessary to ensure that moment redistribution can occur in concrete frames.

The hoop reinforcement provides confinement to the concrete core, prevents premature buckling of the longitudinal bars and acts as shear reinforcement. The cover concrete is unconfined and spalls off once its compressive strength is attained. The core concrete will continue to carry stresses at higher strains. The increase in strength of the confined concrete may be calculated on the basis of the 'effectively confined' concrete area [42]. Confinement of the concrete between the hoops relies on the arching action developed between the hoops. Zones of tensile stresses with no compression in the direction of the confining force develop along the height of the column, as shown in Figure 1.7(c). Thus, the area of effectively confined concrete is less than the nominal core area and is determined by the spacing of the hoops. The maximum confining pressure is governed by the yield strength of the confining steel. As soon as the confining steel yields, the confining pressure remains constant, irrespective of the lateral expansion of the concrete. Strain hardening of the steel results in a limited increase in the confining pressure.

Several empirical failure criterion have been proposed for the strength of concrete confined by lateral steel ties [43-44], and are summarised in Table 1.2. A comparison of the failure stress criterion derived from active and passive confinement is shown in Figure 1.8. The failure strength of concrete predicted by active confinement criteria is significantly greater than strength predicted by passive confinement criteria for high confining pressures. However, the confining stress induced by steel ties is relatively low, typically ranging between 0.50 N/mm^2 to 4.00 N/mm^2, compared to experimental hydrostatic pressures of up to 27 N/mm^2. At these low confining pressures, the differences between active and passive failure criteria are negligible.

Numerous studies have been carried out on the behaviour of concrete confined by lateral reinforcement and have investigated a number of parameters such as the strength of concrete; amount and distribution of longitudinal reinforcement; amount and spacing of transverse reinforcement and strain rate [45-47]. The experimental results for concrete confined by steel ties are compared with the existing failure criteria in Figure 1.9. The high degree of scatter in the experimental data is primarily due to differences in the test parameters, and suggests that the existing failure stress criteria are effective only when used to interpret the proponent's own test results.

The complexities of modelling concrete subject to triaxial confinement can be simplified by the concept of equivalent uniaxial strain [48]. This technique involves the elimination of the non-linear Poisson's effect of the stress-strain behaviour of the concrete, the inelastic triaxial behaviour of the concrete being accounted for by the parameters defining the equivalent uniaxial stress-strain curve.

The early stress-strain model by Kent and Park [49] assumes that the lateral confinement only enhances the ductility of the concrete and not the compressive resistance as shown in Figure 1.10(a). The modified model illustrated in Figure 1.10(b), by Park *et al* [50], included a strength gain factor to account for the increase in compressive resistance as well as ductility. The strength gain factor implied that the degree of enhancement is proportional to the volumetric ratio and yield strength of the lateral steel. The volumetric ratio is the ratio of the volume of lateral steel to the volume of concrete.

The most widely used equivalent uniaxial stress-strain model for confined concrete, which has been extensively tested against experimental data, was proposed by Mander *et al* [43, 45]. The model is based on a fractional expression which represents the complete stress-strain curve, as shown in Figure 1.10(c). The stress-strain model is described by the following

equations:

$$f_c = \frac{f_{cc}\, x\, r}{r - 1 + x^r}$$

Where **(1.12)**

$$x = \frac{\varepsilon_c}{\varepsilon_{cc}} \quad ; \quad r = \frac{E_{ci}}{E_{ci} - E_{sec}} \quad ; \quad E_{sec} = \frac{f_{cc}}{\varepsilon_{cc}}$$

The confined peak strength f_{cc} is expressed in terms of a constant confining pressure f_r using:

$$f_{cc} = -1.254 + 2.254\sqrt{1 + 7.94\frac{f_r}{f_{co}}} - 2\frac{f_r}{f_{co}} \qquad \textbf{(1.13)}$$

$$\varepsilon_{cc} = \varepsilon_{co}\left[1 + 5\left(\frac{f_{cc}}{f_{co}} - 1\right)\right] \qquad \textbf{(1.14)}$$

The critical strain for the confined concrete ε_{cc} is taken from empirical work on actively confined specimens [43]. Thus, whilst the concrete is subjected to passive confinement, the values of ε_{cc} correspond to a constant confining pressure. The equivalent uniaxial stress-strain relationships for confined concrete proposed by different researchers are summarised in Table 1.3.

1.5 CONCRETE CONFINED BY FRP-COMPOSITES

The use of FRP-composites for the confinement of concrete is a relatively new approach, and theoretical and experimental work in this area is limited. Experimental studies on concrete confined by FRP-composites have been carried out in North America [15-24] and Japan [51-53]. These studies have shown that there are fundamental differences in the behaviour of concrete confined by FRP-composites compared to concrete confined by steel. A comparison of the stress-strain behaviour of concrete confined by lateral steel ties, derived using equation 1.12, and concrete confined with an E-glass FRP-composite is shown in Figure 1.11. Despite clear differences in behaviour, previous theoretical studies have used the failure criteria and constitutive equations originally developed for lateral steel confinement [15-16, 21, 54-56] to model the behaviour of FRP-confined concrete.

Unidirectional composites have a linear elastic stress-strain behaviour up to failure and therefore exert a continuously increasing confining pressure. The maximum stress and axial strain in the FRP-confined concrete occur simultaneously and a brittle failure is initiated by failure of the composite jacket. Furthermore, the ability to tailor the properties of the FRP-composite in any direction enables the axial and circumferential stresses to be uncoupled. In

contrast, steel is an elastic-plastic material and therefore, once yield has occurred, the confining pressure remains constant. The peak stress of concrete confined by steel reinforcement occurs at a significantly lower axial strain and corresponds approximately with yielding of the confining steel. Once the confining steel has yielded, the concrete loses strength since the constant confining pressure is unable to counteract the degradation in the stiffness of the concrete due to the formation of mortar cracks.

1.5.1 Concrete confined by FRP-composite wraps

The earliest work on FRP-confined concrete was carried out by Fardis and Khalili [15,16] in 1981-2. Forty-six concrete cylinders confined with FRP-composite wraps were tested in uniaxial compression. Four types of E-glass woven rovings wetted in a polyester resin were used to strengthen the cylinders, resulting in different ratios of circumferential to axial fibres. All the specimens exhibited a significant increase in strength and ductility, and failure was by brittle tensile failure of the FRP in the circumferential direction. Fardis and Khalili used the failure stress criteria proposed by Richart *et al* [29] to predict the strength of FRP-confined concrete. The failure strain of the concrete was found to increase with increasing circumferential stiffness and Fardis and Khalili proposed the following failure strain criterion:

$$\varepsilon_{cc} = \varepsilon_{co} + 0.0005\left(\frac{2t}{D}\right)\frac{E_{\theta\theta}}{f_{co}} \qquad \textbf{(1.15)}$$

Fardis and Khalili proposed that the stress-strain curve for concrete confined by an FRP-composite wrap can be approximated by a hyperbolic function. However, in its published form the expression does not satisfy the boundary condition $(\varepsilon_{cc}, f_{cc})$.

Howie and Karbhari [21, 23] and Picher *et al* [22] extended the work on concrete confined by FRP-composite wraps by investigating the effect of fibre orientation and thickness of composite on the load-carrying efficiency and ductility of the concrete. The concrete specimens used were confined by a unidirectional carbon FRP-composite wrap. The largest increase in load capacity occurred in the specimens confined with fibres orientated predominately in the hoop direction. Wraps orientated at ±45 degrees gave the lowest increase in strength. Thus, the most efficient use of the FRP-composite is achieved when all the fibres are orientated in the hoop direction. Karbhari and Gao [56] proposed that the failure strength of FRP-confined concrete is given by:

$$\frac{f_{cc}}{f_{co}} = 1 + 2.1\left(\frac{f_r}{f_{co}}\right)^{0.87} \qquad \textbf{(1.16)}$$

and the failure strain by:

$$\varepsilon_{cc} = \varepsilon_{co} + 0.01\left(\frac{f_r}{f_{co}}\right) \qquad \textbf{(1.17)}$$

Based on the experimental work of Howie and Karbhari, two theoretical studies [55, 56] have resulted in failure criteria being postulated and these are summarised in Table 1.4. A comparison of the failure criteria with the published results of forty-two specimens confined with carbon FRP-composite wraps [21,22] is shown in Table 1.5. The equation by Karbhari & Gao [56] gives the closest agreement with the experimental failure strengths. The average ratio of the predicted to experimental failure stress is 1.02 with a standard deviation of 7 percent. This equation was derived empirically from experimental results for concrete confined by FRP-composite wraps. The equations proposed by Fardis & Khalili [16] and Hoppel *et al* [55] are based on the Richart *et al* failure criterion for hydrostatic confinement and consequently correlation with the experimental data is poor.

The proposed failure criteria all assume that the hoop strain in the composite jacket at failure is equal to the failure strain of composite coupons with the same lay-up as used in the wraps. The hoop strain at failure in the composite wrap and the failure strains in the coupons tested by Howie and Karbhari [23] are given in Table 1.6. These results show that the failure strain in the composite jacket is significantly lower than the strain obtained from a coupon test on an equivalent FRP-composite. Thus, whilst the proposed failure strength criteria give reasonable agreement with experimental results, they do not satisfy lateral strain compatibility.

The expressions proposed for estimating the strain at peak stress show no correlation with the published experimental data from which they are derived. Furthermore, the axial failure strains published are calculated from the mean axial deformation over the entire specimen length and therefore do not represent the true axial strain of the confined concrete. Axial strains measured indirectly from the platen displacements include the effects of frictional restraint at the ends of the specimens and the deformation of the machine platens. The true axial strain is normally assumed to exist over the middle half of the cylinder where end-zone effects are negligible.

1.5.2 Concrete confined by filament wound FRP-composite tubes

A more recent development in FRP-confinement of concrete is the use of filament wound tubes, which act as both confining reinforcement and permanent formwork. The use of filament wound tubes results in more uniform properties of the composite with a greater degree of repeatability than those achieved by the application of hand wrapped FRP-composite jackets. Three experimental studies on concrete-filled FRP-composite tubes have been carried out in the United States using stub columns [57-60] to ascertain the stress-strain behaviour of the confined concrete.

Mirmiran and Shahawy [58] tested twenty-two 152.5 x 305 mm cylindrical specimens in uniaxial compression. The filament wound tubes consisted of a polyester resin with unidirectional E-glass fibres orientated at $\pm 75^{\circ}$ to the longitudinal axis with three different jacket thicknesses of 6, 10 and 14 plies. Saafi *et al* [60] tested eighteen 152.4 x 435 mm specimens, nine confined with a carbon FRP-composite and nine confined with an E-glass FRP composite. The FRP-composites consisted of 60 percent fibre and 40 percent polyester resin with fibres orientated in the hoop direction only. Three different jacket thicknesses were investigated for each fibre type.

A comparison of the failure strengths of the concrete-filled composite tubes with the experimental failure strength of concrete confined by composite wraps [21-23] is shown in Figure 1.12. The filament wound FRP-composite results in a greater enhancement in compressive strength than the FRP-composite wraps for a given composite hoop modulus. The better performance of the filament wound composites is due to the more uniform nature of the composite which is achieved by the filament winding process compared to hand wrapping. The greater enhancement in strength achieved by filament wound composites requires either new failure strength criteria to be determined or existing failure criteria derived from empirical data on concrete confined by composite wraps to be modified.

Failure criteria for concrete confined by filament wound composites have been proposed by both Samaan *et al* [59] and Saafi *et al* [60] and are given in Table 1.7. These failure criteria define the failure strength of the concrete as a function of the uniaxial failure strength of the FRP-composite. The failure strength criteria proposed by Samaan *et al* [59] and Saafi *et al* [60] show close agreement with the experimental data, as shown in Figures 1.13 and 1.14 respectively. However, the experimental confining pressure at failure is assumed to be equal to the tensile hoop strength of the composite tube derived from uniaxial tests, and thus does not satisfy lateral strain compatibility requirements. Furthermore, the axial strain

measurements in the specimens are based on the total axial deformation of the cylinders, and are therefore not true axial strains.

1.6 OBJECTIVES

The overall aims of this research are to investigate the structural behaviour of concrete-filled FRP-composite columns under short-term monotonic loading, and to develop a methodology for the analysis of concrete-filled FRP-composite columns.

Previous experimental work on the behaviour of FRP-encased concrete is limited to tests on stub columns, where the concrete is subjected to the maximum triaxial confinement. The benefits of triaxial confinement are known to diminish as the column slenderness ratio increases [34], except there is no published experimental data on either stocky columns or slender columns confined with FRP-composites. Therefore, in order to determine the experimental behaviour of concrete columns confined by FRP-composite materials, an extensive experimental testing programme was carried out at the University of Southampton and the Building Research Establishment. The testing programme was designed to investigate some of the main parameters which affect the behaviour of concrete confined by FRP-composites, these being:

- the type of fibre;
- the orientation of the fibres in the composite jacket;
- the column diameter and the thickness of the composite jacket;
- the strength of the concrete;
- the column slenderness ratio.

Other parameters not examined, which may also affect the behaviour of the confined concrete, include the shape of the cross-section, long-term and cyclic loading and the eccentricity of the applied load. The shape of the cross-section was not considered as the study was limited to circular columns subject to short-term monotonic loading. The investigation was also restricted to $0.05D$ the nominal load eccentricity specified in BS 8110 [61]. The experimental programme consisted of three phases:

Phase I Stub columns tested in concentric compression to determine the mechanical properties of the concrete under maximum triaxial confinement.

Phase II The testing of stocky concrete columns externally reinforced with filament wound FRP-composite tubes and subject to eccentric loading.

Phase III The testing of stocky concrete columns reinforced externally by a filament wound FRP-composite tube and by additional longitudinal FRP-composite reinforcement.

The objectives of this research are:

1. To determine failure criteria for concrete confined by FRP-composite materials which satisfy lateral strain compatibility requirements. The existing failure criteria summarised in §1.5 were derived from specimens where the composite fibres were orientated predominately in the hoop direction. Thus, any proposed failure criterion must also account for the orientation of the fibres in the composite jacket.
2. To establish the complete triaxial stress-strain behaviour of concrete encased by FRP-composite materials.
3. To investigate the behaviour of stocky concrete columns confined by FRP-composites under eccentric loading. One of the advantages of FRP-composites is the ability to tailor the properties of the composite to suit the application. Therefore, a longitudinal reinforcing component was incorporated in the winding configuration of some filament wound tubes to determine the effect on the axial and flexural capacity of the column.
4. To ascertain the limiting column slenderness ratio at which the benefits of FRP-confinement diminishes.
5. To develop a practical method for the design of concrete columns reinforced laterally and longitudinally with FRP-composite materials, derived from the experimental research.

Researchers	Date	Failure Strength
Richart *et al.* [29]	1928	$\frac{f_{cc}}{f_{co}} = 1 + 4.1\frac{f_r}{f_{co}}$
Newman and Newman [30]	1971	$\frac{f_{cc}}{f_{co}} = 1 + 3.7\left(\frac{f_r}{f_{co}}\right)^{0.86}$
Ahmad & Shah [31]	1982	$\frac{f_{cc}}{f_{co}} = 1 + 4.26\frac{f_r}{f_{co}}$ $\quad \frac{f_r}{f_{co}} \le 0.68$ $\frac{f_{cc}}{f_{co}} = 1.78 + 3.12\frac{f_r}{f_{co}}$ $\quad \frac{f_r}{f_{co}} > 0.68$
Saatcioglu and Razvi [32]	1992	$\frac{f_{cc}}{f_{co}} = 1 + 6.70\frac{f_r^{0.83}}{f_{co}}$

Table 1.1. Failure stress criteria for actively confined concrete

Researchers	Date	Failure Stress
Mander *et al.* [43]	1988	$\frac{f_{cc}}{f_{co}} = -1.254 + 2.254\sqrt{1 + 7.94\frac{f_r}{f_{co}}} - 2\frac{f_r}{f_{co}}$
Cusson and Paultre [44]	1995	$\frac{f_{cc}}{f_{co}} = 1 + 2.1\left(\frac{f_r}{f_{co}}\right)^{0.70}$

Table 1.2. Failure stress criteria for concrete confined by lateral steel reinforcement

Researcher	Date	Stress-Strain Model	
		Ascending Branch	Descending Branch
Kent and Park [49]	1971	$f_c = f_{co}\left[\frac{2\varepsilon_c}{\varepsilon_{co}} - \left(\frac{\varepsilon_c}{\varepsilon_{co}}\right)^2\right]$	$f_c = f_{co}[1 - Z(\varepsilon_c - \varepsilon_{co})]$ $Z = \frac{0.5}{\varepsilon_{50} - \varepsilon_{co}}$
Park *et al* [50].	1982	$f_c = Kf_{co}\left[\frac{2\varepsilon_c}{K\varepsilon_{co}} - \left(\frac{\varepsilon_c}{K\varepsilon_{co}}\right)^2\right]$	$f_c = Kf_{co}[1 - Z(\varepsilon_c - K\varepsilon_{co})]$ $Z = \frac{0.5}{\varepsilon_{50} - \varepsilon_{co}}$
Mander *et al.* [43]	1988	$f_c = \frac{f_{cc}xr}{r - 1 + x^r}$	$f_c = \frac{f_{cc}xr}{r - 1 + x^r}$
Saatcioglu and Razvi [32]	1992	$f_c = f_{cc}\left[\frac{2\varepsilon_c}{\varepsilon_{cc}} - \left(\frac{\varepsilon_c}{\varepsilon_{cc}}\right)^2\right]^{1/(1+2K)}$	$f_c = f_{cc} - \frac{0.15f_{cc}}{\varepsilon_{85} - \varepsilon_{cc}}(\varepsilon_c - \varepsilon_{cc})$

Table 1.3. Equivalent uniaxial stress-strain models for concrete confined by lateral steel reinforcement

Researcher	Date	Failure Strength	Failure Strain
Fardis & Khalili [16]	1982	$\frac{f_{cc}}{f_{co}} = 1 + 4.1\frac{f_r}{f_{co}}$	$\varepsilon_{cc} = \varepsilon_{co} + 0.0005\left(\frac{2t}{D}\right)\frac{E_{\theta\theta}}{f_{co}}$
Hoppel *et al* [55]	1997	$\frac{f_{cc}}{f_{co}} = 1 + 3.1\nu_c\left(\frac{2t}{D}\right)\frac{E_{\theta\theta}}{E_{ci}} + \frac{f_r}{f_{co}}$	-
Karbhari & Gao [56]	1997	$\frac{f_{cc}}{f_{co}} = 1 + 2.1\left(\frac{f_r}{f_{co}}\right)^{0.87}$	$\varepsilon_{cc} = \varepsilon_{co} + 0.01\frac{f_r}{f_{co}}$

Table 1.4. Failure criteria for concrete confined by FRP-composite wraps

Researcher	Date	Failure Strength		Failure Strain	
		mean $\frac{f_{cc}^{pred}}{f_{cc}^{exp}}$	SD	mean $\frac{\varepsilon_{cc}^{pred}}{\varepsilon_{cc}^{exp}}$	SD
Fardis & Khalili [16]	1982	1.20	0.14	54.83	43.45
Hoppel *et al* [55]	1997	0.85	0.10	-	-
Karbhari & Gao [56]	1997	1.02	0.07	4.03	3.59

Table 1.5. Comparison of existing failure criteria with experimental results for concrete confined with carbon FRP-composite wraps

Laminate Configuration	Uniaxial failure strain of coupon $\mu\varepsilon$	Experimental hoop failure strain of wrap $\mu\varepsilon$	$\frac{\varepsilon_r^{wrap}}{\varepsilon_r^{coupons}}$
[0°]	19,000	8,900	0.47
$[0°]_2$	15,000	11,000	0.73
$[0°]_3$	19,000	11,000	0.58
$[0°]_4$	23,000	6,800	0.30
[0°/90°]	12,000	6,300	0.53
[0°/90°/0°]	16,000	13,400	0.84
[+45°/-45°]	39,000	2,900	0.07
$[+45°/-45°]_2$	54,000	7,100	0.13
$[90°/+45°/-45°/0^0]$	27,000	2,200	0.08

Table 1.6. Comparison of the experimental hoop failure strain of FRP-composite wraps with the failure strain of an equivalent FRP-composite coupon [23]

Researcher	Date	Failure Strength	Failure Strain
Samaan *et al* [59]	1998	$\frac{f_{cc}}{f_{co}} = 1 + 6.0\frac{f_r^{0.7}}{f_{co}}$	-
Saafi *et al* [60]	1999	$\frac{f_{cc}}{f_{co}} = 1 + 2.2\left(\frac{f_r}{f_{co}}\right)^{0.84}$	-

Table 1.7. Postulated failure criteria for concrete confined by filament wound composites tubes

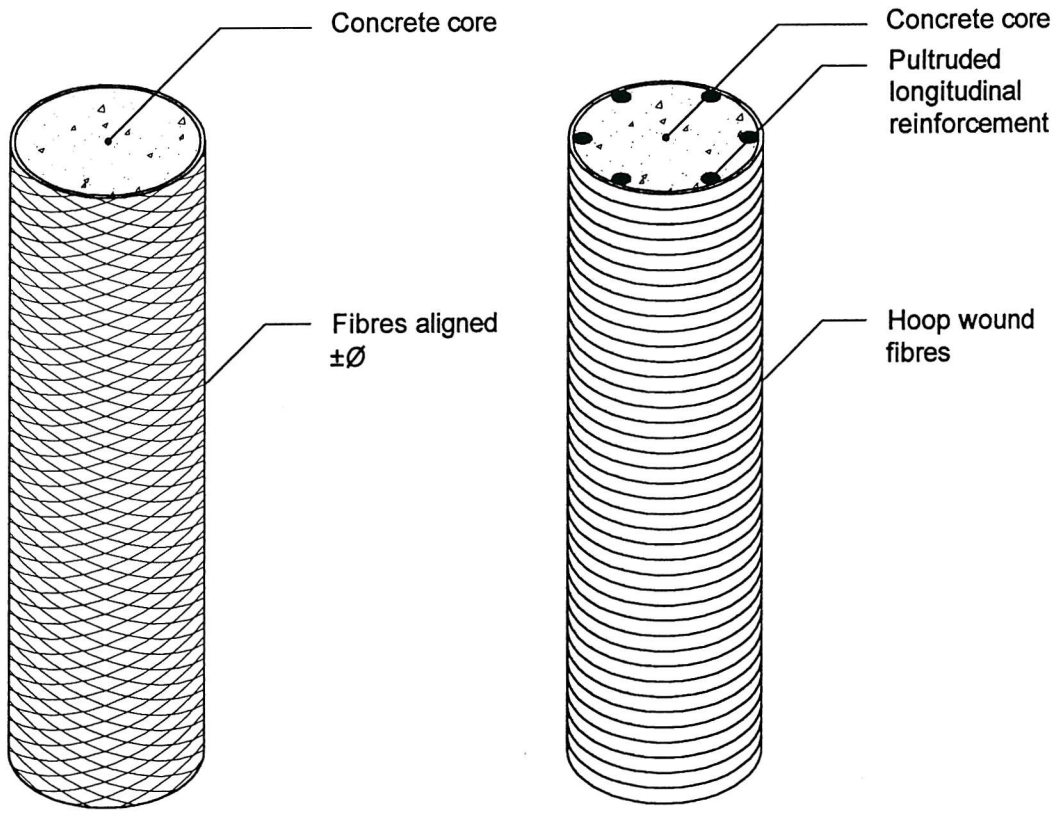

Figure 1.1. Concrete-filled FRP-composite columns

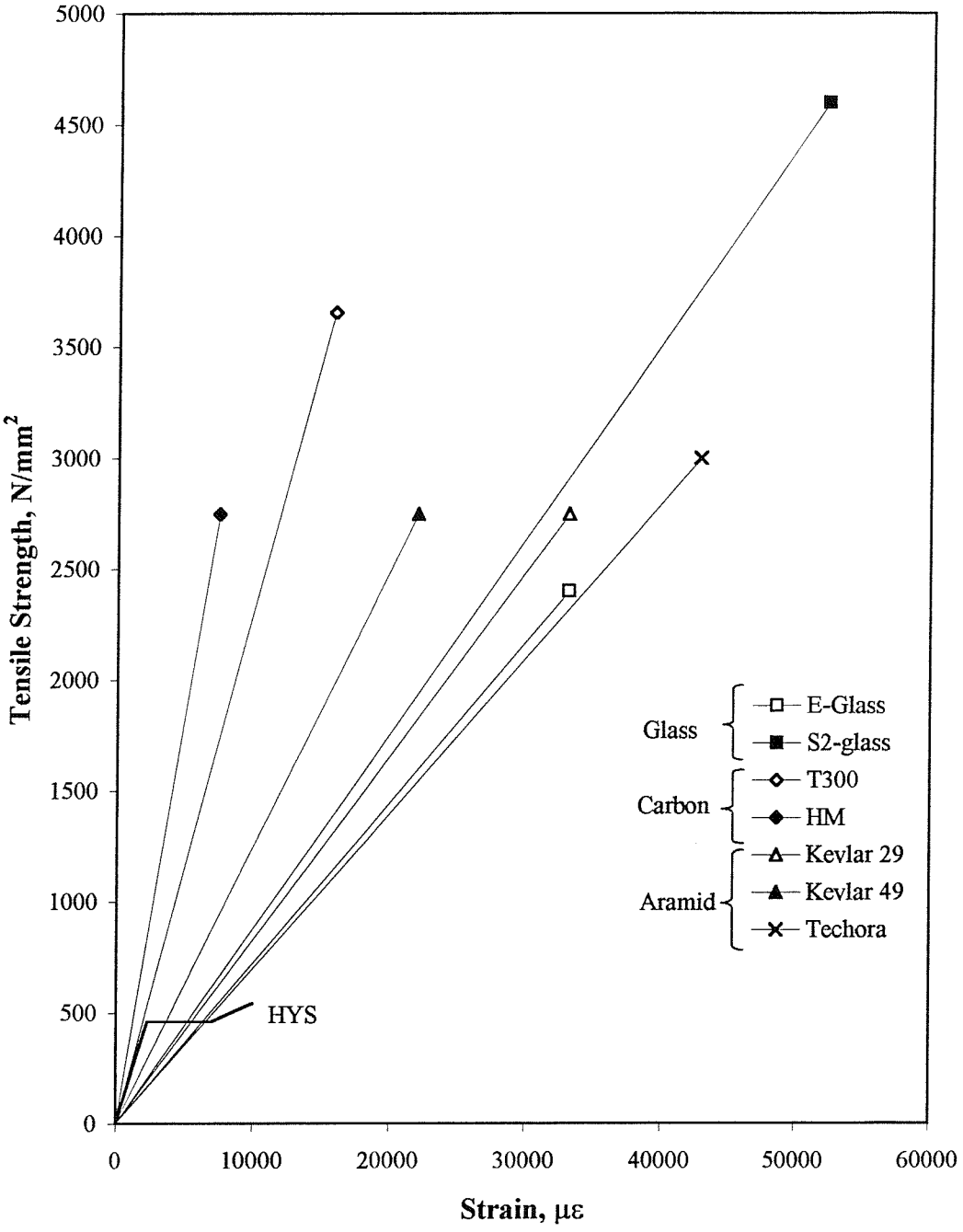

Figure 1.2. Typical stress-strain curves for fibres

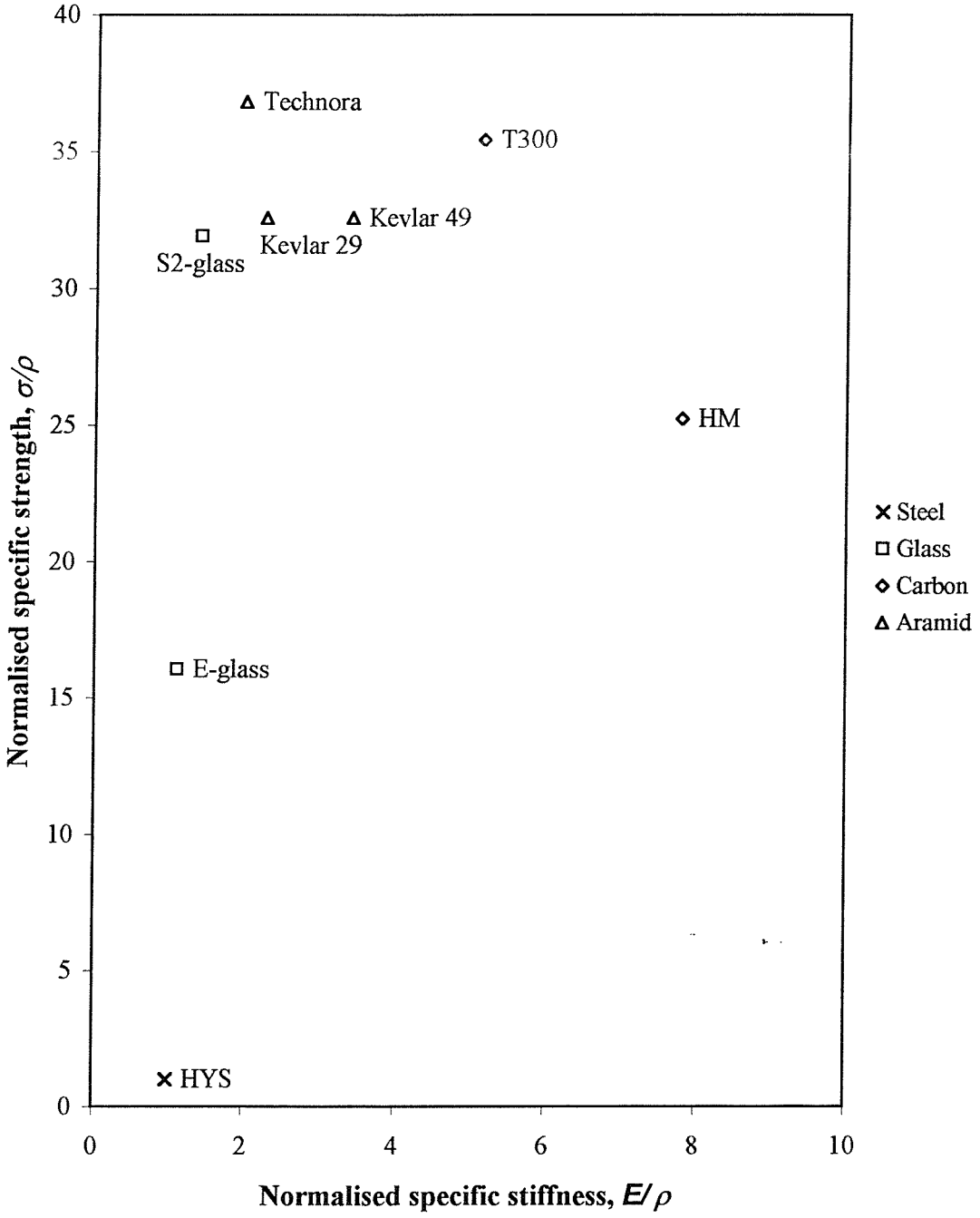

Figure 1.3. Normalised specific strength versus normalised specific stiffness for typical fibres

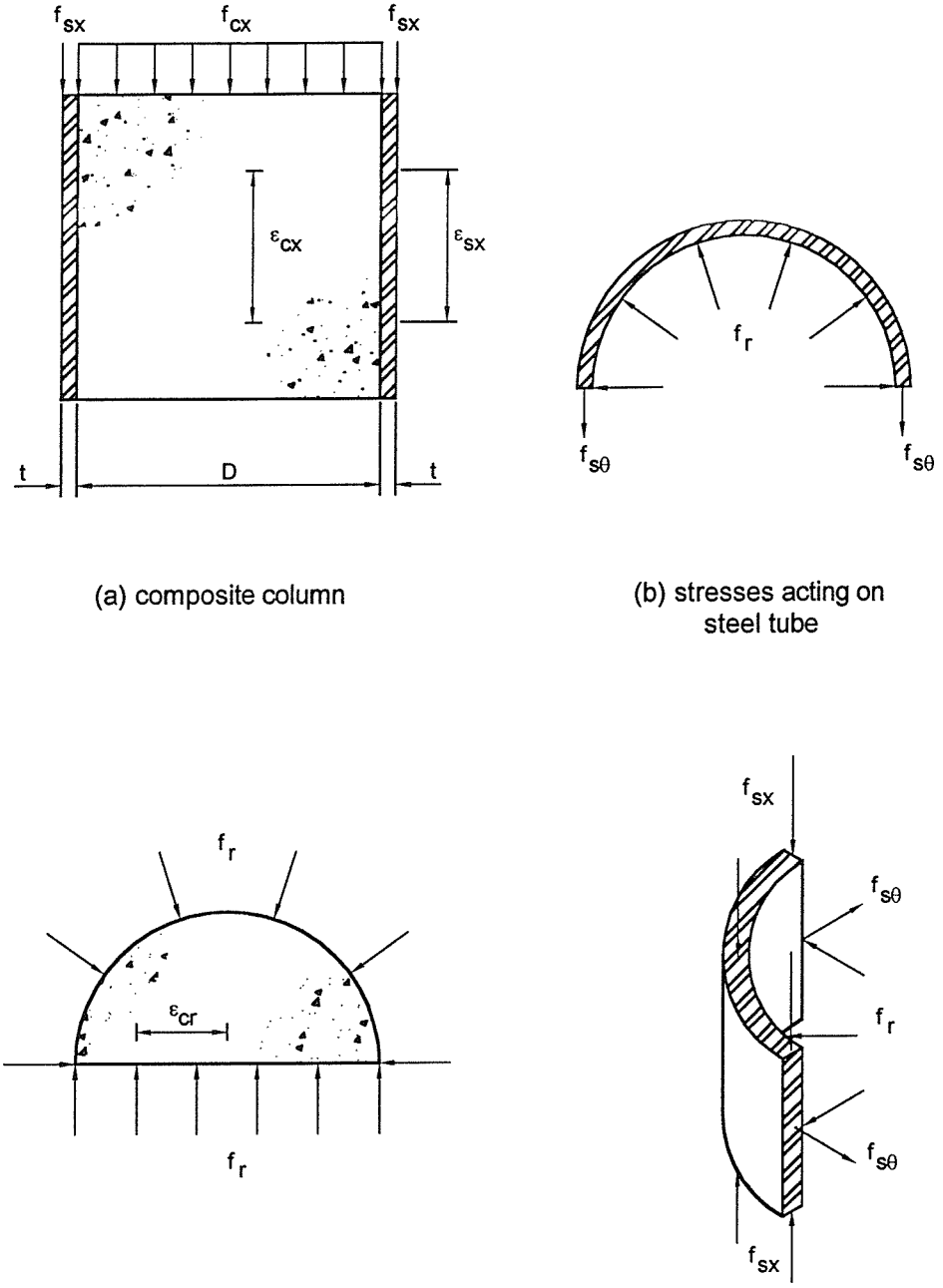

Figure 1.4. Stresses acting on a concrete-filled steel tube

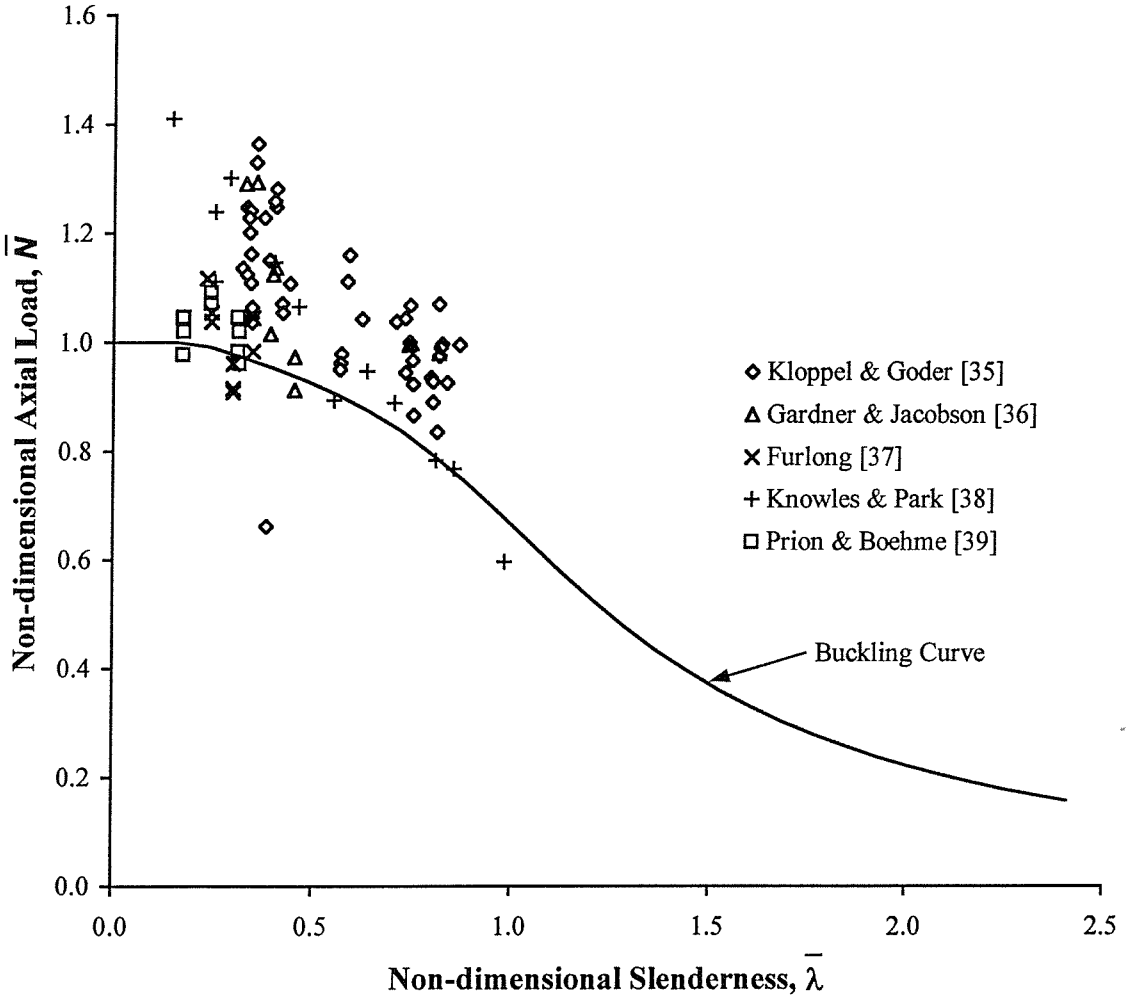

Figure 1.5. Comparison of the experimental failure loads of concrete-filled steel tubes with the non-dimensional column slenderness ratio

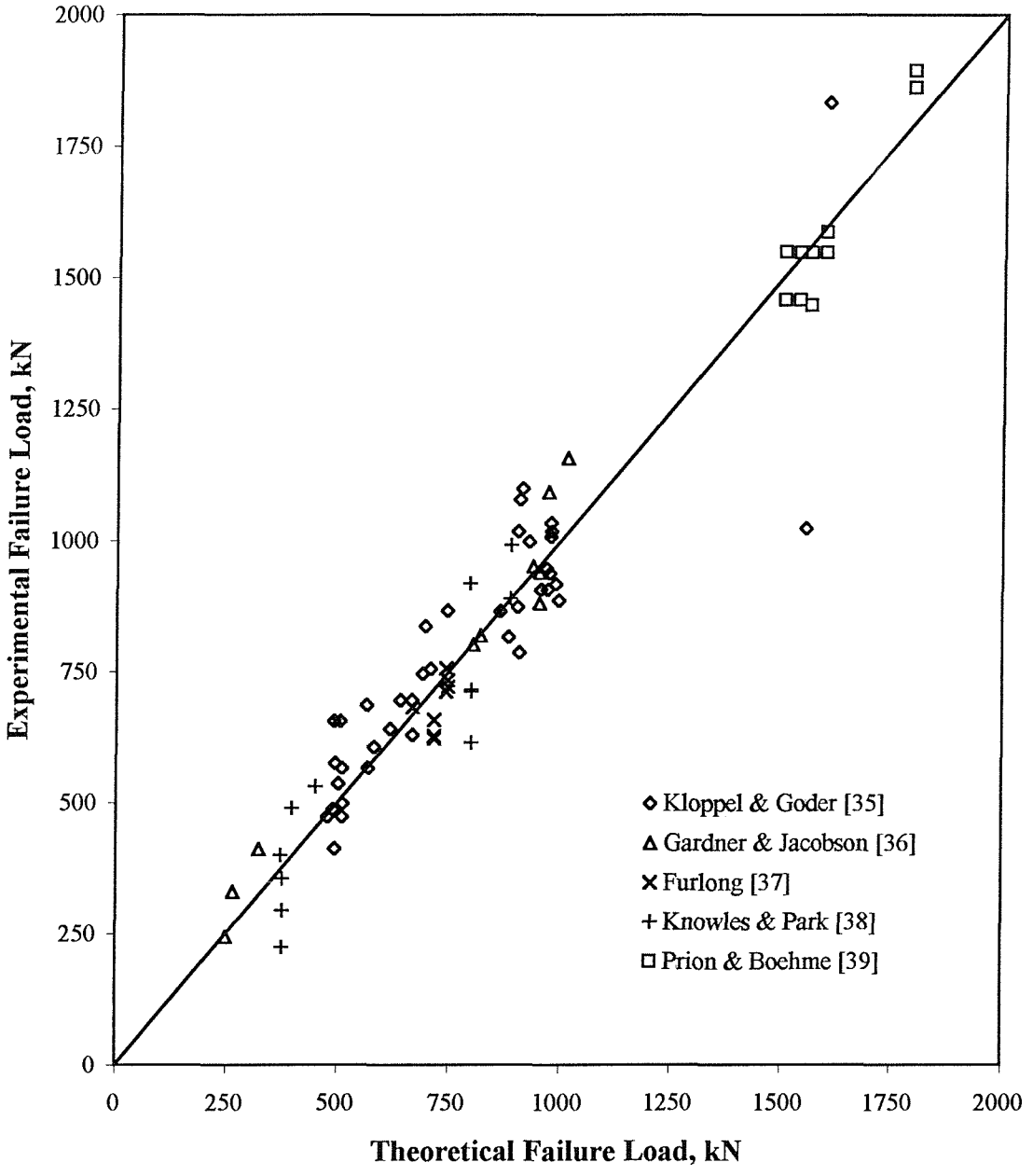

Figure 1.6. Experimental failure loads versus predicted failure loads of concrete-filled steel tubes

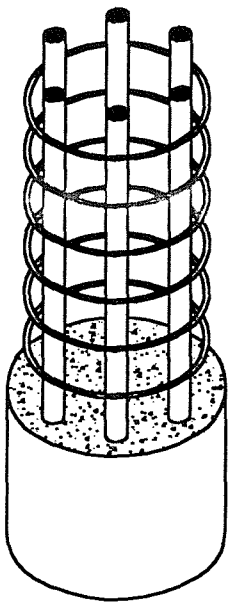

(a) Closely spaced lateral ties

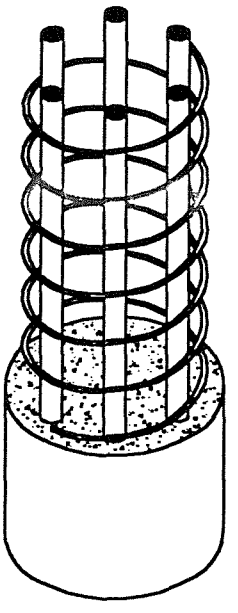

(b) Spiral reinforcement

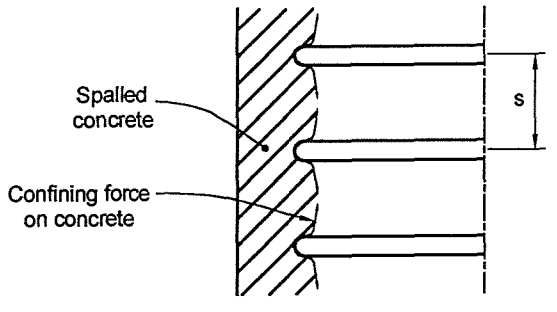

(c) Zones of tensile stresses

Figure 1.7. Traditional methods of achieving confinement in conventional reinforced concrete columns

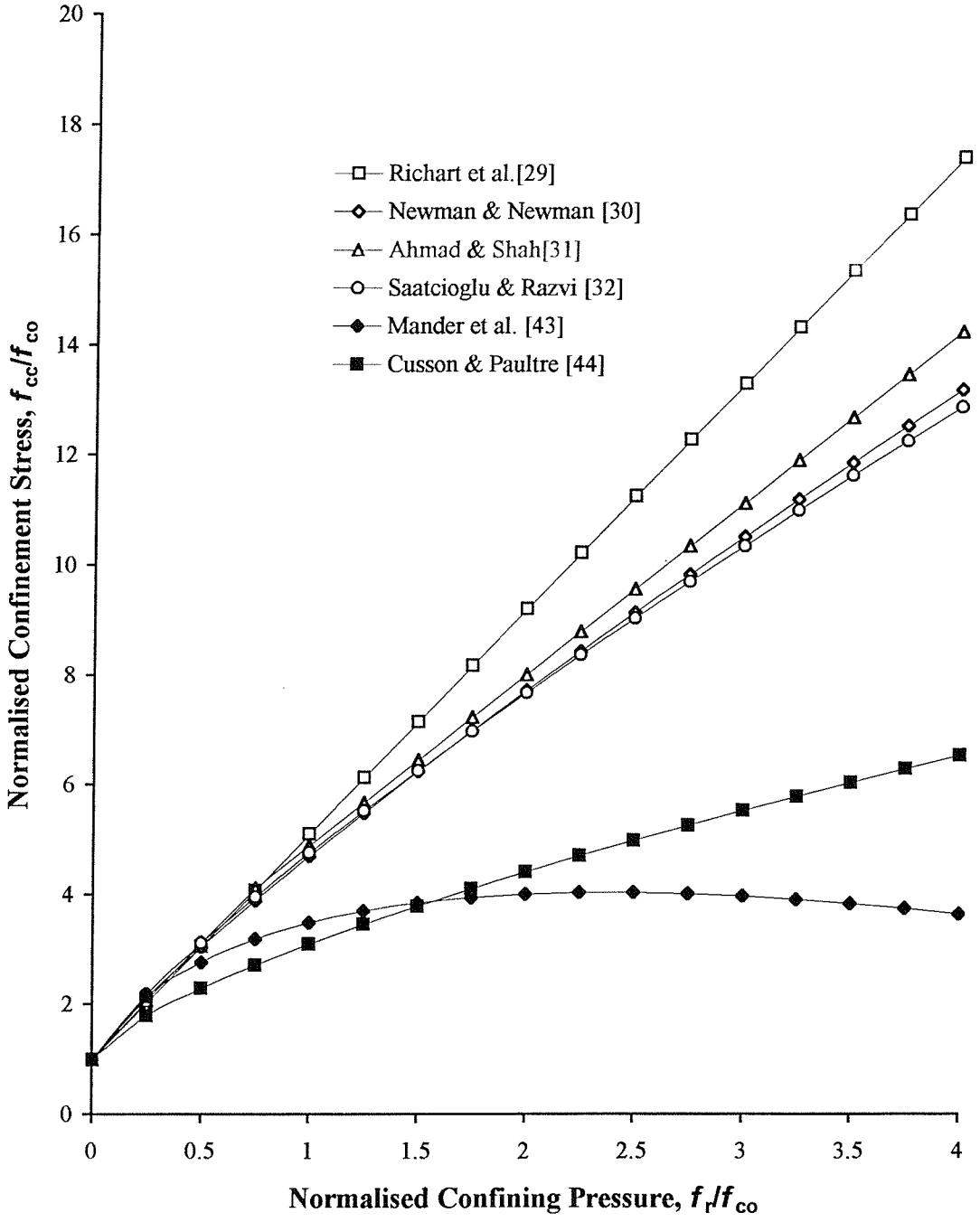

Figure 1.8. Comparison of active and passive failure stress criteria

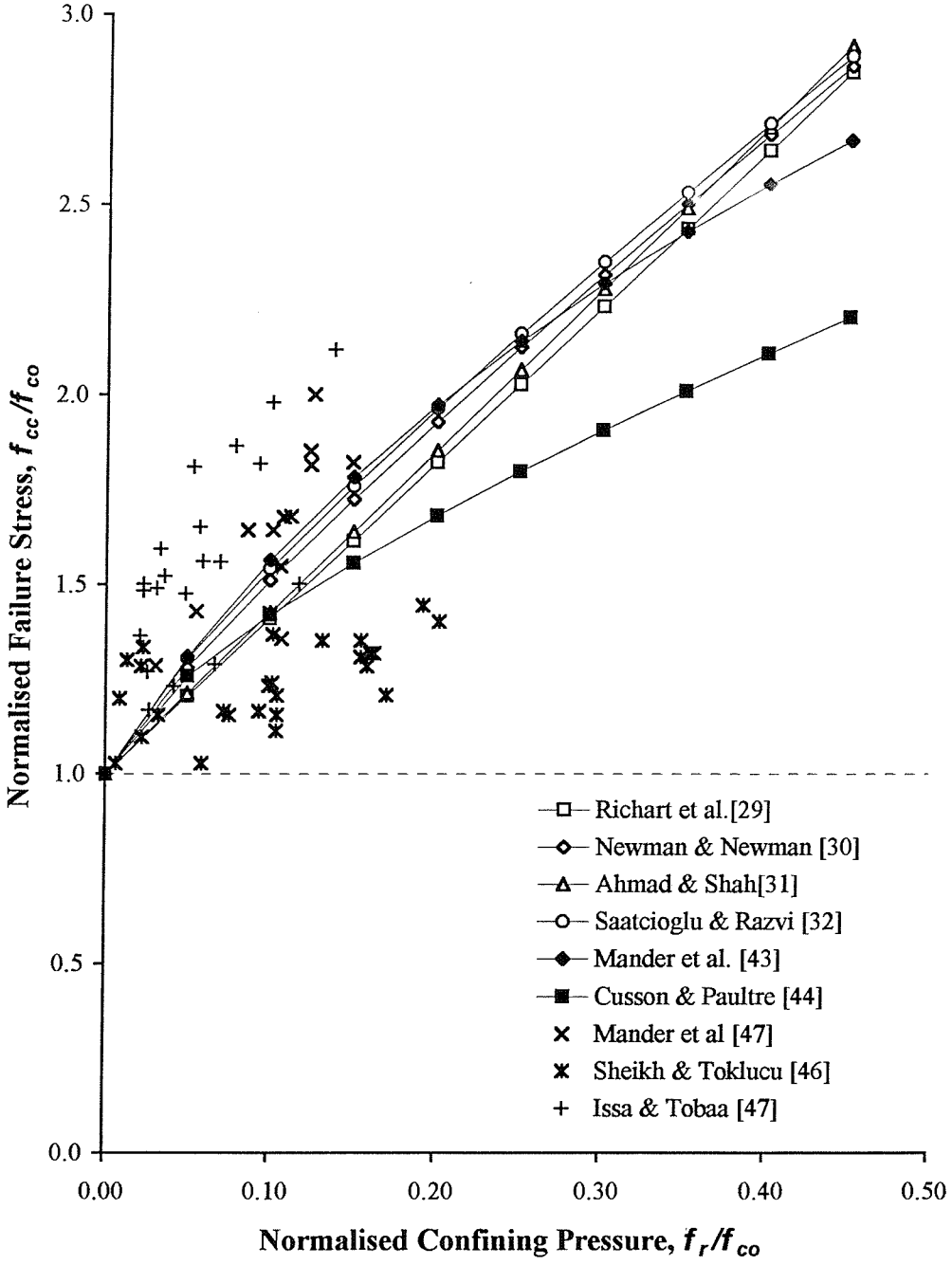

Figure 1.9. Comparison of proposed failure stress criteria with experimental failure loads of concrete specimens confined by lateral steel ties

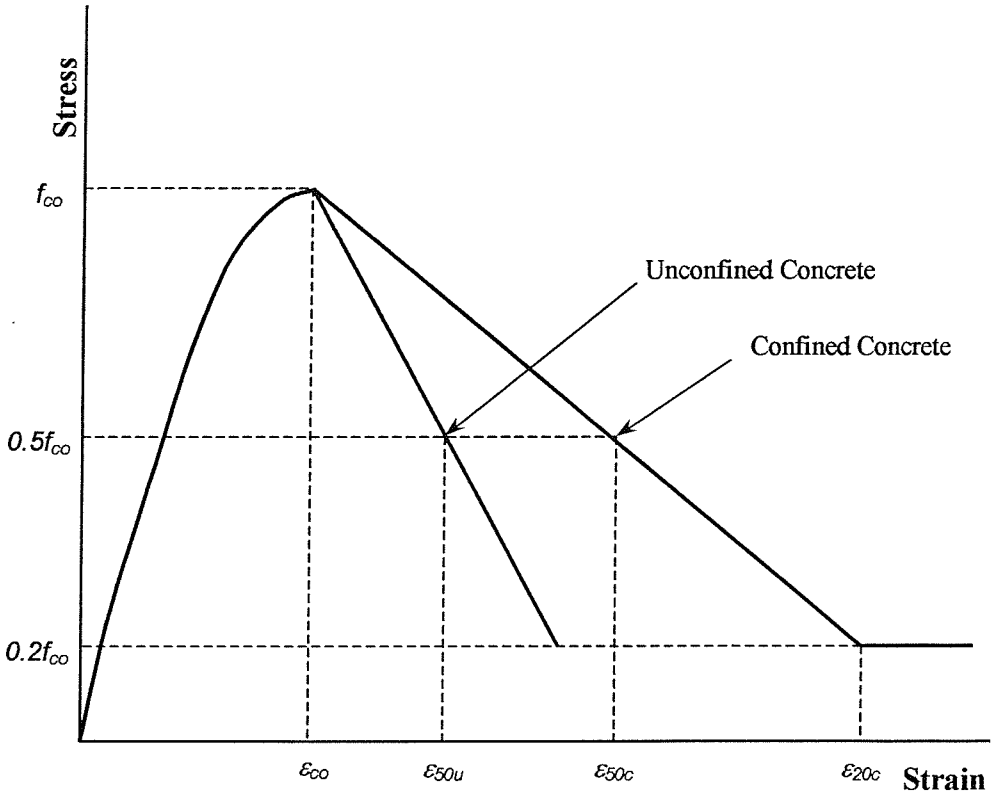

Figure 1.10(a). Kent and Park's equivalent uniaxial stress-strain curve for concrete confined by lateral steel reinforcement [49]

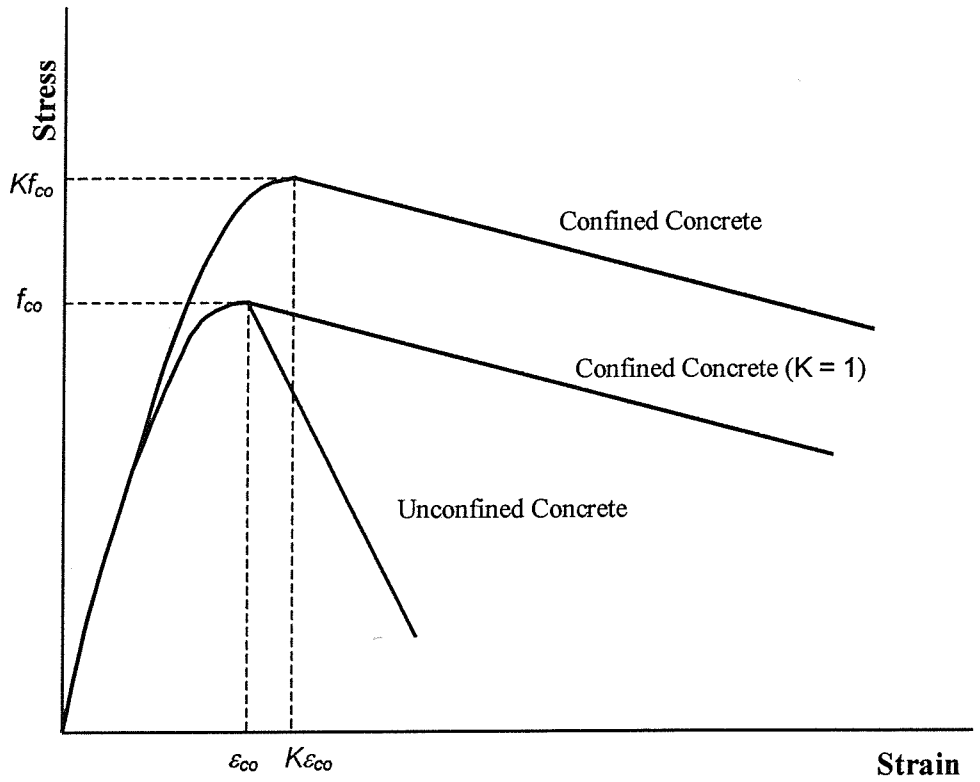

Figure 1.10(b). Modified Kent and Park's equivalent uniaxial stress-strain curve for concrete confined by lateral steel reinforcement [50]

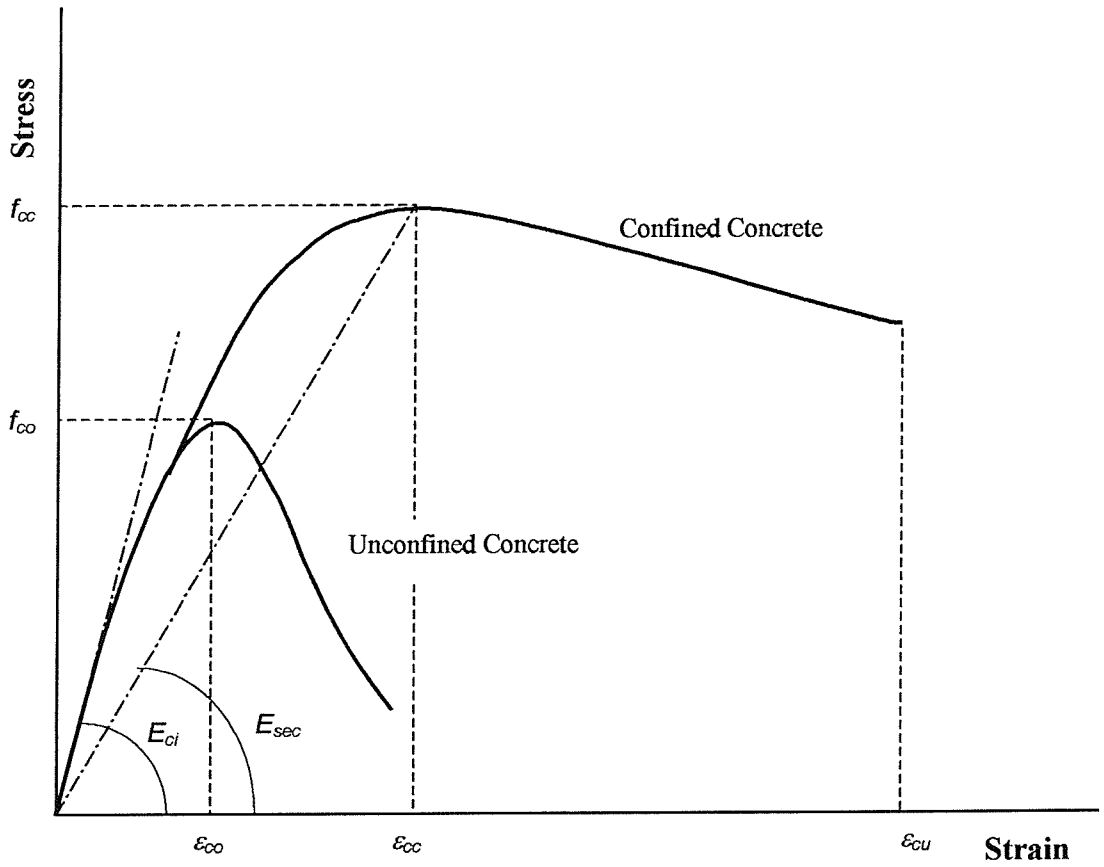

Figure 1.10(c). Mander *et al's* equivalent uniaxial stress-strain curve for concrete confined by lateral steel reinforcement [43]

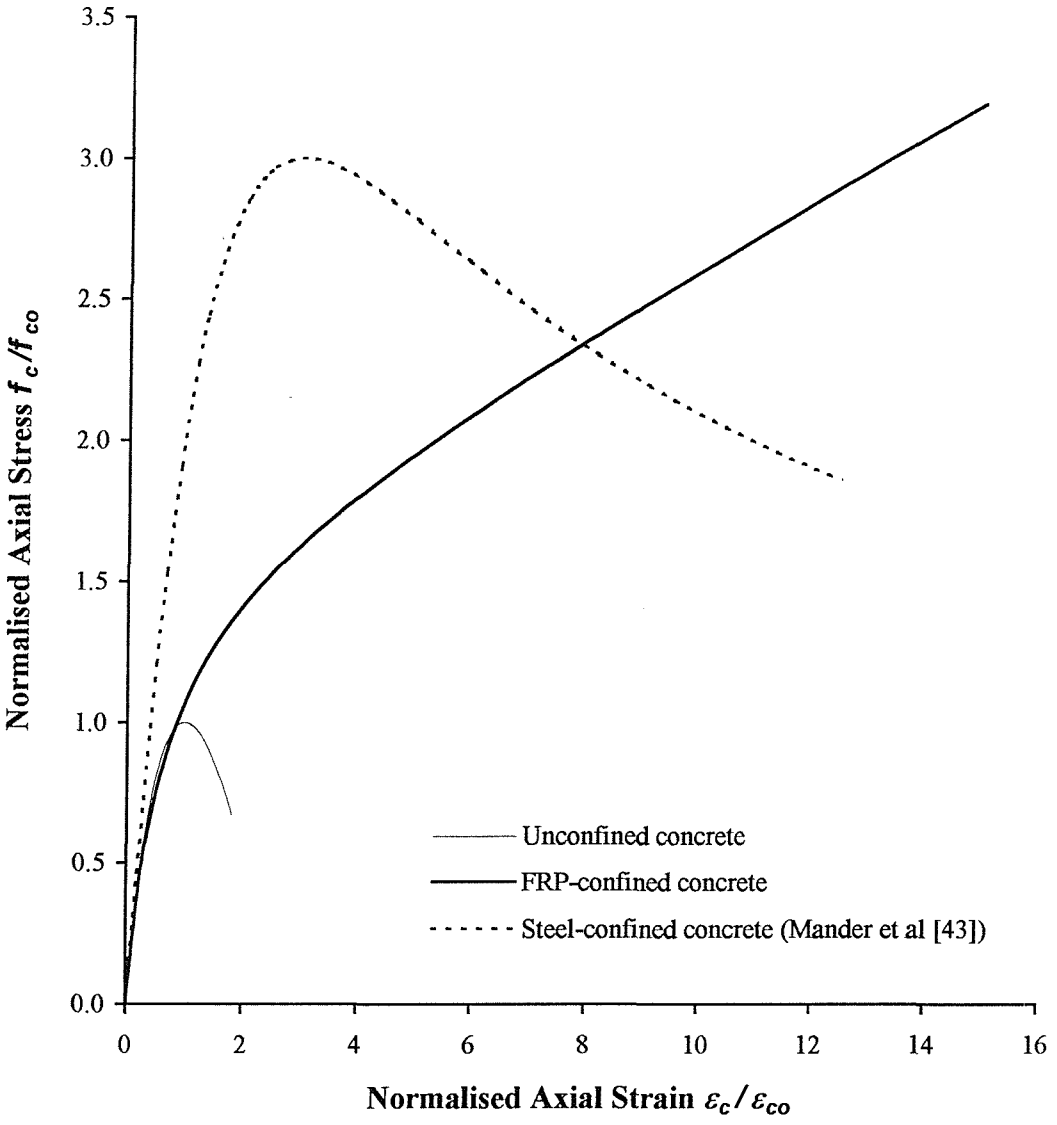

Figure 1.11. Comparison of the behaviour of concrete confined by lateral steel reinforcement and concrete confined by FRP-composite materials

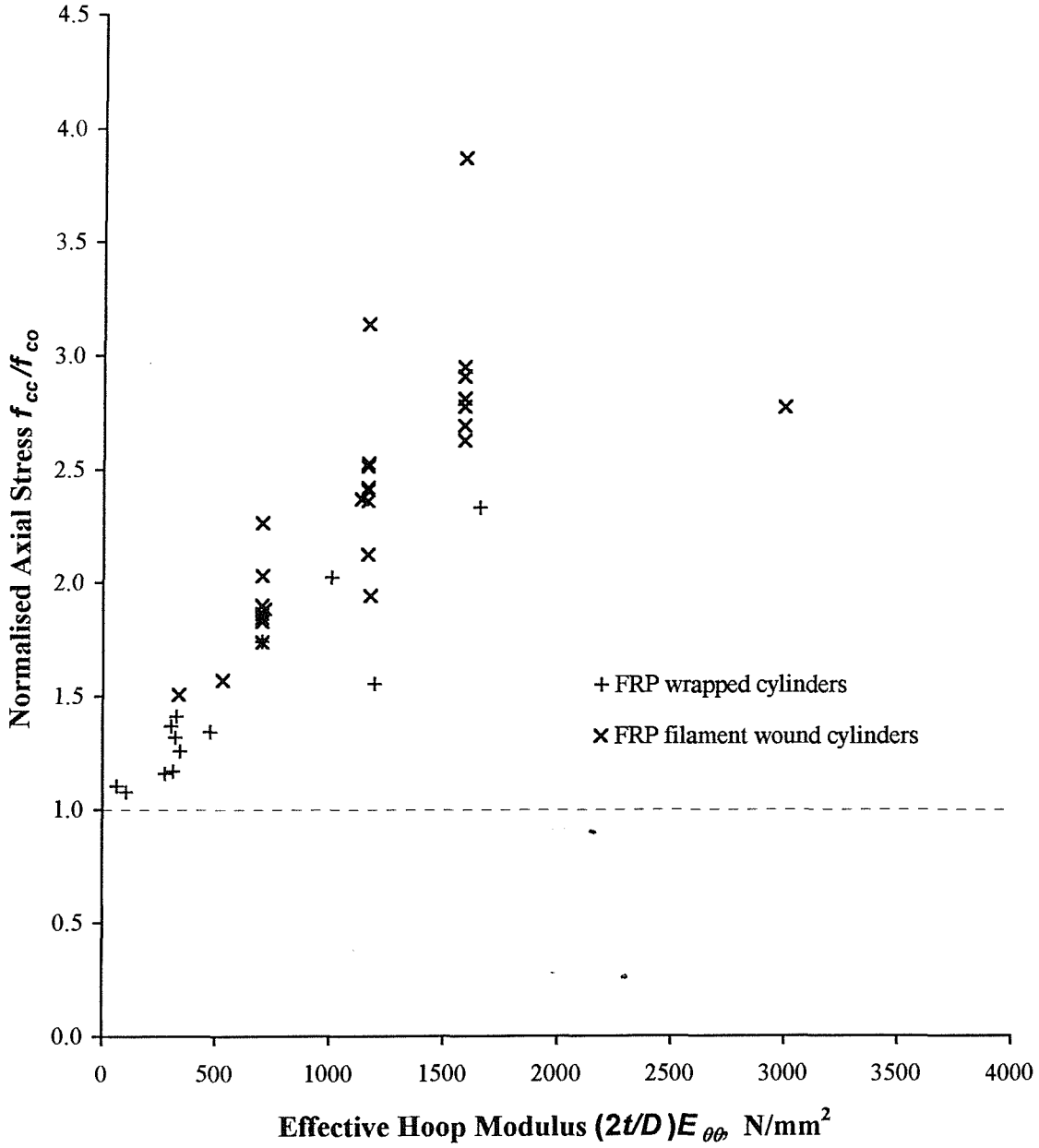

Figure 1.12. Normalised failure strength of FRP wrapped cylinders and concrete filled FRP filament wound cylinders as a function of the composite hoop modulus

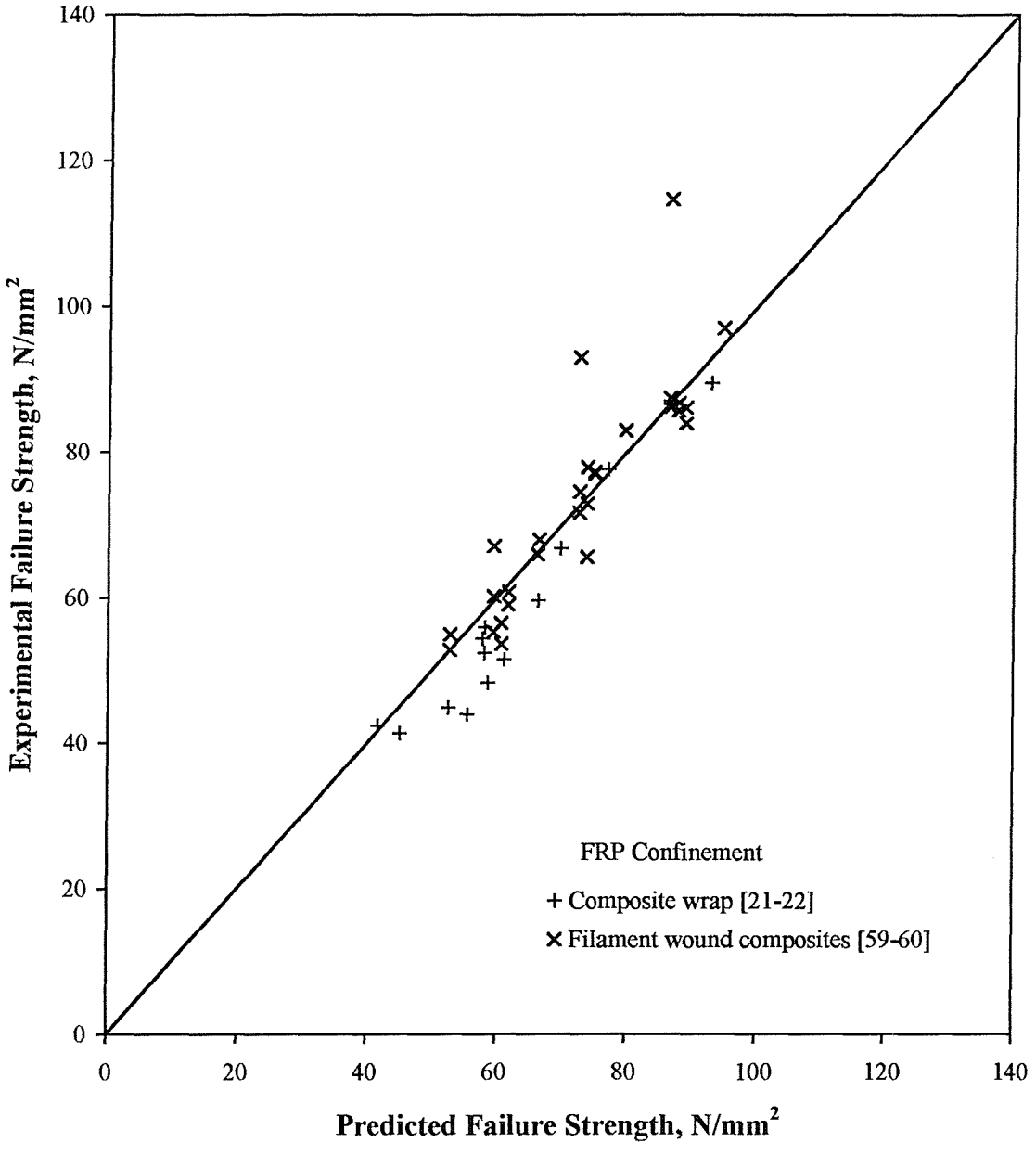

Figure 1.13. Comparison of the experimental compressive strength of FRP-confined concrete with Samaan *et al's* predicted failure strength

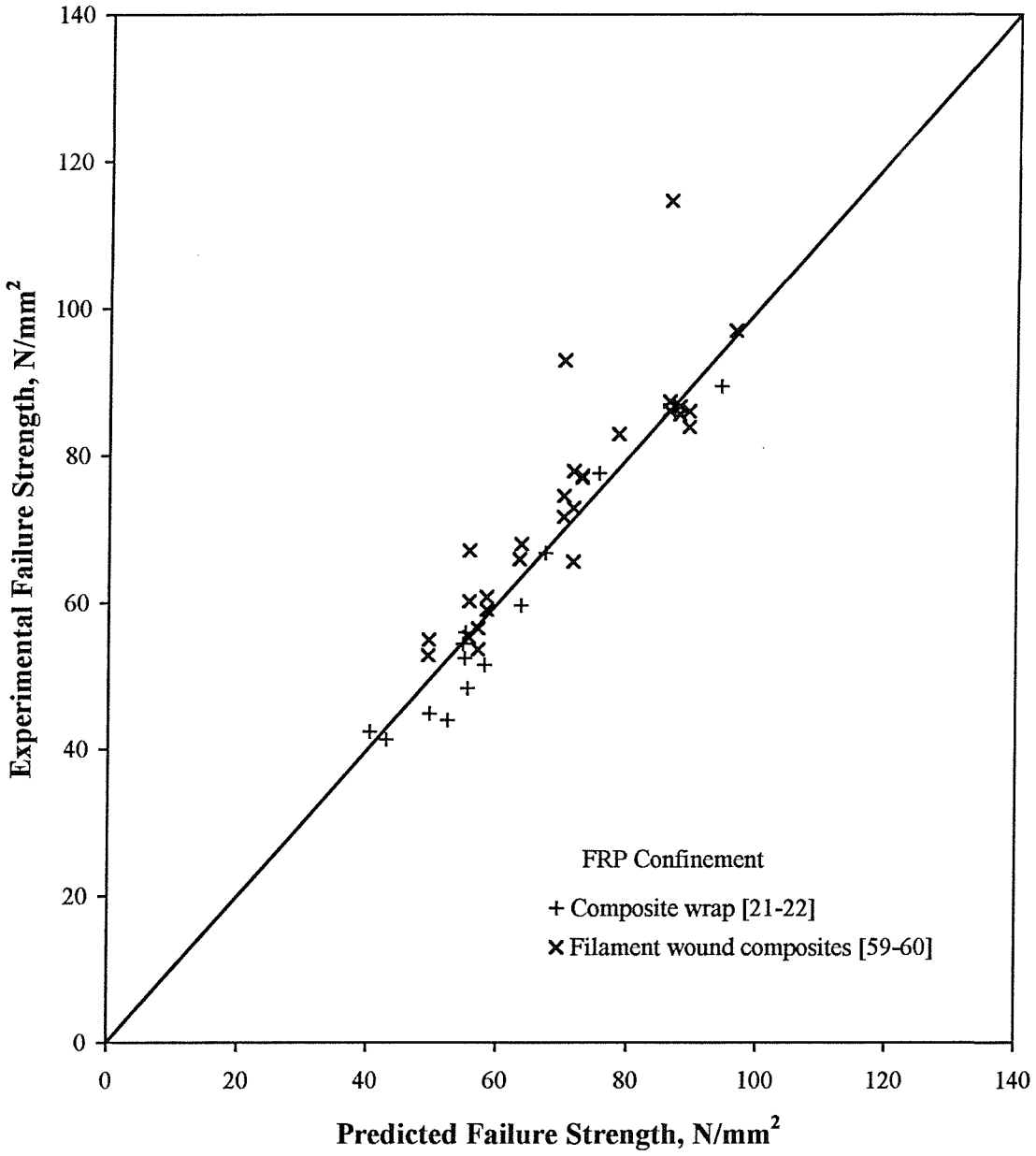

Figure 1.14. Comparison of the experimental compressive strength of FRP-confined concrete with Saafi *et al's* predicted failure strength

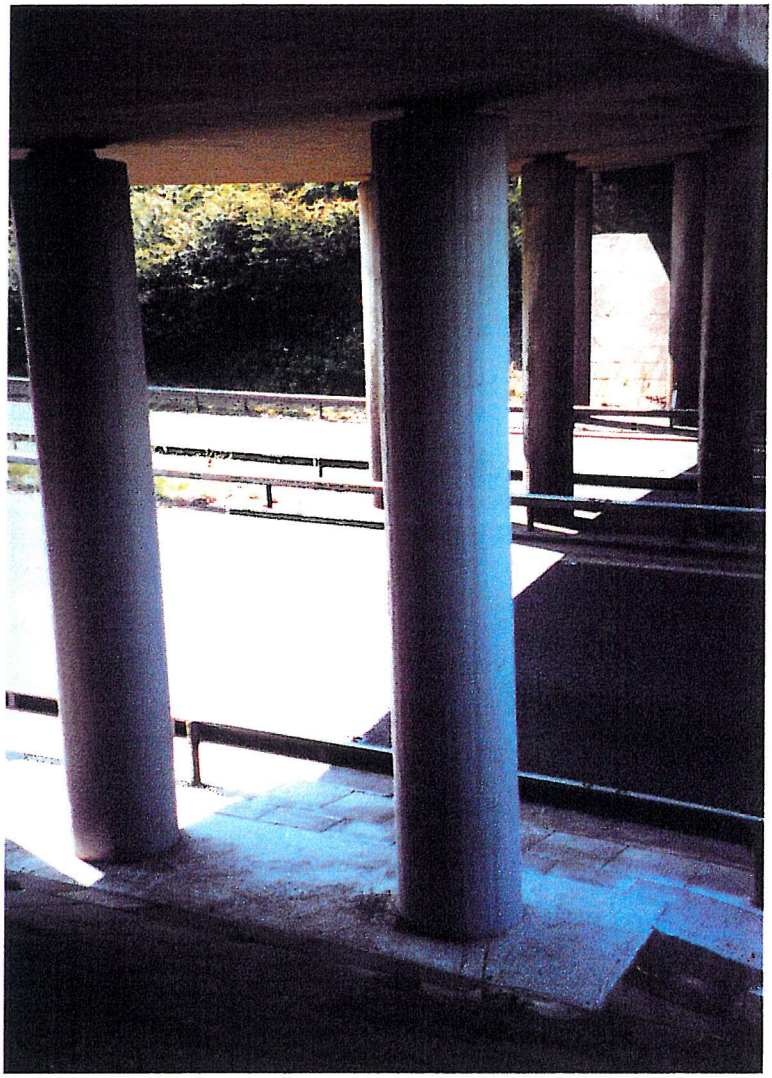

Plate 1.1. FRP-composite wrapped columns on the Bible Christian Overbridge, Cornwall

CHAPTER 2

FIBRE-REINFORCED PLASTIC COMPOSITES FOR CONCRETE STRUCTURES

2.1 INTRODUCTION

Fibre-reinforced plastic (FRP) composites may be used as an alternative form of reinforcement for concrete structures. FRP-composites consist of high strength fibres embedded in a continuous resin matrix. These materials provide the rigidity necessary for ease of fabrication and construction. The perceived inherent durability of FRP-composites eliminates the problems of corrosion and environmentally-induced degradation associated with conventional steel reinforcement.

One advantage of FRP-composites compared to a homogenous isotropic material such as steel is the ability to tailor their properties to a particular requirement, allowing the properties of the FRP composite and the concrete to be more efficiently utilised. The concrete-filled composite tubes that are the subject of this research exploit the dominant mechanical properties of the concrete and the FRP-composite. The composite tubes act as both permanent formwork and as the main structural reinforcement, whilst the compressive properties of the concrete are enhanced by triaxial confinement.

The FRP reinforcing bars for embedding in concrete and the plates for resin bonding are generally manufactured by pultrusion. This method of manufacture produces a unidirectional FRP composite, where the fibres are aligned in the longitudinal direction, see Figure 2.1. A common method of fabricating hollow FRP-composite sections is filament winding. The process of filament winding results in a composite with fibres orientated $\pm\phi$ to the longitudinal axis, see Figure 2.2.

The mechanical properties of the FRP-composite are less than those of the constituent fibres and depend on the type and volume percentage of the fibres. The theoretical analysis of a composite material is divided into two categories, being micromechanics and macromechanics. Micromechanics is used to determine the properties of an elemental layer of the composite based on the constituent properties and their respective volumetric contents. The fibres in an elemental layer are assumed to be aligned in the same direction. Macromechanics determines the global properties of an FRP-composite laminate that consists of a number of elemental layers orientated in different directions.

2.2 PRINCIPAL FIBRES

The fibres are the main component of FRP-composites, since they are the principal load carrying elements and generally occupy the largest volume. The mechanical properties of

FRP-composites, such as the tensile strength, compressive strength and elastic modulus can be designed to suit a particular application by altering the type, volume and orientation of the fibres.

Fibres currently used as reinforcement for concrete structures are glass, carbon and aramid. Typical mechanical properties of the different fibres are given in Table 2.1. As shown in Figure 1.2, the fibres have a linear-elastic stress-strain behaviour up to failure and exhibit no yield point or region of plasticity. The lack of any plasticity prior to failure is one disadvantage of FRP-composites compared to steel. In FRP-composites, local stress concentrations may initiate a premature failure, whereas in steel local stress concentrations may be neglected since these simply cause local yielding and thus redistribution of the stress.

2.2.1 Glass fibres

Glass fibres are made from molten glass, drawn into fine continuous filaments and bundled into yarns and rovings. These rovings are fabricated into chopped fibres, continuous strands, chopped strand mats or woven mats, before being used as reinforcement in composites. The surface of the fibres is coated with size during the manufacturing process to aid wetting by the resin, and enhance the adhesion between the matrix and fibres.

Glass is an amorphous material, since it does not possess the crystalline structure of a solid. The molecular structure of glass consists of a silicon atom bonded to four oxygen atoms to form a tetrahedral molecule. Molten glass is supercooled without devitrification to form an irregular three-dimensional network of the base SiO_4 molecules. Since the molecular structure is three-dimensional, the properties of glass may be assumed to be isotropic. The presence of other elements results in modifications to the mechanical and physical properties of glass [62].

Several types of glass fibre are produced commercially for different applications. The most common are:

1. *E-glass* is the most widely used type of fibre, accounting for nearly 90% of the reinforcing fibres used in composites. This type of glass was originally developed for use in electrical applications because of its insulation properties. The low cost of E-glass is the principal reason for its widespread application in the composites industry;
2. *S-glass* has the highest tensile strength of all commercial fibres. The tensile strength and modulus of elasticity are approximately 32% and 20% greater than

those of E-glass respectively. Originally developed for the aerospace industry, the compositional differences and higher manufacturing costs make it more expensive than E-glass. The higher cost of S-glass tends to prohibit its use in civil engineering applications despite the improved mechanical properties;

3. *Z-glass* is used as a reinforcing fibre for cement mortars and concrete. Zirconia glass has a higher resistance to alkali degradation;
4. *C-glass* is often applied as a surface tissue to composites to improve the chemical resistance at the interface of the composites.

The average tensile strength of freshly drawn E-glass fibres is 3,448 N/mm^2 and 4,585 N/mm^2 for S-glass fibres [63]. However, the strength of the glass fibres depends on the size of surface flaws, which initiate crack propagation. Since fibres are susceptible to damage by abrasion from other fibres or contact with machinery in manufacture, the tensile strength of a processed fibre ranges from 50% to 75% of the virgin value [63]. The modulus of elasticity of glass fibre is not affected during processing, and ranges from approximately 70 kN/mm^2 for E-glass fibres up to 85 kN/mm^2 for S-glass fibres.

The mechanical properties of glass fibres deteriorate in the presence of either water or an alkali environment. This deterioration of mechanical strength is significant if glass fibres are to be used as reinforcement in concrete which has a highly alkaline environment. Embedding the fibres in resin is perceived to provide protection from the environment, but the chemical composition of concrete may create environmental conditions that are highly deleterious to some resins used in FRP composites. Research at the University of Southampton is investigating the long-term durability of glass fibre reinforced plastic composites exposed to cementitious and other aggressive environments [64].

2.2.2 Carbon fibres

Carbon fibres are manufactured by the controlled pyrolysis of a precursor such as polyacrylonitrile (PAN), rayon fibres or pitch. The precursor is processed to achieve a high degree of molecular orientation and stabilised in an oxidising atmosphere before it is carbonised. The temperature at carbonisation ranges between 1000 to 3500°C, the degree of carbonisation determining the mechanical properties of the fibres. The elastic modulus is found to increase constantly throughout the temperature range. However, the maximum tensile strength is achieved at about 1600°C, with further increases in temperature causing the tensile strength to reduce [62].

The structure of carbon fibres is highly anisotropic. The carbon atoms are arranged in crystalline parallel planes of regular hexagons, separated by a distance of 3.35Å. In the basal plane, the carbon atoms are linked by strong covalent bonds, accounting for the high tensile strength and modulus in the direction parallel to the basal plane. Relatively weak *Van der Waals'* bonds hold the layers of carbon atoms together in the direction normal to the basal plane. Consequently, the mechanical properties in this direction are significantly lower.

Carbon fibres are generally used where high stiffness and strength are required. The tensile strength of carbon fibres used in concrete reinforcement is approximately 2,400 kN/mm^2 with an elastic modulus of 230 kN/mm^2. Higher performance carbon fibres are available with tensile strengths of up to 7,000 N/mm^2 and elastic moduli in the region of 300 kN/mm^2.

The disadvantage of carbon fibres is their cost, which is significantly higher than that of glass fibres. Carbon fibres are between 20 and 50 times more expensive (by weight) than E-glass fibres depending on the type of carbon fibres. The higher cost is due to the costly precursors and the expensive manufacturing processes. Nevertheless, the production of carbon fibres is sensitive to market forces, and an increase in demand should result in significant cost savings through economies of scale.

2.2.3 Aramid fibres

Aramid fibres are an organic group of aromatic polyamides where at least 85 percent of the amide linkages are attached to two aromatic rings. Aramid fibres differ from other organic fibres, such as nylon, by having significantly higher strengths and elastic moduli. The aramid fibres are more commonly known by their registered trade names, such as Kevlar[1], Twaron[2] or Techorna[3].

The basic molecular arrangement of aramids consists of linear polymer chains highly orientated in the axial direction. The polymer chains are bonded in the transverse direction by hydrogen bonds. The strong covalent bonds and weaker hydrogen bonds account for the anisotropy of the mechanical properties.

Aramids are characterised as having reasonably high strength, medium modulus and very low density. Although the tensile strength of aramids is similar to that of carbon and glass, their

---

[1] Kevlar is a registered trademark of Du Pont, USA.

[2] Twaron is a registered trademark of Akzo, Holland.

[3] Techorna is a registered trademark of Teijin, Japan.

lower density gives them the highest specific tensile strength. Aramids are classified as either a low modulus fibre with an elastic modulus comparable to glass fibres, of typically 60-70 kN/mm^2, or high moduli with a modulus approximately twice this value. The aramid family is the intermediate fibre in terms of mechanical properties compared to carbon and glass fibres.

Aramid composites have an inherent and fundamental fault when subjected to compressive forces. Compressive loads cause aramid fibres to buckle and form kink bands at significantly lower compressive loads than either glass or carbon [62, 63, 65]. Consequently, aramid composites are not considered suitable as an alternative to steel in concrete members if the fibres are subjected to compressive loads [66].

2.3 RESIN SYSTEMS

The resin matrix is an isotropic material that acts as a load transfer medium between fibres, but also serves several other functions. The matrix protects fibres from abrasion and forms a protective barrier between the fibres and the environment, thus preventing deterioration due to moisture, chemicals or oxidation. Additionally, the shear and compressive properties of the composite are highly dependent on the mechanical characteristics of the matrix. The matrix also governs the thermomechanical performance of the composite. The stiffness and strength of the matrix is lower than that of the fibre. However, the deformation to failure is greater than that of the fibres, enabling the full strength of the fibre to be utilised.

Polymer matrices can be classified as either thermosetting or thermoplastic, according to their structure and behaviour.

Thermoplastic polymers consist of linear molecules which are not interconnected. The chemical valency bond along the chain is extremely strong, with individual molecules held in place by weak secondary bonds. The application of heat to a solid thermoplastic polymer temporarily breaks these bonds, enabling relative movement between the molecules. Upon cooling, the secondary bonds reform, restraining the molecules in their new positions. Therefore, a thermoplastic polymer can be heated and reshaped as required. Thermoplastic polymers are amorphous solids and sometimes have a partly crystalline structure. They have a glass-rubber transition temperature at which their mechanical properties degrade by several orders of magnitude. Incorporation of continuous fibres in thermoplastic polymers is difficult due to their high melting temperatures and viscosity. This low thermal stability of thermoplastic polymers has limited their use in FRP composites due to fire regulations.

In a thermosetting resin, the molecules are chemically bonded by cross-links to form a stable three-dimensional structure. The reactions which occur during curing are usually exothermic and can be accelerated by application of heat. The cross-links are generated during the polymerisation or curing process, which is irreversible. Therefore, thermosetting resins cannot be reshaped by the application of heat.

The suitability of a matrix for a particular fabrication process is determined by factors such as viscosity, shelf life and the curing regime. The most commonly used thermosetting resins in increasing order of chemical and fire resistance, and increasing cost are polyesters, vinyl-esters, epoxies and phenolics [62].

The mechanical behaviour of resins is highly dependent on the magnitude, the time, the rate and the frequency of load application. Thus, it is not possible to obtain a single stress-strain relationship for resins [67]. Typical values for the mechanical properties of thermosetting resins are given in Table 2.2. The quoted shear moduli of the resins are estimates based on the assumption that the resin is a homogenous isotropic material. The shear modulus is given by the elastic constants:

$$G_m = \frac{E_m}{2(1+\nu_m)} \qquad (2.1)$$

2.3.1 Polyester resin systems

The base material for a polyester matrix is unsaturated polyester resin. Additional chemical agents are added to modify the chemical structure between the cross-links to reduce viscosity and prevent premature polymerisation during storage. To initiate the curing reaction, a catalyst is added to the unsaturated polyester resin.

Polyester resins are manufactured with a variety of properties, ranging from hard and brittle, to soft and flexible depending on the density of cross-links. The density of cross-linking is determined by the quantities of raw materials used to manufacture the unsaturated polyester. The advantages of polyester resins are low viscosity, short curing times and low cost.

2.3.2 Vinyl-ester resin systems

Vinyl-esters are derived from the reaction of an epoxy resin with an acrylic or methacrylic acid. The chemical structure of vinyl esters has fewer cross-links than epoxy resins, which results in greater flexibility. Vinyl-ester resins also exhibit an increase in both chemical resistance and mechanical properties over polyester resins. This is due to the inclusion of an epoxy resin component in the manufacture of vinyl-ester resins which influences the

mechanical and physical properties of the cured resin. However, vinyl esters also exhibit the low viscosity and fast curing of polyester resins.

2.3.3 Epoxy resin systems

Epoxy resins consist of low molecular weight organic liquids that contain the epoxy or glycidyl group, which is capable of reaction with compounds containing an active hydrogen atom, such as phenol, amines and carboxylic acids. These curing agents are added to the epoxy resin to initiate polymerisation which results in a three-dimensional stable structure with relatively low shrinkage of approximately 2-3%.

Selection of epoxy resins for commercial applications, as opposed to cheaper polyester or vinyl ester resins, is generally justified by their superior mechanical properties, heat resistance, lower curing shrinkage and excellent bonding to fibres.

2.3.4 Phenolic resin systems

Phenolic resins are the oldest type of thermosetting resins. They are manufactured from the reaction of phenol with formaldehyde. The curing reaction of phenolic resins results in the formation of volatile ethers. Consequently, the manufacturing process is more expensive since pressurisation is required during curing to remove the reaction products and residual solvents [68]. The advantage of composite components made from fibre reinforced phenolic resin systems is their inherent stability to thermal oxidation, low level of smoke emission on burning and the low toxicity of the smoke emissions. Other thermosetting resins require additives in order to achieve good flame retardancy.

2.4 MANUFACTURE OF FRP-COMPOSITES

2.4.1 Pultrusion

Pultrusion produces continuous sections of FRP-composites where the orientation of the fibres is predominately in the longitudinal direction. Fibre rovings are drawn off creels and passed through a resin bath that impregnates the fibres. The resin-impregnated fibres are then forced through a heated forming die under tension to compact the fibres and resin and form the required shape. The heated forming die cures the resin matrix, allowing the finished FRP-composite to be drawn off. A schematic diagram of a typical pultrusion process is illustrated in Figure 2.3.

The maximum section size that can be pultruded is governed by the dimensions and pulling capacity of the machine available. The capacity of pultrusion machines range from 125 mm by 40 mm with a pulling force of 500 kg up to a maximum of 1000 mm by 165 mm with a

pulling force of 15 tonnes. The thickness of the section should be kept to a minimum since thick sections require a longer time for the heat of the die to penetrate. The thicknesses of pultruded sections can range from 1 mm to 50 mm. However, a more practical range is from 2 mm to 20 mm [62]. Line speeds typically range from 25 mm/min to 500 mm/min although a constant speed is required to ensure uniform curing of the resin.

Reinforcing bars for use in concrete are either solid square, rectangular or circular sections with thicknesses ranging from approximate 5 mm up to 20 mm. The pultrusion process can achieve a high fibre content, up to 60-65% by volume and hence the bars have a relatively high strength and stiffness in the longitudinal direction. However, the sections have a smooth surface which provides insufficient bond with concrete. Consequently, an additional surface treatment is required to improve bond. Surface treatments currently used include the application of a sand layer, overwinding with additional fibres to produce a ribbed surface or the application of a peel-ply texture to the rods.

2.4.2 Filament winding

Filament winding is a process in which resin impregnated fibres are wound onto a mandrel in a precise, predetermined pattern. This method is commonly used for the formation of pipes and other hollow sections. A schematic of the filament winding process is illustrated in Figure 2.4.

There are two possible methods of filament winding, namely polar or helical winding. In polar winding the mandrel remains stationary and the fibres are laid by a feeder arm inclined at the required angle, rotating about the longitudinal axis. The mandrel is moved one fibre bandwidth during each revolution of the feeder arm, resulting in adjacent fibre bands. The completed composite is composed of equal numbers of two unidirectional laminae that form a balanced laminate. Polar winding is particularly suited to forming closed hemispherical ends and winding angles that are nearly zero degrees to the longitudinal axis.

The alternative winding pattern is helical. The reinforcement in the form of rovings are gathered off a creel and passed through a resin bath (Plates 2.1–2.2). The resin-impregnated fibres are then guided onto a rotating mandrel via a movable carriage (Plate 2.3). The carriage traverses the mandrel longitudinally at speeds synchronised with the mandrel rotation, controlling the winding angle and the fibre layout rate. The winding angle can be altered between nearly zero (longitudinal winding) to 90 degrees (hoop winding). The normal pattern is a multi-circuit helix. After the first circuit the fibres are not adjacent, and a number of circuits must be traversed before the pattern begins to lay adjacent to earlier windings. The

helical pattern is characterised by fibre crossovers and irregularities in fibre orientation that complicate the formulation of any constitutive equations.

The fabrication of the composite is completed by the curing operation. Cure is achieved by the application of heat from gas-fired or electric ovens (Plate 2.4), autoclaves or microwave ovens, which cause chemical cross-linking. Epoxy and vinyl ester resin systems are generally cured in either gas-fired or electric ovens. Phenolics present a particular problem since they require pressurised curing to remove reaction products and residual solvents [68].

Typical fibre volume fractions of filament wound composites range from 50-60% for helical winding and 60-70% for hoop winding. The actual fibre volume fraction depends on several factors including the type of fibre, resin viscosity, mandrel diameter and the winding angle. Tubes as small as 25 mm and as large as 6000 mm in diameter are commonly made using filament winding. The only limitations on size are those dictated by the geometry of the winding machine and limitations in mandrel size and weight. Typical winding speeds are up to 100 m/min.

2.5 ANALYSIS OF FRP-COMPOSITE MATERIALS

2.5.1 Micromechanical analysis of FRP-composites

Unidirectional composites consist of parallel fibres embedded in a resin matrix. Unidirectional composites exhibit orthotropic behaviour with three planes of symmetry, the greatest stiffness and strength being observed in the direction of the fibres. The properties of the composites depend upon the fibre volume fraction and the mechanical properties of the constituents.

Various micromechanical models are available for predicting the elastic properties of unidirectional composites from their constituent properties. The simplest model is based on the principles of *'law of mixtures'* and *'constant stress'*, and an idealised composite material. The main assumptions of the analysis are:

1. the fibres and matrix are linear-elastic and homogenous;
2. fibres and matrix are free of voids;
3. perfect bond exists at the fibre matrix interface, and there is no transition region;
4. there are no initial stresses in the composite;
5. fibres are uniformly spaced and are parallel.

The elastic properties predicted from the principle of *'law of mixtures'* are given in equations 2.2-2.6. When compared to experimental results, the method predicts acceptable values for the longitudinal modulus, E_{11}, and major Poisson's ratio, ν_{12}, but lower values are predicted for the transverse modulus, E_{22} and modulus of rigidity G_{12} [63].

$$E_{11} = V_f E_f + (1 - V_f) E_m \tag{2.2}$$

$$\nu_{12} = V_f \nu_f + (1 - V_f) \nu_m \tag{2.3}$$

$$E_{22} = \frac{E_f E_m}{E_m V_f + (1 - V_f) E_f} \tag{2.4}$$

$$G_{12} = \frac{G_f G_m}{G_m V_f + (1 - V_f) G_f} \tag{2.5}$$

$$\nu_{21} = \nu_{12} \frac{E_{22}}{E_{11}} \tag{2.6}$$

In a real composite, the fibres are dispersed randomly in the matrix, and fibres may be misaligned. Additionally, a transition region exists between the constituents due to incomplete bond and interaction between the constituents. The fabrication process also influences the elastic properties of the composite and generally results in initial stresses being present in the composite. Consequently, complex mathematical models using formal elasticity theory have been proposed by numerous researchers in an attempt to accurately predict the elastic properties of composites. These rigorous models are found to contribute a negligible correction to the *'law of mixtures'* values for E_{11} and ν_{12}. However, the rigorous solutions for E_{22} and G_{12} are significantly greater than the values predicted by the *'law of mixtures'* model, and are reported to provide good agreement with experimental data [63].

Halpin and Tsai have proposed some semi-empirical relationships for the transverse properties of the composite. These equations result in more accurate predictions of E_{22} and G_{12} compared with the *'law of mixtures'* [63, 65, 69]. The Halpin-Tsai equation for the transverse composite modulus is given by:

$$\frac{E_{22}}{E_m} = \frac{1 + \xi \eta V_f}{1 - \eta V_f} \tag{2.7}$$

where

$$\eta = \frac{(E_f / E_m) - 1}{(E_f / E_m) + \xi}$$

The parameter ξ accounts for the influence of packing arrangements of the fibres. The values of ξ are obtained by the regression analysis with solutions obtained from more formal elasticity theory. Halpin and Tsai have suggested a value of $\xi = 2$ for the determination of the transverse elastic modulus.

The Halpin-Tsai equation for the shear modulus is given by:

$$\frac{G_{12}}{G_m} = \frac{1+\xi\eta V_f}{1-\eta V_f} \qquad \textbf{(2.8)}$$

where

$$\eta = \frac{(G_f/G_m)-1}{(G_f/G_m)+\xi}$$

Again, values of ξ are obtained by regression analysis of solutions obtained using exact elasticity theory, with a value of $\xi = 1$ providing very good agreement [65]. Comparisons of the predicted values for the transverse modulus and shear modulus using the '*law of mixtures*' and the Halpin-Tsai equations are given in Figures 2.5 and 2.6 respectively. In the practical range of fibre volume fractions for pultruded or filament wound composites, it can be seen that the variation in the predicted values of the transverse modulus range from 80 to 100% greater than the '*law of mixtures*'. A similar trend is observed with the predicted values for the shear modulus.

The variations in the manufacture of composites will always cause changes in the elastic constants, and hence in practice it is not possible to determine the exact values of the composite moduli. Therefore, the predicted elastic properties using the Halpin-Tsai equations given above should yield sufficiently accurate results for this research.

2.5.2 Macromechanical analysis of FRP-composites

The constitutive equations of a composite system are derived assuming a two-dimensional stress state. The composite material is assumed to have linear elastic properties and identical characteristics under tension and compression. Under plane stress conditions, the stress-strain relationship for an orthotropic composite is as follows:

$$\begin{Bmatrix}\sigma_{11}\\ \sigma_{22}\\ \sigma_{12}\end{Bmatrix} = \begin{bmatrix}Q_{11} & Q_{12} & 0\\ Q_{12} & Q_{22} & 0\\ 0 & 0 & Q_{33}\end{bmatrix}\begin{Bmatrix}\varepsilon_{11}\\ \varepsilon_{22}\\ \varepsilon_{12}\end{Bmatrix}$$

$$\{\sigma\}_{1,2} = [Q]\{\varepsilon\}_{1,2} \qquad \textbf{(2.9)}$$

Where Q_{ij} are the reduced stiffness constants, and are related to the elastic constants by:

$$Q_{11} = E_{11}/(1-\nu_{12}\nu_{21}) \tag{2.10}$$

$$Q_{22} = E_{22}/(1-\nu_{12}\nu_{21}) \tag{2.11}$$

$$Q_{12} = \nu_{21}E_{11}/(1-\nu_{21}\nu_{12}) \tag{2.12}$$

$$Q_{33} = G_{12} \tag{2.13}$$

The properties of the composite depend upon the properties of the component materials and the arrangement of the fibres. The stresses, strains and stiffness constants can be transformed to an arbitrary co-ordinate system corresponding to a fibre orientation ϕ by the following transformation matrices:

$$\{\sigma\}_{1,2} = [T_1]\{\sigma\}_{x,\theta} \tag{2.14}$$

$$\{\varepsilon\}_{1,2} = [T_2]\{\varepsilon\}_{x,\theta} \tag{2.15}$$

Where,

$$[T_1] = \begin{bmatrix} \cos^2\phi & \sin^2\phi & 2\sin\phi\cos\phi \\ \sin^2\phi & \cos^2\phi & -2\sin\phi\cos\phi \\ -\sin\phi\cos\phi & \sin\phi\cos\phi & \cos^2\phi - \sin^2\phi \end{bmatrix}$$

$$[T_2] = \begin{bmatrix} \cos^2\phi & \sin^2\phi & \sin\phi\cos\phi \\ \sin^2\phi & \cos^2\phi & -\sin\phi\cos\phi \\ -2\sin\phi\cos\phi & 2\sin\phi\cos\phi & \cos^2\phi - \sin^2\phi \end{bmatrix}$$

Substitution of the transformation matrices (equations 2.14-2.15) into the constitutive equation in the principal 1-2 co-ordinate system given by equation 2.9 yields the constitutive equations for the arbitrary co-ordinate system:

$$\{\sigma\}_{x,\theta} = [T_1]^{-1}[Q][T_2]\{\varepsilon\}_{x,\theta}$$

$$\{\sigma\}_{x,\theta} = \left[\overline{Q}\right]\{\varepsilon\}_{x,\theta} \tag{2.16}$$

The transformed reduced stiffness matrix $\left[\overline{Q}\right]$ is a 3x3 matrix where the components are:

$$\overline{Q}_{11} = Q_{11}\cos^4\phi + Q_{22}\sin^4\phi + 2(Q_{12} + 2Q_{33})\sin^2\phi\cos^2\phi$$

$$\overline{Q}_{12} = (Q_{11} + Q_{22} - 4Q_{33})\sin^2\phi\cos^2\phi + Q_{12}\left(\sin^4\phi + \cos^4\phi\right)$$

$$\overline{Q}_{13} = (Q_{11} - Q_{12} - 2Q_{33})\sin\phi\cos^3\phi - (Q_{22} - Q_{12} - 2Q_{33})\sin^3\phi\cos\phi$$

$$\bar{Q}_{22} = Q_{11}\sin^4\phi + Q_{22}\cos^4\phi + 2(Q_{12} + 2Q_{33})\sin^2\phi\cos^2\phi$$

$$\bar{Q}_{23} = (Q_{11} - Q_{12} - 2Q_{33})\sin^3\phi\cos\phi - (Q_{22} - Q_{12} - 2Q_{33})\sin\phi\cos^3\phi$$

$$\bar{Q}_{33} = (Q_{11} + Q_{22} - 2Q_{12} - 2Q_{33})\sin^2\phi\cos^2\phi + Q_{33}(\sin^4\phi + \cos^4\phi)$$

The filament wound tubes are assumed to comprise of alternate lamina layers of unidirectional fibres orientated at $\pm\phi$, uniformly distributed throughout the matrix. To simplify the analysis, irregularities in fibre orientation and the fibre crossovers are neglected. Thus, the behaviour of the idealised filament wound composite is analogous to that of an angle-plied laminate and the analytical methods developed for laminates may be applied to filament wound composites.

Laminates consist of two or more elemental composite layers acting as an integral structural unit, Figure 2.7. The assumptions are that perfect bond exists between any two laminae and that displacement strains are continuous throughout the laminate thickness. The general equation for determining the in-plane and flexural forces in composites is:

$$\begin{Bmatrix} N \\ M \end{Bmatrix}_{x,\theta} = \begin{bmatrix} A & B \\ B & D \end{bmatrix} \begin{Bmatrix} \varepsilon \\ \chi \end{Bmatrix}_{x,\theta} \qquad \textbf{(2.17)}$$

Where:

$$A_{ij} = \sum_{k=1}^{n} \left[\bar{Q}_{ij}\right]_k (h_k - h_{k-1})$$

$$B_{ij} = \frac{1}{2}\sum_{k=1}^{n} \left[\bar{Q}_{ij}\right]_k (h_k^2 - h_{k-1}^2)$$

$$D_{ij} = \frac{1}{3}\sum_{k=1}^{n} \left[\bar{Q}_{ij}\right]_k (h_k^3 - h_{k-1}^3)$$

The matrices *A*, *B* and *D* are the *extensional stiffness matrix, coupling stiffness matrix* and *bending stiffness matrix* respectively. If the lamina layers of the composite are assumed to be balanced with respect to the *x-axis* ($A_{13} = A_{23} = 0$) and symmetrical about the mid-plane axis ($B_{ij} = 0$), it is possible to simplify the in-plane and flexural stress-strain relationships as follows:

$$\begin{Bmatrix} N_{xx} \\ N_{\theta\theta} \\ N_{x\theta} \end{Bmatrix} = \begin{bmatrix} A_{11} & A_{12} & 0 \\ A_{12} & A_{22} & 0 \\ 0 & 0 & A_{33} \end{bmatrix} \begin{Bmatrix} \varepsilon_{xx} \\ \varepsilon_{\theta\theta} \\ \varepsilon_{x\theta} \end{Bmatrix} \qquad \textbf{(2.18)}$$

$$\begin{Bmatrix} M_{xx} \\ M_{\theta\theta} \\ M_{x\theta} \end{Bmatrix} = \begin{bmatrix} D_{11} & D_{12} & 0 \\ D_{12} & D_{22} & 0 \\ 0 & 0 & D_{33} \end{bmatrix} \begin{Bmatrix} \chi_{xx} \\ \chi_{\theta\theta} \\ \chi_{x\theta} \end{Bmatrix} \quad \textbf{(2.19)}$$

Filament winding results in a nearly symmetrical structure about the mid-plane axis, thus the coupling stiffness matrix is approximately zero ($B_{ij} \approx 0$). Therefore, for simplicity it is assumed that there is no coupling between the extensional deformation and bending deformation and equations 2.18 and 2.19 are valid. The elastic constants of a balanced symmetrical composite can then be determined by subjecting the composite to uniaxial stress states:

$$E_{xx} = \frac{\overline{Q}_{11}\overline{Q}_{22} - \overline{Q}_{12}^2}{\overline{Q}_{22}} \quad \textbf{(2.20)}$$

$$E_{\theta\theta} = \frac{\overline{Q}_{11}\overline{Q}_{22} - \overline{Q}_{12}^2}{\overline{Q}_{11}} \quad \textbf{(2.21)}$$

$$G_{x\theta} = \overline{Q}_{33} \quad \textbf{(2.22)}$$

$$\nu_{x\theta} = \frac{\overline{Q}_{12}}{\overline{Q}_{22}} \quad \textbf{(2.23)}$$

$$\nu_{\theta x} = \frac{\overline{Q}_{12}}{\overline{Q}_{11}} \quad \textbf{(2.24)}$$

The variation in the elastic hoop modulus $E_{\theta\theta}$ with fibre orientation for a typical E-glass/epoxy composite is illustrated in Figure 2.8. The elastic hoop modulus $E_{\theta\theta}$ decreases from E_{11} at $\phi = 90^\circ$ to E_{22} at $\phi = 0^\circ$. If the angle of fibre orientation is reduced from $\phi = 90^\circ$ to $\phi = 80^\circ$, $E_{\theta\theta}$ decreases by 10 percent. However, as the fibre orientation tends further towards 0°, the decrease in elastic hoop modulus becomes significant.

The magnitude of the concrete confinement is influenced by the hoop modulus of the composite. The largest confinement stresses develop in the composites with fibres orientated predominately in the hoop direction. Therefore, to achieve maximum confinement from the composite, the angle of fibre orientation should not be less than 80°. However, incorporating a longitudinal reinforcement component in the winding configuration may provide other benefits by increasing the shear and flexural capacity of the column.

2.6 FAILURE STRENGTH OF FRP-COMPOSITES

Under axial compression, the failure of a hollow cylindrical FRP-composite column for which $L > D$ may be due to axial compression strength failure of the wall material, Euler buckling of the column, or local buckling of the cylinder wall. The addition of a solid concrete core changes the failure modes of the composite. The concrete core prevents the cylinder wall from buckling inwards, eliminating the potential for local buckling. However, failure may occur due to tensile strength failure of the wall material resulting from the lateral expansion of the concrete core.

The failure of a composite may result from fibre failure, matrix failure, or failure of the fibre-matrix interface. The actual mode of failure depends on the orientation of the fibres and the direction of load.

2.6.1 Longitudinal tensile failure

In a unidirectional composite subjected to a longitudinal tensile load, failure is initiated when the fibres are strained to their fracture strain. The longitudinal tensile failure strength can be estimated by the *'law of mixtures'* equation, given by:

$$\sigma_{11}^{t} = \sigma_f^t V_f + \sigma_m (1 - V_f) \qquad \textbf{(2.25)}$$

2.6.2 Transverse tensile strength

The transverse failure mode is illustrated in Figure 2.9. The transverse strength of a unidirectional composite is governed by a number of factors, such as the properties of the fibre and the matrix and the adhesion between the fibres and the matrix. The tensile strength of brittle resins is affected by flaws in the material and stress concentrations that develop at the fibre/matrix interface. Consequently, the transverse tensile strength is usually less than the tensile strength of the matrix material [67].

2.6.3 Longitudinal compressive failure

Failure modes of composites subjected to longitudinal compression may be classified as [63]:

- fibre buckling;
- transverse tensile failure;
- shear failure.

The compressive strength of unidirectional composites is largely dependent on the buckling of the fibres. The fibres are assumed to act independently of each other and adjacent fibres will buckle with equal wave lengths at the ultimate load either out-of-phase (an extensional mode) with each other or in-phase with each other (shear mode) [63]. The fibre buckling

modes of a unidirectional composite are illustrated in Figure 2.9. The extensional fibre buckling mode is only possible when the inter-fibre distance is quite large, which corresponds to a low fibre volume fraction. The critical compressive strength of a composite failing in the extensional mode is given by [67]:

$$\sigma_{11}^{c} = 2V_f\left[\frac{E_f E_m V_f}{3(1-V_f)}\right]^{1/2} \tag{2.26}$$

The shear mode of buckling is more common and tends to dominate the practical range of V_f for civil engineering applications. The critical compressive strength of a composite failing in the shear mode is given by [67]:

$$\sigma_{11}^{c} = \frac{G_m}{1-V_f} \tag{2.27}$$

Compressive failure of a unidirectional composite loaded in the fibre direction may be initiated by a transverse tensile failure resulting from the Poisson's effect. The transverse strain resulting from longitudinal compression may exceed the ultimate transverse strain capacity of the composite. The failure criterion for transverse tensile failure is given by [63]:

$$\sigma_{11}^{c} = \frac{\left[E_f V_f + E_m(1-V_f)\right]\left[1-V_f^{1/3}\right]\varepsilon_{mu}}{\nu_f V_f + \nu_m(1-V_f)} \tag{2.28}$$

2.6.4 Transverse compression strength

A unidirectional composite subjected to transverse compression loads generally fails by shear failure of the matrix, which may also include debonding of the constituent materials or crushing of the fibres. The shear failure mode of a unidirectional composite subject to transverse compression is shown in Figure 2.9.

PROPERTY	E-glass	HS Carbon	HM Carbon	Kevlar 49
Specific Gravity	2.56	1.80	1.97	1.44
Tensile Strength σ_{11}, N/mm^2	3448	2414	1724	3620
Elastic Modulus E_{11}, kN/mm^2	75.90	221	379	124
Elastic Modulus E_{22}, kN/mm^2	75.90	13.79	6.21	4.14
Shear Modulus G_{12}, kN/mm^2	31.11	8.96	7.59	2.90
Shear Modulus G_{23}, kN/mm^2	31.11	4.83	4.83	1.52
Poisson's ratio ν_{12}	0.22	0.20	0.20	0.35
Poisson's ratio ν_{23}	0.22	0.25	0.25	0.35

Table 2.1. Typical mechanical properties of fibres

Property	Polyester	Vinyl Ester	Epoxy	Phenolic
Specific gravity	1.23	1.15	1.20	1.25
Tensile Strength σ_m, N/mm^2	53	73	85	55
Elastic Modulus E_m, kN/mm^2	3.7	3.5	2.35	5.5
Shear Modulus G_m, kN/mm^2	1.35	-	0.89	2.00
Poisson's ratio ν_m	0.37	-	0.32	0.37

Table 2.2. Typical mechanical properties of thermosetting resins

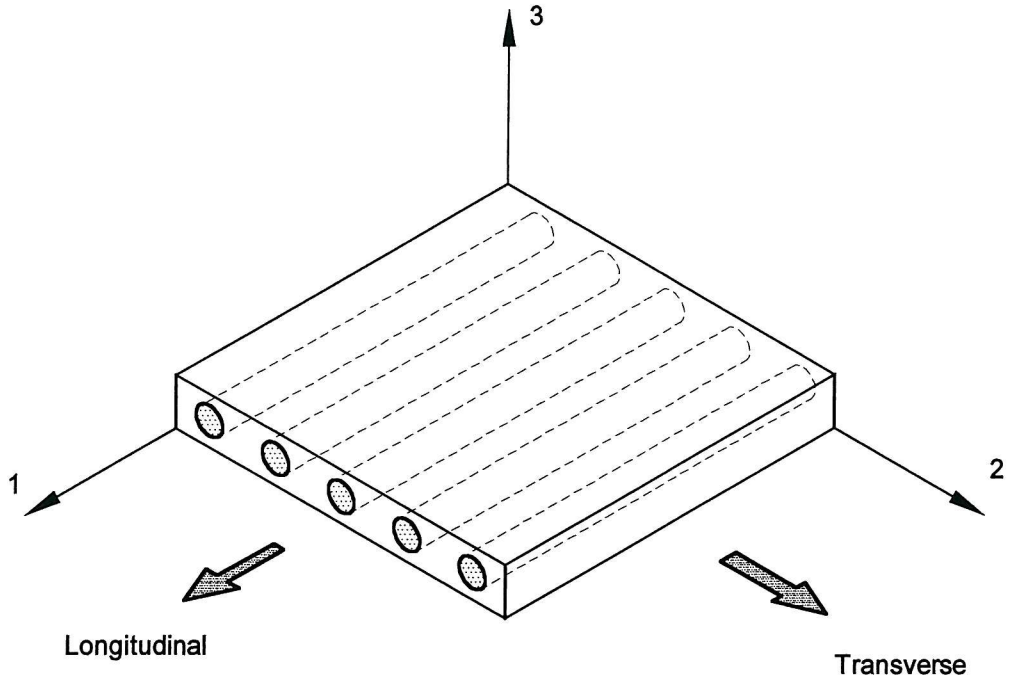

Figure 2.1. Idealised unidirectional FRP-composite laminate

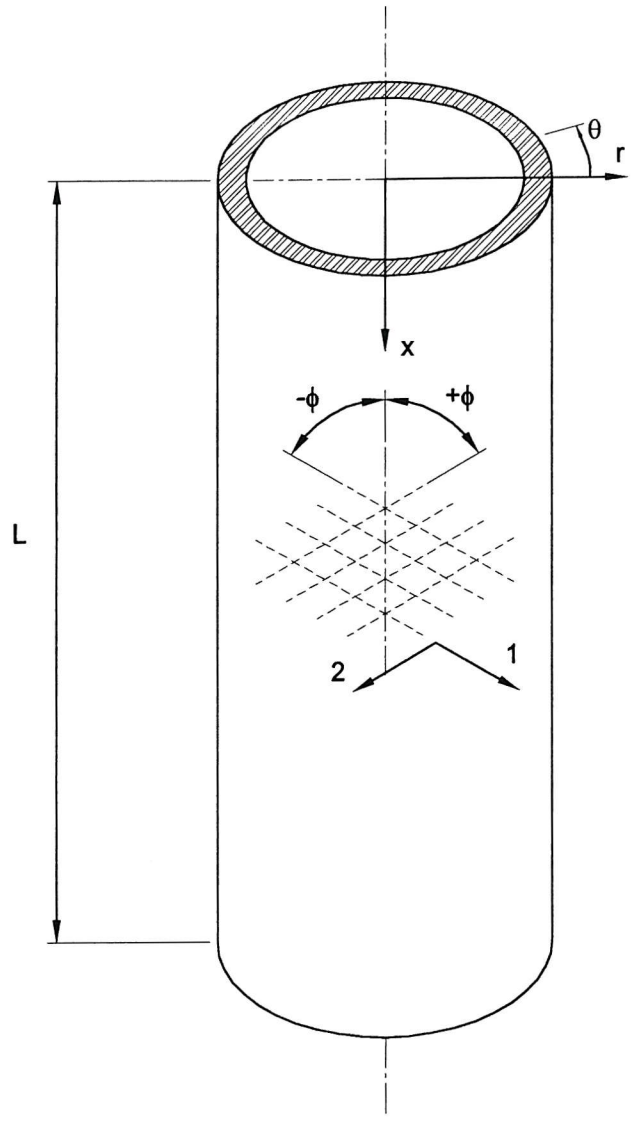

Figure 2.2. Filament wound FRP-composite tube with fibres orientated at $\pm\phi$

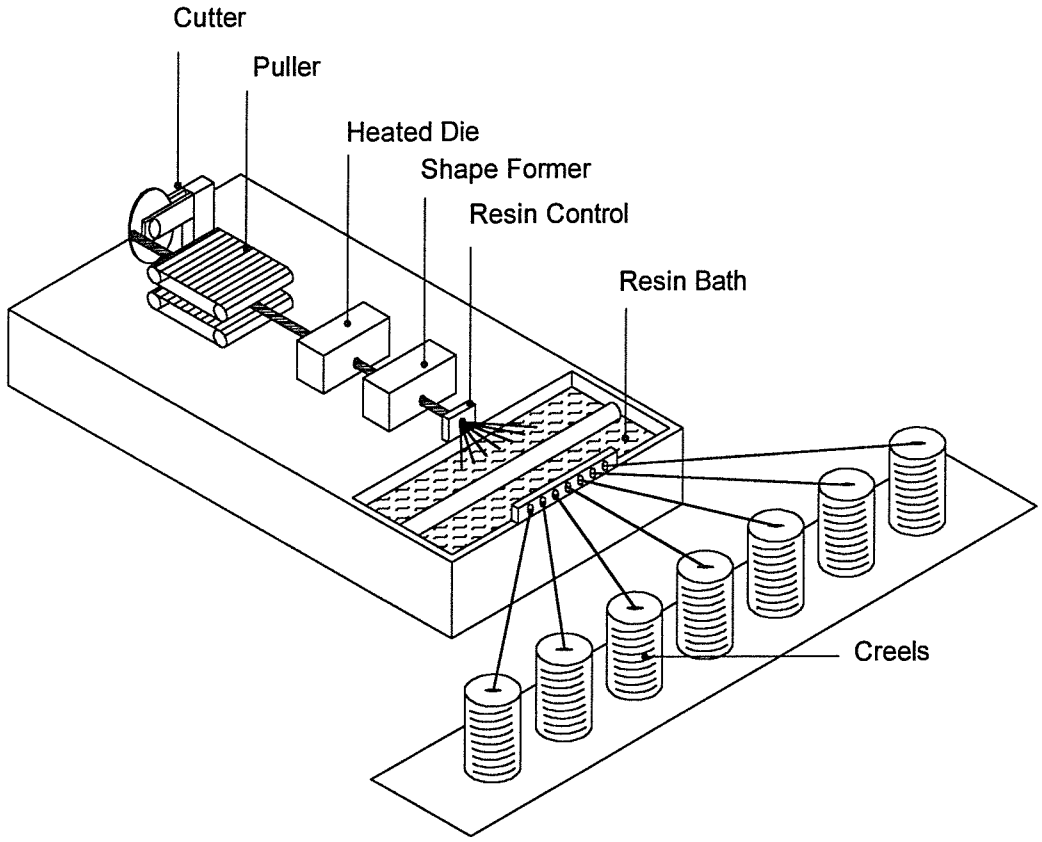

Figure 2.3. The pultrusion process

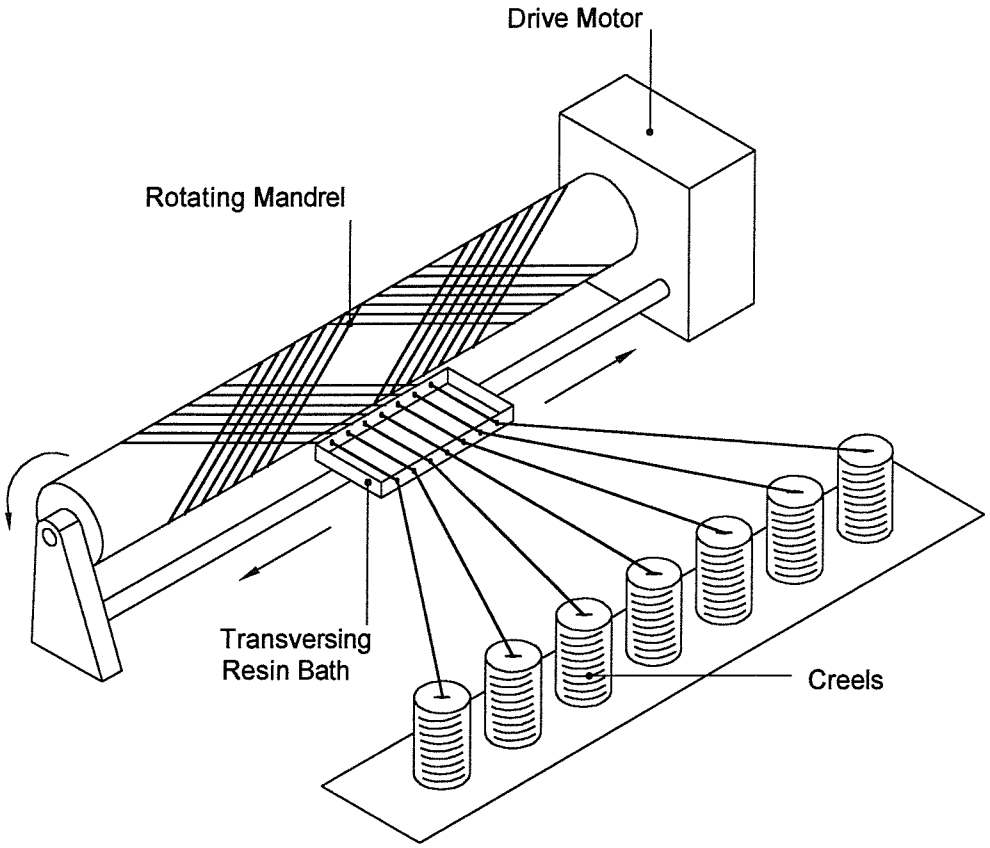

Figure 2.4. The filament winding process

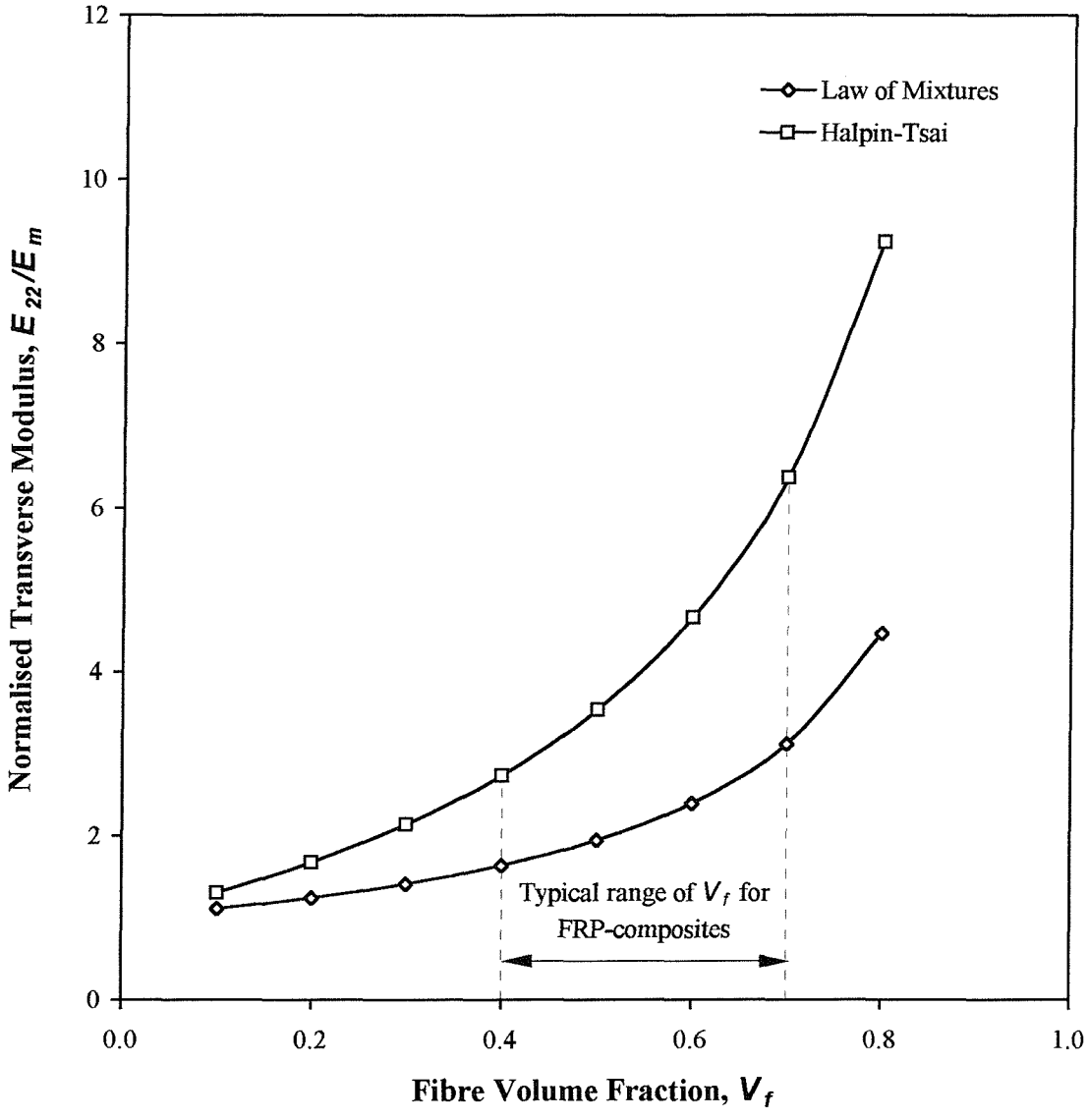

Figure 2.5. Comparison of the transverse modulus of elasticity of a FRP-composite predicted by the *'law of mixtures'* and the Halpin-Tsai equations

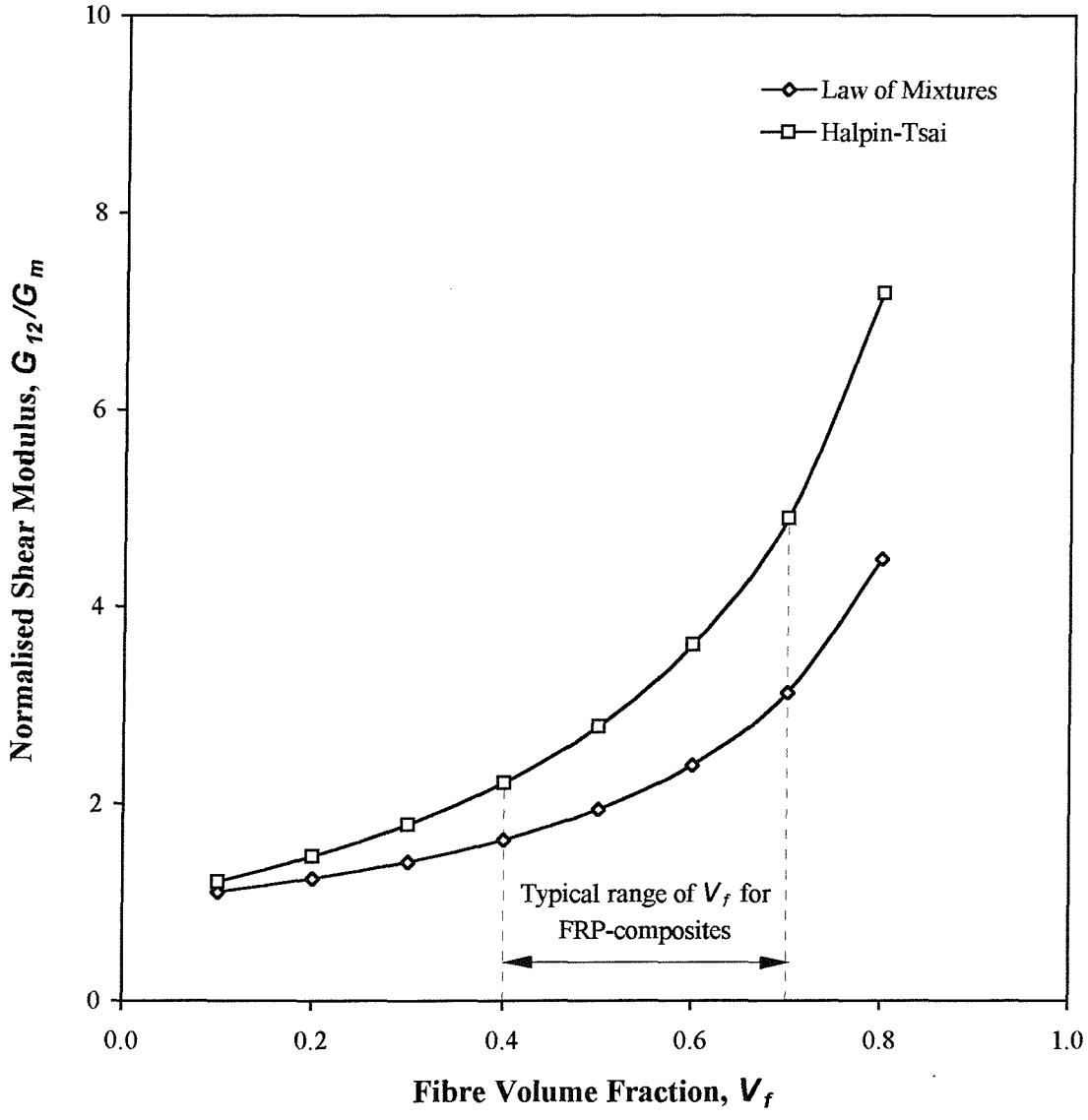

Figure 2.6. Comparison of the shear modulus of a FRP-composite predicted by the *'law of mixtures'* and the Halpin-Tsai equations

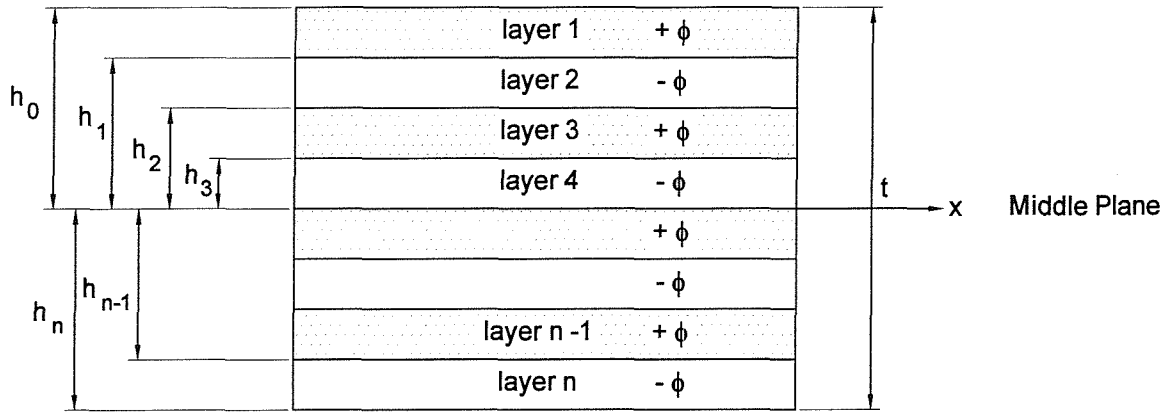

Figure 2.7. Geometry of a multilayered $\pm\phi$ filament wound FRP-composite

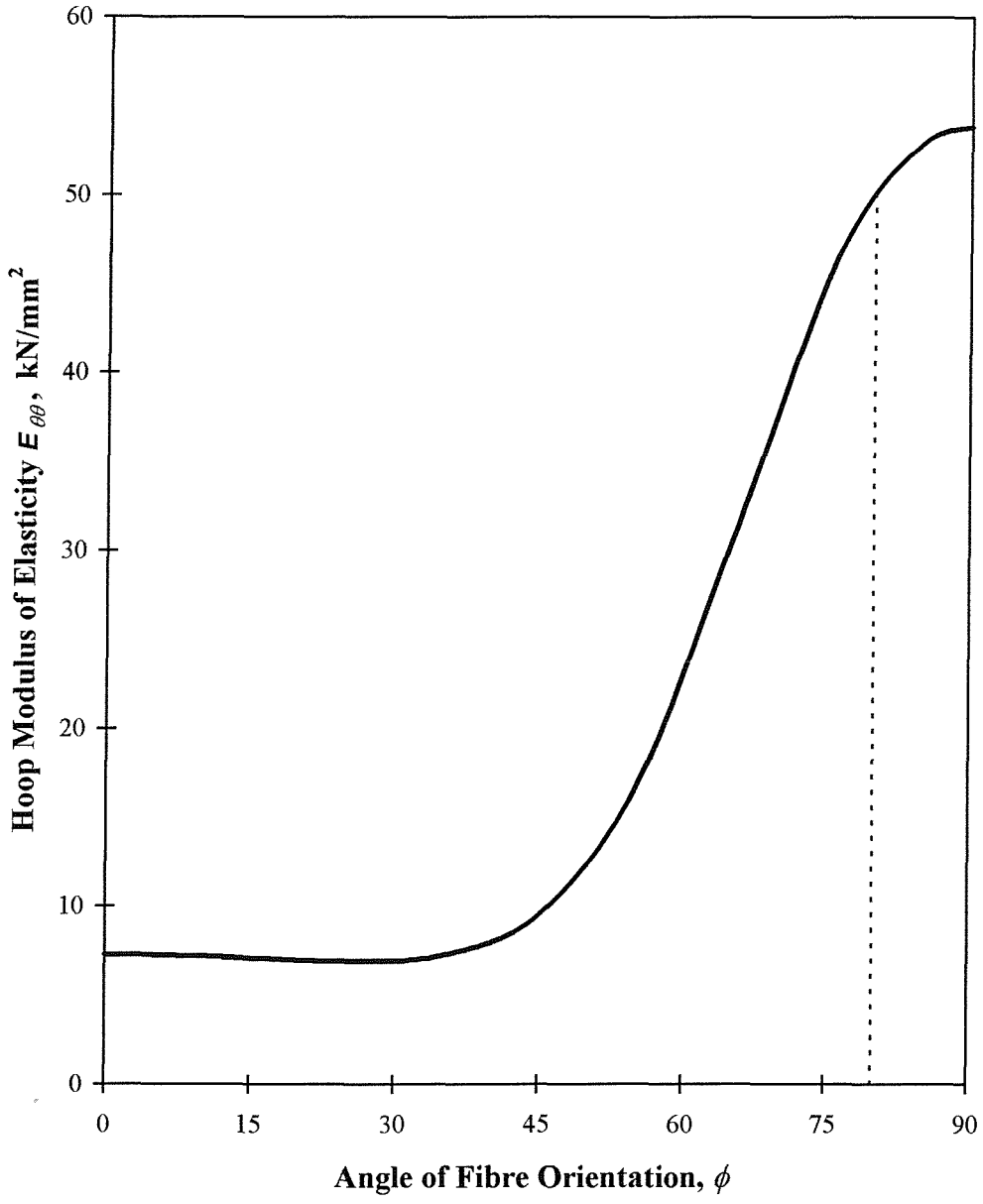

Figure 2.8. Variation in the hoop elastic modulus with fibre orientation for a typical E-glass/epoxy composite

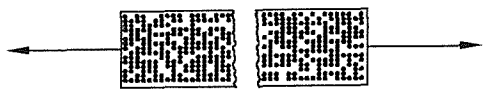

Transverse tensile failure

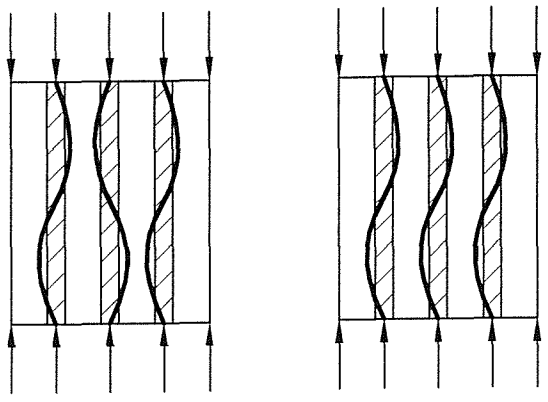

(i) Extensional mode (i) Shear mode

Longitudinal compressive failure

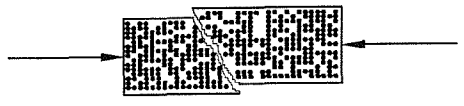

Transverse compressive failure

Figure 2.9. Failure modes of a unidirectional FRP-composite

Plate 2.1. E-glass fibres stored on creels

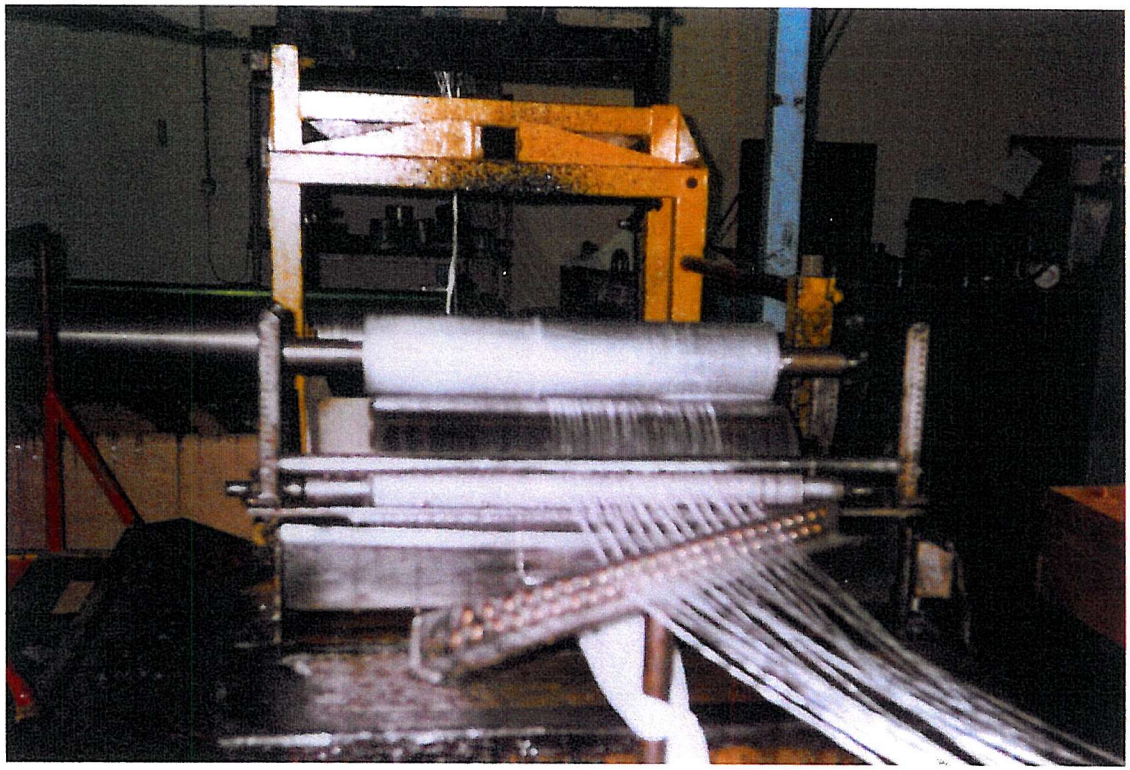

Plate 2.2. E-glass fibres passing through a resin bath

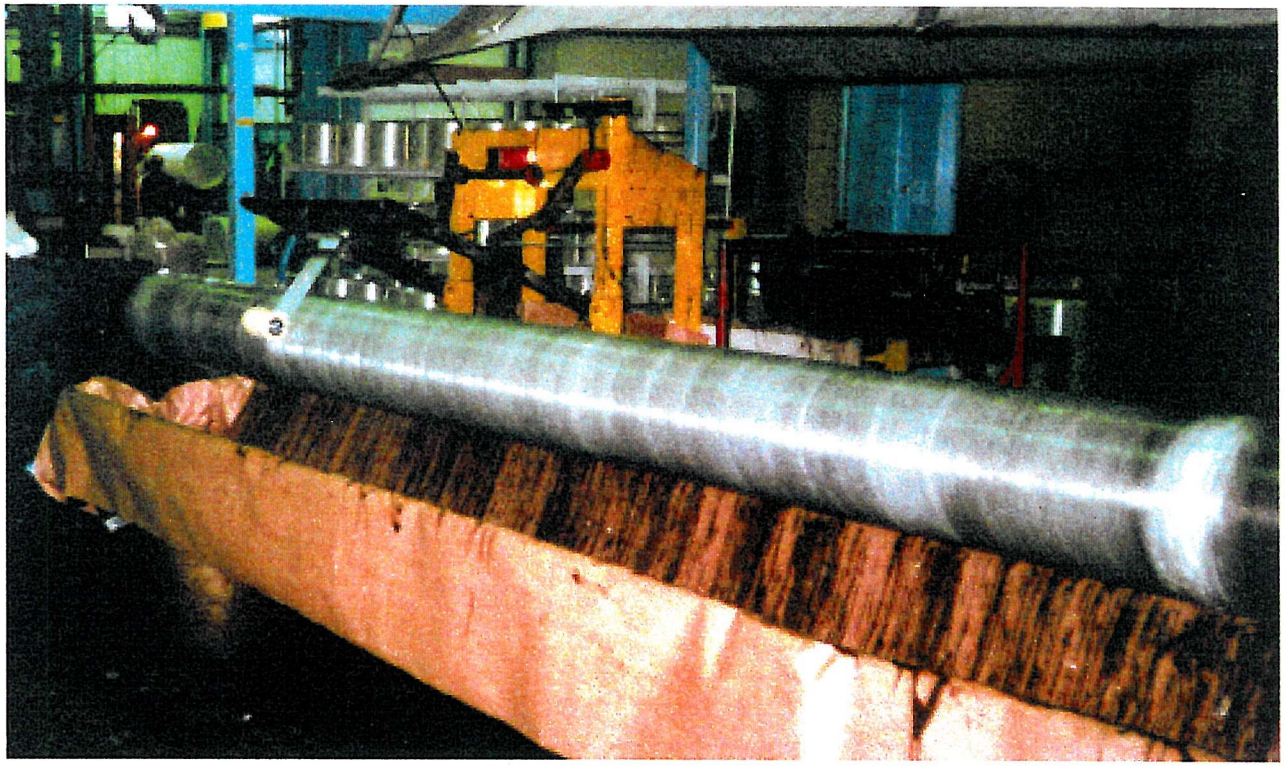

Plate 2.3. Fibres being positioned on the mandrel via the moving carriage

Plate 2.4. Curing of filament wound tubes in electric ovens

CHAPTER 3

EXPERIMENTAL BEHAVIOUR OF CONCRETE CONFINED BY FRP-COMPOSITES

3.1 INTRODUCTION

When concrete is subjected to a state of triaxial compression, both the compressive strength and ductility are enhanced. The degree of enhancement is a function of the magnitude of the confining pressure. However, due to the heterogeneous nature of concrete, analysis of its physical properties and behaviour under various stress combinations is extremely complex. Consequently, no exact theory exists to describe the behaviour of concrete subjected to a multi-stress state.

The proposed FRP-composite reinforcing system for concrete columns consists of a concrete-filled prefabricated filament wound FRP-composite tube. This proposed method of construction is analogous to the more traditional form of construction using concrete-filled steel tubes, both methods exploiting the augmented strength and ductility of the triaxially confined concrete. The FRP-composite tube acts as lateral reinforcement, thereby providing triaxial confinement to the concrete core. Furthermore, the tube acts as:

- permanent formwork, thereby eliminating the need for the erection and subsequent removal of shuttering;
- and as a barrier to the ingress of water and atmospheric gases, thus increasing the durability of the concrete core.

When an axial compressive strain is applied to concrete, lateral deformations occur due to Poisson's effect. The lateral expansion causes tensile stresses to develop in the tube, which induce a lateral confining pressure on the concrete core. The presence of a triaxial state of stress enhances the strength and ductility of the concrete core, the degree of enhancement being proportional to the magnitude of applied lateral pressure. As the axial strain increases, the lateral confining pressure on the concrete also increases, thereby further increasing the strength and ductility of the concrete. Buckling of the wall of the tube is prevented by the concrete core.

The FRP-composite tube is a multi-layered fibre composite with the fibres orientated at $\pm\phi$ in alternate layers. Utilising the FRP-composite around the periphery of the column enables the FRP composite to act more efficiently in circumferential tension, as opposed to longitudinal compression. Since the FRP-composite effectively consists of alternating layers of angle-plies, the circumferential and longitudinal reinforcing components are incorporated in the winding configuration. The magnitudes of the reinforcing components in the two principal

directions are determined by the angle of fibre orientation ϕ.

To determine the mechanical properties of concrete confined by FRP-composites, twenty-six stub columns with a length-to-diameter ratio of 2 were tested to failure. The stub columns consisted of E-glass FRP-composite tubes, filled with normal weight concrete. The nominal tube diameters and the angle of fibre winding are summarised in Table 3.1. The majority of the stub columns were tested in a 2000 kN Losenhausen compression rig at the University of Southampton. Testing of the large diameter columns was carried out in collaboration with the Building Research Establishment (BRE) at Garston.

3.2 MATERIAL PROPERTIES

3.2.1 Concrete

Concrete mixes with nominal 28-day cube strengths of 25 N/mm^2 or 35 N/mm^2 were used for all the test specimens. The maximum strength of the unconfined concrete was limited to 35 N/mm^2 to ensure failure of the FRP-confined concrete was achieved. To minimise segregation of the concrete, three grades of sea-dredged aggregate were blended to a type 4 grading curve to produce a cohesive concrete. The three grades of aggregate were a single size 20 mm, a single size 10 mm and fine sand. The concrete for the columns tested at the Building Research Establishment used a Thames Valley aggregate. The concrete mix designs are given in Table 3.2.

The stub columns were cast in the vertical position, as would normally be the case in construction. The casting of a stub column is shown in Plate 3.1. Compaction of the concrete was achieved using either a vibrating poker, or for the smaller diameter stub columns, using a vibrating table and a steel punner. After casting, the ends of the columns were sealed with polythene and air cured for 28-days.

The uniaxial properties of the concrete were determined from standard concrete specimens. Six 100 mm cubes were taken from each batch of concrete, half were air cured in polythene to replicate the curing regime of the columns whilst the remainder were water cured. The mean initial tangent modulus of the concrete was determined from 100 mm diameter concrete cylinders which were air cured in polythene.

3.2.2 Filament wound tubes

The filament wound tubes consist of Vetrotex RO 99 2400 P122 E-glass fibres embedded in a Bisphenol epoxy resin, Epophen resin EL-62. The tubes were produced by a commercial manufacturer using a multi-circuit helical winding process. The lay-up of the tube consisted

of a resin rich layer of C-glass tissue to improve the durability of the composite, and eight layers of E-glass fibres orientated at $\pm\phi$ to the longitudinal axis.

Eight different internal tube diameters were tested, which were nominally 60 mm, 80 mm, 100 mm, 125 mm, 150 mm, 200 mm, 300 mm and 400 mm. The wall thickness of the tubes were designed to be 2.5 mm for the 60 mm to 200 mm diameter tubes inclusive, and 3.6 mm and 5.0 mm for the 300 mm and 400 mm diameter tubes respectively. The wall thicknesses of the tubes used were the minimum thickness required to provide sufficient structural strength for the extraction of the steel mandrel.

Three different fibre orientations were investigated to determine the effect of including axial and hoop fibre reinforcement components. The three notional winding angles were 90 degrees, 67½ degrees and 45 degrees. However, limitations imposed by the winding machinery meant that the actual winding angles differed from the notional winding angles, depending on the tube diameter. The dimensions of the fibre composite tubes are given in Table 3.3.

The mechanical properties of the composite were determined theoretically using micromechanical analysis of the constituent materials and classical lamination theory. The mechanical properties of the constituent materials and the properties of the FRP-composite tubes are given in Table 3.4 and Table 3.5 respectively. The fibre volume fraction of the composite was determined by resin burn-off tests carried out in accordance with BS 2782 [70]. The theoretical mechanical properties were comparable with extrapolated experimental values provided by the composite manufacturer.

The behaviour of the FRP-composite tubes with different wall thicknesses, diameters and fibre orientations are compared by the parameter termed the *effective hoop modulus*, defined by:

$$\overline{E}_{\theta\theta} = \left(\frac{2t}{D}\right) E_{\theta\theta} \qquad (3.1)$$

The effective hoop moduli of the FRP-composite tubes are given in Table 3.5.

3.3 TEST METHODOLOGY

3.3.1 Instrumentation

Longitudinal strains were measured using an extensometer. The average longitudinal strains in the specimens were measured over the middle half of the specimens to eliminate the

influence of platen restraint at the ends of the specimens. The extensometer consisted of four ±2.5 mm linear voltage displacement transducers (LVDT) positioned at orthogonal points coinciding with the principal axes. The accuracy of the LVDTs used to measure axial strain were ±0.01 mm at full scale. The gauge length for strain measurements was set equal to the internal diameter of the column, up to a maximum of 150 mm, using steel spacer-blocks. A schematic diagram of the axial extensometer is shown in Figure 3.1. In addition to measuring the true axial strains, the mean axial strain over the total length of the stub columns was also measured.

The mean circumferential expansion of the cylinder was measured using a ±10.0 mm LVDT connected to a circumferential extensometer, shown in Figure 3.2. One end of the cable was attached to the LVDT, whilst the opposite end of the cable and sheath were attached to a clamp to prevent movement. As the column expanded, the relative linear displacement was measured by the LVDT. The accuracy of the LVDT used to measure the circumferential expansion was ±0.01 mm at full scale. Measurement readings for all the instrumentation including applied load were taken once every second by an Amplicon PC226 data acquisition board and logged on a Pentium computer.

3.3.2 Loading regime

Specimens up to 150 mm diameter were tested in a 2,000 kN Losenhausen test machine, operating in displacement control. The 300 mm and 400 mm diameter specimens were tested at the BRE in a 10,000 kN Amsler test rig. The specimens were aligned centrally in the testing machine using specially fabricated steel plates with a 5 mm recess to locate the specimen. A thin layer of cement grout was used to remove any surface imperfections, and a pre-load of 1.5 N/mm^2 was applied to the specimen for 24 hours whilst the grout hardened. The end details of the specimens were such that the FRP-composite and concrete were loaded simultaneously with identical overall strain. The instrumentation and general test arrangement is shown in Plate 3.2.

The majority of specimens were tested in monotonically increasing uniaxial compression with a constant displacement increment. The platen displacement rate was proportional to the diameter of the specimen and calculated using the following relationship:

$$\text{Platen displacement rate} = 0.002D \text{ mm/min}$$

Due to limitations imposed by the test machines at the BRE, the 300 mm and 400 mm diameter stub columns were tested under constant load increments. The loading rate used in

all the tests was 1.5 N/mm^2/min. The duration of a test was approximately 40 minutes. Measurements of applied axial load, platen displacement, axial strain and circumferential strain were taken continuously throughout the test.

3.4 EXPERIMENTAL BEHAVIOUR

The stub columns were tested 28 days after casting. Until 50 percent of the ultimate load was applied, there were no visible signs of distress to the stub columns. As the load increased, the failure of individual fibres could be heard and whitening of the resin occurred at discrete intervals along the length of the column, due to light reflection from the interfaces where localised bond breakdown occurred between the fibres and resin. The observed peak strength in the columns generally corresponded to failure of the FRP-composite, except when the angle of fibre orientation was less than 45 degrees. Once the FRP-composite failed, and there was no confinement to the concrete core, the specimen failed in a sudden brittle manner. The failure loads of the confined stub columns and the measured axial and circumferential strains are summarised in Table 3.6 and Table 3.7.

The angle of fibre orientation in the FRP-composite influenced the failure mode of the stub columns. The failure mode of the stub columns reinforced with a 90 degree fibre orientation are typified by the fibres rupturing and unwrapping about the middle third of the specimens. The failure mode of a stub column reinforced with a 90 degree fibre orientation is illustrated in Plate 3.3. Stub columns confined by a 67½ degree fibre orientation failed by the FRP-composite rupturing in a single vertical split along the entire length of the composite, as shown in Plate 3.4. This mode of failure was more sudden and catastrophic than the failure of the 90 degree stub columns. Initial signs of failure in the stub columns reinforced with a 45 degree FRP-composite was local buckling of the FRP-composite tube and delamination of the outer fibres. Ultimate failure of the stub columns was again due to rupture of the FRP-composite which was characterised by the zigzag pattern of angle tears shown in Plate 3.5. The zigzag pattern of angle tears was a result of localised imperfection due to the fibre crossovers that occur in helical wound FRP-composites. A comparison of the three different modes of failure described above are illustrated in Plate 3.6.

3.4.1 Ultimate failure

All the confined concrete specimens exhibited an increase in compressive strength and ductility compared to plain concrete, as shown in Figure 3.3. The greatest enhancement in strength was observed in the specimens with a nominal 90 degree fibre orientation, for a

given specimen diameter and thickness of FRP-composite. As the angle of fibre orientation tended towards 45 degrees, the enhancement in strength and ductility was found to diminish.

The experimental failure strength of the confined concrete ranges from 30.9 N/mm^2 for a FRP-composite with an effective hoop modulus of 305 N/mm^2, to 186.4 N/mm^2 for an effective hoop modulus of 2,717 N/mm^2. The relationship between the ultimate failure strength of the FRP-confined concrete and the effective hoop modulus of the composite jacket is given in Figure 3.4. The ultimate failure strength of the confined concrete is linearly proportional to the effective hoop modulus of the FRP-composite jacket. The higher compressive strengths achieved using FRP-composite confinement are comparable to or exceed the compressive strengths obtained by high-strength concrete but use traditional concrete mix specifications.

3.4.2 Stress-strain characteristics

The stress-strain behaviour of concrete confined by an FRP-composite material is approximately bilinear. Generally, no descending branch to the curve was observed, accept when the concrete was confined by a nominal 45 degree fibre orientation. Typical stress-strain curves for concrete confined by FRP-composites with different angles of fibre orientation are shown in Figure 3.5 and Figure 3.6. Initially, there is no confining action from the FRP-composite, and the behaviour is similar to plain concrete. Increasing axial compression causes the concrete to expand laterally due to Poisson's effects, causing tensile hoop stress to develop in the FRP-composite tube, and a lateral confining pressure on the concrete.

Further increases in axial compression cause micro-cracks to develop in the concrete, resulting in an increase in the rate of lateral expansion of the concrete and the magnitude of the confining pressure. However, associated with this increasing rate of lateral expansion due to crack propagation, is a reduction in the axial stiffness of the concrete. The stress-strain curve enters a transition zone, where the FRP-composite exerts a lateral pressure on the concrete, inhibiting crack propagation and counteracting the reduction in axial stiffness of the concrete. Once the unconfined strength of the concrete is exceeded, the concrete enters a post-crushing region where the stiffness has stabilised to a constant value. The stiffness of the concrete in the post-crushing region depends on the fibre orientation of the composite, with the greatest stiffness being observed for hoop wound composites.

In Figure 3.7, which shows the stress-strain curves for the 60 mm specimens, the stress-strain curve is extremely unstable with large drops in load. The maximum size of the aggregate

used to fill the 60 mm diameter FRP composite tubes was 20 mm. Consequently scaling factors influenced the specimens and the measured strains were predominately the strains in individual aggregate particles. Furthermore, movement of the aggregate particles within the tubes resulted in the sudden drops in load-carrying capacity. Therefore, the results for the 60 mm specimens are neglected in the subsequent analysis of the experimental data.

The stress-strain behaviour and the failure mode of specimens with a nominal 45 degree winding angle were unique. The initial stress-strain behaviour of the confined concrete shown in Figure 3.8 was similar to that of plain concrete. However, once the curve enters the transition zone, the low effective hoop modulus of the FRP-composite was unable to prevent the stress-strain curve decaying due to unstable crack propagation in the concrete. Disruption of the concrete was prevented by the FRP composite which allowed the specimens to undergo a significant axial deformation beyond the peak stress. Load was removed before complete failure of the FRP-composite was achieved in the specimens, although there was extensive delamination of the outer fibre layers.

Stress-strain curves for all the specimens are given in Appendix B. The stress-strain behaviour of the majority of the specimens were similar, with the three typical regions being observed:

- the initial unconfined behaviour;
- the transition zone;
- and the post-crushing region.

3.4.3 Initial tangent modulus

The initial modulus of elasticity of plain concrete is a function of the compressive strength, with higher values of the modulus corresponding to higher concrete strengths. The traditional empirical relationship between the compressive strength and initial modulus of elasticity of concrete is typically of the form:

$$E_{ci} = m f_c^{1/n} \qquad (3.2)$$

Where m and n are empirically derived constants. Substituting the constants defined in the CEB-FIP Model Code [71] into equation 3.2, the initial tangent modulus of unconfined concrete is defined by the expression:

$$E_{ci} = 21500 \left(\frac{f_{co}}{10} \right)^{1/3} \qquad (3.3)$$

Experimental values for the initial tangent modulus of concrete confined by FRP-composites are given in Table 3.8. The experimental initial tangent moduli were determined from the slope of the stress-strain curves at a stress of $0.30f_{co}$. A comparison of the initial tangent modulus of confined concrete with the initial tangent modulus of control specimens, shown in Figure 3.9, illustrates that presence of confinement from FRP-composite reinforcement has a negligible effect on the initial tangent modulus of concrete. This is because the confinement provided is passive and negligible confining stresses are present when the axial stress level in the concrete is below $0.30f_{co}$ [72].

3.4.4 Post-crushing tangent modulus

The main characteristic of concrete confined by FRP-composites is the quasi linear-elastic behaviour of concrete beyond its unconfined compressive strength. The stiffness of the confined concrete beyond its unconfined compressive strength has been termed the post-crushing tangent modulus. Experimental values for the post-crushing tangent modulus of the confined concrete are given in Table 3.8. The experimental values for the post-crushing modulus were determined using linear regression analysis between axial strains of approximately $6{,}000\mu\varepsilon$ and ε_{cc}. Figure 3.10 illustrates that the tangential stiffness of the concrete in the post-crushing region increases as the orientation of fibres in the FRP-composite tends towards 90 degrees. The post-crushing tangent moduli for the specimens confined by FRP-composites with fibre orientations of approximately 45 degrees were found to have a negative slope. When the angle of fibre orientation was increased to 57.8 degrees, the post-crushing tangent modulus increased to 1,264 N/mm^2.

The influence of the effective hoop modulus on the post-crushing tangent modulus is shown in Figure 3.11. Provided the effective hoop modulus is greater than 977 N/mm^2, the relationship is found to be linear. However, if the effective hoop modulus is less than 590 N/mm^2, full confinement of the concrete does not occur and the post-crushing tangent modulus becomes negative.

3.4.5 Stress-volumetric strain characteristics

In a polar axisymmetric state of stress, volumetric strain is defined as the volume change per unit volume.

$$\begin{aligned}\varepsilon_v &= \frac{\Delta V}{V} = (1+\varepsilon_x)(1+\varepsilon_r)^2 - 1 \\ &= \varepsilon_x + 2\varepsilon_r + 2\varepsilon_x\varepsilon_r + \varepsilon_x\varepsilon_r^2 + \varepsilon_r^2 \\ &\approx \varepsilon_x + 2\varepsilon_r \qquad \text{for small strains}\end{aligned} \tag{3.4}$$

The typical volumetric strain behaviour of concrete in uniaxial compression is illustrated in Figure 3.12. The initial σ–ε_v behaviour of plain concrete is approximately linear and represents the pre-cracked elastic response of the material. The concrete undergoes a net volume reduction up to about $0.75f_{co}$ to $0.90f_{co}$. Beyond this stress level, the direction of change in volumetric strain is reversed, resulting in an unstable inelastic volume expansion at a stress level of approximately f_{co}. The stress corresponding to the minimum value of volumetric strain is termed the *critical stress* [72]. The *critical stress* corresponds to the development of unstable crack propagation in the concrete matrix where the level of internal energy exceeds the crack release energy.

Typical plots of the volumetric strain behaviour of concrete confined by FRP composites are shown in Figure 3.13 and Figure 3.14. Stress-volumetric strain curves for all the specimens are given in Appendix C. Initially, the behaviour is identical to plain concrete for all fibre orientations, with the concrete undergoing a net volume reduction up to the critical stress. Beyond the critical stress, a check on the contraction or a small net volumetric expansion is observed in the concrete confined by hoop wound fibres. Finally, the confining pressure overcomes the volume expansion and re-establishes the original direction of volumetric change. This final phenomenon was not observed in specimens confined by composites with either a 45 degree or 67½ degree fibre orientation due to their lower elastic hoop modulus. Thus, provided the effective hoop modulus of a hoop wound fibre composite is greater than 1,137 N/mm^2, the propagation of micro-cracks in the concrete can be inhibited, thereby curtailing the unstable volumetric expansion of the concrete.

3.4.6 Poisson's ratio

The Poisson's ratio was taken as the ratio between the mean circumferential strain and the mean axial strain. The initial Poisson's ratio for specimens varied from between 0.12 to 0.25. The Poisson's ratio for normal weight concrete subjected to uniaxial compressive stress in the elastic region is generally in the range 0.11 to 0.21, with 0.20 being a representative value [73]. The non-linear behaviour of concrete at higher strains causes the Poisson's ratio to increase rapidly due to the formation of cracks. This increase in the Poisson's ratio of concrete results in the dilatancy phenomenon observed in unconfined concrete as it approaches its ultimate strength.

The true Poisson's ratio of any homogenous material cannot exceed $\nu = 0.50$, the Poisson's ratio for an incompressible material. However, the concrete is no longer a continuous solid material due to the formation of cracks and therefore, only an 'apparent' Poisson's ratio is

measured. The 'apparent' Poisson's ratio of concrete can exceed the limiting value of an incompressible material due to wedging action and the opening of cleavage planes in the concrete and also due to local buckling of the FRP-composite tube. This behaviour is consistent with that of concrete-filled steel tubes, where the measured apparent Poisson's ratio has been found to vary from 0.11 to 0.75 [36, 40].

The apparent Poisson's ratios of the concrete-filled fibre composite tubes before failure are given in Table 3.7. The variation of the measured apparent Poisson's ratio with the angle of fibre orientation is shown in Figure 3.15. The apparent Poisson ratio is generally less than 0.50 for the specimens confined by hoop wound fibres. However, as the angle of fibre orientation tends towards 45 degrees, the value of the apparent Poisson's ratio increases significantly. This increase in the apparent Poisson's ratio is due to the low hoop modulus of elasticity of the FRP composite which enables cleavage planes and wedging action to form more easily in the concrete core. Local buckling of the FRP-composite was also observed in the 45 degree specimens.

3.5 SUMMARY

FRP-composite materials can be used as lateral confinement to enhance the compressive strength and ductility of concrete. The degree of strength enhancement was found to be linearly proportional to the effective hoop modulus of the FRP-composite. The magnitude of the effective hoop modulus is highly dependent on the orientation of fibres in the composite. Consequently, the greatest enhancement in strength was observed in specimens where the fibres were orientated predominately in the hoop direction, with strength enhancements between $2.29f_{cu}$ and $9.46f_{co}$. The corresponding increase in ductility ranged from $9.27\varepsilon_{co}$ to $20.35\varepsilon_{co}$.

As the orientation of the fibres tends towards 45 degrees, the magnitude of the effective hoop modulus diminishes. Consequently, there is a smaller strength enhancement observed in the specimens with off-axis lateral reinforcement. However, the specimens with fibre orientations of 67.5 degrees and 45 degrees still exhibited an enhancement in ductility since structural integrity of the concrete was maintained by the FRP-composite.

The stress-strain behaviour of the concrete consists of three distinct regions:

1. Initially, the behaviour of the concrete is identical to unconfined concrete, since any initial confining stresses are small.

2. As axial strains increase, the rate of lateral expansion of the concrete increases, causing tensile hoop stresses to develop in the FRP-composite. There is also an associated reduction in the axial stiffness of the concrete due to the development of concrete micro-cracks. However, the increasing lateral confinement inhibits crack propagation and counteracts the reduction in stiffness of the concrete core.
3. Once the unconfined strength of concrete has been exceeded, the axial stiffness of the concrete stabilises to a constant value. This region has been termed the *post-crushing zone*. The axial stiffness of the concrete in the post-crushing zone is found to be directly proportional to the effective hoop modulus of the concrete.

Diameter mm	Angle of Fibre Orientation		
	90°	67½°	45°
60	2		
80	2	2	2
100	2	2	2
125	2		
150	2	2	2
300	2		
400	2		

Table 3.1. Summary of stub column tests for concrete-filled FRP-composite tubes

Institution	Cube Strength	Ordinary Portland Cement	Water	Aggregate, kg		
	N/mm^2	kg	kg	Sand	10 mm	20 mm
University of Southampton	25	271	190	792	405	645
	35	345	190	786	402	640
Building Research Establishment	25	210	197	830	367	734
	35	262	197	755	377	755

Table 3.2 Concrete mix specification

Average Internal Diameter† mm	S. D. mm	Average Thickness‡ mm	S. D. mm	Angle of Wind	Fibre Volume Fraction
59.90	0.02	2.53	0.14	75.5	0.57
79.89	0.08	2.45	0.10	78.1	0.63
79.90	0.04	2.58	0.34	57.8	0.55
79.91	0.06	2.63	0.15	43.4	0.55
100.09	0.18	2.48	0.17	80.4	0.62
100.08	0.13	2.28	0.13	71.4	0.53
100.14	0.15	2.22	0.09	49.9	0.51
125.64	0.12	2.24	0.23	82.3	0.62
150.40	0.17	2.46	0.10	83.6	0.61
150.08	0.19	2.35	0.26	71.3	0.52
150.35	0.21	2.61	0.49	48.0	0.47
200.64	0.18	2.12	0.08	85.2	0.62
300.67	0.05	3.48	0.07	86.8	0.64
299.53	0.07	4.12	0.08	86.8	0.64
399.67	0.16	5.06	0.08	87.6	0.61
400.08	0.14	5.08	0.05	87.6	0.61

† The average internal diameter is based on five measurements taken at both ends of all the tubes.

‡ The average wall thickness is based on five measurements taken at both ends of all the tubes

Table 3.3. Geometry and dimensions of filament wound tubes

Property	E-glass RO99 2400 P122	Epophen Resin EL-62
Specific Gravity	2.56	1.20
Tensile strength, N/mm^2	3448	85
Modulus of Elasticity, kN/mm^2	75.90	2.35
Shear Modulus, kN/mm^2	31.11	0.89
Poisson's ratio	0.22	0.32

Table 3.4 Mechanical properties of the E-glass fibres and epoxy resin

Nominal Diameter	Angle of Wind	E_{xx} kN/mm^2	$E_{\theta\theta}$ kN/mm^2	$G_{x\theta}$ kN/mm^2	$\nu_{x\theta}$	$\nu_{\theta x}$	$\bar{E}_{\theta\theta}$ kN/mm^2
60	75.5	9.51	38.19	5.19	0.12	0.48	3.226
80	78.1	11.49	44.30	5.19	0.10	0.40	2.717
	57.8	7.95	17.86	10.28	0.38	0.85	1.153
	43.4	10.00	8.97	11.97	0.71	0.64	0.590
100	80.4	11.28	45.14	4.51	0.09	0.35	2.237
	71.4	8.28	31.89	5.92	0.16	0.62	1.453
	49.9	7.54	10.56	10.87	0.56	0.79	0.468
125	82.3	11.37	46.15	4.12	0.08	0.32	1.645
150	83.6	11.09	45.99	3.80	0.07	0.30	1.504
	71.3	8.06	31.19	5.83	0.16	0.62	0.977
	48.0	7.12	8.80	10.17	0.61	0.75	0.305
200	85.2	11.47	47.25	3.69	0.07	0.28	0.998
300	86.8	12.22	49.10	3.74	0.07	0.27	1.137
400	87.6	11.19	47.04	3.38	0.06	0.27	1.191

Table 3.5. Mechanical properties of filament wound tubes

Diameter mm	Angle of wind	Cube strength f_{cu} N/mm^2	Concrete strength f_{co} N/mm^2	Failure stress f_{cc} N/mm^2	$\frac{f_{cc}}{f_{co}}$
60	75.5	21.5	17.8	158.0	8.88
		27.2	22.6	147.7	6.54
80	78.1	23.4	18.7	177.3	9.46
		35.2	28.1	186.4	6.62
	57.8	22.6	18.1	114.2	6.32
		32.8	26.3	154.5	5.88
	43.4	29.5	23.6	49.7	2.10
		31.3	23.6	46.6	1.98
100	80.4	19.7	16.1	123.9	7.68
		36.2	29.7	144.2	4.85
	71.4	28.2	23.1	104.3	5.04
		25.6	17.6	116.3	5.93
	49.9	31.2	25.6	50.5	1.97
		24.6	20.2	52.6	2.60
125	82.3	29.2	23.9	119.0	4.98
		37.5	30.8	118.9	3.86
150	83.6	27.4	22.5	103.5	4.60
		46.3	37.8	109.9‡	2.91
	71.3	32.7	26.8	77.0	2.87
		31.7	26.0	78.4	2.70
	48.0	27.6	22.6	30.9	1.37
		44.7	36.6	45.0	1.23
300	86.8	34.0	28.2	84.9	3.01
		38.6	32.0	85.9	2.68
400	87.6	32.3	26.8	80.8‡	3.02
		40.8	33.9	77.6‡	2.29

‡ Failure load exceeded capacity of testing machine

Table 3.6. Confined compressive strength of axially loaded FRP-confined concrete stub columns

Diameter mm	Angle of wind	Cube strength f_{cu} N/mm^2	Axial strain $\mu\varepsilon_{cc}$	Circumferential strain $\mu\varepsilon_{\theta\theta}$	Apparent Poisson's ratio ν_a
60	75.5	21.5	44,600	-12,500	0.28
		27.2	40,500	-11,600	0.29
80	78.1	23.4	46,100	-16,300	0.35
		35.2	48,300	-15,700	0.32
	57.8	22.6	76,200	-49,800	0.65
		32.8	54,400	-30,800	0.57
	43.4	29.5	10,900	-12,100	1.11
		31.3	11,400	-14,600	1.28
100	80.4	19.7	38,300	-13,000	0.34
		36.2	31,700	-12,300	0.39
	71.4	25.6	51,600	-34,200	0.66
		28.2	53,600	-32,800	0.61
	49.9	24.6	39,300	-39,400	1.00
		31.2	59,100	-54,600	0.92
125	82.3	29.2	38,500	-14,100	0.37
		37.5	34,000	-12,800	0.38
150	83.6	27.4	37,100	-13,600	0.37
		46.3	25,000	-12,800	0.51
	71.3	32.7	32,300	-18,900	0.58
		31.7	33,900	-20,400	0.60
	48.0	27.6	20,000	-19,400	0.97
		44.7	9,700	-11,800	1.21
300	86.8	34.0	32,200	-13,400	0.42
		38.6	22,400	-13,200	0.59
400	87.6	32.3	28,000	-12,900	0.46
		40.8	21,900	-12,900	0.60

Table 3.7. Ultimate axial strains and circumferential strains measured in axially loaded FRP-confined concrete stub columns

Diameter mm	Angle of wind	Cube strength f_{cu} N/mm^2	Initial tangent modulus E_{ci} N/mm^2	Post-crushing tangent modulus E_{px} N/mm^2
60	75.5	21.5	19,860	2,920
		27.2	21,010	2,560
80	78.1	23.4	23,430	3,315
		35.2	35,170	3,320
	57.8	22.6	22,570	1,264
		32.8	32,830	1,702
	43.4	29.5	29,530	-200
		31.3	28,521	-400
100	80.4	19.7	25,214	2,841
		36.2	30,913	2,856
	71.4	25.6	28,421	1,772
		28.2	22,664	1,623
	49.9	24.6	29,764	98
		31.2	18,589	61
125	82.3	29.2	23,980	2,151
		37.5	27,928	2,094
150	83.6	27.4	27,248	2,004
		46.3	37,943	2,091
	71.3	32.7	29,860	1,250
		31.7	30,303	1,234
	48.0	27.6	31,067	-100
		44.7	33,974	-500
300	86.8	34.0	34,628	1,743
		38.6	35,770	1,786
400	87.6	32.3	21,843	1,989
		40.8	36,948	1,628

Table 3.8. Initial tangent moduli and post-crushing tangent moduli of axially loaded FRP-confined concrete stub columns

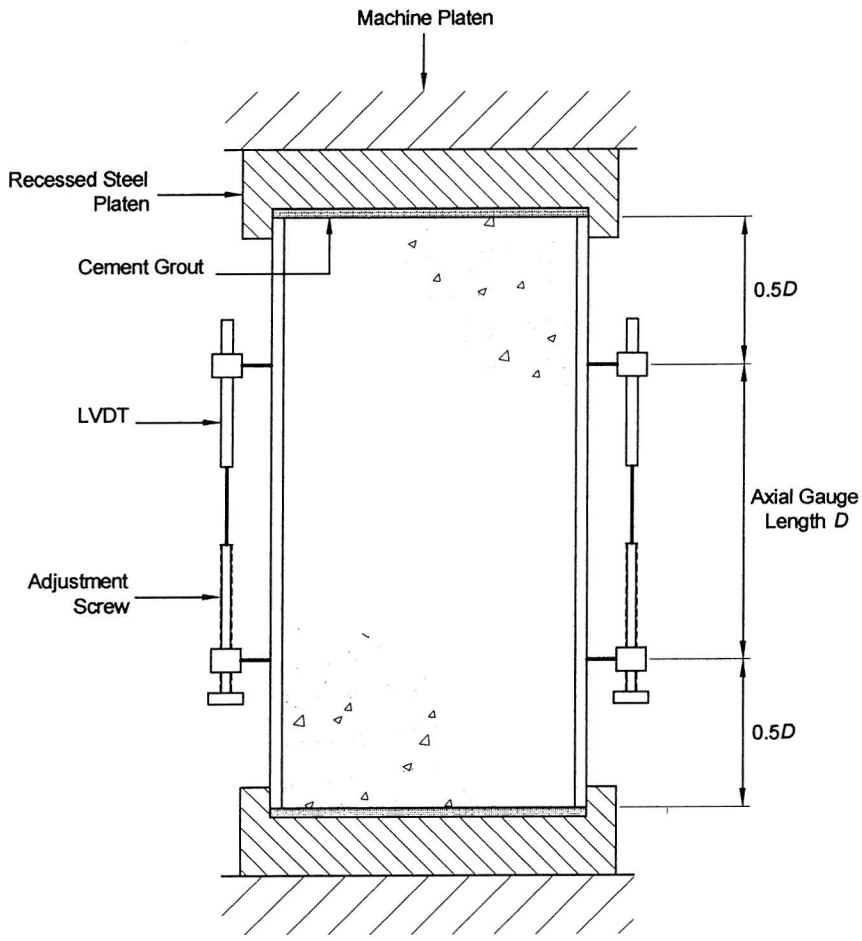

Figure 3.1. Axial extensometer

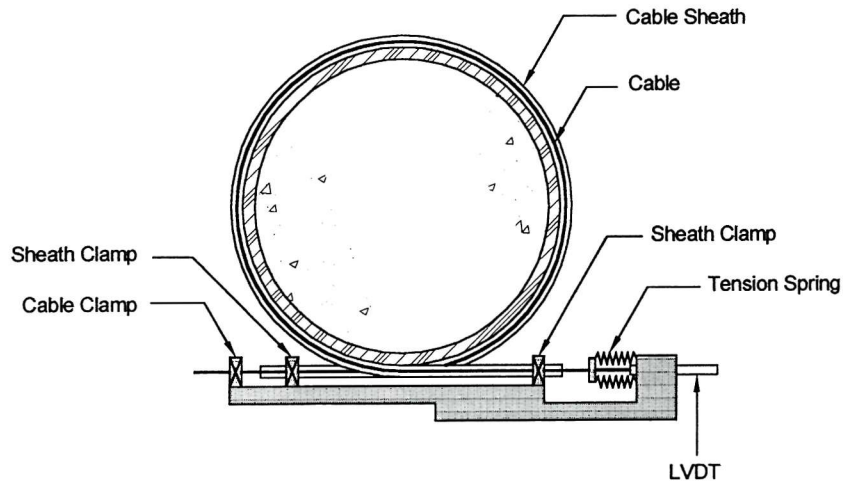

Figure 3.2. Circumferential extensometer

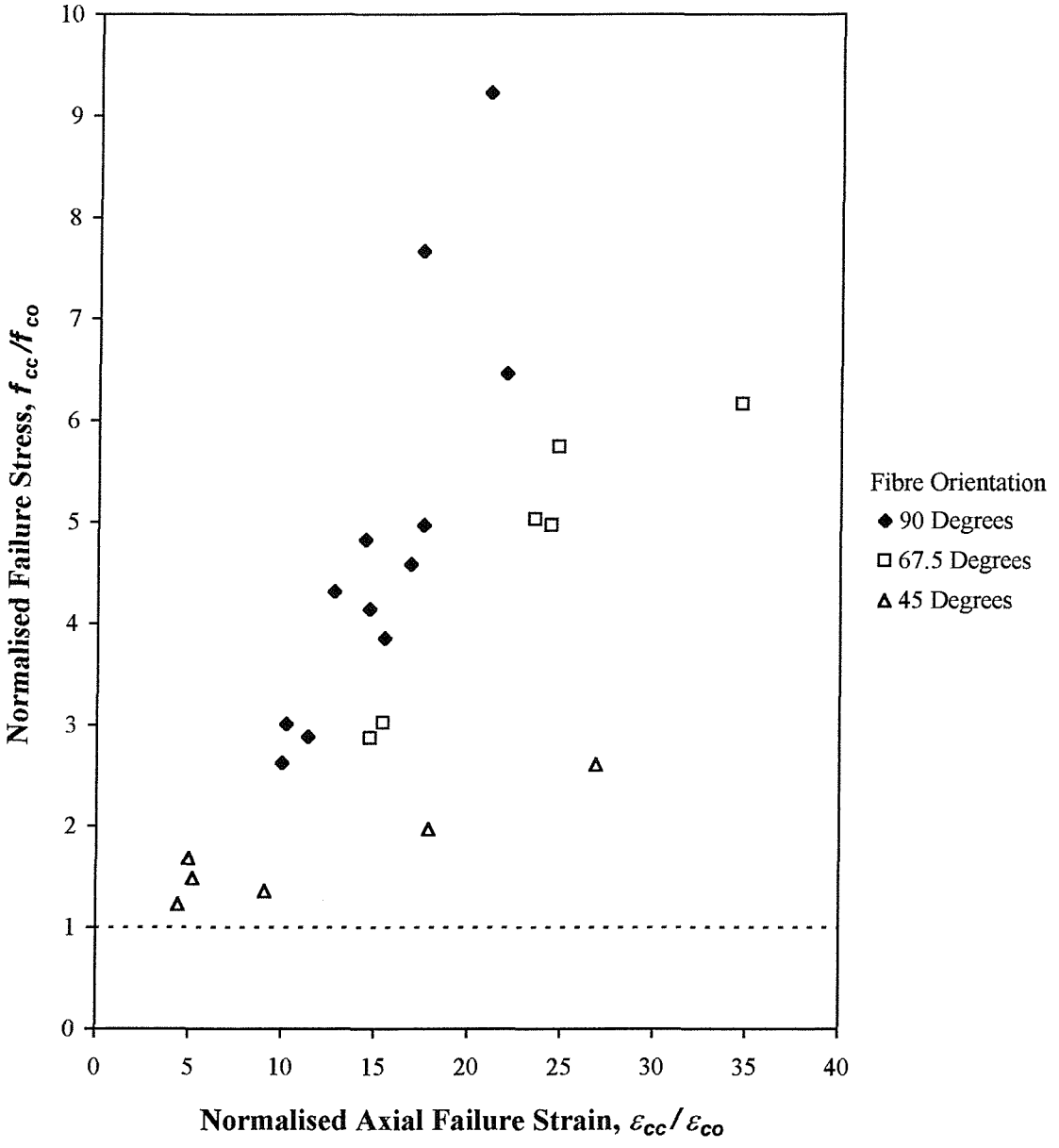

Figure 3.3. Normalised failure stress versus normalised axial failure strain of FRP-confined concrete stub columns

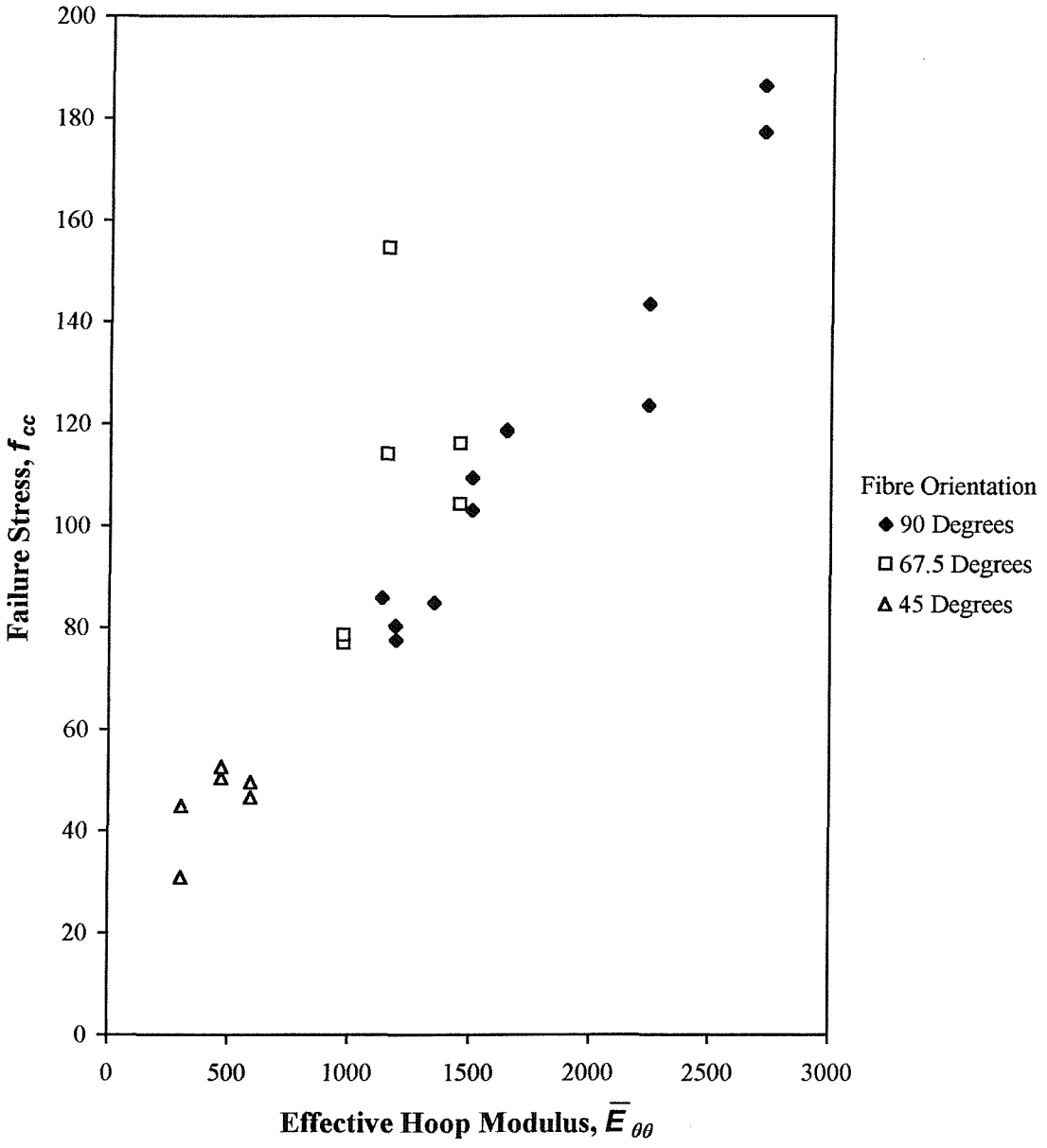

Figure 3.4. The influence of the effective hoop modulus of the composite jacket on the ultimate failure stress of confined concrete

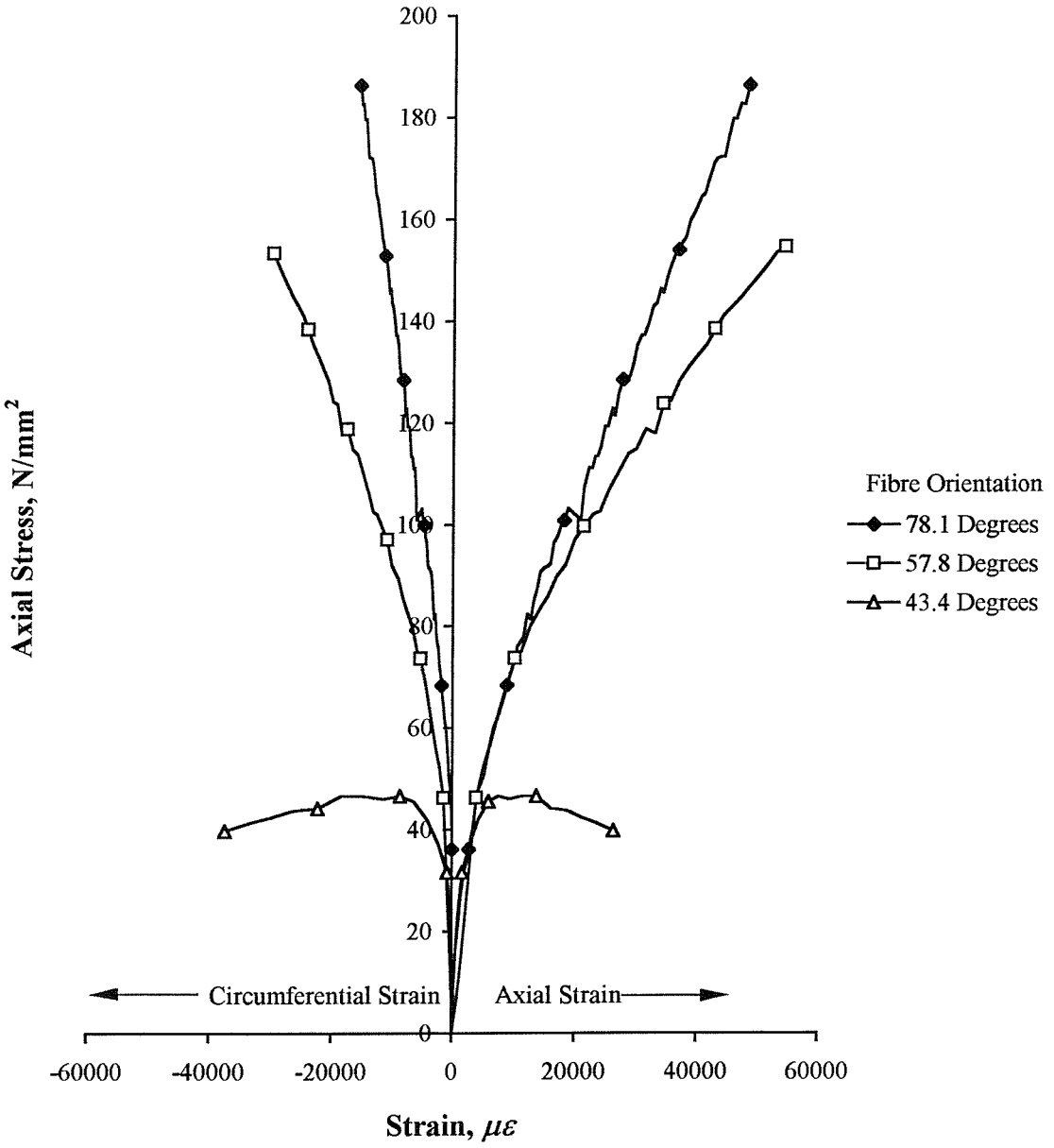

Figure 3.5. Stress-strain curves for the 80 mm diameter concrete-filled filament wound tubes

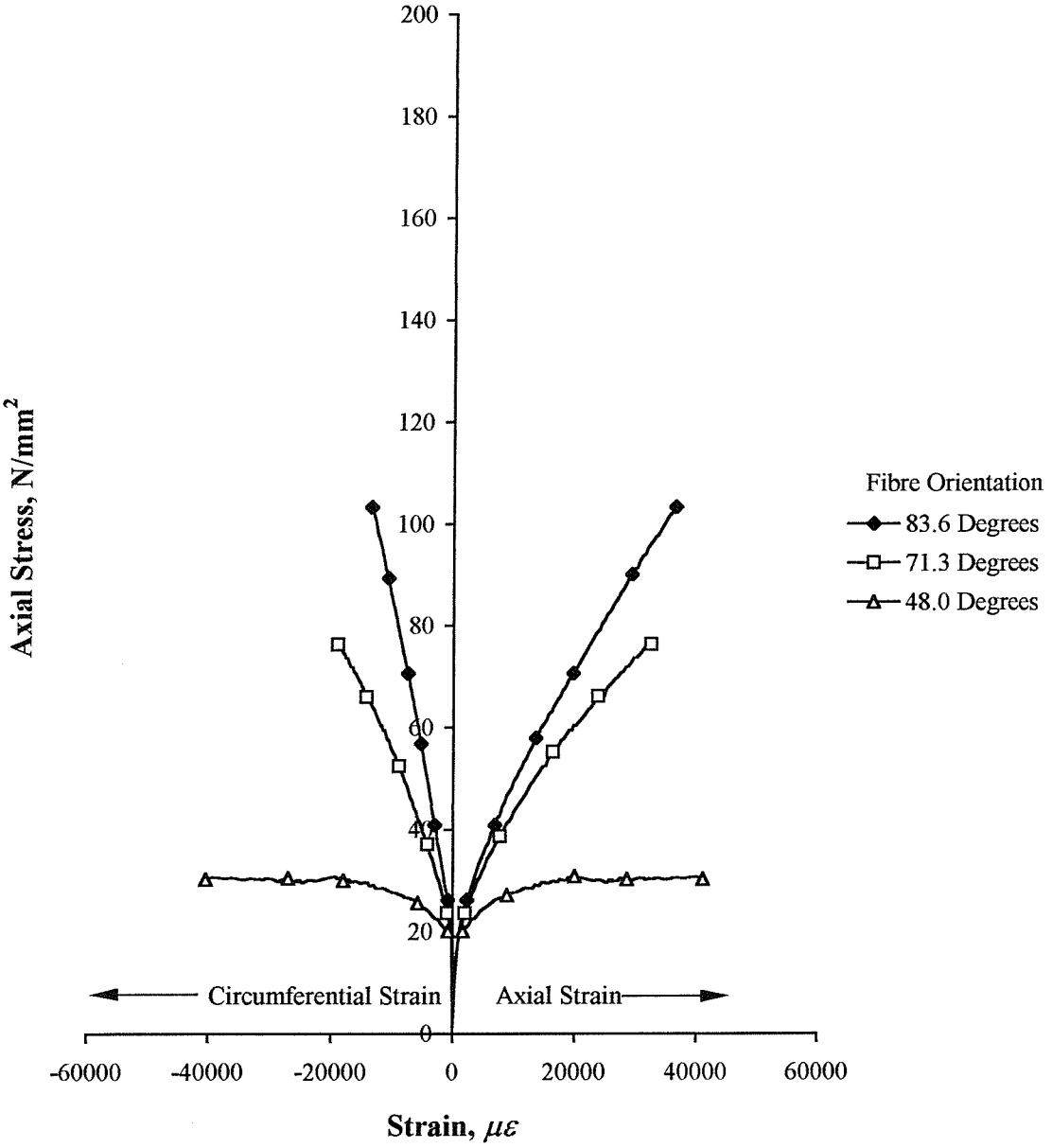

Figure 3.6. Stress-strain curves for the 150 mm diameter concrete-filled filament wound tubes

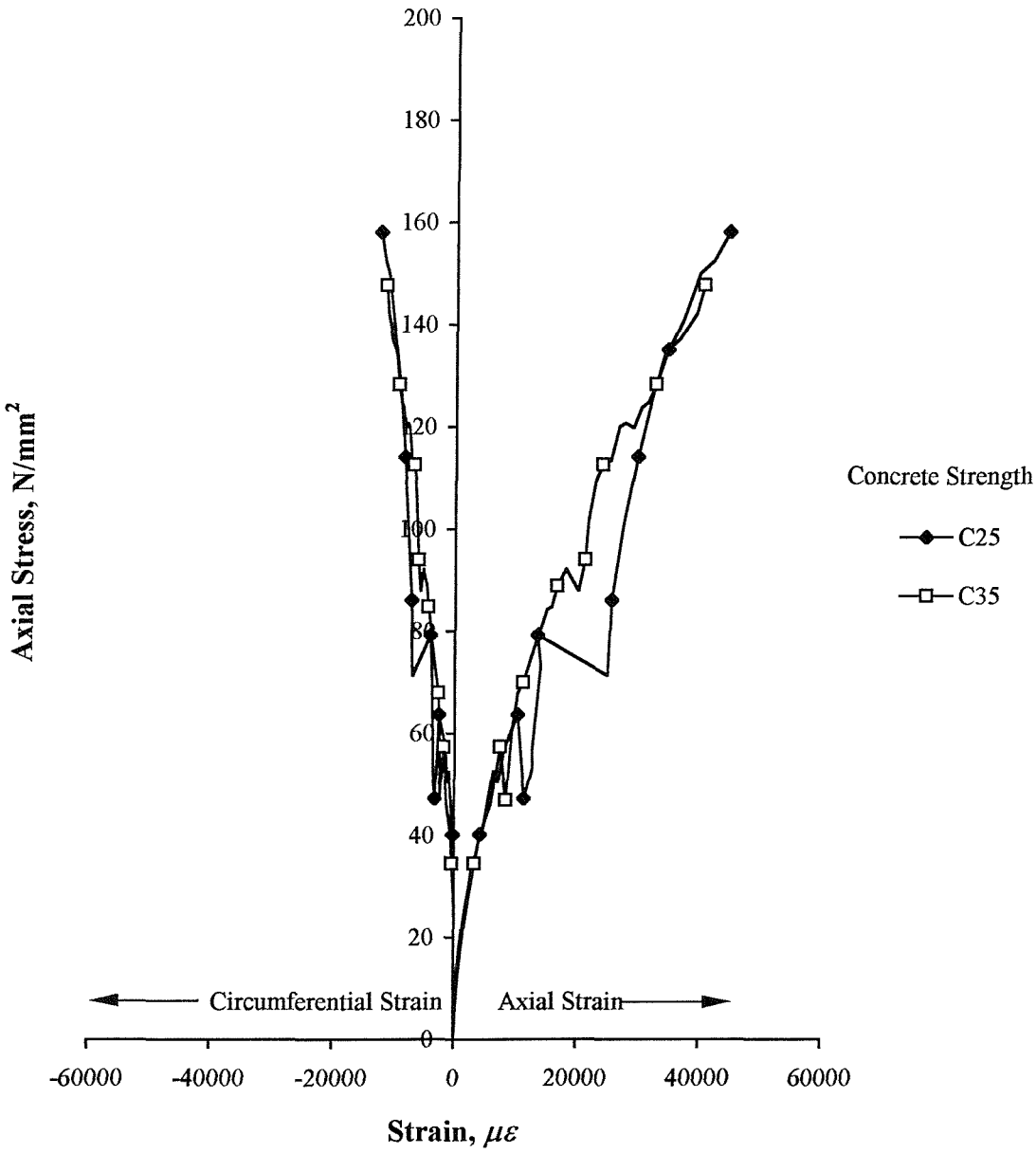

Figure 3.7. Stress-strain curves for the 60 mm diameter concrete-filled filament wound tubes

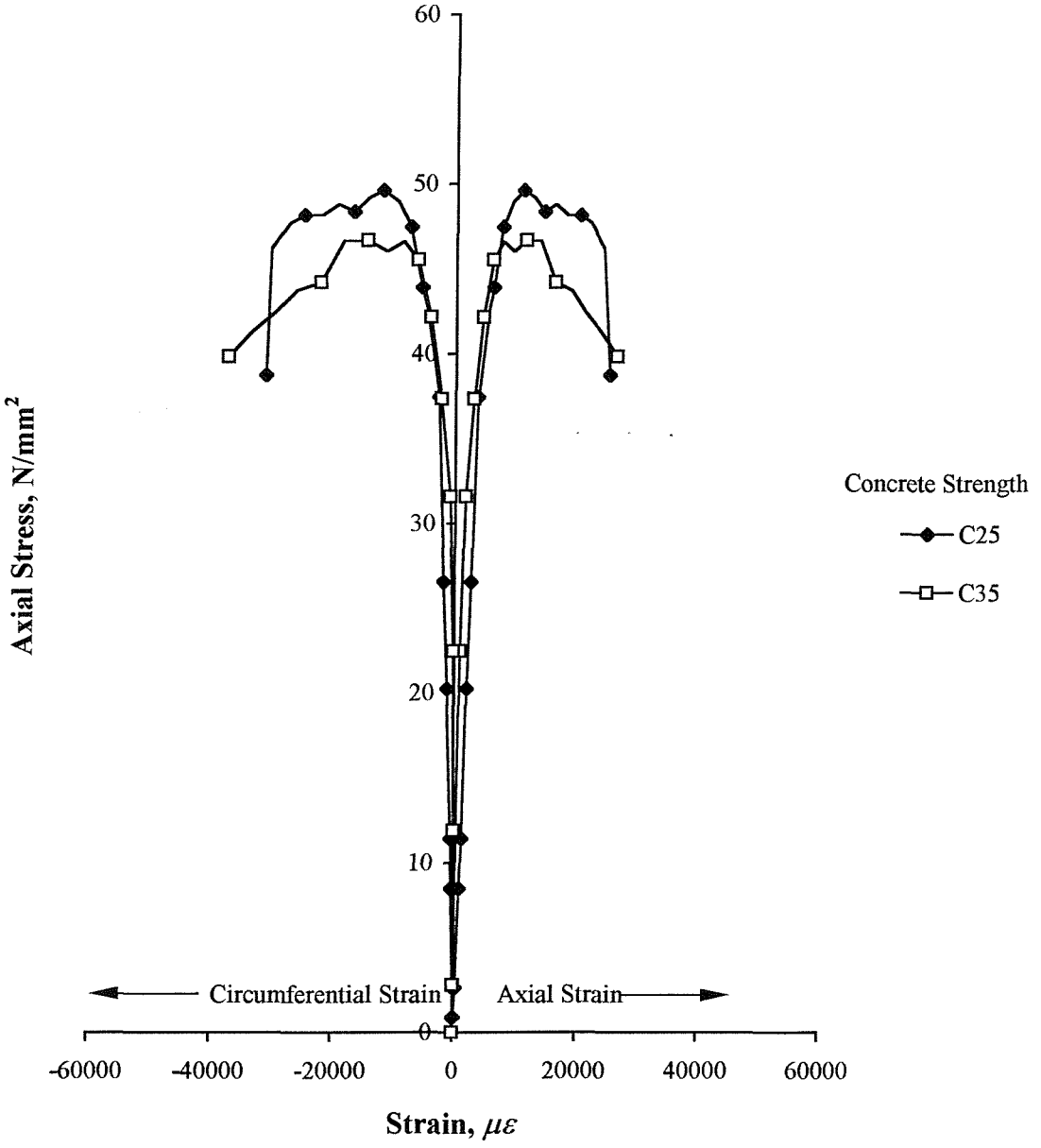

Figure 3.8. Stress-strain curves for the 80 mm diameter concrete-filled filament wound tubes with a fibre orientation of 43.4 degrees

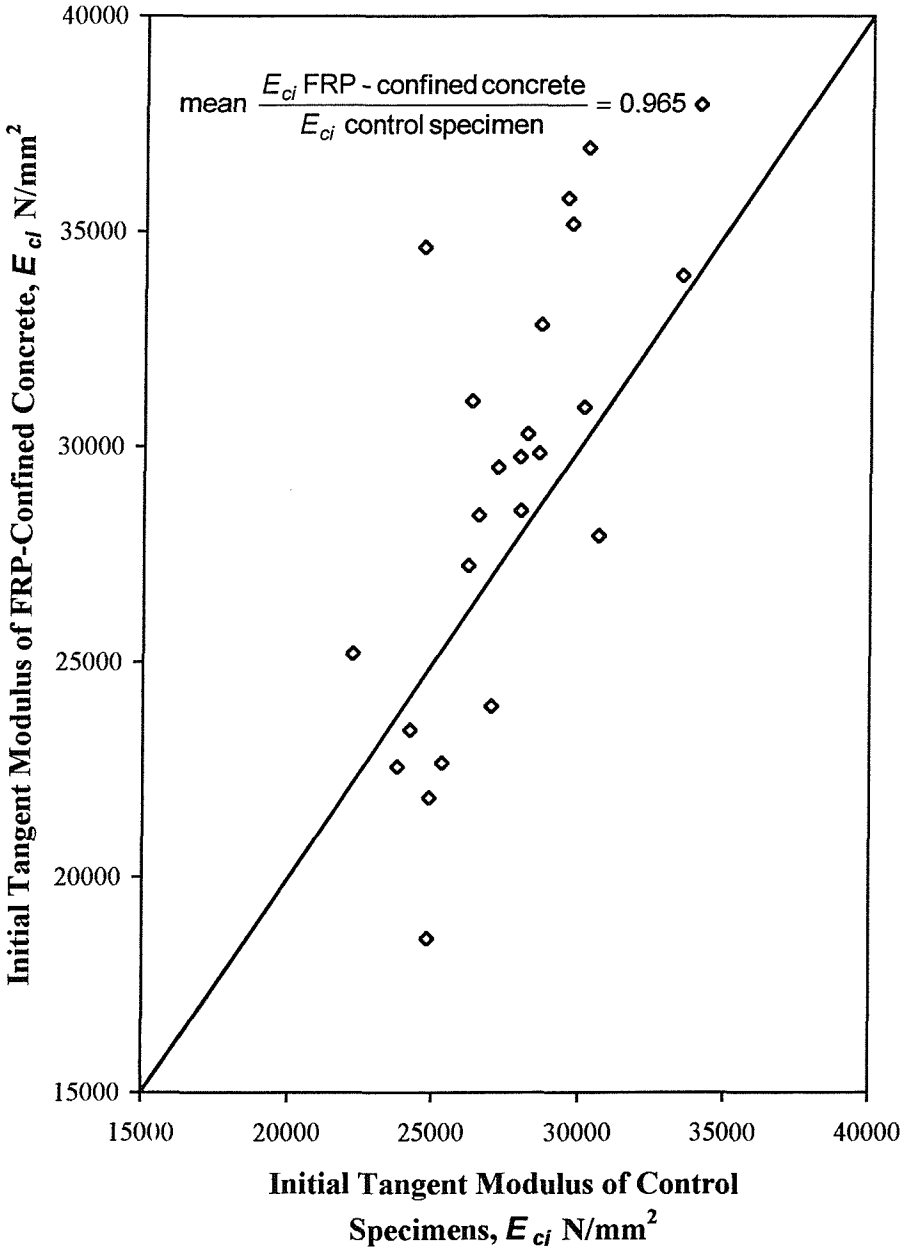

Figure 3.9. Initial tangent modulus of control specimens versus the initial tangent modulus of FRP-confined concrete

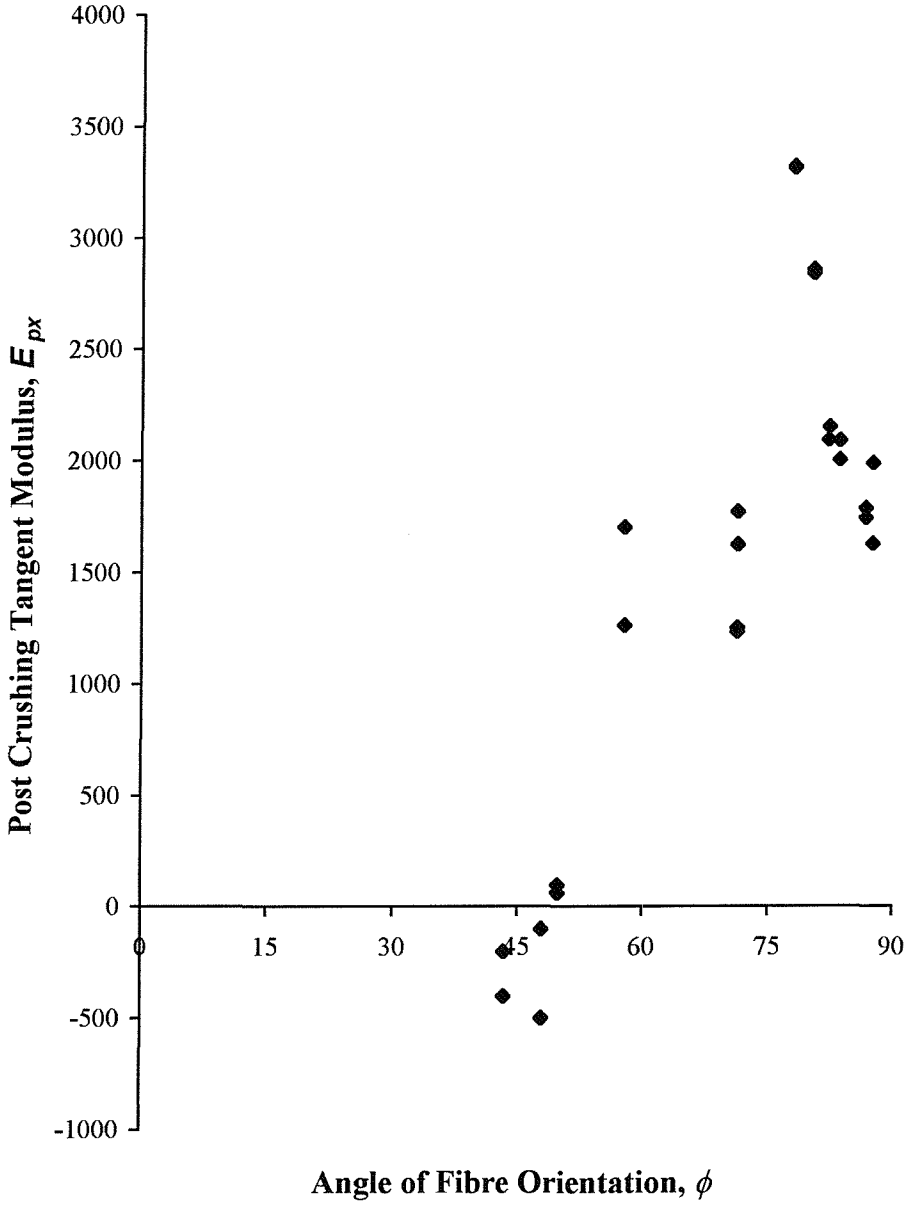

Figure 3.10. The variation in the post-crushing tangent modulus of FRP-confined concrete with fibre orientation

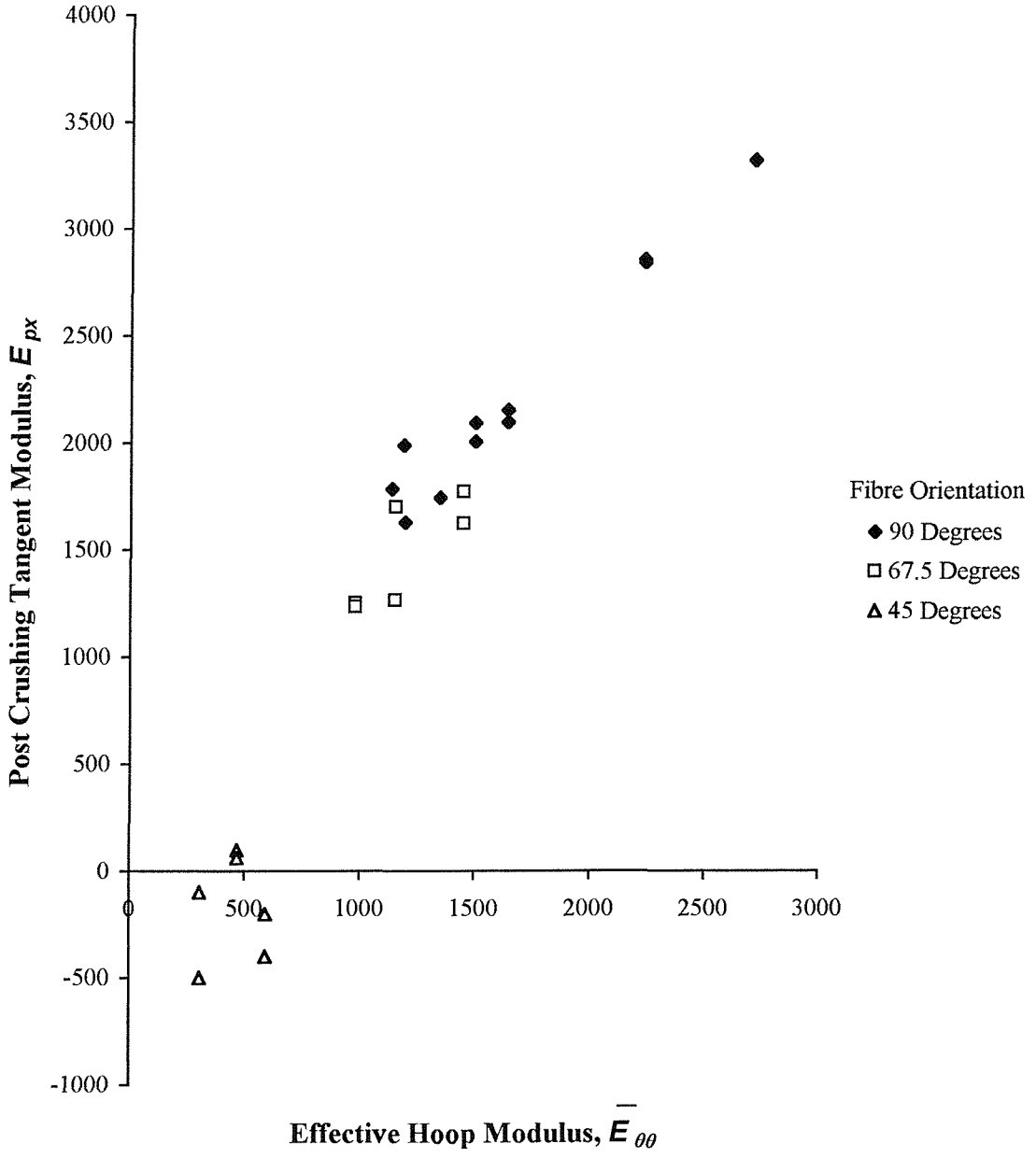

Figure 3.11. The post-crushing tangent modulus of FRP-confined concrete as a function of the effective hoop modulus of the FRP- composite

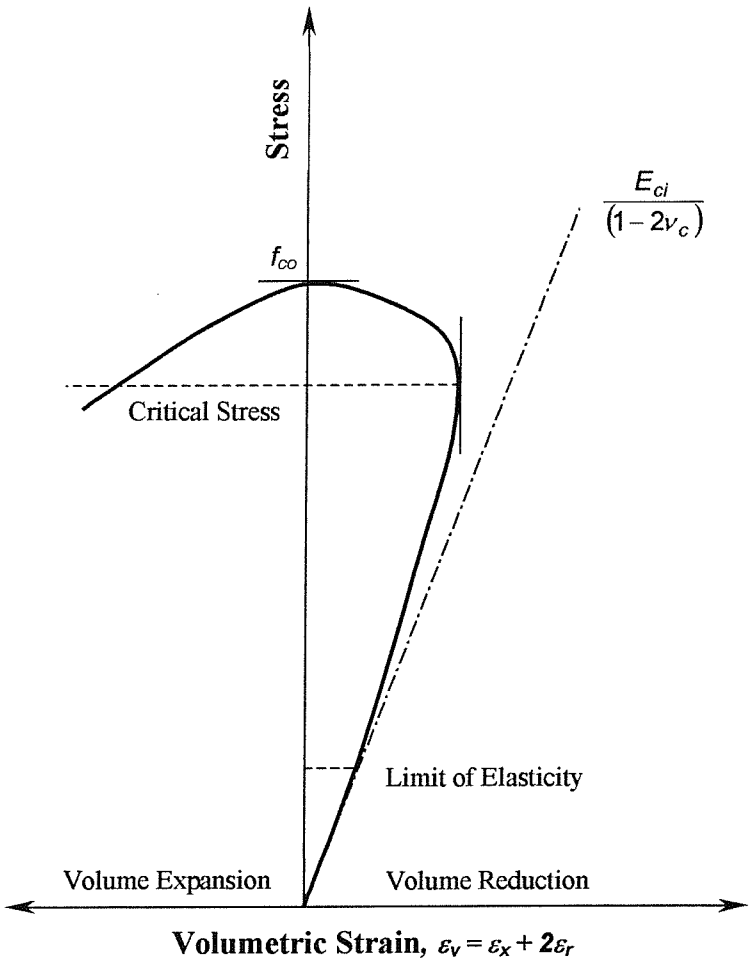

Figure 3.12. Typical stress-volumetric strain behaviour of concrete in uniaxial compression

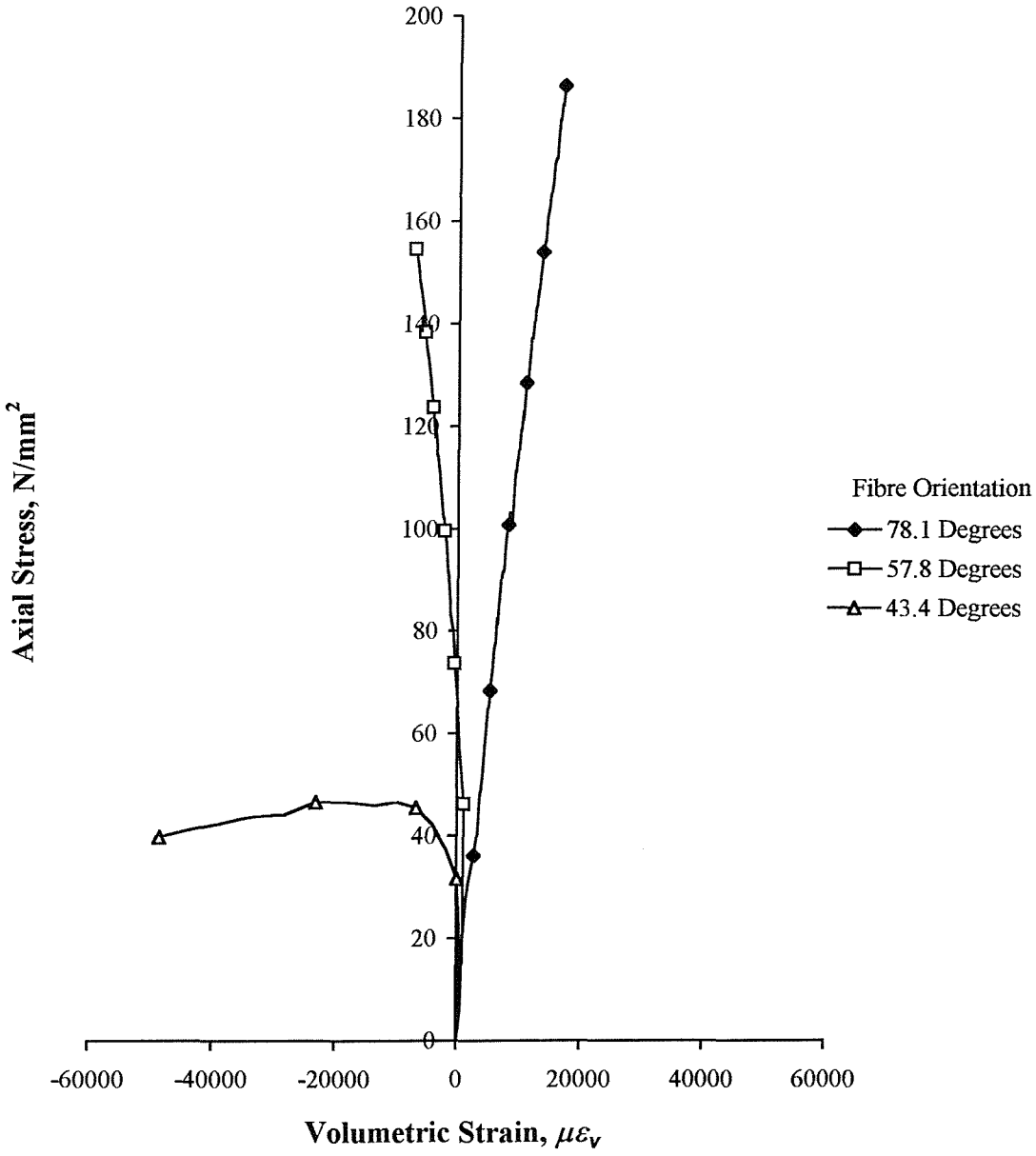

Figure 3.13. Stress-volumetric strain curves for the 80 mm diameter concrete-filled filament wound tubes

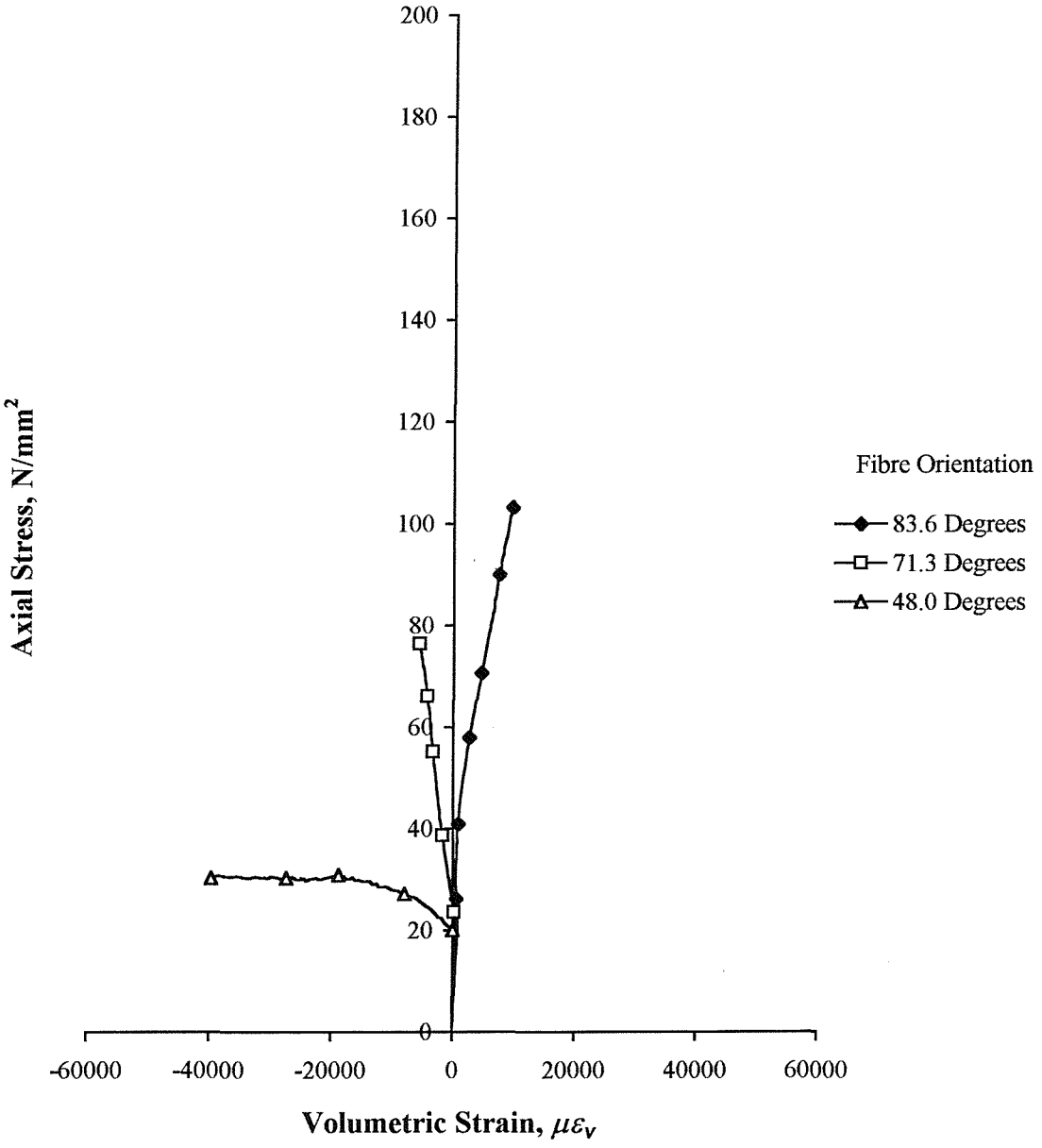

Figure 3.14. Stress-volumetric strain curves for the 150 mm diameter concrete-filled filament wound tubes

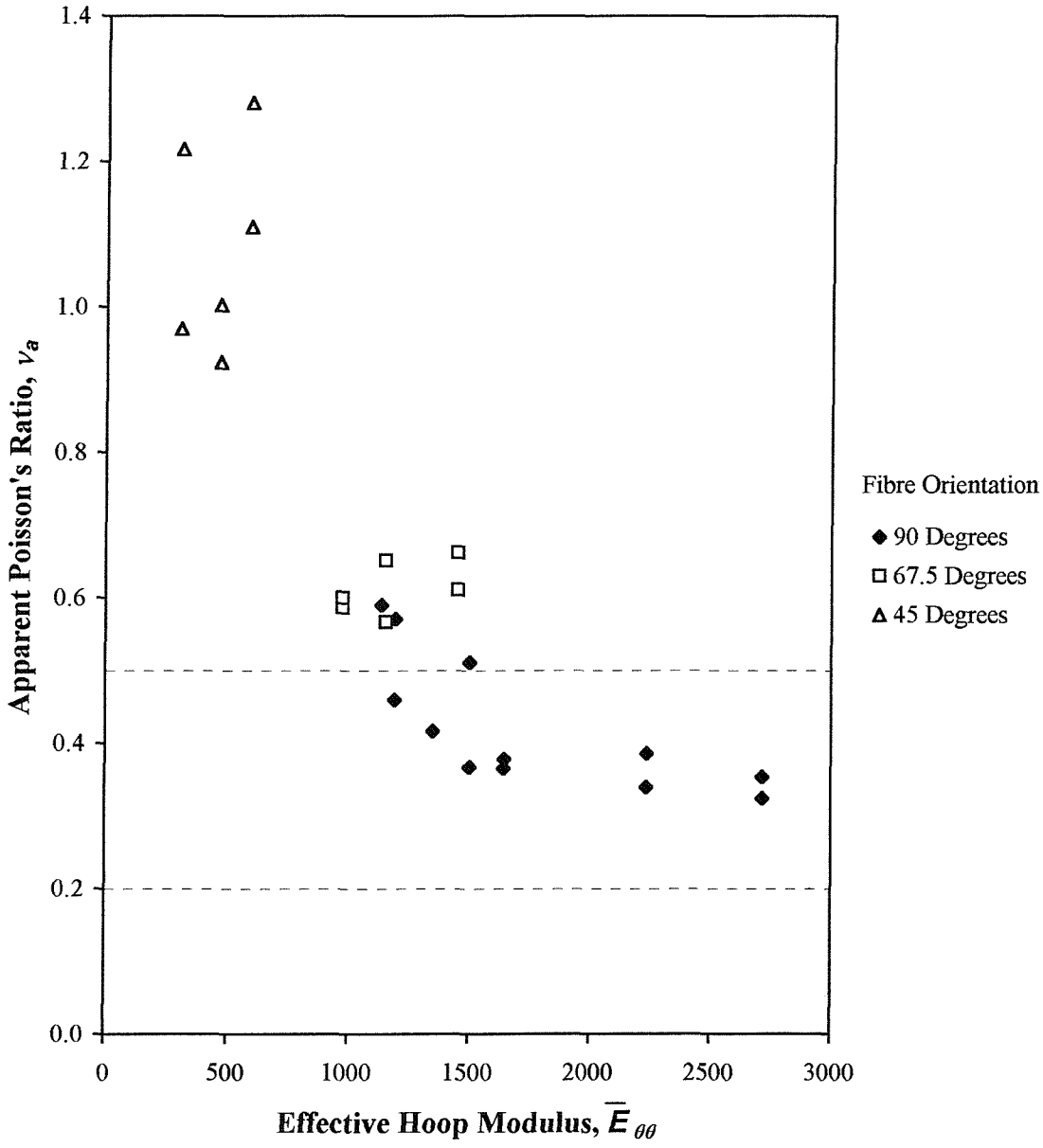

Figure 3.15. The apparent Poisson's ratio of FRP-confined concrete at failure as a function of the effective hoop modulus of the FRP-composite

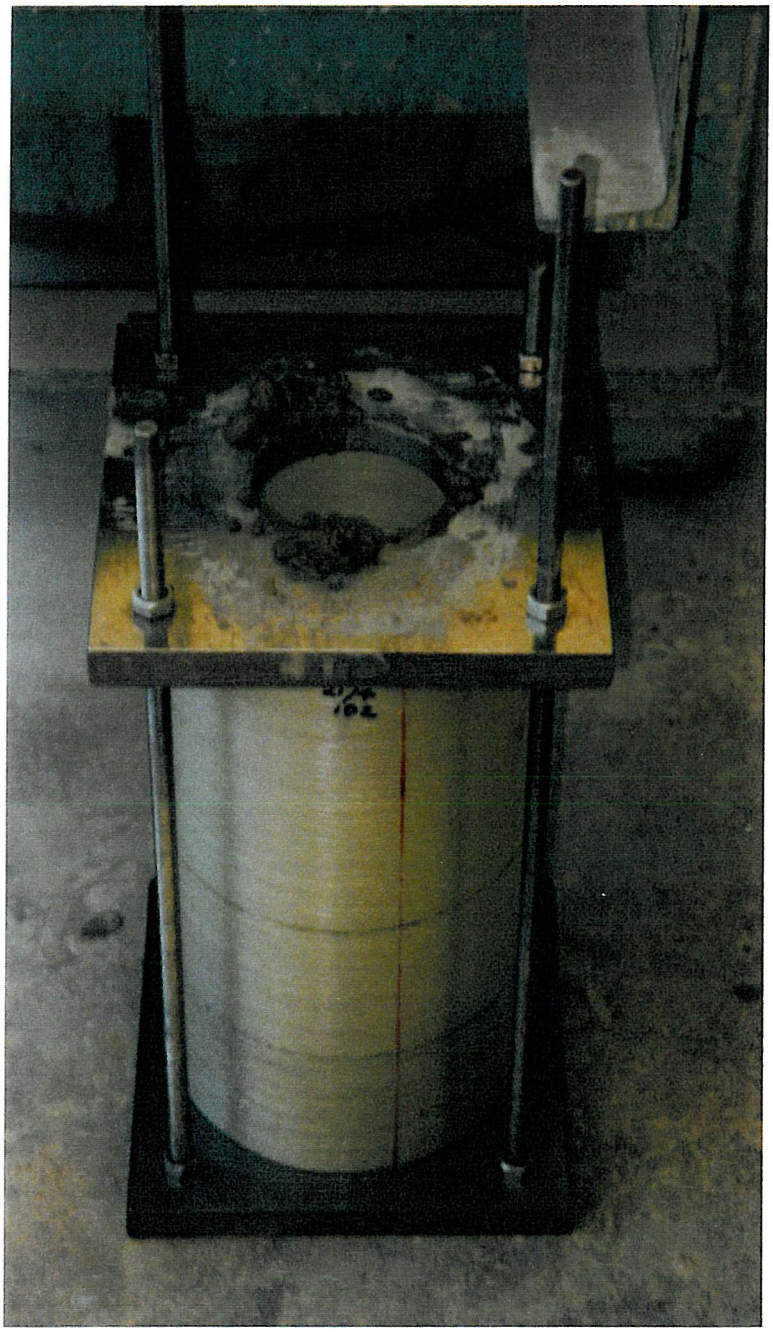

Plate 3.1. Casting a concrete-filled FRP-composite column

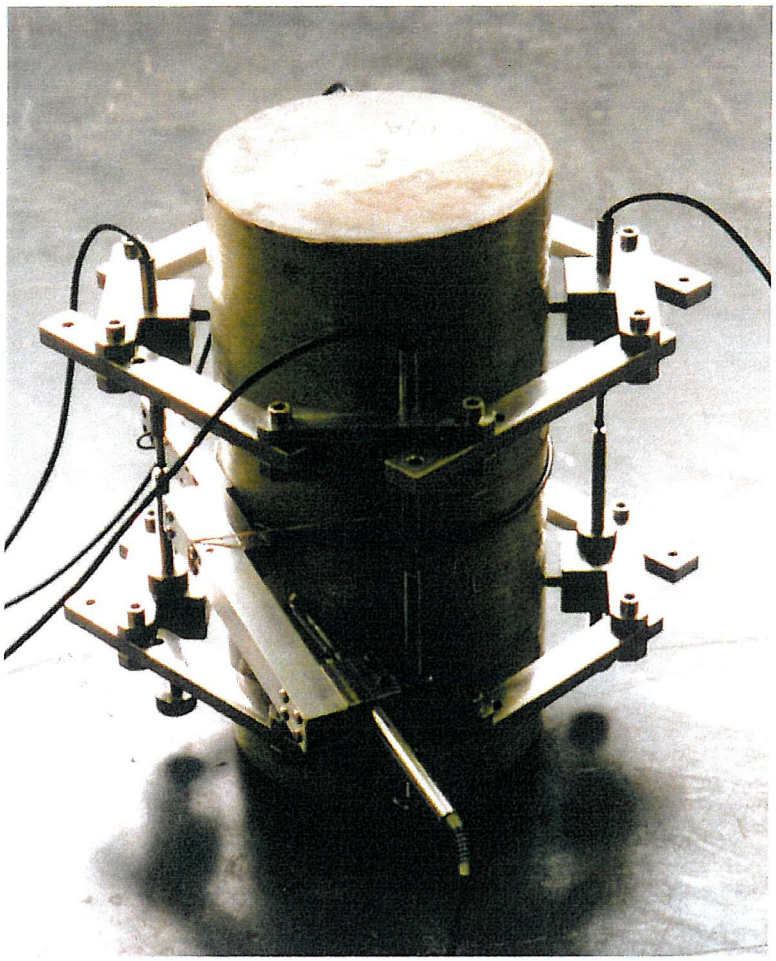

Plate 3.2. Axial and circumferential extensometers on a stub column

Plate 3.3. Failure mode of a stub column confined by an FRP-composite with a nominal 90 degree fibre orientation

Plate 3.4. Failure mode of a stub column confined by an FRP-composite with a nominal 67½ degree fibre orientation

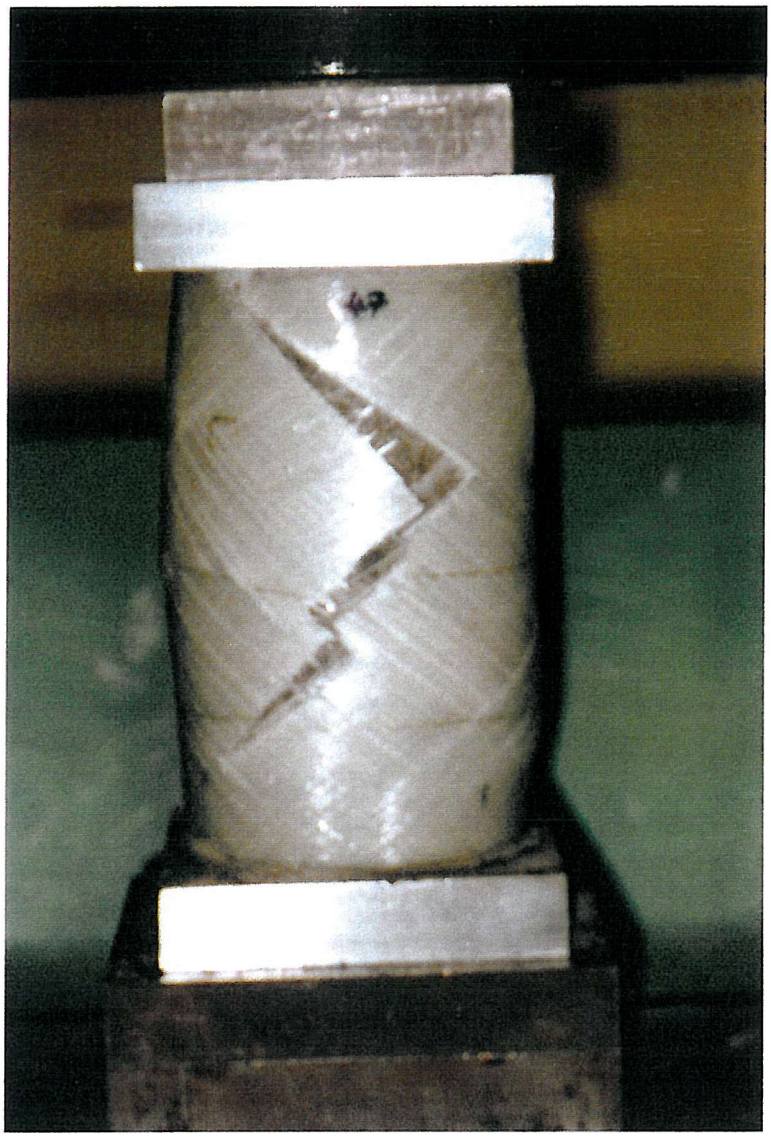

Plate 3.5. Failure mode of a stub column confined by an FRP-composite with a nominal 45 degree fibre orientation

Plate 3.6. Comparison of the failure modes of FRP-confined concrete stub columns

CHAPTER 4

MODELLING THE BEHAVIOUR OF CONCRETE CONFINED BY FRP-COMPOSITES

4.1 CONFINEMENT MODEL

The mechanical behaviour of concrete subjected to a state of triaxial stress cannot be completely described by the constitutive theories of elasticity or plasticity. Concrete is inherently anisotropic and heterogeneous, and the mechanical behaviour is influenced by a large number of parameters, such as:

- softening of the resistance with increasing axial strain;
- instability beyond the peak strength in uniaxial compression;
- increases in strength and stiffness in the presence of lateral confinement;
- elastic-plastic behaviour when subjected to a state of triaxial compression.

The confinement of concrete by permanent formwork or unstressed fibre wrapped FRP-composite materials is passive, since the confining pressure is developed by the lateral expansion of the concrete under an applied axial strain. Therefore, the mechanical behaviour of the confinement will depend on the Poisson's ratio of the concrete core and the hoop stiffness of the FRP-composite.

The proposed concrete confinement model assumes that the circumferential strain in the concrete at the interface between the concrete and lateral reinforcement is equal to the circumferential strain in the lateral reinforcement.

$$\varepsilon_{\theta}^{\text{concrete}} = \varepsilon_{\theta}^{\text{reinforcement}} \qquad \textbf{(4.1)}$$

The thickness of the lateral reinforcement is assumed to be significantly smaller than the diameter of the concrete core. Thus, the lateral reinforcement can be described as a thin shell, and the lateral confining pressure which acts on the core is derived from the assumption that the internal forces are in equilibrium.

$$f_r = \left(\frac{2t}{D}\right) f_{\theta} \qquad \textbf{(4.2)}$$

The derivation of equation 4.2 is given in Appendix A. For concrete strain compatibility the strain in the radial direction must equal the strain in the hoop direction. In addition, conditions of equilibrium require that the radial stress in the concrete is equal to the radial stress applied by the FRP-composite and, at all points, the hoop stress in the concrete is equal to the radial stress.

Furthermore, it is assumed that:

- there is no bond between the FRP-composite and the concrete;
- the FRP-composite carries negligible axial load due to the low axial compression modulus of the FRP-composite compared to concrete;
- the axial strain in the FRP-composite and the concrete is equal.

4.1.1 Ultimate failure stress

The existing failure criteria for confined concrete define the failure strength as a function of the applied lateral pressure. In the case of concrete confined by lateral steel reinforcement, the maximum confining pressure induced is limited to the yield strength of the steel and is relatively constant once yield has occurred. However, the confining pressure induced by FRP-confinement increases continuously as the axial strain in the concrete core increases, but the stiffness of the confining system remains constant.

The existing failure criteria for FRP-confined concrete assume that at failure the hoop strain in the composite jacket is equal to the uniaxial tensile failure strain of the composite. However, the experimental work presented in Chapter 3 and Table 1.6 have shown that at failure the hoop strain in the composite jacket is less than the uniaxial tensile failure strain of the composite. Thus, whilst existing failure criteria proposed by Samaan *et al* [59] and Saafi *et al* [60] give good correlation with experimental results, they do not satisfy lateral strain compatibility requirements.

The proposed failure criterion presented in this work is based on the hoop stiffness of the FRP-composite jacket, which is assumed to remain constant. A failure criterion based on the confining stiffness as opposed to the confinement pressure, has the following advantages:

- The failure criterion does not require prior knowledge of the lateral expansion of the concrete core.
- Unlike the tensile strength of E-glass fibres, the elastic modulus of the fibres is not reduced by mechanical abrasion during manufacturing processes.

Figure 4.1 compares the experimental compressive failure strength of concrete confined with the effective hoop stiffness of the FRP-composite for the present study, with those by Samaan *et al* [59] for concrete-filled E-glass fibre filament wound tubes, Howie & Karbhari [23] and Picher *et al* [22] for carbon fibre wrapped concrete cylinders, and Saafi

et al [60] for concrete-filled E-glass and carbon-fibre filament wound tubes. The compressive failure strength of the confined concrete was found to be linearly proportional to the effective hoop stiffness of the FRP-composite and is given by:

$$\frac{f_{cc}}{f_{co}} = 1 + \alpha\left(\frac{2t}{D}\right)\frac{E_{\theta\theta}}{f_{co}} \qquad (4.3)$$

Where α is an empirical constant. Linear regression analysis of the experimental data determined $\alpha = 0.05$ with a coefficient of correlation of 0.92.

4.2 STRESS-STRAIN CONSTITUTIVE EQUATION

The proposed model is based on the equivalent uniaxial strain concept [48]. The model is defined by a stress-strain equation where the material parameters account for the enhancement due to triaxial confinement. The equivalent axial stress-strain relationship of concrete confined by an FRP-composite material is assumed to be bilinear, and is described by a four-parameter elastic-plastic stress-strain relationship [74]:

$$f_c = \frac{E_{1x}\varepsilon_c}{\left[1+\left(\frac{E_{1x}\varepsilon_c}{f_{ox}}\right)^n\right]^{1/n}} + E_{px}\varepsilon_c \qquad (f_c \le f_{cc})$$

$$E_{1x} = E_{ci} - E_{px} \qquad (4.4)$$

The idealised bilinear model and the parameters defining the curve are shown in Figure 4.2. The shape parameter, n, controls the behaviour of the stress-strain curve in the transition zone whereas f_{ox} defines the axial plastic stress. The parameters used to establish the stress-strain curve are determined using only the experimental data presented in Chapter 3.

4.2.1 Initial tangent modulus

The benefits of the passive confinement induced by the FRP-composite are only fully realised at stress levels which exceed the peak stress of unconfined concrete. Hence, passive FRP-composite confinement does not significantly increase the initial tangent modulus of the concrete core. The initial tangent modulus is determined by the empirical expression given in the CEB-FIP Model Code [71].

$$E_{ci} = 21500\left(\frac{f_{co}}{10}\right)^{1/3} \qquad (4.5)$$

Equation 4.5 was found to give close agreement with the measured initial tangent moduli of unconfined concrete, as shown in Figure 3.9. Research by Guo [75] on the different empirical expressions for the initial tangent modulus of concrete has shown that equation 4.5 also gives the closest agreement between finite element analysis prediction and experimental data for concrete strengths up to 50 N/mm^2.

4.2.2 Axial post-crushing tangent modulus

The slope of the stress-strain curve in the pseudo-plastic region of the confined concrete has been termed the post-crushing tangent modulus. As the axial strain enters the pseudo-plastic region, microcracking of the concrete becomes more extensive and the structure of the concrete is assumed to be a highly fissured, discontinuous material. Structural stability of the concrete is only maintained by the restraining action of the FRP-composite. Therefore, the magnitude of the post-crushing tangent modulus is a function of the stiffness of the confinement system and is independent of the concrete properties, assuming the concrete consists of a dense, stiff aggregate.

A plot of the post-crushing modulus versus the effective hoop modulus of the FRP-composite is shown in Figure 4.3. The magnitude of the post-crushing modulus is linearly proportional to the effective hoop modulus, provided the effective hoop modulus is greater than 977 N/mm^2. An empirical expression for the post-crushing tangent modulus, determined using regression analysis of the experimental data with $\overline{E}_{\theta\theta} \geq 977\,\text{N/mm}^2$, resulted in the following linear relationship with a correlation coefficient of 92%:

$$E_{px} = 1.282\,\overline{E}_{\theta\theta} \qquad \left(\overline{E}_{\theta\theta} \geq 977\ \text{N/mm}^2\right) \qquad \textbf{(4.6)}$$

For FRP confinement with an effective hoop modulus of less than 977 N/mm^2, the low degree of lateral restraint cannot inhibit the onset of unstable crack propagation in the concrete and the corresponding increased lateral expansion. Thus, once the unconfined concrete strength has been exceeded, a descending branching is observed in the stress-strain curve. Specimens with an effective hoop modulus of less than 977 N/mm^2 should therefore be designed as if unconfined.

4.2.3 Shape parameter

The shape parameter n is determined by forcing the analytical expression through two points on the experimental stress-strain curve either side of the transition zone, namely (ε_a, f_a) and (ε_b, f_b), as shown in Figure 4.2.The resulting expression is:

$$\left(A^n - 1\right) - \left(\frac{\varepsilon_a}{\varepsilon_b}\right)^n \left(B^n - 1\right) = 0 \qquad (4.7)$$

where: $A = \frac{E_{1x}}{E_a - E_{px}}$ $B = \frac{E_{1x}}{E_b - E_{px}}$ $E_a = \frac{f_a}{\varepsilon_a}$ $E_b = \frac{f_b}{\varepsilon_b}$

The shape parameter can be determined by numerical iteration of equation 4.7. Values for n have been evaluated from the experimental data presented in Chapter 3 for all stub column tests. The mean experimental value for the shape parameter was 1.013 with a standard deviation of 0.082. However, the curve was also found to be insensitive to changes in n in the range $0.931 \le n \le 1.095$, and therefore a constant value of 1.00 has been adopted. Thus, equation 4.4 reduces to the form:

$$f_c = \frac{E_{1x}\varepsilon_c}{1 + \left(\frac{E_{1x}\varepsilon_c}{f_{ox}}\right)} + E_{px}\varepsilon_c \qquad \left(\begin{array}{c} 0 \le f_c \le f_{cc} \\ \overline{E}_{\theta\theta} \ge 977\ \text{N/mm}^2 \end{array}\right) \qquad (4.8)$$

4.2.4 Axial plastic stress

The axial plastic stress defines the intercept of post-crushing tangent modulus with the stress axis. Experimental values of f_{ox} were determined from the intercept of the linear regression analysis used to determine the axial post-crushing modulus in §3.4.4. Analysis of the experimental data showed that the reference plastic stress is linearly proportional to unconfined concrete strength:

$$f_{ox} = \left(\frac{E_{ci} - E_{px}}{E_{ci} - E_{c1}}\right) f_{co} \qquad (4.9)$$

The comparison of the experimental and predicted values for the reference plastic stress in Figure 4.4 shows a positive correlation between the values, with a correlation coefficient of 0.90 for the entire range of effective hoop moduli tested in this study.

4.3 LATERAL STRAIN

The relationship between the applied axial stress and the measured lateral strain in the confined concrete is also assumed to be bilinear. Furthermore, since the transition zone occurs at the same axial stress level, the lateral strains can be modelled using the same elastic-plastic stress-strain relationship proposed in §4.2. Rearranging equation 4.8 and substituting in the parameters defining the radial plastic stress and radial post-crushing modulus, the radial strain is given by:

$$\varepsilon_r = \frac{1}{2}\left(\frac{f_{or}}{E_{1r}} + \frac{f_{or} - f_c}{E_{pr}}\right) - \left[\frac{1}{4}\left(\frac{f_{or}}{E_{1r}} + \frac{f_{or} - f_c}{E_{pr}}\right)^2 + \frac{f_{or}}{E_{pr}}\frac{f_c}{E_{1r}}\right]^{1/2} \quad \textbf{(4.10)}$$

4.3.1 Initial radial tangent modulus

Assuming the initial behaviour of concrete is linear-elastic, traditional elastic theory gives the initial slope of the axial stress – radial strain to be:

$$\sigma_x = -\left(\frac{E_x}{\nu}\right)\varepsilon_r \quad \textbf{(4.11)}$$

Therefore, the initial radial tangent modulus of the concrete is given by:

$$E_{cr} = \frac{E_{ci}}{\nu_c} \quad \textbf{(4.12)}$$

Where ν_c is the initial Poisson's ratio for the uncracked response of concrete, which is assumed to be 0.20.

4.3.2 Radial post-crushing modulus

The radial post-crushing modulus is a measure of the lateral expansion of the restrained concrete core. Since the lateral expansion of the concrete is governed by the stiffness of the confinement, the radial post-crushing modulus must be a function of the effective hoop modulus. The experimental value for the radial post-crushing modulus was determined using linear regression analysis over the same stress range used to establish the axial post-crushing modulus. The experimental values for the radial post-crushing modulus are plotted in Figure 4.5 as a function of the effective hoop modulus. Regression analysis of the experimental data resulted in the following linear expression:

$$E_{pr} = 4.52\bar{E}_{\theta\theta} - 1909 \quad \left(\bar{E}_{\theta\theta} \geq 977 \text{ N/mm}^2\right) \quad \textbf{(4.13)}$$

4.3.3 Radial plastic stress

Experimental values of the radial plastic stress were determined from the intercept of the linear regression analysis using to determine the radial post-crushing modulus. By inspection, it was found that the radial plastic stress was linearly proportional to the axial plastic stress, as shown in Figure 4.6.

$$f_{or} = 0.566 f_{ox} + 8.96 \quad \textbf{(4.14)}$$

The correlation coefficient between predicted and experimental values is 0.94, provided the effective hoop modulus is greater than 977 N/mm^2.

4.4 VALIDATION OF THE MODEL

4.4.1 Axial failure stress

A comparison of the experimental failure stress of FRP-confined concrete with the failure stress predicted by equation 4.3 is given in Figure 4.7. Good correlation is achieved between the experimental and predicted failure stress irrespective of the angle of orientation of the confining fibres. Figure 4.8 shows the predicted strength of the confined concrete versus both the experimental results of this study and those published by other researchers [22-23,59-60]. As illustrated in Figure 4.8, equation 4.3 gives good correlation with the experimental failure stresses for concrete confined by hand-wrapped FRP-composites or filament wound tubes using either E-glass or carbon fibres.

4.4.2 Axial failure strain

The ultimate axial failure strain may be determined directly from equation 4.3 and equation 4.8. The resulting expression is:

$$\varepsilon_{cc} = -\frac{1}{2}\left[\frac{f_{ox}}{E_{1x}} + \frac{f_{ox} - f_{cc}}{E_{px}}\right] + \left[\frac{1}{4}\left(\frac{f_{ox}}{E_{1x}} + \frac{f_{ox} - f_{cc}}{E_{px}}\right)^2 + \frac{f_{ox} f_{cc}}{E_{px} E_{1x}}\right]^{1/2} \quad \textbf{(4.15)}$$

A comparison of the experimental failure strains and predicted failure strains is given in Figure 4.9. Very good agreement is observed in the specimens confined by the nominal 90 degree fibre orientations, this being primarily due to the stable volumetric behaviour which results from the confining system. As the fibre orientation of the confining fibres tends towards 67½ degrees, equation 4.15 predicts lower axial failure strains than were measured in the experimental work. Comparisons for specimens confined with fibres orientated at 45 degrees are not given since their effective hoop moduli are less than the minimum 977 N/mm^2, and therefore beyond the validity of equation 4.6.

The unstable crack propagation and associated volumetric expansion which occurs prior to the failure of unconfined concrete causes variability in the magnitude of the axial failure strain. The specimens with poor correlation between the experimental and predicted axial failure strains exhibited unstable volumetric expansion prior to failure which results in unrestrained axial deformations. Comparison of predicted axial failure strains with previous studies is not possible due to differences in the measurement of the axial strain.

4.4.3 Hoop failure strain

The comparison of the experimental and predicted hoop failure strains is shown in Figure 4.10. The experimental values for the tensile hoop failure strains ranged from 12,300$\mu\varepsilon$ to 16,300$\mu\varepsilon$ for concrete confined by a nominal 90 degree fibre orientation. As illustrated in Figure 4.10, the predicted tensile hoop failure strains in the 90 degree specimens give close correlation with the experimental results. However, as the fibre orientation of the specimens is reduced to 67½ degrees, the unstable volumetric expansion of the confined concrete results in poor correlation between the experimental and predicted hoop failure strains. The predicted hoop failure strain is also found to give reasonable correlation with the experimental hoop failure strains measured in previous studies [23, 59] which are shown in Figure 4.10.

4.4.4 Experimental versus predicted stress-strain behaviour

Figure 4.11 shows the predicted versus experimental stress-strain curves for a 80 mm diameter specimen and a 150 mm diameter specimen confined by a nominal 90 degree fibre. Comparisons of the predicted versus experimental stress-strain curves for all the specimens confined by a nominal 90 degree fibre orientation are given in Appendix D. As shown in Figure 4.11 and Appendix D, good correlation is achieved in both axial and circumferential directions over the entire load history for the specimens. Further confirmation of the close agreement between predicted and experimental behaviour is given by the stress-volumetric curves which are shown in Appendix E. The modelling of volumetric strain gives poorer agreement with experimental results than the axial strain modelling since the errors in predicting axial strains and radial strains are cumulative.

The comparisons of the predicted versus experimental stress-strain curves for the specimens confined by a 67½ degree fibre orientation are given in Appendix F. Whilst it has already been shown that both the axial failure strain and hoop failure strain are underestimated, the predicted stress- axial strain curves give reasonable correlation with the experimental curves in the axial direction. Stress-strain predictions in the circumferential direction show good agreement with the experimental curves up to the unconfined concrete strength. However, beyond this stress level the predicted behaviour deviates from the experimental behaviour.

4.5 DESIGN METHODOLOGY

4.5.1 Ultimate design failure strength

To account for differences in actual and laboratory values, local imperfections and long-term effects on the modulus of elasticity for FRP-composites, it is necessary to apply a partial safety factor. Based on the guidance given by the Institution of Structural Engineers a partial safety factor $\gamma_{me} = 1.80$ [76] has been used to determine the design modulus of elasticity for E-glass composites.

The experimental analysis is based on the mean value of the concrete compressive strength. To account for the variability of concrete manufacture, the design is normally based on the characteristic compressive strength which is defined as *'that strength below which 5% of all possible strength measurements for the specified concrete may be expected to fall'* [71]. An estimate of the characteristic compressive strength of concrete is given by:

$$f_{ck} = f_{co} - 8 \quad \text{N/mm}^2 \tag{4.16}$$

The design compressive strength of concrete is normally determined based on a partial safety factor, $\gamma_{mc} = 1.50$ [61]. Thus, the design compressive strength of concrete confined by a FRP-composite jacket is given by:

$$\begin{aligned} f_{ccd} &= \frac{f_{ck}}{\gamma_{mc}} + 0.05\frac{\overline{E}_{\theta\theta}}{\gamma_{me}} \\ \gamma_{mc} &= 1.50 \\ \gamma_{me} &= 1.80 \text{ for concrete - filled FRP - composite tubes} \end{aligned} \tag{4.17}$$

and the design post-crushing tangent modulus is given by:

$$E_{pd} = 1.282\frac{\overline{E}_{\theta\theta}}{\gamma_{me}} \qquad \left(\overline{E}_{\theta\theta} \geq 977 \text{ N/mm}^2\right) \tag{4.18}$$

Figure 4.12 shows a comparison of the experimental failure strength with the design failure strength calculated using equation 4.17. Using partial safety factors of 1.50 for the strength of the unconfined concrete and 1.80 for the modulus of elasticity of the FRP-composite, resulted in one unsafe design for a post-wrapped concrete cylinder using a hand lay-up. The mechanical properties of FRP-composites produced by hand lay-up are extremely variable, and therefore it can be argued that a higher partial safety factor should be used for concrete confined by hand wrapped FRP-composites.

4.5.2 Design working strength

The experimental work has shown that significant enhancements in compressive strength can be achieved using FRP-composite confinement. Furthermore, the ultimate failure strength of the confined concrete can be predicted safely and with a high degree of confidence for fibre orientations between 45 degrees and 90 degrees using either glass or carbon fibre composites for both concrete-filled filament wound tubes and post wrapped concrete cylinders. However, because the concrete core is a highly fissured material, structural integrity of the system is only maintained due to the confining action induced by the FRP-composite. Disruption of the confining action of the fibre composite due to abrasion or accidental damage would result in a sudden brittle failure. Therefore, it is proposed that the design working stress be based on the limited failure strain criterion of $3500\mu\varepsilon$ for unconfined concrete. This proposed design method eliminates the possibility of such a failure. The remaining axial load capacity due to confinement can be used as a factor of safety against accidental overload.

A typical equivalent uniaxial stress-strain strain curve and the corresponding design curve for the ultimate limit state with the proposed partial factors of safety are given in Figure 4.13. Also shown in Figure 4.13 is the limiting strain criterion for the design working strength to illustrate the magnitude of the safety factor against brittle failure occurring.

4.6 SUMMARY

Previous studies on FRP-confined concrete have defined the compressive failure strength as a function of the confining pressure. However, since the confining pressure increases constantly, the actual confining pressure at failure cannot be determined without prior knowledge of the lateral expansion of the concrete which is also a function of the confining pressure. The proposed failure stress criterion defines the compressive failure strength as a function of the hoop stiffness of the FRP-composite, which is assumed to be constant. The proposed failure strength criterion has been shown to give good correlation with experimental results for concrete confined with E-glass or carbon fibre composites using either filament wound tubes or post-wrapped confinement systems.

The stress-strain curve for concrete confined by a FRP-composite material consists of three regions:

1. an initial slope corresponding to the unconfined concrete;
2. a transition zone as the confining pressure develops;

3. a linear post-crushing region which is a function of the hoop stiffness of the FRP-composite.

The complete stress-strain curves in the axial and circumferential directions can be defined using the three parameter elastic-plastic relationships given by equations 4.8 and 4.10 respectively. The model gives good agreement with experimental results for specimens confined by a nominal 90 degree fibre orientation. The model also enables the mean volumetric strain behaviour of the confined concrete to be evaluated at a given axial strain level. A flow diagram summarising the procedure for the proposed confinement model is illustrated in Figure 4.14.

For specimens confined by a nominal 67½ degree fibre orientation, the proposed model gives reasonable agreement with experimental results in the axial direction, although hoop failure strain is underestimated by the model.

The design curves based on the characteristic unconfined concrete strength and partial safety factors of 1.50 for concrete and 1.80 for the modulus of elasticity of the FRP-composite result in a safe prediction of the ultimate load capacity. However, at this load capacity, the concrete core is a highly fissured material, and structural integrity is only maintained due to the confining action induced by the FRP-composite tube. The loss of the confining action from accidental or malicious damage to the FRP-composite may result in a sudden brittle failure. Therefore, it is proposed that the design working stress be based on the limiting failure strain criteria of $3500\mu\varepsilon$.

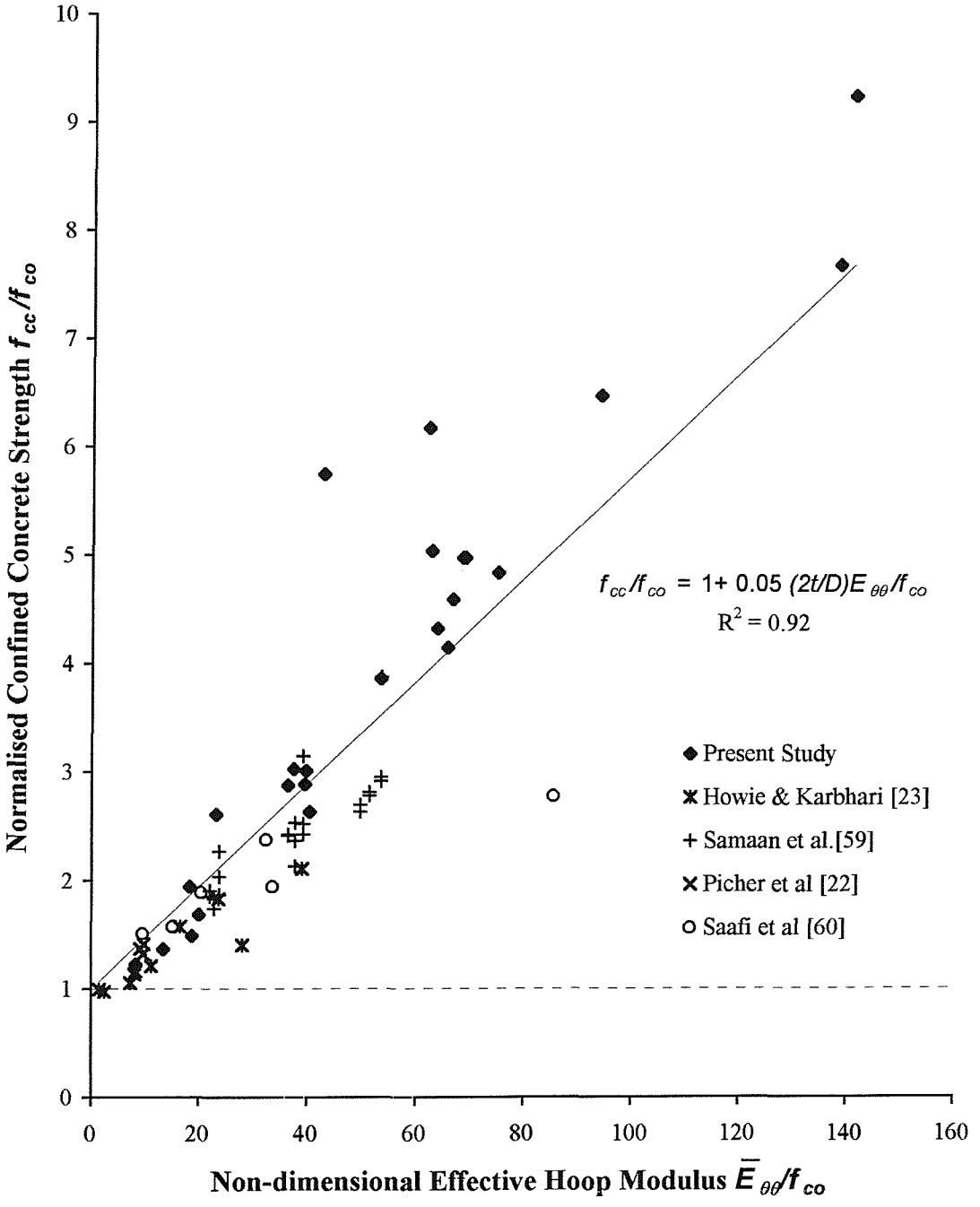

Figure 4.1. Normalised failure strength of FRP-confined concrete versus the non-dimensional effective hoop modulus of the confining FRP-composite

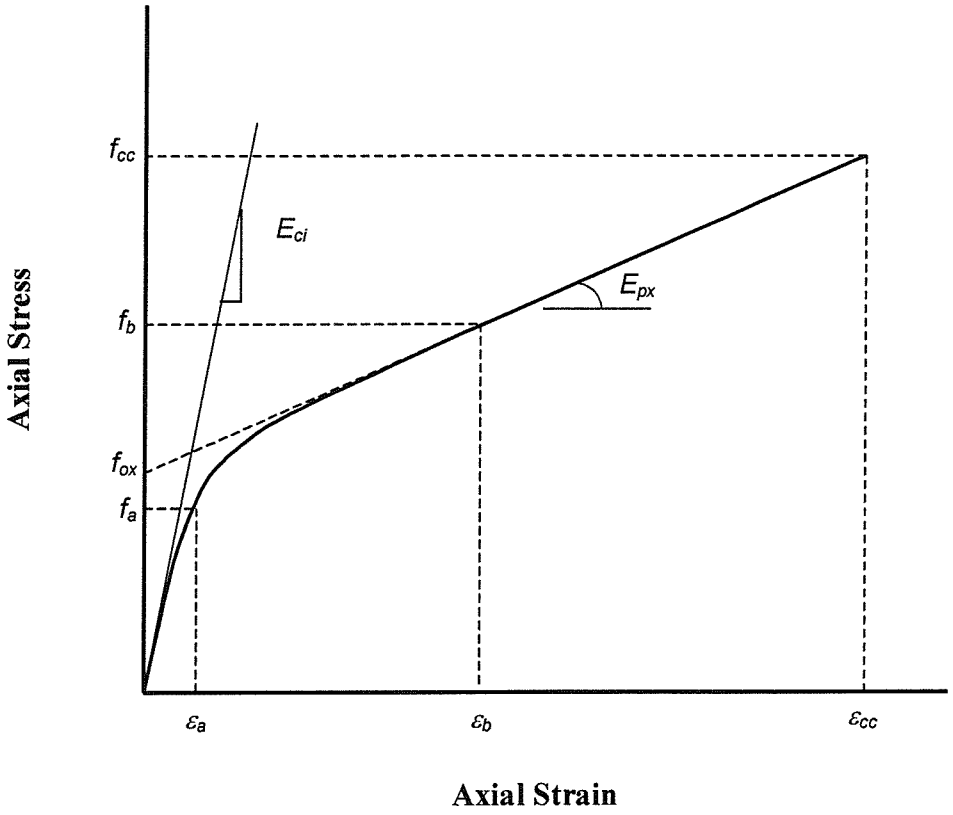

Figure 4.2. Idealised stress-strain curve for FRP-confined concrete

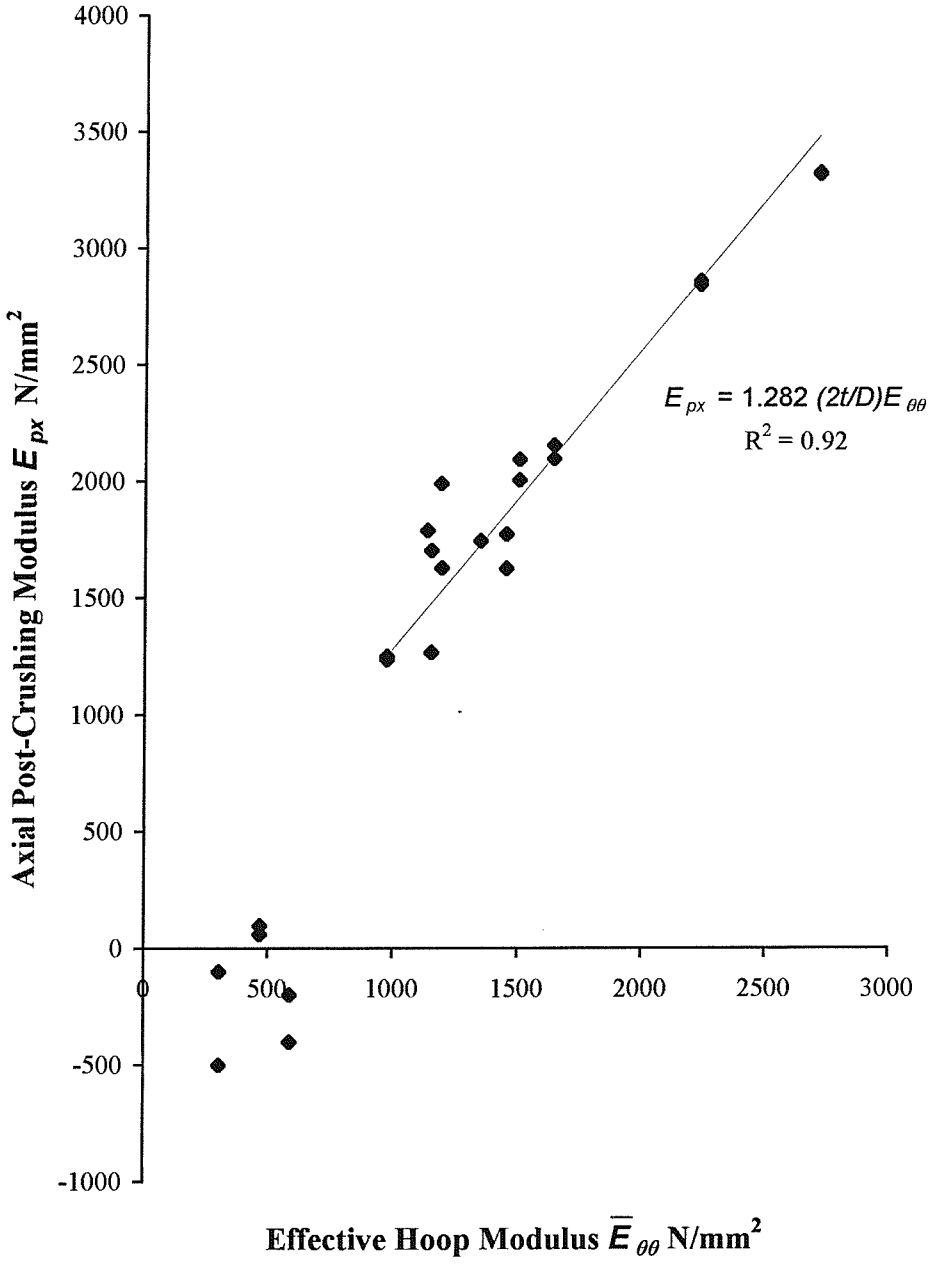

Figure 4.3. Axial post-crushing tangent modulus versus the effective hoop modulus of the FRP-composite

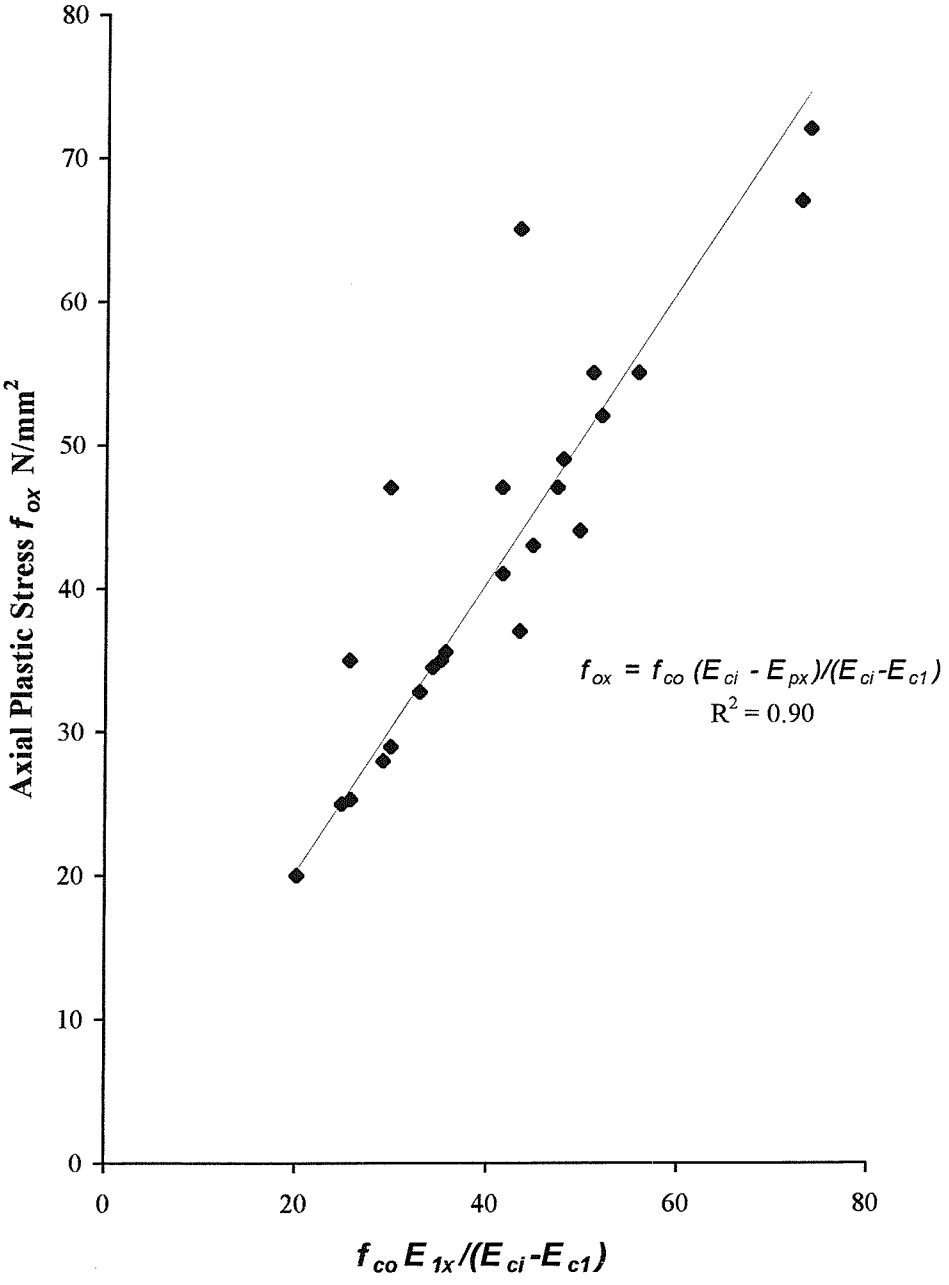

Figure 4.4. Axial plastic stress as a function of the mechanical properties of the confined and unconfined concrete

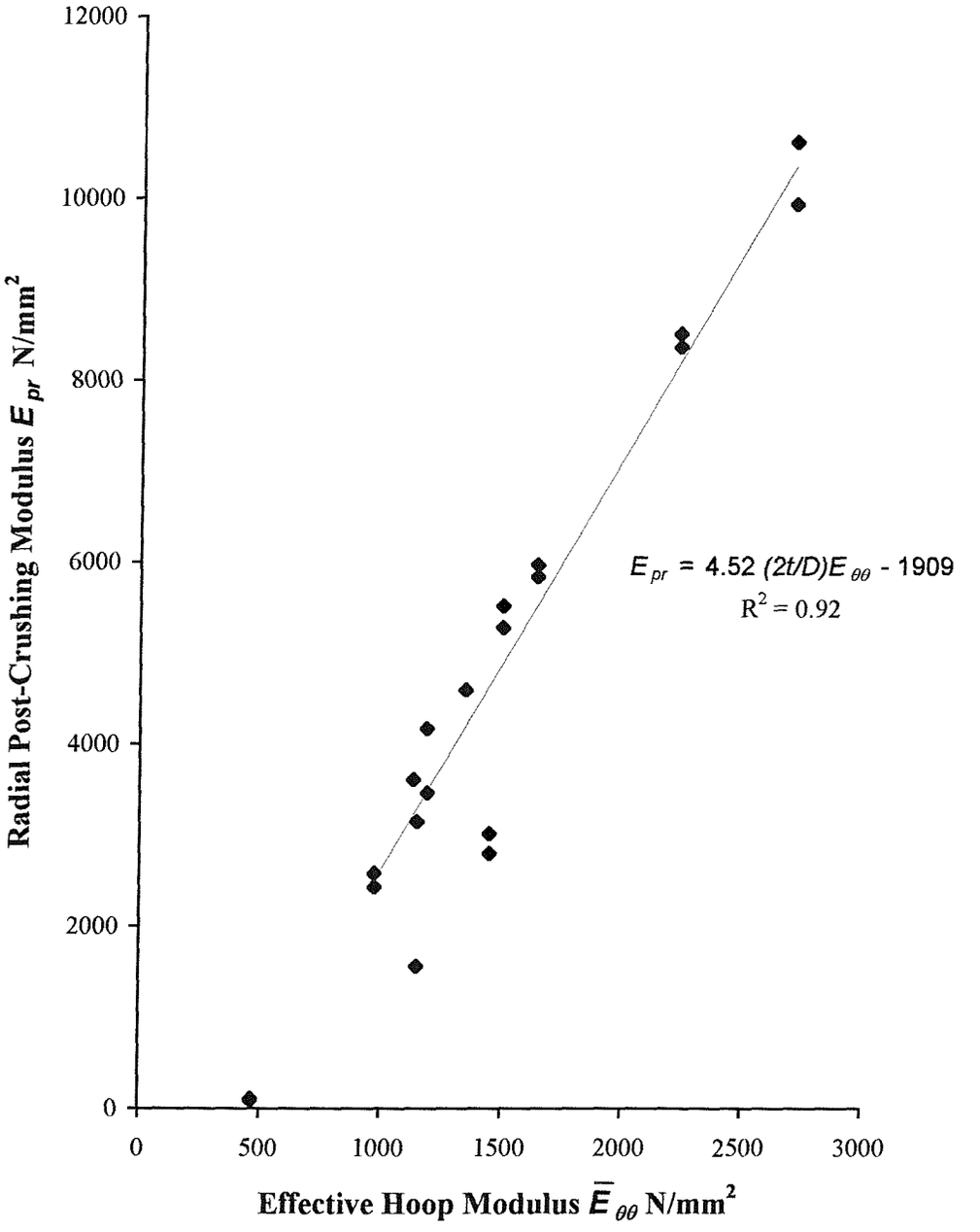

Figure 4.5. Radial post-crushing tangent modulus versus the effective hoop modulus of the FRP-composite

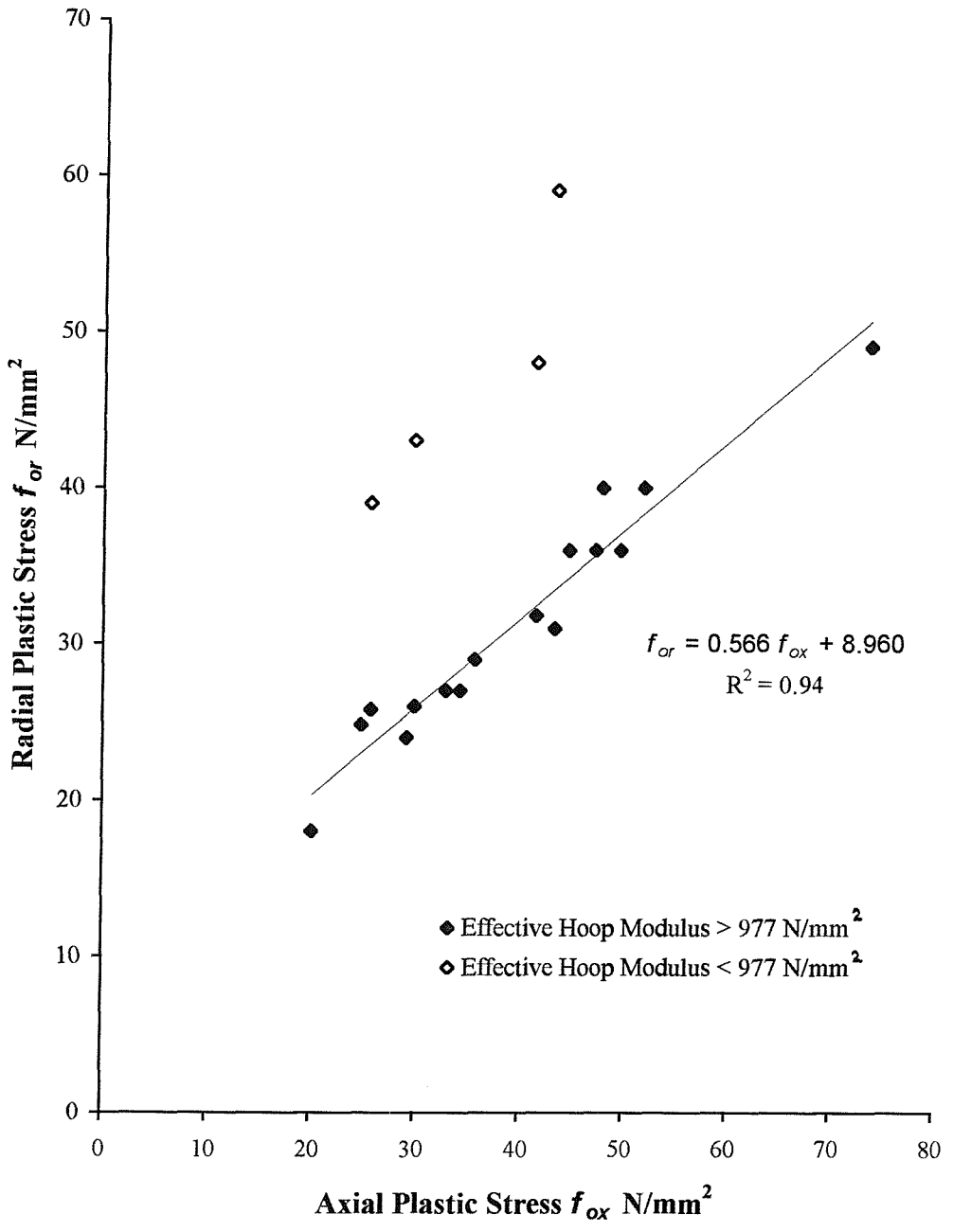

Figure 4.6. Radial plastic stress versus the axial plastic stress

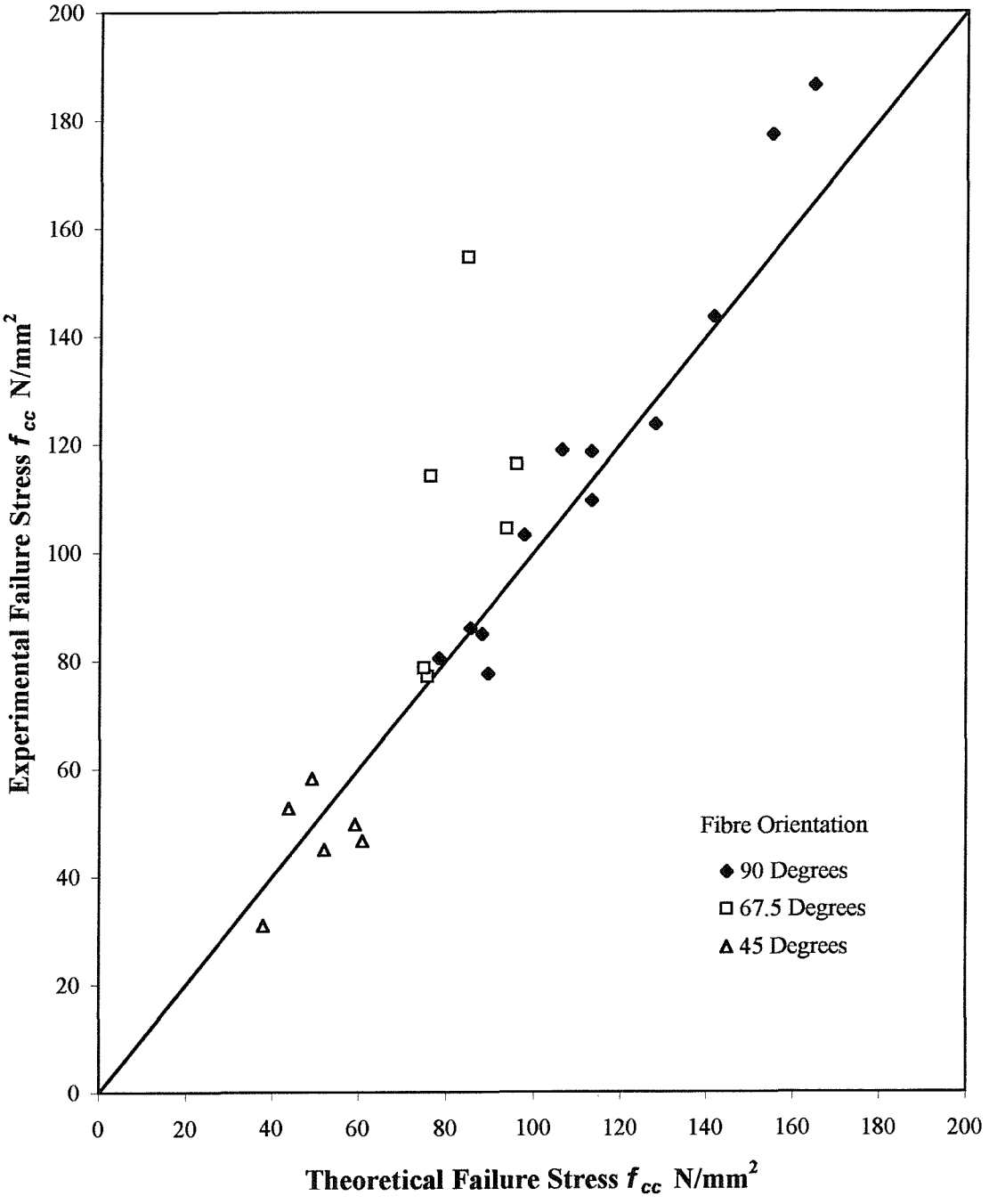

Figure 4.7. Comparison of the theoretical failure stresses with experimental results from the present study

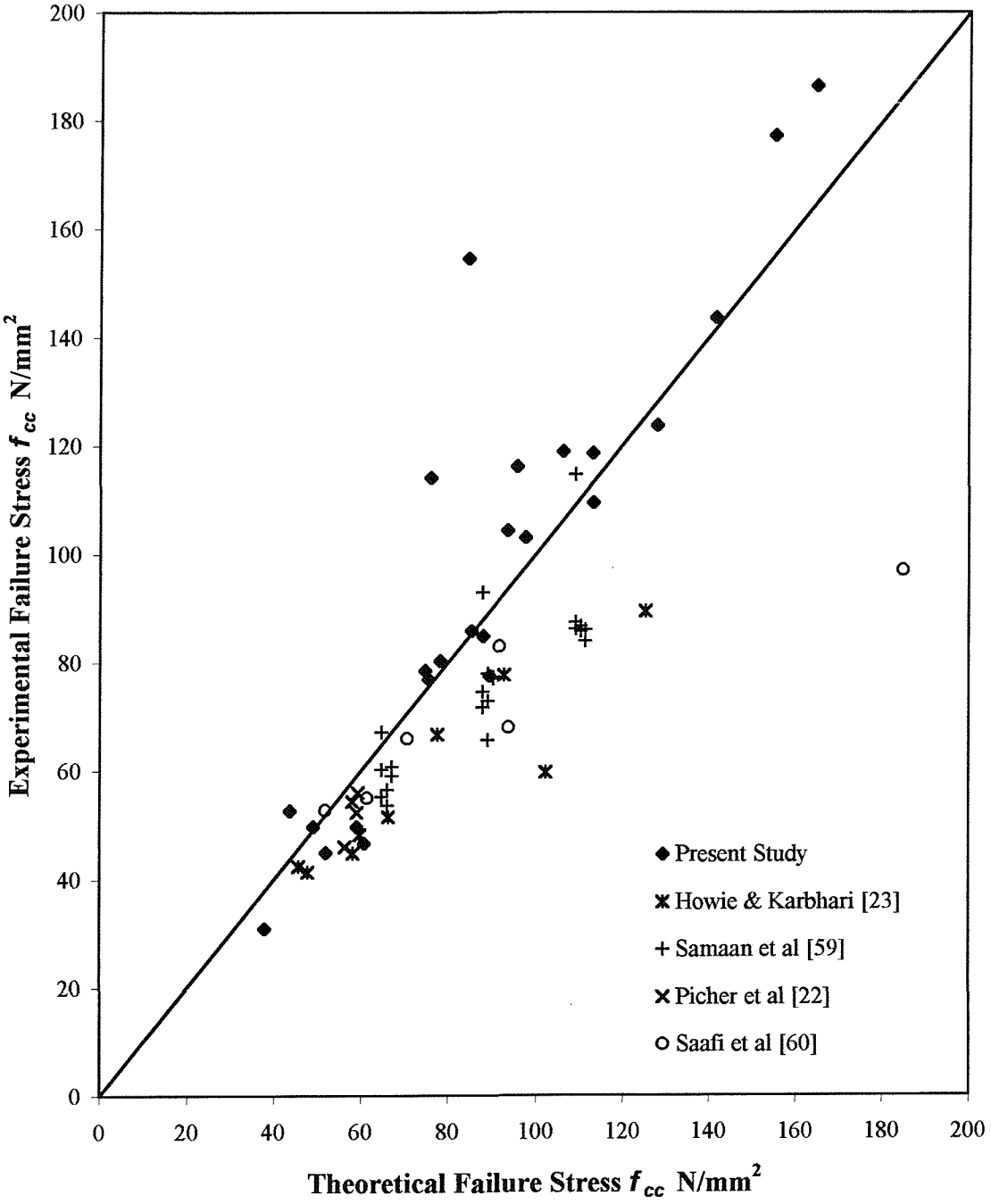

Figure 4.8. Comparison of the theoretical failure stresses with experimental results from the previous studies on FRP-confined concrete

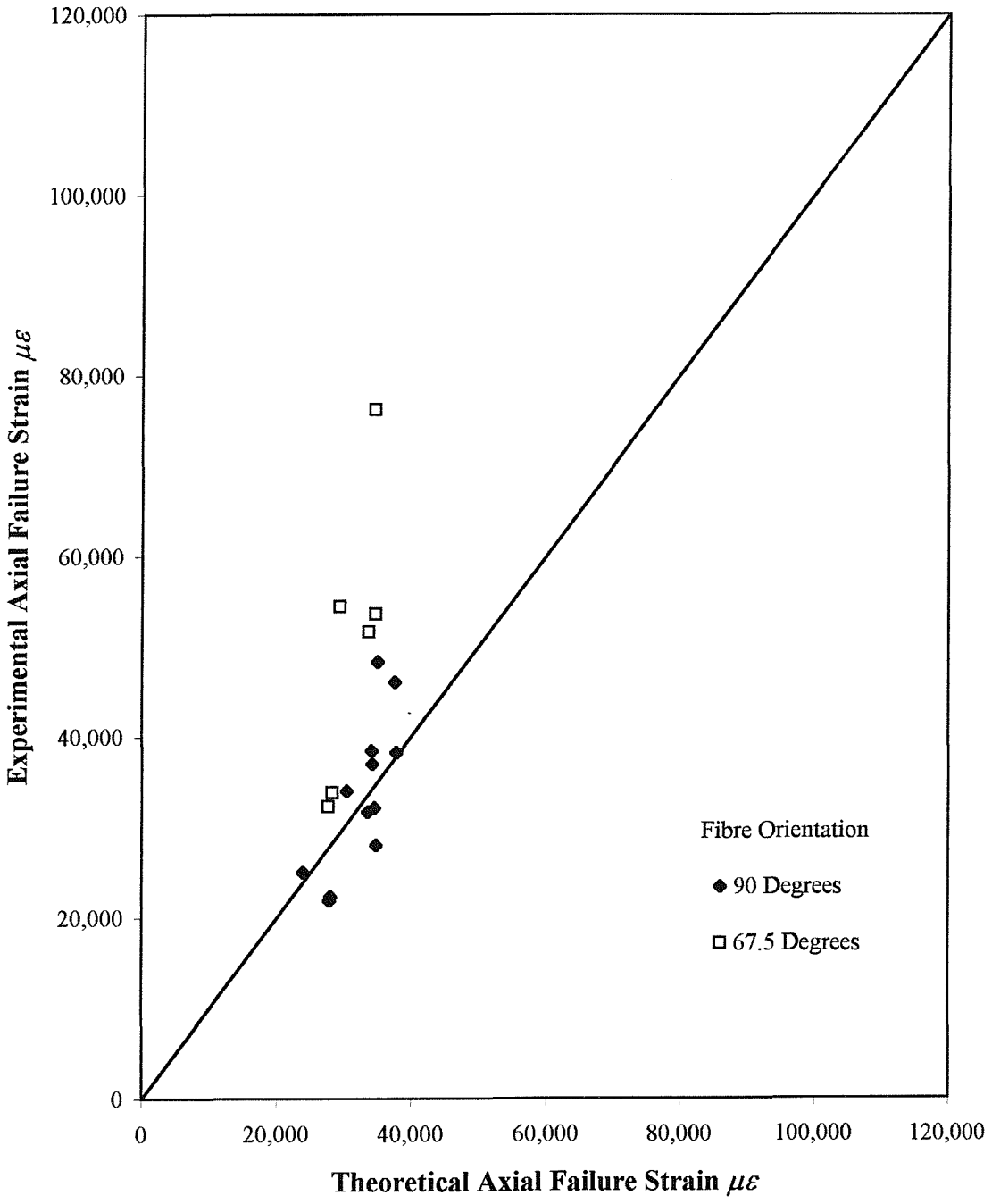

Figure 4.9. Comparison of the theoretical axial failure strains with experimental results from the present study

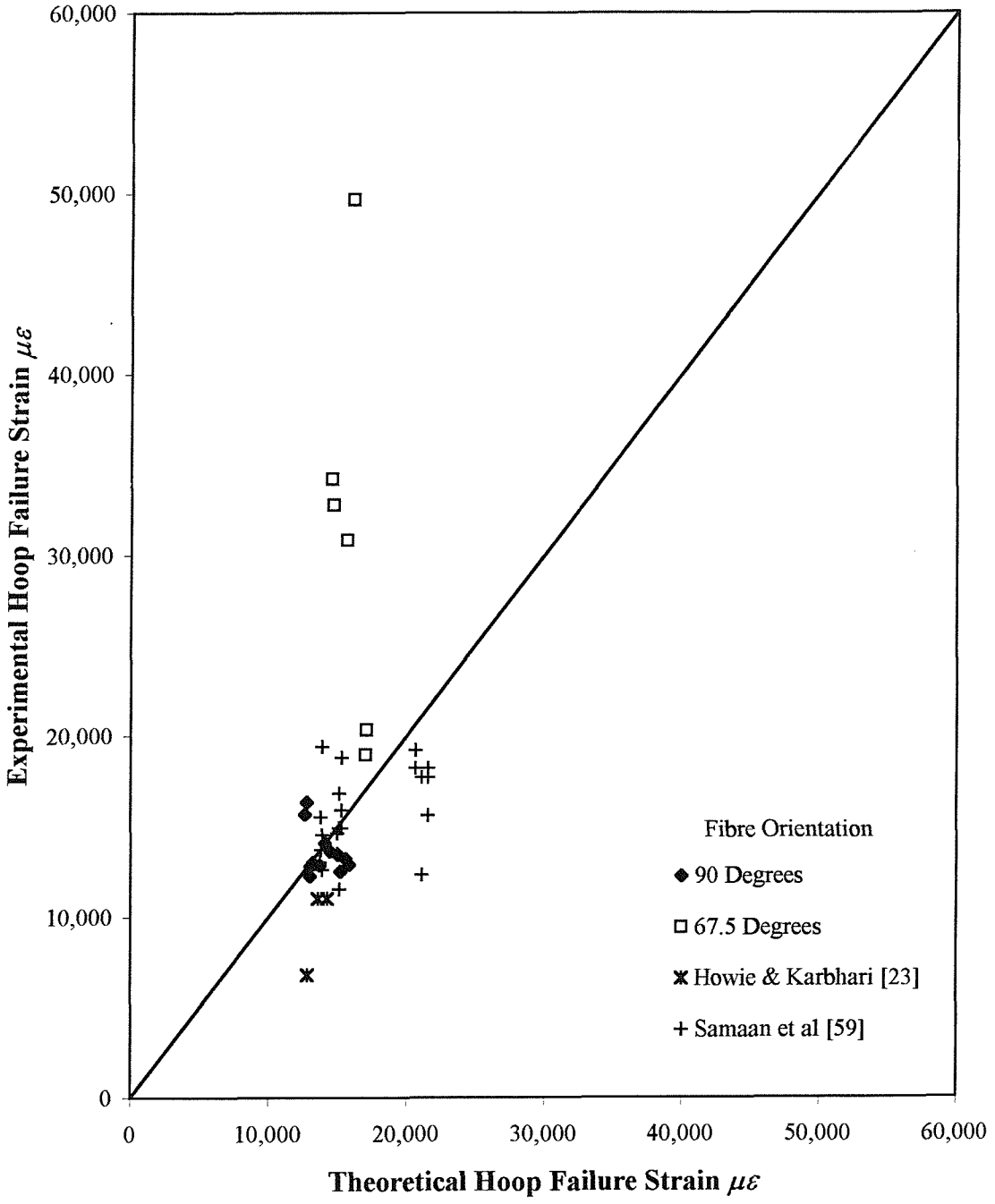

Figure 4.10. Comparison of the theoretical hoop failure strain with experimental results

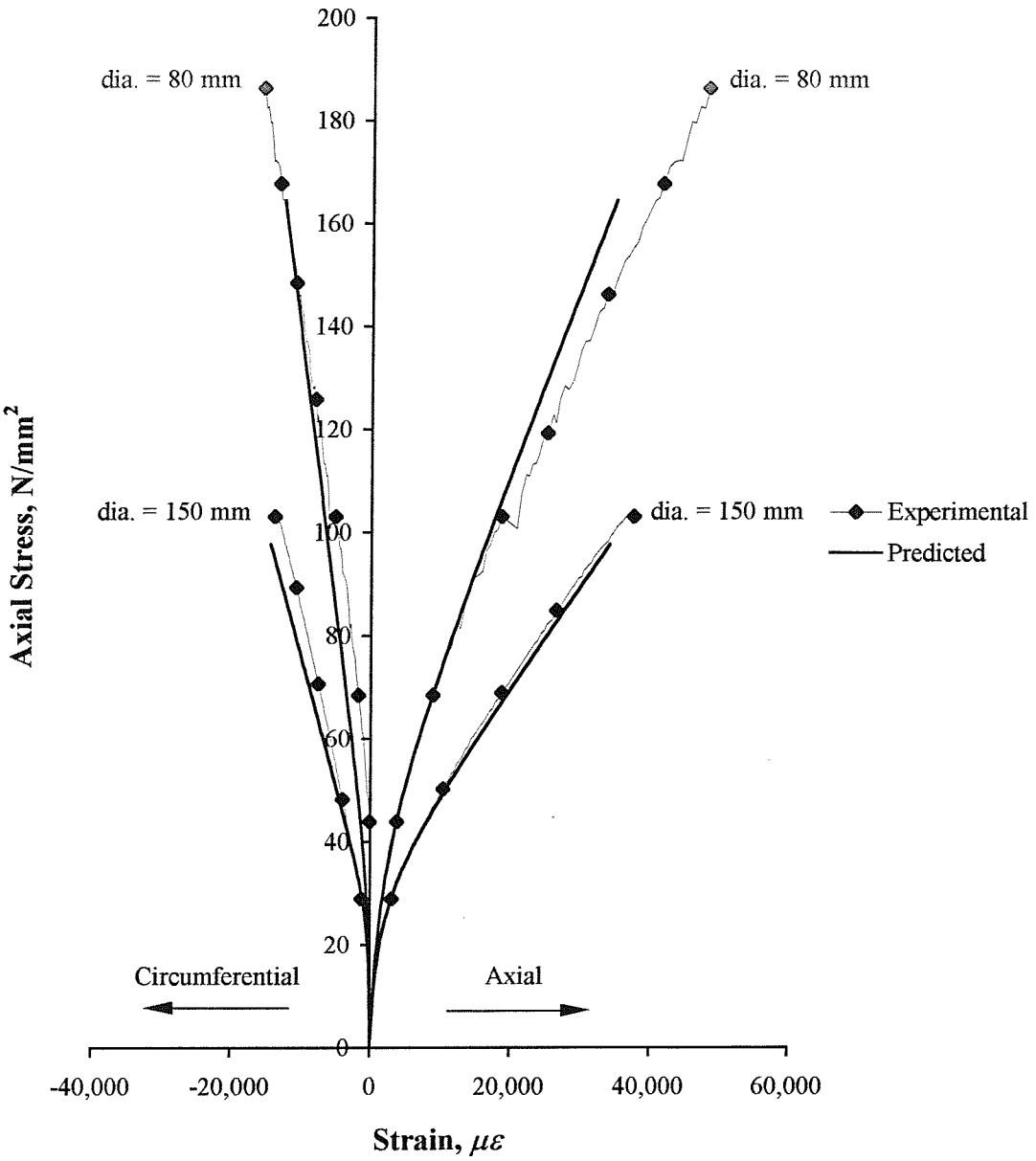

Figure 4.11. Comparison of the proposed stress-strain model with experimental results

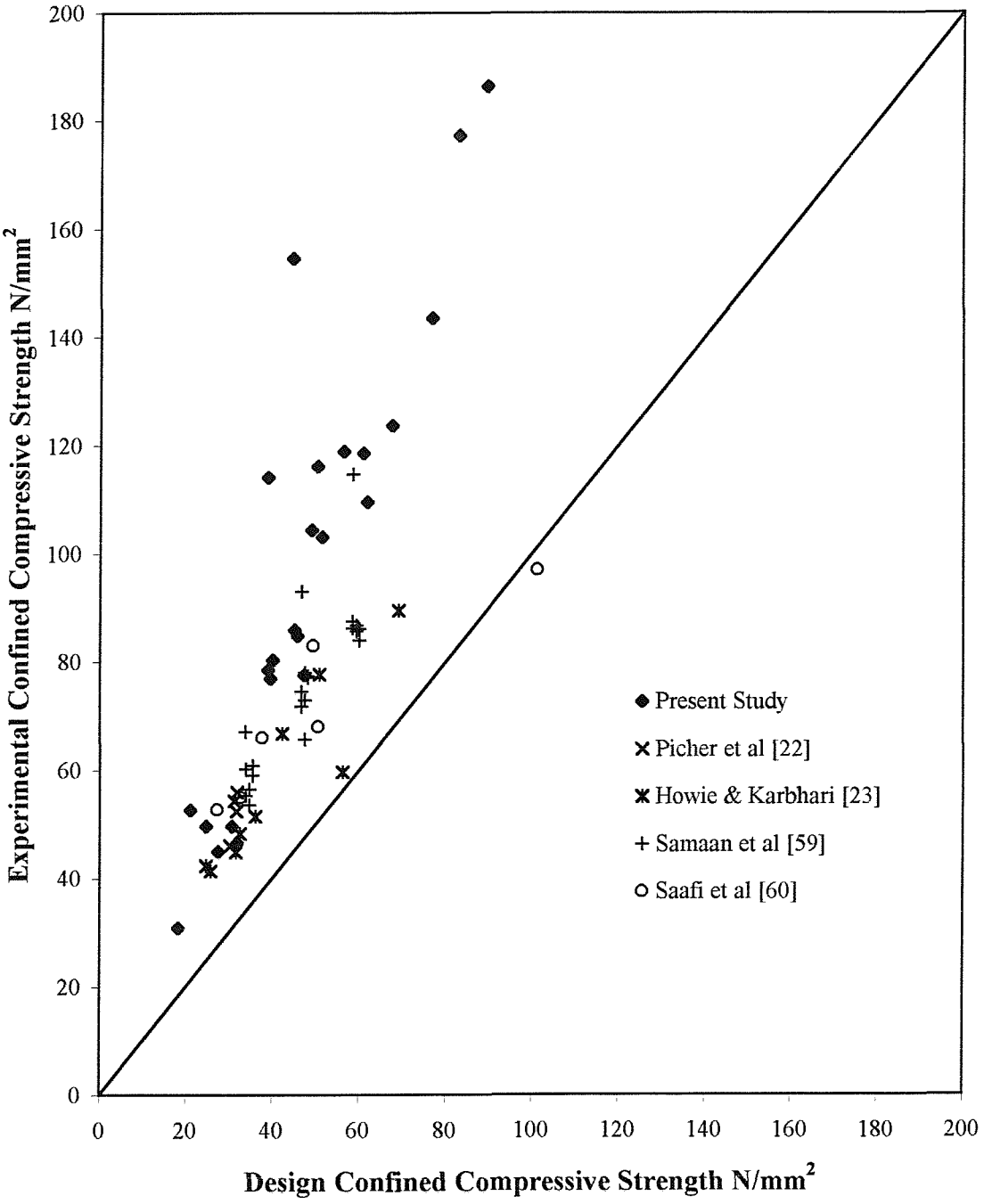

Figure 4.12. Comparison of experimental failure strength with the design failure strength of FRP-confined concrete

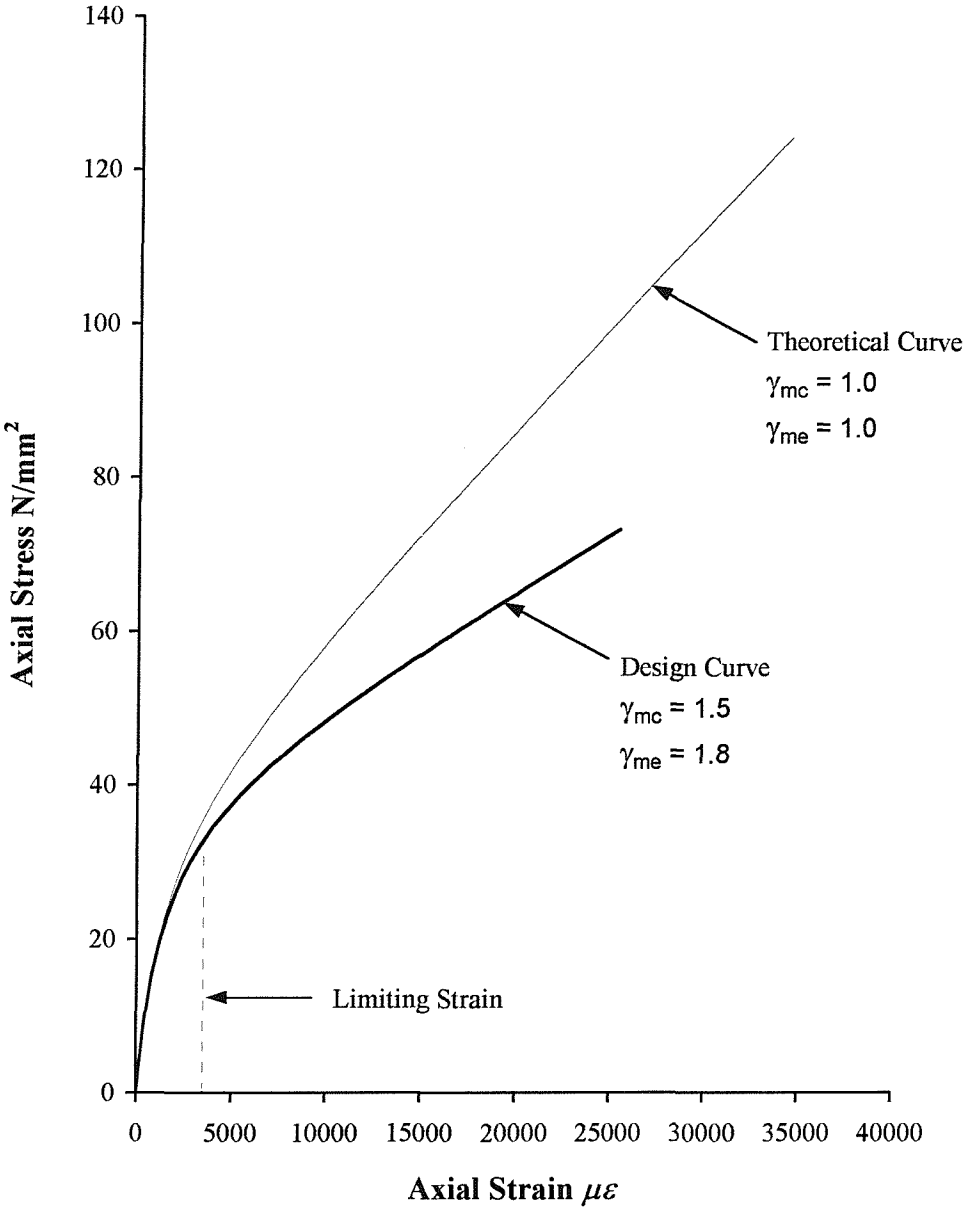

Figure 4.13. Typical design curve for FRP-confined concrete

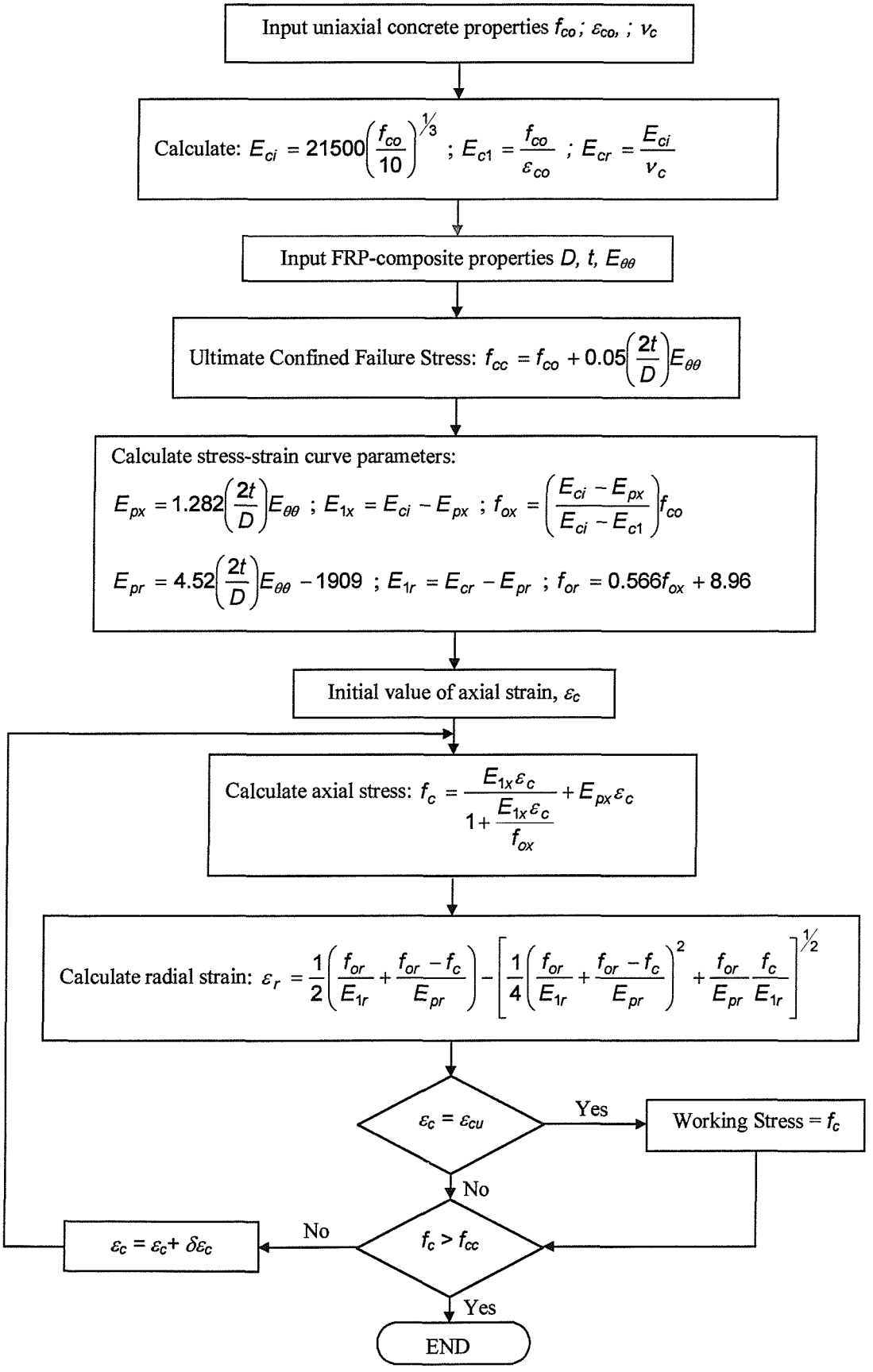

Figure 4.14. Confinement model flow diagram

CHAPTER 5

CONCRETE FILLED E-GLASS FRP-COMPOSITE COLUMNS

5.1 INTRODUCTION

Concrete columns can fail either due to material failure, instability or a combination of both. Material failures can normally be predicted from equilibrium conditions of the initial shape of the structure. Conversely, the failure prediction due to structural instability requires equations of equilibrium based on the deformed shape of the structure. Since the deformed shape is not known in advance, the problem is in principle non-linear.

Structural failures caused by the failure of the material are governed by the strength of the material, which is independent of structural geometry and size. However, the load at which a structure becomes unstable may be regarded as independent of the material strength; instead it is primarily governed by the material stiffness and geometric slenderness.

Unless the column is very stocky, material failures will generally be preceded by inelastic behaviour that destabilises the column due to the non-linear behaviour of concrete. This inelastic behaviour reduces the capacity of the column and therefore must be accounted for in any realistic model.

The parameters that affect the mechanical properties of concrete confined by FRP-composites are presented in Chapter 3. The mechanical properties and constitutive relationships for the FRP-confined concrete are based on specimens subjected to a uniform distribution of axial strain across the column section. Thus, the concrete is subjected to maximum triaxial confinement. Experimental work on the behaviour of concrete-filled steel tubes [40] and columns confined by steel ties [32] has shown that the effects of triaxial confinement diminish as the column slenderness increases or as the end moment of the column increases.

The limiting slenderness ratio at which the triaxial effects become negligible can only be approximated. Virdi and Dowling [34] proposed that the effects of triaxial confinement be ignored for concrete-filled steel tubes with $L/D > 25$. For columns in the range $0 < L/D < 25$, the augmented strength of confined concrete is assumed to be inversely proportional to the slenderness ratio:

$$f_{cc} = f_{co} + 0.25\left(25 - \frac{L}{D}\right)f_r \qquad \textbf{(5.1)}$$

Most practical applications for columns involve a degree of eccentric loading, which results in a strain gradient across the column cross-section. The effect of a strain gradient on the unconfined concrete is generally neglected [77]. However, the magnitude of the

confining pressure due to passive confinement is a function of the circumferential strain, which in turn is a function of the applied axial strain. Therefore, the magnitude of the confinement pressure under a strain gradient across the column section will be less than the confining pressure under a uniform compressive strain.

5.2 EXPERIMENTAL INVESTIGATION

To investigate the behaviour of FRP-confined concrete columns, forty-nine columns were tested to failure in eccentric compression. The concrete strengths and properties of the E-glass/epoxy filament wound tubes were identical to those described in Chapter 3. The influence of second-order effects on the load capacity of conventional reinforced concrete columns are negligible provided $L/D < 12$ [78]. Therefore, the two column slenderness ratios used in the investigation were $L/D = 5$ and $L/D = 10$. The columns were tested with a constant end eccentricity equal to $0.05D$, the minimum notional eccentricity of concrete columns specified in BS8110 [61].

Three different fibre orientations were investigated to determine the effects of incorporating axial and hoop reinforcing components in the tube manufacturing process. The three notional winding angles were 90 degrees, 67½ degrees and 45 degrees.

5.2.1 Loading regime

The columns were tested under monotonically increasing axial compression with constant end eccentricity, using a 1,500 kN Instron test machine operating in displacement-control. Three 300 mm and three 400 mm diameter columns were tested using the 10,000 kN Amsler test rig at the BRE. The testing arrangement at the BRE was identical to the arrangement used at the Southampton, except that constant load increments were used in the test. Load was applied through steel end plates and rollers that provided a constant end eccentricity and simulated pin-ended supports. The end-plate details, shown in Figure 5.1, resulted in both the FRP-composite tube and the concrete being loaded simultaneously.

5.2.2 Instrumentation

Longitudinal and circumferential strains and the curvature at mid-height of the columns were measured using a similar test arrangement to the concentrically loaded specimens. The curvature at mid-height being calculated from the gradient of the longitudinal strains at the concave and convex faces. In addition to the measurement of strains at the column mid-height, lateral deflection at quarter and mid-height positions were measured using ±100.00 mm LVDT's. The load and crosshead displacements were recorded automatically

from the Instron control panel. The testing arrangement for the eccentrically loaded columns is shown in Plate 5.1.

5.3 EXPERIMENTAL BEHAVIOUR

The eccentric load was applied to the columns by increasing the platen displacement or load increments at the same constant rate used in the axial tests. As the axial load increased, whitening of the resin matrix occurred at discrete intervals along the entire length of the column, as shown in Plate 5.2. The whitening of the resin is due to light reflection where localised bond breakdown occurred between the fibres and resin. The deflected shape of the columns at peak load was symmetrical, as shown in Plate 5.3.

Localised buckling of the FRP-composite tube did not occur in any of the columns confined by tubes with fibre orientations greater than 55 degrees. The columns confined by the FRP composite with a nominal 45 degree fibre orientation exhibited localised buckling of the FRP-composite tube. Plate 5.4 shows a column confined by a 43.4 degree fibre orientation which has undergone localised buckling of the tube. The wavelength of the localised buckling was approximately equal to the tube diameter, and corresponded approximately with the positions of the fibre crossovers which resulted from the manufacturing process.

At the peak load, the FRP composite tube remained integral, the only visible signs of distress to the composite were the lines of plastic flow due to the localised bond breakdown between the fibres and resin, and the large lateral deflections of the column. Tensile rupture of the composite was only caused by a significant increase in the lateral deflection beyond the peak load. Typical ultimate failures of the FRP-composite tubes are shown in Plates 5.5 to 5.7, for composites with 90 degree, 67½ degree and 45 degree fibre orientations respectively. Rupture of the composite with a 45 degree fibre orientation did not occur at mid-height but at the intersection of the fibre crossovers which result in points of weakness in the composite. Inspection of the concrete core after failure showed the concrete to be of a highly fissured nature, but re-compacted under the high triaxial state of stress.

5.3.1 Ultimate failure load

The ultimate axial and moment capacity of a column is dependent on the relative magnitudes of the applied axial load and bending moment. Considering a small element of the column to avoid second-order effects, an axial load is applied to the element at a

constant eccentricity, Figure 5.2(a). The load-point displacement is increased in small increments and the corresponding capacity of the element is calculated from the basic principles of equilibrium and the constitutive equations for the concrete, assuming the cross-section remains plane.

The axial capacity of the column is plotted in Figure 5.2(b) as a function of vertical displacement. If the slope of the load-displacement curve is positive, then the column is in a state of stable equilibrium, and cannot fail due to instability. Failure of the column with a positive load-displacement slope is classified as a material failure. However, when the slope becomes negative the column is unstable and is deemed to have failed. The critical point for a stability failure is where the slope of the load-displacement curve is zero.

The column failure loads and corresponding deflections for the eccentrically loaded columns are given in Table 5.1 and Table 5.2. The effective length of the columns was taken as the distance between the centres of the rollers used to applied the eccentric loading. In order to compare the failure loads for different column diameters, the column strength is non-dimensionalised with respect to the squash load of unconfined concrete, thus:

$$\overline{N} = \frac{N_u}{f_{co} A_c} \qquad \textbf{(5.2)}$$

The variation in $\overline{N}$ with the effective hoop stiffness of the FRP-composite is shown in Figure 5.3. Axial load capacity increases as the effective hoop stiffness of the FRP-composite increases. Thus, for a given diameter of column and percentage of confinement reinforcement, the largest axial load capacities were achieved with the reinforcing fibres aligned predominately in the hoop direction.

5.3.2 Column slenderness

Comparison of the failure loads and moments given in Table 5.1, Table 5.2 and Figure 5.4, indicates a significant reduction in both the axial load capacity and the moment capacity of the columns as the slenderness ratio increased from 5 to 10. However, all the confined columns continued to exhibit a degree of strength enhancement, due to triaxial containment. The largest reductions in triaxial enhancement due to increasing slenderness were observed in the columns with the largest effective hoop modulus. The reduction in axial load capacity for the hoop wound specimens as the slenderness ratio increased from 5 to 10 ranged from between 46-65%, depending on the effective hoop stiffness of the FRP-composite and unconfined strength of concrete.

The influence of second order effects on the load capacity of conventional reinforced concrete columns are negligible provided $L/D < 12$ [78]. Therefore, the influences of second-order effects on FRP-confined columns are more significant at a lower slenderness ratio than in conventional reinforced concrete columns. Furthermore, as the slenderness ratio of the column increases the benefits of triaxial confinement from the FRP-composite diminishes.

5.3.3 Load-deflection response

Typical load-deflection curves for the eccentrically loaded columns are shown in Figure 5.5. The load-deflection curves for all the columns are given in Appendix G. Initially, the load-deflection response is approximately linear. However, as the axial load increases, the non-linear behaviour of concrete causes the rate of lateral deflection to increase in all the columns. Once the peak load has been exceeded, lateral deflections continue to increase until rupture of the FRP composite results in a brittle failure.

The load-deflection response of the confined columns is dependent on the fibre orientation of the FRP composite shell. Initially, the lateral deflections of columns with the same diameter, effective length and unconfined strength of concrete are similar, irrespective of the orientation of the fibres in the FRP composite. At higher load intensities[1], the lateral deflections increase due to softening of the resistance of the concrete. However, the rate of increase in lateral deflection is governed by orientation of the fibres in the FRP-composite. The rate of increase in the lateral deflections reduces as the fibre orientation of the FRP-composite tends towards a hoop winding. The larger effective hoop stiffness obtained from a hoop winding inhibits the softening of the concrete. This corresponds to the experimental work in Chapter 3, where the post-crushing tangent modulus of the confined concrete was found to increase proportionally with the effective hoop stiffness of the FRP-composite.

5.3.4 Load-strain characteristics

The load-strain curves for the eccentrically loaded columns are shown in Figure 5.6 and Appendix H. Initially, since the behaviour of the columns at failure was unknown and expected to be extremely brittle, the extensometers were removed before the peak load was achieved. Consequently, the failure strains were not measured for column diameters in the

---

[1] The load intensity at which the second-order effects become significant is governed by the column slenderness ratio L/D and unconfined concrete strength.

range 60 mm to 100 mm.

The maximum compressive strains in the extreme concrete fibres greatly exceed the perceived $3500\mu\varepsilon$ compressive failure strain of concrete. The largest compressive and tensile strains to failure were achieved by columns confined by FRP-composites with a 90 degree fibre orientation. The failure strains were smaller for columns confined with a smaller effective hoop modulus or for columns with a larger slenderness ratio.

The load-strain behaviour of the confined columns is analogous to the load deflection response. Initially, the load-strain behaviour of confined columns with similar unconfined concrete strengths and slenderness ratios are the same. As the axial strain increases, softening of the resistance of the concrete results in the observed non-linear behaviour. The rate of softening in resistance of the concrete is determined by the confinement provided by the FRP-composite shell.

5.3.5 Moment-curvature behaviour

The moment-curvature curves for the columns are given in Figure 5.7 and Appendix I. The curvature at mid-height of the column is given by:

$$\chi = \frac{|\varepsilon_1 - \varepsilon_2|}{D} \qquad \textbf{(5.3)}$$

The moment-curvature relationships for all the columns are approximately bilinear. The initial almost linear response of the columns indicates a rapid increase in moment with only a small increase in curvature. The initial slope is not affected by the angle of fibre orientation since the confining stresses in the composite are not utilised at these low strains. The magnitude of this slope is equal to the initial stiffness of an unconfined concrete column, given by:

$$k_c = E_{ci} I_c \qquad \textbf{(5.4)}$$

As micro-cracks develop in the concrete, the slope of the curve decreases to give larger curvatures. The secondary slope of the moment-curvature relationship is governed by the effective hoop modulus of the FRP-composite, with increasing stiffness being measured as the orientation of the fibres tends towards the hoop direction. The large curvatures give rise to the large deflections observed during the tests. These large deflections warn of impending failure, which occurs by the concrete crushing.

5.4 LIMITING STRAIN FAILURE CRITERION

Immediately prior to failure, the concrete is an extremely fissured and fractured material, and without the presence of the FRP composite, the concrete would have no structural integrity. Therefore, whilst this method of construction enables the concrete to undergo extreme compressive strains, the need for structural integrity will prevent these strains being utilised in normal design procedures. The failure loads, deflections and moments measured in the columns at a compressive strain of $3500\mu\varepsilon$ are given in Table 5.3 and Table 5.4.

The effects of slenderness on the axial load capacity of the columns at the limiting strain criterion are negligible, as illustrated in Figure 5.8. Furthermore, even at the significantly lower compressive strain the columns exhibit a load capacity that is comparable to the squash load of unconfined concrete, despite the presence of the eccentricity of load.

5.5 SUMMARY

The experimental work has shown that triaxial confinement from FRP-composites increases the load carrying capacity of concrete columns. The enhancement in strength and ductility of the confined columns increased in proportion to the effective hoop modulus of the confining FRP-composite shell. The use of an angle-ply FRP-composite to provide both circumferential and longitudinal reinforcement does not increase the flexural capacity of the columns. The increased longitudinal stiffness of the FRP-composite does not offset the reduction in the augmented strength of the confined concrete. Thus, a 90 degree fibre orientation is the most efficient winding arrangement for increasing the axial and flexural strength of FRP-confined concrete columns.

The benefits of triaxial confinement were also found to diminish as the slenderness ratio of the column increased. Reductions in axial capacity of up to 65% were observed for the hoop wound specimens as the slenderness ratio was increased from 5 to 10. All the specimens exhibited instability at failure due to the non-linear behaviour of the confined concrete. Therefore, second-order effects on the ultimate load capacity of FRP-confined columns must be included in any design methodology, even for columns with relatively low slenderness ratios of $L/D = 5$.

The influence of second-order effects at $3500\mu\varepsilon$ compressive strain are negligible if the column slenderness, $L/D < 12$. Therefore, existing codes of practice for concrete construction [61] may be used for the design of the column, with a simple strength modification factor to account for the confined concrete strength at $3500\mu\varepsilon$.

Diameter mm	Angle of wind °	Initial Eccentricity mm	Effective Length mm	f_{cu} N/mm^2	N_u kN	δ_v mm	M_u kNm	$\mu\varepsilon_{1u}$
59.90	75.5	3.00	370.0	27.9	167	6.67	1.62	-
			370.0	36.2	172	7.94	1.88	-
			670.2	32.3	92	8.80	1.09	-
79.89	78.1	4.00	467.8	19.7	312	11.13	4.72	-
			469.6	36.4	431	-	-	-
			869.7	25.6	171	10.72	2.52	-
			867.9	31.2	200	11.85	3.18	-
100.09	80.4	5.00	569.7	23.4	447	13.77	8.40	-
			569.9	35.2	568	11.98	9.65	-
			1,068.9	22.6	278	11.38	4.56	-
			1,070.3	32.8	312	10.66	4.88	-
125.64	82.3	6.25	694.9	27.4	584	14.31	12.04	30,500
			694.7	31.7	627	15.66	13.73	27,500
			1,320.0	46.3	454	13.55	9.00	7,100
150.40	83.6	7.50	869.6	33.9	866	19.82	23.67	34,400
			1,620.0	28.4	399	18.55	10.39	8,700
			1,620.0	37.8	486	17.68	12.24	8,400
200.64	85.2	10.00	1,120.6	24.6	1,072	22.09	34.39	28,500
			1,120.4	43.7	1,397	10.43	28.55	24,500
			2,120.8	27.7	627	22.08	20.10	7,300
300.67	86.8	15.00	1,650.0	25.3	2,530	-	-	-
			1,650.0	36.8	3,300	-	-	-
			3,150.0	39.7	2,100	-	-	-
399.67	87.6	20.00	2,150.0	29.0	5,050	-	-	-
			2,150.0	40.5	5,860	-	-	-
			4,150.0	36.5	3,300	-	-	-

Table 5.1. Failure loads of eccentrically loaded columns confined by fibres orientated predominately in the hoop direction

Diameter mm	Angle of wind °	Initial Eccentricity mm	Effective Length mm	f_{cu} N/mm^2	N_u kN	δ_v mm	M_u kNm	$\mu\varepsilon_{1u}$
79.90	57.8	4.00	469.6	24.6	213	6.72	2.28	-
			469.1	28.1	243	7.54	2.80	-
			869.0	21.5	131	7.82	1.55	-
			869.7	27.2	188	4.44	1.59	10,649
100.08	71.4	5.00	569.6	29.5	392	11.50	6.47	-
			569.9	31.3	398	9.58	5.81	-
			1,069.1	21.4	189	11.69	3.15	11,900
			1,069.8	33.2	237	11.46	3.90	9,200
150.08	71.3	7.50	770.0	27.2	532	18.76	13.96	32,400
			770.0	36.7	669	18.38	17.32	30,900
			1,620.1	24.6	290	13.98	6.24	6,100
			1,619.8	36.6	431	13.86	9.21	6,300
79.91	43.4	4.00	469.1	30.7	172	2.55	1.13	13,200
			469.9	34.4	185	3.20	1.33	15,425
			789.9	34.3	150	5.35	1.40	4,319
100.14	49.9	5.00	569.9	33.9	240	6.49	2.76	17,960
			569.9	40.1	273	5.67	2.91	17,150
			1,068.7	29.3	177	7.91	2.28	4,794
			1,069.3	30.0	154	8.91	2.15	5,629
150.35	48.0	7.50	869.8	24.2	345	9.73	5.94	19,100
			869.9	36.7	453	8.29	7.15	14,600
			1,616.8	25.9	286	9.45	4.85	4,200
			1,620.3	37.1	339	10.48	6.10	5,000

Table 5.2. Failure loads of eccentrically loaded columns confined by fibres orientated at 67½ degrees or 45 degrees

Diameter mm	Angle of wind °	Initial Eccentricity mm	Effective Length mm	f_{cu} N/mm^2	3,500$\mu\varepsilon$ Compressive Strain		
					N kN	δ mm	M kNm
59.90	75.5	3.00	370.0	27.9	71	0.49	0.25
			370.0	36.2	76	0.50	0.27
			670.2	32.3	66	2.50	0.36
79.89	78.1	4.00	467.8	19.7	94	0.60	0.43
			469.6	36.4	172	0.29	0.74
			869.7	25.6	104	2.22	0.64
			867.9	31.2	128	2.06	0.77
100.09	80.4	5.00	569.7	23.4	158	0.18	0.82
			569.9	35.2	231	0.11	1.18
			1,068.9	22.6	179	1.58	1.18
			1,070.3	32.8	226	1.43	1.45
125.64	82.3	6.25	694.9	27.4	290	1.08	2.13
			694.7	31.7	361	1.92	2.95
			1,320.0	46.3	417	6.16	5.18
150.40	83.6	7.50	869.6	33.9	488	1.49	4.39
			1,620.0	28.4	334	5.72	4.43
			1,620.0	37.8	414	5.16	5.24
200.64	85.2	10.00	1,120.6	24.6	623	1.88	7.39
			1,120.4	43.7	916	2.08	11.07
			2,120.8	27.7	580	10.12	11.66
300.67	86.8	15.00	1,650.0	25.3	1,500	3.25	27.38
			1,650.0	36.8	-	-	-
			3,150.0	39.7	-	-	-
399.67	87.6	20.00	2,150.0	29.0	-	-	-
			2,150.0	40.5	3,680	4.89	91.59
			4,150.0	36.5	-	-	-

Table 5.3. Experimental results at a compressive strain of 3500$\mu\varepsilon$ for eccentrically loaded columns confined by fibre orientated predominately in the hoop direction

Diameter mm	Angle of wind °	Initial Eccentricity mm	Effective Length mm	f_{cu} N/mm^2	3500$\mu\varepsilon$ Compressive Strain		
					N kN	δ mm	M kNm
79.90	57.8	4.00	469.6	24.6	92	0.48	0.41
			469.1	28.1	122	0.52	0.55
			869.0	21.5	115	2.10	0.70
			869.7	27.2	136	0.13	0.56
100.08	71.4	5.00	569.6	29.5	228	0.44	1.24
			569.9	31.3	223	0.84	1.30
			1,069.1	21.4	169	3.42	1.42
			1,069.8	33.2	219	4.05	1.98
150.08	71.3	7.50	770.0	27.2	310	1.54	2.80
			770.0	36.7	452	1.76	4.19
			1,620.1	24.6	276	7.48	4.13
			1,619.8	36.6	413	6.74	5.88
79.91	43.4	4.00	469.1	30.7	130	0.43	0.57
			469.9	34.4	153	0.81	0.74
			789.9	34.3	146	2.35	0.92
100.14	49.9	5.00	569.9	33.9	148	0.74	0.85
			569.9	40.1	211	0.50	1.16
			1,068.7	29.3	172	4.88	1.69
			1,069.3	30.0	147	4.04	1.33
150.35	48.0	7.50	869.8	24.2	299	1.71	2.75
			869.9	36.7	425	1.33	3.75
			1,616.8	25.9	285	7.65	4.32
			1,620.3	37.1	335	6.95	4.84

Table 5.4. Experimental results at a compressive strain of 3500$\mu\varepsilon$ for eccentrically loaded columns confined by fibre orientated at 67½ degrees or 45 degrees

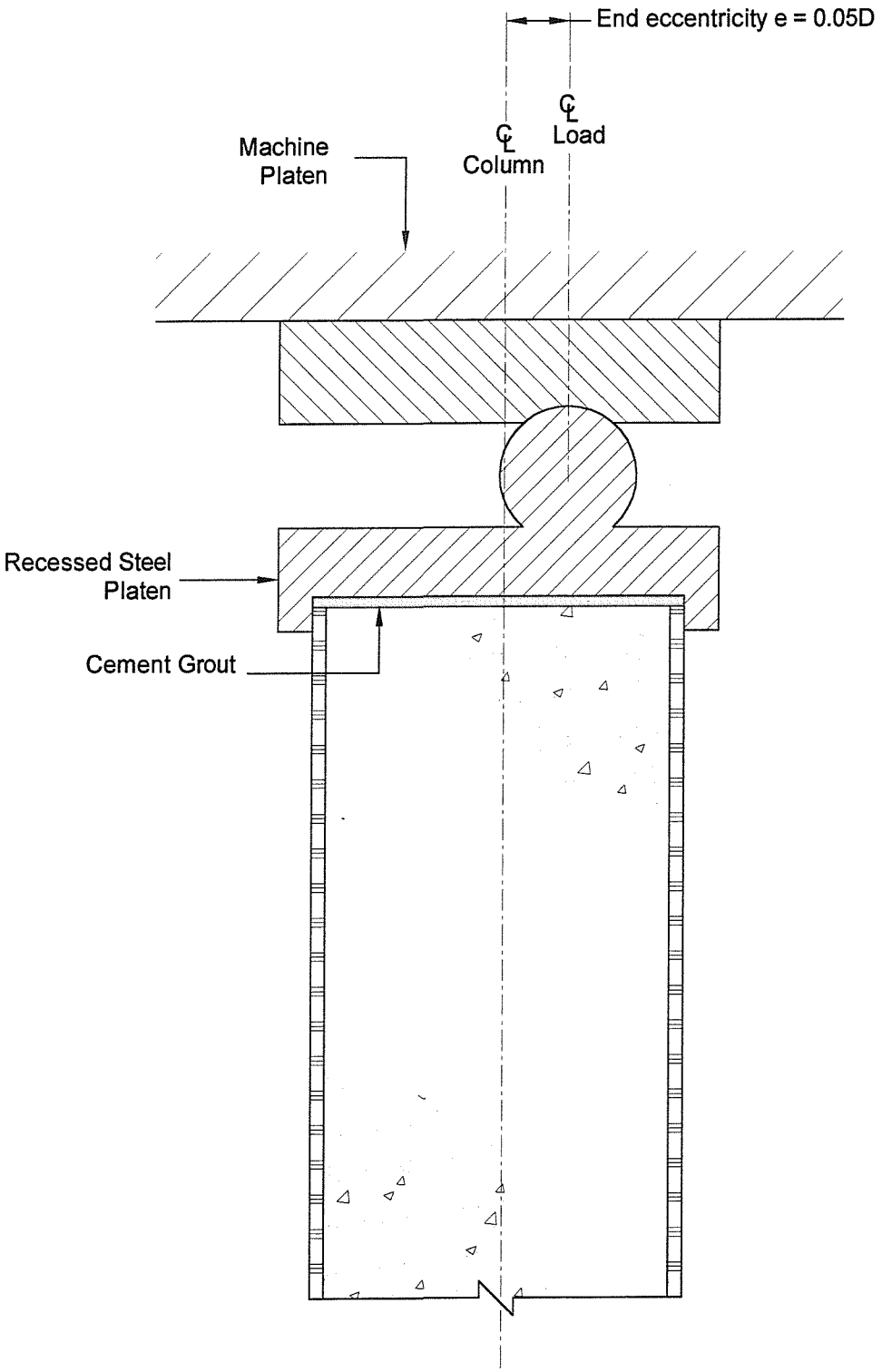

Figure 5.1. End detail of the eccentrically loaded columns

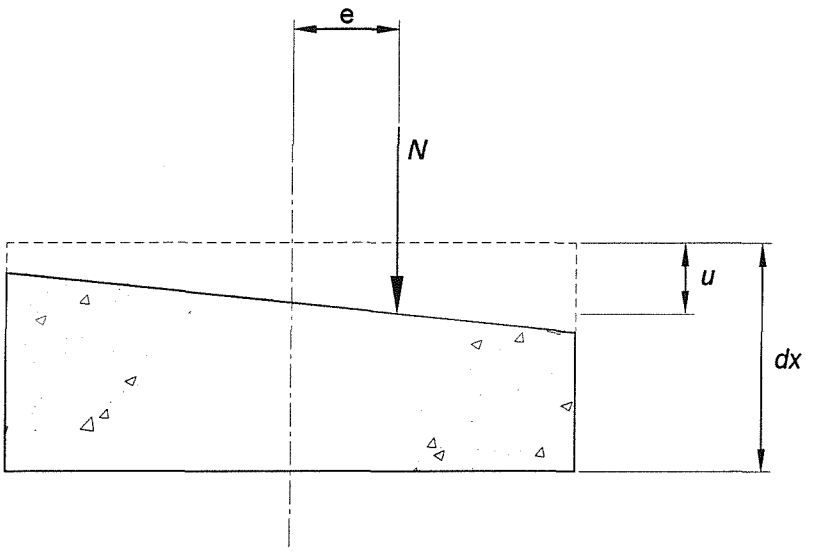

(a) Concrete column element

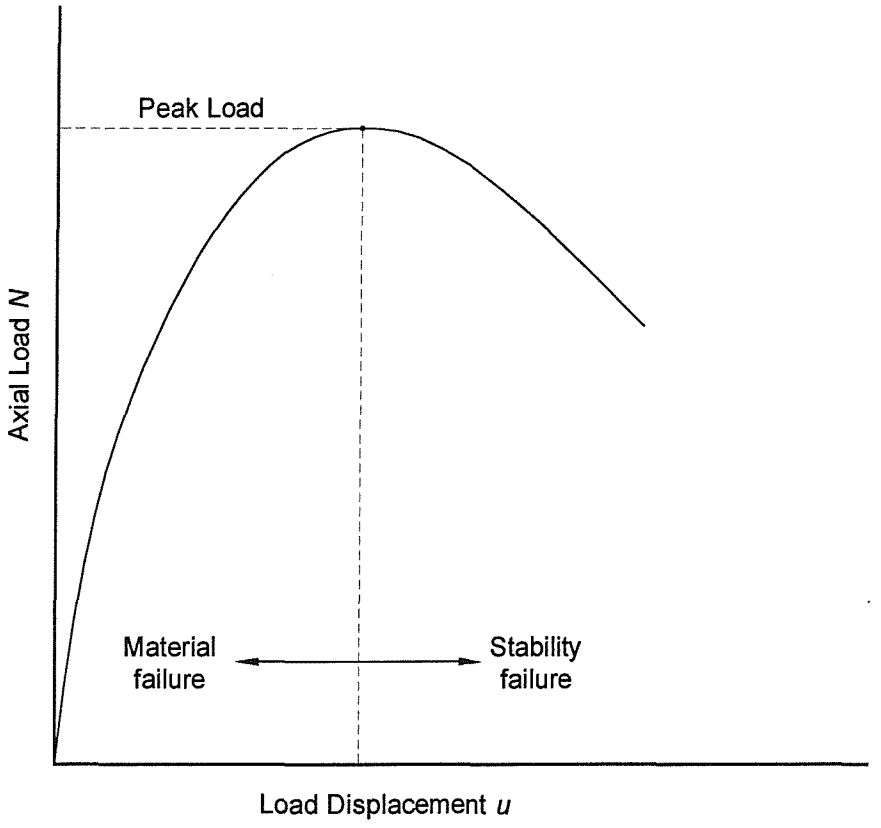

(b) Load-displacement curve

Figure 5.2. Failure mode of eccentrically loaded columns

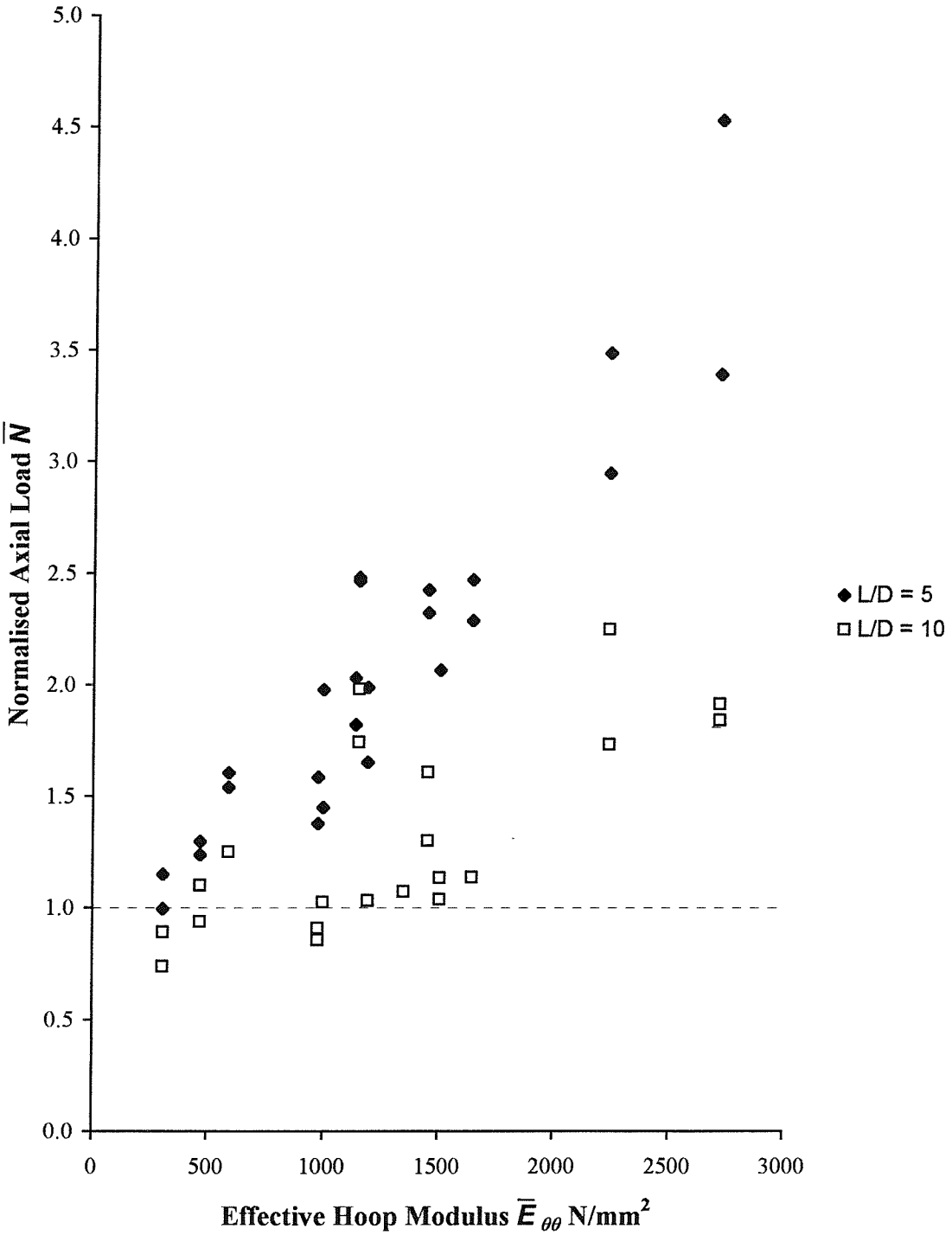

Figure 5.3. Influence of the effective hoop modulus of the FRP-composite confinement on the ultimate axial load capacity

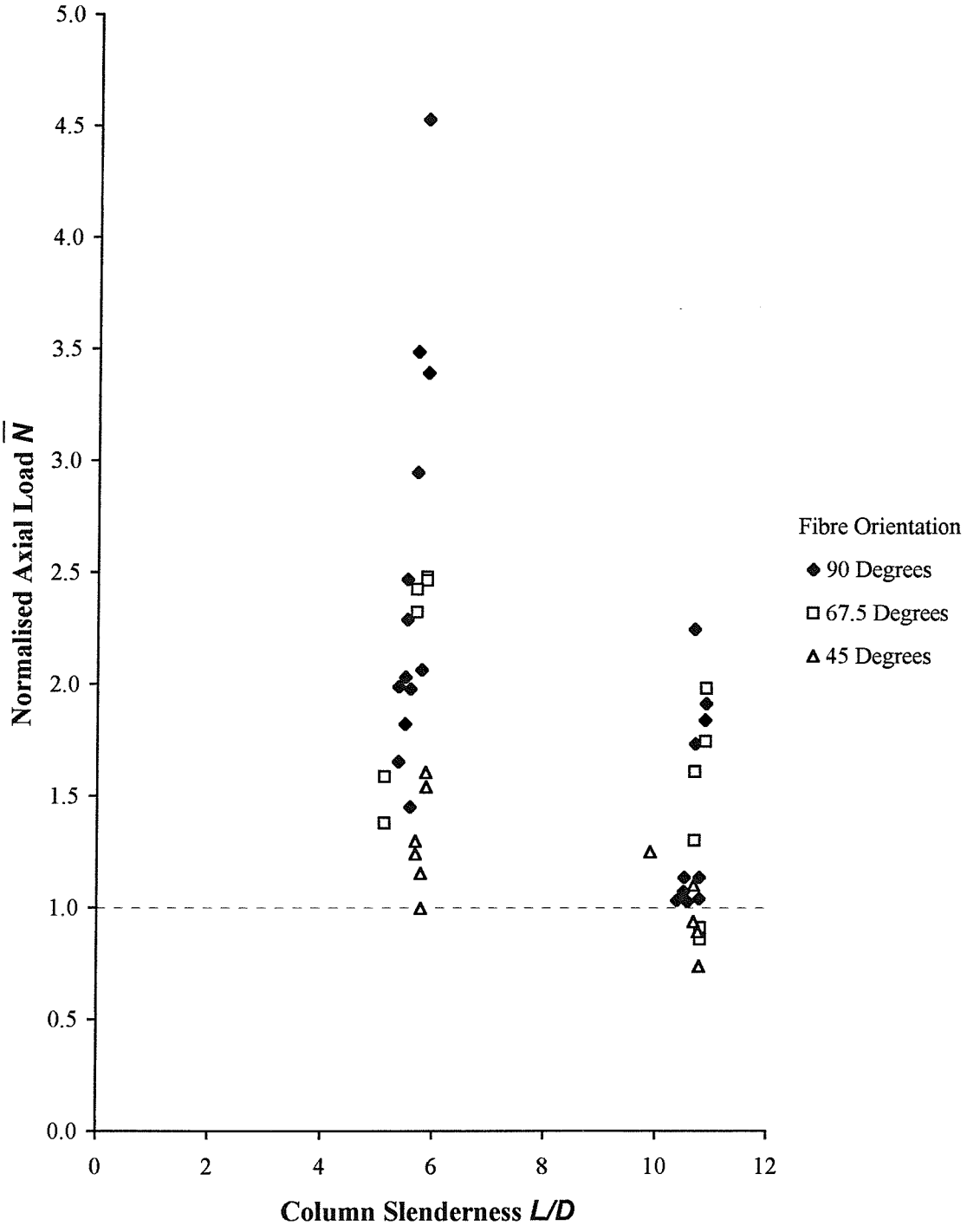

Figure 5.4. Influence of column slenderness on the ultimate axial load capacity of FRP-confined columns

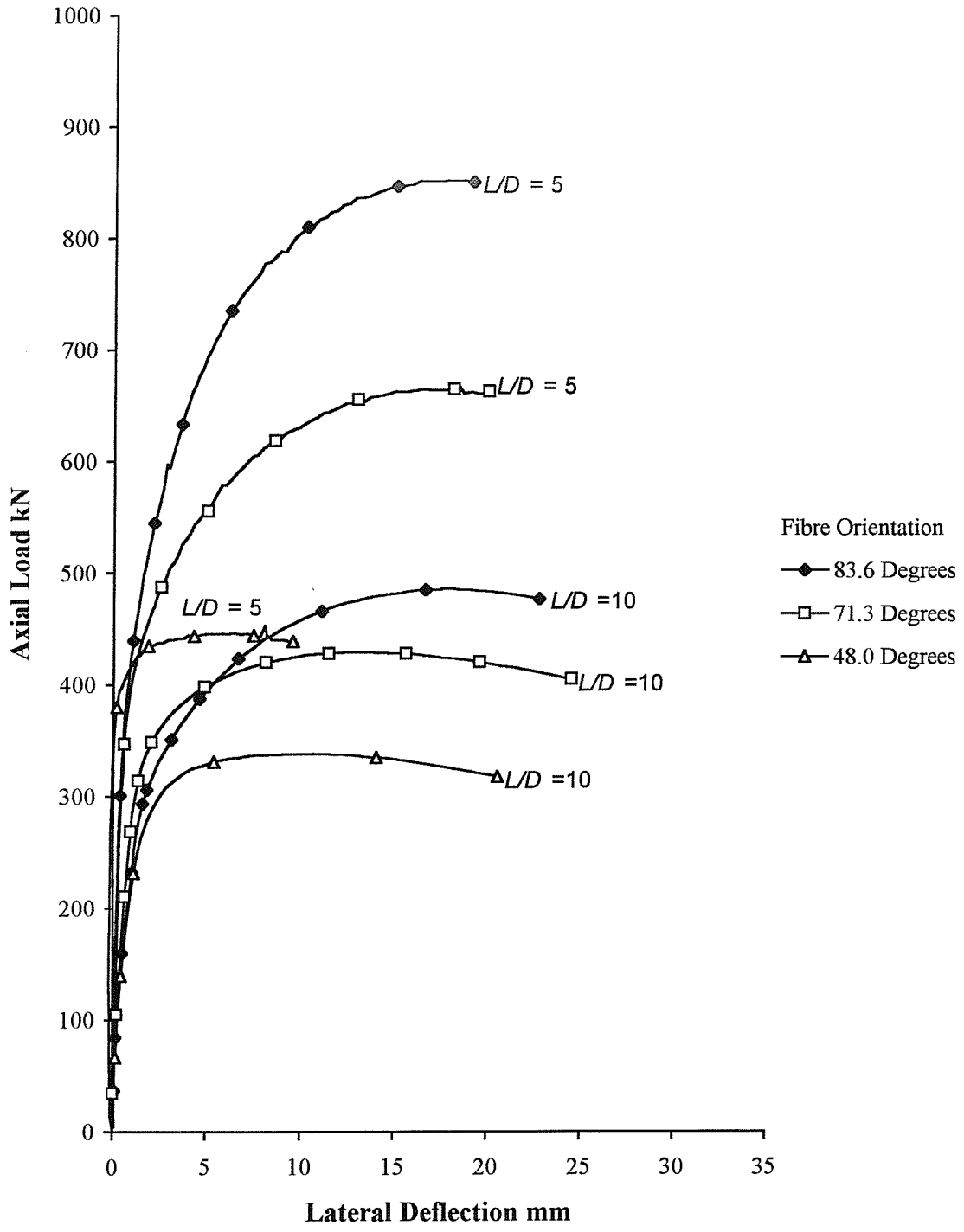

Figure 5.5. Typical load-deflection curves for FRP-confined columns subjected to eccentric loading

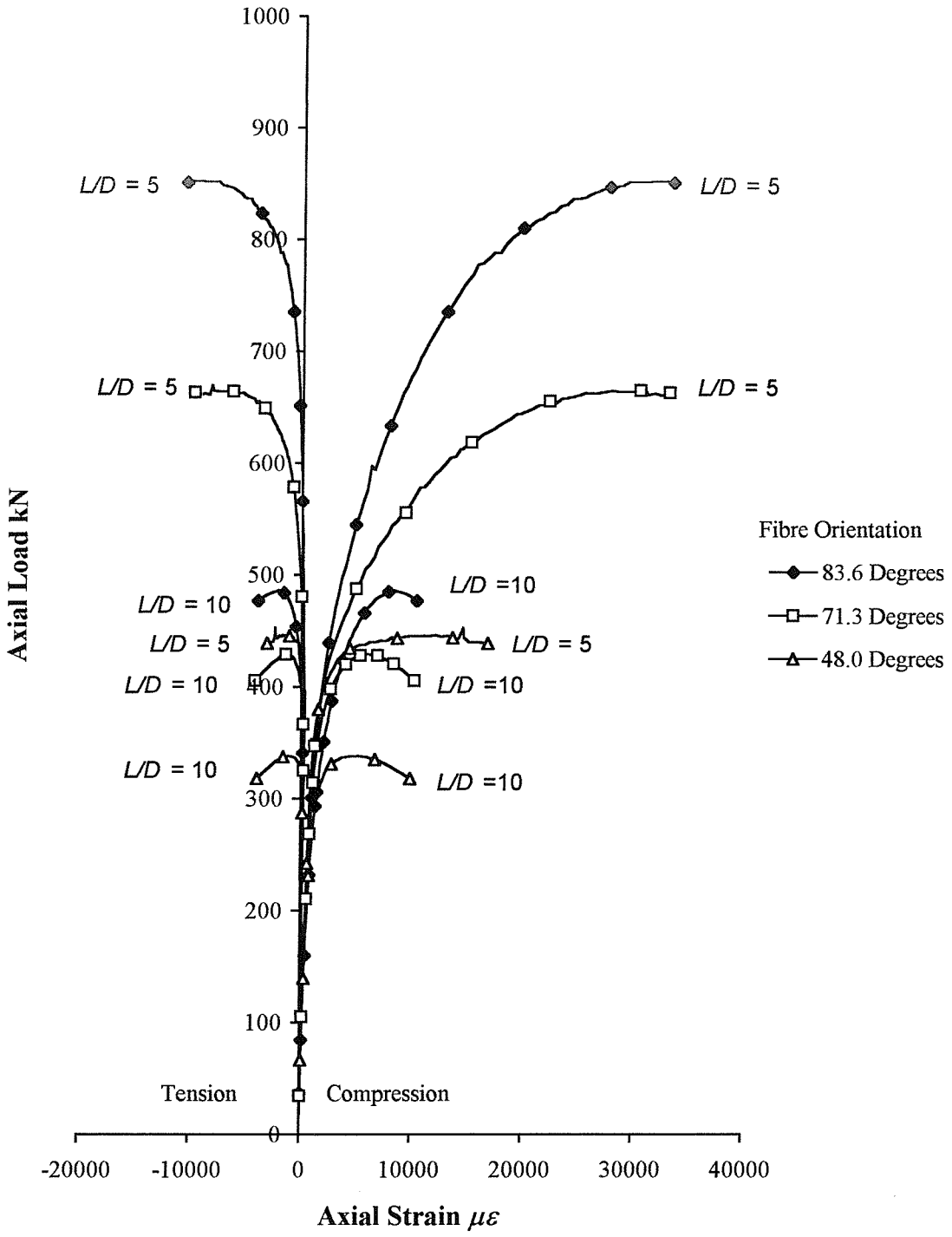

Figure 5.6. Typical load-strain curves for FRP-confined columns subjected to eccentric loading

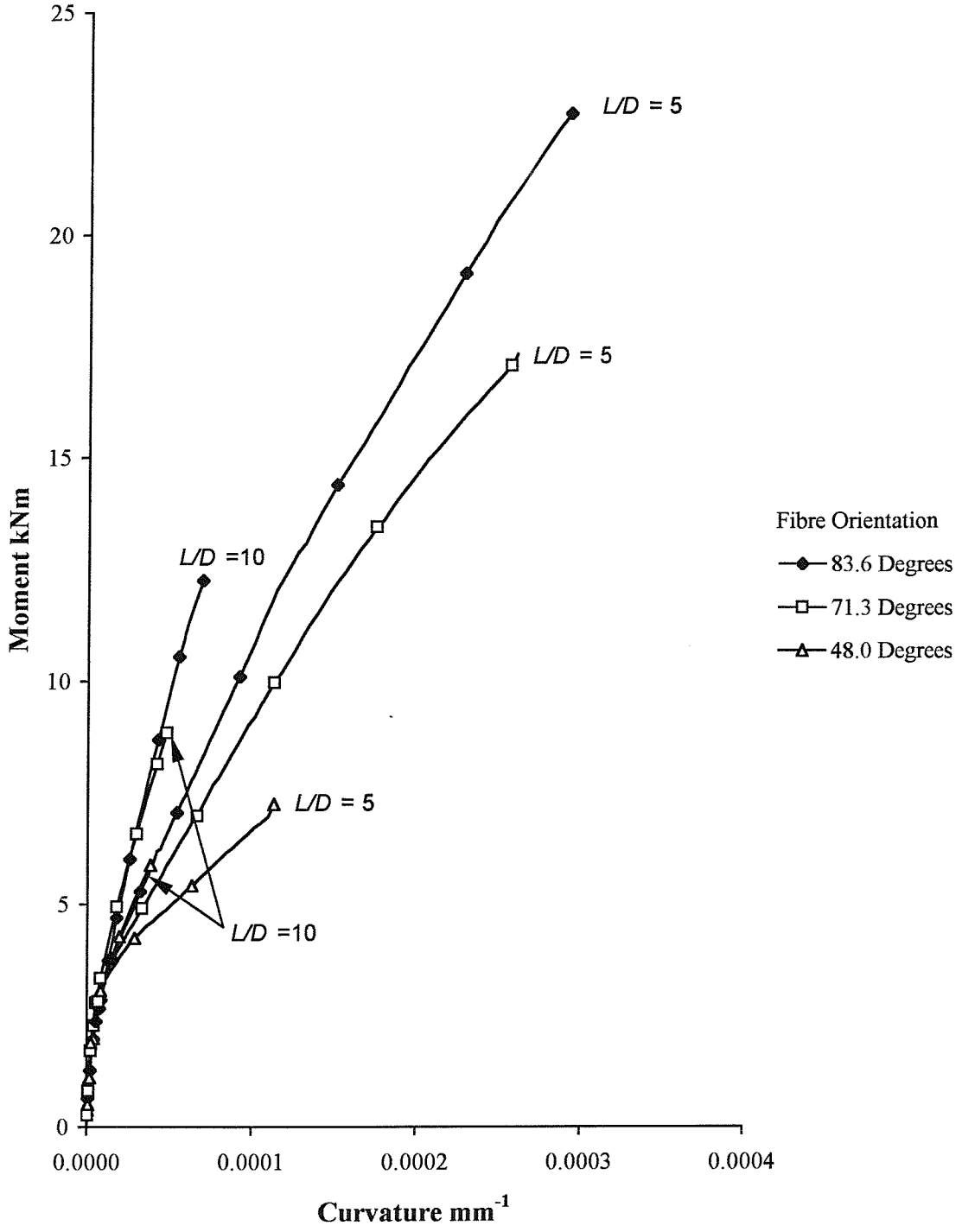

Figure 5.7. Typical moment-curvature curves for FRP-confined columns subjected to eccentric loading

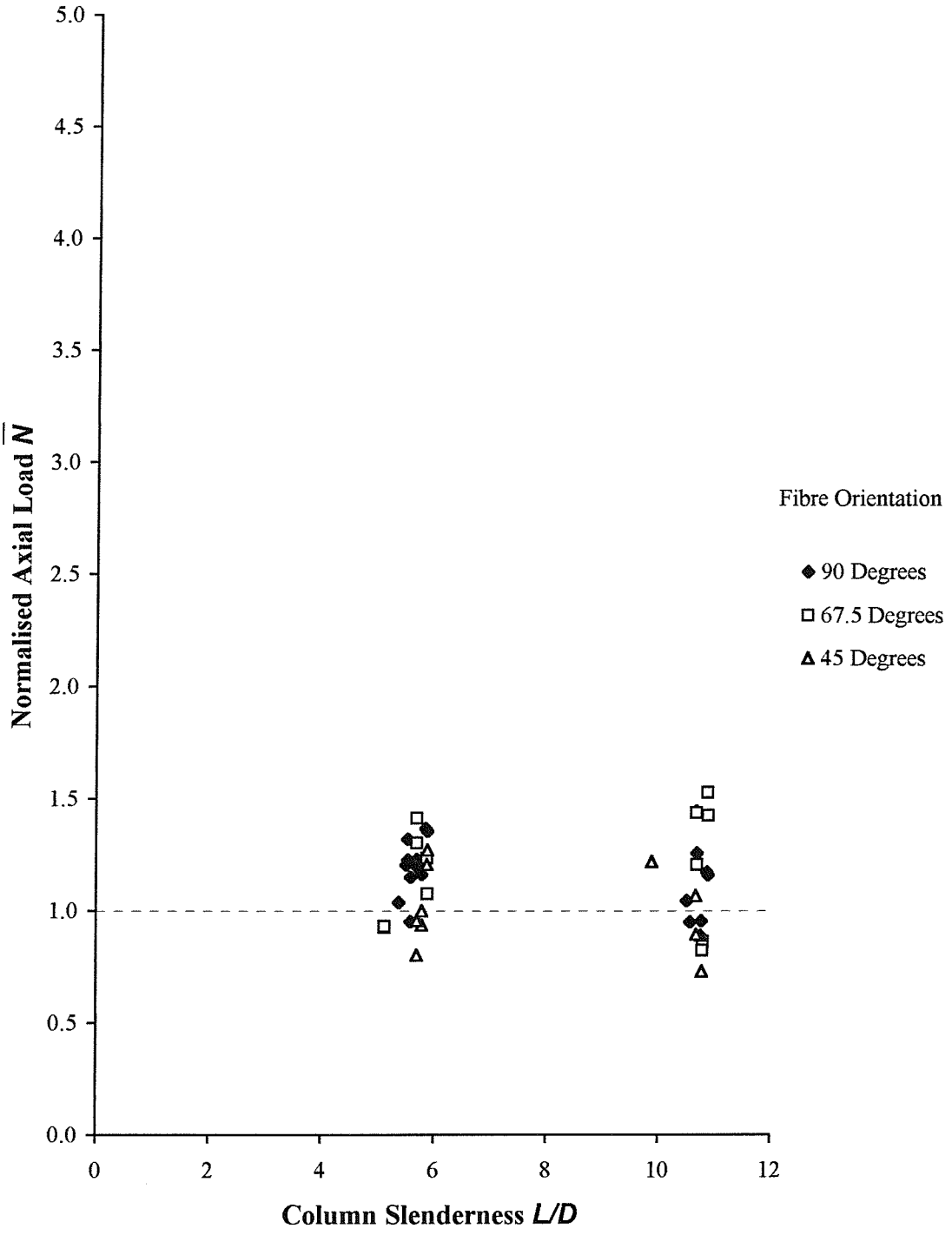

Figure 5.8. Influence of column slenderness on the axial load capacity of FRP-confined columns at 3500$\mu\varepsilon$ compressive strain

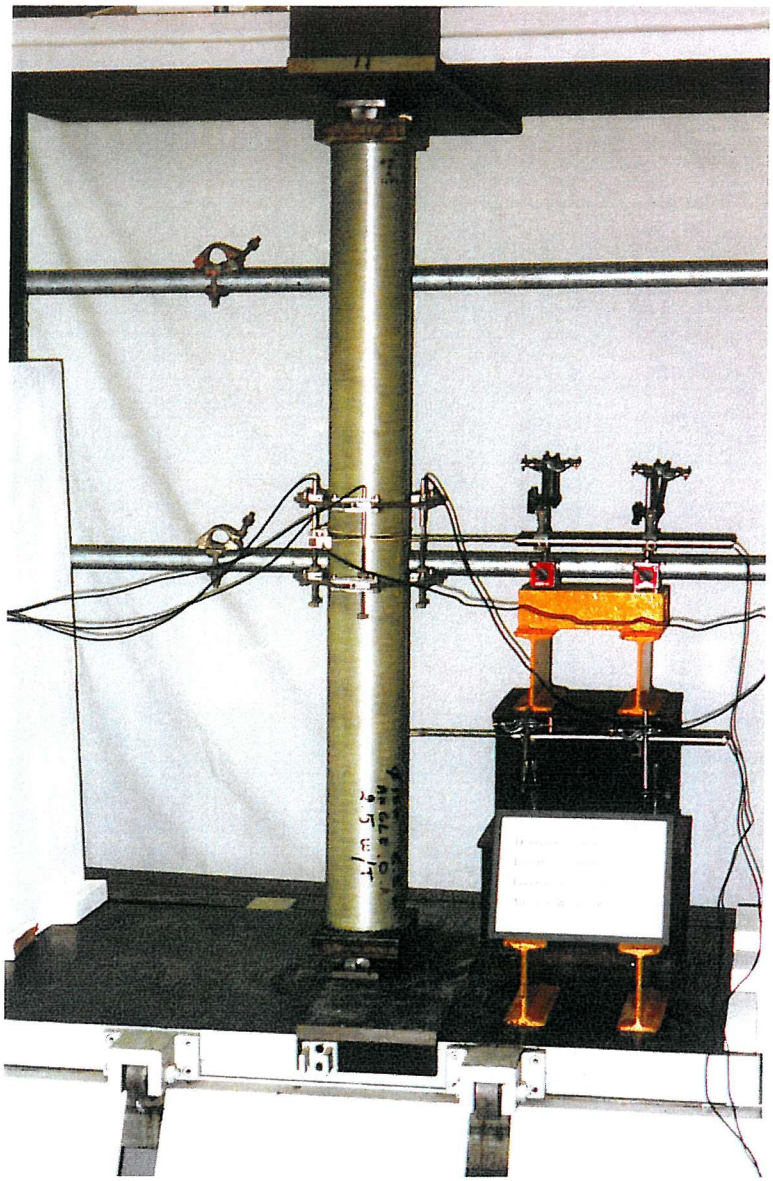

Plate 5.1. Typical test arrangement for an eccentrically loaded column

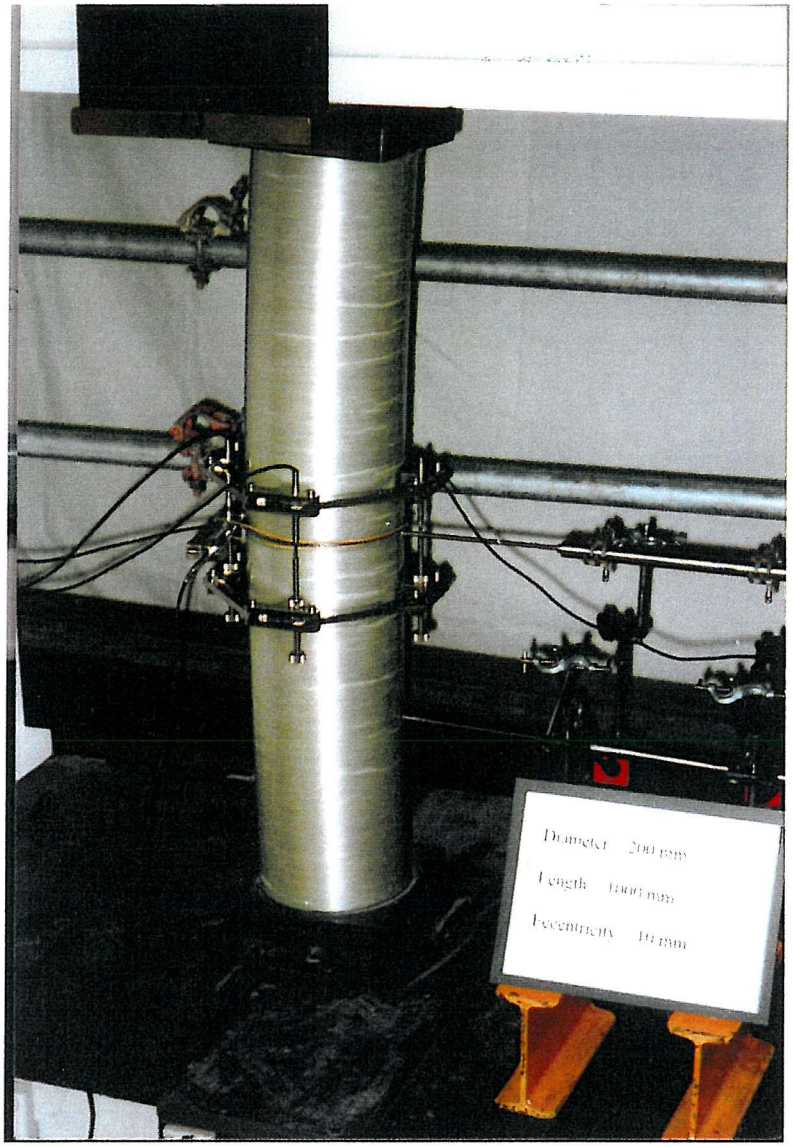

Plate 5.2. Whitening of the resin matrix due to localised bond breakdown between the fibres and resin

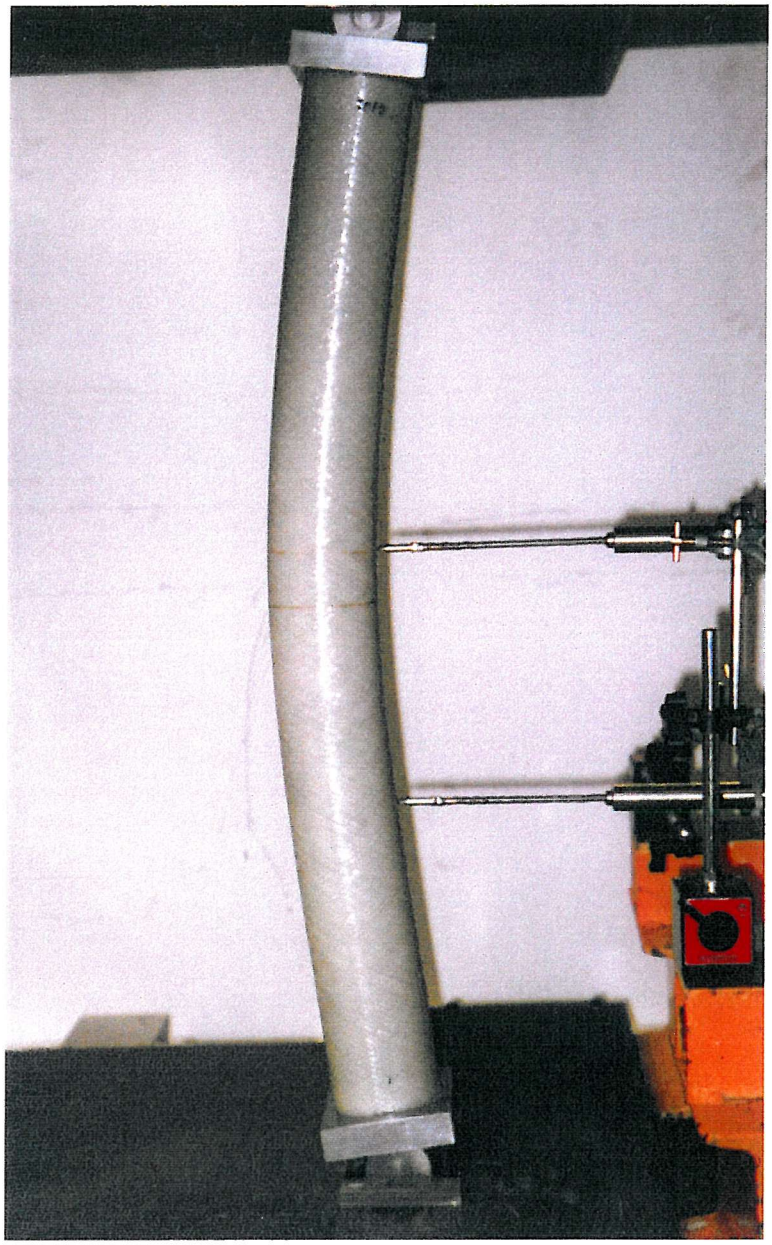

Plate 5.3. Deflected profile of an eccentrically loaded column at peak load

Plate 5.4. Localised buckling of an FRP-composite tube with a fibre orientation of 43.4 degrees

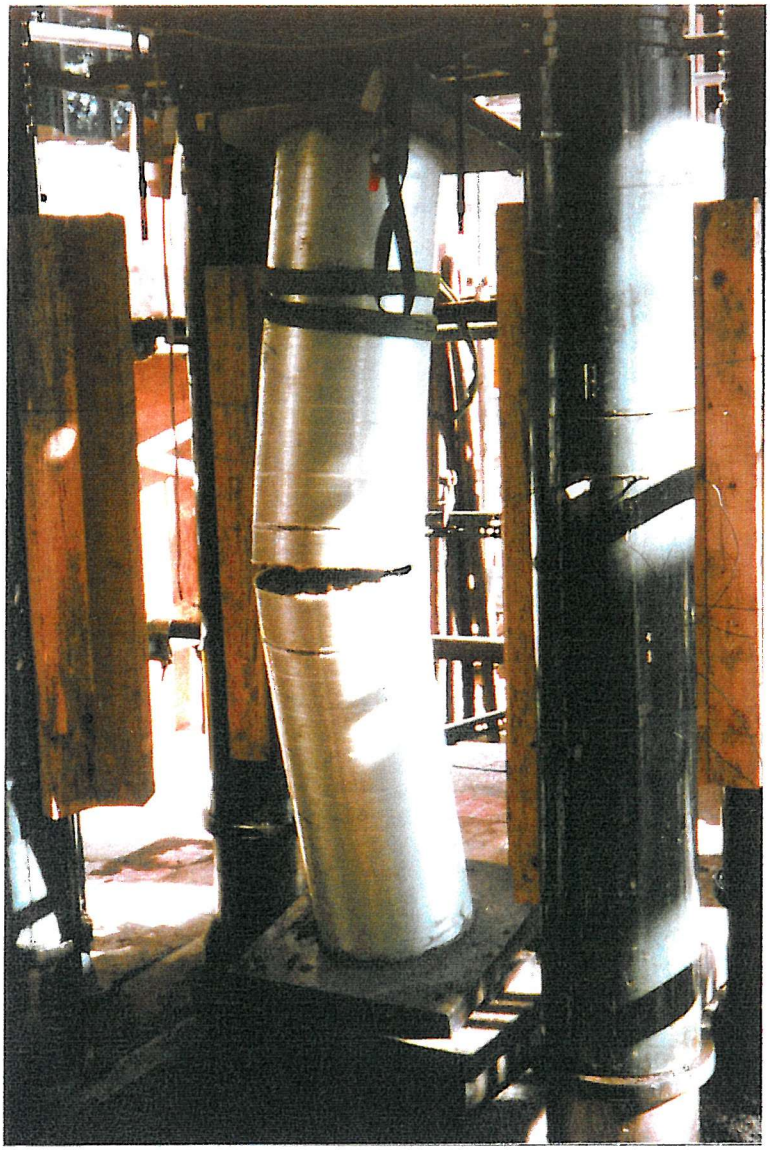

Plate 5.5. Typical ultimate failure mode of a concrete-filled FRP-composite column with confining fibres orientated at 90 degrees

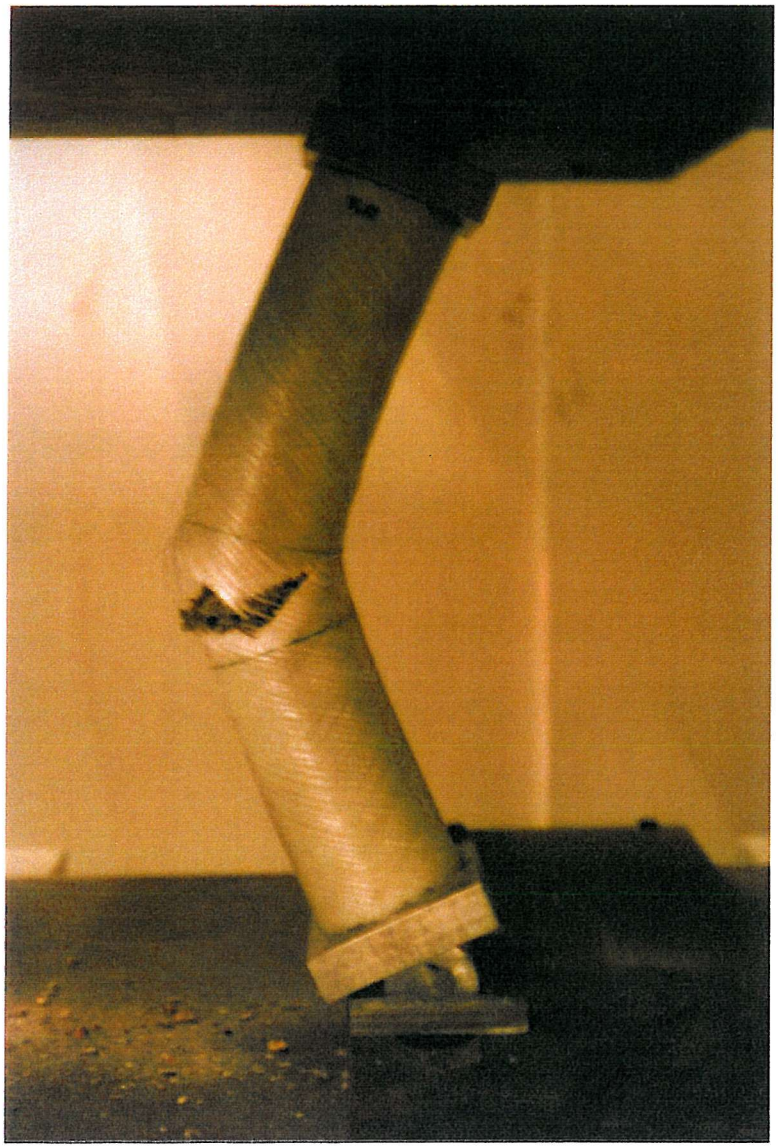

Plate 5.6. Typical ultimate failure mode of a concrete-filled FRP-composite column with confining fibres orientated at 67½ degrees

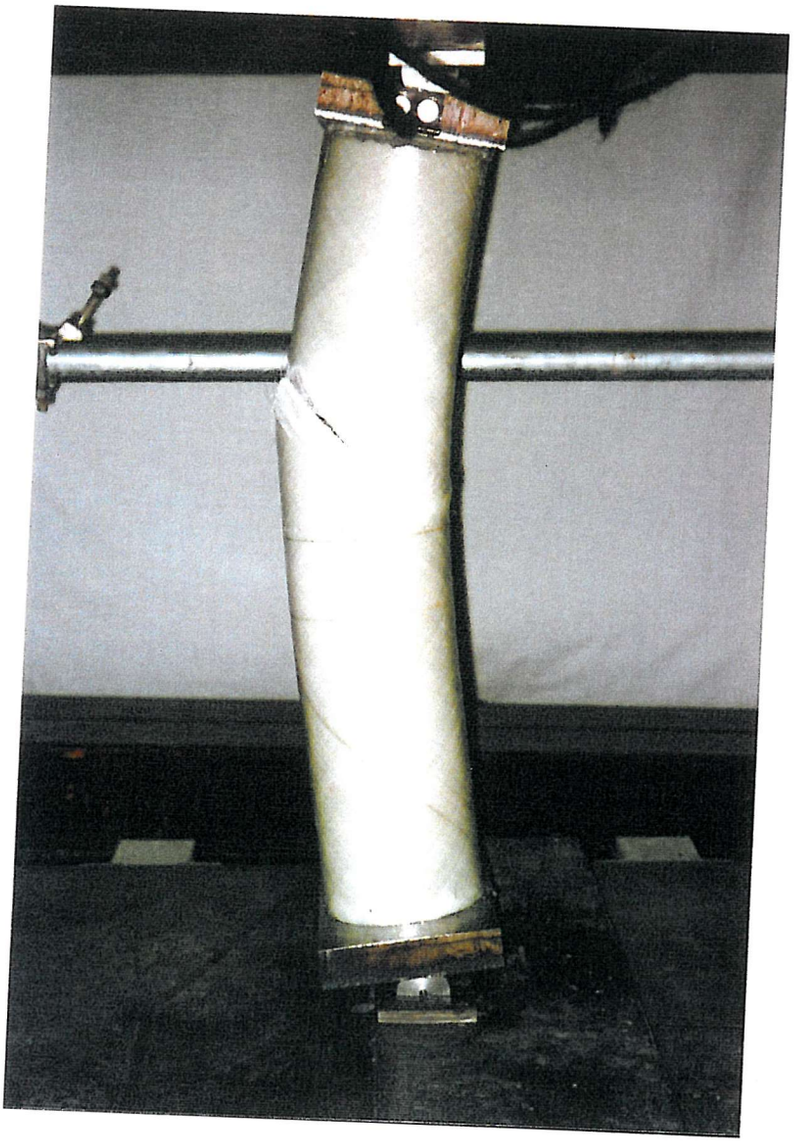

Plate 5.7. Typical ultimate failure mode of a concrete-filled FRP-composite column with confining fibres orientated at 45 degrees

CHAPTER 6

NUMERICAL MODELLING OF CONCRETE FILLED FRP-COMPOSITE COLUMNS

6.1 COLUMN THEORY

All structures deflect under loading. Generally, the effect of deflections on the overall geometry of a structural element may be neglected. However, in the particular case of columns, the deflections may result in significant additional moment. Thus, the accurate analysis of columns requires the use of complex second-order differential equations to represent the final deformed shape of the column. The non-linear behaviour of concrete results in the second-order differential equations becoming intractable and solutions may only be obtained using numerical methods.

The maximum axial load capacity of a very short column is governed by the material properties of the concrete. Thus, the maximum squash load of an FRP-confined concrete column in the absence of any moment on the cross-section is given by:

$$N_{uz} = A_c f_{cc} \tag{6.1}$$

As the column slenderness increases, the failure of the column is governed by stability. The failure load of a pinned-end column was first solved by Euler (circa 1744) who demonstrated that such a column remains stable until a critical load is reached at which lateral deflections develop. The critical load of the column is given by:

$$N_{crit} = \frac{\pi^2 EI}{L_e^2} \tag{6.2}$$

The calculation of the critical buckling load of a column requires the flexural stiffness EI of the column, which is the slope of the relationship between moment and curvature. However, as shown in Appendix I, the moment-curvature response of FRP-confined concrete columns is non-linear, and the critical buckling load cannot be determined directly.

6.1.1 Column slenderness

Values of N_{uz} and N_{crit} have been calculated for a circular concrete column with an unconfined ultimate strength of 25 N/mm^2. The concrete was assumed to be uncracked, and the modulus of elasticity of the concrete was determined from equation 4.5. Figure 6.1 gives the values of N_{crit} / N_{uz} over a range of slenderness ratios, L_e/D. If the value of N_{crit} / N_{uz} is greater than 5, the effects of stability on the collapse load are negligible and second-order effects can be neglected [78]. The limiting criterion $N_{crit} / N_{uz} > 5$ corresponds to a slenderness ratio of less than or equal to 12 for conventional steel reinforced concrete

columns, and is the limit adopted by BS 8110 [61] for the design of stocky columns. The limiting slenderness ratio for FRP-confined concrete circular columns may be determined using the following expression:

$$\frac{N_{crit}}{N_{uz}} = 5 = \frac{\pi^2 EI}{L_e^2 A_c f_{cc}}$$

$$\frac{L_e}{D} = \left(\frac{\pi^2 E_{ci}}{80 f_{cc}}\right)^{0.5} \qquad \textbf{(6.3)}$$

The effect of increasing the confinement index, f_{cc}/f_{co} on the limiting slenderness ratio is also illustrated in Figure 6.1. Maintaining the limiting criterion of $N_{crit} / N_u > 5$ to minimise the effects of stability, it can be seen that as the confinement index increases the limiting slenderness ratio decreases significantly. This is because FRP-composite confinement only increases the load capacity of the column whilst the column stiffness is virtually unchanged.

6.2 NUMERICAL ANALYSIS

The ultimate compressive load and the ultimate bending moment for a concrete column are related by an interaction diagram or failure envelope. Interaction diagrams are commonly used by engineers to avoid complex calculations. A typical interaction diagram for conventional reinforced concrete columns is shown in Figure 6.2. Whilst it is possible to produce interaction diagrams for FRP-confined concrete columns, they are impractical due to the range of possible fibre orientations and wall thicknesses and the greater influence of second-order effects at lower slenderness ratios.

Therefore, a computational algorithm has been developed as part of this research which enables the load-deflection behaviour and the moment-curvature relationships of concrete-filled FRP-composite tubes to be studied up to and beyond the maximum load. The CONcrete conFINEment (CONFINE) algorithm for eccentrically loaded FRP-confined concrete columns gives the load-deflection curve for the columns tested, thus allowing a full comparison to be made between theoretical and experimental results.

The analysis is based on the following assumptions:

1. Plane sections remain plane after deformation.
2. The stress in the concrete is derived using the equivalent uniaxial stress-strain relationship for FRP-confined concrete proposed in §4.2.

3. The longitudinal stress in the FRP-composite tube is determined using the transformed reduced stiffness constants.
4. The tensile strength of concrete is neglected.
5. The deflected shape of the column is approximated by a sinusoidal curve.
6. The peak load of the load deflection curve at mid-height is taken as the failure load of all eccentrically loaded columns.
7. Effects of axial shortening are neglected.

6.2.1 Column analysis algorithm

A schematic diagram of the proposed deflected profile is shown in Figure 6.3. The differential equation satisfying equilibrium of the column is derived by equating the internal and external forces and moments at the displaced section.

$$-EIw'' = Nw \tag{6.4}$$

The deflected shape may be calculated by integrating equation 6.4 along the length of the column. However, since the flexural stiffness EI is not constant, the integration of equation 6.4 becomes intractable. To simplify the calculation, the deflected shape is approximated by a sinusoidal curve with equilibrium satisfied only at the mid-height of the column. The total deflection, w and curvature, χ at any point (x, w) are given by:

$$w = w_o \cos\left(\frac{\pi x}{\lambda}\right) \tag{6.5}$$

$$w'' = -\chi = -\left(\frac{\pi}{\lambda}\right)^2 w_o \cos\left(\frac{\pi x}{\lambda}\right) \tag{6.6}$$

Substitution of the boundary condition $w = e$ when $x = L_e/2$ into equation 6.5 gives:

$$e = w_o \cos\left(\frac{\pi L_e}{2\lambda}\right) \tag{6.7}$$

The curvature at mid-height ($x = 0$) from equation 6.6 then becomes:

$$\chi_o = -\frac{4}{L_e^2}\left[\cos^{-1}\left(\frac{e}{w_o}\right)\right]^2 w_o \tag{6.8}$$

When $e = 0$, equation 6.8 reduces to the general form:

$$\chi_o = -\frac{\pi^2}{L_e^2} w_o \tag{6.9}$$

The analysis consists of successively increasing the mid-height deflection by a predetermined incremental value and finding the axial load and bending moment that satisfies equilibrium. The method of solution is iterative. An initial strain profile for the section is proposed, and the corresponding internal forces and moments are calculated. If equilibrium is satisfied, the strain profile is taken as correct. Otherwise, the strain profile is modified and the procedure repeated.

To facilitate the analysis the concrete cross-section and the composite cross-section of the column are subdivided horizontally into n and m number of strip elements respectively, as shown in Figure 6.4. Fifty element strips were used in all the computational analyses. Since plane sections remain plane after deformation, the strain distribution in any element is defined by the curvature χ and the distance Y_o from the neutral axis to the centroid of the column. Since the elements of the cross-section are small, the stresses in each element are assumed to be uniform. The internal forces and moments at mid-height are calculated from the strain distributions by the equations:

$$N^{\text{int}} = \sum_{i=1}^{n} f_{ci} A_{ci} + \sum_{j=1}^{m} f_{tj} A_{tj} \qquad \textbf{(6.10)}$$

$$M^{\text{int}} = \sum_{i=1}^{n} f_{ci} A_{ci} \bar{y}_i + \sum_{j=1}^{m} f_{tj} A_{tj} \bar{y}_j \qquad \textbf{(6.11)}$$

The position of the neutral axis is given when the moment residual is zero. Where the moment residual is defined as:

$$M^r = M^{ext} - M^{\text{int}} \qquad \textbf{(6.12)}$$

The position of the neutral axis is determined using the *Regula Falsi* method of interpolation [79]. The interpolation method initially involves guessing the solution interval end points (Y_1, Y_2) for the neutral axis position. The internal axial forces and moments are calculated from equations 6.10 and 6.11 respectively, for Y_1 and Y_2. The corresponding external moments are given by:

$$M_j^{ext} = N_j^{ext} w_o = N_j^{\text{int}} (e + \delta_o) \quad (j = 1,2) \qquad \textbf{(6.13)}$$

The position of the neutral axis is determined by interpolating between the interval endpoints, using the following equation:

$$Y_o = \frac{Y_1 M_2^r - Y_2 M_1^r}{M_2^r - M_1^r} \qquad \textbf{(6.14)}$$

and the moment residual M^r is calculated for the new neutral axis position. If M_1^r and M^r have opposite signs, then the neutral axis must be in the interval (Y_1, Y_o). Conversely, if M_2^r and M^r have opposite signs then the position of the neutral axis must be in the interval (Y_o, Y_2). The neutral axis position is determined by replacing either Y_1 or Y_2 accordingly by the value of Y_o, and repeating the procedure. The procedure ends when the moment residual for Y_o satisfies:

$$\frac{|M^r|}{M^{ext}} \leq 0.005 \qquad \textbf{(6.15)}$$

To determine the maximum axial load, the internal axial load is compared with the axial load calculated in the previous iteration. If the internal axial load is greater than the axial load in the previous iteration, N_{max} is updated. By successive incrementing of the central deflection δ_o, and repeating the above procedure for each value of δ_o, the complete load deflection curve of the column is defined. The solution interval end points for the position of the neutral axis are taken as (Y_1, Y_o), where Y_o is the previous solution for the position of the neutral axis. The algorithm used for calculating the load-deflection curve is given in Figure 6.5.

6.2.2 Failure load criterion

The failure load of the column coincides with the peak load on the load-deflection curve. The load-deflection curve may also be used to determine the mode of failure of the column. If the slope of the load-deflection curve is positive when the extreme compressive strain in the concrete equals ε_{cc}, then a material failure governs. However, if the slope of the load deflection curve is negative when the extreme compressive strain in the concrete equals ε_{cc}, then a stability failure governs. Once a stability failure has been detected, CONFINE continues to calculate the load-defection until the load has decreased by 5 percent.

6.3 MATERIAL PROPERTIES

6.3.1 Equivalent uniaxial stress-strain curve for FRP-confined concrete

The stresses in the concrete are derived from the equivalent stress-strain curve for FRP-confined concrete proposed in §4.2. However, the presence of a strain gradient is known to reduce the maximum compressive strength of both unconfined and confined concrete

[77, 80]. The reduction in strength of unconfined concrete is accounted for in design codes in the coefficient 0.67 for compressive strengths obtained from cubes or 0.85 for cylinders.

The theoretical predictions of the behaviour of the columns were initially carried out using a coefficient of 0.85 to account for the strain gradient. This resulted in a poor correlation with experimental failure loads. Research by Hognestad *et al* [77] on the flexural strength of unconfined concrete found that the value of the coefficient decreased with increasing cylinder strength. Hognestad *et al* postulated that the compressive stress in a member subject to flexure is reduced by the coefficient k, given by:

$$k = \frac{27 + 0.35 f_{co}}{22 + f_{co}} \tag{6.16}$$

The coefficient k is applied to the reference plastic stress.

$$f_{ox} = \left(\frac{E_{ci} - E_{px}}{E_{ci} - E_{c1}} \right) k f_{co} \tag{6.17}$$

This ensures that the initial stiffness of the column and the stiffness in the post-crushing region are not influenced by the strength reduction coefficient.

The equivalent stress-strain curve for triaxial enhancement of both strength and ductility is only utilised for columns with effective hoop stiffness greater than 977 N/mm^2. For columns confined with effective hoop stiffnesses of less than 977 N/mm^2 only ductility is enhanced, the maximum compressive strength in the concrete being restricted to the unconfined strength.

6.3.2 Stress-strain equations for the FRP-composite tube

The longitudinal stress in the FRP-composite tube is determined using the effective axial modulus calculated in §2.5.2.

$$\sigma_x = E_{xx} \varepsilon_x \tag{6.18}$$

The stresses in the circumferential direction are ignored in the CONFINE algorithm. The benefits of triaxial confinement of the concrete are accounted for by the equivalent uniaxial stress-strain relationship. Failure of the FRP-composite is governed by the maximum stress failure criterion, which assumes that failure occurs when the longitudinal component of the stress attains its limiting value. Thus, a 'safe' condition for the maximum stress failure criterion based on a netting analysis is given by:

$$X_c \sin^2 \phi < \sigma_x < X_T \sin^2 \phi \tag{6.19}$$

The magnitude of the strains in the circumferential direction cannot be quantified due to the non-linear expansion of the concrete. The lateral expansion of the concrete core is a function of the applied axial strain. Therefore, the presence of a strain gradient results in a non-uniform expansion of the core. The circumferential strains near the extreme concrete compressive fibre may be comparable to the circumferential strains obtained in concentric compression tests. However, the concrete near the neutral axis is subjected to relatively low longitudinal compressive strains and hence lower circumferential strains.

Experimental values of the mean circumferential strain at mid-height indicate that at failure the mean circumferential strain is an order of magnitude smaller than the maximum longitudinal compressive strain.

6.4 COMPARISON OF THEORETICAL AND EXPERIMENTAL RESULTS

6.4.1 Ultimate load capacity

The comparison between the predicted failure loads from CONFINE and experimental results is given in Figure 6.6 and Table 6.1. Generally, good agreement is obtained between the theoretical and experimental failure loads for all the column diameters, with a correlation coefficient of 0.922.

Whilst the ultimate load capacity of the columns can be predicted with a high degree of confidence, the large compressive strains associated with the ultimate failure load would result in a catastrophic failure if passive confinement were lost. In the absence of additional research to establish a limiting strain criterion that maintains the structural integrity of the column in the event of a partial or total loss of confining action, the usual limiting compressive strain criterion of $3500\mu\varepsilon$ has been adopted. The load capacity beyond the limiting strain then becomes a strength reserve factor against accidental overload. A comparison of the experimental loads at $3500\mu\varepsilon$ compressive strain with the predicted design loads is given in Figure 6.7.

The enhancement in strength above the limiting compressive strain is shown in Figure 6.8. The degree of enhancement is a function of both the column slenderness and the effective hoop modulus of the composite. The experimental load ratios $N_{(\varepsilon=3500)}/N_u$ ranged from 0.302 to 0.656 for slenderness ratios $L/D \approx 5$ and 0.606 to 0.925 for slenderness ratios $L/D \approx 10$. The larger the effective hoop modulus, the greater the enhancement in strength. However, as the slenderness ratio increases, the strength reserve factor reduces significantly.

The theoretical curves derived from the CONFINE program, also shown in Figure 6.8, give reasonable agreement with the experimental values. Variation between the theoretical and experimental results is primarily due to the small variations in the actual slenderness ratios.

6.4.2 Ultimate moment capacity

A comparison of the applied moments and predicted moments at failure and $3500\mu\varepsilon$ are given in Figures 6.9 and 6.10 respectively. Reasonable correlation is achieved between the theoretical and experimental moment capacities at failure, with correlation coefficients of 0.854 and 0.815 respectively. The lower correlation coefficients observed for the moment capacities are due to variation in both the predicted axial load capacity and lateral deflections of the columns.

6.4.3 Ultimate failure strain

Good correlation, $R^2 = 0.914$, is achieved between the experimental and predicted ultimate strains as shown in Figure 6.11. However, this improves as the slenderness of the column increases. One possible explanation for the larger degree of scatter at low slenderness ratios is the variability of the transverse properties of the filament wound tubes. The large compressive strains observed in the low slenderness columns indicate that the behaviour is highly dependent on the compressive failure mechanism of the FRP-composite in the transverse direction. The observed failure mechanism involved debonding of the fibres from the matrix at discrete intervals, indicated by whitening of the resin matrix and bunching of the adjacent fibre bundles. This behaviour is highly dependent on the fabrication process and imperfections resulting from fibre crossovers. As the slenderness ratio increases, the transverse mechanical properties of the FRP-tube become less dominant, resulting in the greater degree of correlation.

6.4.4 Load-deflection curves

The load-deflection curves are calculated using the sinusoidal waveform method described in §6.2. In all cases, the ascending part of the curve is virtually identical up to approximately 80 percent of the maximum load. Comparisons of the experimental and theoretical load-deflection curves are given in Figures 6.12(a-f) for a range of column diameters and fibre orientations.

6.4.5 Load-strain relationships

The predicted longitudinal strains on the concave side of the central section are compared with the experimental values in Figures 6.13(a-f). Good agreement is again obtained in the ascending parts of the curves. Generally, the calculated values for the longitudinal strains

at the concave side are slightly greater than the experimental results. For the limited number of tests in which the instrumentation was removed after the peak load was attained, the experimental strains at the concave side were generally larger than the sinusoidal waveform values. This implies that the post-failure central curvature calculated by the sinusoidal waveform assumption is smaller than the experimental values.

6.4.6 Moment-curvature behaviour

The moment-curvature relationships calculated by the CONFINE algorithm give reasonable agreement with the experimental curves shown in Figure 6.14(a-f). The theoretical moment-curvature relationship is approximately bilinear, as observed in the experimental work. The initial stiffness of the column is approximately equal to the stiffness of the concrete section, since the stiffness component of the FRP-composite tube is negligible in comparison. The initial stiffness of the column is approximately equal to:

$$(EI)_c \approx (E_{ci}I)_{concrete} \qquad (6.20)$$

Increasing axial load causes the slope of the curve to decrease due to the non-linear behaviour of concrete. The stiffness of the columns beyond a compressive strain of approximately $3500\mu\varepsilon$ is relatively constant, indicated by the linear nature of the curve. The secondary stiffness of the column increases as the fibre orientation tends toward the hoop direction and hence the post-crushing modulus of the concrete increases.

6.5 INFLUENCE OF COLUMN SLENDERNESS

The influence of second-order effects in conventional concrete columns can generally be neglected for slenderness ratios less than 12 [61]. However, the experimental work found that the benefits of triaxial confinement diminished significantly as the slenderness increased from 5 to 10.

Theoretical curves predicting the load enhancement for increasing effective hoop modulus and column slenderness are given in Figure 6.15, based on an initial load eccentricity of $0.05D$. The load enhancement is the failure load ratio of the confined column and an identical unconfined column. It can be seen that the largest enhancement in load is achieved at low slenderness ratios and increases with increasing effective hoop modulus. For slenderness ratios greater than 10, there is no enhancement in strength if the effective hoop modulus is less than 977 N/mm^2. Extrapolated results for slenderness ratios of 12 and 15, indicate that there is negligible strength enhancement for slenderness ratios of 12 within

practical limits of the effective hoop modulus range. Thus, it is proposed that the effects of triaxial confinement are ignored for slenderness ratios greater than $L/D = 12$.

6.6 COMPARISON WITH CONVENTIONAL R.C. COLUMNS

To compare the performance of the concrete-filled fibre composite tubes with conventional reinforced concrete columns, the experimental failure loads are plotted against the failure envelopes for increasing percentages of longitudinal steel reinforcement on Figure 6.16. The failure envelopes for the conventional reinforced concrete columns are based on the assumptions that high yield steel is used for the longitudinal reinforcement and minimum cover is provided. It can be seen from Figure 6.16 that the load capacity of columns with the fibre composite orientated predominately in the hoop direction varied from being equivalent to a column with 2 percent longitudinal steel reinforcement to greatly exceeding the load capacity of an equivalent column with 6 percent longitudinal reinforcement. 6 percent longitudinal steel reinforcement is the maximum amount of steel permitted in the UK concrete design code [61].

The large variation of load capacity is due to the range of the effective hoop moduli for the 90 degree wound specimens. The effective hoop modulus varied from 1.137 kN/mm^2 for the 300 mm diameter column up to 3.226 kN/mm^2 for the 60 mm diameter columns.

The load capacity of the column designed using the $3500\mu\varepsilon$ limitation is compared to the load capacity of conventional reinforced columns in an *N-M* interaction chart, as shown in Figure 6.17. The capacity of the columns is equivalent to providing between 1 percent to 5 percent longitudinal steel reinforcement. The angle of fibre orientation is less critical at the limiting strain criterion, with comparable load capacities being observed for the nominal 90 degree and 67½ degree windings. However, columns confined with the nominal 45 degree fibre orientation have lower load capacities.

6.7 SUMMARY

The proposed analysis of FRP-confined concrete columns using the CONFINE algorithm gives good correlation with experimental data. The validation of the CONFINE algorithm is however limited to columns subject to a notional eccentricity of $0.05D$.

The use of a sinusoidal waveform to approximate the deflected profile of the column gives good agreement with the experimental behaviour. The CONFINE model has been shown

to predict the axial load, moment capacity and compressive strain to failure with a high degree of confidence.

The experimental investigations found that the column capacity of FRP-confined concrete was influenced by second-order effects at significantly lower slenderness ratios than conventional reinforcement concrete columns. The slenderness ratio for FRP-confined concrete columns at which second-order effects must be considered is a function of the effective hoop modulus of the FRP-composite confinement. The benefits of triaxial confinement are also found to diminish as the slenderness ratio of the column increases due to the greater influence of second-order effects. Extrapolation of the experimental data using the CONFINE model shows that there is no enhancement in the strength of columns if the slenderness ratio is greater than 12. Therefore, the design of columns with slenderness ratios greater than 12 should be based on the unconfined concrete core and the FRP-composite jacket ignored.

The performance of concrete-filled FRP-composite columns was compared with conventional reinforced concrete columns using *N-M* interaction diagrams. It was found that columns confined by a notional 90 degree fibre orientation exhibited a minimum ultimate load capacity comparable to a column with 6 percent longitudinal high yield steel reinforcement. The maximum load capacity of the columns greatly exceeds the load capacity of a conventional reinforced concrete column.

In the absence of additional research to establish a limiting strain criterion that maintains the structural integrity of the column in the event of a partial or total loss of confining action, it is proposed that maximum compressive strain for the design is limited to the usual $3500\mu\varepsilon$. The load capacity beyond the limiting strain then becomes a strength reserve factor against accidental overload. The load capacities of concrete-filled FRP-composite columns at $3500\mu\varepsilon$ are comparable with the strength of conventional reinforced concrete columns. Therefore, concrete-filled FRP-composite columns offer similar strengths to conventional reinforced concrete columns but also provide:

- increased construction rates since the FRP-composite tube acts as permanent formwork;
- a more durable structure since the FRP-composite acts as a barrier to the ingress of aggressive agents;
- an increased factor of safety against accidental overload of the column.

Diameter mm	Angle of wind °	f_{cu} N/mm^2	$\frac{L}{D}$	Experimental Ultimate Load kN	$\frac{N_T}{N_{Exp}}$
79.89	78.1	19.7	5.86	312	1.066
79.89	78.1	36.4	5.88	431	0.825
79.89	78.1	25.6	10.90	171	0.976
79.89	78.1	31.2	10.88	200	0.777
100.09	80.4	23.4	5.69	447	1.017
100.09	80.4	35.2	5.69	568	0.858
100.09	80.4	22.6	10.68	278	0.746
100.09	80.4	32.8	10.69	312	0.768
125.64	82.3	27.4	5.53	584	1.002
125.64	82.3	31.7	5.53	627	0.971
125.64	82.3	46.3	10.51	454	0.908
150.40	83.6	33.9	5.78	866	0.915
150.40	83.6	28.4	10.77	399	1.009
150.40	83.6	28.4	10.77	486	0.988
200.64	85.2	24.6	5.58	1,072	0.924
200.64	85.2	43.7	5.58	1,397	0.982
200.64	85.2	27.7	10.57	627	0.984
300.67	86.8	25.3	5.49	2,530	0.985
300.67	86.8	36.8	5.49	3,300	0.889
299.53	86.8	39.7	10.52	2,100	0.931
399.67	87.6	29.0	5.38	5,050	0.966
399.67	87.6	40.5	5.38	5,860	0.977
400.08	87.6	36.5	10.37	3,300	0.964

Table 6.1. Comparison of theoretical and experimental ultimate failure loads

Diameter mm	Angle of wind °	f_{cu} N/mm^2	$\frac{L}{D}$	Experimental Ultimate Load kN	$\frac{N_T}{N_{Exp}}$
79.90	57.8	24.6	5.88	213	0.967
79.90	57.8	28.1	5.87	243	0.881
79.90	57.8	21.5	10.88	131	0.810
79.90	57.8	27.2	10.88	188	0.616
100.08	71.4	29.5	5.69	392	0.900
100.08	71.4	31.3	5.69	398	0.903
100.08	71.4	21.4	10.68	189	0.840
100.08	71.4	33.2	10.69	237	0.837
150.08	71.3	27.2	5.13	532	1.239
150.40	83.6	36.7	5.13	669	1.129
150.40	83.6	24.6	10.79	290	1.088
150.40	83.6	36.6	10.79	431	0.969
79.91	43.4	30.7	5.87	172	0.870
79.91	43.4	34.4	5.88	185	0.873
79.91	43.4	34.3	9.88	150	0.860
100.14	49.9	33.9	5.69	240	0.899
100.14	49.9	40.1	5.69	273	0.902
100.14	49.9	29.3	10.67	177	0.873
100.14	49.9	30.0	10.68	154	1.022
150.35	48.0	24.2	5.79	345	1.013
150.35	48.0	36.7	5.79	453	1.066
150.35	48.0	25.9	10.75	286	1.056
150.35	48.0	37.1	10.87	339	1.244

Table 6.1. Comparison of theoretical and experimental ultimate failure loads (cont.)

Diameter mm	Angle of wind °	f_{cu} N/mm^2	$\frac{L}{D}$	Experimental Ultimate Load kN	$\frac{N_T}{N_{Exp}}$
79.89	78.1	19.7	5.86	94	1.228
79.89	78.1	36.4	5.88	172	1.910
79.89	78.1	25.6	10.90	104	1.221
79.89	78.1	31.2	10.88	128	0.893
100.09	80.4	23.4	5.69	158	1.131
100.09	80.4	35.2	5.69	231	0.973
100.09	80.4	22.6	10.68	179	0.867
100.09	80.4	32.8	10.69	226	0.845
125.64	82.3	27.4	5.53	290	0.953
125.64	82.3	31.7	5.53	361	0.842
125.64	82.3	46.3	10.51	417	0.857
150.40	83.6	33.9	5.78	488	0.911
150.40	83.6	28.4	10.77	336	1.041
150.40	83.6	28.4	10.77	414	1.030
200.64	85.2	24.6	5.58	622	0.933
200.64	85.2	43.7	5.58	916	0.988
200.64	85.2	27.7	10.57	580	0.973
300.67	86.8	25.3	5.49	1,500	0.914
300.67	86.8	36.8	5.49	†	†
299.53	86.8	39.7	10.52	†	†
399.67	87.6	29.0	5.38	†	†
399.67	87.6	40.5	5.38	3,680	0.940
400.08	87.6	36.5	10.37	†	†

† Axial extensometer removed at load less than 3500$\mu\varepsilon$

Table 6.2. Comparison of theoretical and experimental loads at 3500$\mu\varepsilon$ compressive strain

Diameter mm	Angle of wind °	f_{cu} N/mm^2	$\frac{L}{D}$	Experimental Ultimate Load kN	$\frac{N_T}{N_{Exp}}$
79.90	57.8	24.6	5.88	92	1.116
79.90	57.8	28.1	5.87	122	0.921
79.90	57.8	21.5	10.88	115	0.738
79.90	57.8	27.2	10.88	136	0.721
100.08	71.4	29.5	5.69	228	0.787
100.08	71.4	31.3	5.69	223	0.837
100.08	71.4	21.4	10.68	169	0.775
100.08	71.4	33.2	10.69	219	0.789
150.08	71.3	27.2	5.13	310	1.138
150.40	83.6	36.7	5.13	452	0.979
150.40	83.6	24.6	10.79	276	1.050
150.40	83.6	36.6	10.79	413	0.939
79.91	43.4	30.7	5.87	130	0.959
79.91	43.4	34.4	5.88	153	0.893
79.91	43.4	34.3	9.88	146	0.863
100.14	49.9	33.9	5.69	148	1.324
100.14	49.9	40.1	5.69	211	1.089
100.14	49.9	29.3	10.67	172	0.900
100.14	49.9	30.0	10.68	147	1.072
150.35	48.0	24.2	5.79	299	1.058
150.35	48.0	36.7	5.79	425	1.096
150.35	48.0	25.9	10.75	285	1.058
150.35	48.0	37.1	10.87	335	1.259

Table 6.2. Comparison of theoretical and experimental loads at 3500$\mu\varepsilon$ compressive strain (cont.)

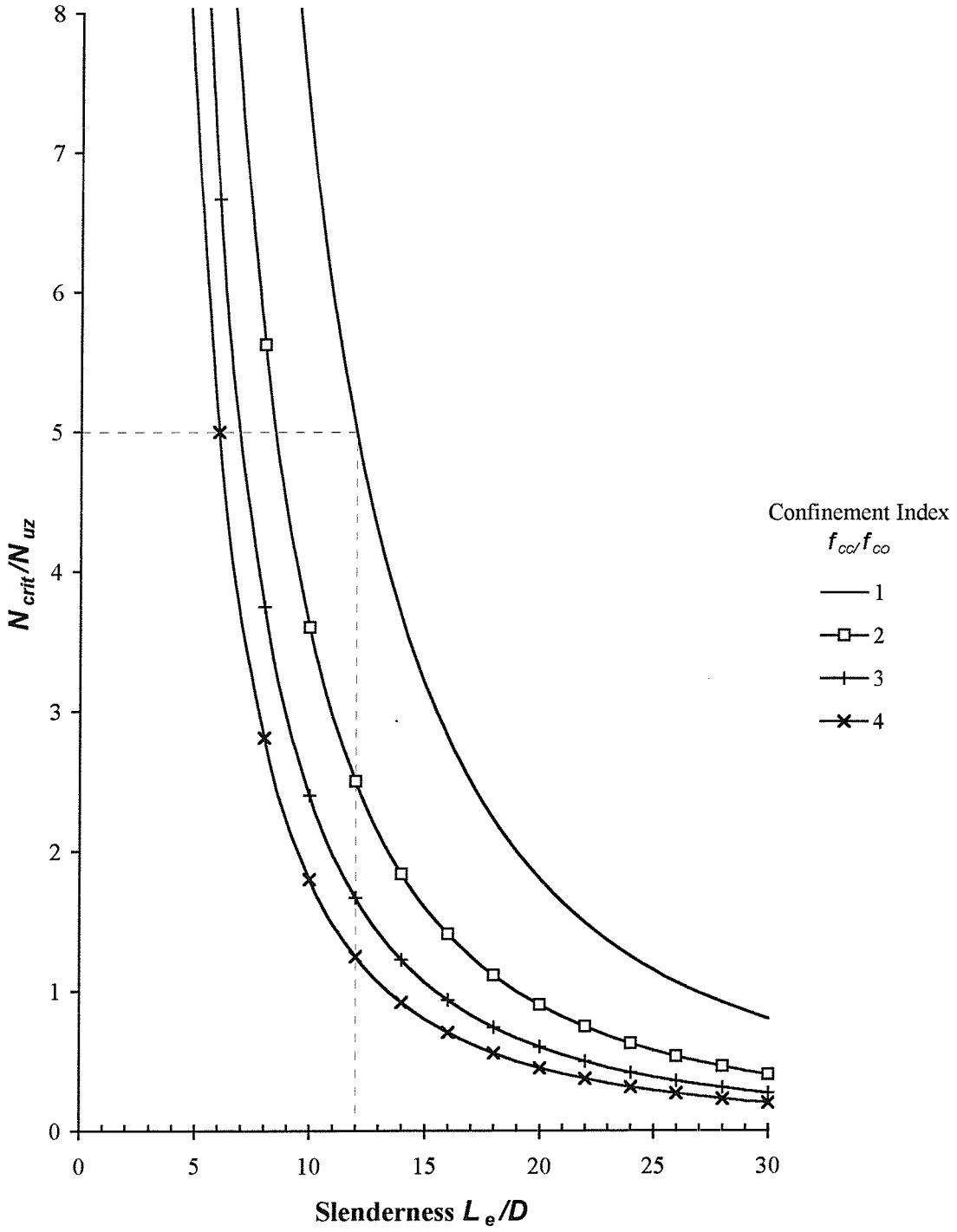

Figure 6.1. Influence of column slenderness on the axial load capacity of FRP-confined concrete columns

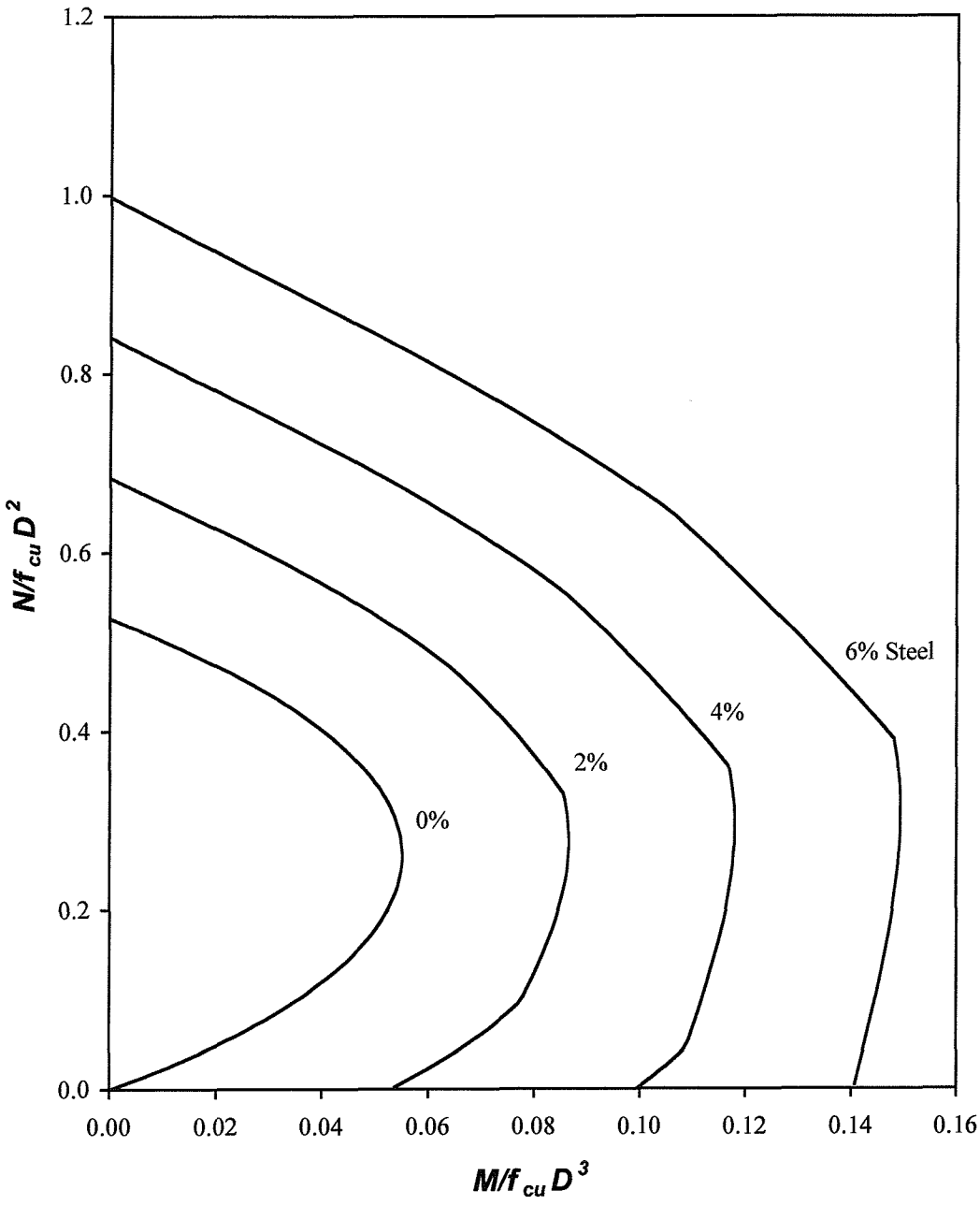

Figure 6.2. Typical *N-M* interaction diagram for conventional reinforced concrete columns

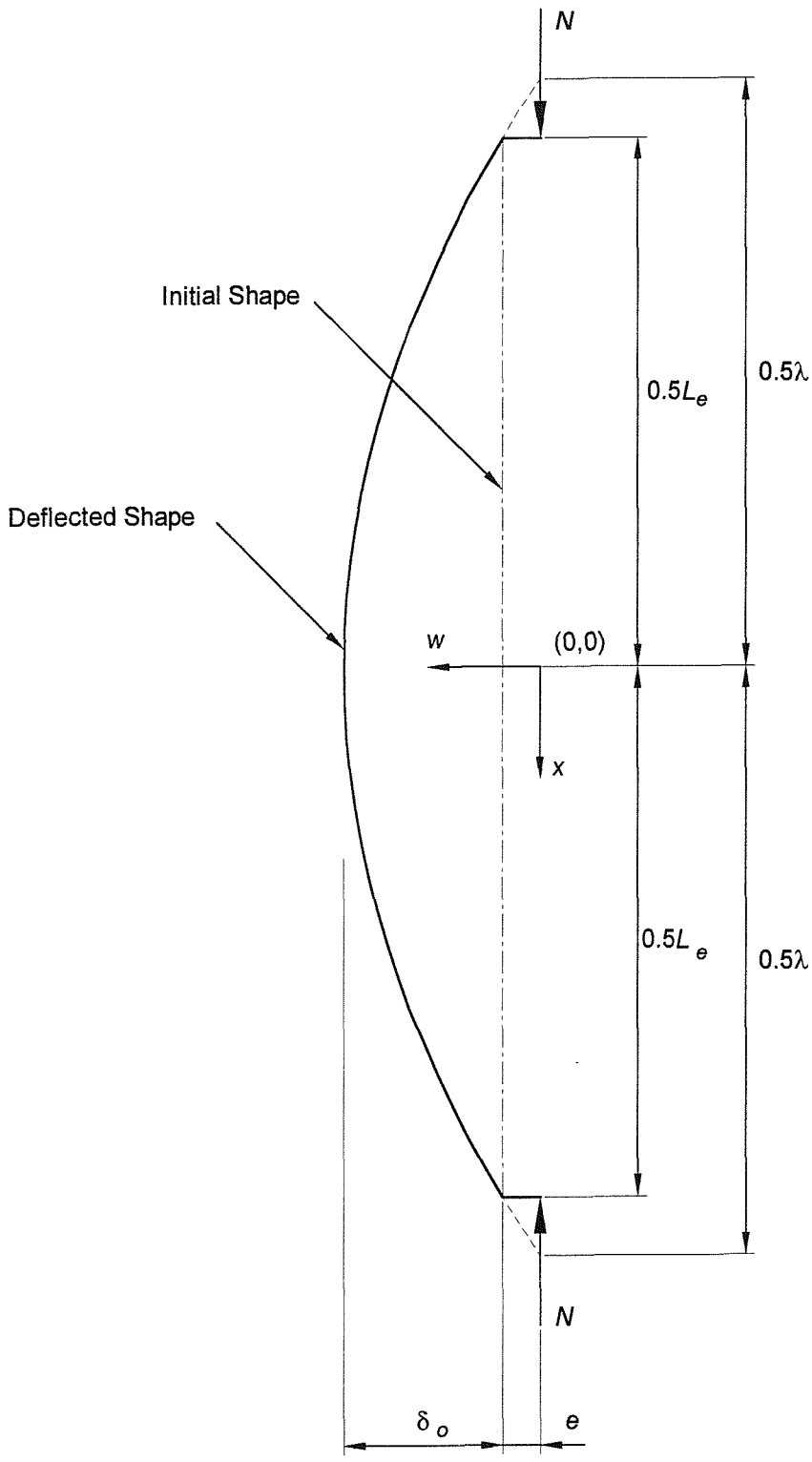

Figure 6.3. Sinusoidal deflected profile of column

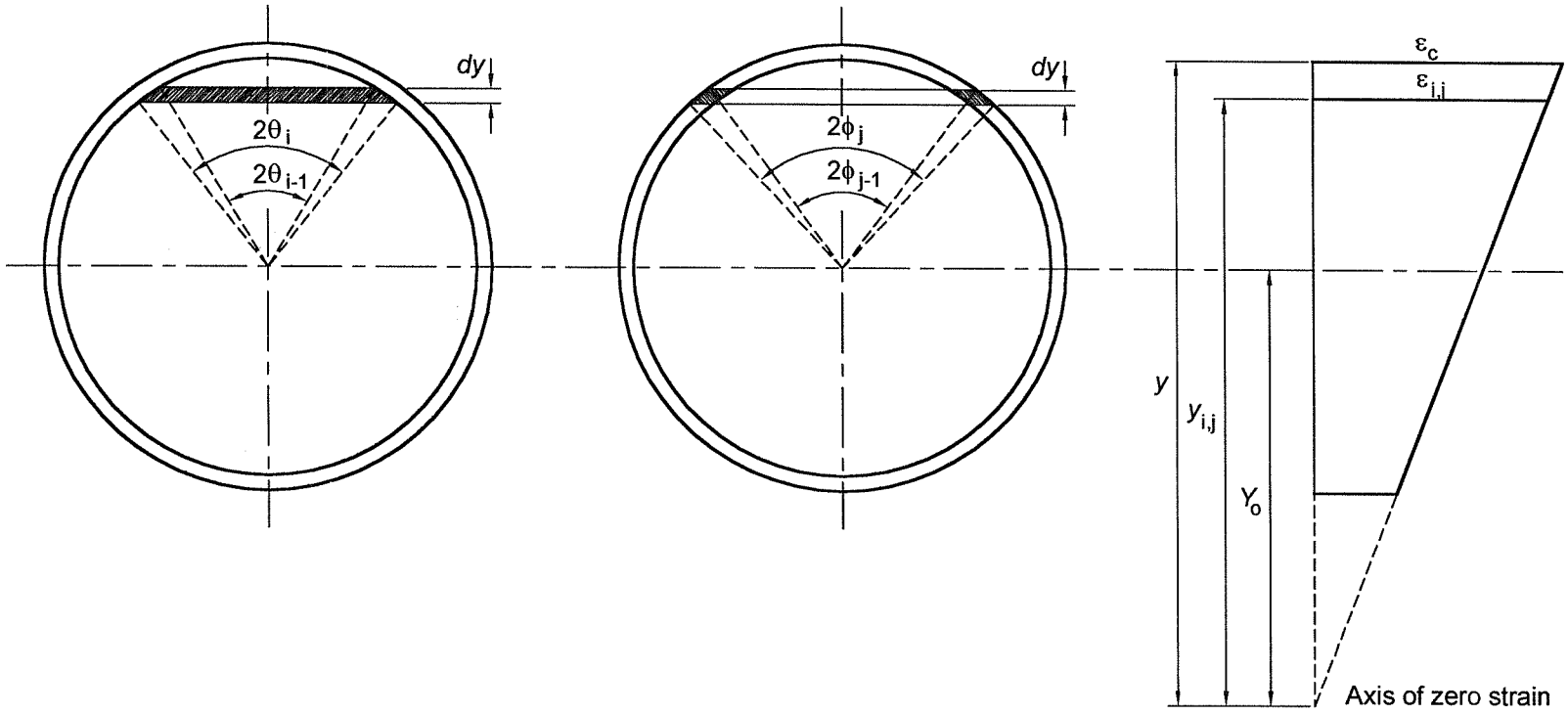

(a) Concrete strip element

(b) FRP-composite strip element

(c) Strain distribution

Figure 6.4. Column cross-section and strain distribution

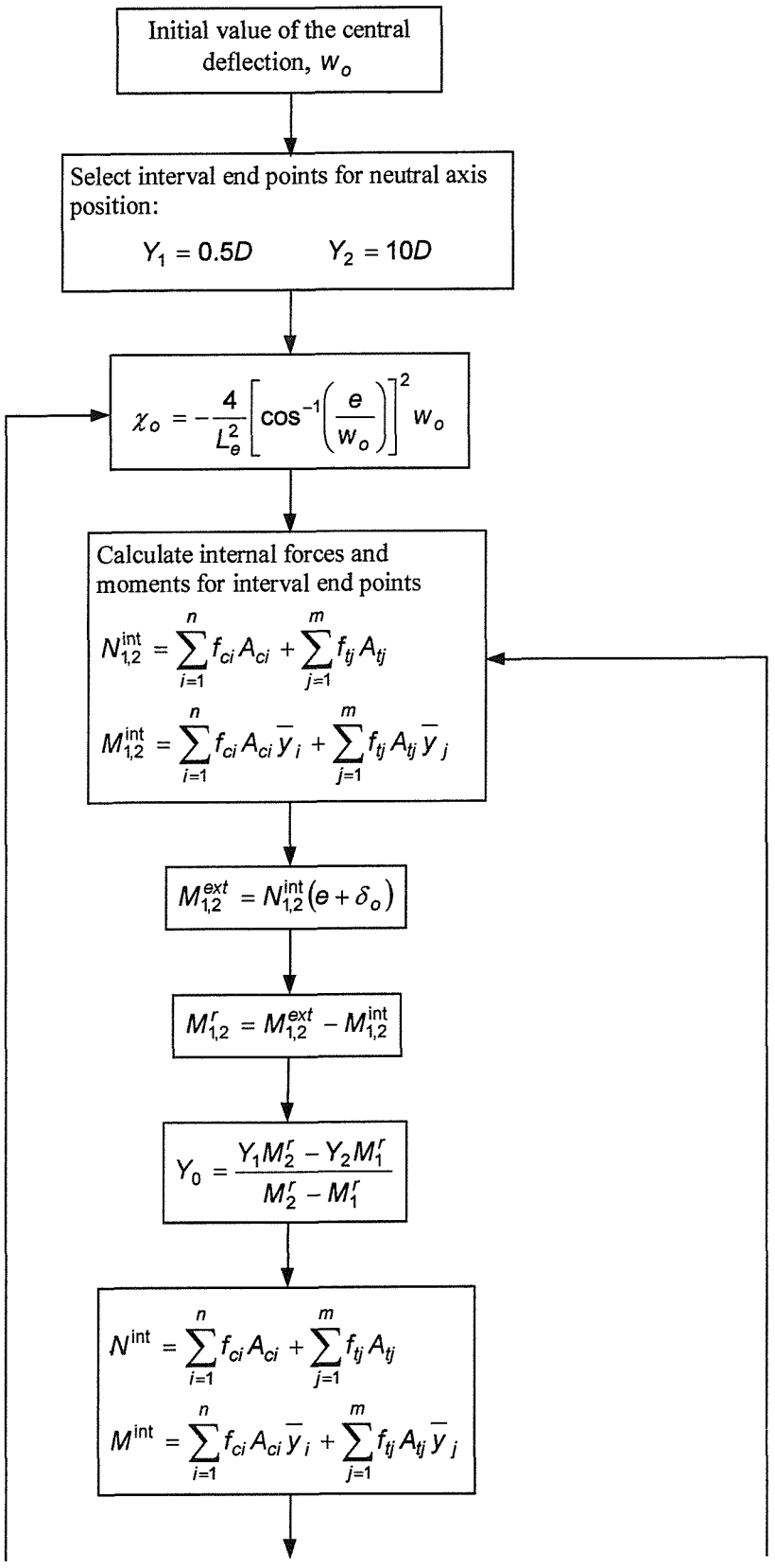

Figure 6.5. Confined concrete column load-deflection algorithm

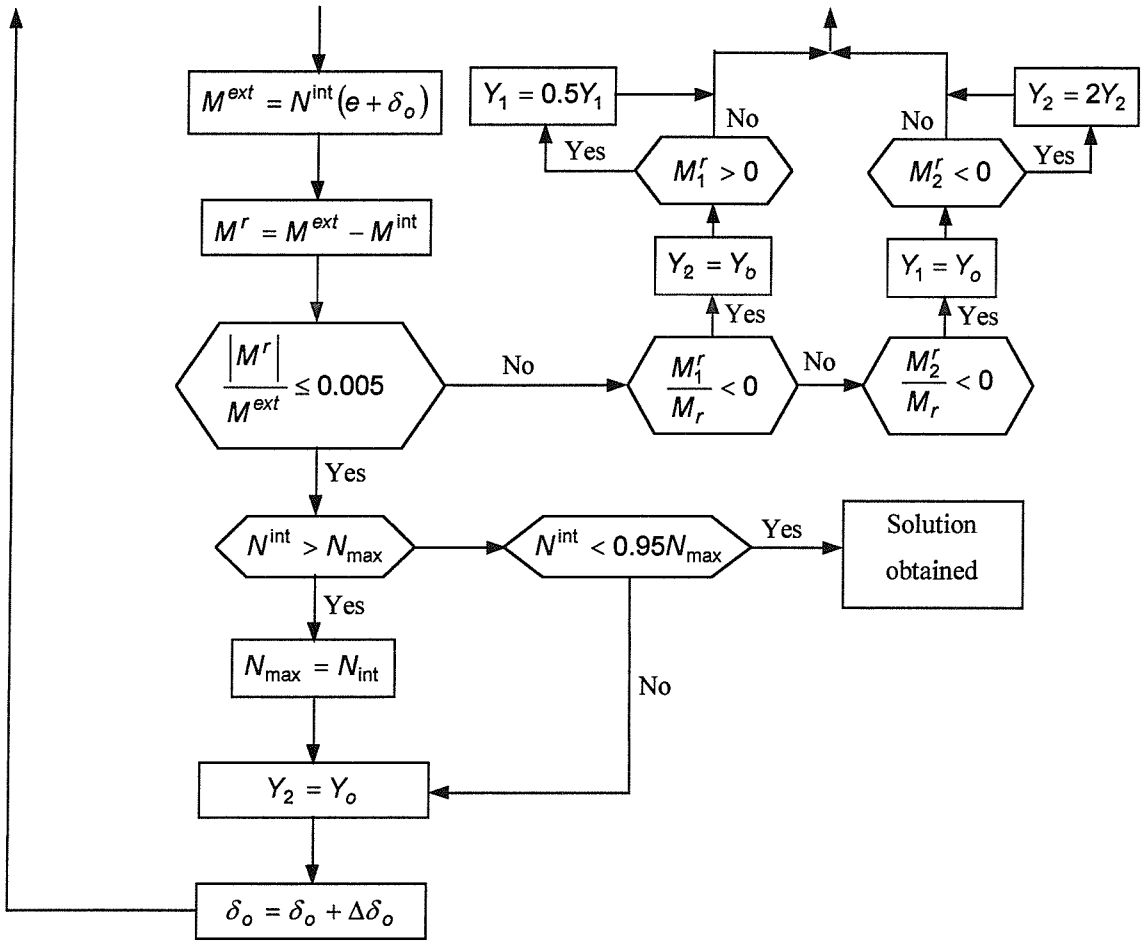

Figure 6.5. Confined concrete column load-deflection algorithm (cont.)

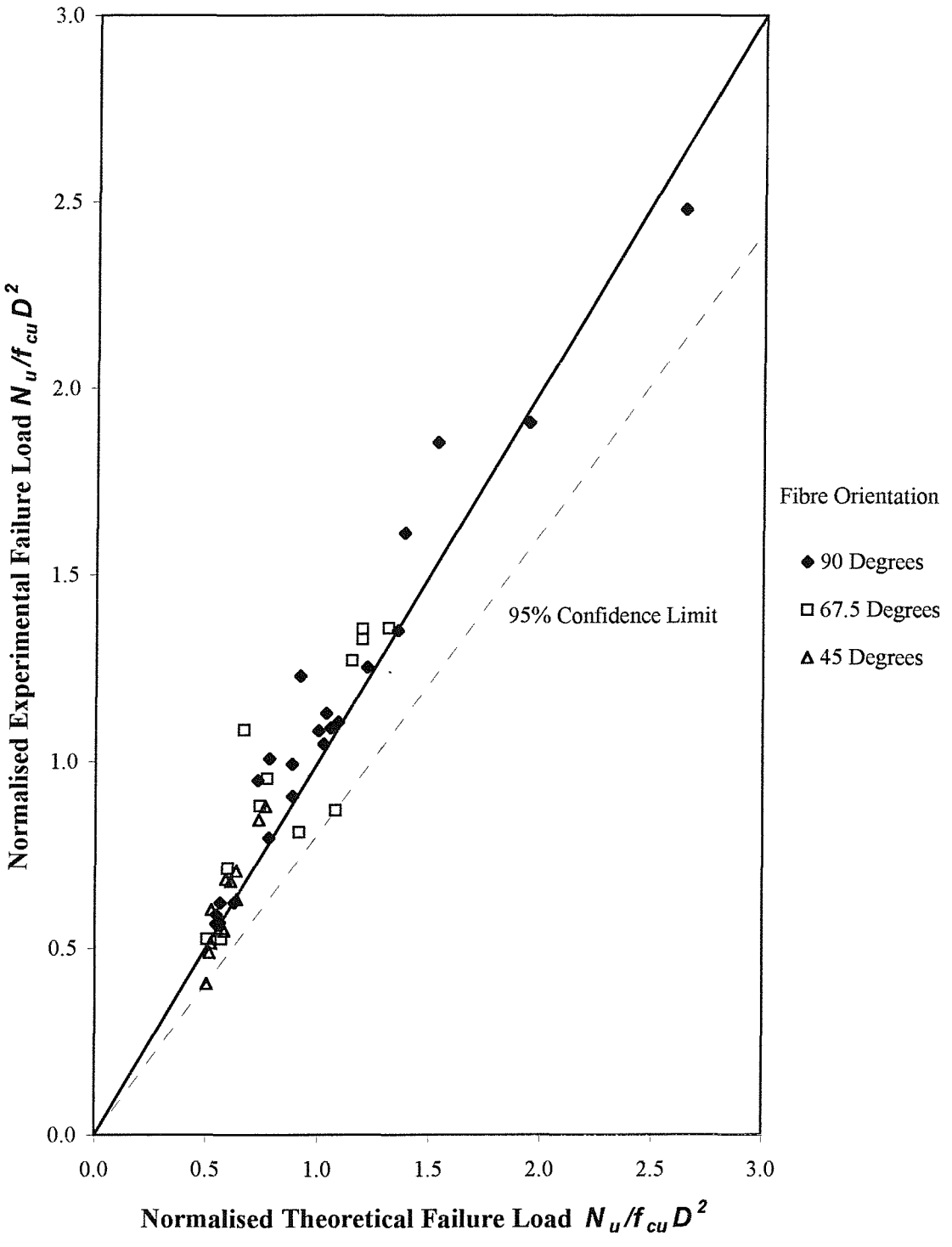

Figure 6.6. Comparison of the theoretical axial failure loads with the experimental results

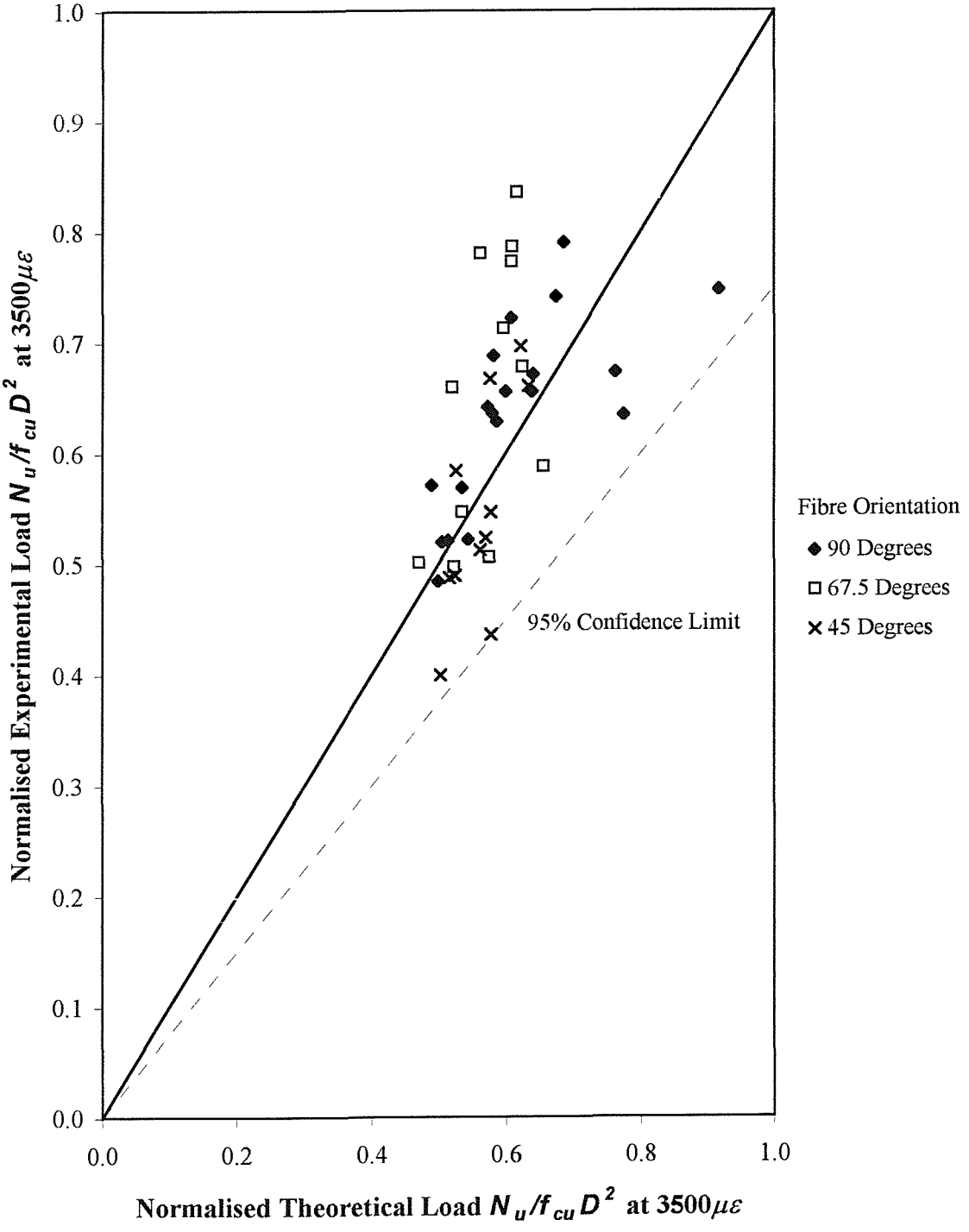

Figure 6.7. Comparison of the theoretical load capacity at 3500$\mu\varepsilon$ compressive strain with experimental results

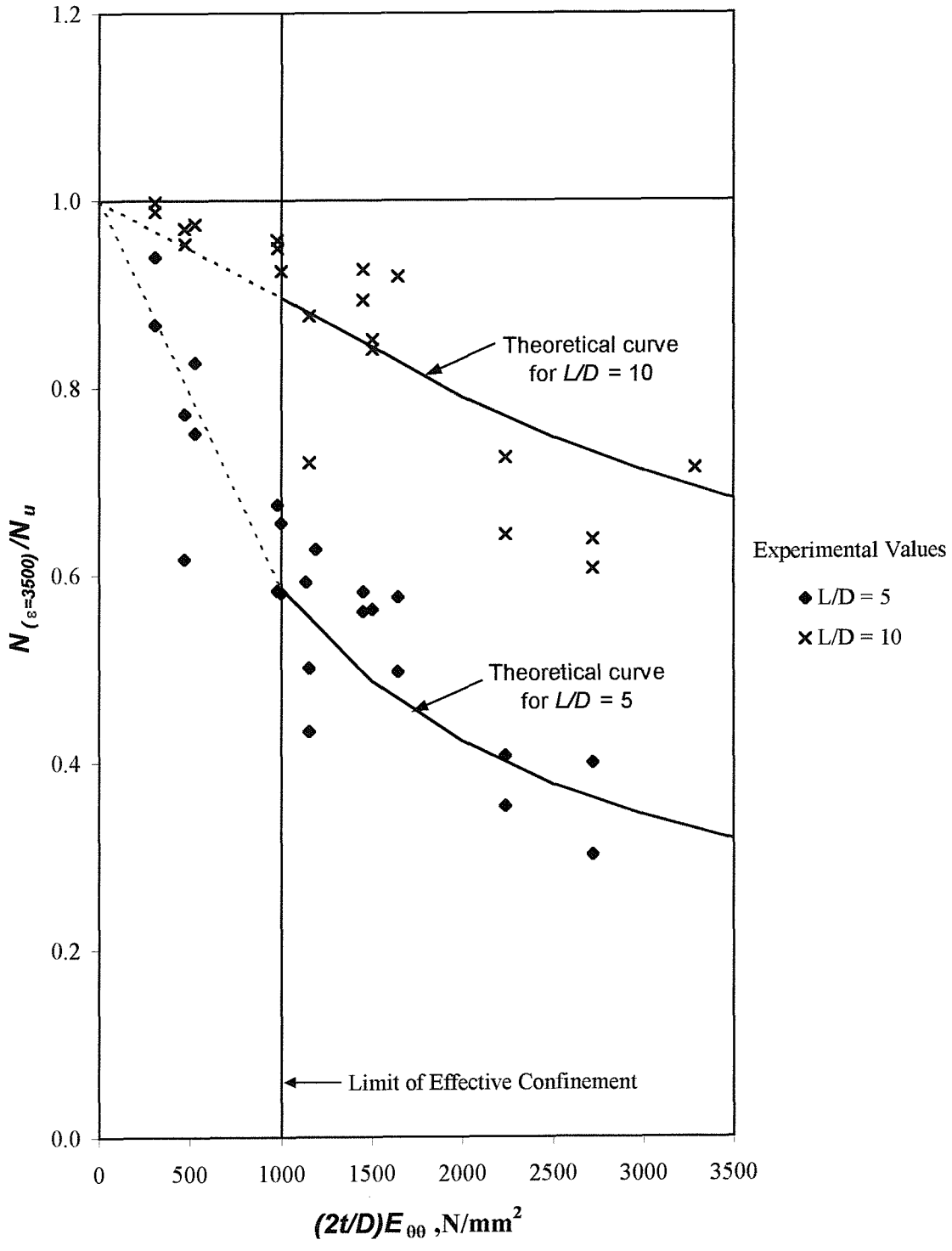

Figure 6.8. Axial load capacity of FRP-confined columns beyond the $3500\mu\varepsilon$ compressive strain failure criterion

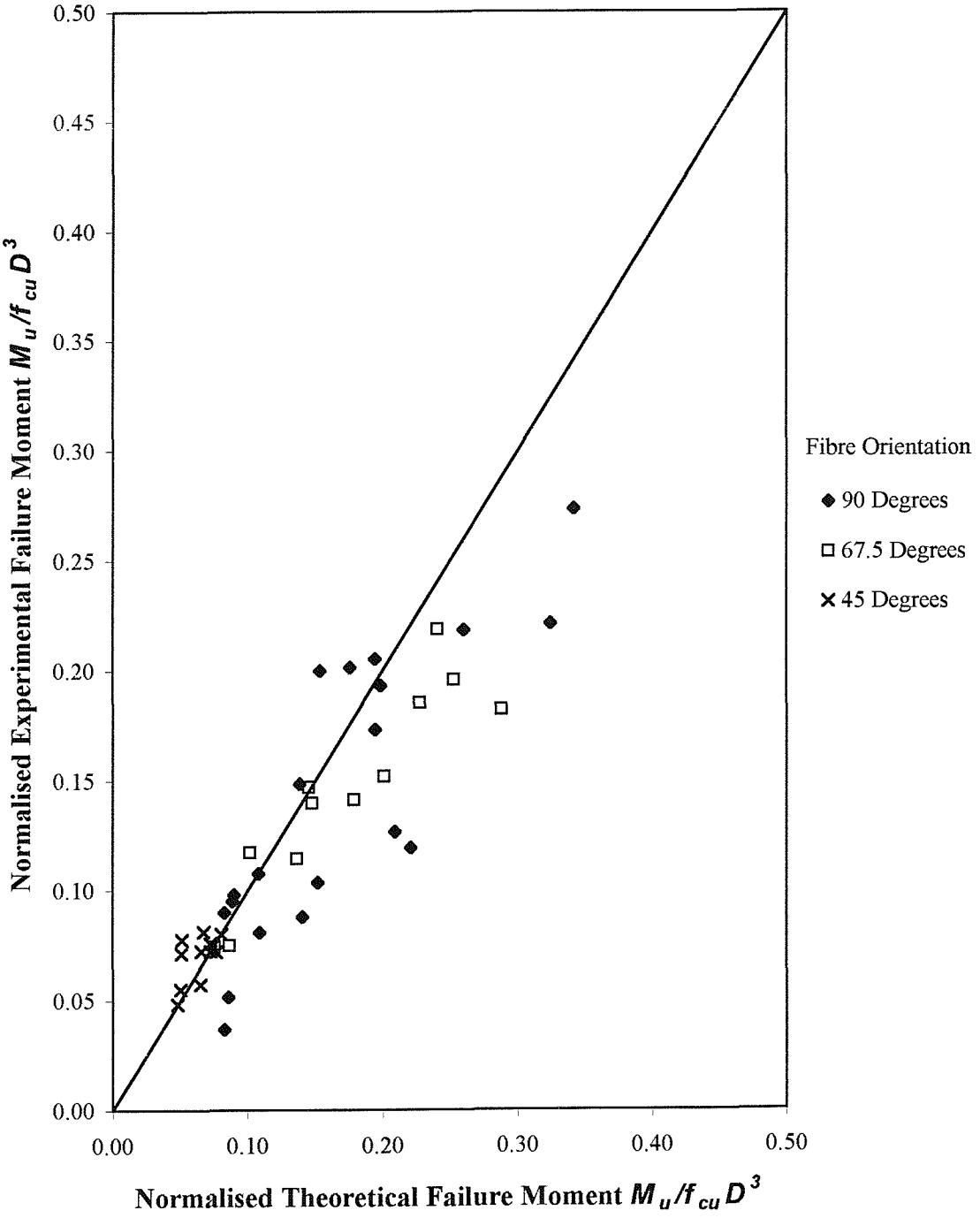

Figure 6.9. Comparison of the theoretical ultimate moment capacity with experimental results

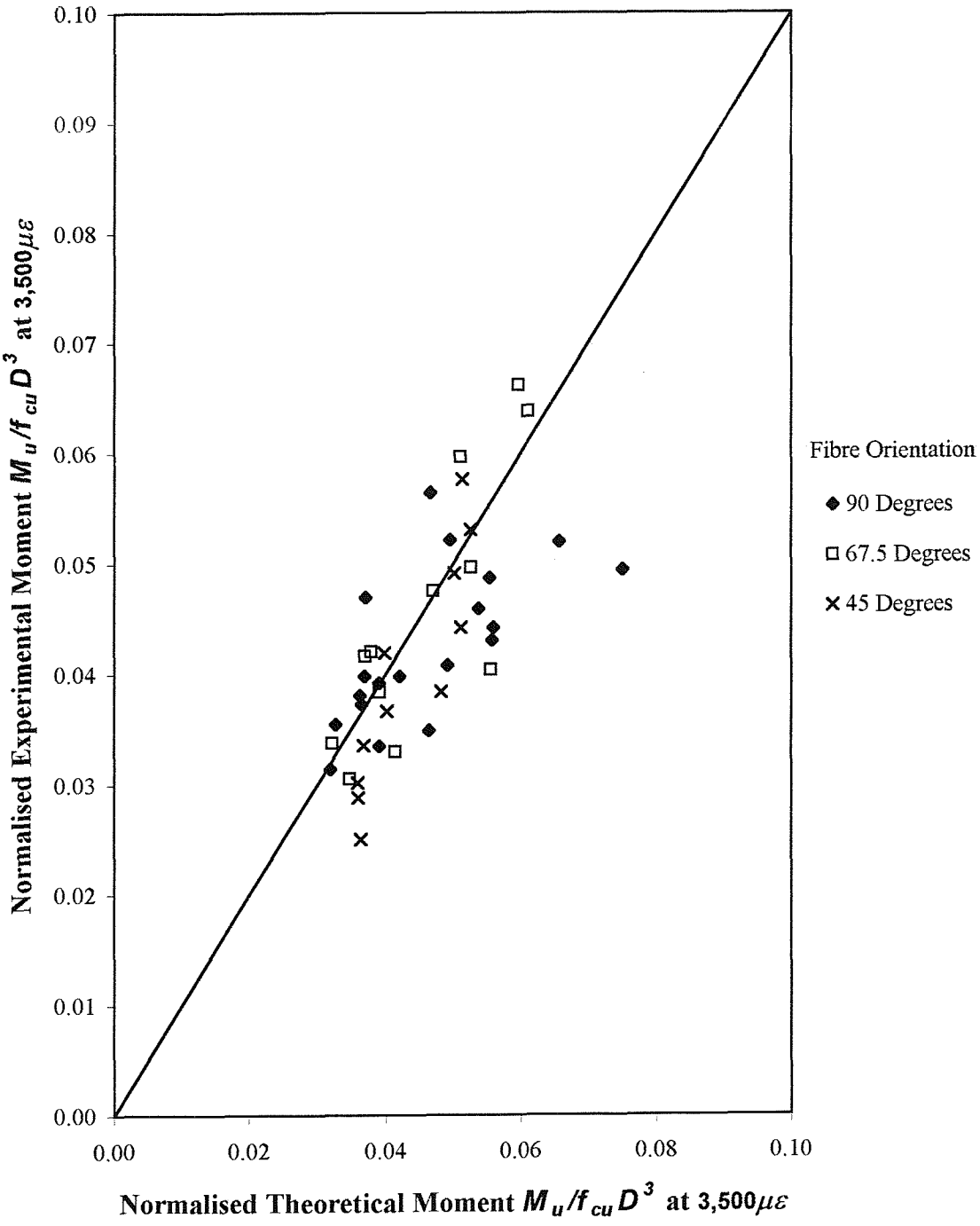

Figure 6.10. Comparison of the theoretical moment capacity at 3500$\mu\varepsilon$ compressive strain with experimental results

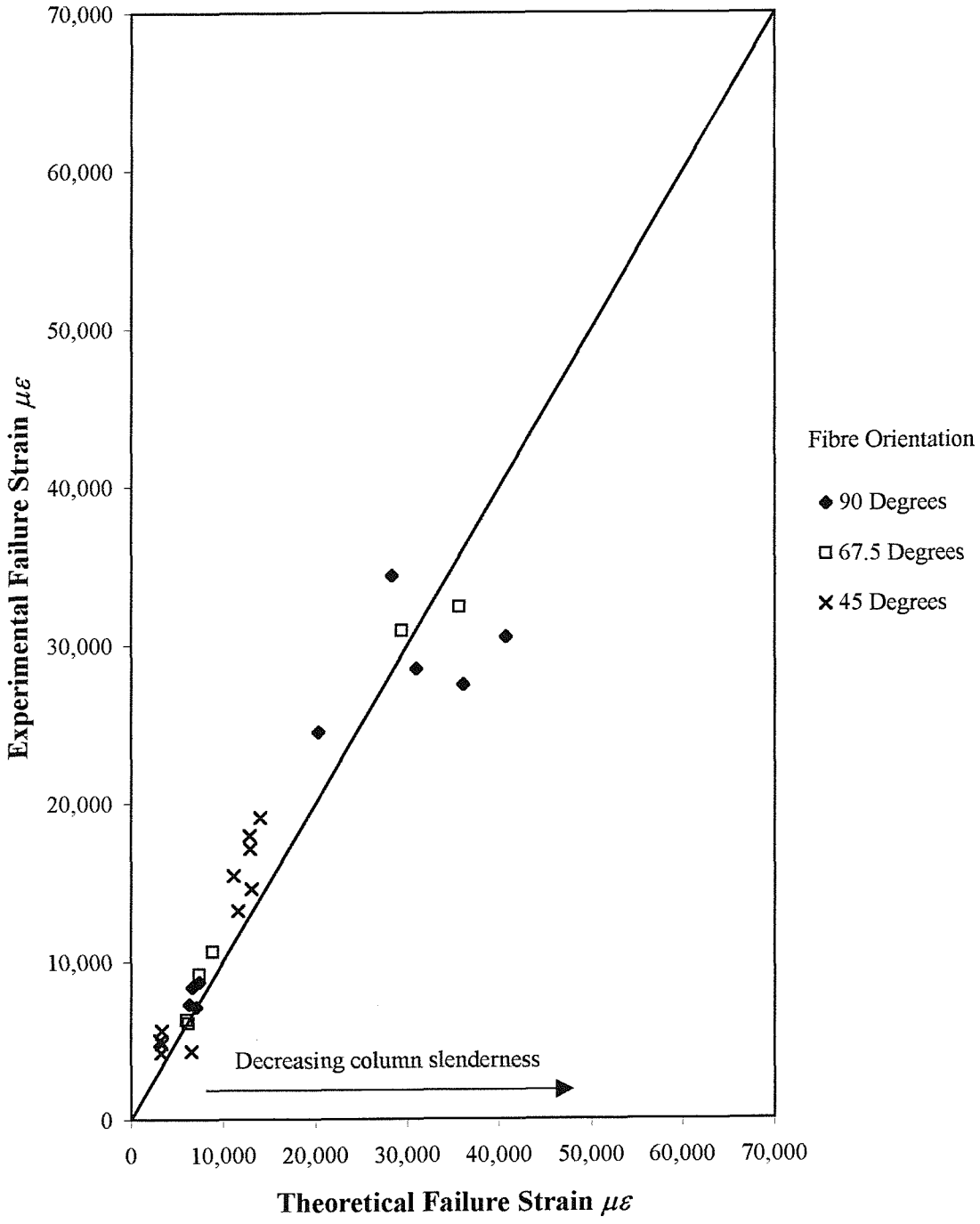

Figure 6.11. Comparison of the theoretical maximum compressive failure strain with experimental results

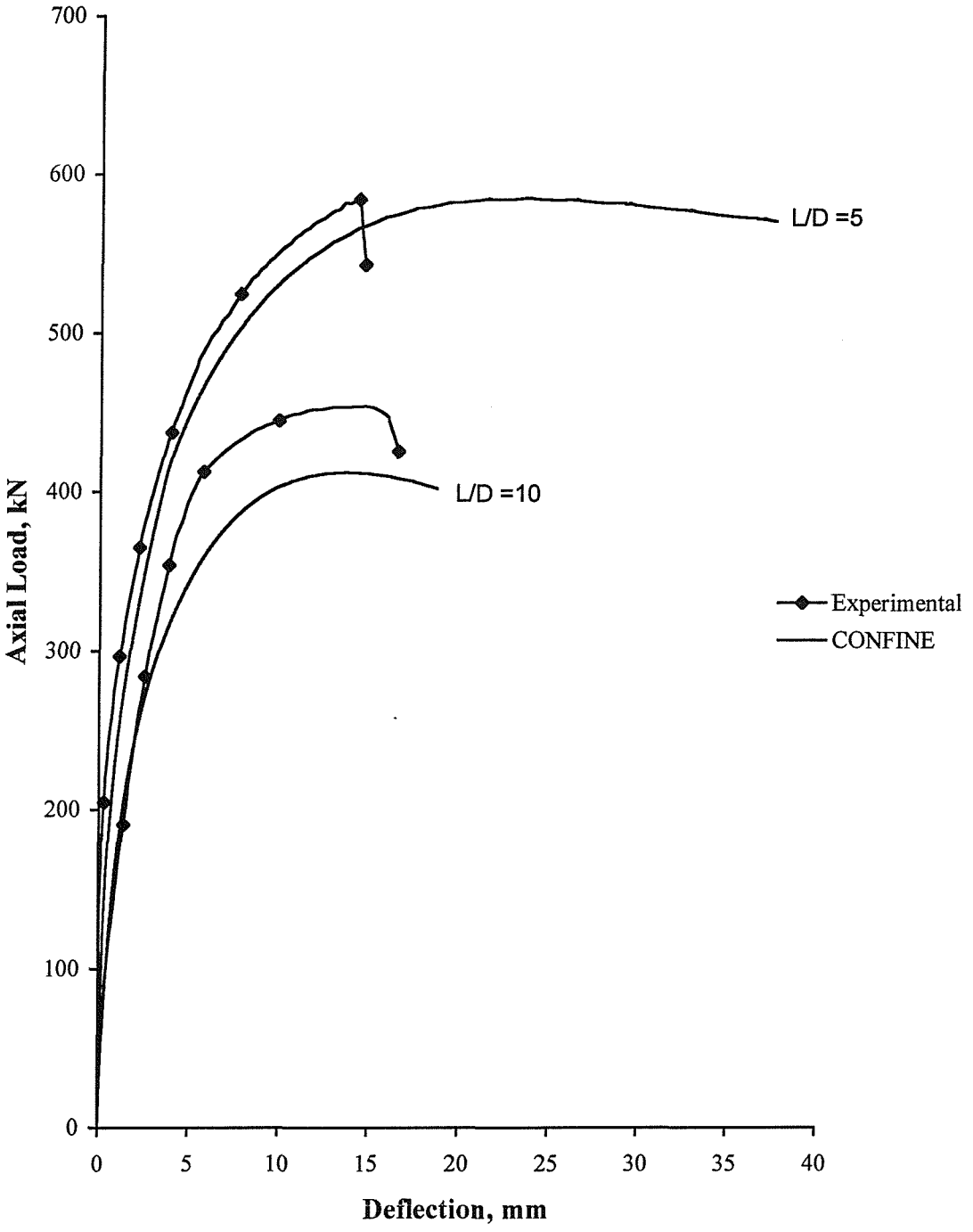

Figure 6.12(a). Comparison of the theoretical load-deflection behaviour with experimental results for the 125 mm diameter columns confined by fibres orientated at 82.3 degrees

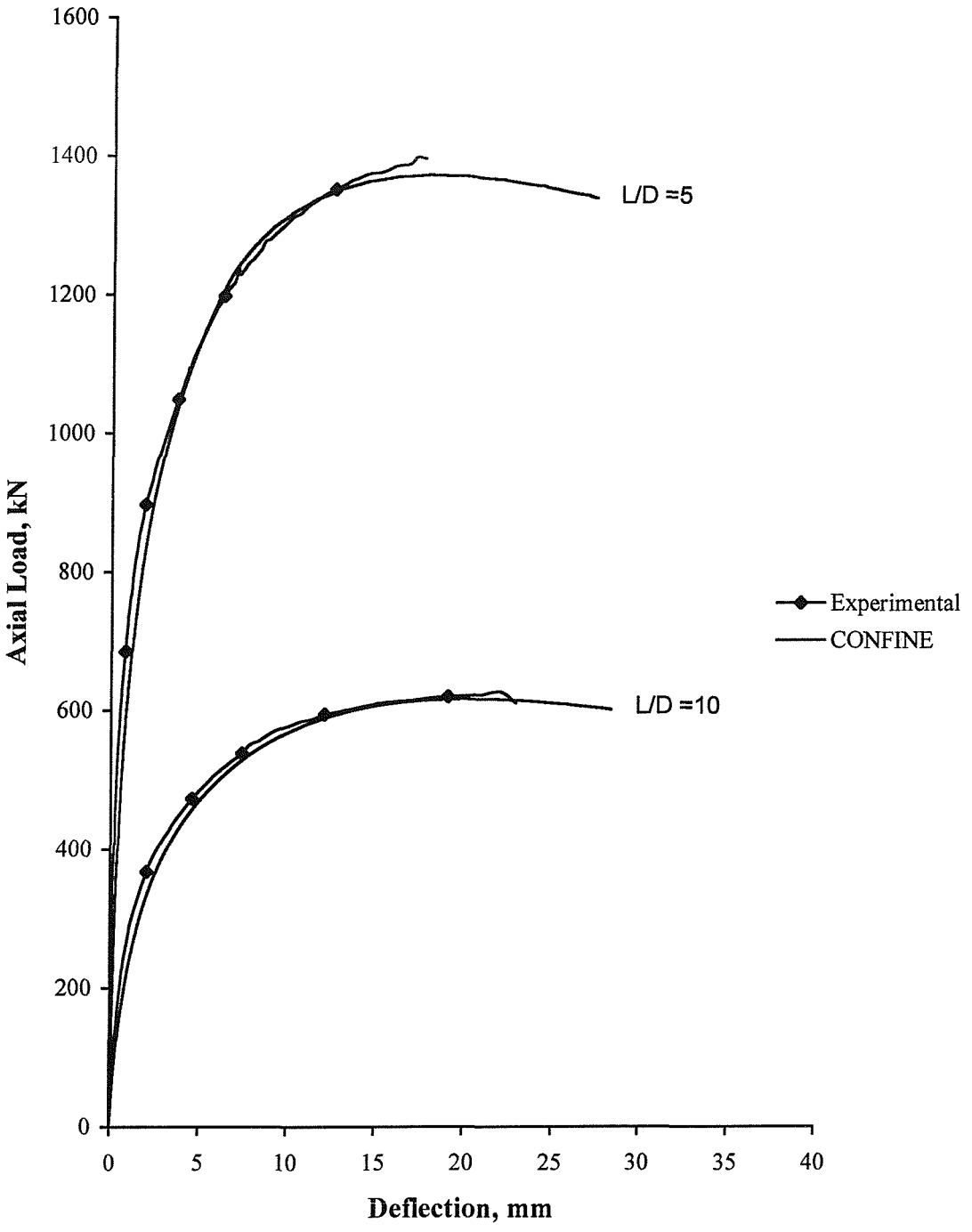

Figure 6.12(b). Comparison of the theoretical load-deflection behaviour with experimental results for the 200 mm diameter columns confined by fibres orientated at 85.2 degrees

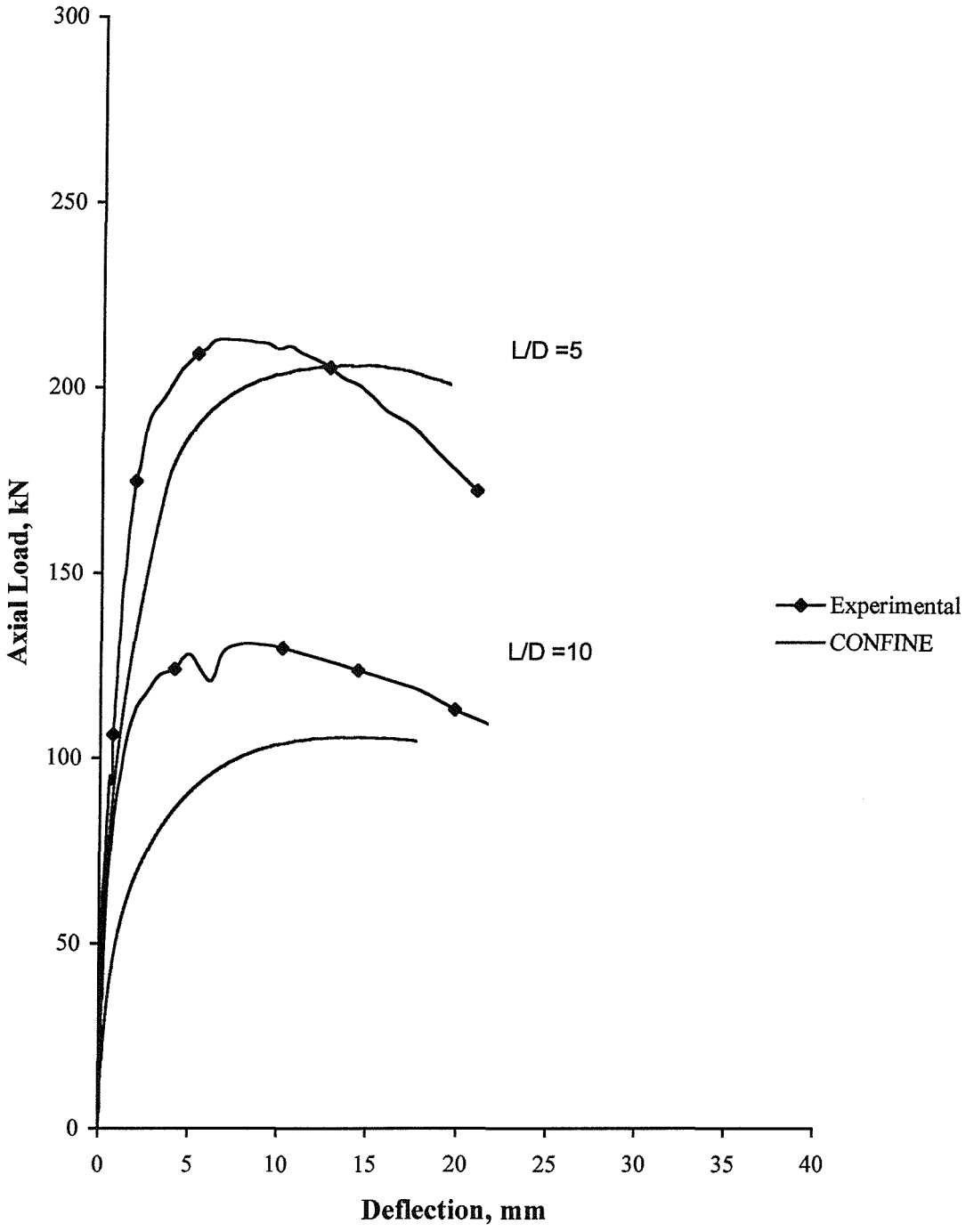

Figure 6.12(c). Comparison of the theoretical load-deflection behaviour with experimental results for the 80 mm diameter columns confined by fibres orientated at 57.8 degrees

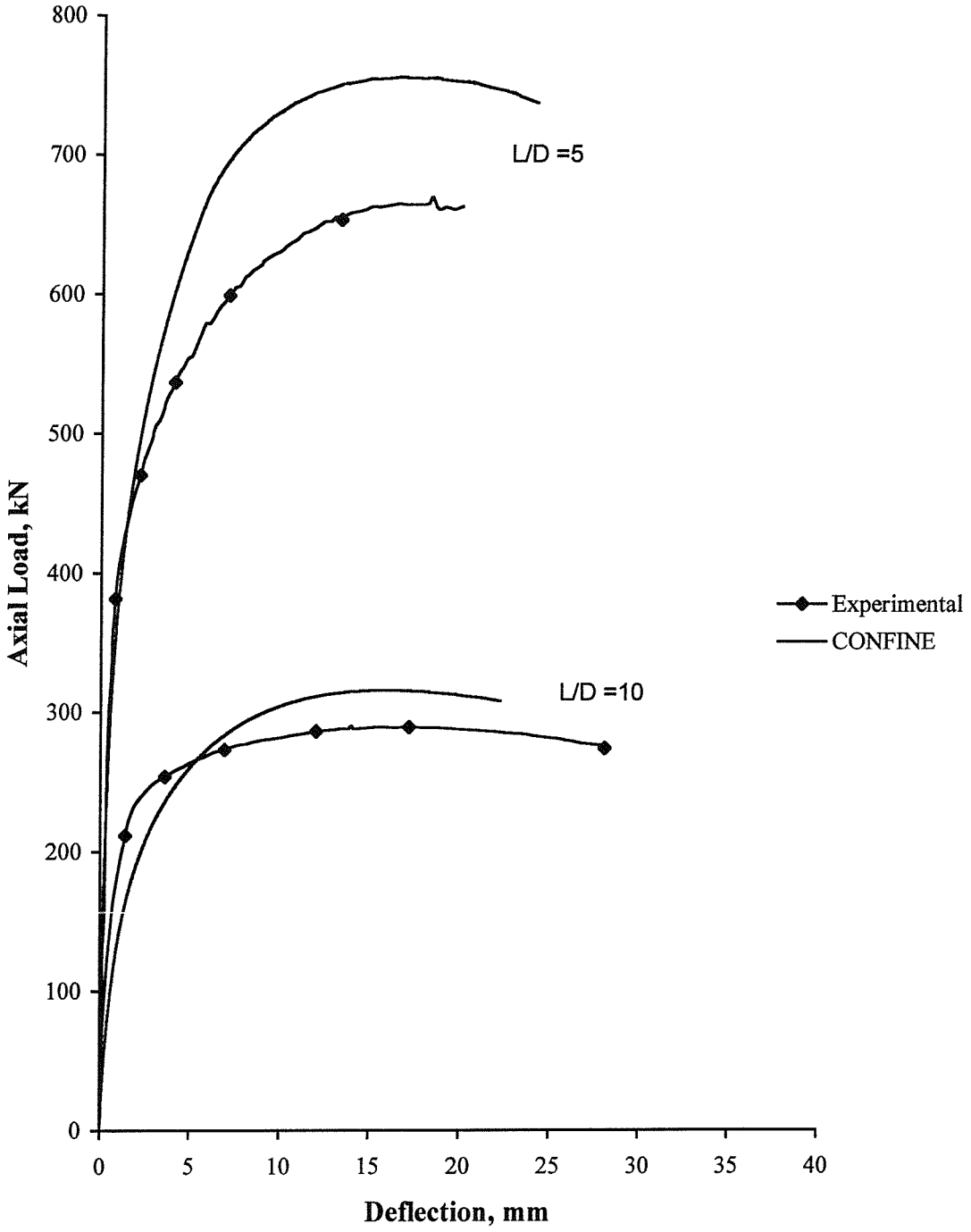

Figure 6.12(d). Comparison of the theoretical load-deflection behaviour with experimental results for the 150 mm diameter columns confined by fibres orientated at 71.3 degrees

PAGES MISSING
NOT AVAILABLE

figure 6.12.(e)

191

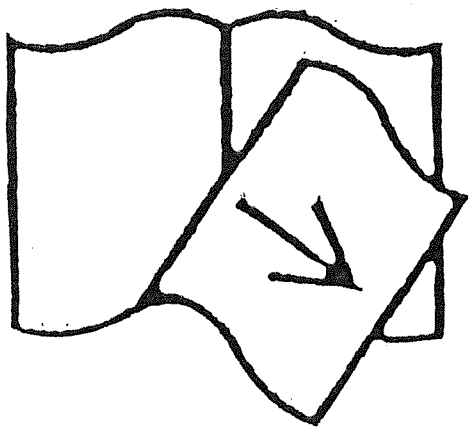

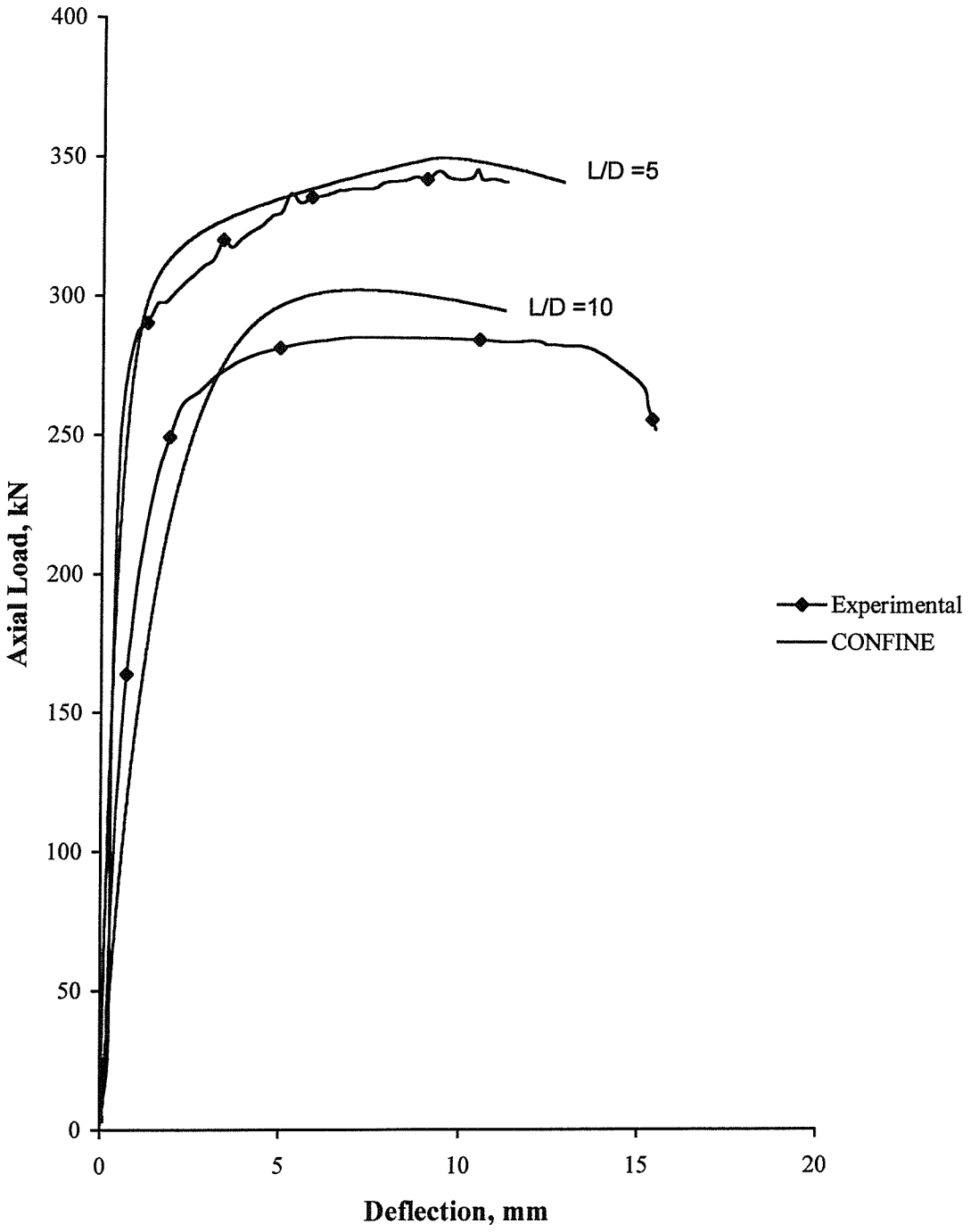

Figure 6.12(f). Comparison of the theoretical load-deflection behaviour with experimental results for the 150 mm diameter columns confined by fibres orientated at 48.0 degrees

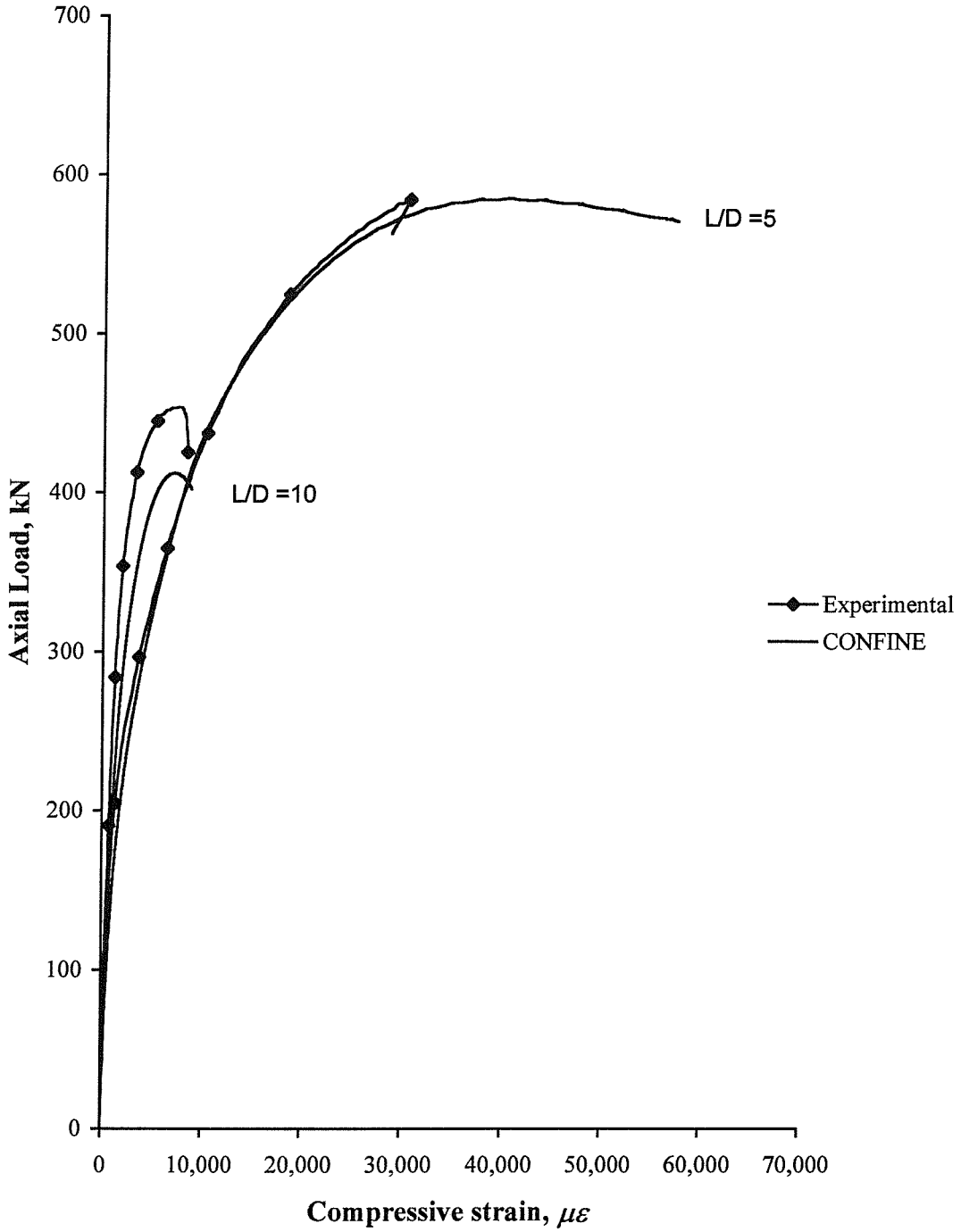

Figure 6.13(a). Comparison of the theoretical load-strain curves with experimental results for the 125 mm diameter columns confined by fibres orientated at 82.3 degrees

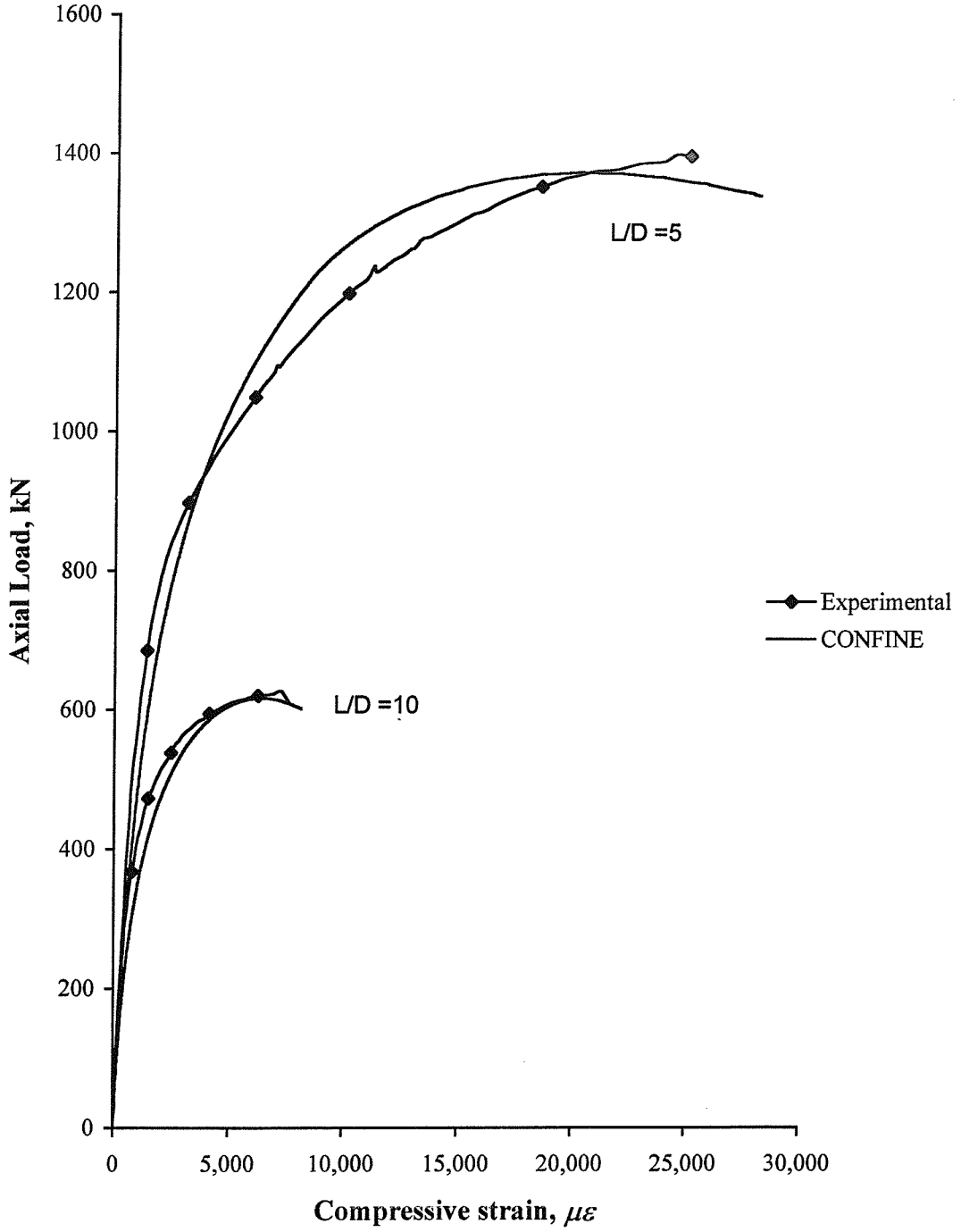

Figure 6.13(b). Comparison of the theoretical load-strain curves with experimental results for the 200 mm diameter columns confined by fibres orientated at 85.2 degrees

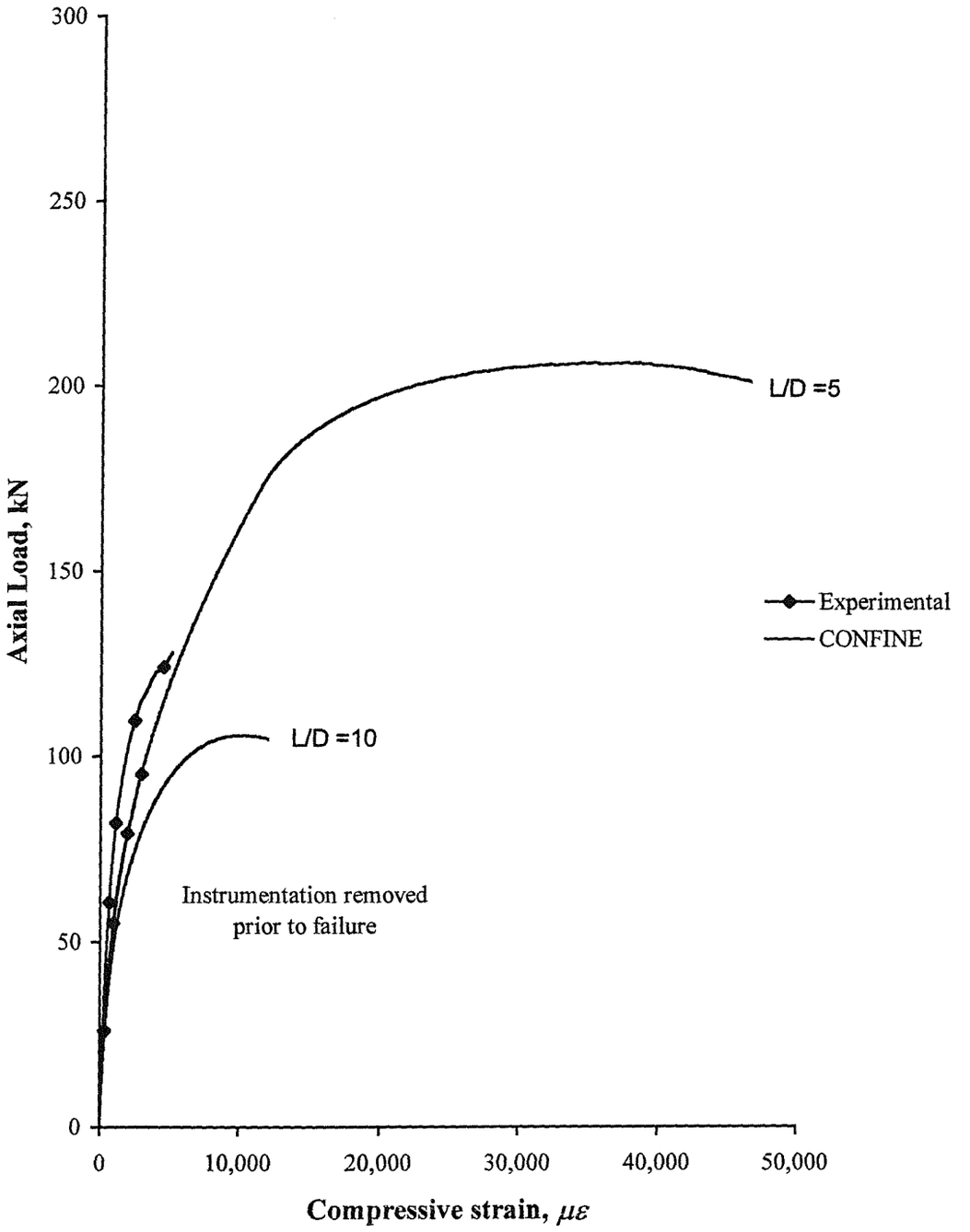

Figure 6.13(c). Comparison of the theoretical load-strain curves with experimental results for the 80 mm diameter columns confined by fibres orientated at 57.8 degrees

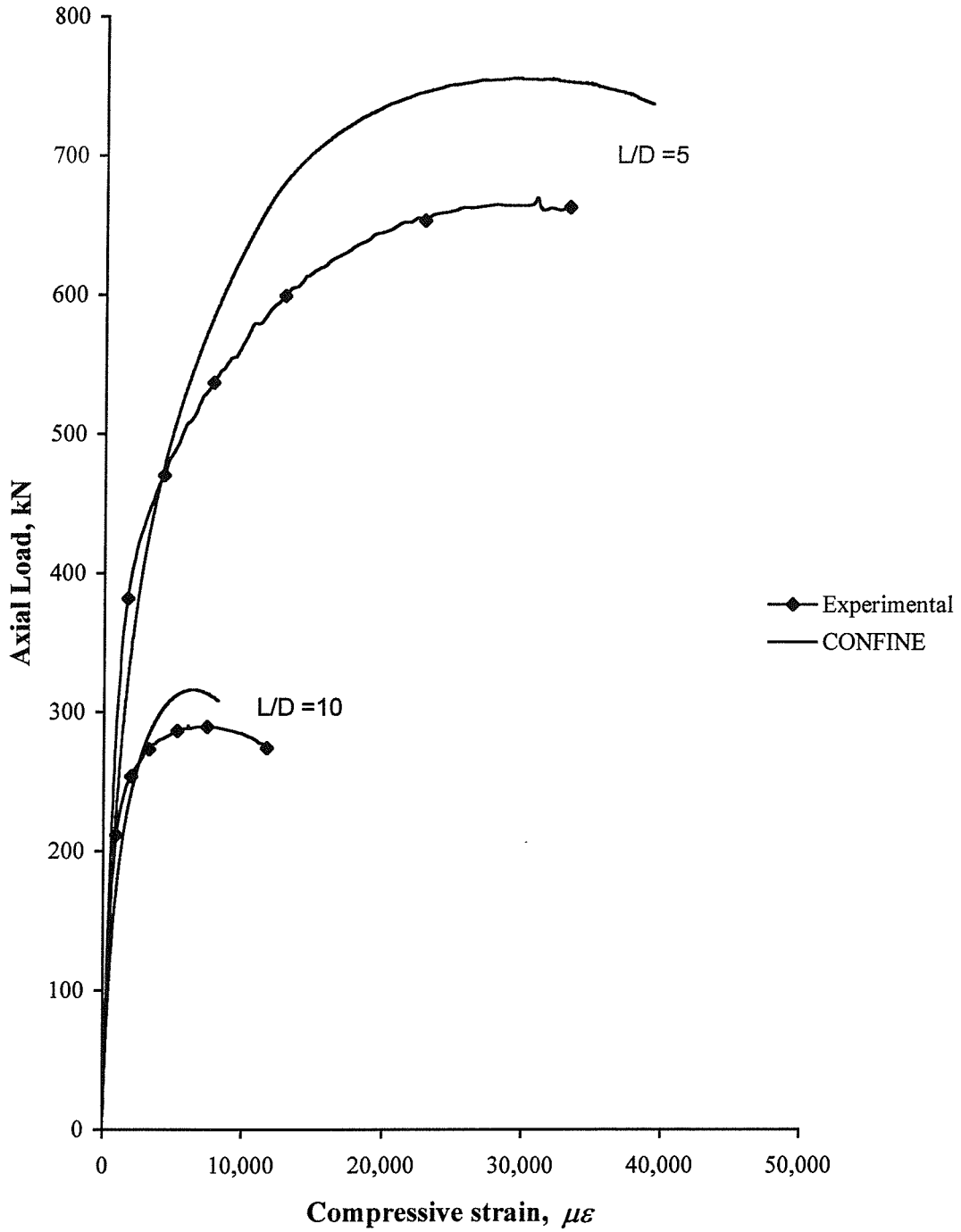

Figure 6.13(d). Comparison of the theoretical load-strain curves with experimental results for the 150 mm diameter columns confined by fibres orientated at 71.3 degrees

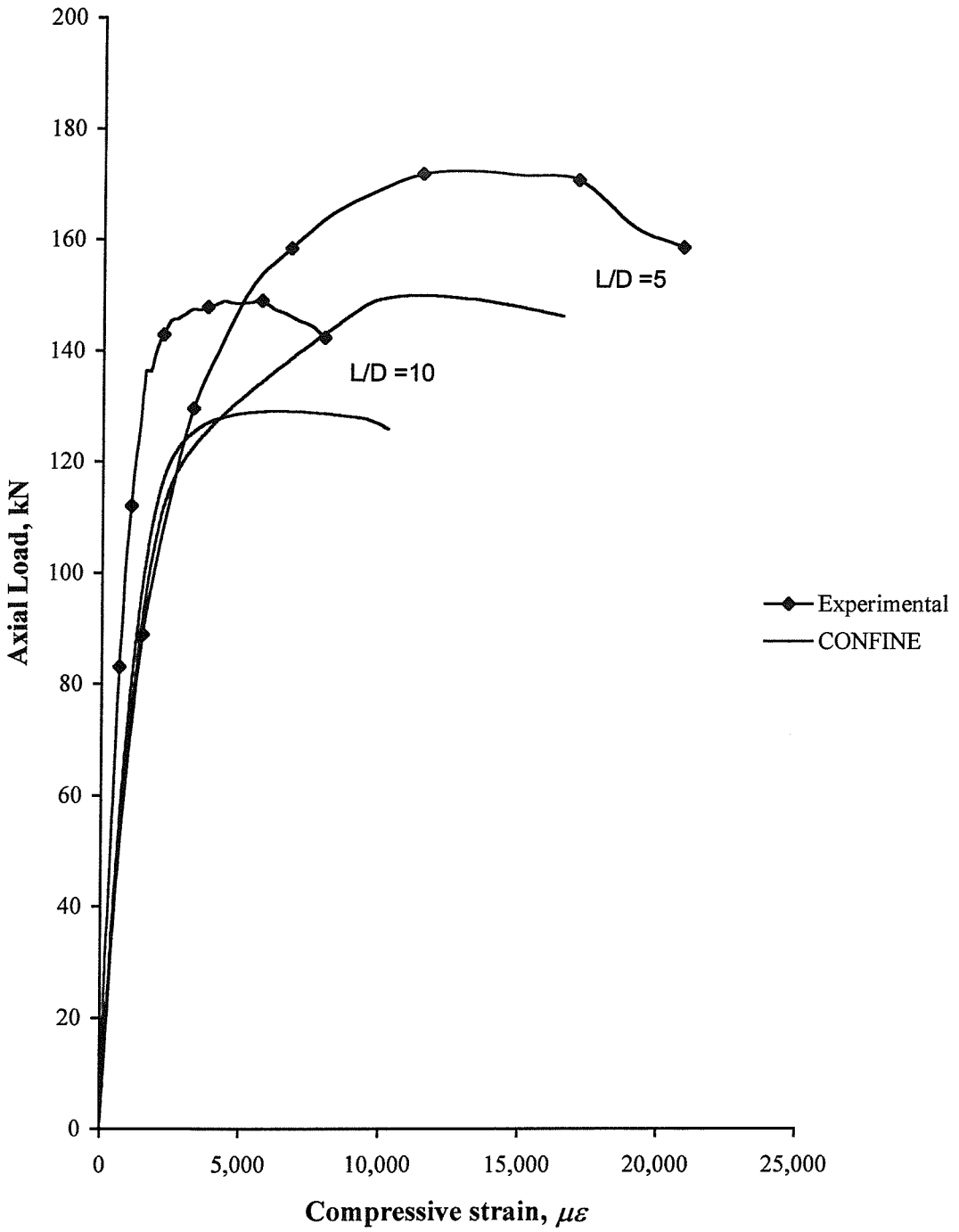

Figure 6.13(e). Comparison of the theoretical load-strain curves with experimental results for the 80 mm diameter columns confined by fibres orientated at 43.3 degrees

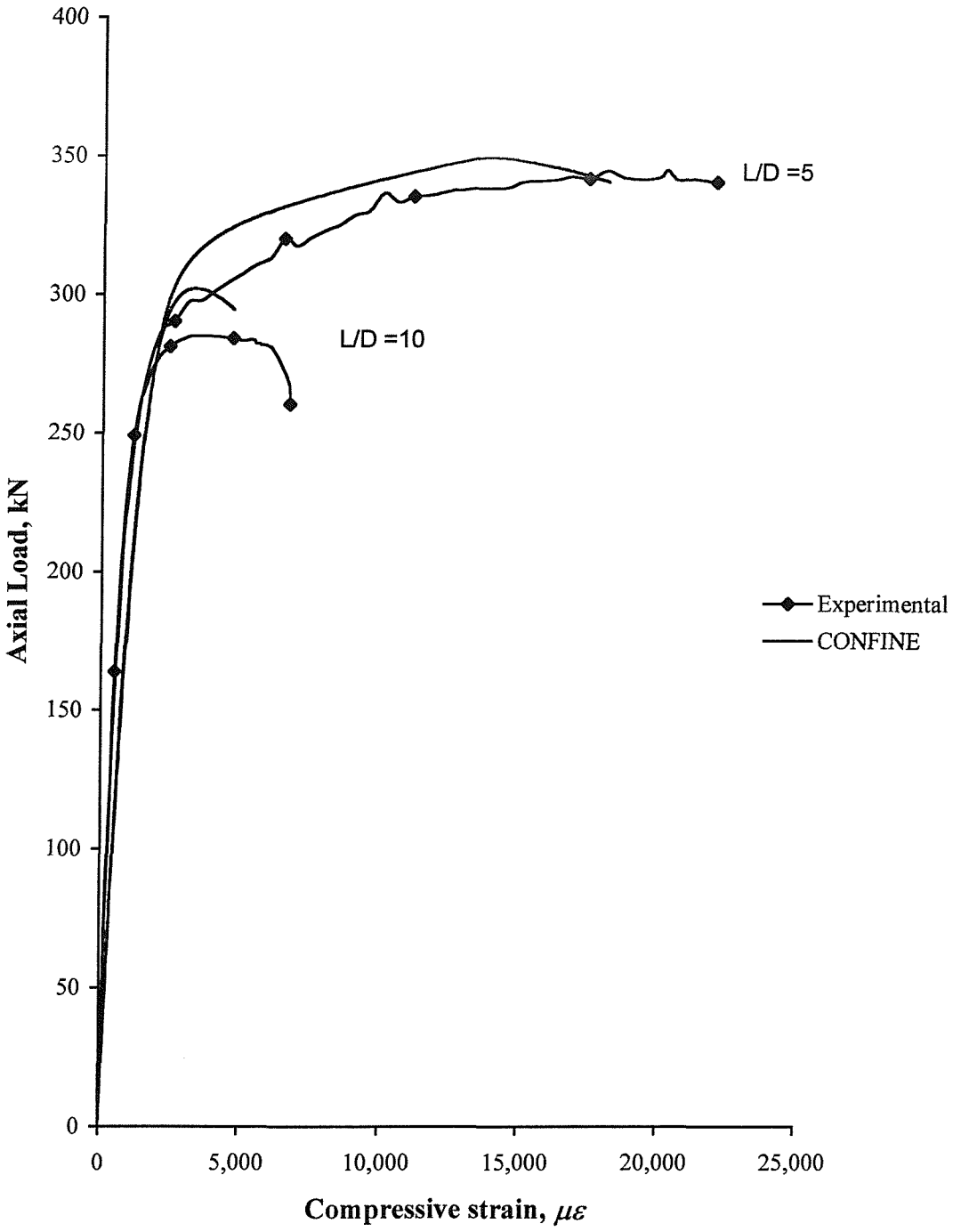

Figure 6.13(f). Comparison of the theoretical load-strain curves with experimental results for the 150 mm diameter columns confined by fibres orientated at 48.0 degrees

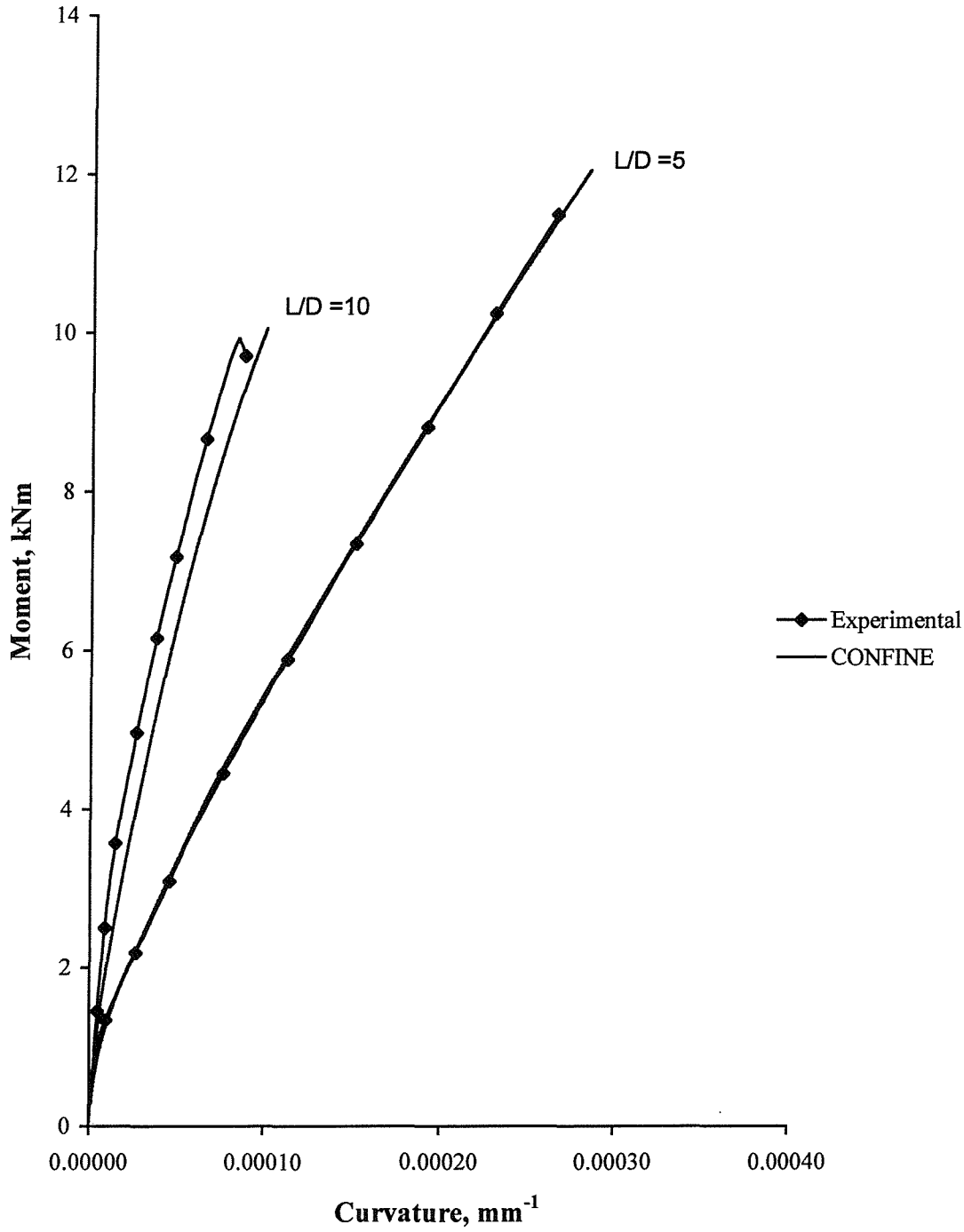

Figure 6.14(a). Comparison of the theoretical moment-curvature relationships with experimental results for the 125 mm diameter columns confined by fibres orientated at 82.3 degrees

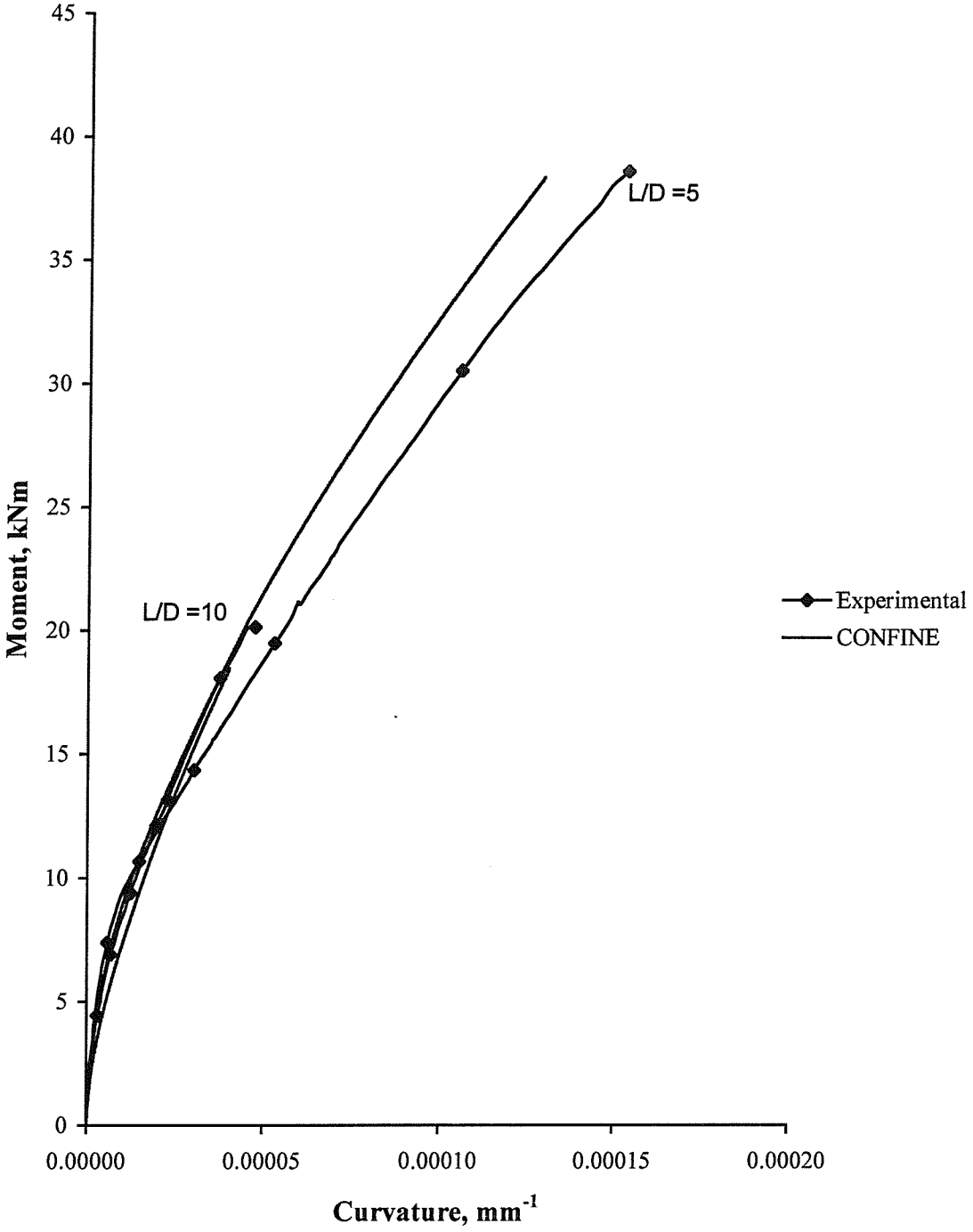

Figure 6.14(b). Comparison of the theoretical moment-curvature relationships with experimental results for the 200 mm diameter columns confined by fibres orientated at 85.2 degrees

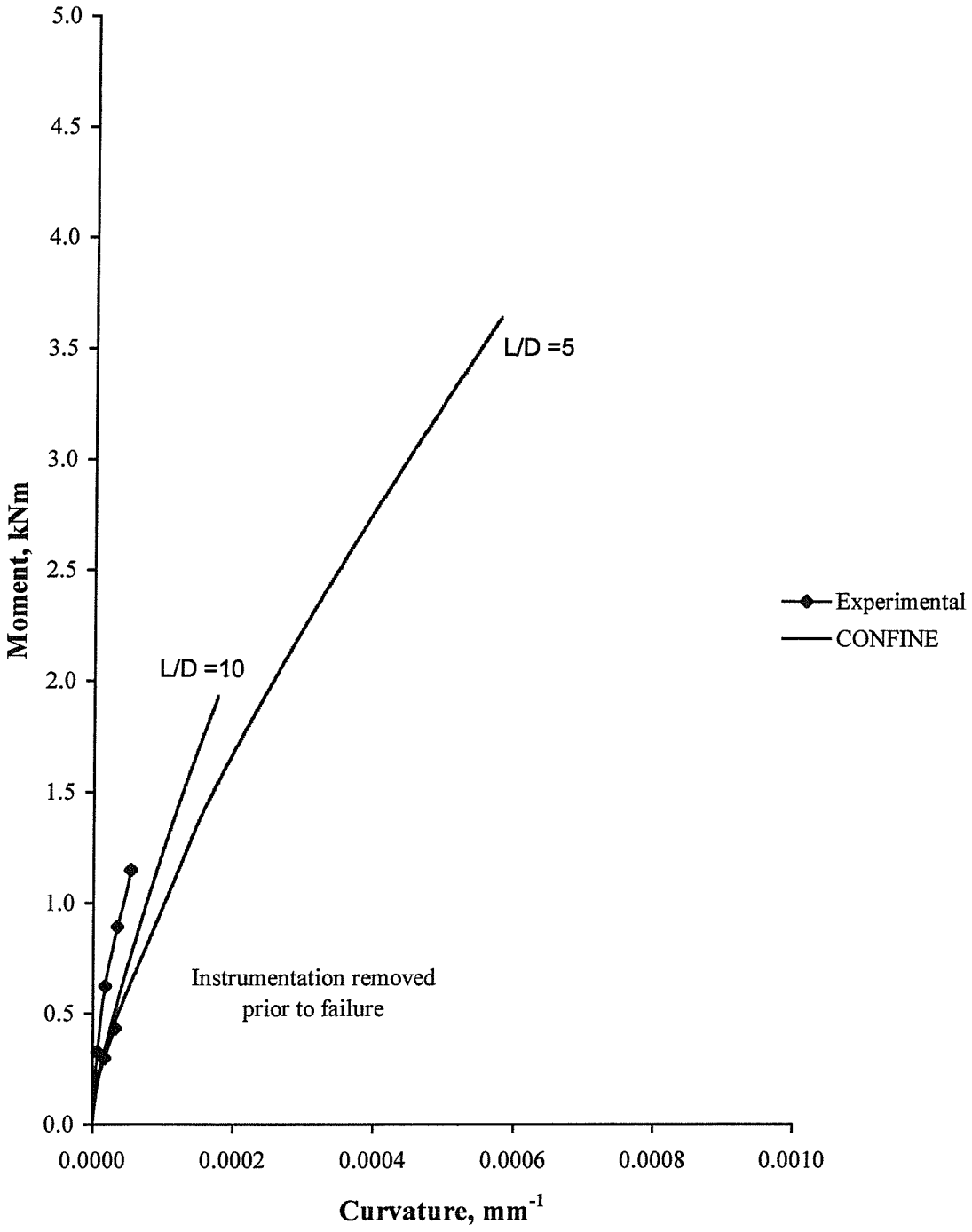

Figure 6.14(c). Comparison of the theoretical moment-curvature relationships with experimental results for the 80 mm diameter columns confined by fibres orientated at 57.8 degrees

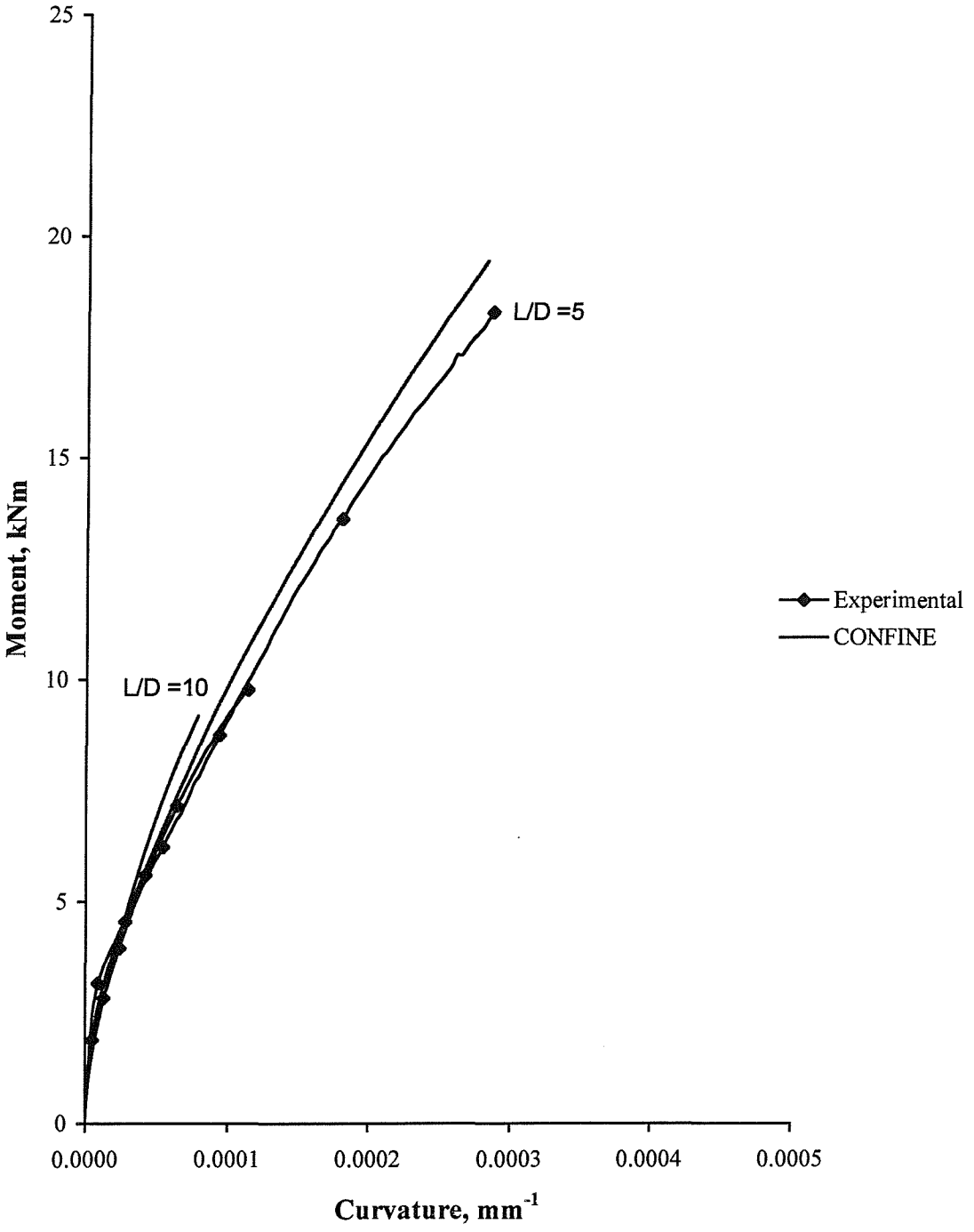

Figure 6.14(d). Comparison of the theoretical moment-curvature relationships with experimental results for the 150 mm diameter columns confined by fibres orientated at 71.3 degrees

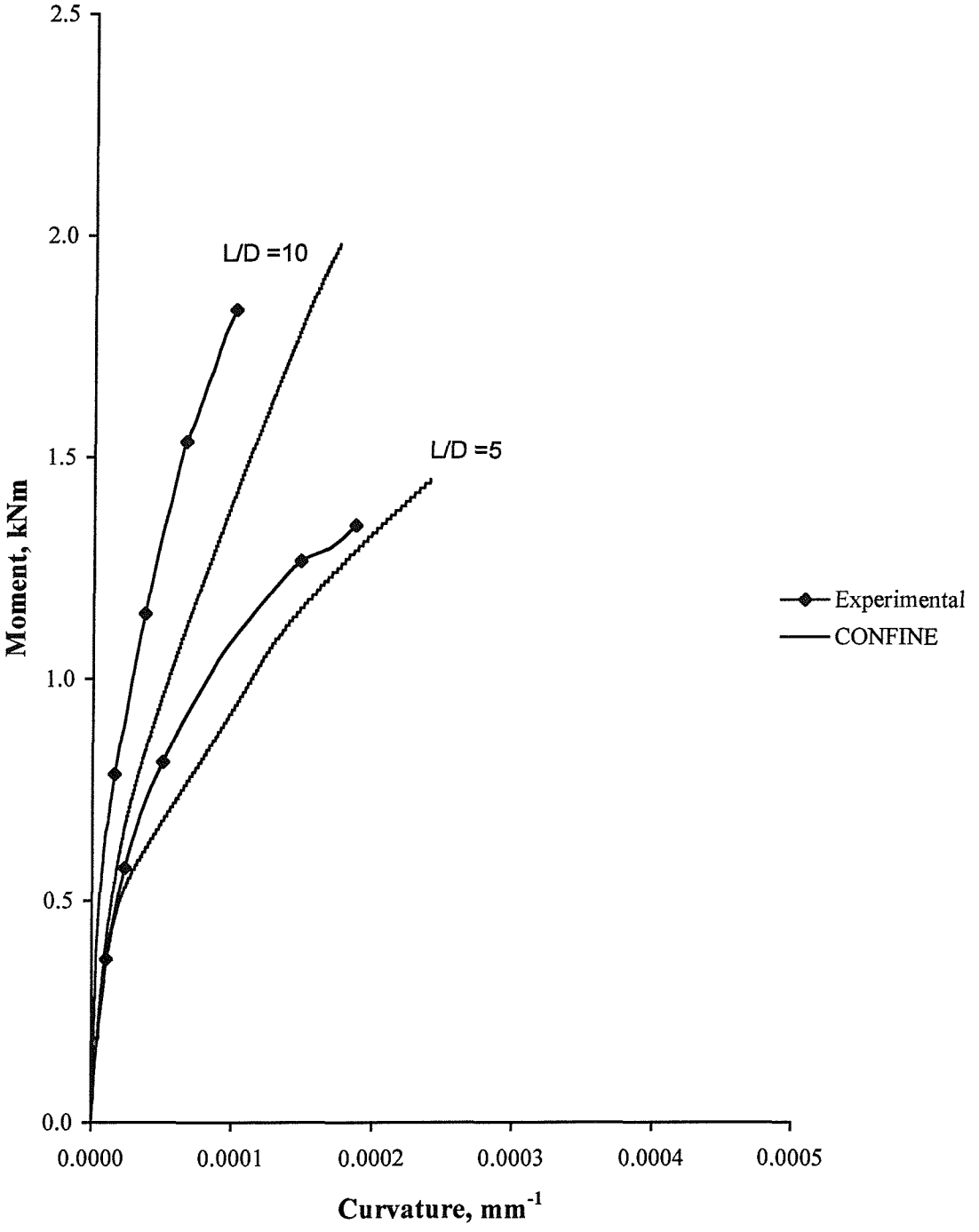

Figure 6.14(e). Comparison of the theoretical moment-curvature relationships with experimental results for the 80 mm diameter columns confined by fibres orientated at 43.3 degrees

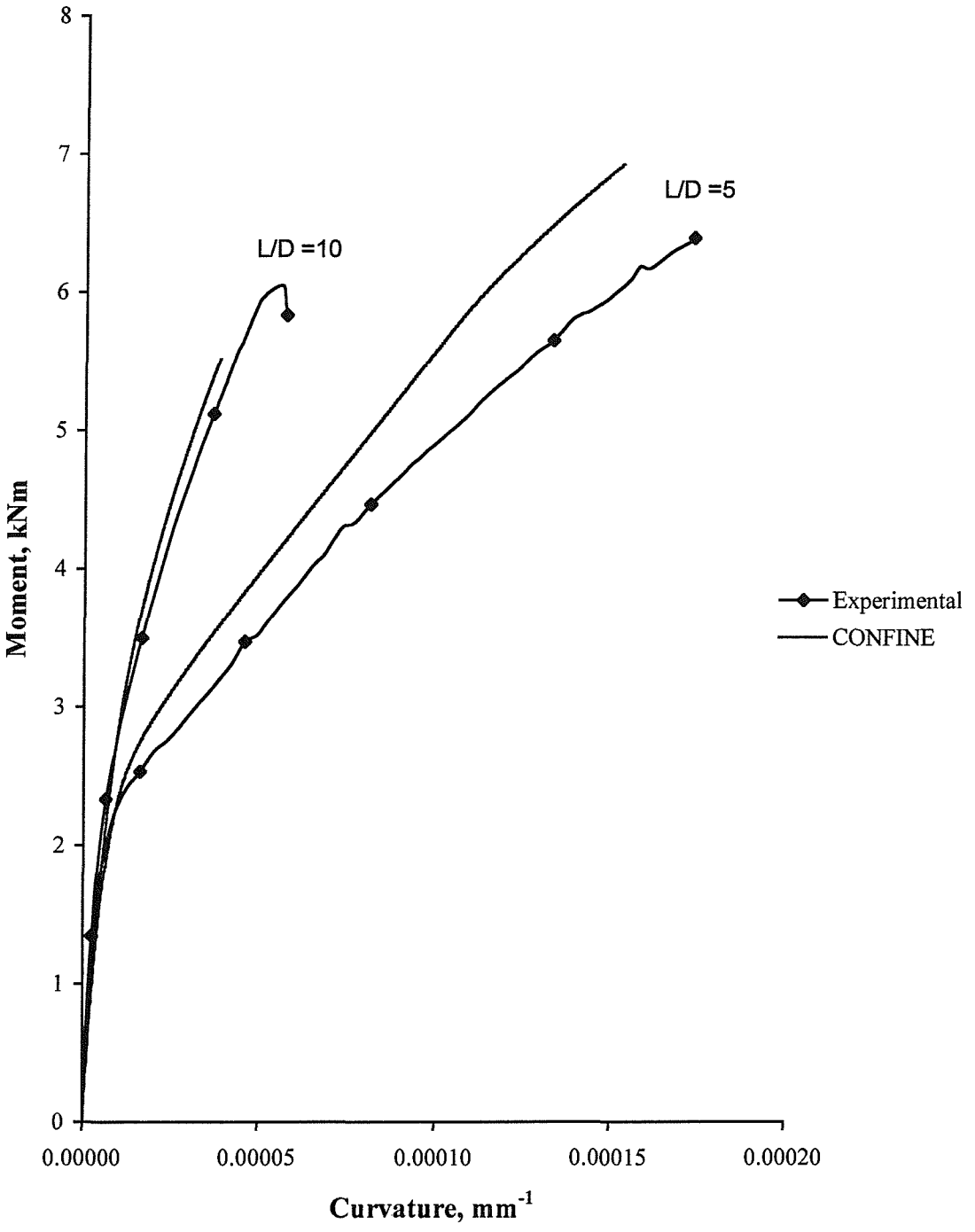

Figure 6.14(f). Comparison of the theoretical moment-curvature relationships with experimental results for the 150 mm diameter columns confined by fibres orientated at 48.0 degrees

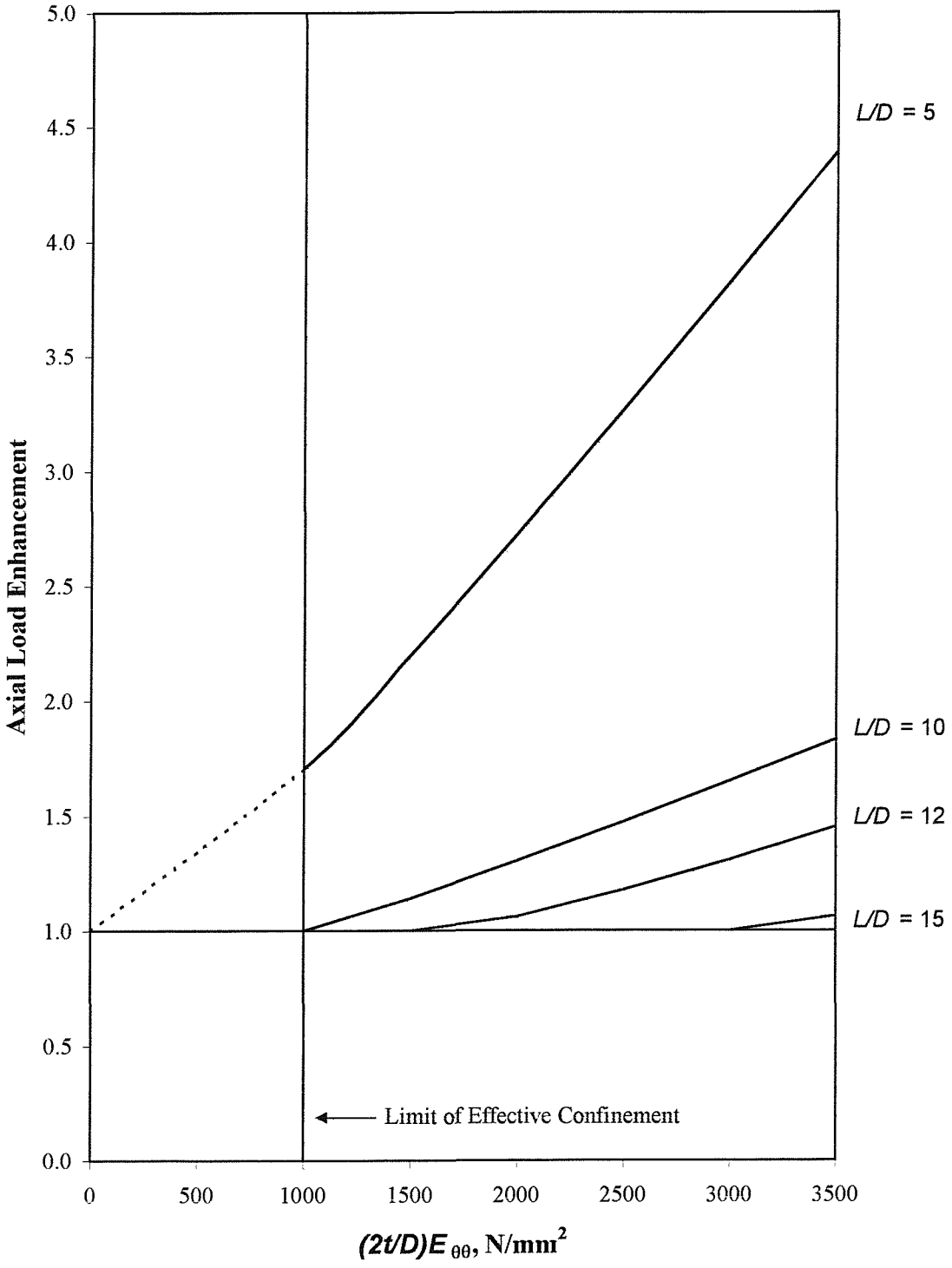

Figure 6.15. Load enhancement of FRP-confined concrete columns with increasing effective hoop modulus and column slenderness for a load eccentricity of 0.05*D*

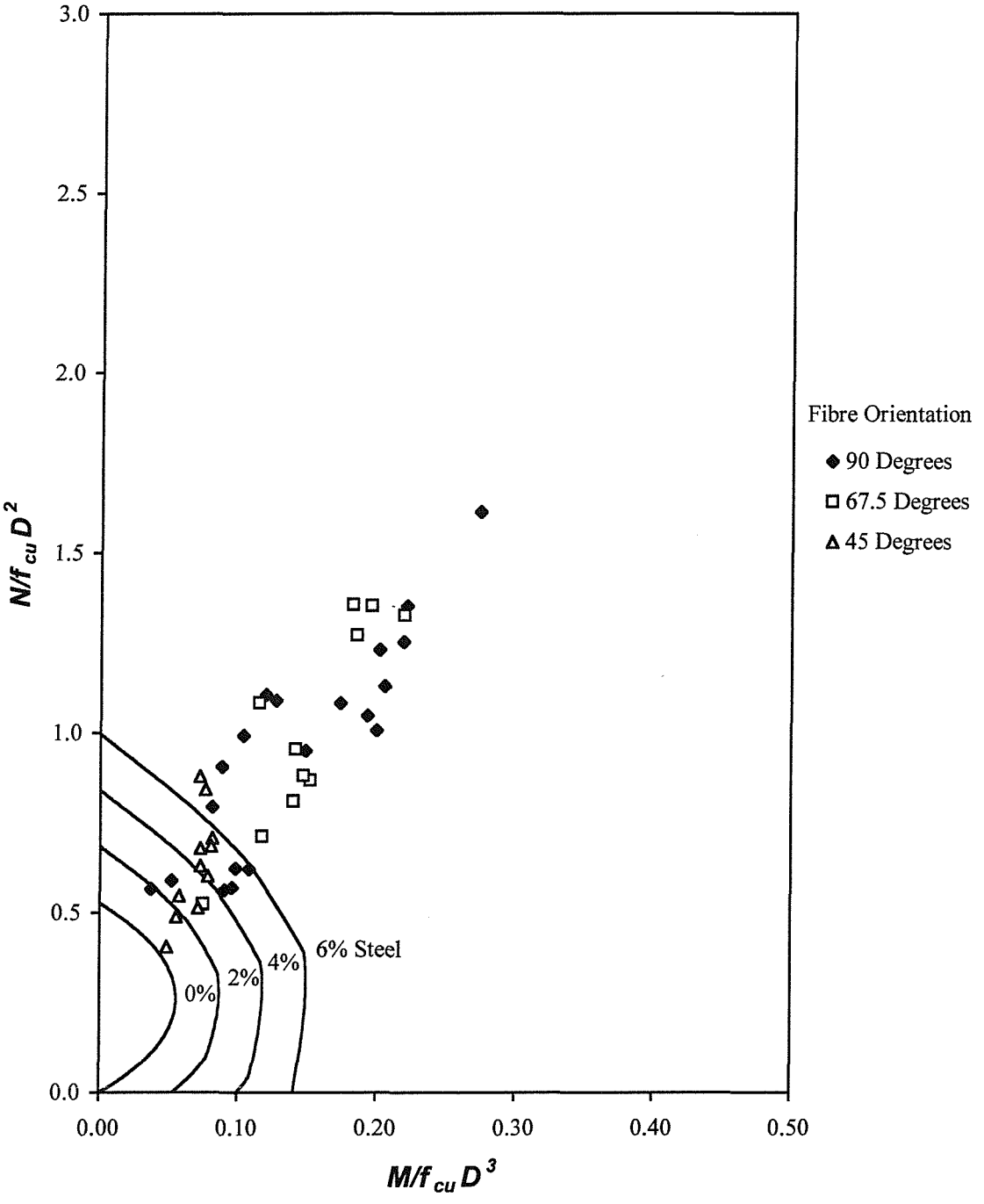

Figure 6.16. Comparison of the ultimate failure strength of FRP-confined concrete with conventional reinforced concrete columns

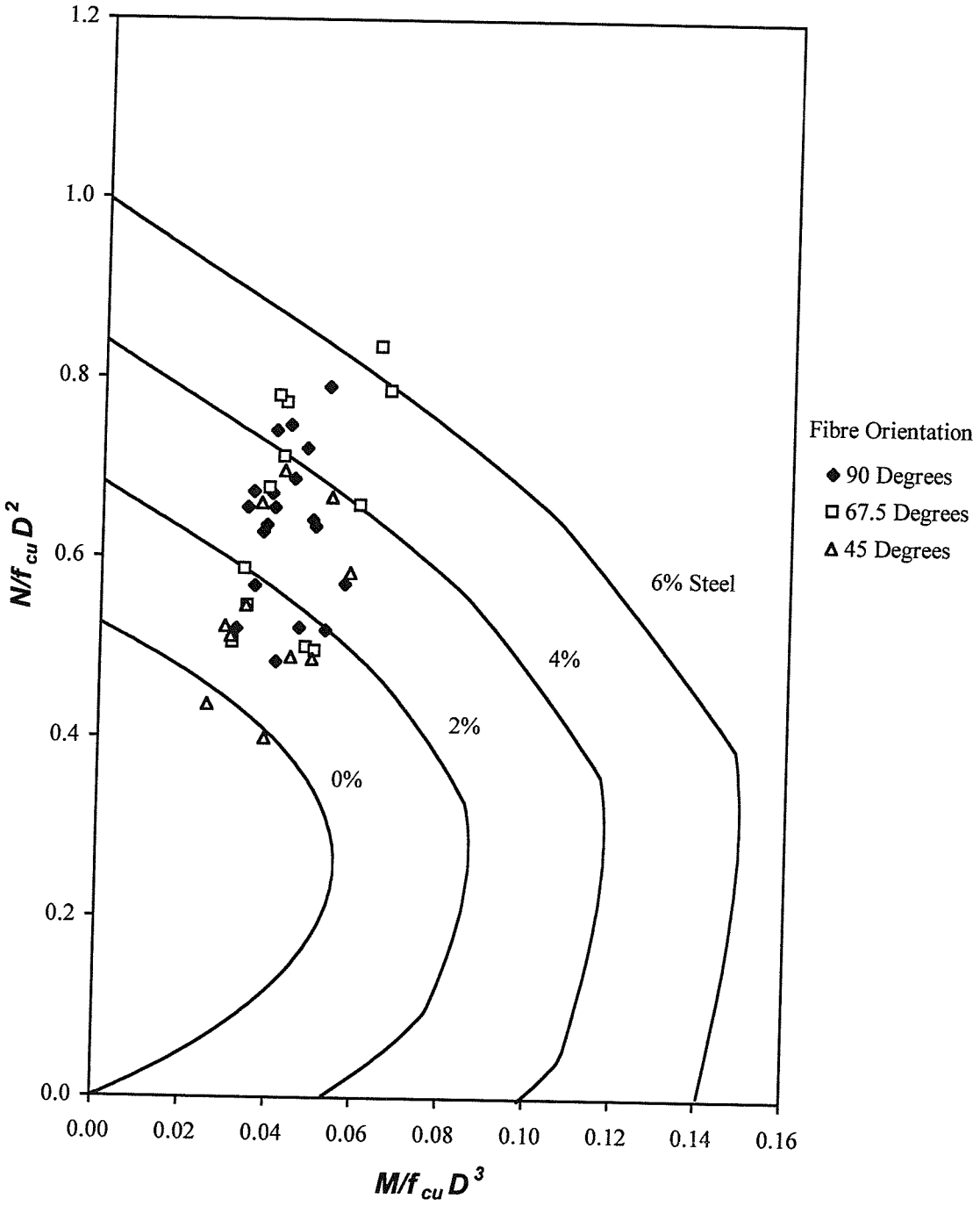

Figure 6.17. Comparison of the strength of FRP-confined concrete at 3500$\mu\varepsilon$ compressive strain with conventional reinforced concrete columns

CHAPTER 7

CONCRETE-FHLLED E-GLASS FRP-COMPOSITE COLUMNS WITH ADDITIONAL LONGITUDINAL FRP-COMPOSITE REINFORCEMENT

7.1 INTRODUCTION

The use of prefabricated filament wound tubes as both permanent formwork and the main reinforcement for concrete columns results in a significant enhancement in the load capacity of the column, provided the effective elastic hoop modulus of the FRP-composite is greater than 1,000 N/mm^2. However, strain softening of the concrete and the low axial modulus of elasticity of the FRP-composite give rise to significant lateral deflections. The lateral deflections of the column can only be reduced by increasing the stiffness *EI* of the column. The stiffness of the column may be increased by either increasing the diameter of the column, or by incorporating longitudinal reinforcement in the column cross-section.

The overall objective of this research is to develop a non-ferrous reinforced concrete column. Therefore, the increase in column stiffness is achieved by including FRP-composite bars as longitudinal reinforcement. Several types of FRP-composite bar have been developed specifically to act as reinforcement in concrete structures, these include the Eurocrete reinforcement bar [81], the ComBAR manufactured by Schöck [82] and the Kodiak bar produced by International Gratings [83]. These FRP composite bars are manufactured using the pultrusion process, which results in a unidirectional FRP composite with relatively high tensile strength and stiffness in the longitudinal direction.

Experimental research on the compressive behaviour of concrete reinforced with FRP bars is limited to a study by Kobayashi and Fujisaki [66]. They found that the compressive elastic moduli of FRP bars were the same as their tensile elastic moduli. However, the compressive strength of carbon, glass and aramid FRP bars are approximately 30%, 30% and 10% of their tensile strengths respectively [66]. The low longitudinal compressive strength of unidirectional composites is due to the low transverse tensile strength or the tendency for fibre buckling to occur.

7.2 EUROCRETE FRP-COMPOSITE BAR

The FRP-composite bars used in this research as longitudinal reinforcement were those developed by the Eurocrete project [81] specifically as an alternative form of reinforcement for concrete. The pultruded bars consist of unidirectional E-glass fibres or carbon Zoltek fibres and a vinyl-ester resin matrix. To improve the bond characteristics of the rod with concrete, a peel-ply texture is applied to the surface of the rod.

Two diameters of E-glass FRP rod were used to provide longitudinal reinforcement, a nominal 8.0 mm diameter and a 13.5 mm diameter. The tensile strength of the E-glass bars was 1,000 N/mm^2 with an elastic modulus of 45.0 kN/mm^2. The carbon FRP bars were a nominal 8.0 mm diameter, with a tensile strength of 2,408 N/mm^2 and an elastic modulus of 152.5 kN/mm^2 [81].

7.3 EXPERIMENTAL INVESTIGATION

All the columns were reinforced with six FRP bars equally spaced around the periphery of the column as shown in Plate 7.1. The columns were each reinforced with bars of one diameter and fibre type. The bars were bonded to the interior of the filament wound tubes using an epoxy resin, and allowed to cure fully before casting the concrete.

The parameters investigated were the:

- type of longitudinal fibre;
- percentage of longitudinal reinforcement;
- column slenderness;
- diameter of FRP-composite tube;
- orientation of the fibres.

The different tube diameters and combinations of FRP-composite tubes and longitudinal reinforcement are summarised in Table 7.1.

The testing arrangement for the eccentrically loaded columns with longitudinal reinforcement was identical to the testing arrangement described in §5.2. Two column slenderness ratios of $L/D = 5$ and $L/D = 10$ were again investigated, and all the columns were tested with a constant end eccentricity of $0.05D$.

7.4 EXPERIMENTAL BEHAVIOUR

The eccentric load was applied to the columns by increasing the platen displacement at a constant rate of $0.002D$ mm/min, the same displacement rate used in phases I and II. As the load on the column increased, the characteristic matrix whitening of the FRP-composite tubes was observed at discrete intervals along the entire length of the column. Two different modes of failure were observed during the testing of the longitudinally reinforced columns. The failure modes of the columns are summarised in Table 7.2.

The first mode of failure was the same as the confined columns with no longitudinal reinforcement. The failure of the column was governed by stability. During the loading

regime, the columns exhibit an increase in load with increasing platen displacement until the peak load is reached. Further increases in the platen displacement resulted in a drop in the load capacity.

The second mode of failure is initiated by the failure of the FRP bar at the extreme compressive face. All the columns reinforced with the carbon FRP bars were characterised by this mode of failure. This mode of failure also occurred in columns reinforced with the E-glass FRP bars with a slenderness ratio equal to 5. The failure of the E-glass FRP bars caused the confining tube to rupture due to the release of strain energy and the volumetric expansion of the bar. The rupture of the FRP-composite tube by the FRP bar, as shown in Plate 7.2, results in a loss of confining pressure and a sudden reduction in the load capacity.

7.5 ULTIMATE FAILURE

The failure of the confined columns with longitudinal reinforcement is taken as either the peak load if stability governs, or the load corresponding to first failure of the FRP bar. The load at first failure of the FRP bar was identified by a sudden drop in load capacity and an audible failure. The load, deflection and compressive strain of the columns at failure are summarised in Table 7.3.

Failure of the columns reinforced with carbon FRP bars was initiated by the failure of the reinforcement at the extreme compressive face. The mean compressive strain at which failure of the carbon FRP bars occurred was 5,629$\mu\varepsilon$ with a standard deviation of 434$\mu\varepsilon$. Inclusion of longitudinal reinforcement reduced the load capacity of the confined columns with a slenderness equal to 5, except for columns confined by composites with a low effective hoop modulus.

The ultimate failure load of the confined columns was increased by the E-glass longitudinal reinforcement. The greater the percentage of longitudinal reinforcement, the larger the increase in axial load. The lateral deflections at failure are similar to the lateral deflections of FRP-confined columns without longitudinal reinforcement.

Comparisons of the load capacity of columns with and without longitudinal reinforcement for slenderness ratios of 5 and 10 are given in Figures 7.1 and 7.2 respectively. The lower load capacity is due to the failure of the carbon FRP bar before the full benefits of the triaxial enhancement are utilised. When the column slenderness L/D equals 10, an increase in load capacity is observed in the confined columns with longitudinal reinforcement.

However, the increase in load capacity due to the reinforcement diminishes as the magnitude of the confining stiffness increases.

The primary function of the longitudinal reinforcement was to increase the stiffness of the column and hence reduce the lateral deflections. The experimental results given in Table 7.3 show that the longitudinal carbon FRP bars reduce the lateral deflections of the columns at failure. Typical load-deflection curves for confined columns with and without longitudinal carbon FRP reinforcement are shown in Figures 7.3(a-b). The complete set of load-deflection curves for columns with additional longitudinal carbon FRP reinforcement is given in Appendix J.

The load-deflection responses of the FRP-confined columns reinforced with E-glass FRP bars are compared with FRP-confined columns with no longitudinal reinforcement in Figures 7.4(a-b). The complete set of load-deflection curves for columns with additional longitudinal E-glass FRP reinforcement is given in Appendix K. The initial load deflection behaviour of the columns is the same, since the elastic moduli of the E-glass FRP bar and normal weight concrete are very similar. The elastic modulus of the E-glass FRP bar is 45 kN/mm^2, whereas the initial tangent modulus of normal weight concrete is approximately 28 kN/mm^2 to 45 kN/mm^2 depending on the compressive strength.

A comparison of the load-deflection behaviour of the columns reinforced with either carbon or E-glass FRP bars is given in Figure 7.5. The carbon FRP-composite reinforcement reduced the lateral deflection of the column but resulted in a brittle failure mode initiated by a compressive failure of the longitudinal reinforcement. The use of E-glass bars as longitudinal reinforcement was not found to increase the flexural stiffness of the columns. However, columns reinforced longitudinally with E-glass bars do exhibit an enhanced axial load capacity compared to columns reinforced with carbon FRP bars or no longitudinal bars.

The stiffness of the column is given by the slope of the moment-curvature relationship. Typical moment-curvature relationships for reinforced and unreinforced columns are given in Figures 7.6(a-b) and Appendix L. The moment-curvature curves for all the columns are approximately bi-linear. The initial stiffness of the column is given by:

$$k_c = E_{ci}\left(\frac{\pi D^4}{64}\right) + (E_r - E_{ci})I_r \qquad (7.1)$$

Since the elastic modulus of the E-glass FRP bar and concrete are similar, the initial stiffness of the column is not increased by E-glass FRP reinforcement.

The secondary slope of the moment-curvature relationship is a function of the degree of confinement and the percentage of longitudinal reinforcement. The secondary slope increases as the confining pressure increases, as discussed in §5.3.5. The secondary stiffness is also increased by the E-glass FRP reinforcement. The magnitude of the increase in stiffness is proportional to the percentage of longitudinal reinforcement, as shown in Figure 7.6(b).

Typical load-strain curves for the longitudinally reinforced columns are shown in Figures 7.7(a-b). Columns reinforced with E-glass FRP bars were able to undergo much larger compressive strains than the columns reinforced with the carbon FRP bars. However, the lower elastic modulus of the E-glass bar resulted in stability failures for columns with L/D = 10, as shown in Figure 7.7(b). Based on a tensile failure strength of 1000 N/mm^2 and a modulus of elasticity of 45 kN/mm^2, the tensile failure strain of the E-glass bar is 22,200$\mu\varepsilon$. Compressive failure strains in the short columns ranged between 16,800$\mu\varepsilon$ to 32,700$\mu\varepsilon$, depending of the orientation of the confining fibres. Thus, triaxial confinement enables compressive strains to occur in the FRP-composite bar that are comparable to or greater than the tensile failure strain. The failures of the columns where the compressive strains exceed 22,200$\mu\varepsilon$ were characterised by the reinforcement rupturing the FRP-composite tube. The load-strain curves for all the columns with longitudinal reinforcement are given in Appendix M.

Differences in the behaviour of the carbon- and E-glass FRP bars are due to the microstructure of the fibres. The carbon FRP bar failed by inter-laminar shear due to the weak transverse strength of the fibres. The failure of the E-glass FRP bar was typified by the bar crushing longitudinally as a result of the triaxial confinement. The strain energy released at failure and the volumetric expansion of the material caused the FRP-composite tube to rupture. The crushing failure mode of an E-glass bar in compression is shown in Plate 7.3.

7.5.1 Column slenderness

The ultimate axial load capacity of the columns was, as expected, found to decrease with increasing column slenderness. The influence of column slenderness on the ultimate load capacity of confined columns reinforced with high modulus carbon FRP bars or low

modulus E-glass FRP bars is shown in Figures 7.8 and 7.9 respectively. Columns reinforced with the higher modulus carbon FRP bars exhibit a smaller reduction in axial load capacity as the slenderness is increased. The failure of the columns is initiated by the carbon FRP bar failing at a mean compressive strain of 5,629$\mu\varepsilon$, preventing full triaxial confinement developing in the column. Since the reduction in axial load capacity is due to the diminishing benefits of triaxial confinement with increasing slenderness, the apparent reduction in second-order effects at ultimate load is due to the lower compressive failure strain of the column. Columns reinforced longitudinally with the lower modulus E-glass FRP bar retained full confinement and hence exhibited a greater reduction in triaxial confinement as the slenderness increased.

7.6 NUMERICAL MODELLING OF CONFINED BEHAVIOUR

The FRP reinforcement is modelled as discrete elements in the CONFINE algorithm. The idealisation of the cross-section is shown in Figure 7.10. To account for the longitudinal FRP reinforcement, equation 6.10 and equation 6.11 of the CONFINE algorithm are modified to include the strength contribution of the FRP-composite bars. The internal forces and moments at mid-height of the column are calculated from the strain distributions by the equations:

$$N^{\text{int}} = \sum_{i=1}^{n} f_{ci} A_{ci} + \sum_{j=1}^{m} f_{tj} A_{tj} + \sum_{k=1}^{p} (f_{rk} - f_{ck}) A_{rk} \qquad (7.2)$$

$$M^{\text{int}} = \sum_{i=1}^{n} f_{ci} A_{ci} \bar{y}_i + \sum_{j=1}^{m} f_{tj} A_{tj} \bar{y}_j + \sum_{k=1}^{p} (f_{rk} - f_{ck}) A_{rk} \bar{y}_k \qquad (7.3)$$

The last term in equation 7.2 and equation 7.3 represents the strength contribution of the FRP-composite bars.

7.6.1 Stress-strain characteristics of FRP reinforcement

The FRP reinforcement is assumed to be linear-elastic to failure in both tension and compression. The elastic modulus of the FRP reinforcement is also assumed to be the same in both tension and compression [66]. The failure criterion for the FRP reinforcement is dependent on the type of fibre.

The experimental work on columns reinforced with carbon FRP bars found that for the range of column slenderness ratios tested, the failure was governed by compressive failure of the FRP bar. The mean empirically derived failure strain criterion of 4,900$\mu\varepsilon$ has been

adopted, based on the 95th percentile of the mean failure strain $5{,}629\mu\varepsilon \pm 434\mu\varepsilon$. This compressive failure strain is approximately 30% of the tensile value, which agrees with the findings of Kobayashi and Fujisaki [66].

The compressive failure strain criterion for E-glass FRP bars is assumed to be the same as the tensile failure strain, due to the triaxial confinement. Whilst larger compressive strains were observed in the experimental work, the potential loss of confinement due to rupture of the FRP-composite tube is a limiting criterion. Therefore, in the case of confined columns reinforced with E-glass FRP bars, the compressive failure strain criterion is assumed to be $22{,}200\mu\varepsilon$.

7.7 COMPARISON BETWEEN THEORETICAL AND EXPERIMENTAL RESULTS

The comparison between the predicted failure loads from CONFINE and the experimental results are given in Table 7.4. Good agreement is obtained between the theoretical and experimental failure loads for both carbon- and E-glass FRP longitudinal reinforcement, with correlation coefficients of 0.96 for carbon and 0.98 for E-glass FRP bars. Comparisons of the experimental and theoretical failure loads for carbon- and E-glass reinforcement are shown in Figure 7.11 and Figure 7.12 respectively.

Comparison of the predicted ultimate moment capacity of the columns also gives good agreement with experimental data. The comparisons of the experimental and theoretical ultimate moments for carbon- and E-glass reinforcement are shown in Figure 7.13 and Figure 7.14 respectively.

7.7.1 Load response

Comparisons of the theoretical and experimental load-deflection, moment-curvature and load-strain curves are given in Figures 7.15(a-d), Figures 7.16(a-d) and Figures 7.17(a-d) respectively. Good agreement is achieved in all the columns for the entire load history of the column to failure, irrespective of the type and percentage of longitudinal reinforcement, winding angle of the confining fibres or the column slenderness.

7.7.2 Limiting concrete compressive strain criterion

The experimental loads and deflections for the columns at $3{,}500\mu\varepsilon$ are tabulated in Table 7.5. Comparison of the experimental and predicted loads at the limiting compressive strain for columns reinforced with carbon and E-glass FRP bars are given in Figure 7.18 and Figure 7.19 respectively. The mean value of the N_{exp}/N_T ratios for all the columns with

additional longitudinal reinforcement was 0.93. The N_{exp}/N_T ratios have been calculated by setting the partial safety factors for the concrete and FRP-composite to unity. In design, the appropriate safety factors of 1.5 for concrete and 1.8 for the modulus of elasticity of the FRP-composite [76] would be used.

7.8 COMPARISON WITH CONVENTIONAL REINFORCED CONCRETE COLUMNS

To compare the performance of concrete-filled FRP-composite tubes reinforced longitudinally with FRP-composite bars to conventional reinforced concrete columns with an eccentricity of $0.05D$, the experimental failure strengths are plotted on *N-M* interaction diagrams for *L/D* equals 5 and *L/D* equals 10 in Figure 7.20 and Figure 7.21 respectively. The failure envelopes for conventional reinforced concrete columns with unit partial factors of safety are given for increasing percentages of high tensile steel reinforcement. All the columns with additional longitudinal FRP reinforcement exhibited ultimate failure strengths greater than the capacity of a conventional reinforced concrete column with 6 percent longitudinal reinforcement.

The comparisons of the load capacities at $3{,}500\mu\varepsilon$ compressive strain for *L/D* equals 5 and *L/D* equals 10 are given in Figure 7.22 and Figure 7.23 respectively. At the limiting strain, the hybrid system of longitudinal carbon fibres with E-glass confining fibres resulted in the largest enhancements in strength compared to the E-glass confinement systems. At the limiting strain criterion, columns reinforced with carbon FRP bars all exhibited axial load capacities greater than the axial load capacity of an equivalent conventional steel reinforced concrete column, as shown in Figure 7.24. However, the lower modulus of elasticity of the E-glass bars resulted in lower axial loads being achieved than the axial load capacity of an equivalent conventional steel reinforced concrete column, as shown in Figure 7.25

7.9 SUMMARY

The behaviour of concrete-filled FRP-composite columns with additional longitudinal FRP-reinforcement is dependent on the type of longitudinal FRP fibre. The use of high-modulus carbon FRP bars results in an increase in the initial stiffness of the columns and hence lower deflections at serviceability loads. However, the carbon FRP bars have a low compressive failure strain of $4{,}900\mu\varepsilon$ that prevents the full benefits of triaxial confinement being utilised. Therefore, the ultimate failure load of the column is reduced by the

inclusion of carbon FRP reinforcement. For the range of column slenderness ratios investigated, the ultimate failure load of the column was governed by the material failure of the carbon FRP reinforcement.

The lower modulus E-glass FRP bars do not increase the initial stiffness of the columns, but do increase the post-crushing stiffness and ultimate load capacity of the column. The magnitudes of the increases in the post-crushing column stiffness and load capacity are proportional to the percentage of longitudinal reinforcement. The E-glass FRP reinforcement was also able to sustain greater compressive strains than the carbon FRP bars. Under triaxial compressive loads, the compressive failure strain of the E-glass reinforcement was found to be comparable to or greater than the tensile failure strain.

The use of E-glass FRP bars reduces the deflections of the columns at serviceability loads. However, the axial load capacity of the columns is also lower than conventional reinforced columns with an identical amount of longitudinal steel reinforcement. At the limiting strain criterion, the hybrid reinforcing system of longitudinal carbon fibres and E-glass confining fibres results in an enhanced serviceability load capacity compared to conventional reinforced concrete columns, although there is a reduction in the ultimate load capacity and ductility of these columns.

The ultimate load capacity of the longitudinally reinforced confined columns is predictable using the CONFINE algorithm with considerable accuracy. The CONFINE algorithm also gives good agreement for the entire load history of the columns, accounting for differences in the diameter, winding angle of the confining FRP-composite and the type and percentage of longitudinal FRP reinforcement.

Properties of FRP tube		Properties of longitudinal reinforcement	
Diameter mm	**Angle of wind °**	**Fibre type**	**$100A_f/A_c$**
80	78.1	E-Glass	6.00
	78.1	Carbon	6.00
	57.8		
	43.4		
100	80.4	E-Glass	3.84
	80.4	Carbon	3.84
	71.4		
	49.9		
150	83.6	Carbon	1.71
	83.6	E-Glass	1.71
	83.6	E-Glass	5.94
	71.3		
	48.0		

Table 7.1. Experimental parameters for FRP-confined concrete columns with additional longitudinal reinforcement

Properties of FRP tube		Properties of longitudinal reinforcement		L/D	Failure Mode
Diameter mm	Angle of wind °	Fibre type	$100A_f/A_c$		
80	78.1	E-Glass	6.00	5	Material
				10	Stability
	78.1	Carbon	6.00	5	Material
				10	Material
	57.8	Carbon	6.00	5	Material
				10	Material
	43.4	Carbon	6.00	5	Material
				10	Material
100	80.4	E-Glass	3.84	5	Material
				10	Stability
	80.4	Carbon	3.84	5	Material
				10	Material
	71.4	Carbon	3.84	5	Material
				10	Material
	49.9	Carbon	3.84	5	Material
				10	Material
150	83.6	Carbon	1.71	5	Material
				10	Material
	83.6	E-Glass	1.71	5	Material
				10	Stability
	83.6	E-Glass	5.94	5	Material
				10	Stability
	71.3	E-Glass	5.94	5	Material
				10	Stability
	48.0	E-Glass	5.94	5	Material
				10	Stability

Table 7.2. Summary of failure mode, for FRP-confined concrete columns with additional longitudinal reinforcement

D	Longitudinal Reinforcement		Angle of wind	Effective Length	f_{cu}	N_u	δ_u	Strain
mm	Fibre	%	°	mm	N/mm^2	kN	mm	$\mu\varepsilon$
80	Carbon	6.00	78.1	464.2	28.3	318	0.39	5,700
				868.7	29.3	265	4.62	5,500
			57.8	469.0	28.3	272	0.56	5,800
				867.3	29.3	231	4.65	5,400
			43.8	468.7	28.3	261	0.89	5,200
				869.0	29.3	211	4.39	4,700
	E-glass	6.00	78.1	469.7	24.2	418	7.54	25,400
				870.1	24.2	211	18.77	15,300
100	Carbon	3.84	80.4	569.6	27.6	383	1.54	6,400
				1069.0	29.8	328	7.29	5,700
			71.4	569.9	27.6	322	1.44	5,700
				1069.3	29.8	270	5.65	5,200
			49.9	569.9	27.5	315	1.56	6,300
				1070.0	29.8	291	7.20	5,800
	E-glass	3.84	80.4	570.2	24.6	534	8.75	32,700
				1070.1	24.6	268	17.43	18,200
150	Carbon	1.71	83.6	870.0	27.7	626	2.65	5,800
				1620.0	27.7	447	13.05	5,600
	E-glass	1.71	83.6	870.0	32.4	923	14.93	26,300
				1620.0	32.4	442	20.14	9,200
	E-glass	5.94	83.6	870.2	27.3	1475	14.19	26,300
				870.0	42.8	1471	8.90	18,500
				1619.8	22.1	655	28.89	13,500
				1619.7	39.1	788	30.39	13,500
			71.3	870.0	29.2	1224	10.92	22,600
				870.1	37.5	1210	10.26	19,400
				1620.2	24.1	548	27.68	12,100
				1620.3	30.9	617	33.53	14,400
			48.0	870.2	28.8	856	10.16	19,900
				870.0	42.8	962	9.76	16,800
				1620.0	28.8	520	28.86	15,500
				1619.9	34.7	546	30.89	13,200

Table 7.3. Failure loads of eccentrically loaded FRP-confined concrete columns with additional longitudinal reinforcement

D	Longitudinal Reinforcement		Angle of wind	Effective Length	f_{cu}	N_u	$\frac{N_T}{N_u}$
mm	Fibre	%	°	mm	N/mm^2	kN	
80	Carbon	6.00	78.1	464.2	28.3	318	1.051
				868.7	29.3	265	1.077
			57.8	469.0	28.3	272	1.096
				867.3	29.3	231	1.114
			43.8	468.7	28.3	261	1.088
				869.0	29.3	211	1.178
	E-glass	6.00	78.1	469.7	24.2	418	1.049
				870.1	24.2	211	0.989
100	Carbon	3.84	80.4	569.6	27.6	383	1.056
				1069.0	29.8	328	1.072
			71.4	569.9	27.6	322	1.149
				1069.3	29.8	270	1.199
			49.9	569.9	27.5	315	1.042
				1070.0	29.8	291	1.016
	E-glass	3.84	80.4	570.2	24.6	534	1.016
				1070.1	24.6	268	1.000
150	Carbon	1.71	83.6	870.0	27.7	626	0.955
				1620.0	27.7	447	1.136
	E-glass	1.71	83.6	870.0	32.4	923	0.978
				1620.0	32.4	442	1.088
	E-glass	5.94	83.6	870.2	27.3	1475	0.875
				870.0	42.8	1471	0.989
				1619.8	22.1	655	0.921
				1619.7	39.1	788	0.894
			71.3	870.0	29.2	1224	0.956
				870.1	37.5	1210	1.039
				1620.2	24.1	548	1.010
				1620.3	30.9	617	0.968
			48.0	870.2	28.8	856	1.076
				870.0	42.8	962	1.053
				1620.0	28.8	520	0.955
				1619.9	34.7	546	0.968

Table 7.4. Comparison of experimental and predicted failure loads of eccentrically loaded FRP-confined concrete columns with additional longitudinal reinforcement

D	Longitudinal Reinforcement		Angle of wind	Effective Length	f_{cu}	N	δ
mm	Fibre	%	°	mm	N/mm^2	kN	mm
80	Carbon	6.00	78.1	464.2	28.3	229	0.21
				868.7	29.3	209	2.63
			57.8	469.0	28.3	184	0.34
				867.3	29.3	187	2.59
			43.8	468.7	28.3	203	0.74
				869.0	29.3	188	2.80
	E-glass	6.00	78.1	469.7	24.2	144	0.94
				870.1	24.2	124	2.87
100	Carbon	3.84	80.4	569.6	27.6	268	0.71
				1069.0	29.8	259	3.74
			71.4	569.9	27.6	245	0.57
				1069.3	29.8	228	3.42
			49.9	569.9	27.5	244	0.69
				1070.0	29.8	243	3.51
	E-glass	3.84	80.4	570.2	24.6	169	0.96
				1070.1	24.6	160	2.80
150	Carbon	1.71	83.6	870.0	27.7	503	1.44
				1620.0	27.7	399	7.03
	E-glass	1.71	83.6	870.0	32.4	460	1.53
				1620.0	32.4	338	6.00
	E-glass	5.94	83.6	870.2	27.3	503	1.38
				870.0	42.8	697	1.07
				1619.8	22.1	414	5.54
				1619.7	39.1	538	5.31
			71.3	870.0	29.2	482	1.56
				870.1	37.5	577	1.75
				1620.2	24.1	402	6.68
				1620.3	30.9	432	5.88
			48.0	870.2	28.8	393	1.72
				870.0	42.8	568	1.65
				1620.0	28.8	382	5.84
				1619.9	34.7	427	7.10

Table 7.5. Load capacities of eccentrically loaded FRP-confined concrete columns with additional longitudinal reinforcement at 3,500$\mu\varepsilon$ compressive strain

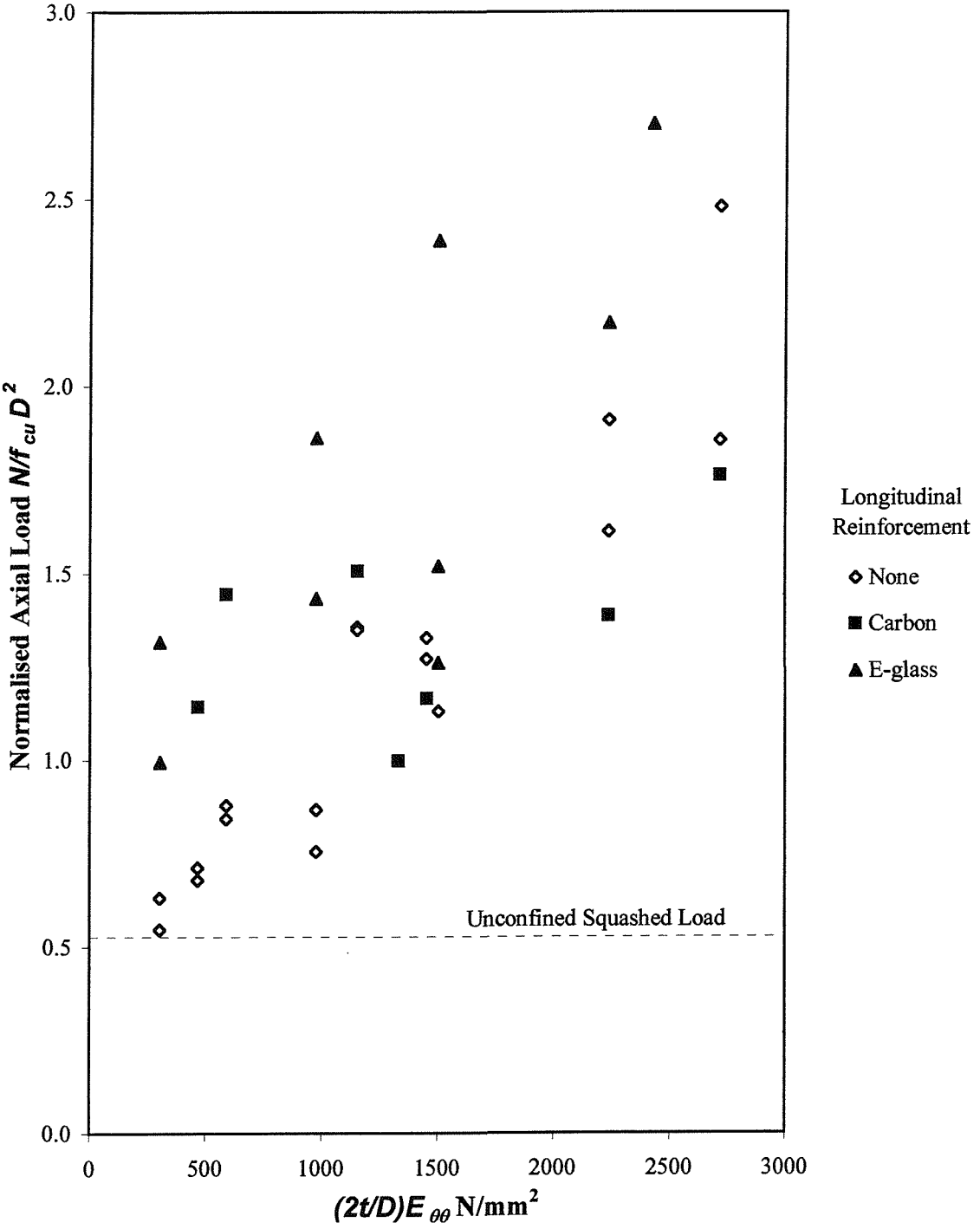

Figure 7.1. Normalised axial load capacity of concrete-filled E-glass FRP-composite columns with longitudinal FRP reinforcement (slenderness ratio = 5)

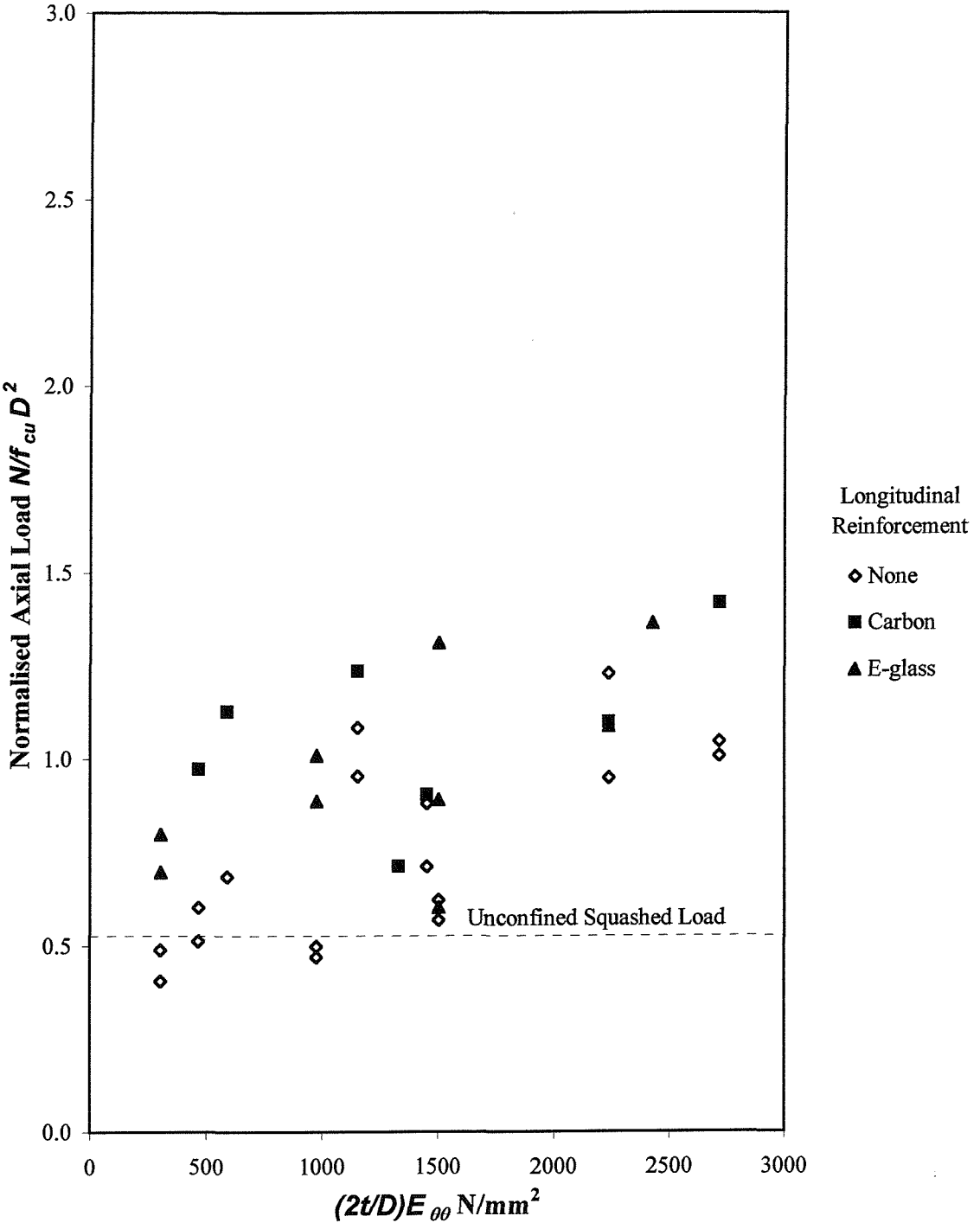

Figure 7.2. Normalised axial load capacity of concrete-filled E-glass FRP-composite columns with longitudinal FRP reinforcement (slenderness ratio = 10)

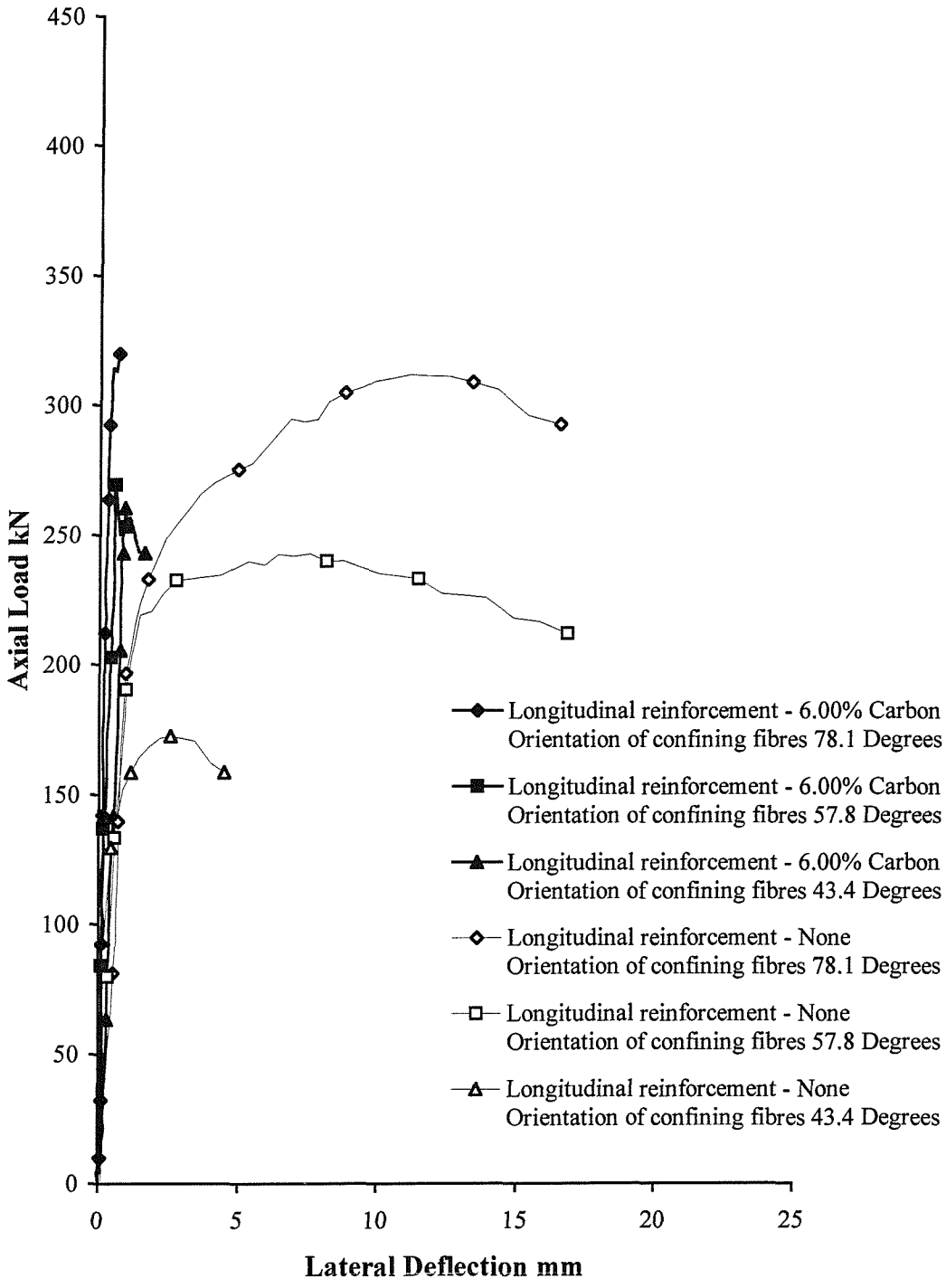

Figure 7.3(a). Load-deflection curves for the 80 mm diameter columns, with and without longitudinal carbon FRP reinforcement (slenderness ratio = 5)

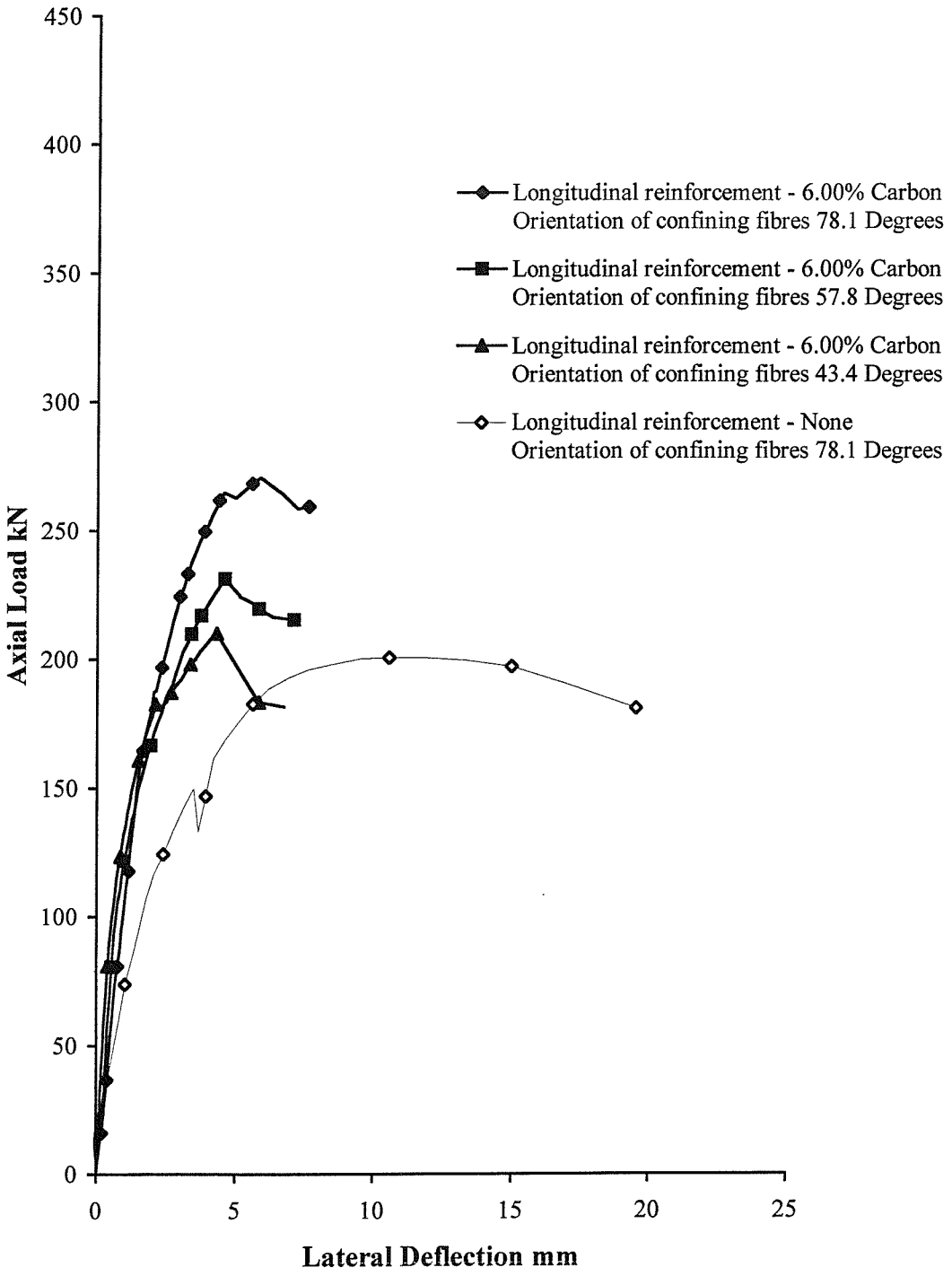

Figure 7.3(b). Load-deflection curves for the 80 mm diameter columns, with and without longitudinal carbon FRP reinforcement (slenderness ratio = 10)

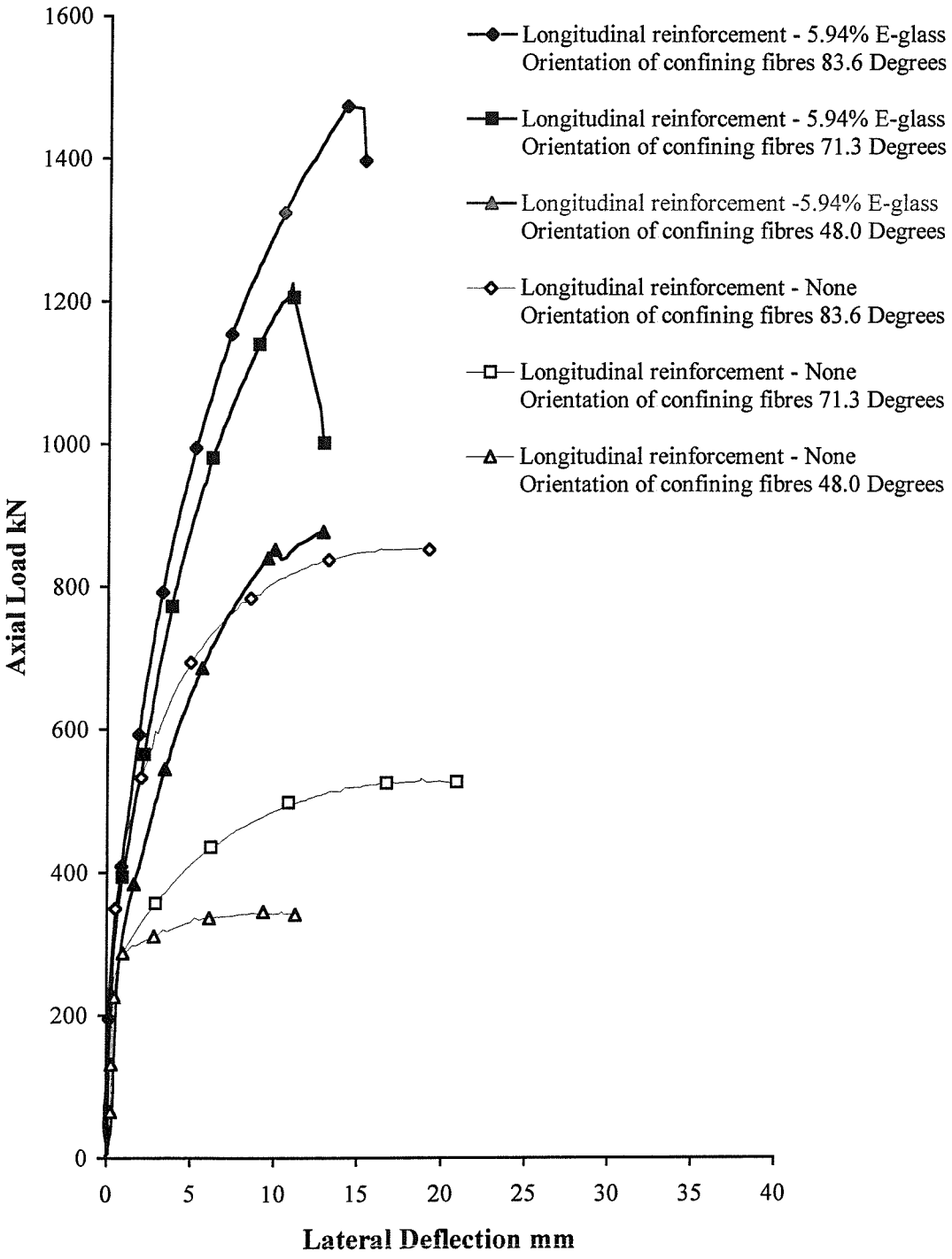

Figure 7.4(a). Load-deflection curves for the 150 mm diameter columns, with and without longitudinal E-glass FRP reinforcement (slenderness ratio = 5)

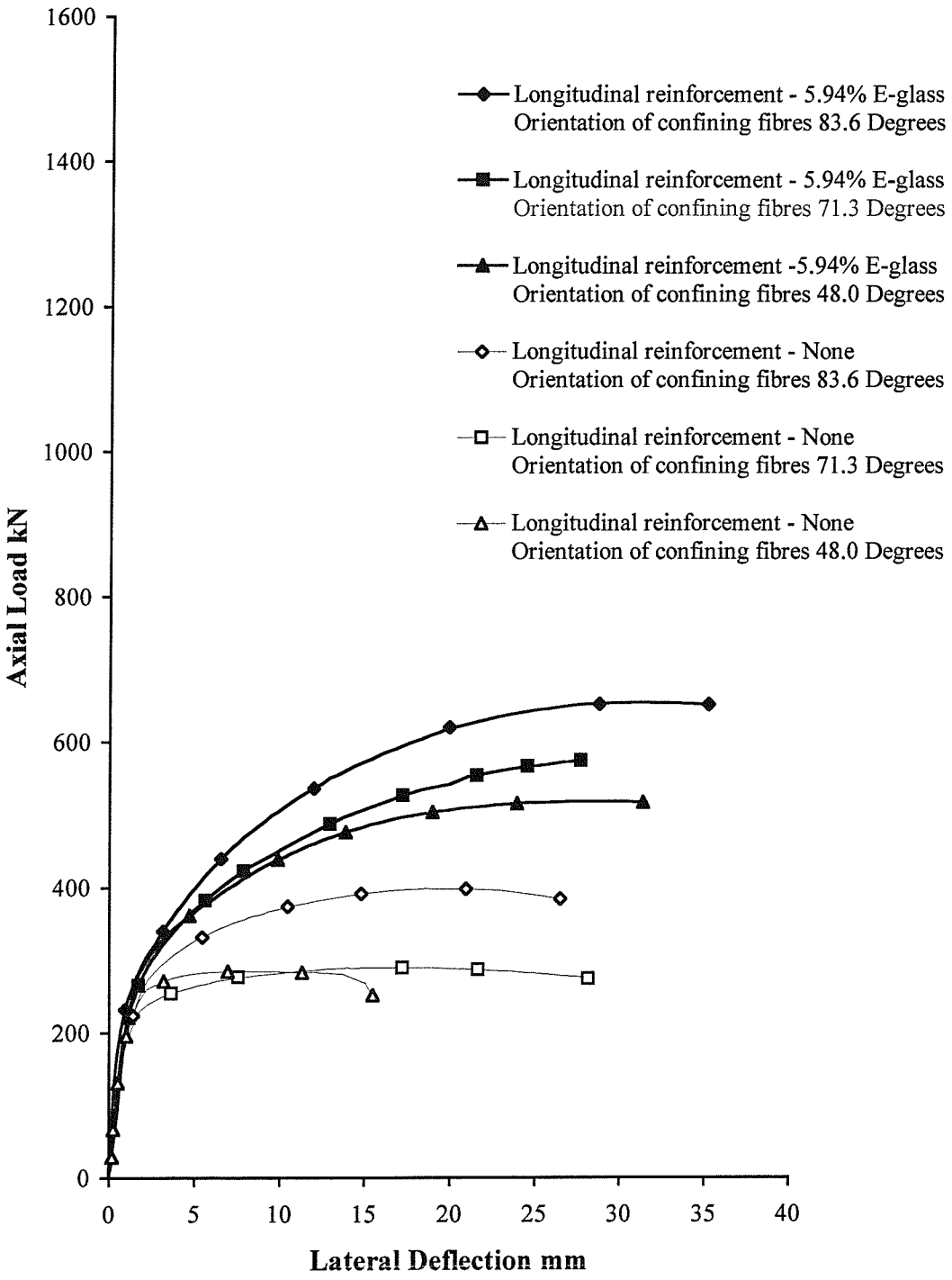

Figure 7.4(b). Load-deflection curves for the 150 mm diameter columns, with and without longitudinal E-glass FRP reinforcement (slenderness ratio = 10)

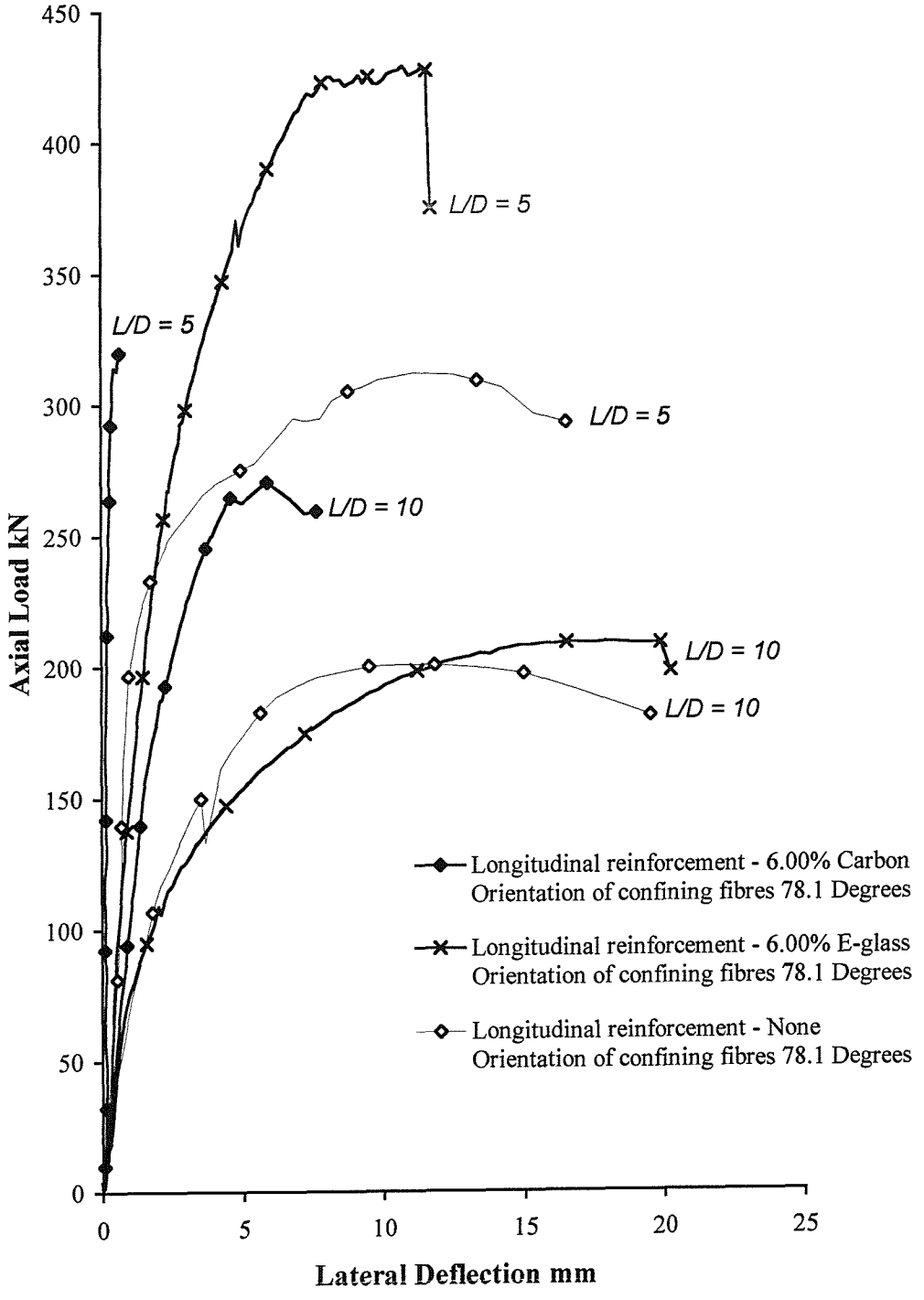

Figure 7.5. Comparison of the load-deflection behaviour of columns longitudinally reinforced with either carbon or E-glass FRP reinforcement

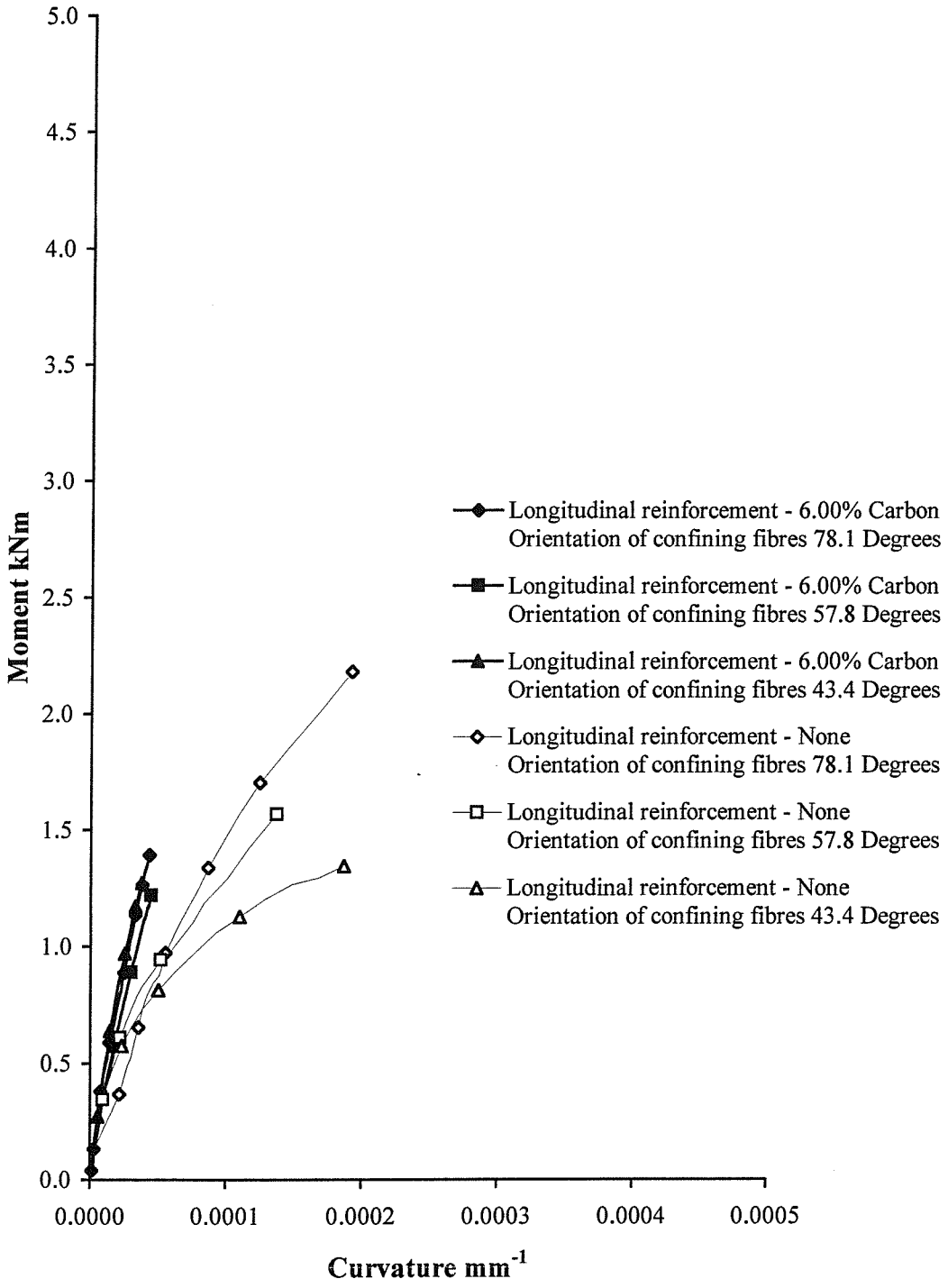

Figure 7.6(a). Moment-curvature relationships for the 80 mm diameter columns, with and without longitudinal carbon FRP reinforcement

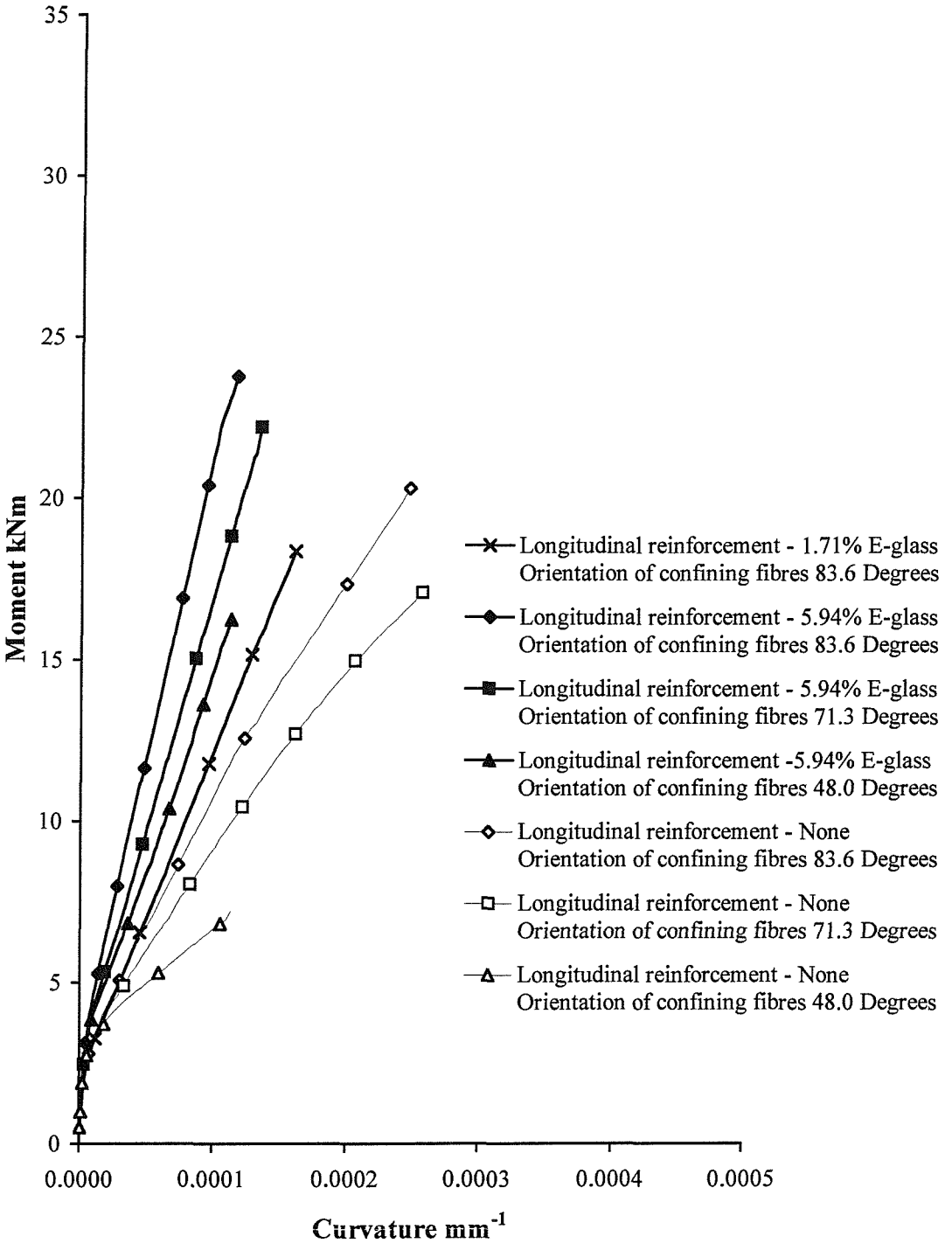

Figure 7.6(b). Moment-curvature relationships for the 150 mm diameter columns, with and without longitudinal E-glass FRP reinforcement

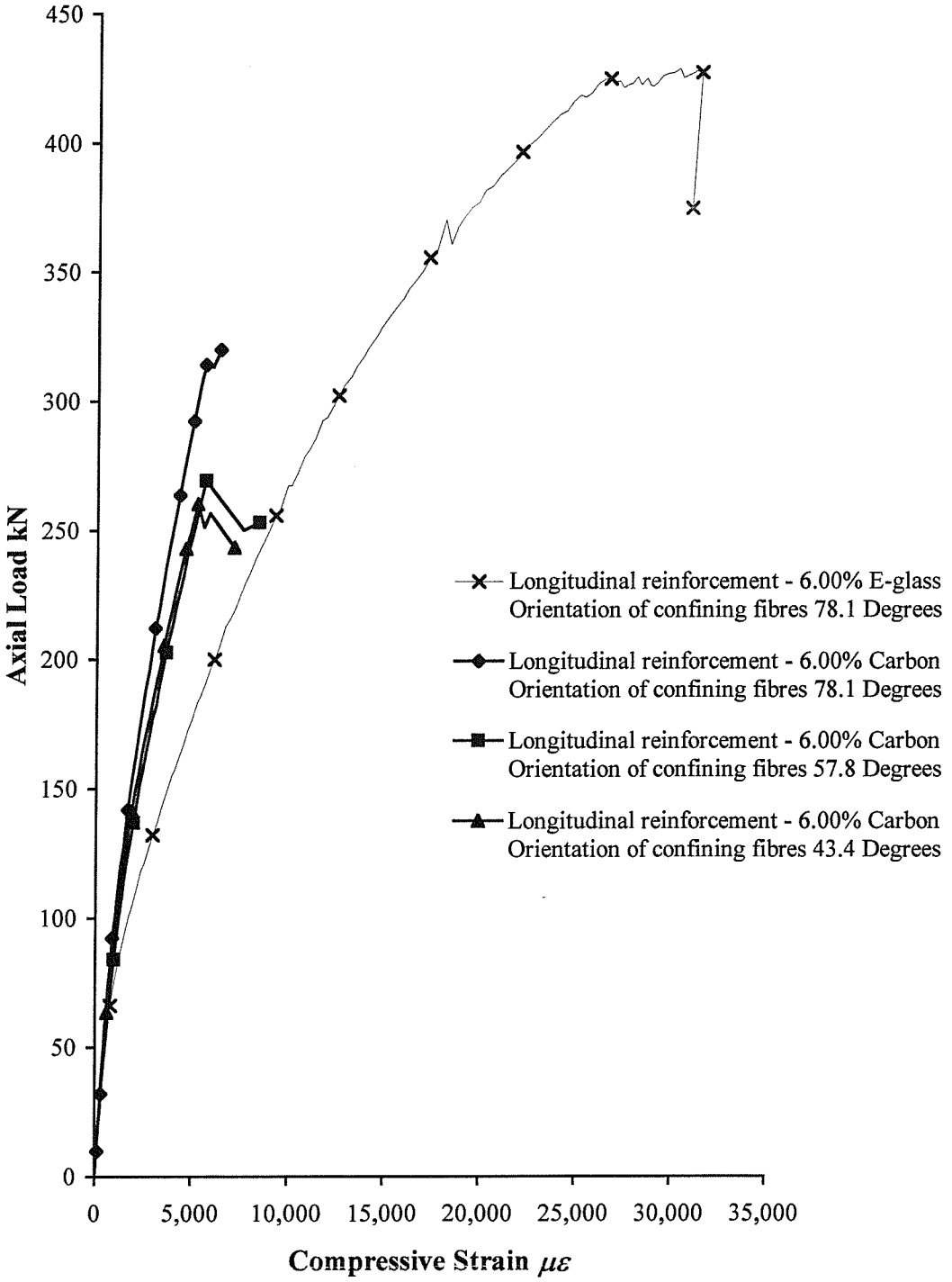

Figure 7.7(a). Comparison of the load-strain curves for the 80 mm diameter columns longitudinally reinforced with either carbon or E-glass FRP reinforcement

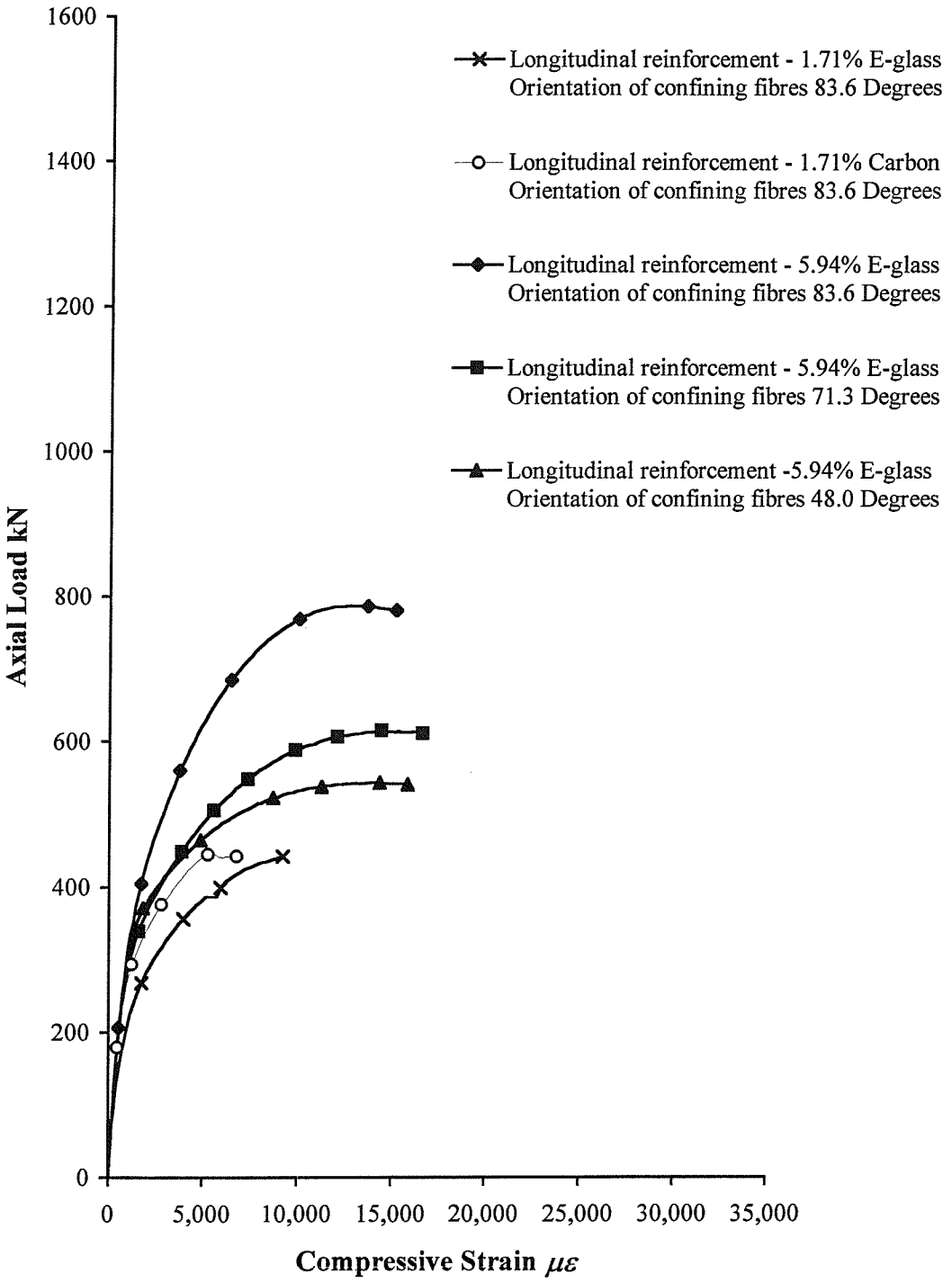

Figure 7.7(b). Comparison of the load-strain curves for the 150 mm diameter columns longitudinally reinforced with either carbon or E-glass FRP reinforcement

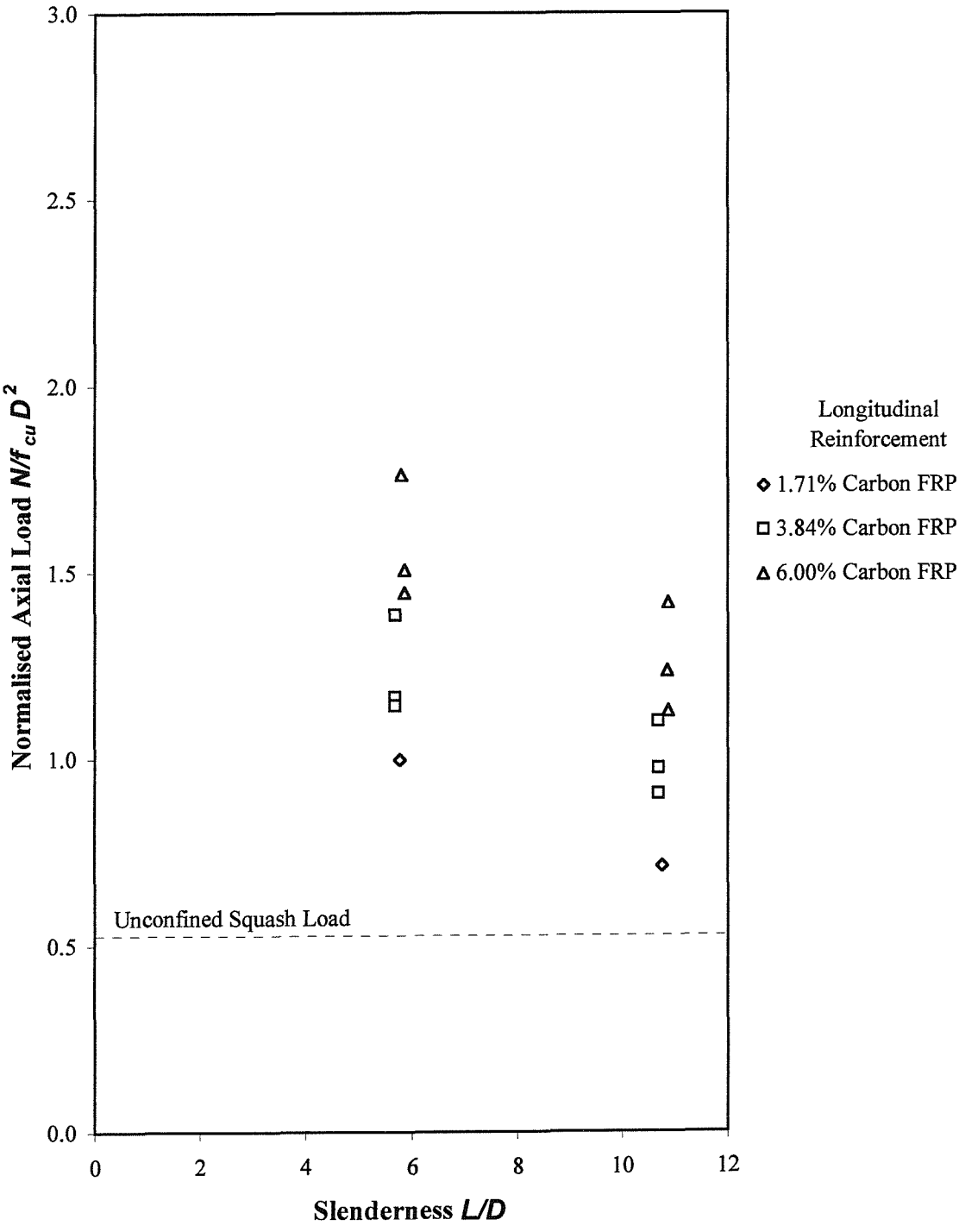

Figure 7.8. The influence of column slenderness on the axial load capacity of concrete-filled E-glass FRP composite columns reinforced longitudinally with carbon FRP reinforcement

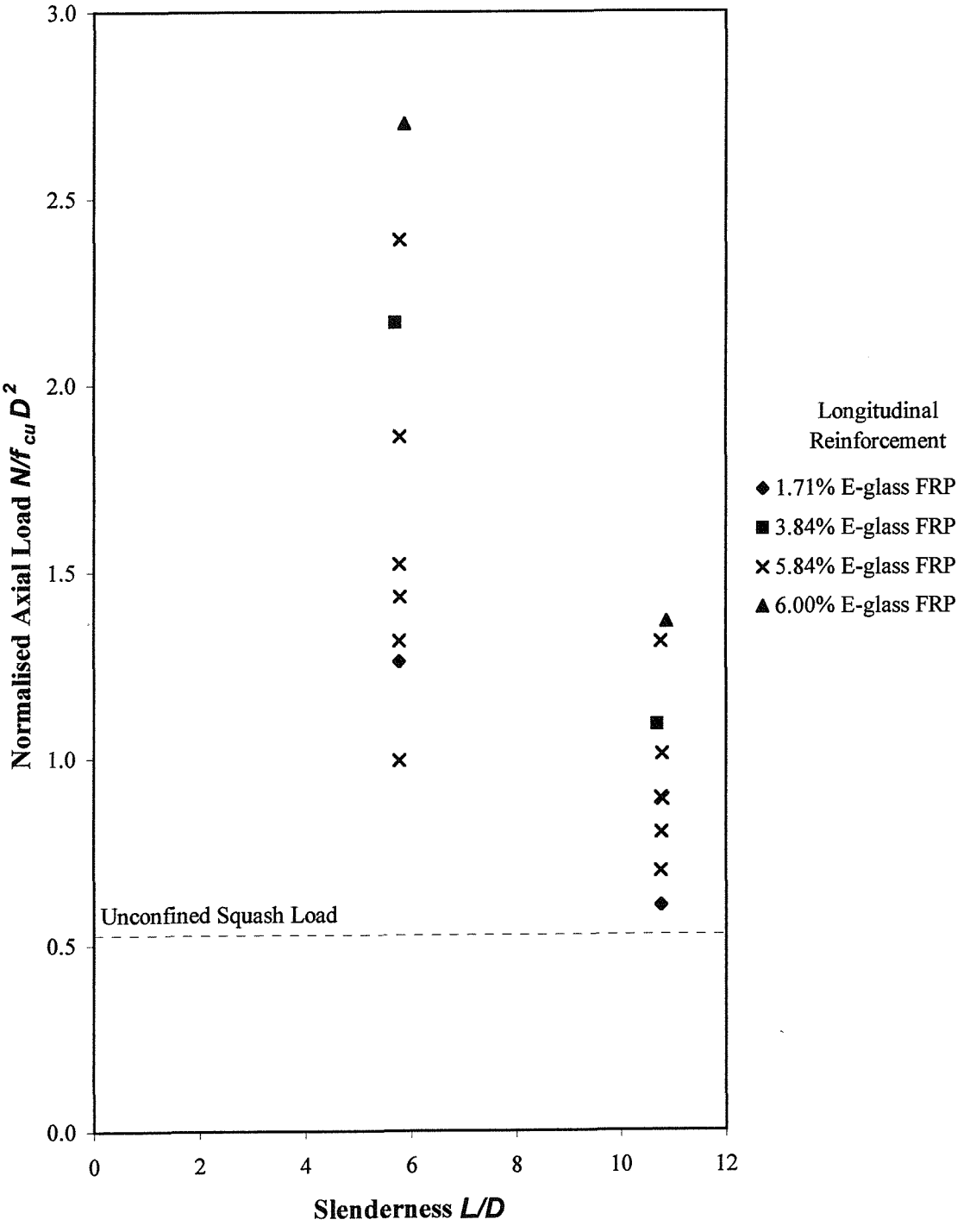

Figure 7.9. The influence of column slenderness on the axial load capacity of concrete-filled E-glass FRP composite columns reinforced longitudinally with E-glass FRP reinforcement

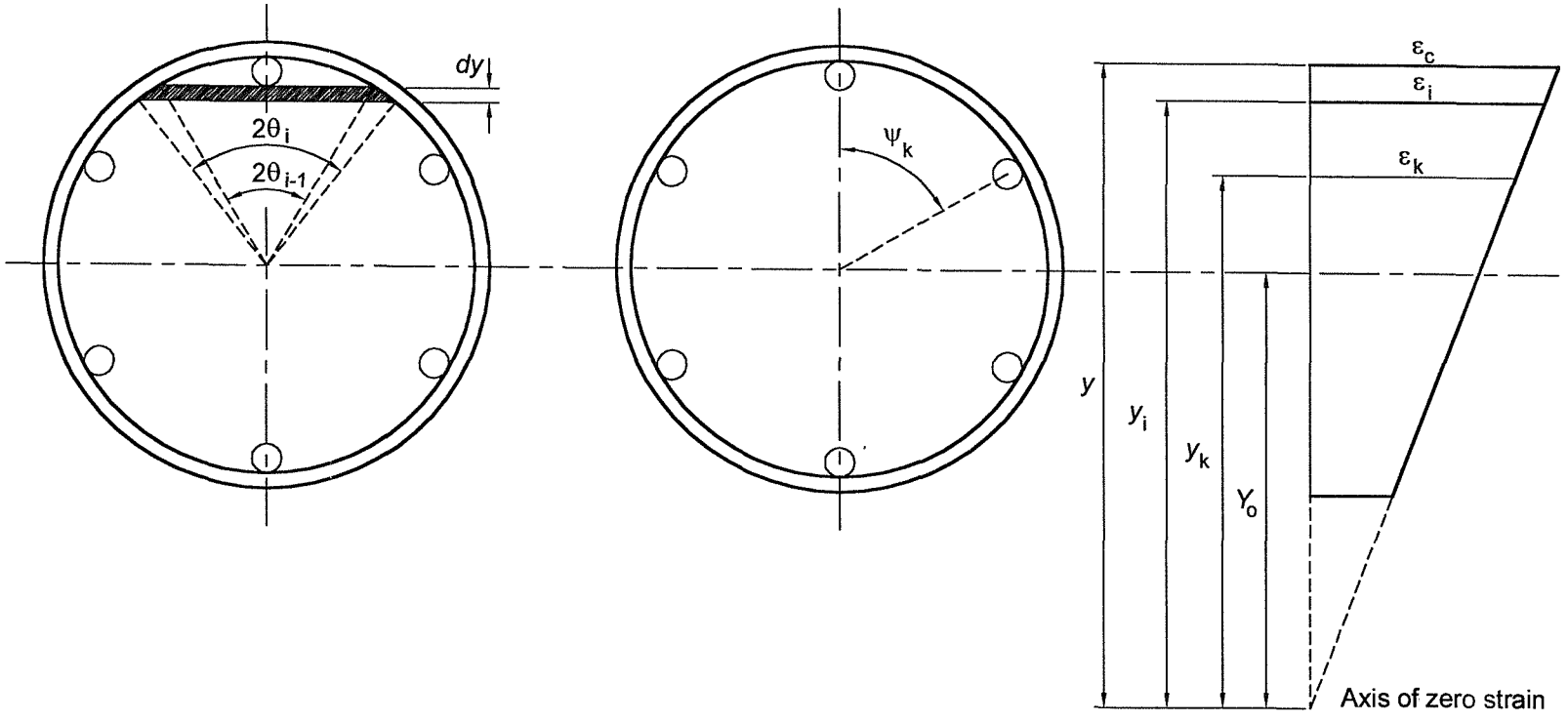

Figure 7.10. Idealised column cross-section and strain distribution in a longitudinally reinforced column

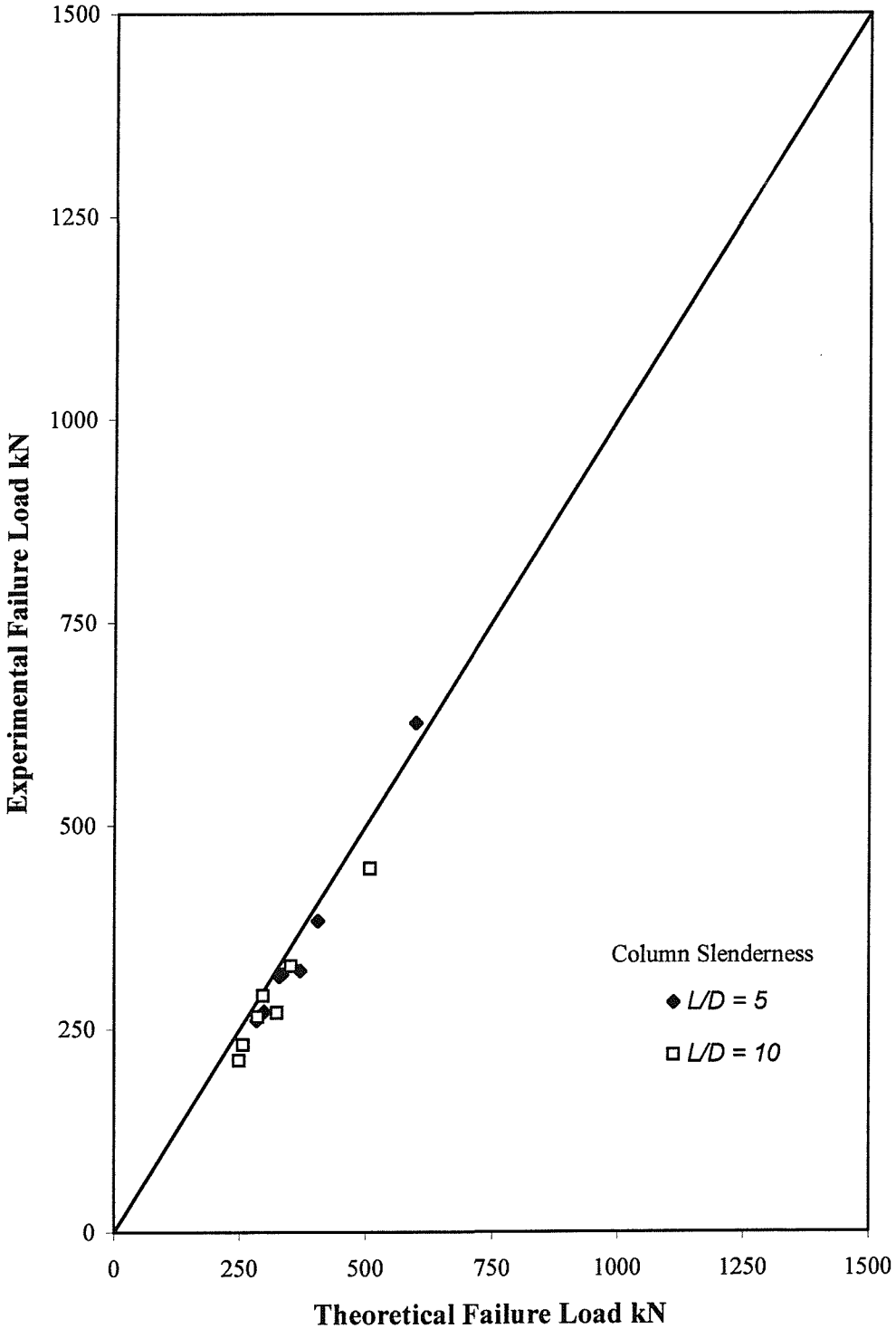

Figure 7.11. Comparison of the theoretical ultimate failure load of columns with longitudinal carbon FRP reinforcement with experimental results

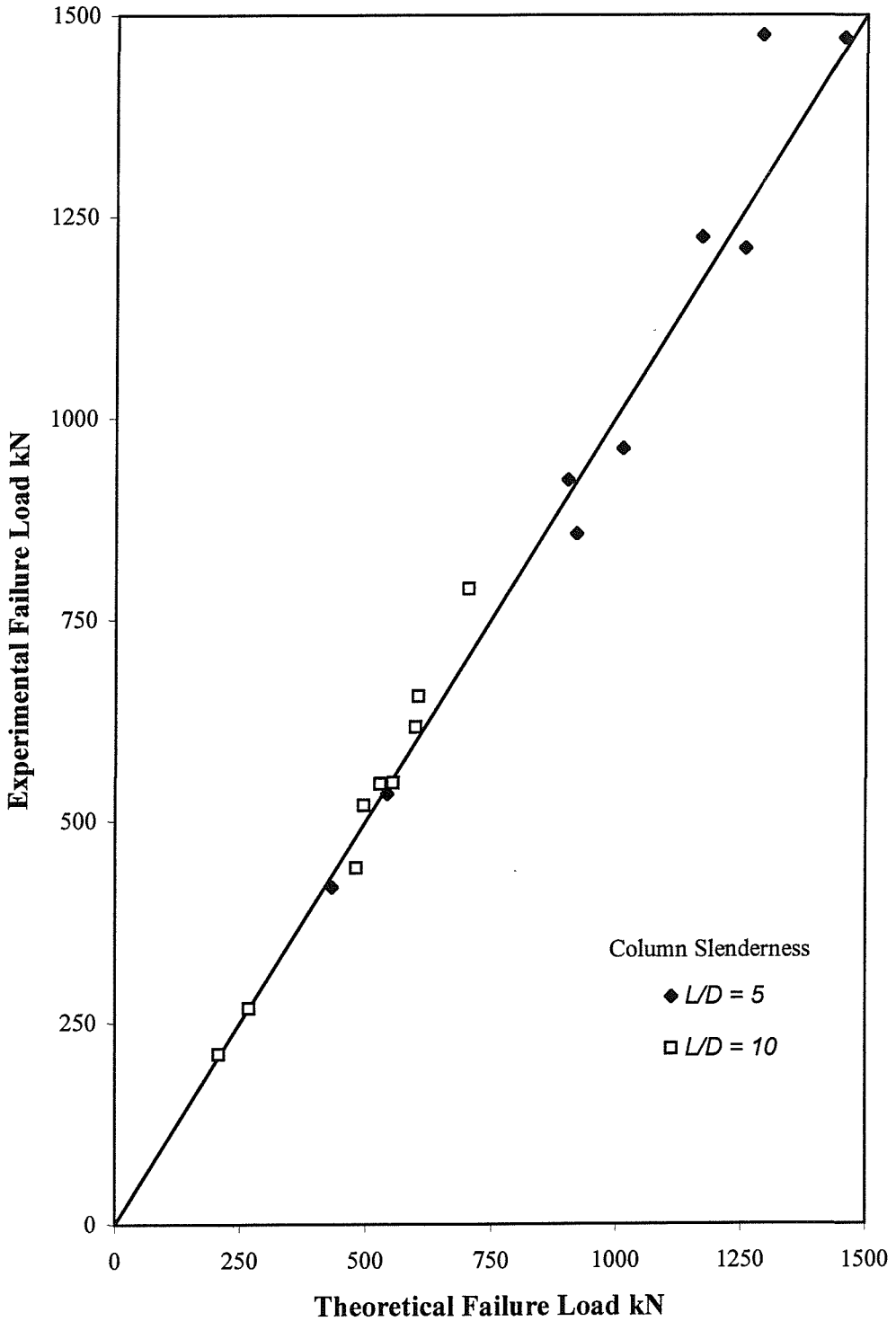

Figure 7.12. Comparison of the theoretical ultimate failure load of columns with longitudinal E-glass FRP reinforcement with experimental results

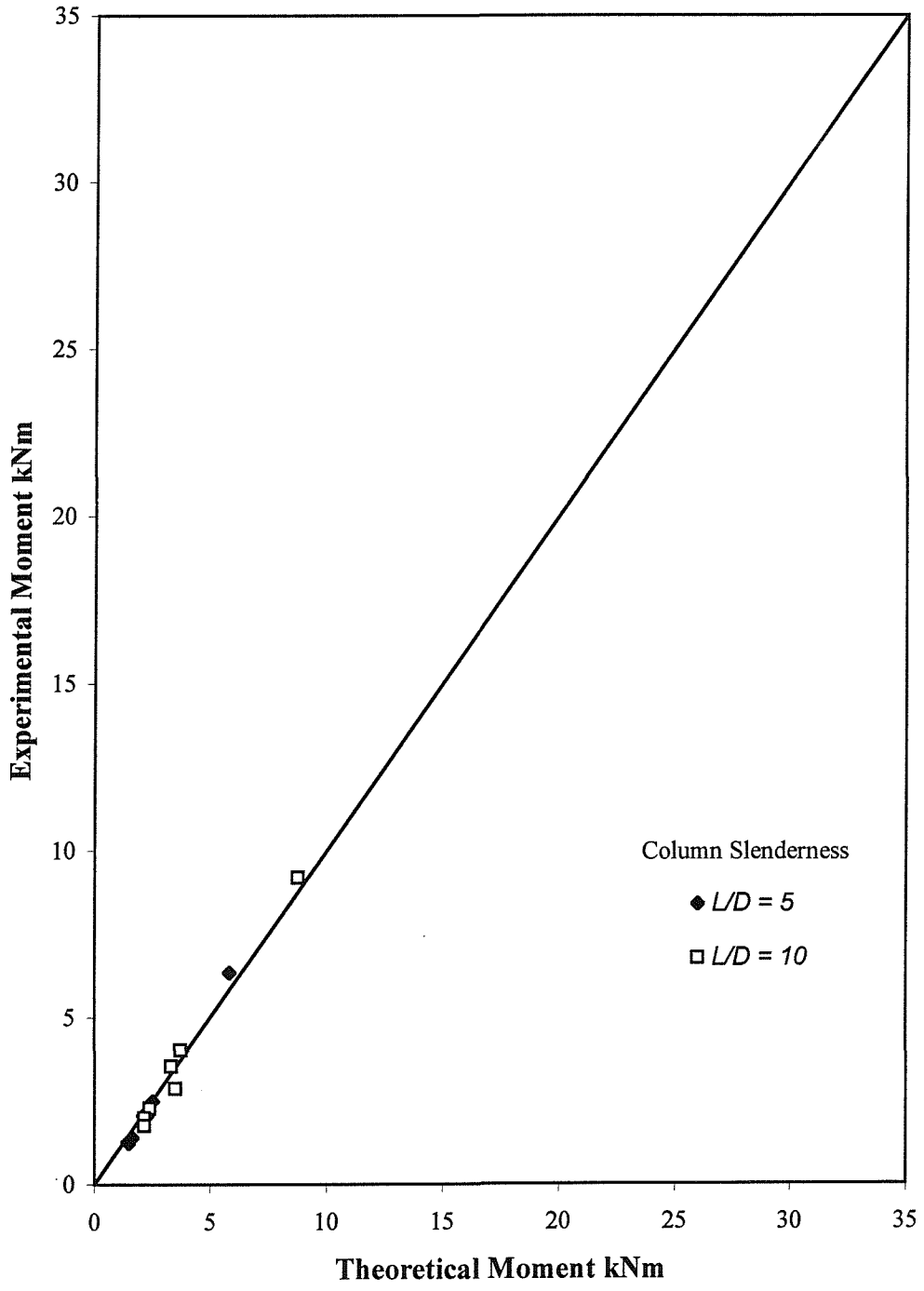

Figure 7.13. Comparison of the theoretical ultimate moment of columns with longitudinal carbon FRP reinforcement with experimental results

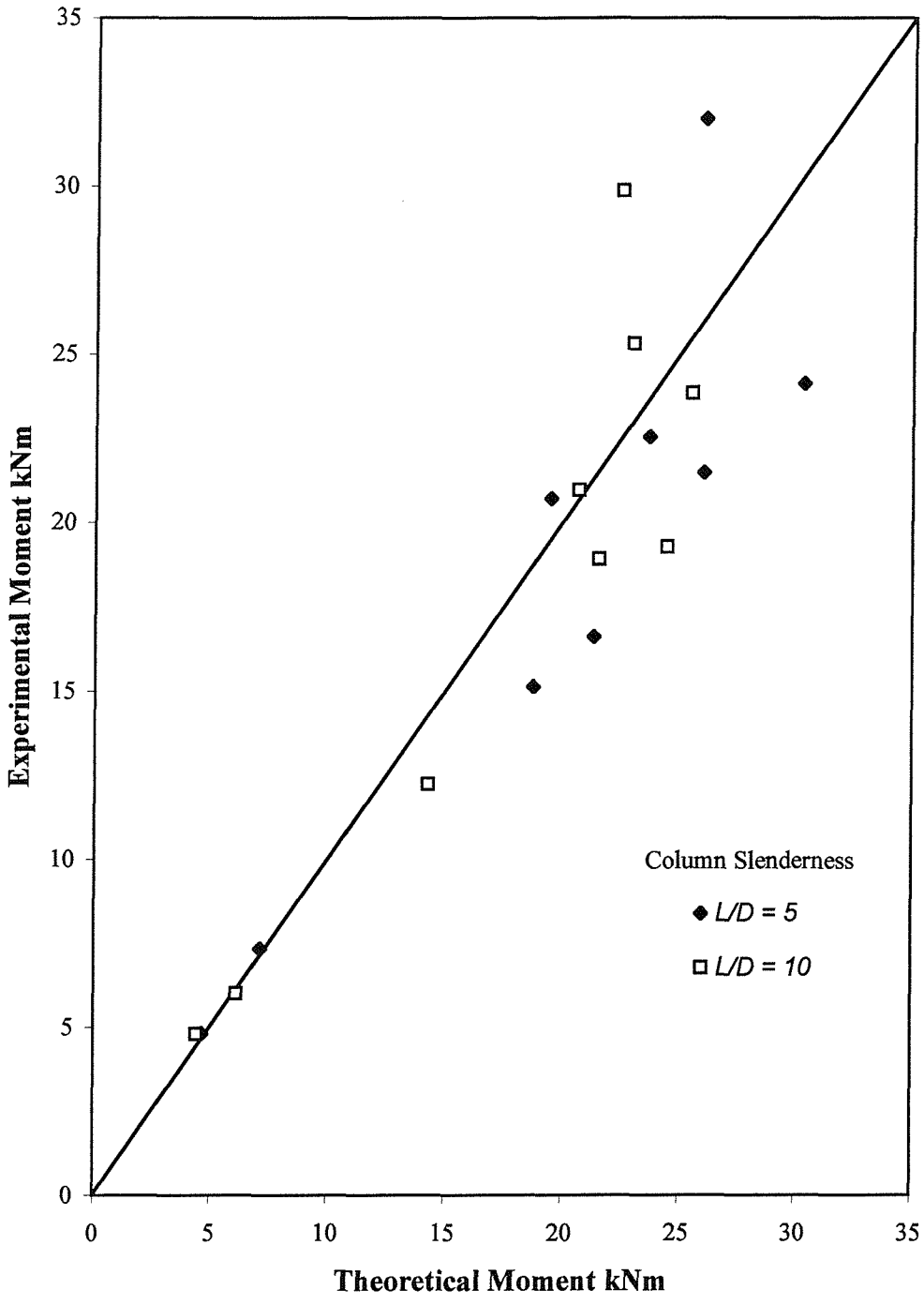

Figure 7.14. Comparison of the theoretical ultimate moment of columns with longitudinal E-glass FRP reinforcement with experimental results

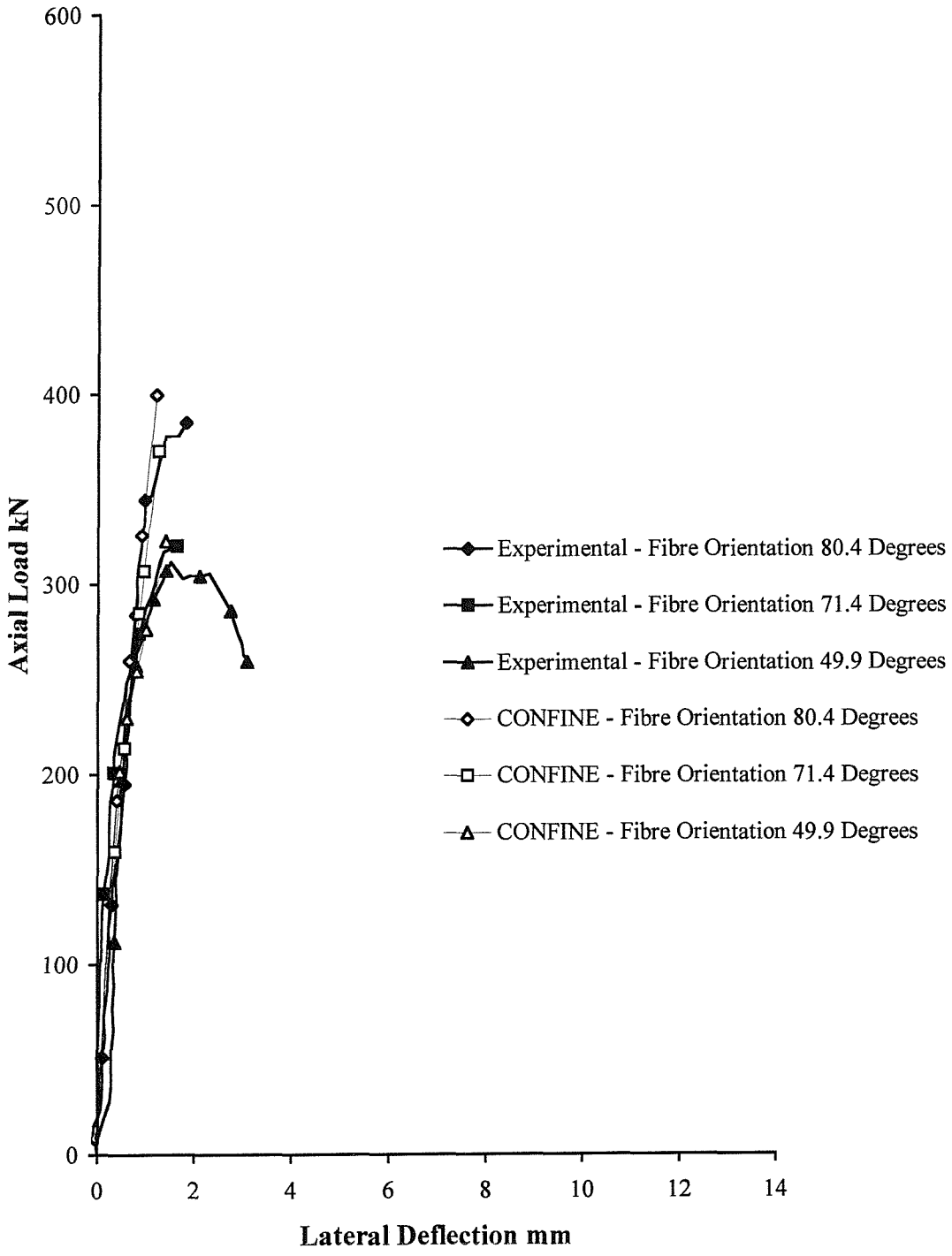

Figure 7.15(a). Comparison of the theoretical load-deflection curves with experimental results for the 100 mm diameter columns reinforced longitudinally with carbon FRP reinforcement (slenderness ratio = 5)

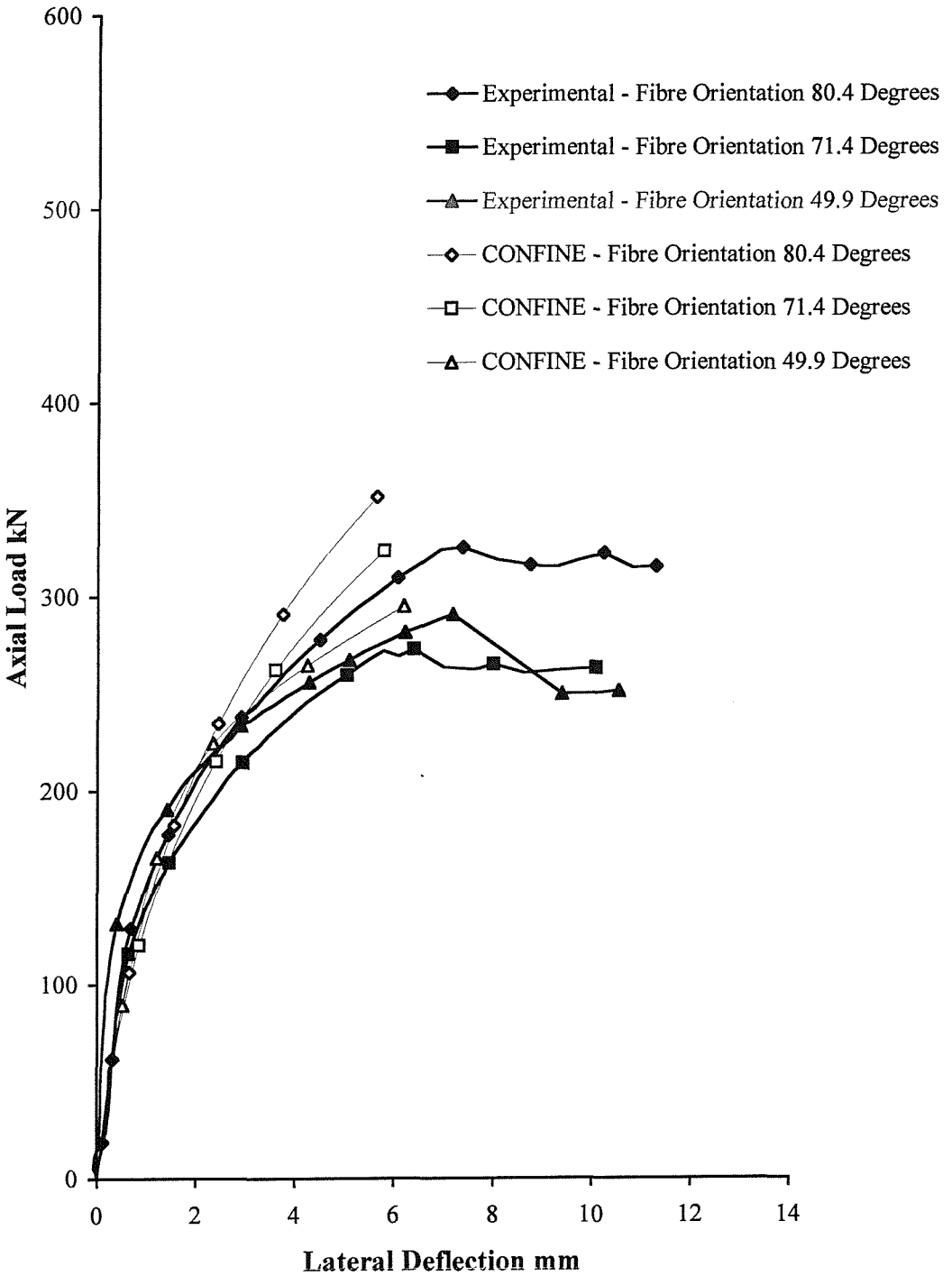

Figure 7.15(b). Comparison of the theoretical load-deflection curves with experimental results for the 100 mm diameter columns reinforced longitudinally with carbon FRP reinforcement (slenderness ratio = 10)

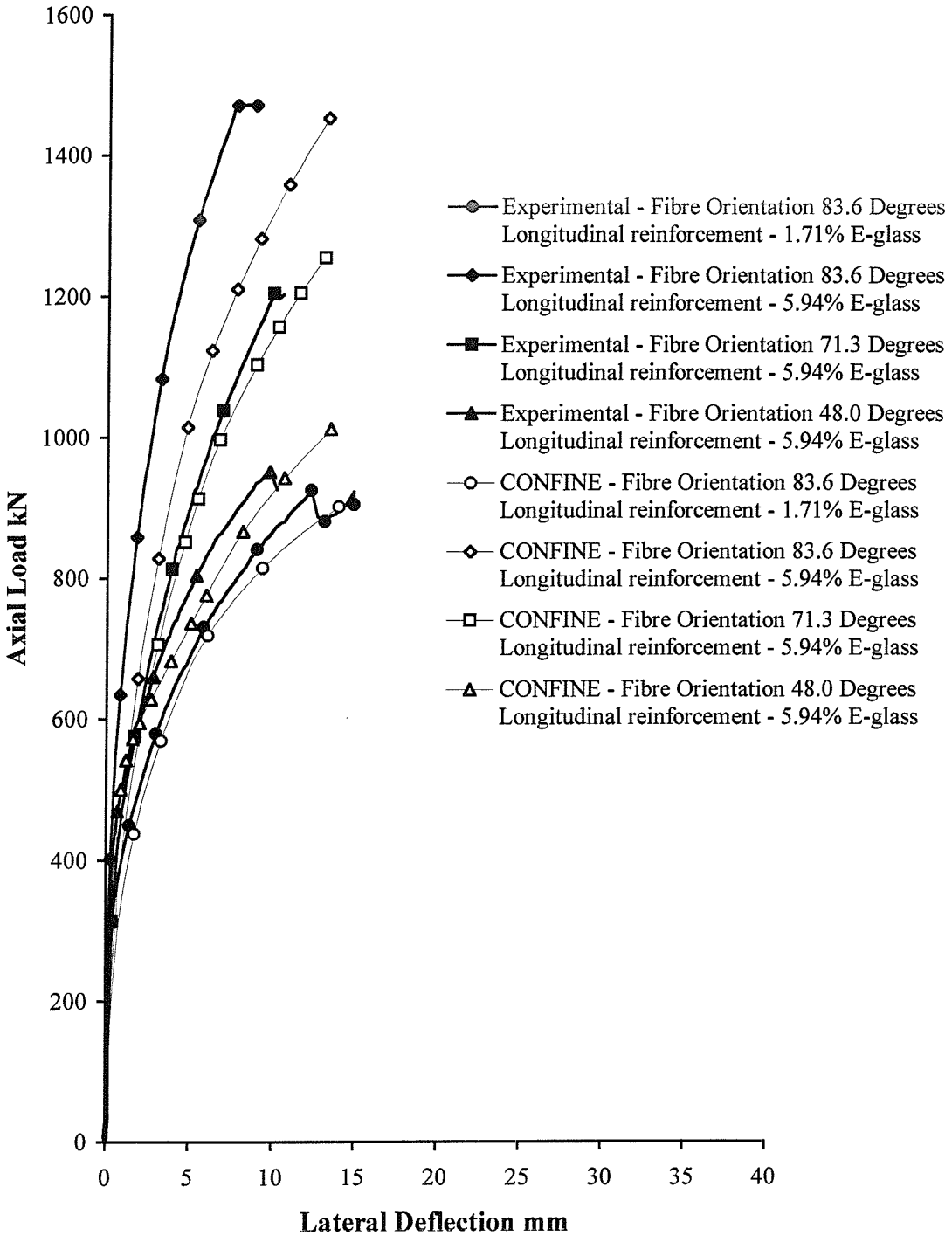

Figure 7.15(c). Comparison of the theoretical load-deflection curves with experimental results for the 150 mm diameter columns reinforced longitudinally with E-glass FRP reinforcement (slenderness ratio = 5)

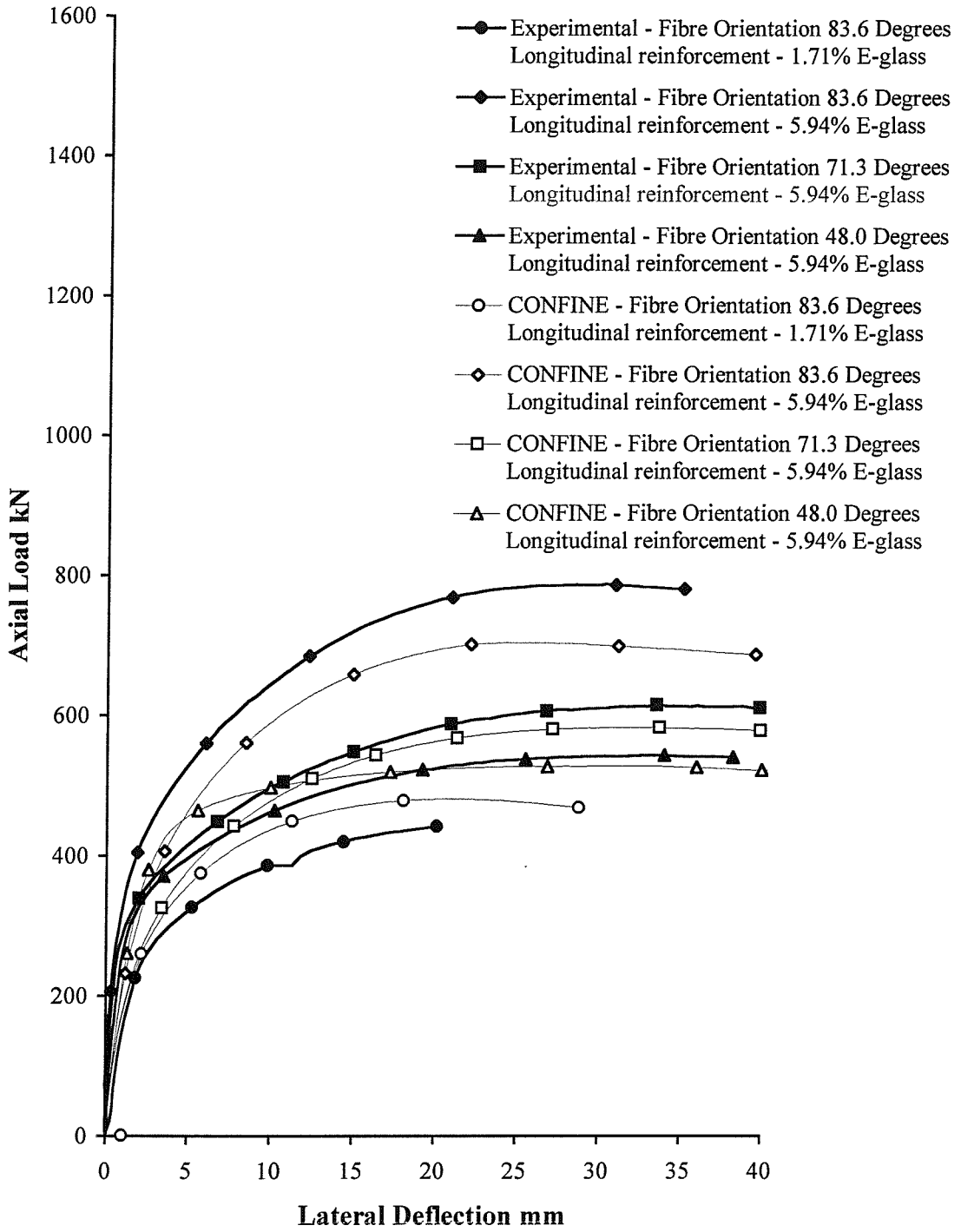

Figure 7.15(d). Comparison of the theoretical load-deflection curves with experimental results for the 150 mm diameter columns reinforced longitudinally with E-glass FRP reinforcement (slenderness ratio = 10)

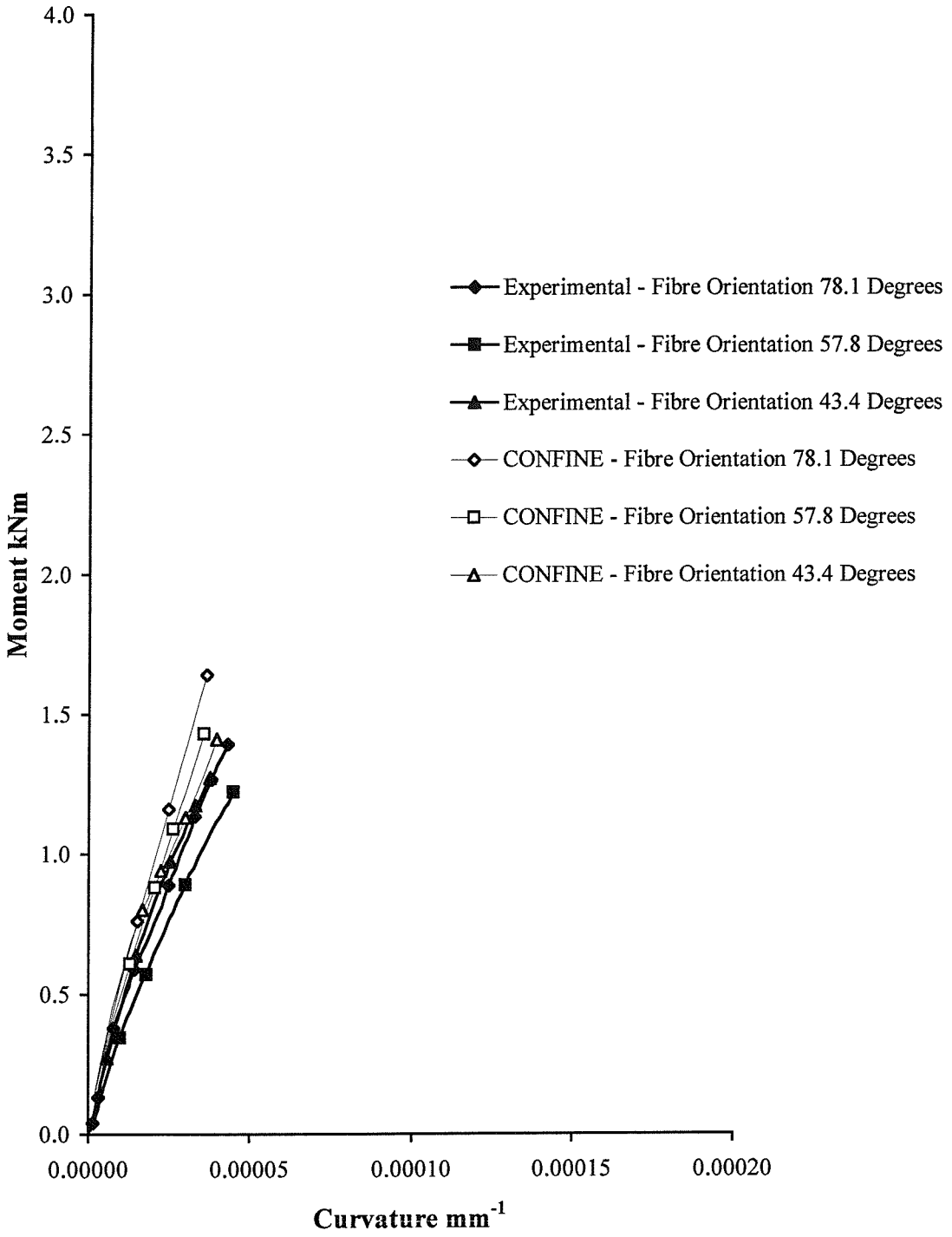

Figure 7.16(a). Comparison of the theoretical moment-curvature relationships with experimental results for the 80 mm diameter columns reinforced longitudinally with carbon FRP reinforcement (slenderness ratio = 5)

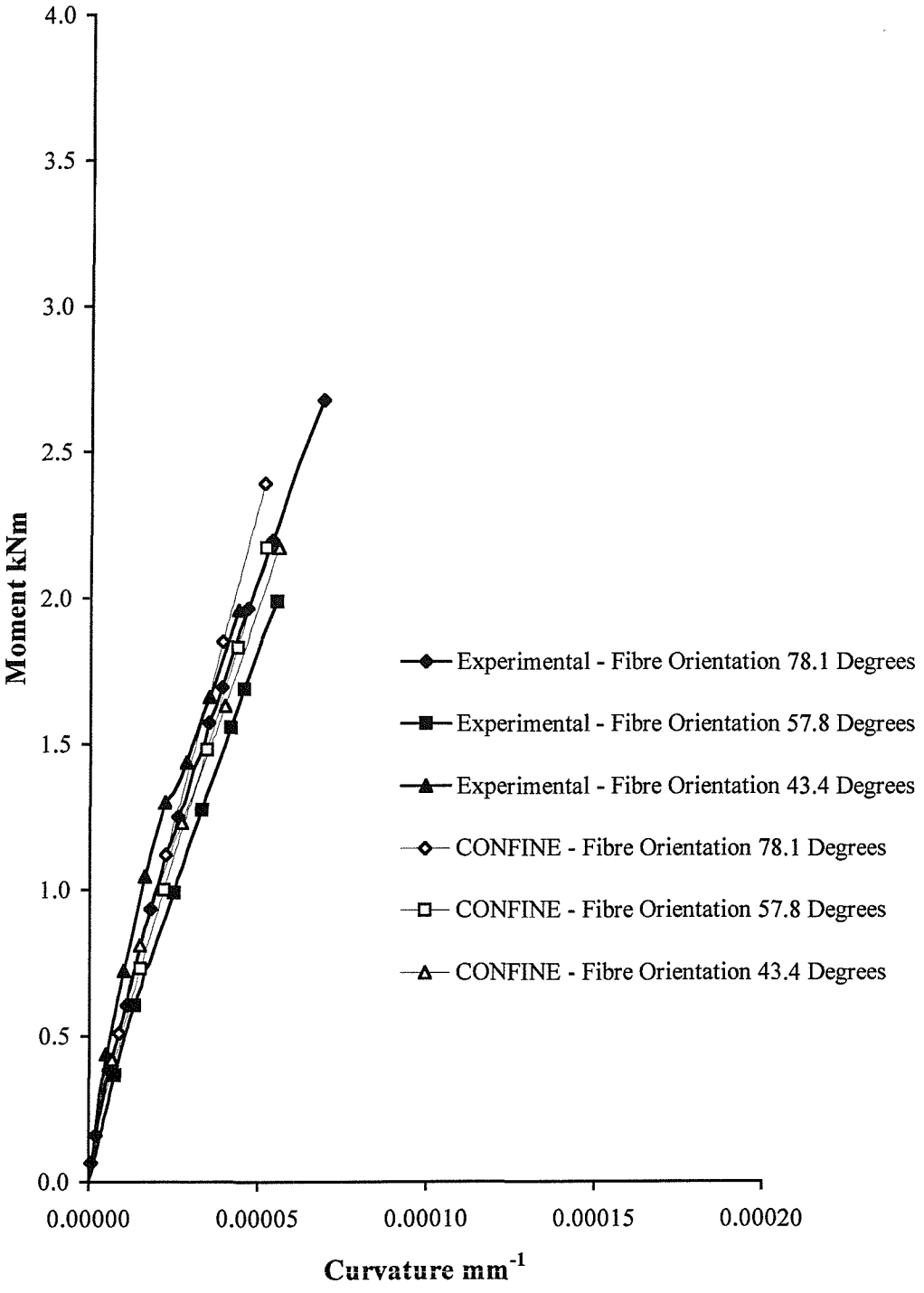

Figure 7.16(b). Comparison of the theoretical moment-curvature relationships with experimental results for the 80 mm diameter columns reinforced longitudinally with carbon FRP reinforcement (slenderness ratio = 10)

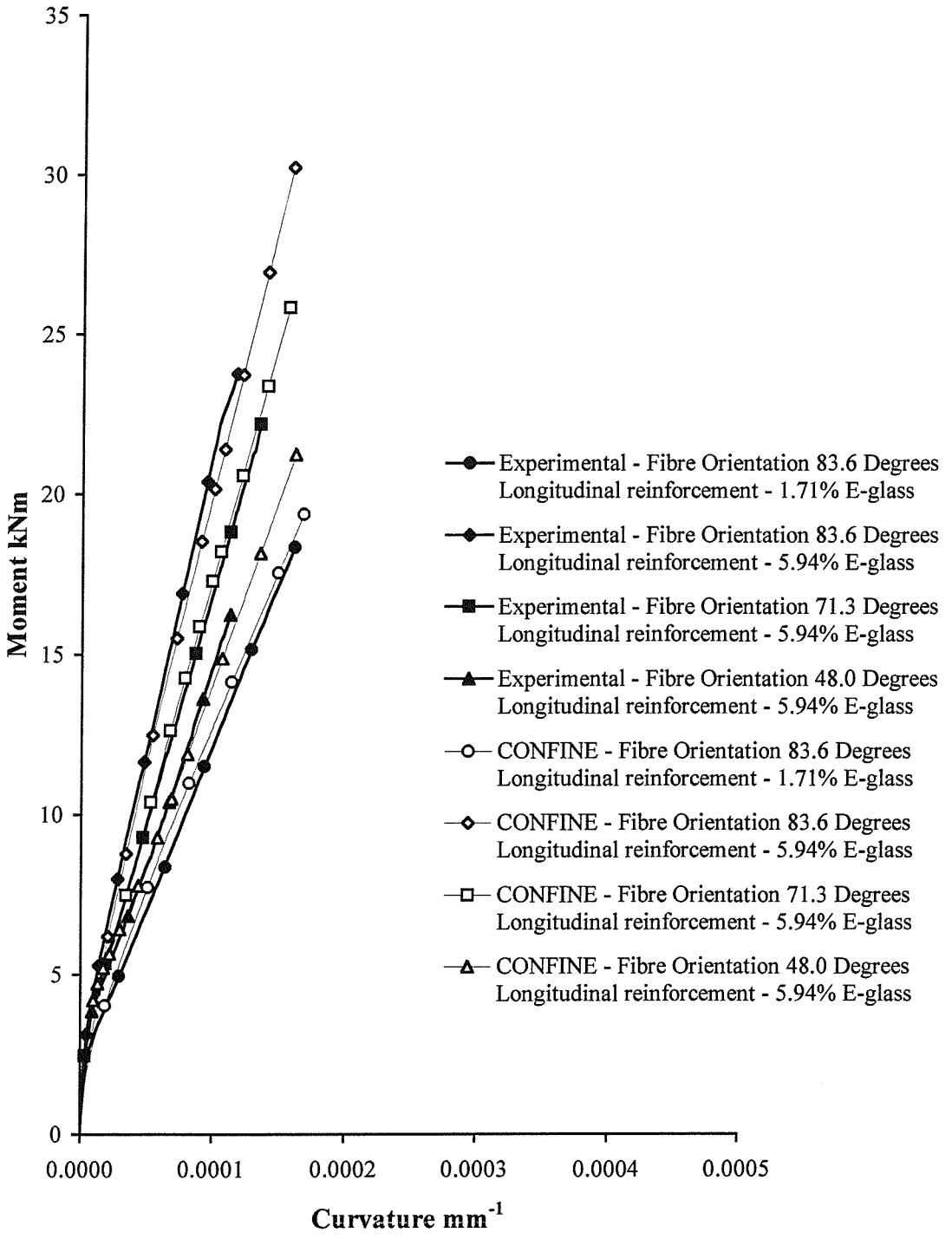

Figure 7.16(c). Comparison of the theoretical moment-curvature relationships with experimental results for the 150 mm diameter columns reinforced longitudinally with E-glass FRP reinforcement (slenderness ratio = 5)

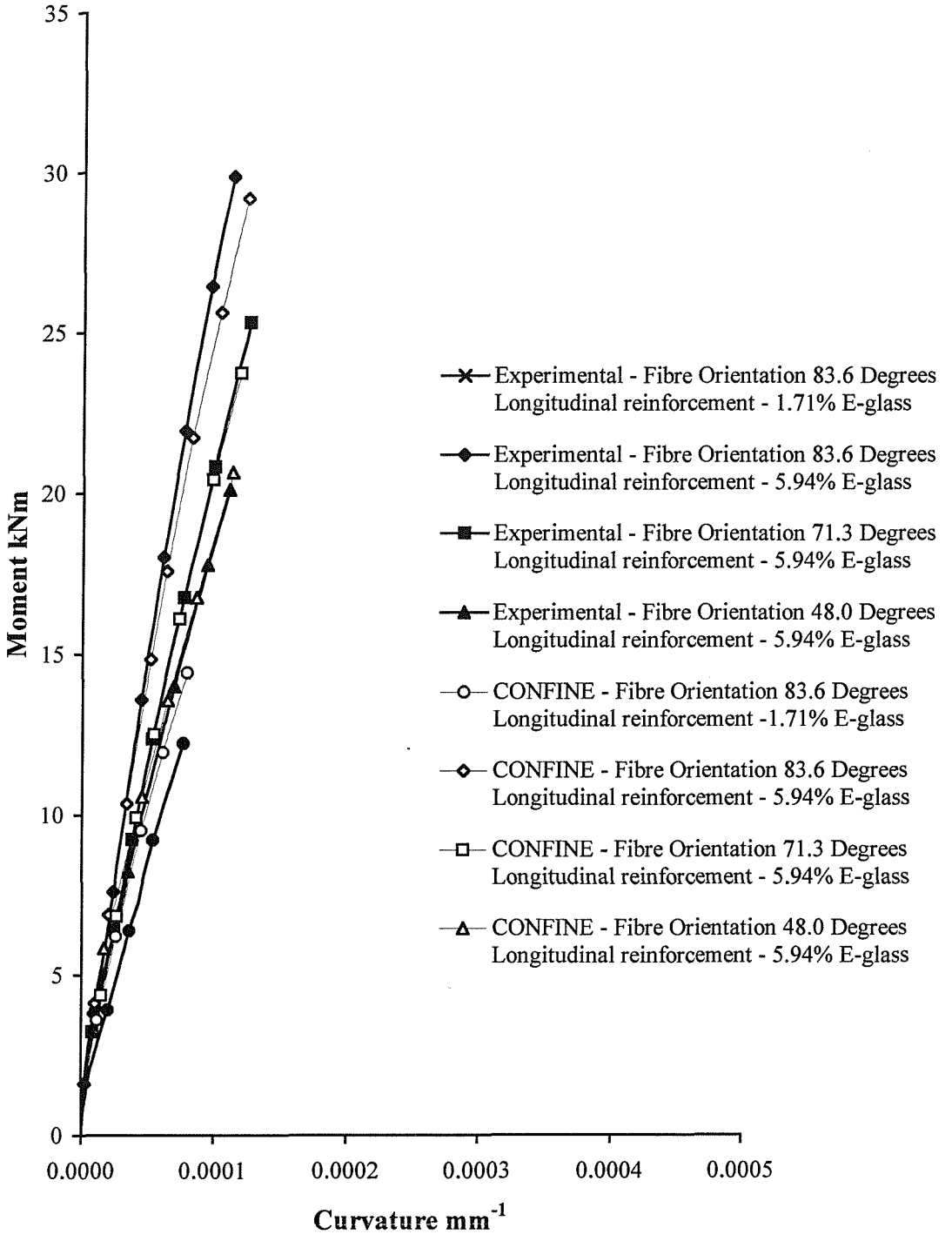

Figure 7.16(d). Comparison of the theoretical moment-curvature relationships with experimental results for the 150 mm diameter columns reinforced longitudinally with E-glass FRP reinforcement (slenderness ratio = 10)

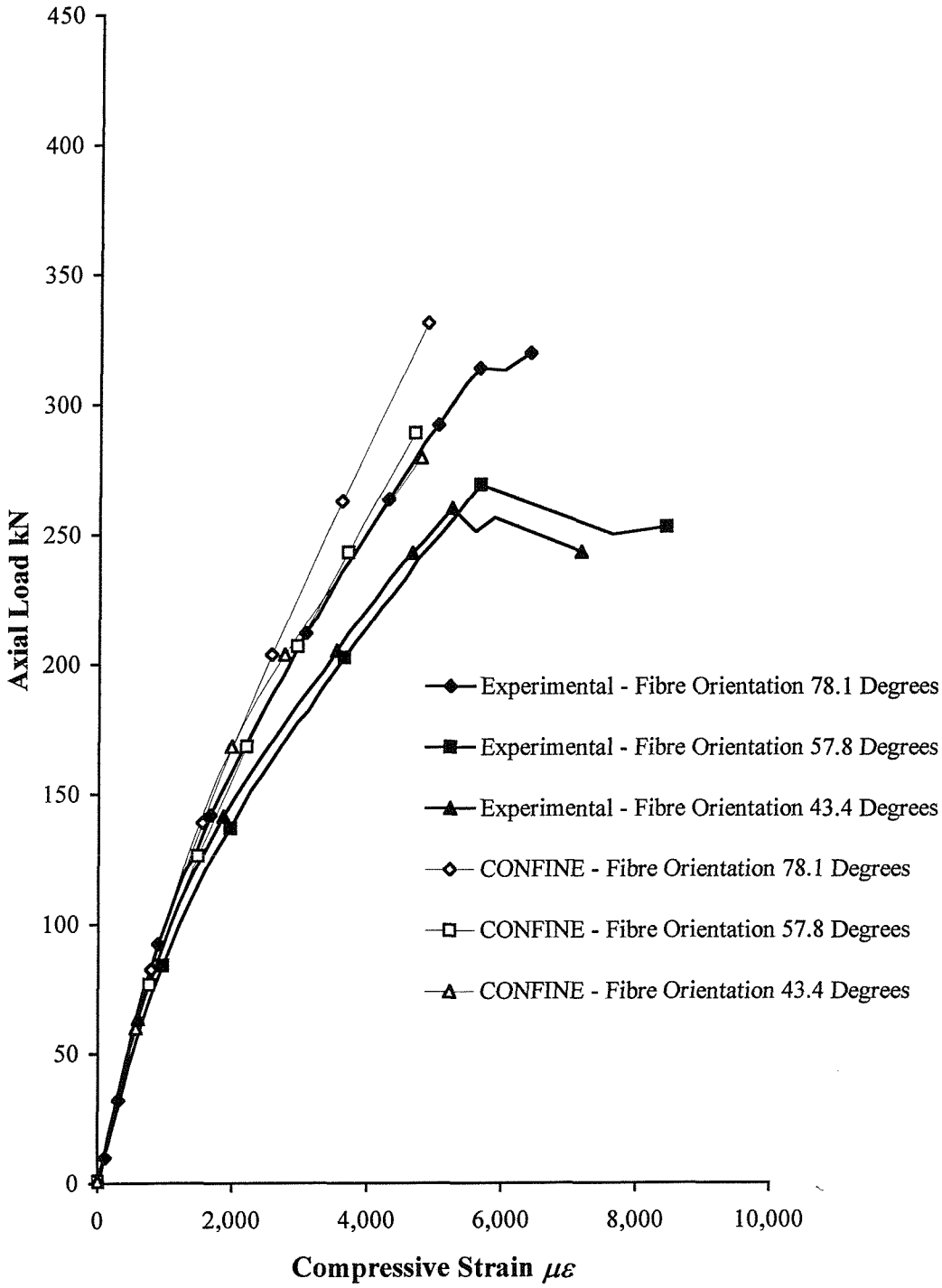

Figure 7.17(a). Comparison of the theoretical load-strain curves with experimental results for the 80 mm diameter columns reinforced longitudinally with carbon FRP reinforcement (slenderness ratio = 5)

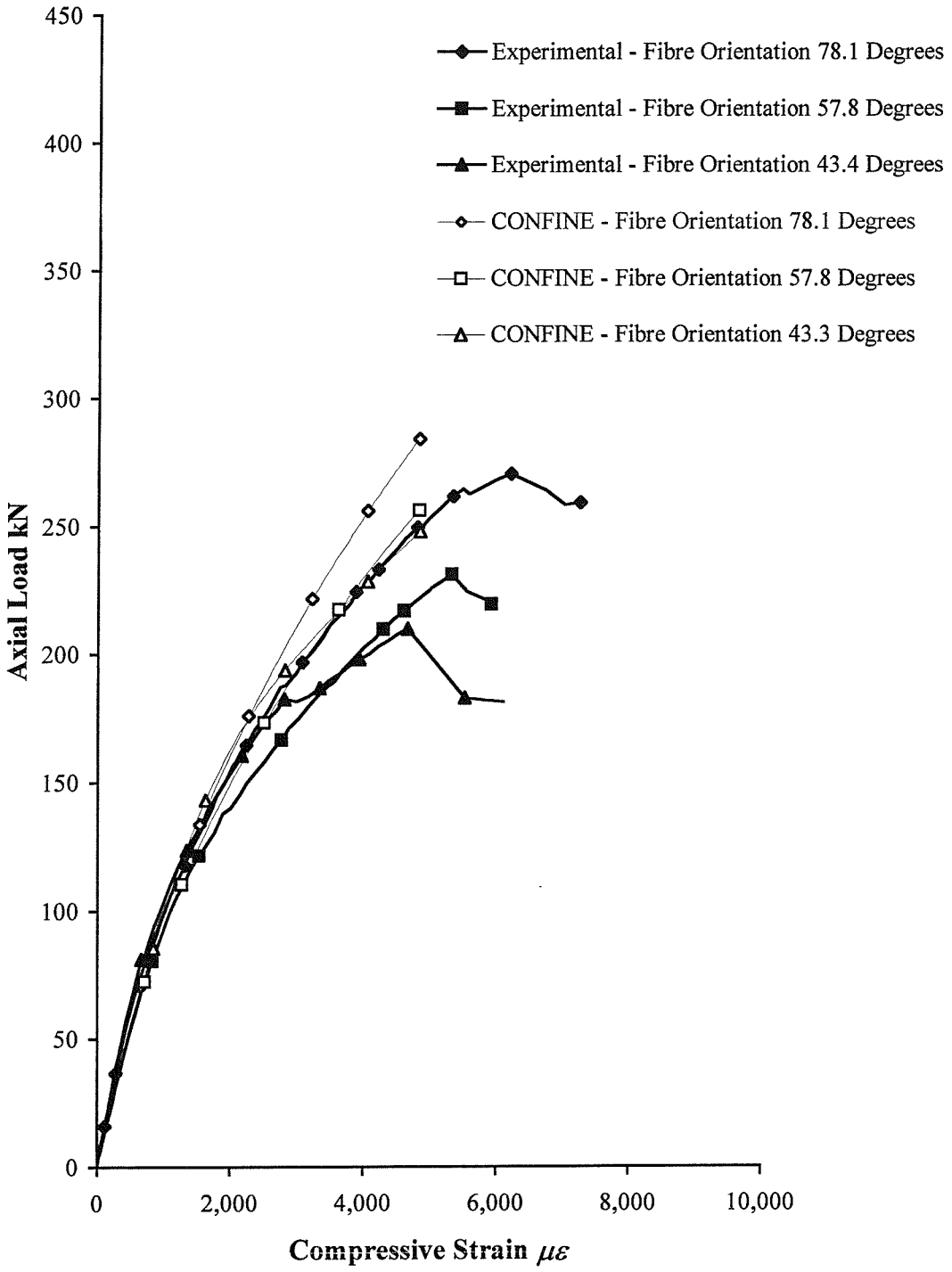

Figure 7.17(b). Comparison of the theoretical load-strain curves with experimental results for the 80 mm diameter columns reinforced longitudinally with carbon FRP reinforcement (slenderness ratio = 10)

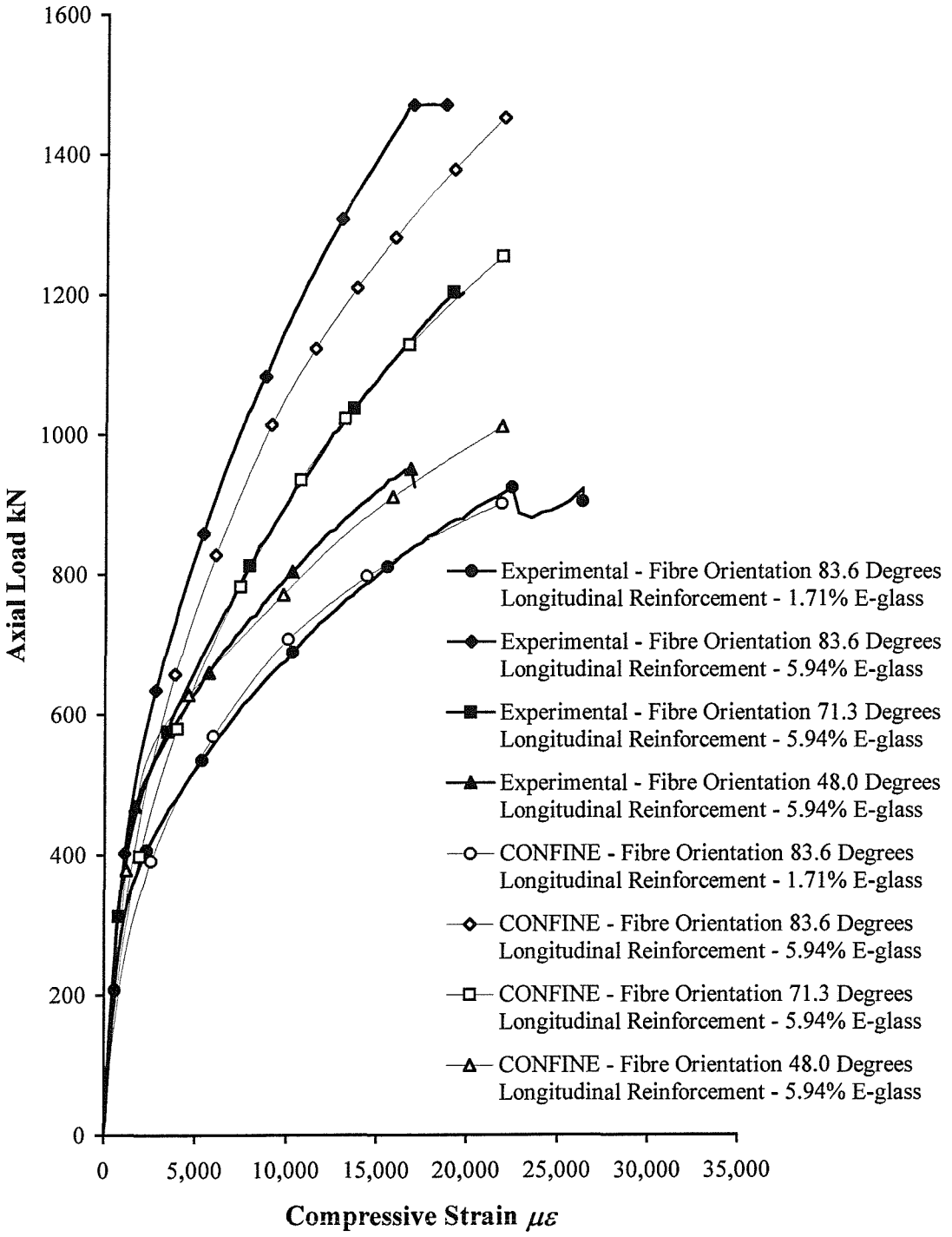

Figure 7.17(c). Comparison of the theoretical load-strain curves with experimental results for the 150 mm diameter columns reinforced longitudinally with E-glass FRP reinforcement (slenderness ratio = 5)

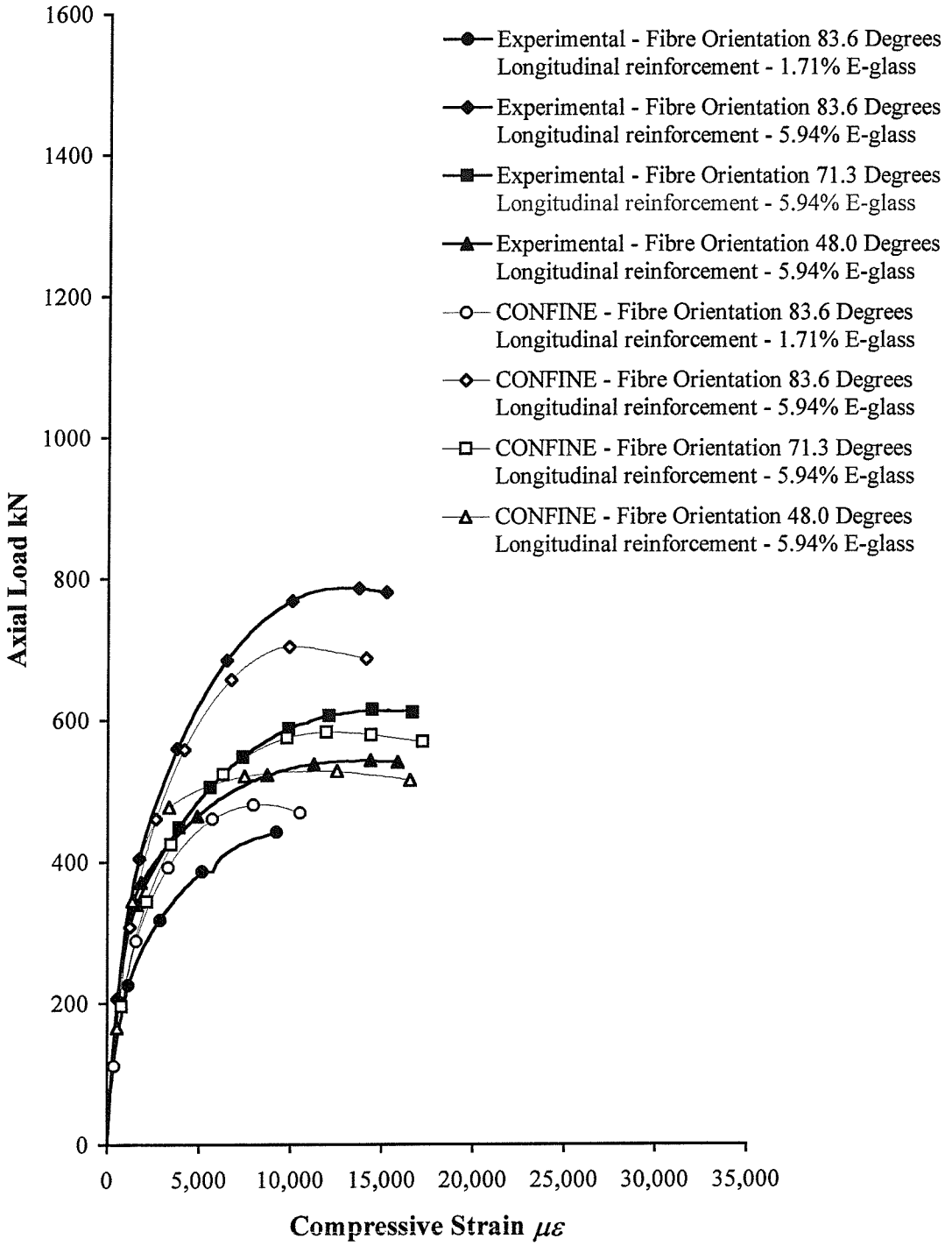

Figure 7.17(d). Comparison of the theoretical load-strain curves with experimental results for the 150 mm diameter columns reinforced longitudinally with E-glass FRP reinforcement (slenderness ratio = 10)

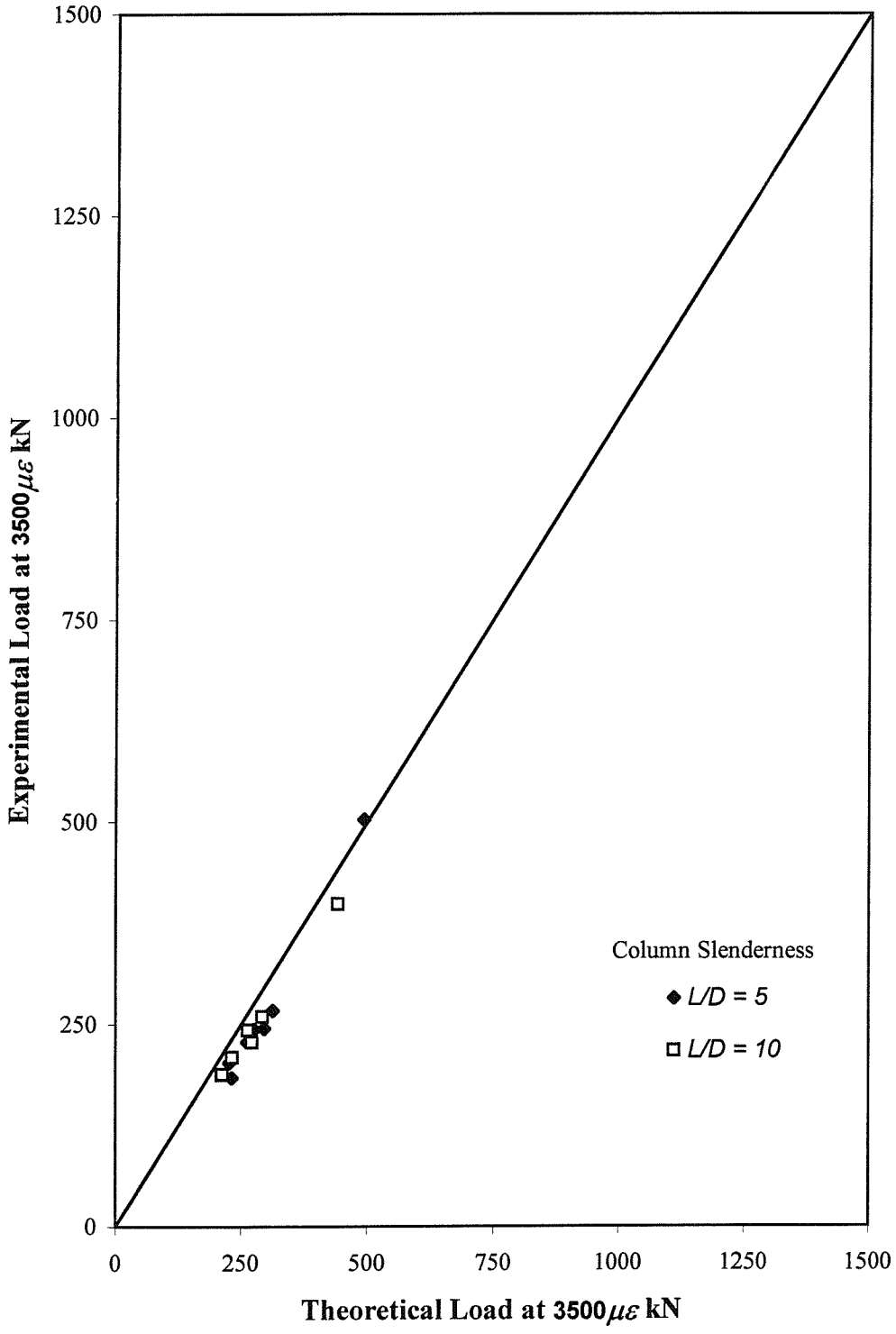

Figure 7.18. Comparison of the theoretical load at a compressive strain of 3,500$\mu\varepsilon$ with experimental results for columns with longitudinal carbon FRP reinforcement

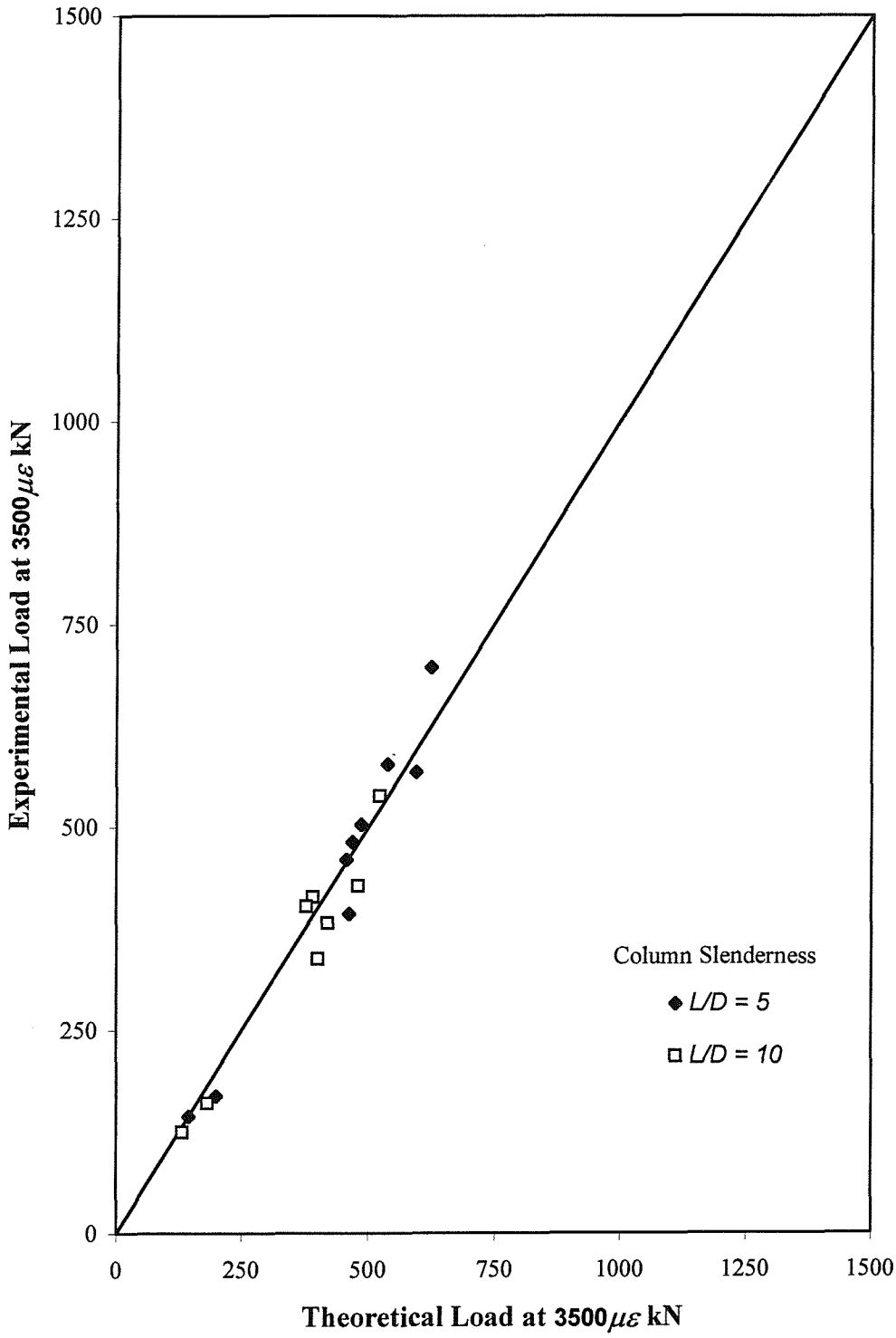

Figure 7.19. Comparison of the theoretical load at a compressive strain of 3,500$\mu\varepsilon$ with experimental results for columns with longitudinal E-glass FRP reinforcement

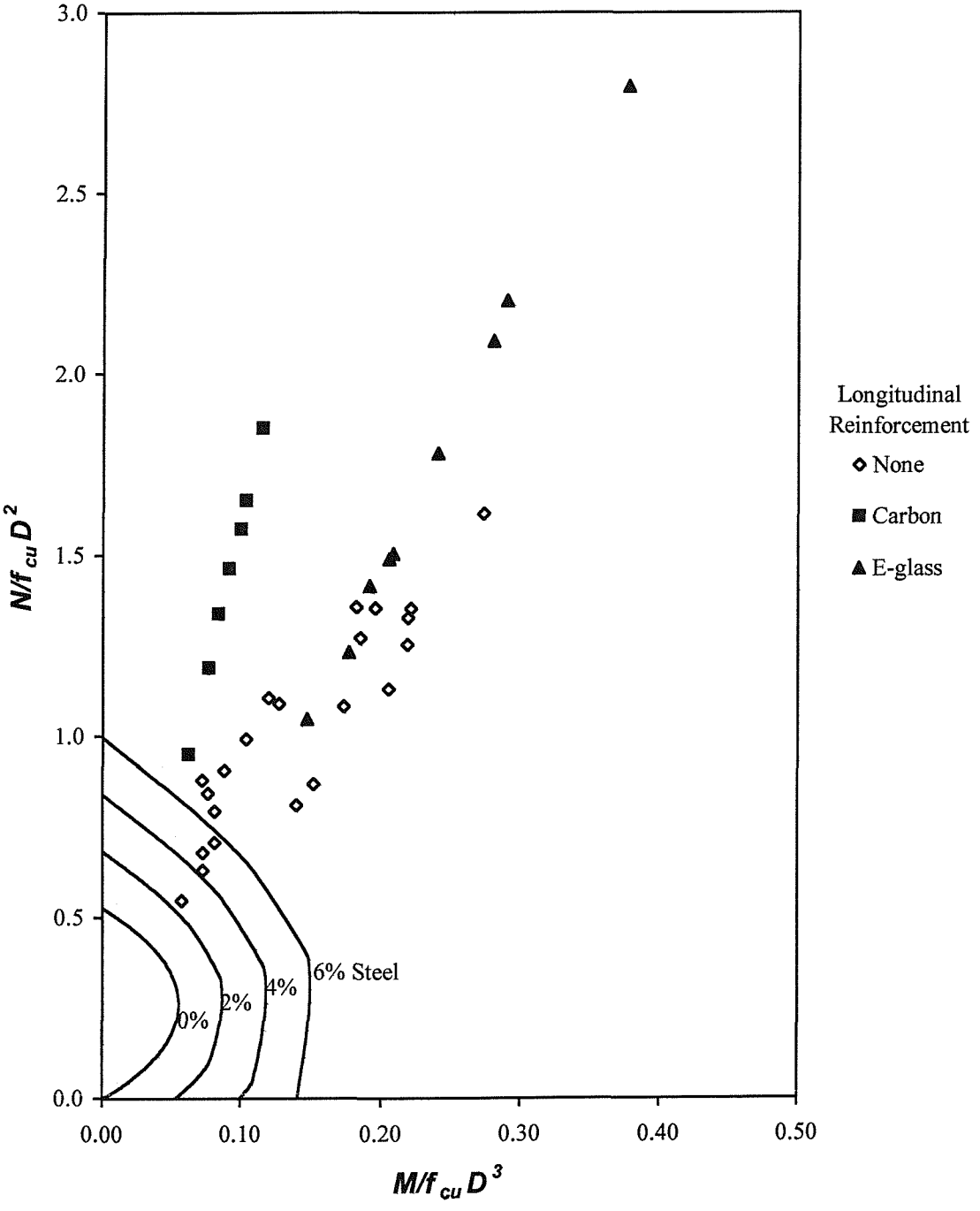

Figure 7.20. Comparison of the ultimate load capacity of longitudinally reinforced concrete-filled E-glass FRP composite columns with conventional steel reinforced concrete columns (slenderness ratio = 5)

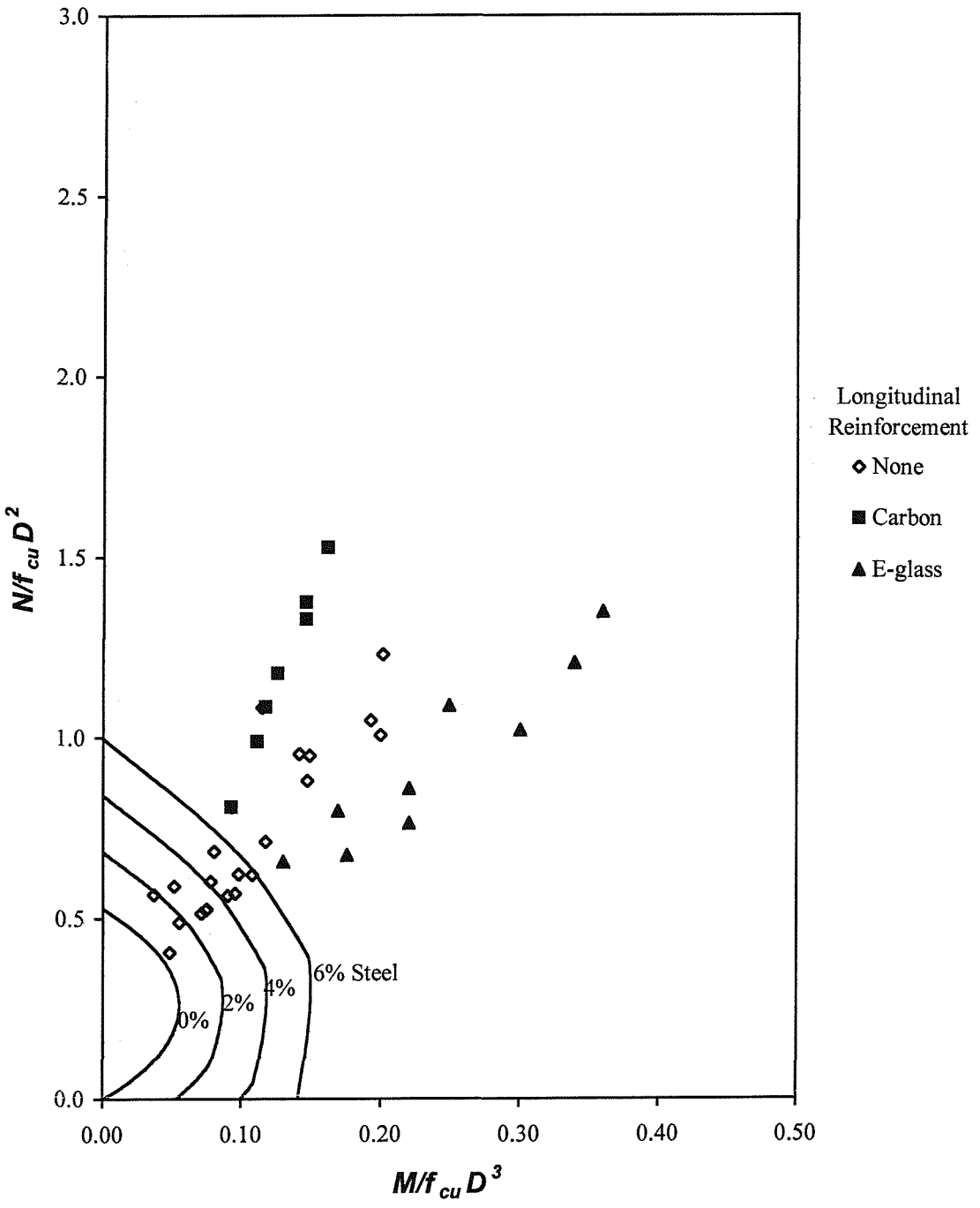

Figure 7.21. Comparison of the ultimate load capacity of longitudinally reinforced concrete-filled E-glass FRP composite columns with conventional steel reinforced concrete columns (slenderness ratio = 10)

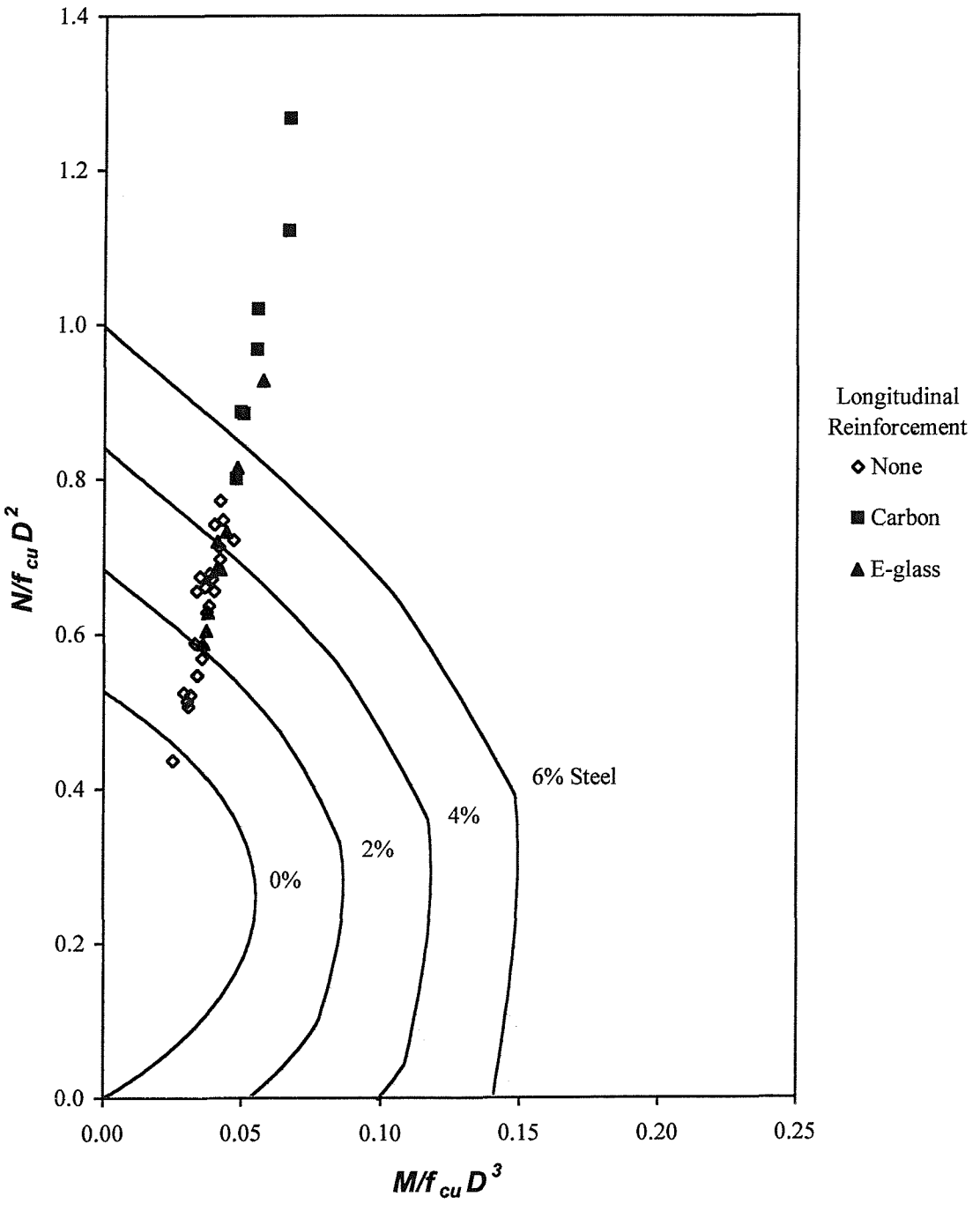

Figure 7.22. Comparison of the load capacity at a compressive strain of $3500\mu\varepsilon$ of longitudinally reinforced concrete-filled E-glass FRP composite columns with conventional steel reinforced concrete columns (slenderness ratio = 5)

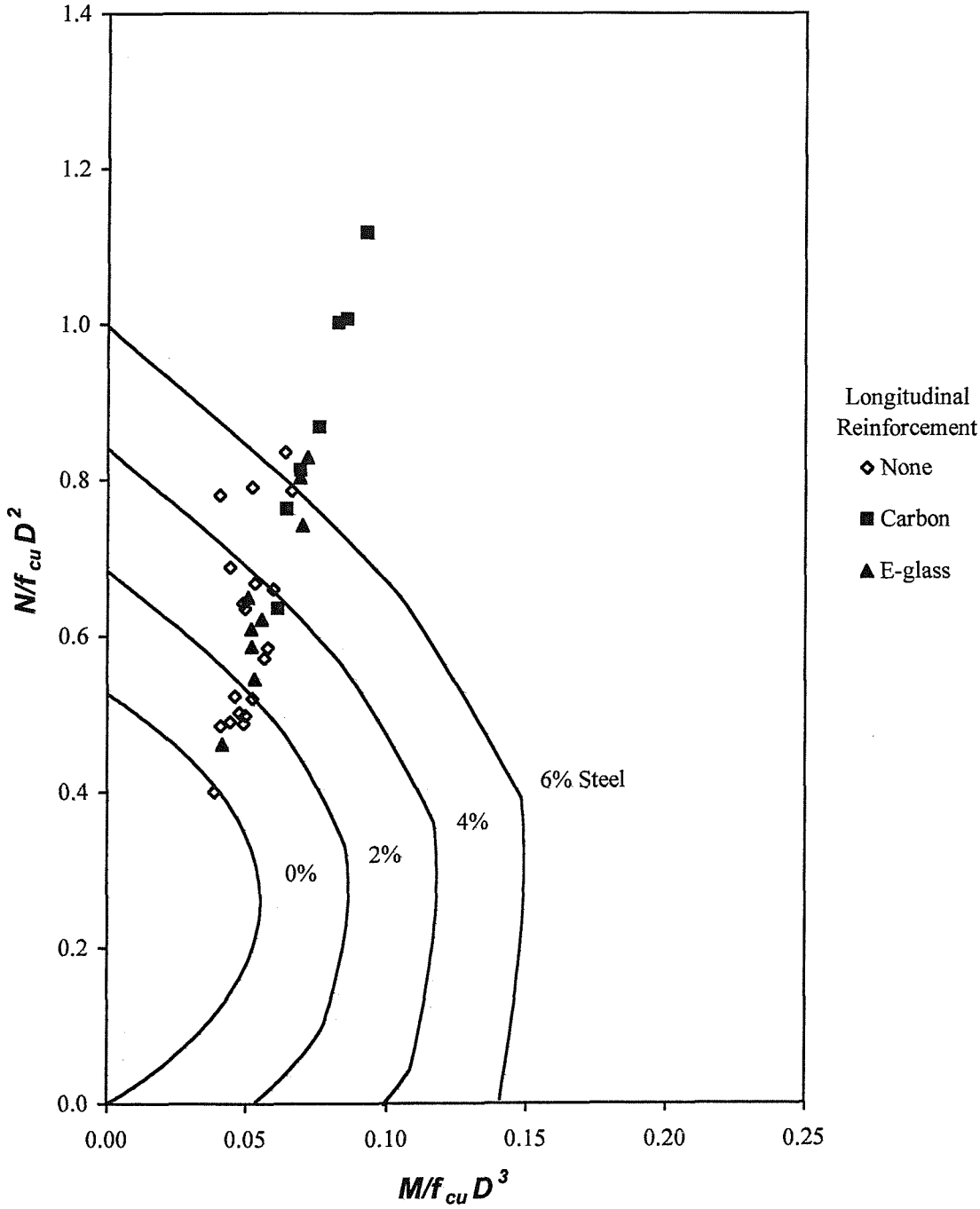

Figure 7.23. Comparison of the load capacity at a compressive strain of $3500\mu\varepsilon$ of longitudinally reinforced concrete-filled E-glass FRP composite columns with conventional steel reinforced concrete columns (slenderness ratio = 10)

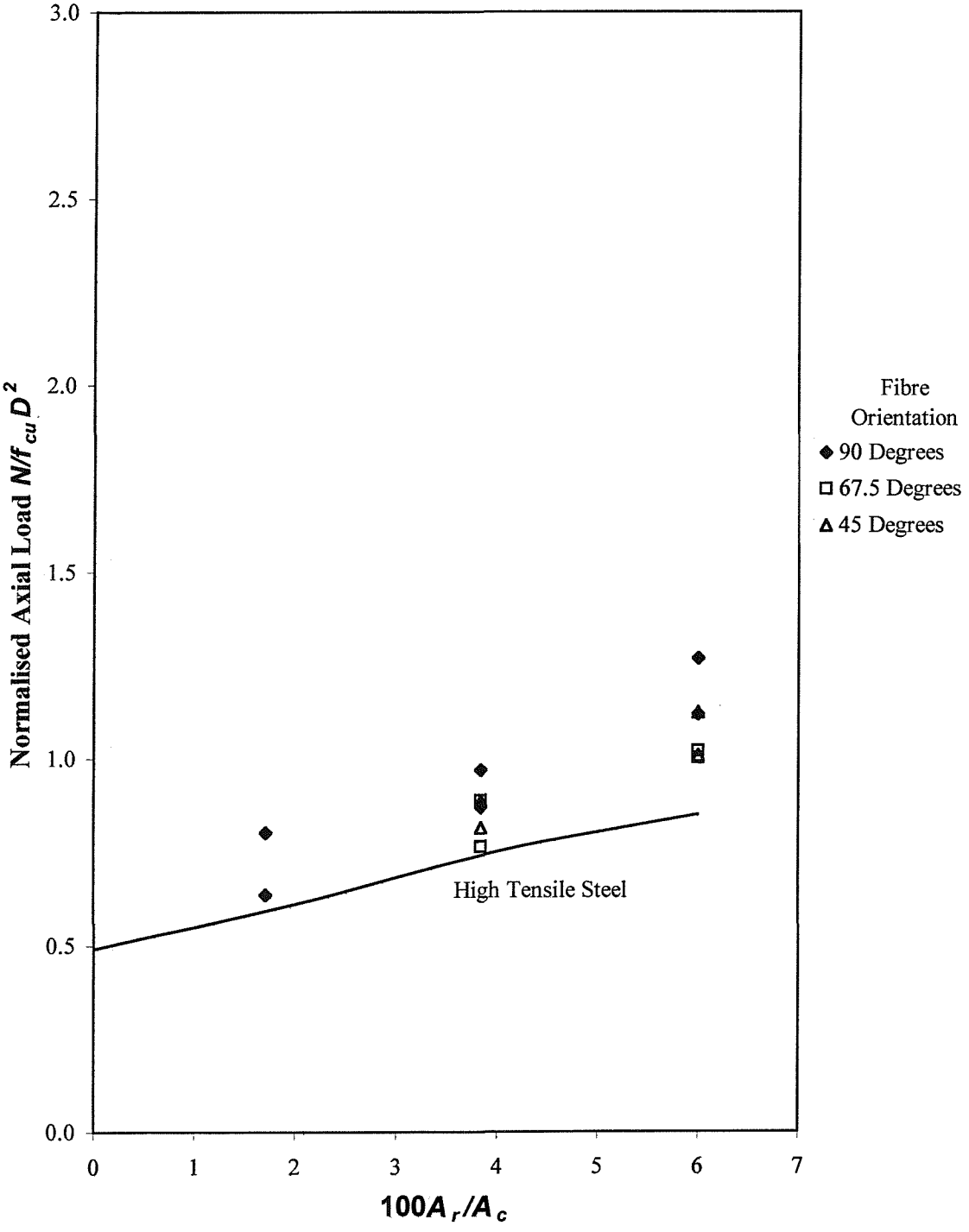

Figure 7.24. Comparison of the axial load capacity at a compressive strain of $3500\mu\varepsilon$ of concrete-filled E-glass FRP composite columns with conventional steel reinforced concrete columns for increasing percentages of longitudinal carbon FRP reinforcement

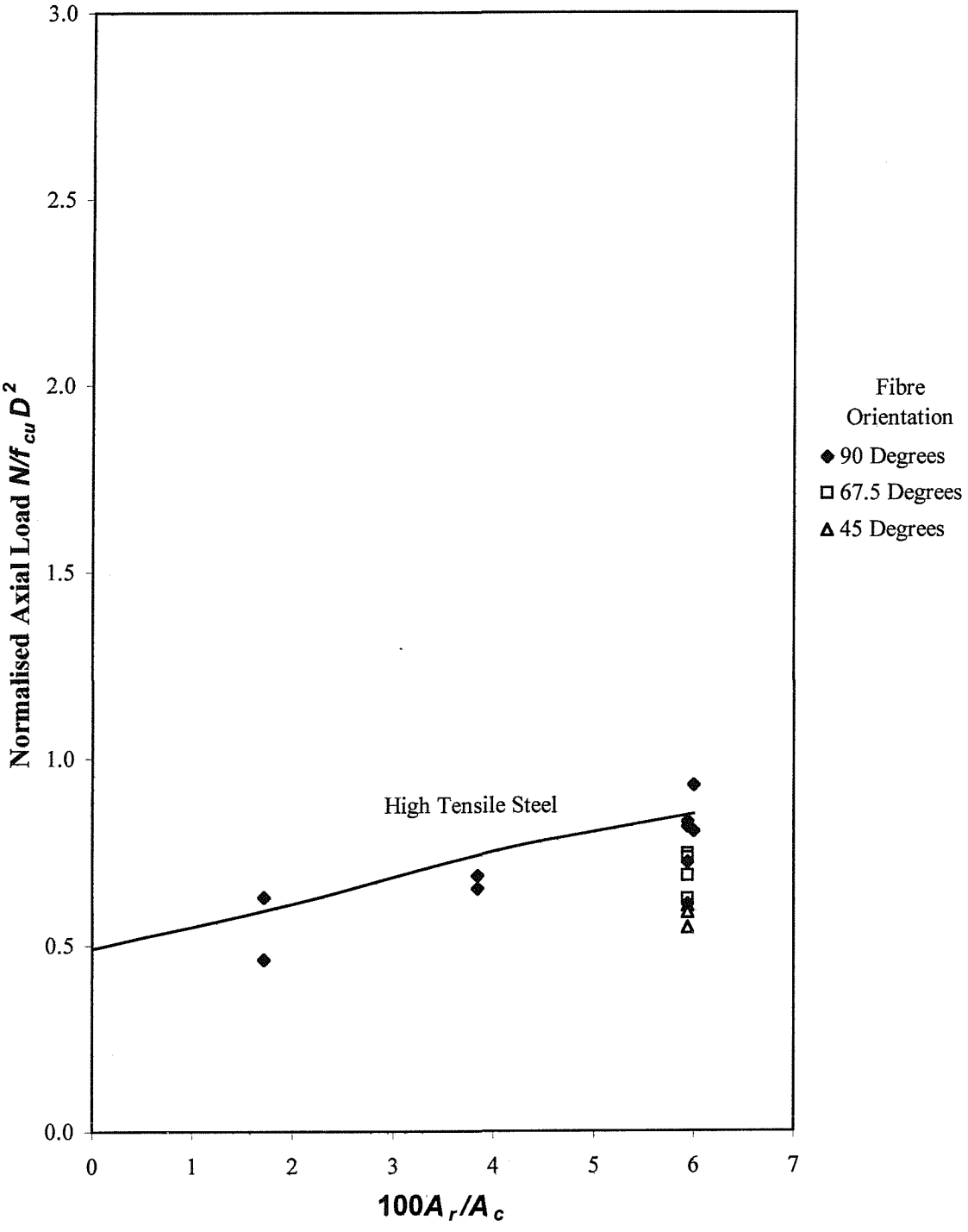

Figure 7.25. Comparison of the axial load capacity at a compressive strain of $3500\mu\varepsilon$ of concrete-filled E-glass FRP composite columns with conventional steel reinforced concrete columns for increasing percentages of longitudinal E-glass FRP reinforcement

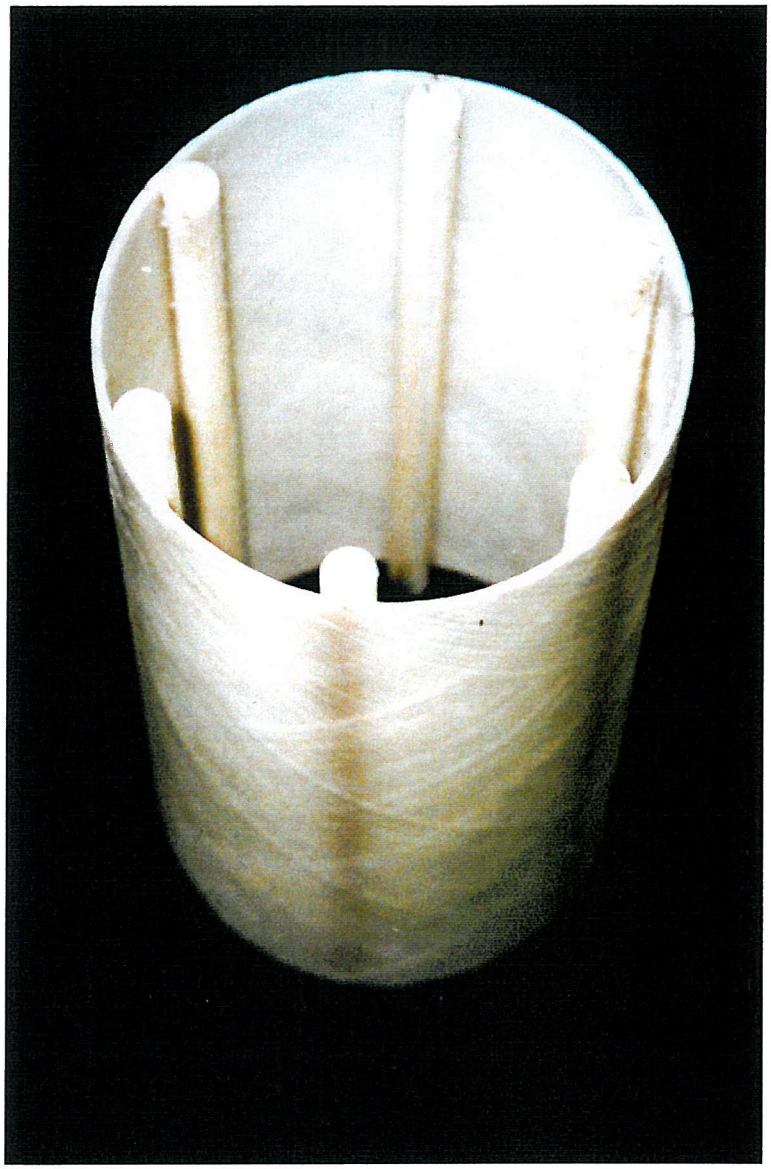

Plate 7.1. An E-glass filament wound tube reinforced longitudinally with six 13.5 mm diameter E-glass FRP-composite bars

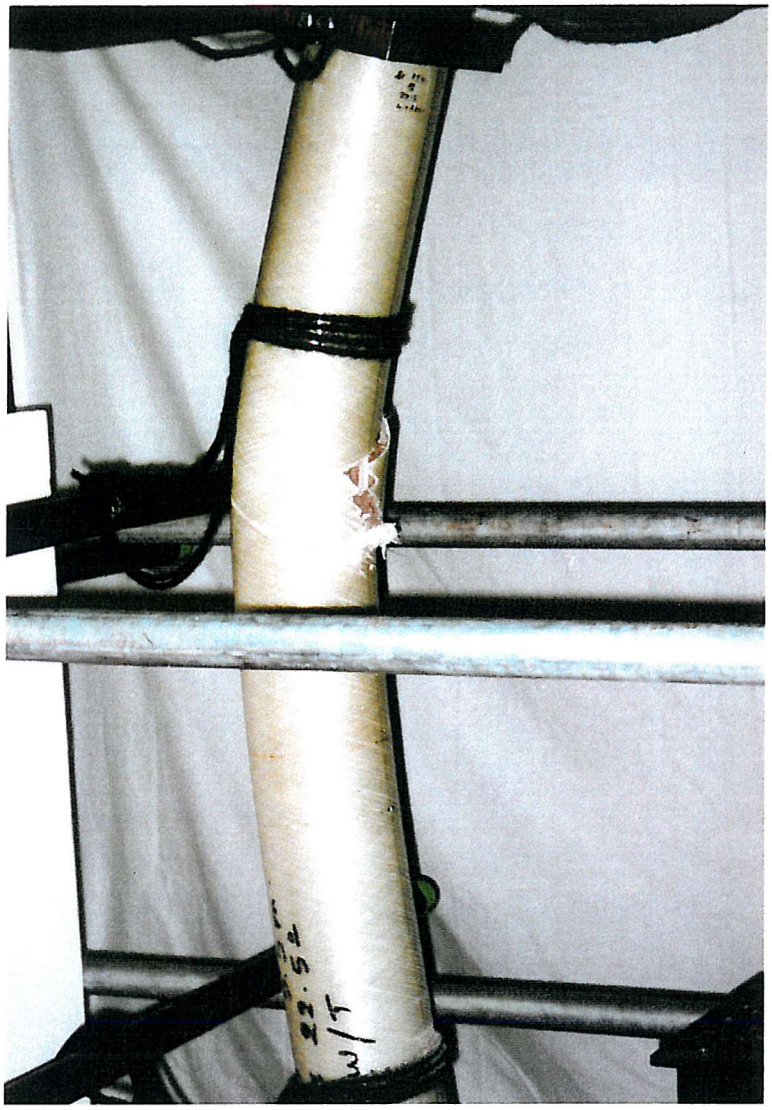

Plate 7.2. Compressive failure of a longitudinal FRP-composite bar

Plate 7.3. Crushing failure mode of an E-glass FRP-composite bar in compression

CHAPTER 8

CONCRETE-FILLED CARBON FRP-COMPOSITE COLUMNS

8.1 INTRODUCTION

The CONFINE model developed in this research has been derived from empirical data for concrete confined with E-glass FRP-composites. E-glass FRP-composites have the lowest elastic modulus of the three main families of FRP-composites currently used for civil engineering applications. To verify the validity of the CONFINE algorithm for concrete confined with a high modulus FRP-composite, two concentrically loaded stub columns and four eccentrically loaded concrete columns confined with a carbon fibre composite were tested to ultimate failure. The early experimental work using E-glass FRP-composite tubes found there to be no benefit of incorporating a longitudinal reinforcing component in the winding configuration. Therefore, the fibre orientation was limited to a nominal 90 degree winding for the carbon FRP-composite tubes. A further four eccentrically loaded concrete-filled carbon fibre composite tubes with additional longitudinal carbon FRP bars were also tested to ultimate failure.

8.2 MATERIAL PROPERTIES

The carbon FRP composite tubes consisted of a Bisphenol epoxy resin with unidirectional T300 carbon fibres. The tubes were fabricated using a helical filament winding configuration resulting in eight symmetrical layers orientated at $\pm\phi$. The mechanical properties of T300 carbon fibre are specified in Table 8.1.

Two nominal carbon FRP-composite tube diameters were tested, namely a 100mm and 150mm diameter, with three different column slenderness ratios of L/D = 2, L/D = 5 and L/D = 10. The geometrical and mechanical properties of the tubes are specified in Table 8.2. The mechanical properties of the tubes were derived using classical laminate theory.

The carbon FRP bars used as longitudinal reinforcement were 8mm diameter unidirectional pultruded Eurocrete bars. The bars had a tensile strength of 2,408 N/mm^2 and a modulus of elasticity of 152.5 kN/mm^2.The bars were bonded to the interior of the filament wound tubes using an epoxy resin, and allowed to cure fully before casting of the concrete.

8.3 EXPERIMENTAL INVESTIGATION

8.3.1 Stub columns

The stub columns were tested under monotonically increasing axial compression using a 2,000 kN Losenhausen test machine operating in displacement-control. The platen

displacement was increased at a constant rate of $0.002D$ mm/min. The end-plate details resulted in both the FRP-composite tube and the concrete being loaded simultaneously.

Longitudinal and circumferential strains were measured over the middle half of the columns using an identical testing arrangement to the E-glass specimens. The testing arrangement for the 100 mm diameter column is shown in Plate 8.1. The load and crosshead displacements were recorded automatically from the Losenhausen control panel.

8.3.2 Eccentrically loaded columns

The columns were tested under monotonically increasing axial compression with constant end eccentricity of $0.05D$, using a 1,500 kN Instron test machine operating in displacement-control. The platen displacement was increased at a constant rate of $0.002D$ mm/min. Load was applied through steel end plates and rollers that provided a constant end eccentricity and simulated pin-ended supports. The end-plate details resulted in both the FRP-composite tube and the concrete being loaded simultaneously.

Longitudinal and circumferential strains and the curvature at mid-height of the columns were measured using a similar testing arrangement to the concentrically loaded specimens. In addition to the measurement of strains at the column mid-height, lateral deflections at quarter and mid-height positions were measured using ±100.00 mm LVDT's. The accuracy of the LVDTs used to measure axial strain were ±0.01 mm at full scale. The load and crosshead displacements were recorded automatically from the Instron control panel. The testing arrangement for the eccentrically loaded columns is shown in Plate 8.2.

8.4 CONCENTRICALLY LOADED STUB COLUMNS

8.4.1 Experimental behaviour

Failure of concentrically loaded stub columns was extremely brittle. During the loading of the columns there were no visible signs of distress in the composite tube although the failure of individual fibres could be heard in the latter stages. At failure, the carbon fibre tube ruptured explosively into several pieces, resulting in the column's complete loss of structural integrity.

The failure loads and strains measured in the stub columns are summarised in Table 8.3. Due to a failure of the platen displacement control system on the machine, incomplete results were obtained for the 150 mm diameter specimen.

The stress-strain behaviour of the 100 mm diameter specimen is shown in Figure 8.1. The shape of the stress-strain curve for concrete confined by carbon is similar to that of E-glass, consisting of three basic regions, namely:

- an unconfined initial response;
- a transition zone;
- and a linear post-crushing region.

The initial tangent modulus of the confined concrete was 33.1 kN/mm^2, which compares to an initial tangent modulus for the unconfined control specimens of 29.5 kN/mm^2. The increase in the initial tangent modulus of the confined concrete is relatively small and, due to the limited test data, it is not possible to determine whether the increase is due to experimental scatter or to the contribution from the carbon fibre tube.

The circumferential failure strain of the confined concrete was 11,400$\mu\varepsilon$. The uniaxial breaking strain for a T300 carbon fibre is 11,440$\mu\varepsilon$. Thus, unlike concrete confined by E-glass FRP-composite tubes, the ultimate failure of concrete confined by a carbon FRP-composite tube is governed by the uniaxial breaking strain of the carbon fibre.

8.4.2 Comparison of CONFINE with experimental behaviour

The predicted mechanical properties of concrete filled carbon FRP-composite tubes using the CONFINE model are compared with the experimental results in Table 8.4. The ultimate failure stress of the confined concrete was determined using equation 4.3 together with the empirical coefficient derived from the research on concrete confined by E-glass FRP-composites reported in Chapter 4. The ratio of predicted failure stress to the experimental failure stress was 0.844, which suggests the higher modulus fibres are less effective and therefore a lower coefficient is required.

The experimental values of post-crushing tangent moduli for concrete confined by E-glass and carbon fibres are shown in Figure 8.2. The axial post-crushing tangent modulus was determined from equation 4.6 and gives poor agreement with the experimental value. The ratio of the predicted value to the experimental value of the post-crushing tangent modulus is 0.539. Based on the experimental work for concrete confined by low modulus E-glass fibres, the experimental value of the post-crushing tangent modulus for confinement from the higher modulus carbon fibres is significantly lower than expected. The post-crushing tangent modulus of concrete confined by E-glass fibres was found to be linearly proportional to the effective hoop modulus of the confining composite, for effective hoop

modulus values ranging from 1,000 N/mm^2 up to 3,000 N/mm^2. Figure 8.2 implies that the axial post-crushing modulus of concrete confined by FRP-composites is asymptotic to an upper bound value of 3,466 N/mm^2, with the fibres becoming less effective as the effective hoop modulus increases.

Figure 8.3 compares the experimental stress-strain curve for concrete confined by carbon fibres with the predicted equivalent uniaxial stress-strain curve. As expected, poor correlation exists between the predicted and experimental curves due to the overestimation of the post-crushing tangent modulus by equation 4.6. However, on the basis of the one test for concrete confined by a filament wound carbon FRP-composite, the parameters required to define the equivalent uniaxial stress-strain curve for concrete confined by carbon fibres cannot be quantified.

Also shown in Figure 8.3 is the theoretical stress-strain curve for concrete confined by an identical E-glass fibre tube. The higher modulus carbon fibre tube results in larger enhancements in both the strength and ductility of the concrete. However, the circumferential failure strains are comparable with an experimental circumferential strain to failure of 11,400$\mu\varepsilon$ for carbon confinement and a predicted circumferential strain to failure of 13,610$\mu\varepsilon$ for E-glass confinement.

8.5 ECCENTRICALLY LOADED COLUMNS

8.5.1 Experimental behaviour

The experimental behaviour of the concrete-filled carbon FRP-composite tubes was similar to that observed for the columns confined with E-glass fibre, with no visible signs of damage to the FRP-composite at peak load. Plate 8.3 shows the structural integrity of a 150 mm diameter column at peak load. The failure loads for the columns are given in Table 8.5. Ultimate failure of the column was initiated by the tensile rupture of the carbon fibre tube and resulted in a very brittle failure, as shown in Plate 8.4.

The failure of the columns with longitudinal carbon FRP bars was governed by the compressive failure of the bars. The mean compressive failure strain of the longitudinally reinforced columns is 5,875$\mu\varepsilon$, which is comparable to a mean compressive failure strain of 5,629$\mu\varepsilon$ obtained for concrete-filled E-glass tubes with longitudinal carbon FRP bars. Thus, the compressive failure strain of the longitudinal reinforcement is independent of the type of confining fibre and the 95th percentile value of 4,900$\mu\varepsilon$ can be taken as representative for the Eurocrete carbon FRP bar.

A direct comparison of the experimental behaviour of concrete columns confined with either E-glass or carbon FRP-composite is not possible due to differences in the thickness of the composite and the fibre volume fraction. Therefore, theoretical models of columns confined by an E-glass/epoxy composite with identical geometric properties and fibre volume fractions as the carbon/epoxy composite have been carried out using the CONFINE model.

A comparison of the load capacities of columns confined with E-glass or carbon FRP-composite is given in Table 8.6. Confinement using a carbon FRP-composite resulted in load capacities of between 30.6 percent to 47.5 percent greater than a column confined with an identical amount of E-glass FRP-composite. However, when the slenderness ratio increased to 10, the increase in load capacity ranged from 14.8 percent to 22.1 percent. Thus, as the column slenderness ratio increases, the benefits of using the more expensive high modulus carbon fibres for confinement diminish.

Carbon FRP-composite confinement resulted in a greater axial load capacity than an equivalent volume E-glass FRP-composite confinement, as shown in Table 8.6. However, comparable axial load capacities can be achieved by increasing the volume of E-glass FRP-confinement. Using the geometric parameters for the columns confined by carbon fibres, the CONFINE model was used to determine the volume of E-glass FRP composite confinement required to achieve the same axial load capacity. The analysis was carried out using a fibre volume fraction of 51 percent, and the increased volumes in E-glass fibre are given in Table 8.7. The volume of E-glass fibres necessary to attain the same axial load capacity was between 1.212 to 1.668 times greater than the volume of carbon fibres.

Comparison of the load capacities of columns confined by E-glass or carbon FRP-composites with additional longitudinal carbon FRP reinforcement are given in Table 8.8. The increase in axial load capacity gained from using the higher modulus fibre reduces since compressive failure of the carbon FRP bars prevents the full confinement developing. For the range of concrete-filled carbon FRP columns tested, the maximum increase in axial load capacity compared to an identical column confined with E-glass fibres was 11.1 percent. Thus, in terms of short-term axial load capacity, there are no benefits from using the more expensive carbon fibres for the confinement of concrete. However, carbon fibres may offer other advantages such as greater resistance to environmental degradation.

8.5.2 Load-deflection response

The experimental load-deflection curves for the 100 mm diameter columns and 150 mm diameter columns are given in Figure 8.4 and Figure 8.5 respectively. The initial load-deflection behaviour of the columns is linear. However, as the axial load increases, the non-linear behaviour of the concrete causes the rate of lateral deflection to increase. The rate of increase in non-linear behaviour increases as the slenderness ratio increases. Additional longitudinal carbon FRP reinforcement increased the axial stiffness of the column, reducing the lateral deflections of the column. The compressive failure of the carbon FRP reinforcing bars results in a sharp reduction in the slope of the load-deflection curve which is shown in Figure 8.4 and Figure 8.5.

The experimental load-deflection behaviour of columns confined with carbon fibres is compared with the theoretical behaviour of identical columns confined by E-glass fibres in Figure 8.6. The fibre volume fraction, thickness of FRP-composite and angle of fibre orientation used in the CONFINE model for the E-glass column were the same as the experimental values. The initial load-deflection response of the columns is similar and the behaviour is independent of the hoop modulus of the confining material. As the load increases, larger lateral deflections occur in the columns confined with the E-glass composite. However, at the peak column load, the lateral deflections in the columns are similar, with significant deflections occurring irrespective of the confining material.

Figure 8.7 compares the experimental behaviour of the concrete-filled carbon FRP-composite columns with additional longitudinal carbon FRP reinforcement, with the predicted load-deflection behaviour of columns confined with an E-glass FRP-composite. The experimental load-deflection curves only show the behaviour of the columns up to the compressive failure of the longitudinal reinforcement. Figure 8.7 shows that the behaviour of the columns confined by E-glass fibres is virtually identical to the columns confined by the more expensive carbon fibres with little or no enhancement in load capacity. Since the failure of the columns is governed by the compressive failure of the longitudinal carbon FRP reinforcement at a mean compressive strain of $5{,}875\mu\varepsilon$, the full benefits of triaxial confinement cannot be utilised.

8.5.3 Load-strain behaviour

The load-strain curves for the columns are shown in Figure 8.8 and Figure 8.9 for the 100 mm and 150 mm diameter columns respectively. Initially the mechanical properties of the concrete are dominant and determine the early behaviour of the column. As the axial

strains in the concrete increase, softening of the concrete occurs due to the propagation of mortar cracks. However, the degree of strain softening is determined by the magnitude of the confining pressure, which inhibits crack development. Thus, the higher modulus carbon FRP-composite slows down the non-linear behaviour of the concrete more effectively than an E-glass FRP-composite.

Columns reinforced longitudinally with carbon FRP bars exhibited an increase in the slope of the load-strain curves compared to the columns with no longitudinal reinforcement. The increase in the slope of the load-strain curve was proportional to the amount of longitudinal reinforcement. The compressive failure of the carbon FRP reinforcing bars caused a sudden reduction in the slope of the curve, at a compressive strain of approximately 5,875$\mu\varepsilon$. Whilst the columns with a slenderness ratio of 5, were able to resist increases in the axial load beyond the compressive strain of 5,875$\mu\varepsilon$, the compressive failure of the longitudinal FRP bars initiated failure in the more slender columns.

8.5.4 Comparison with theoretical behaviour

The behaviour of the eccentrically loaded concrete-filled carbon FRP columns predicted by the CONFINE model gave poor agreement with the experimental results. The existing CONFINE model was found to over-predict the load capacity and axial stiffness of the columns due to the errors in estimating the post-crushing tangent modulus of the confined concrete. Further experimental work to quantify the parameters defining the equivalent uniaxial stress-strain behaviour is required to validate the CONFINE model for concrete confined by high modulus fibres.

8.6 SUMMARY

The experimental work on concrete confined by carbon FRP-composites has shown that the semi-empirical equations derived for concrete confined by E-glass FRP-composites are not valid for the concrete confined by the higher modulus fibres. The limited amount of experimental data obtained from this research does not enable the parameters defining the equivalent stress-strain curve for carbon fibre confinement to be determined. However, it was clear that the benefits of triaxial confinement are less effective for the high modulus fibres.

The experimental behaviour of the eccentrically loaded columns was found to be similar to the behaviour of concrete-filled E-glass FRP-composite columns. Confinement by carbon FRP-composites resulted in axial load capacities of between 14.8 to 47.5 percent greater

than columns confined by identical E-glass FRP-composites. However, due to the reduction in the effective triaxial confinement achieved with carbon fibres, confinement using carbon FRP-composites is unlikely to be economic compared to E-glass fibres.

Property	T300 Carbon Fibre
Specific gravity	1.8
Longitudinal tensile strength σ_{11}, N/mm^2	2414.0
Longitudinal elastic modulus E_{11}, kN/mm^2	211.0
Transverse elastic modulus E_{22}, kN/mm^2	13.8
Longitudinal shear modulus G_{12}, Kn/mm^2	9.0
Transverse shear modulus G_{23}, kN/mm^2	4.8
Poisson's ratio ν_{12}	0.20
Poisson's ratio ν_{23}	0.25

Table 8.1. Mechanical properties of T300 carbon fibre [84]

Property	ϕ100	ϕ150
Fibre orientation	80.40°	83.60°
Internal diameter, mm	100.06 ± 0.16	150.13 ± 0.16
Thickness, mm	2.38 ± 0.06	2.43 ± 0.07
Fibre volume fraction	0.51	0.51
Axial elastic modulus E_{xx}, kN/mm^2	9.0	9.1
Hoop elastic modulus $E_{\theta\theta}$, kN/mm^2	105.4	110.3
Shear modulus $G_{x\theta}$, kN/mm^2	5.2	3.5
Poisson's ratio $\nu_{x\theta}$	0.05	0.03
Poisson's ratio $\nu_{\theta x}$	0.58	0.41

Table 8.2. Geometric and mechanical properties of carbon FRP-composite

Property	Diameter, mm	
	100.06	**150.13**
Concrete strength, N/mm^2	21.0	22.9
Axial load, N/mm^2	229.8	-
Axial Post-crushing modulus, N/mm^2	3466	-
Axial strain, $\mu\varepsilon$	60,200	-
Lateral strain, $\mu\varepsilon$	11,400	-

Table 8.3. Experimental results of the concrete filled carbon FRP-composite stub columns

Property	Experimental	Predicted	$\frac{\text{Experimental}}{\text{Predicted}}$
Axial load, N/mm^2	229.8	272.2	0.844
Axial Post-crushing modulus, N/mm^2	3466	6428	0.539
Axial strain, $\mu\varepsilon$	60,200	38,400	1.568
Lateral strain, $\mu\varepsilon$	11,400	11,975	0.952

Table 8.4. Comparison of experimental and predicted behaviour of the 100 mm diameter concrete filled carbon FRP-composite stub column

D mm	Angle of wind °	Eccentricity mm	$100\frac{A_r}{A_c}$	Effective Length mm	f_{cu} N/mm^2	N_u kN	δ_u mm	Strain $\mu\varepsilon$
100.06	80.4	5	0.00	571	26.2	500	15.84	>30,800†
				1071	26.2	212	14.09	9,700
			3.84	571	35.6	419	1.63	5,800
				1071	35.6	390	6.34	5,800
150.13	83.6	7.5	0.00	870	28.6	982	19.79	>26,800†
				1621	28.6	448	17.29	7,300
			1.71	871	32.5	751	2.93	6,100
				1620	32.5	581	12.02	5,800

† Last recorded compressive strain before axial extensometer was removed.

Table 8.5. Failure loads of eccentrically loaded carbon FRP-confined concrete columns

Diameter mm	f_{cu} N/mm^2	L/D	Axial Load, kN		$\frac{N^{\text{Carbon}}}{N^{\text{E-glass}}}$
			E-glass tube†	Carbon tube‡	
100.06	26.2	5	382	500	1.306
		10	185	212	1.148
150.13	28.3	5	666	983	1.475
		10	367	448	1.221

† Theoretical values based on geometric properties of the carbon fibre tube.

‡ Experimental values

Table 8.6. Comparison of the axial load capacity of concrete filled FRP-composite columns

Diameter mm	f_{cu} N/mm^2	L/D	Axial Load kN	Tube Thickness, mm		$\frac{V^{\text{E-glass}}}{V^{\text{Carbon}}}$
				Carbon	E-glass	
100.06	26.2	5	500	2.38	3.30	1.373
		10	212	2.38	2.90	1.212
150.13	28.3	5	983	2.43	4.10	1.668
		10	448	2.43	3.80	1.549

Table 8.7. Comparison of the thickness of FRP-composite confinement required for a given axial load capacity, based on a fibre volume fraction of 51 percent.

Diameter mm	f_{cu} N/mm^2	L/D	Axial Load, kN		$\frac{N^{\text{Carbon}}}{N^{\text{E-glass}}}$
			E-glass tube †	Carbon tube‡	
100.06	35.6	5	412	419	1.017
		10	351	390	1.111
150.13	32.5	5	693	751	1.084
		10	543	581	1.070

† Theoretical values based on geometric properties of the carbon fibre tube.

‡ Experimental values

Table 8.8. Comparison of the axial load capacity of concrete filled FRP-composite columns reinforced with carbon FRP bars

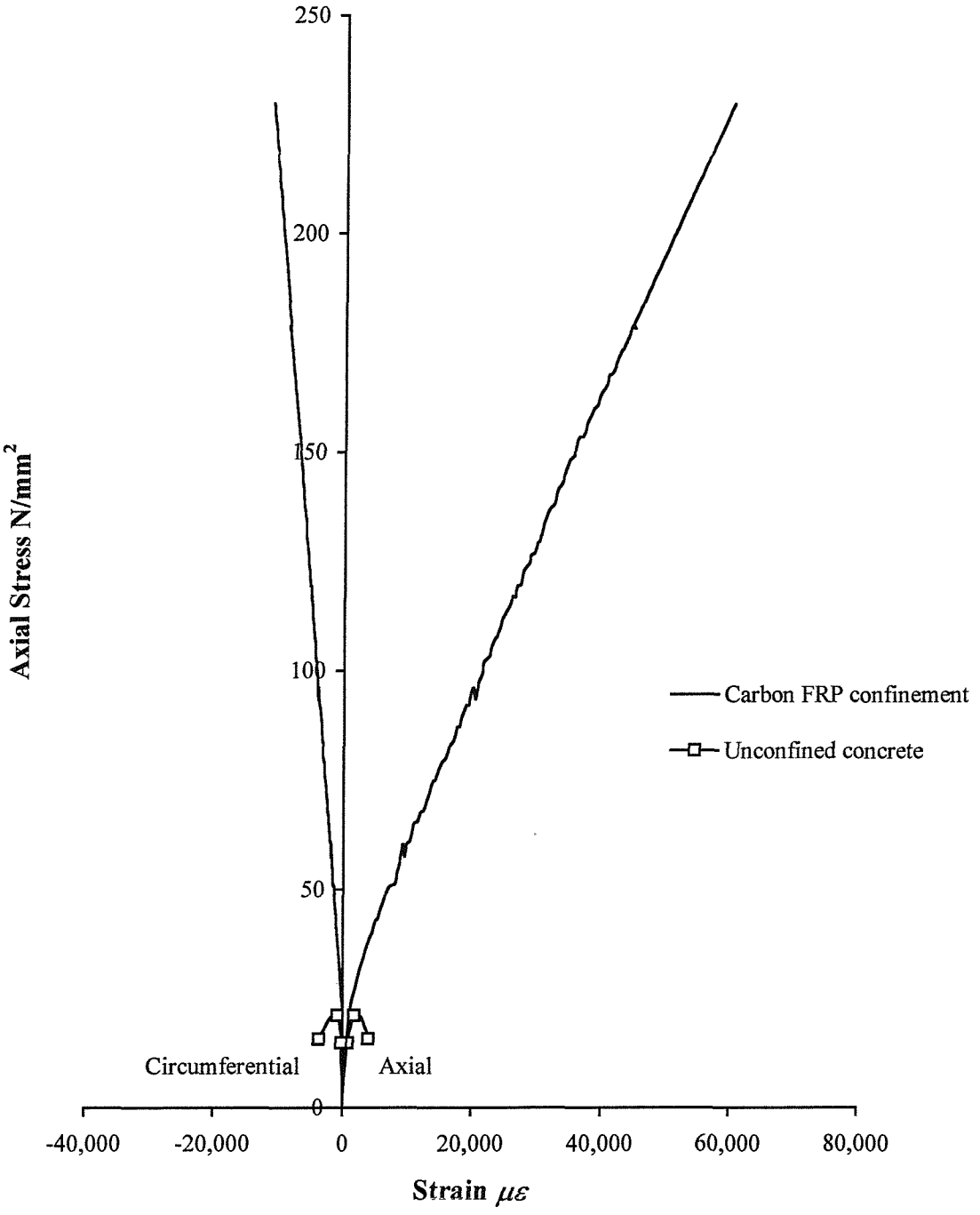

Figure 8.1. Stress-strain curves for the 100 mm diameter concrete-filled carbon FRP-composite tube

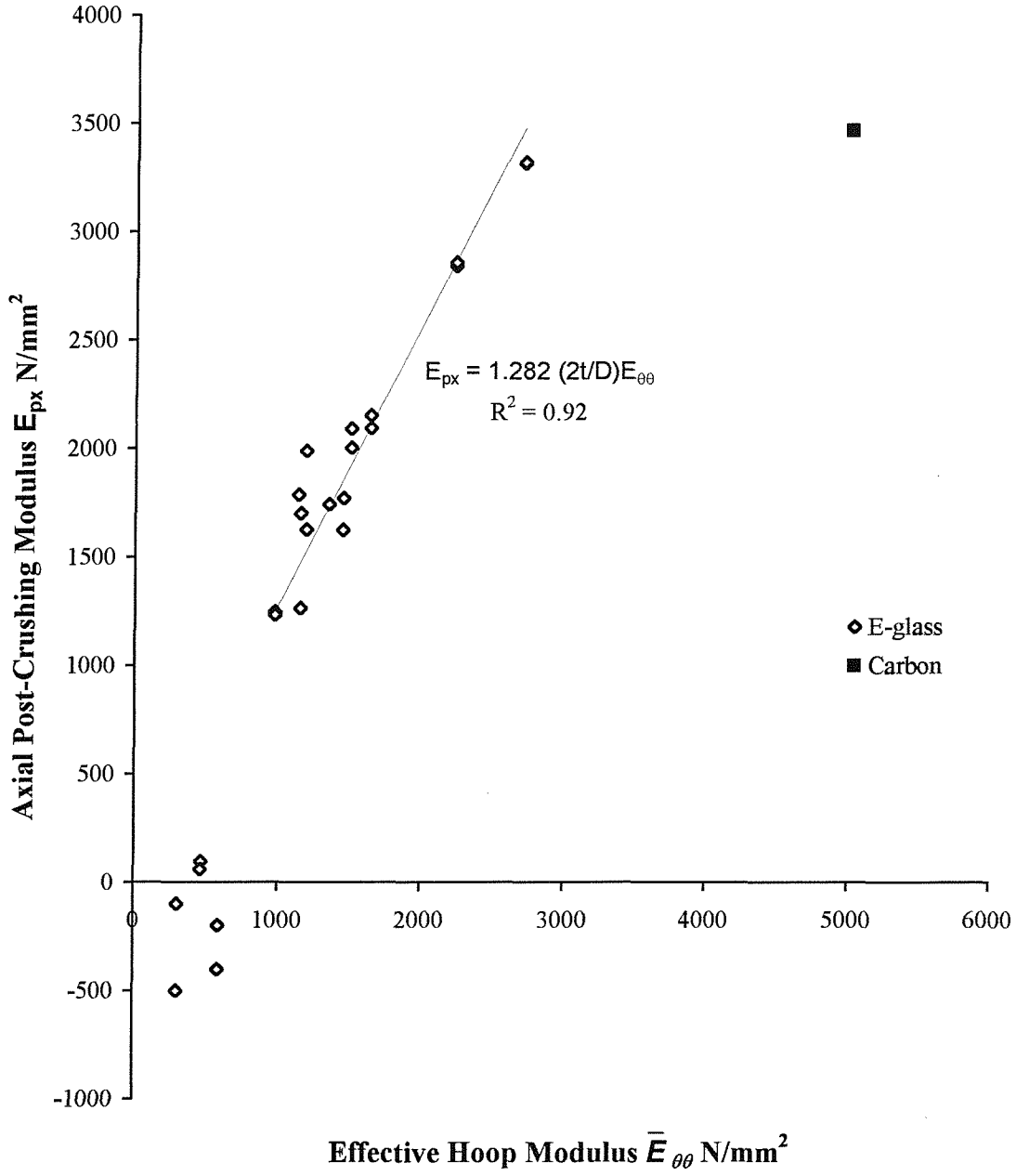

Figure 8.2. Comparison of the axial post-crushing tangent modulus of concrete confined by a carbon FRP-composite with the axial post-crushing modulus of concrete confined by E-glass FRP-composites

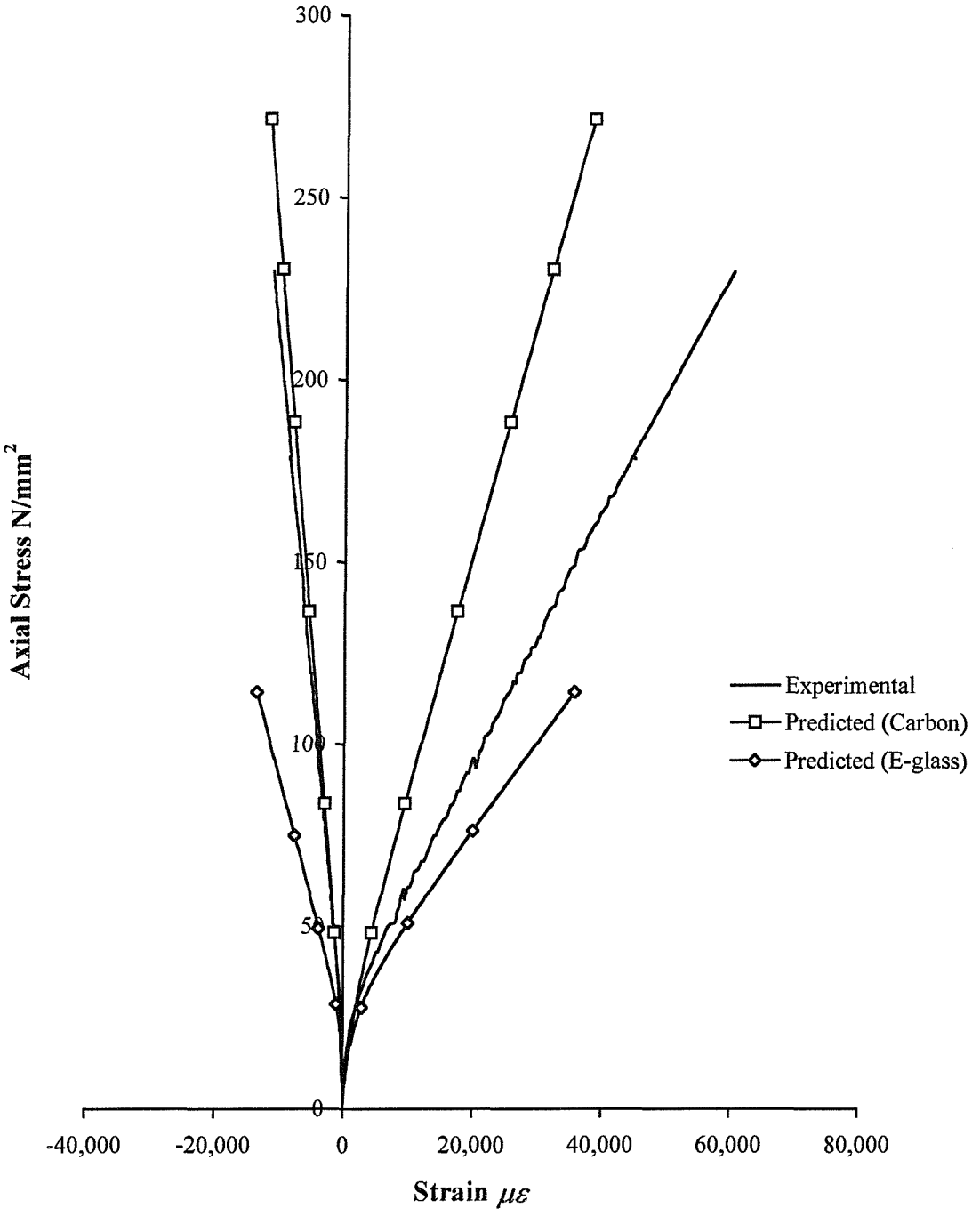

Figure 8.3. Comparison of the experimental stress-strain curve for concrete confined by a carbon FRP-composite with the predicted stress-strain curves for concrete confined with either carbon or E-glass FRP-composites

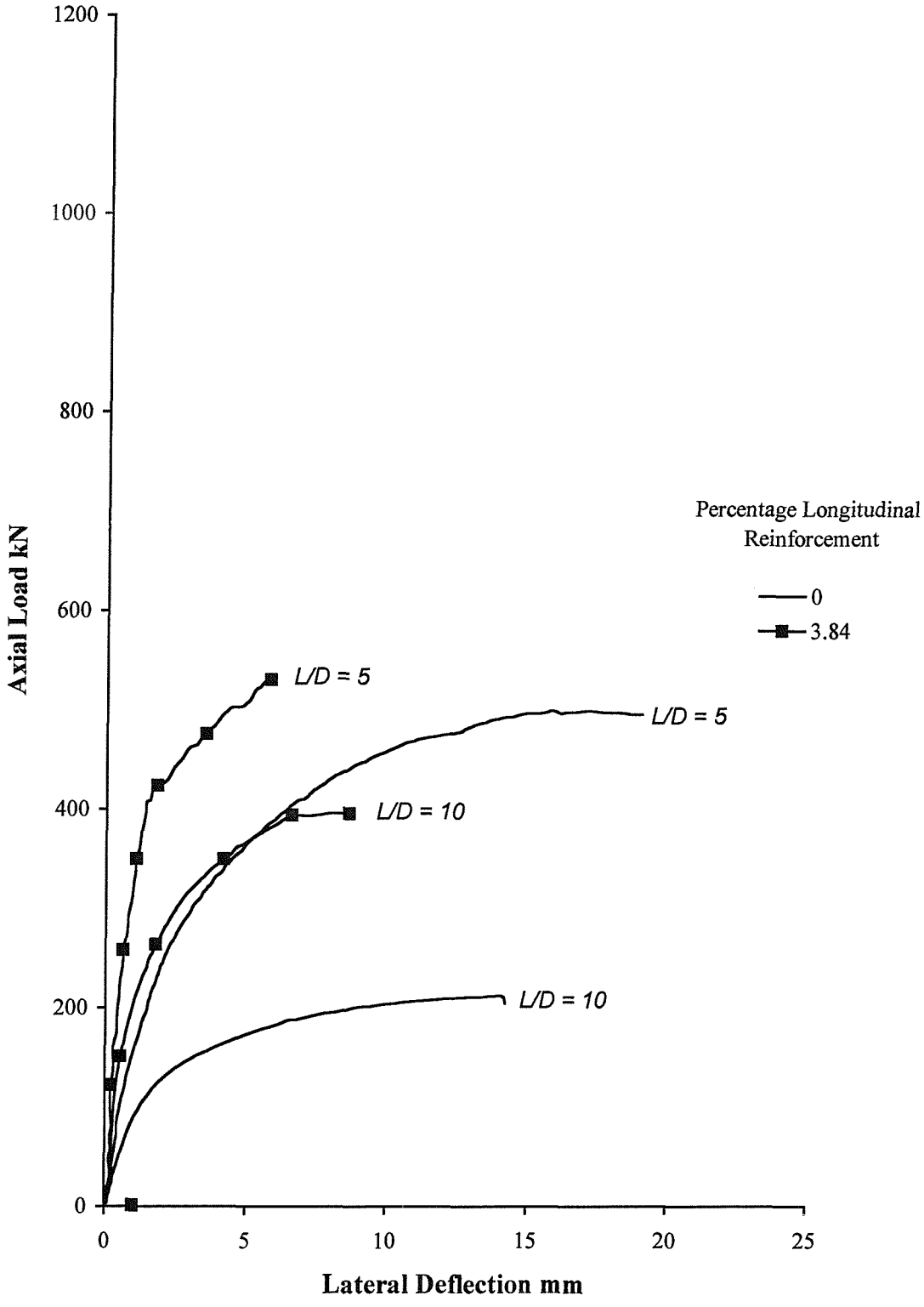

Figure 8.4. Load-deflection curves for the 100 mm diameter concrete-filled carbon FRP-composite columns subjected to eccentric loading

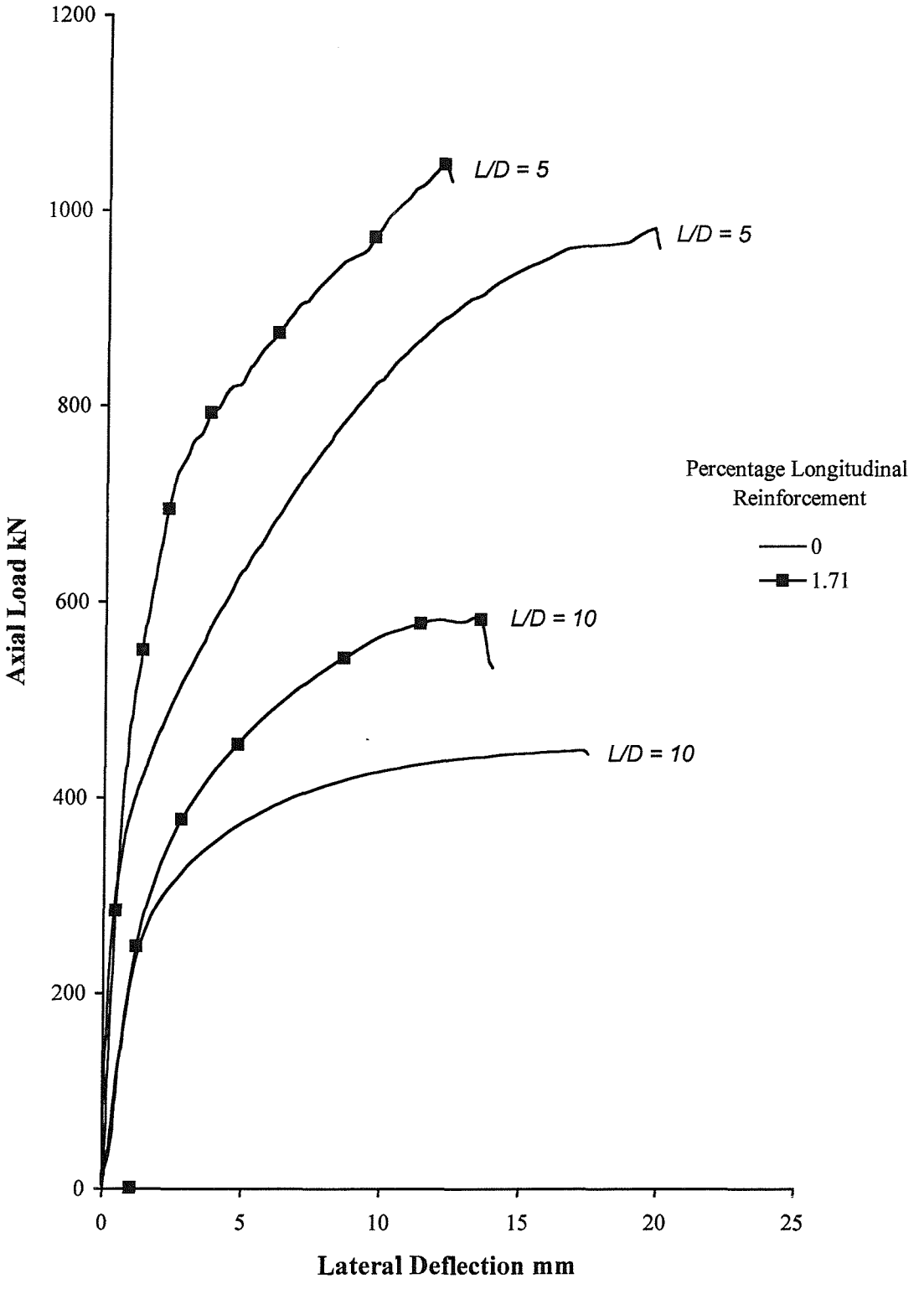

Figure 8.5. Load-deflection curves for the 150 mm diameter concrete-filled carbon FRP-composite columns subjected to eccentric loading

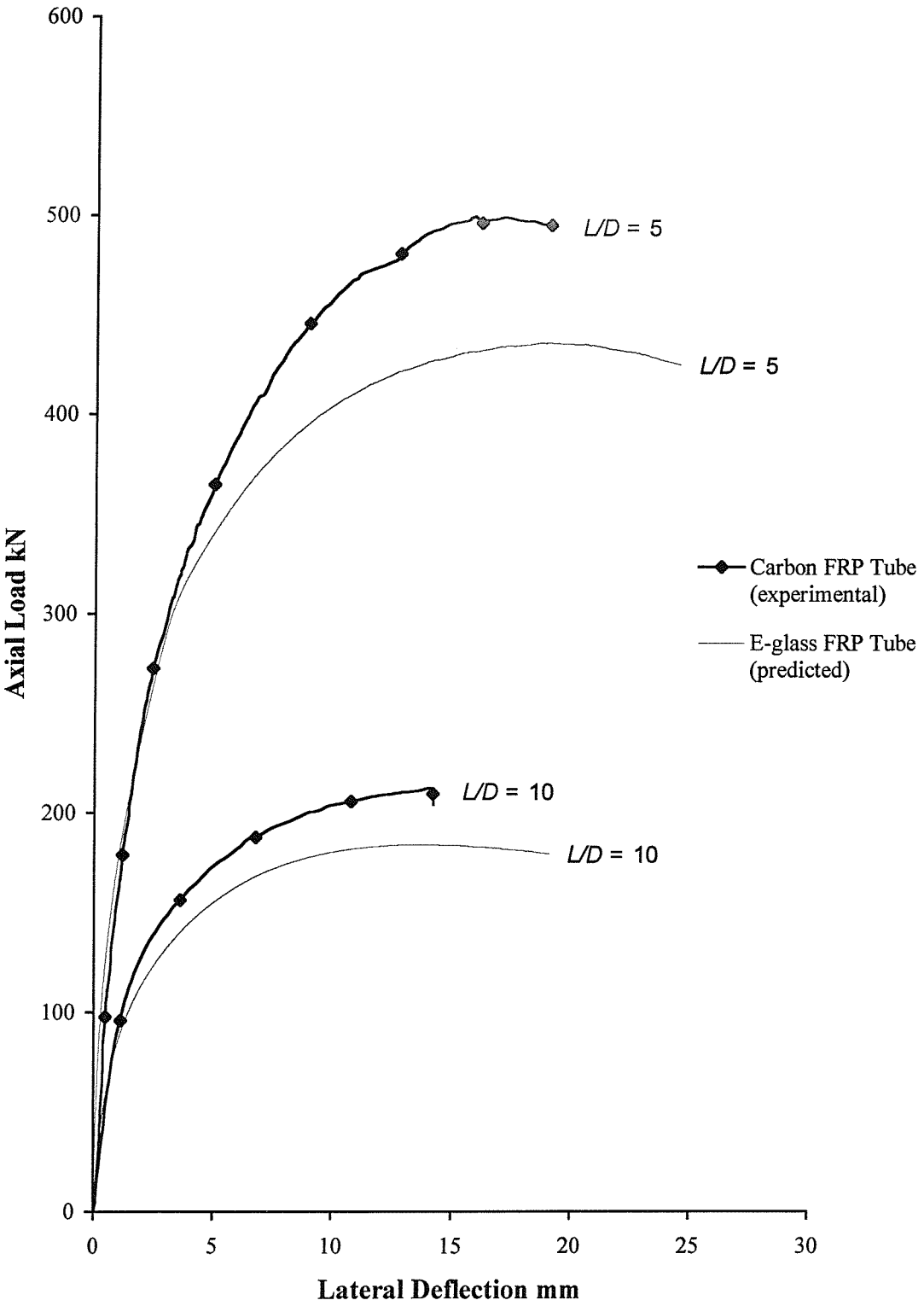

Figure 8.6. Comparison of the experimental load-deflection behaviour of the 100 mm diameter concrete-filled carbon FRP-composite column with no longitudinal reinforcement with the theoretical behaviour of an identical column confined with an E-glass FRP-composite

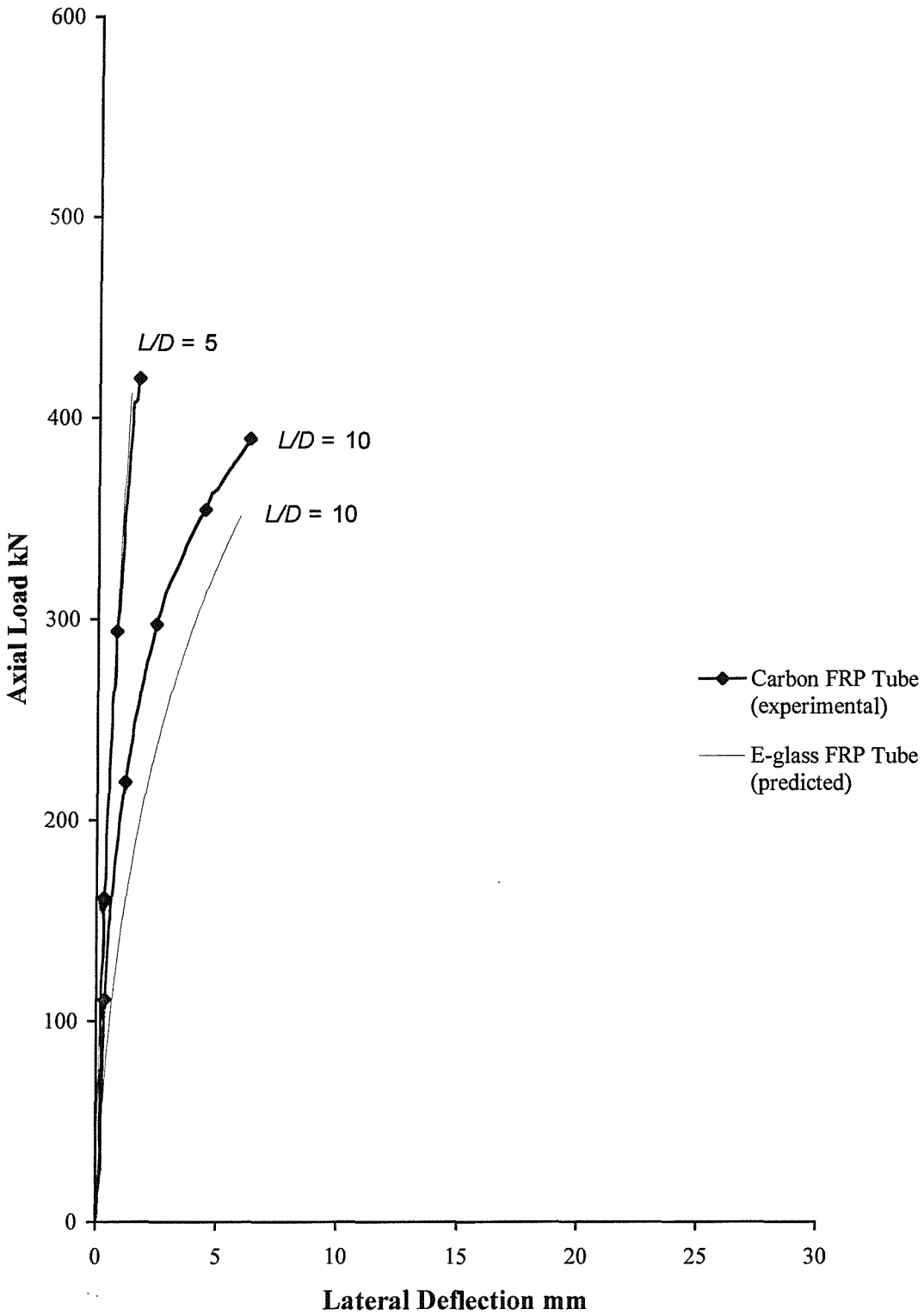

Figure 8.7. Comparison of the experimental load-deflection behaviour of the 100 mm diameter concrete-filled carbon FRP-composite column with longitudinal carbon FRP-composite reinforcement with the theoretical behaviour of an identical column confined with an E-glass FRP-composite

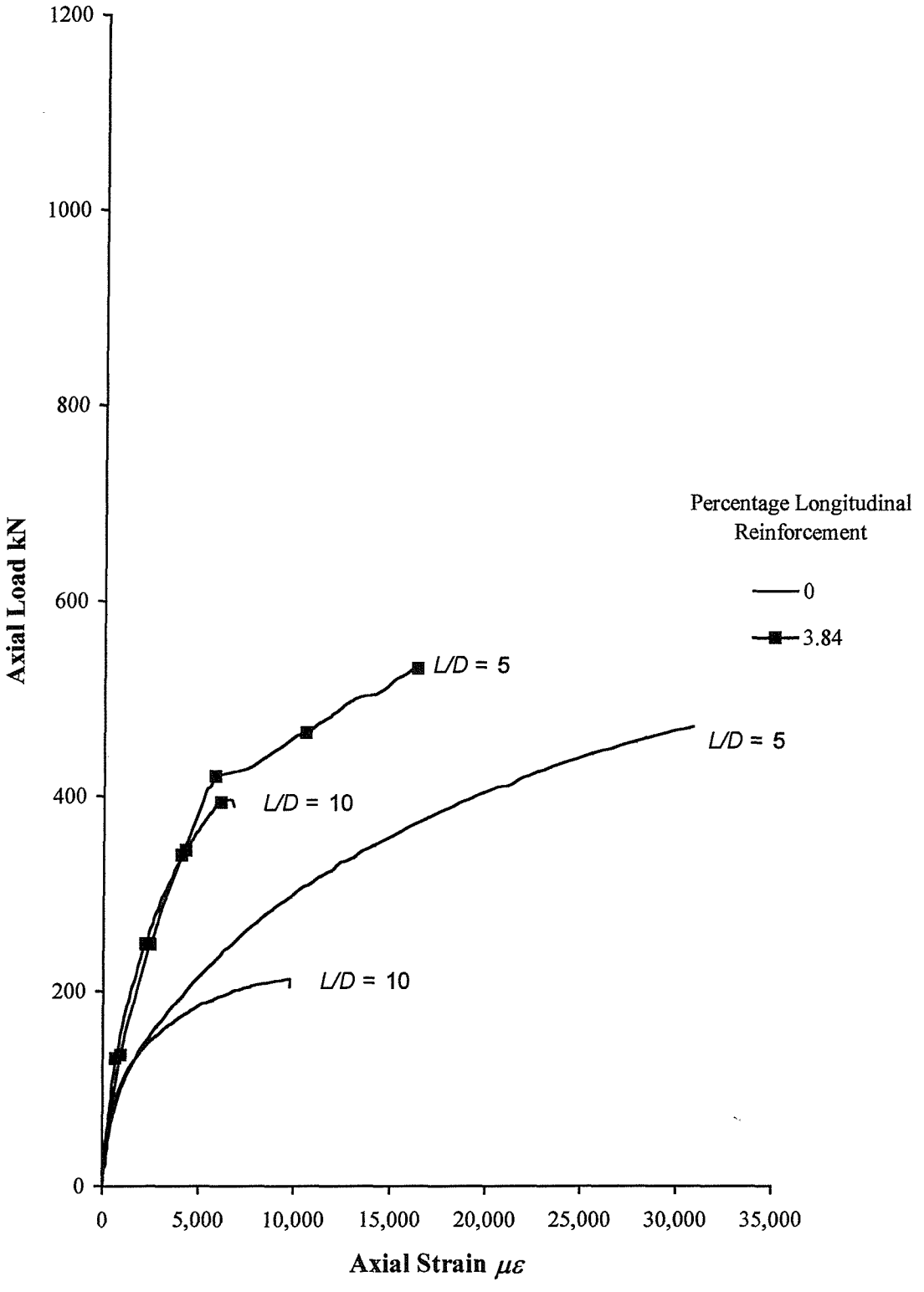

Figure 8.8. Load-strain curves for the 100 mm diameter concrete-filled carbon FRP-composite columns subjected to eccentric loading

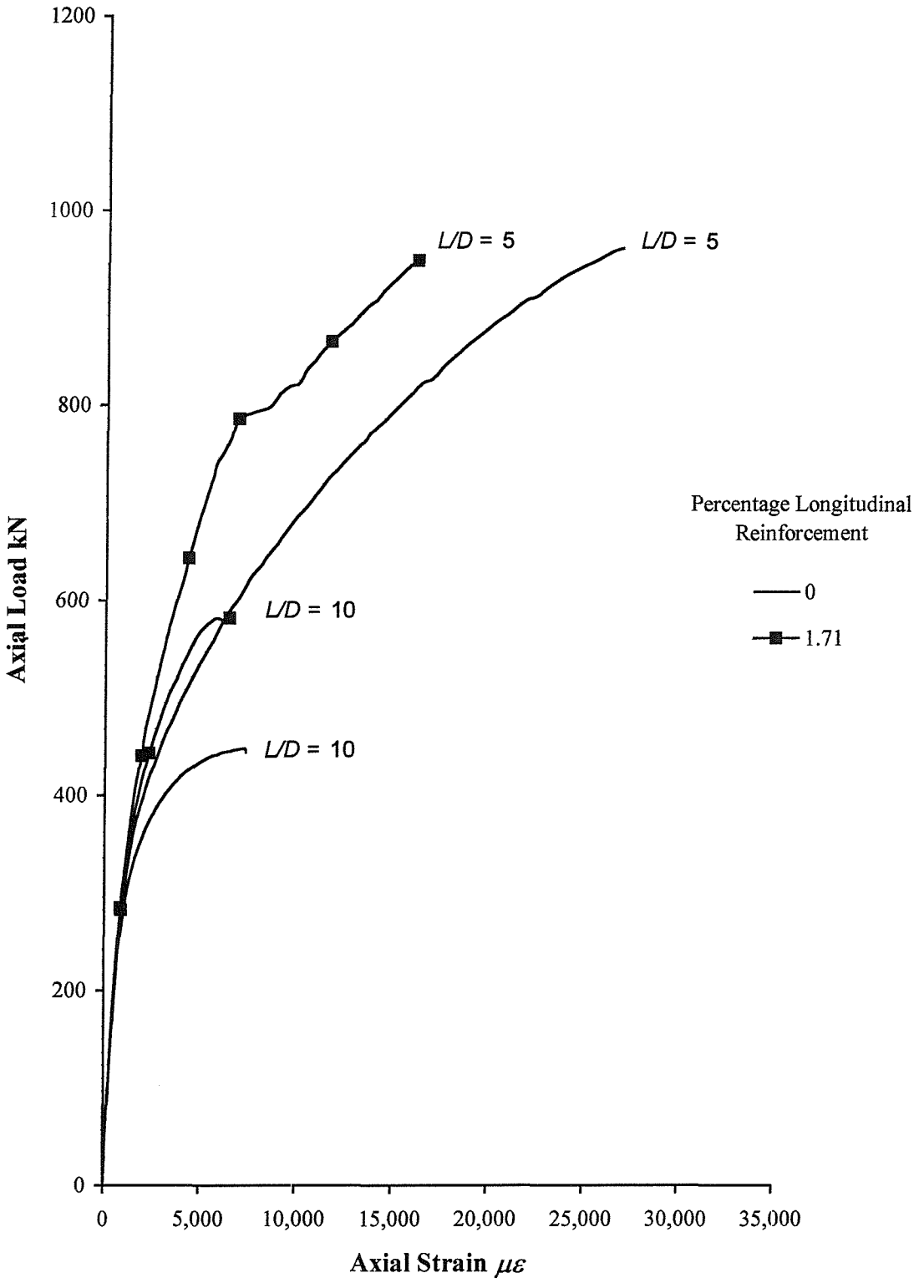

Figure 8.9. Load-deflection curves for the 150 mm diameter concrete-filled carbon FRP-composite columns subjected to eccentric loading

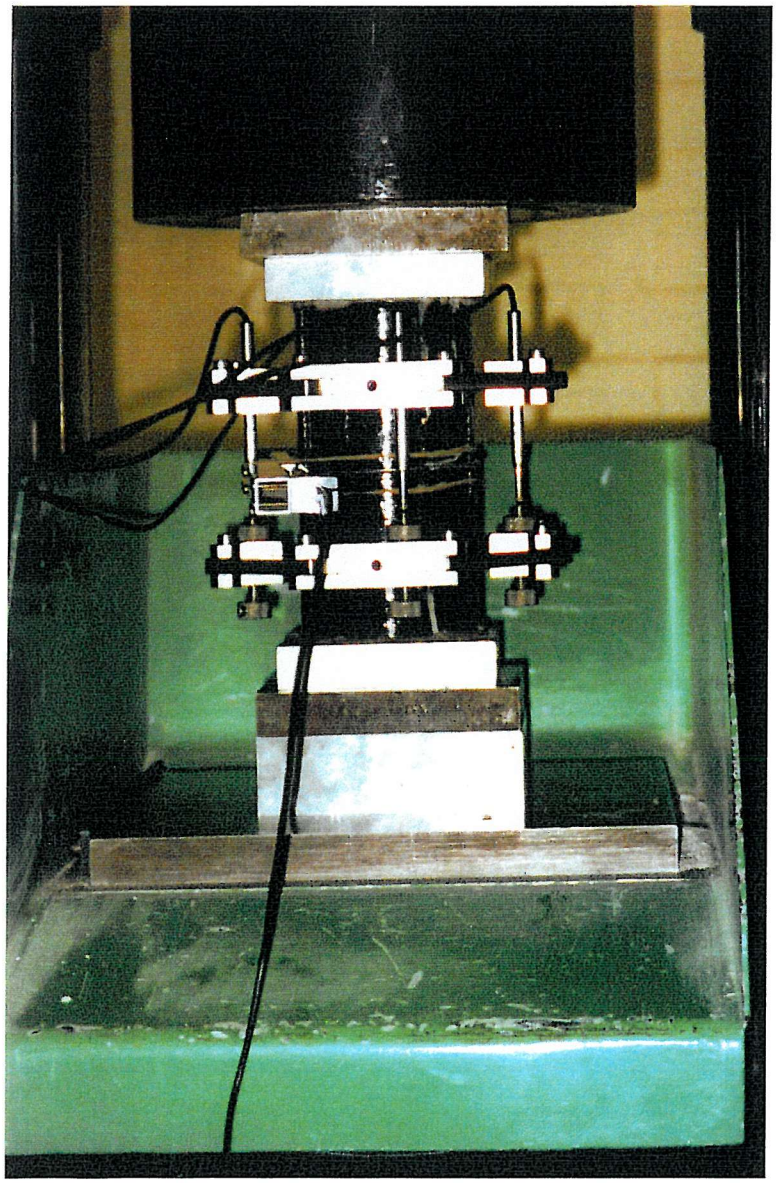

Plate 8.1. A concrete-filled carbon fibre composite stub column

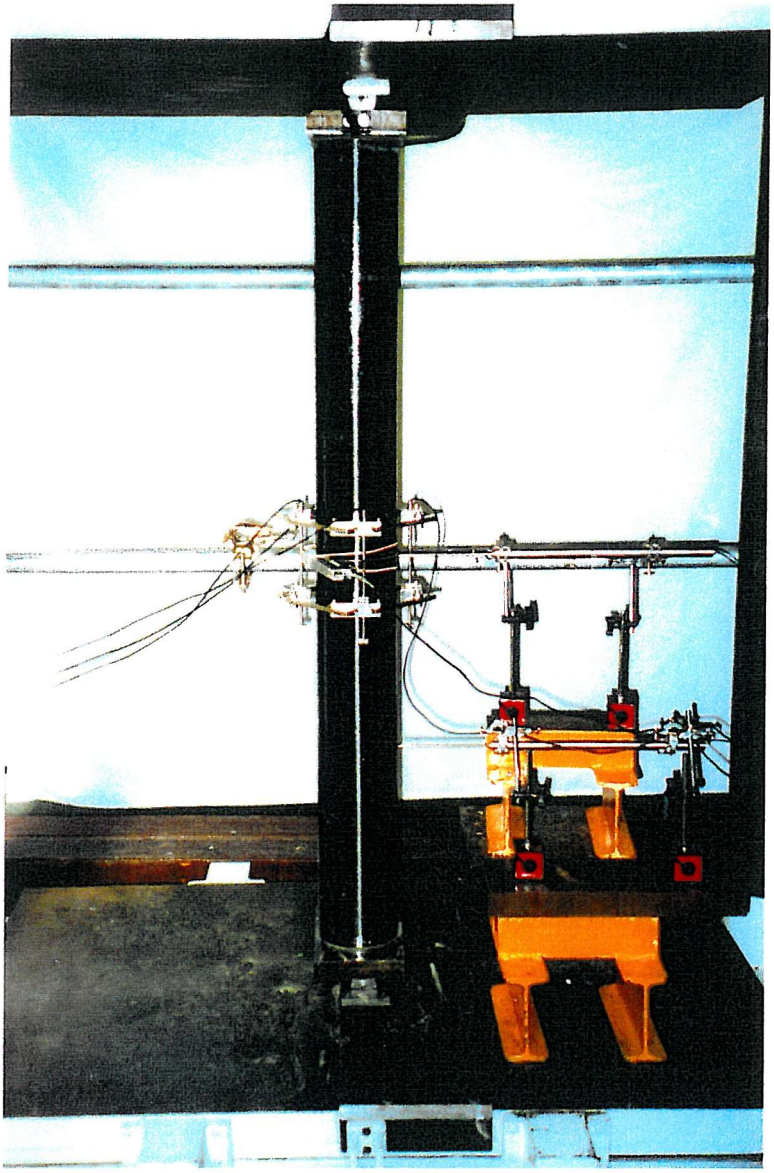

Plate 8.2. The testing arrangement for eccentrically loaded columns

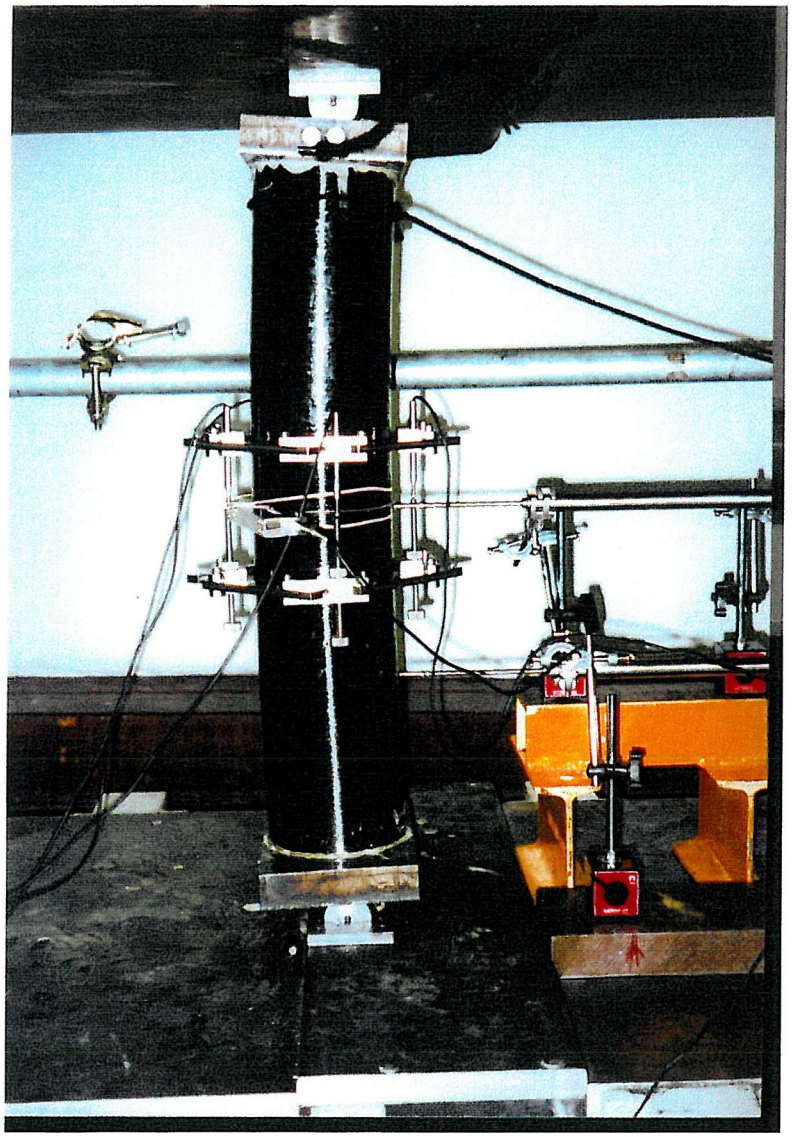

Plate 8.3. Concrete filled carbon fibre composite column at peak load

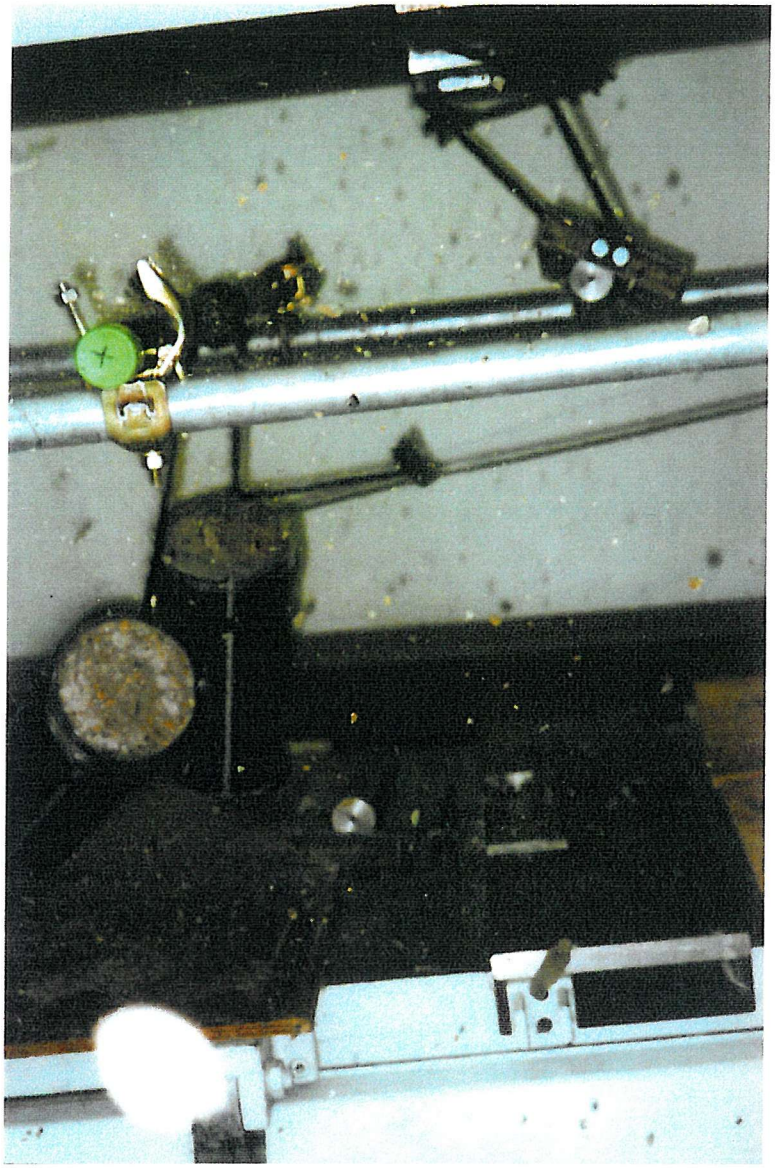

Plate 8.4. Brittle failure of the column due to tensile rupture of the carbon fibre tube

CHAPTER 9

CONCLUSIONS

9.1 CONCLUSIONS

The aim of this research was to develop constitutive equations for the mechanical properties of concrete confined by fibre reinforced composite materials in order to model and predict the short-term behaviour of concrete-filled FRP composite columns.

Traditional methods of construction that exploit the augmented strength of confined concrete use lateral steel reinforcement as the confining mechanism. The equations for the uniaxial stress-strain behaviour and the failure criterion are based on a constant confining pressure, since once the lateral steel reinforcement has yielded, there is a negligible increase in the confining pressure. This work has shown that there are fundamental differences in the behaviour of concrete confined by an elastic-plastic material such as steel, and concrete confined by a linear elastic FRP-composite.

The use of FRP-composites for the confinement of concrete is a relatively new concept, and theoretical and experimental work in this area is limited. Consequently, an extensive experimental programme involving 117 columns was carried out as part of this research to investigate the influence of:

- the type of fibre
- the orientation of the fibres in the composite jacket
- the column diameter and thickness of the composite jacket
- the strength of the concrete
- the column slenderness ratio
- carbon or glass FRP-composite bars as additional longitudinal reinforcement.

9.1.1 Mechanical properties of FRP-confined concrete

To ascertain the mechanical properties of FRP-confined concrete subjected to the maximum state of triaxial containment, twenty-six stub columns confined by E-glass/epoxy FRP-composites were tested to ultimate failure.

The failure mode of the stub columns was governed by the orientation of the confining fibres. The failure mode of the stub columns reinforced with a 90 degree fibre orientation was typified by the fibres rupturing and unwrapping about the middle third of the specimens. Stub columns confined by a 67½ degree fibre orientation failed by the FRP-composite rupturing in a single vertical split along the entire length of the composite. This mode of failure was more sudden and catastrophic than the failure of the 90 degree stub columns. Initial signs of failure in the stub columns reinforced with a 45 degree

FRP-composite was local buckling of the FRP-composite tube and delamination of the outer fibres. Ultimate failure of the stub columns was again due to rupture of the FRP-composite, which was characterised by a zigzag pattern of angle tears. The zigzag pattern of angle tears was a result of localised imperfection due to the fibre crossovers that occur in helically wound FRP-composites.

The failure stress criterion proposed in this thesis is based on the effective hoop modulus of the FRP-composite as opposed to the maximum confining pressure. Thus, no prior knowledge of the lateral expansion of the concrete core is required to determine the confined failure stress. Unlike the tensile strength of E-glass fibres, the elastic modulus is not reduced by mechanical abrasion and therefore is less sensitive to differences in manufacturing processes. The proposed failure criterion has been shown to give good correlation with experimental results for concrete confined with E-glass or carbon FRP-composites using either filament wound tubes or post-wrapping confinement systems.

The strength and ductility of concrete is greatly enhanced when confined by an FRP-composite material. The concrete core immediately prior to failure is a highly fissured material and the structural integrity of the system is only maintained by the confining action induced by the FRP-composite. This, coupled with the brittle nature of the FRP-composite, means that the full benefits of triaxial enhancement cannot be utilised in design. Therefore, it is proposed that the design working stress be based on the limiting failure strain criterion of $3{,}500\mu\varepsilon$, the current limiting UK design strain criterion for unconfined concrete. The remaining axial load capacity due to the confinement can be used as a factor of safety against accidental overload. It is proposed that the ultimate design load is determined using partial safety factors of 1.5 for concrete and 1.8 for the modulus of elasticity of the FRP-composite.

The stress-strain behaviour of FRP-confined concrete is approximately bilinear in both the axial and circumferential directions. The initial behaviour is similar to that of plain concrete since there are negligible confining stresses. Increasing axial compression causes micro-cracks to develop in the concrete core, resulting in an increase in the lateral expansion and an associated reduction in the stiffness of the concrete. At a stress level that corresponds approximately to the critical stress of unconfined concrete, the stress-strain curve enters a transition zone. In this transition zone, the FRP-composite exerts a lateral pressure on the concrete, inhibiting mortar crack development and thus counteracting the reduction in stiffness of the concrete. Once the unconfined strength has been exceeded, the

curve enters a post-crushing region where the stiffness stabilises to a constant value. The slope of the curve in the post-crushing region is highly dependent on the magnitude of the effective hoop modulus of the FRP-composite. For the range of FRP-composite tubes tested, it was found that the stiffness of the confined concrete in the post-crushing region was linearly proportional to the effective hoop modulus, provided the effective hoop modulus was greater than 977 N/mm^2.

The confinement model is based on an equivalent uniaxial strain. The triaxial behaviour of the concrete is defined by the empirically derived parameters. The proposed confinement model gives good agreement with the experimental results for specimens confined by fibres orientated predominately in the hoop direction. As the angle of fibre orientation tends towards 67½ degrees, the model tends to underestimate the axial and circumferential failure strains.

The experimental work on concrete-filled carbon FRP-composite tubes found that the benefits of triaxial confinement from higher modulus carbon fibres were less marked than the benefits from E-glass fibres. The limited empirical data available using carbon FRP confinement prevented the parameters defining the triaxial behaviour from being determined. Therefore, the confinement model proposed in this thesis is restricted to concrete confined by E-glass FRP-composite filament wound tubes.

The main conclusions from this research on the mechanical properties of concrete confined by E-glass FRP-composites can be summarised as follows:

1. The compressive strength and ductility of concrete are enhanced by confinement from E-glass FRP-composite materials. The augmented strength of confined concrete is linearly proportional to the effective hoop modulus of the confining FRP-composite. The largest enhancement in strength is achieved when the confining fibres are orientated in the hoop direction.
2. The stress-strain response of concrete confined by FRP-composites is approximately bilinear. The initial slope of the stress-strain curve is identical to that of unconfined concrete. The secondary slope of the curve is linearly proportional to the effective hoop modulus of the composite provided $\overline{E}_{\theta\theta} \geq 977$ N/mm^2.
3. The failure mode of the column is governed by the orientation of the confining fibres.

4. A confinement model has been proposed, the mathematics of which are capable of reproducing all the characteristics of the stress-strain curves observed in the experimental specimens provided the stiffness of the confining system is adequate.
5. The parameters defining the triaxial behaviour of concrete are dependent on the type of confining fibre.
6. The slope of the stress-strain curve in the post-crushing region is increased by using carbon fibres. However, the benefits of confinement from the higher modulus carbon fibres are not proportional to the increase in the modulus of elasticity nor is the ultimate strength increased proportionally.
7. The design stress-strain curve of FRP-confined concrete should be determined using partial safetly factors of 1.5 for concrete and 1.8 for the modulus of elasticity of the FRP-composite.

9.1.2 Concrete-filled FRP-composite columns

One of the objectives of this research was to investigate different angles of fibre orientation in the FRP-composite tubes. The use of an angle-ply FRP-composite to provide both circumferential and longitudinal reinforcement was not found to increase the flexural capacity of the columns. The use of an off axis winding configuration as opposed to a hoop winding configuration increases the axial modulus of elasticity of the FRP-composite tube with a corresponding reduction in the hoop modulus of elasticity that results in a low confining stiffness. However, the increase in the axial stiffness of the composite tube does not offset the reduction in the augmented strength of the concrete, which results in lower axial failure loads. The use of an off-axis winding configuration may however have other benefits such as increasing the shear capacity of the column. Shear was not investigated in this research programme.

The behaviour of concrete-filled FRP-composite columns with additional longitudinal reinforcement is dependent on the type of longitudinal fibres. The use of higher modulus carbon FRP bars resulted in an increase in the initial stiffness of the columns. Ultimate failure of the column was initiated by failure of the carbon FRP bar at the extreme compressive face of the column at a compressive strain of $4{,}900\mu\varepsilon$. The low compressive failure strain prevents the full benefits of triaxial confinement being utilised and thus reduces the axial failure load when using longitudinal carbon FRP reinforcement.

The initial stiffness of columns is not increased when E-glass FRP bars are used as longitudinal reinforcement. However, E-glass FRP bars do increase the post-crushing stiffness and ultimate load capacity of the columns. The magnitude of the increases in the post-crushing column stiffness and load capacity are proportional to the amount of longitudinal reinforcement. Under triaxial loading, the compressive failure strain of E-glass FRP bars was found to be comparable to or greater than the tensile failure strain. The experimental work and analysis described in this thesis has been developed using the Eurocrete FRP-composite reinforcing bar.

The proposed design method for concrete-filled FRP-composite columns uses the CONFINE computer model developed as part of this research. The deflected profile of the column is assumed to be approximated by a part sinusoidal waveform. The analysis of the column is carried out by successively increasing the mid-height deflection by a predetermined incremental value and calculating the axial load and internal moment that satisfy equilibrium. Due to the non-linearity of the FRP-confined concrete, the solution is iterative.

The CONFINE model gives good correlation with the experimental data for concrete-filled E-glass FRP-composite columns subjected to small eccentricities of load. The mathematics of the model enables predictions of the deflections, curvature and strains in the columns over the entire load history with a high degree of confidence. The behaviour of concrete-filled carbon FRP-composite columns cannot currently be modelled using the CONFINE model, since the parameters defining the equivalent uniaxial stress-strain relationship have not been determined.

The column slenderness ratio at which second-order effects reduce the axial load capacity of concrete-filled FRP-composite columns is lower than that for conventional reinforced concrete columns due to the lower longitudinal stiffness. The limiting slenderness ratio below which second-order effects can be neglected is a function of the degree of confinement. Extrapolation of the experimental data showed that there is no enhancement in load capacity when the slenderness ratio is approximately 12. The ultimate load capacity of columns with slenderness ratios greater than 12 should be calculated on the unconfined concrete core and confinement from the FRP-composite jacket should be ignored.

In the absence of additional research to establish a limiting strain criterion that maintains the structural stability of the column in the event of a partial or total loss of confining pressure, it is proposed that the design load is limited to a maximum compressive strain of

3,500$\mu\varepsilon$. The influences of second-order effects at this limiting compressive strain are negligible provided the column slenderness ratio is less than 12.

The main conclusions from this research on the behaviour of concrete-filled E-glass FRP-composite columns can be summarised as follows:

1. The greatest enhancement in load capacity is achieved using FRP-composites with fibres orientated in the hoop direction.
2. The axial load capacity of columns with slenderness ratios greater than 12 should be based on the unconfined concrete strength, ignoring any confinement induced by the FRP-composite jacket.
3. The ultimate failure strain of concrete-filled FRP-composite columns with additional carbon FRP-composite bars is 4,900$\mu\varepsilon$. Whilst the initial stiffness of the columns is increased, the ultimate failure load is reduced since the low compressive failure strain prevents the full benefits of triaxial containment being utilised.
4. Additional E-glass FRP-composite bars as longitudinal reinforcement increases the post-crushing stiffness and the ultimate load capacity of the column. The compressive failure strain of the E-glass reinforcement with triaxial confinement was comparable to the tensile failure strain.
5. The maximum compressive strain for design should not exceed 3,500$\mu\varepsilon$ to prevent the possibility of brittle failure occurring under normal working loads.
6. The proposed method of analysis is a computer program based on a part sinusoidal deflected waveform. The CONFINE model is capable of reproducing the characteristics observed in the experimental specimens. Second-order effects in the columns are accounted for by the part-sinusoidal deflected waveform.

Concrete-filled FRP-composite columns represent a viable alternative form of construction in aggressive environments where the corrosion of conventional steel reinforcement would be problematic. The proposed columns offer similar axial load capacities to conventional reinforced concrete columns but also offer:

- increased construction rates since the FRP-composite tube acts as permanent formwork;
- a more durable structure since the FRP-composite acts as a barrier to the ingress of aggressive agents;

- an increased factor of safety against accidental overload of the column.

9.2 RECOMMENDATIONS FOR FURTHER RESEARCH

This research has investigated several of the main parameters that affect the behaviour of concrete-filled FRP-composite columns. The experiments carried out as part of this research have provided an extensive database of the detailed response on concrete-filled FRP-composite columns. However, this is a relatively new construction concept and thus there are numerous avenues for future research. Proposals to extend and supplement the research can be categorised as either:

- those aimed at improving the confinement model and extending its application to all types of FRP-composites;
- those that would extend the range of experimental data concerning the behaviour of concrete-filled FRP-composite columns.

A confinement model for FRP-confined concrete has been proposed as part of this research. However, the validity of the proposed model is limited to concrete confined by E-glass FRP-composites with an effective hoop modulus greater than 977 N/mm^2. The mechanical properties of concrete confined by carbon or aramid FRP-composites need to be determined. Further testing of concrete confined by hoop wound E-glass FRP-composites with effective hoop moduli less than 977 N/mm^2 is also required to establish the minimum requirements for adequate FRP-composite confinement.

This work examined the behaviour of columns subjected to short-term monotonic loading. However, the long-term stability of the concrete-filled FRP-composite columns is of significant importance. One of the main recommendations of the work presented in this thesis is the adoption of a design compressive strain of $3{,}500\mu\varepsilon$ to prevent a brittle failure of the column from occurring. The adoption of a $3{,}500\mu\varepsilon$ limiting strain criterion is a conservative approach and future experimental work on the long-term behaviour of the columns may result in this value being increased.

Any work on long-term loading should also investigate the potential for the FRP-composite to creep rupture. Under long-term loads, FRP-composites no longer exhibit linear elastic behaviour. The mechanical properties of the resin matrix are time-, frequency- and rate-dependent. Thus, under sustained stress, the strain in the FRP-composite continues to increase while the magnitude of stress needed to produce rupture

diminishes with time. The behaviour is complex and is influenced by temperature and the environment.

Dynamic fatigue loading of an FRP-composite results in micro-damage such as resin cracking, initiating bond breakdown between the fibres and the resin. E-glass FRP-composites are more sensitive to fatigue than higher modulus FRP-composites. Due to their low modulus of elasticity, E-glass FRP-composites work at relatively high strains which approach the cracking strain of the resin matrix and in turn results in a reduced fatigue life.

The degree of triaxial confinement has been shown to diminish as the column slenderness increases. This thesis proposes that the effects of triaxial confinement be ignored for concrete-filled FRP-composite tubes with $L/D > 12$. The benefits of triaxial confinement are also known to diminish as the end moment increases. However, the validity of the CONFINE model has only been verified for columns subject to the minimum end eccentricity for a nominally axially loaded column. To verify the CONFINE model, further experimental work is required on stocky columns subjected to larger eccentricities and pure bending.

One of the aims of this research was to develop a non-ferrous reinforcing system for concrete columns in aggressive environments. The reinforcing system used in this research comprised of filament wound tubes with additional longitudinal FRP bars epoxy bonded to the interior wall of the tubes. However, epoxy bonding the FRP bars to the interior surface of the tubes was labour intensive. If this form of column reinforcement is to be used in the construction industry, a fully automated fabrication process is required. The envisaged form for the reinforcing system consists of a pultruded FRP-composite tube with longitudinal ribs and fibres over-wound in the hoop direction to provide the confinement.

The development of a connection between concrete-filled FRP-composite columns and beams is essential if this form of construction is to be used in civil engineering. However, connections in the FRP-composites present enormous complexities due to the anisotropic nature of composite materials.

An alternative application to the aggressive environments for concrete-filled FRP-composite columns is seismic design due to the enhanced ductility of the concrete. FRP-composite wrapping of columns is currently being using in the United States to strengthen bridge piers against earthquake loading. Whilst the ductility of the concrete under

monotonic loading is significantly enhanced by FRP-confinement, the performance of the columns under load reversal needs quantifying.

One disadvantage of this form of construction is the slow development of any confining action. The initial behaviour of concrete-filled FRP-composite columns may be improved by using an expanding agent, such as aluminium oxide, in the concrete mix to provide active confinement prior to axial load being applied. The use of an expanding agent may increase the initial confined strength of the concrete, thus improving the design failure load at 3,500$\mu\varepsilon$.

The above proposals for further avenues of research highlight the need for a greater understanding of the mechanics of concrete confined by fibre reinforced composite materials. This is essential to make the safest and most economic use of an innovative form of construction.

REFERENCES

1. Hobbs, D.W.: (1996) 'Chloride ingress and chloride induced corrosion in reinforced concrete members', *4th International Symposium on Corrosion in Concrete Construction*, The Royal Society of Chemistry, pp 124-135.
2. Faza, S.S. and GangaRao, H.V.S.: (1993) 'Glass FRP reinforcing bars for concrete', *Fiber-Reinforced-Plastic (FRP) for Concrete Structures: Properties and Applications*, (Ed. A. Nanni), Elsevier Science Publishing B.V., pp 167-188.
3. Faza, S.S. and GangaRao, H.V.S.: (1993) 'Theoretical and experimental correlation of behaviour of concrete beams reinforced with fiber reinforced plastic rebars', *Fiber-Reinforced-Plastic Reinforcement for Concrete Structures* (Eds. A. Nanni and C.W. Dolan), SP-138, American Concrete Institute, Detroit, pp 599-614.
4. Nanni, A.: (1993) 'Flexural behaviour and design of RC members using FRP reinforcement', *Journal of Structural Engineering, Proc. ASCE*, Vol. 119, No. 11, pp 3344-3359.
5. Clarke, J.L. and Waldron, P.: (1996) 'The reinforcement of concrete structures with advanced composites', *The Structural Engineer,* Vol. 74, No. 17, pp 283-288.
6. Dolan, C.W.: (1990) 'Developments in non-metallic prestressing tendons', *PCI Journal,* September-October, pp 80-88.
7. Tsuji, Y., Kanda, M.M. and Tamura, T.: (1993) 'Applications of FRP materials to prestressed concrete bridges and other structures in Japan', *PCI Journal,* July-August, pp 50-58.
8. Zia, P., Ahmad S.H., Garg, R.K. and Hanes, K.: (1992) 'Flexural and shear behaviour of concrete beams reinforced with 3-D continuous carbon fibre fabric', *Concrete International,* December, pp 48-52.
9. Meier, U.: (1992) 'Carbon fibre-reinforced polymers: modern materials in bridge engineering', *Structural Engineering International*, IABSE, Vol. 2, No. 1, pp 7-12.
10. Garden, H.N., Hollaway, L.C. and Thorne, A.M.: (1997) 'A preliminary evaluation of carbon fibre reinforced polymer plates for strengthening concrete members', *Proc. Institution of Civil Engineers: Structures and Buildings*, Vol. 123, May, pp 127-142.

11. Priestley, M.J.N.; Seible, F. and Fyfe, E.: (1992) 'Column seismic retrofit using fibreglass/epoxy jackets', *Advanced composite materials in bridges and structures,* (Eds. K.W. Neale and P. Labossière), Canadian Society for Civil Engineering, Montreal, pp 287-297.

12. Fyfe, E.R.: (1994) 'New concept for wrapping columns with a high strength fiber/epoxy system', *Proc. 3rd Materials Engineering Conference - Infrastructure: New Materials and Methods of Repair*, (Ed K.D. Basham), San Diego, California, pp1156-1162.

13. Watson, R.J.: (1994) 'Column retrofit of short and medium span bridges and structures using high strength fiber composites', *Developments in Short and Medium Span Bridge Engineering,* (Eds. A.A Mufti; B. Bakht and L.G. Jaeger), Canadian Society for Civil Engineering, Montreal, pp 983-994.

14. Cercone, L. and Korff, J.: (1997) 'Putting the wraps on quakes', *Civil Engineering*, Vol. 67, No. 7, pp 60-61.

15. Fardis, M.N. and Khalili, H.H.: (1981) 'Concrete encased in fiberglass-reinforced plastic', *Journal of the American Concrete Institute*, Vol. 78, No. 6, pp 440-446.

16. Fardis, M.N. and Khalili, H.H.: (1982) 'FRP-encased concrete as a structural material', *Magazine of Concrete Research*, Vol. 34, No. 121, pp 191-202.

17. Ahmad, S.H., Khaloo, A.R. and Irshaid, A.: (1991) 'Behaviour of concrete spirally confined by fibreglass filaments', *Magazine of Concrete Research*, Vol. 43, No. 156, pp 143-148.

18. Harmon, T.G. and Slattery, K.T.: (1992) 'Advanced composite confinement of concrete', *Advanced composite materials in bridges and structures,* (Eds. K.W. Neale and P. Labossière), Canadian Society for Civil Engineering, Montreal, pp 299-306.

19. Nanni, A., Norris, M.S. and Bradford, N.M.: (1993) 'Lateral confinement of concrete using FRP reinforcement', *Fiber-Reinforced-Plastic Reinforcement for Concrete Structures* (Eds. A. Nanni and C.W. Dolan), SP-138, American Concrete Institute, Detroit, pp 193-209.

20. Saadatmanesh, H.: (1995) 'Wrapping with composite materials', *Non-metallic (FRP) Reinforcement for Concrete Structures* (Ed. L. Taerwe), E & FN Spon, London, pp 593-600.

21. Howie, I. and Karbhari, V.M.: (1995) 'Effect of tow sheet composite wrap architecture on strengthening of concrete due to confinement: I - experimental studies', *Journal of Reinforced Plastics and Composites*, Vol. 14, No. 9, pp 1008-1030.

22. Picher, F., Rochette, P. and Labossière, P.: (1996) 'Confinement of concrete cylinders with CFRP', *ICCI '96 Fiber Composites in Infrastructure,* (Eds. H. Saadatmanesh and M.R. Ehsani), University of Arizona, Tucson, pp 829-841.

23. Howie, I. and Karbhari, V.M.: (1997) 'Effect of tow sheet composite wrap architecture on strengthening of concrete due to confinement: II – strain and damage effects', *Journal of Reinforced Plastics and Composites*, Vol. 16, No. 11, pp 1039-1063.

24. Demer, M. and Neale, K.W.: (1999) 'Confinement of reinforced concrete columns with fibre-reinforced composite sheets – an experimental study', *Canadian Journal of Civil Engineering,* Vol. 26, No. 3, pp 226-241.

25. Parker, D.: (1998) 'Keeping damage under wraps', *New Civil Engineer,* 20/27 August, pp 31-31.

26. Vassie, P.: (1984) 'Reinforcement corrosion and durability of concrete bridges', *Proceedings of the Institution of Civil Engineers*, Part 1, Vol. 76, Aug, pp 713-723.

27. Hobbs, D.W.; Marsh, B.K.; Matthews, J.D. and Petit, S.: (1998) 'Minimum requirements for concrete to resist carbonation-induced corrosion of reinforcement', *Minimum requirements for durable concrete* (Ed. D.W. Hobbs), British Cement Association, Crowthorne, pp 11-42.

28. Locke, C.E.: (1986) 'Corrosion of steel in Portland cement concrete: fundamental studies', *Corrosion Effects of Stray Currents and Techniques for Evaluating Corrosion of Rebars in Concrete* (Ed. V. Chalker), ASTM STP-906, pp 5-14.

29. Richart, F.E., Brandtzaeg, A. and Brown, R.L.: (1928) 'A study of the failure of concrete under compressive stresses', *Engineering Experimental Station,* Bulletin No. 185, University of Illinois, pp 104.

30. Newman, K. and Newman, J.B.: (1971) 'Failure theories and design criteria for plain concrete', *Structures, Solid Mechanics and Engineering Design: The Proceedings of the Southampton 1969 Engineering Materials Conference*, Wiley-Interscience, New York, pp 963-995.

31. Ahmad, S.H. and Shah, S.P.: (1982) 'Complete triaxial stress-strain curves for concrete', *Journal of the Structural Division, Proc. ASCE*, Vol. 108, No. ST4, pp 728-742.

32. Saatcioglu, M. and Razvi, S.A.: (1992) 'Strength and ductility of confined concrete', *Journal of Structural Engineering, Proc. ACSE,* Vol. 118, No. 6, pp 1590-1607.

33. Chung, K.F. and Narayanan, R.: (1994) *P142: Composite column design to Eurocode 4*, The Steel Construction Institute, Ascot, pp106.

34. Virdi, K.S. and Dowling, P.J.: (1976) 'A unified design method for composite columns', *International Symposium,* IABSE, Vol. 36(II), Zurich, pp165-184.

35. Klöppel, K. and Goder, W.: (1957) 'Traglastversuche mit ausbetonierten Stahlrohren und Aufstellung einer Bemessungformel', *Der Stahlbau*, Berlin, Vol. 26, No. 1.

36. Gardner, N.J. and Jacobson, E.R.: (1969) 'Structural behaviour of concrete filled steel tubes', *Journal of the American Concrete Institute*, Vol. 64, No. 7, pp 404-413.

37. Furlong, R.W.: (1967) 'Strength of steel-encased concrete beam columns', *Journal of the Structural Division, Proc. ASCE,* Vol. 93, No. ST5, pp 113-124.

38. Knowles, R.B. and Park, R.: (1969) 'Strength of concrete filled steel tubular columns', *Journal of the Structural Division, Proc. ASCE,* Vol. 95, No. ST12, pp 2565-2587.

39. Prion, H.G.L and Boehme, J.: (1994) 'Beam-column behaviour of steel tubes filled with high-strength concrete', *Canadian Journal of Civil Engineering,* Vol. 21, No. 2, pp 207-218.

40. Sen, H.K.: (1969) 'Triaxial effects in concrete filled tubular steel columns', Ph.D. Thesis, University of London, 1969.

41. British Standards Institution: (1994) *DD ENV 1994-1-1 Eurocode 4: Design of composite and concrete structures Part1.1 General rules and rules for buildings,* BSI, London.

42. Sheikh, S.A. and Uzumeri, S.M.: (1980) 'Strength and ductility of tied concrete columns', *Journal of the Structural Division, Proc. ASCE*, Vol. 106, No. ST5, pp 1079-1102.

43. Mander, J.B., Priestly, M.J.N. and Park, R.: (1988) 'Theoretical stress-strain model for confined concrete', *Journal of Structural Engineering, Proc. ASCE,* Vol. 114, No. 8, pp 1804-1826.

44. Cusson, D. and Paultre, P.: (1995) 'Stress-strain model for confined high-strength concrete', *Journal of Structural Engineering, Proc. ASCE*, Vol. 121, No. 3, pp 468-477.

45. Mander, J.B., Priestly, M.J.N. and Park, R.: (1988) 'Observed stress-strain behaviour of confined concrete', *Journal of Structural Engineering, Proc. ASCE,* Vol. 114, No. 8, pp 1827-1849.

46. Sheikh, S.A. and Toklucu, M.T.: (1993) 'Reinforced concrete columns confined by circular spirals and hoops', *ACI Structural Journal,* Vol. 90, No. 5, pp 542-553.

47. Issa, M.A. and Tobaa, H.: (1994) 'Strength and ductility enhancement in high-strength confined concrete', *Magazine of Concrete Research,* Vol. 46, No. 168, pp 177-189.

48. Chen, W.F. and Saleeb, A.F.: (1994) *Constitutive Equations for Engineering Materials Volume 1: Elasticity and Modeling*, Elsevier, Amsterdam.

49. Kent, D.C. and Park, R.: (1971) 'Flexural members with confined concrete', *Journal of the Structural Division, Proc. ASCE*, Vol. 97, No. ST7, pp 1969-1990.

50. Park, R.; Priestly, M.J.N. and Gill, W.D.: (1982) 'Ductility of square-confined concrete columns', *Journal of the Structural Division, Proc. ACSE*, Vol. 108, No. ST4, pp 929-950.

51. Watanabe, K., Sonobe, Y. and Okamoto, T.: (1991) 'Centrally loaded compression test of concrete columns reinforced with braided aramid fibre rods', *Proc. of Japan Concrete Institute*, Vol. 13, No. 2, pp 801-806.

52. Kobota, T. and Murakami, M.: (1991) 'Experimental study on stress-strain relationship of confined concrete reinforced by FRP bars', *Proc. of Japan Concrete Institute*, Vol. 13, No. 2, pp 843-848.

53. Hosoi, R., Mutsuyoshi, H., Tanaguchi, H. and Kita, T.: (1992) 'Compressive properties of concrete members reinforced with FRP as transverse reinforcement', *Proc. of Japan Concrete Institute*, Vol. 14, No. 2, pp 637-642.

54. Saadatmanesh, H.; Ehsani, M.R. and Li, M.W.: (1994) 'Strength and ductility of concrete columns externally reinforced with fiber composite straps', *American Concrete Institute Structural Journal*, Vol. 91, No. 4, pp 434-447.

55. Hoppel, C.P.R, Bogetti, T.A. and Gillespie, J.W.: (1997) 'Design and analysis of composite wraps for concrete columns', *Journal of Reinforced Plastics and Composites*, Vol. 16, No. 7, pp 588-602.

56. Karbhari, V.M. and Gao, Y.: (1997) 'Composite jacketed concrete under uniaxial compression – verification of simple design equations', *Journal of Materials in Civil Engineering, Proc. ASCE,* Vol. 9, No. 4, pp 185-193.

57. Harmon, T. Slattery, K. and Ramakrishnan, S.: (1995) 'The effect of confinement stiffness on confined concrete', *Non-metallic (FRP) Reinforcement for Concrete Structures* (Ed. L. Taerwe), E & FN Spon, London, pp 585-592.

58. Mirmiran, A. and Shahawy, M.: (1997) 'Behaviour of concrete columns confined by fibre composites', *Journal of Structural Engineering, Proc. ASCE*, Vol. 123, No. 5, pp 583-590.

59. Samaan, M.; Mirmiran, A. and Shahawy, M.: (1998) 'Model of concrete confined by fiber composites', *Journal of Structural Engineering, Proc. ASCE*, Vol. 124, No. 9, pp 1025-1031.

60. Saafi, M.; Toutanji, H.A. and Li, Z.: (1999) 'Behaviour of concrete columns confined with fibre reinforced polymer tubes', *American Concrete Institute Materials Journal*, Vol. 96, No. 4, pp 500-509.

61. British Standards Institution: (1985) *Structural Use of Concrete: Code of Practice for Design and Construction.* BS 8110, Part 1, BSI, London.

62. Phillips, L.N. (Ed): (1989) *Design with Advanced Composite Materials*, The Design Council, London.

63. Agarwal, B.D. and Broutman, L.J.: (1990) *Analysis and Performance of Fiber Composites (2nd Edition),* John Wiley & Sons, New York.

64. Thomas, S.J. and Jolly, C.K.: (1997) 'Durability of fibre-composite reinforcement in contact with cementitious materials and aggressive environments', *4th CANMET/ACI International Conference on Durability of Concrete*, Sydney, pp 1-21.

65. Morley, J.G.: (1987) *High-Performance Fibre Composites,* Academic Press, London, pp 89-119.

66. Kobayashi, K. and Fujisaki, T.: (1995) 'Compressive behaviour of FRP reinforcement in non-prestressed concrete members', *Non-metallic (FRP) Reinforcement for Concrete Structures* (Ed. Taerwe, L.), E & FN Spon, London, pp 267-274.

67. Hollaway, L.C. (Ed): (1990) *Polymers and Polymer Composites in Construction,* Thomas Telford, London, pp 19.

68. Lubin, G. (Ed): (1982) *Handbook of Composites,* Van Nostand, New York, pp449-478.

69. Chou, T.W.: (1992) *Microstructural Design of Fiber Composites,* Cambridge University Press, pp 29-39.

70. British Standards Institution: (1977) *Determination of Loss on Ignition.* BS2782, Part 10, Method 1002, BSI, London.

71. CEB-FIP Model Code: (1990) Comite Euro-International du Beton, Lausanne.

72. Chen, W.F.: (1994) *Constitutive Equations for Engineering Materials Volume 2: Plasticity and Modeling,* Elsevier, Amsterdam, pp 1-26.

73. Neville, A.M.: (1981) *Properties of Concrete 3rd Edition,* Longman Scientific & Technical, London, pp 370-371.

74. Richard, R.M. and Abbott, B.J.: (1975) 'Versatile elastic-plastic stress-strain formula', *Journal of the Engineering Mechanics Division, Proc. ASCE*, Vol. 101, No. EM4, pp 511-515.

75. Guo, M.: (1998) *Finite Element Analysis of Confined Concrete in Building Frame Components and Joints*, PhD Thesis, University of Southampton.

76. Institution of Structural Engineers: (1999) *Interim Guidance on the Design of Reinforced Concrete Structures using Fibre Composite Reinforcement*, The Institution of Structural Engineers, London, pp 25-26

77. Hognestad, E.; Hanson, N.R. and McHenry, D.: (1955) 'Concrete stress distribution in ultimate strength design', *Journal of the American Concrete Institute*, Vol. 27, No. 4, pp 455-479.

78. Cranson, W.B.: (1972) *Analysis and Design of Reinforced Concrete Columns*, Research Report No. 20, Cement & Concrete Association, London, pp 54.

79. Weltner, K.; Grosjean, J.; Schuster, P. and Weber, W.J.: (1986) *Mathematics for Engineers and Scientists*, Stanley Thornes, Cheltenham, pp 408-409.

80. Saatcioglu, M; Salamat, A.H. and Razvi, S.R.: (1995) 'Confined columns under eccentric loading', *Journal of Structural Engineering, Proc. ASCE*, Vol. 121, No. 11, pp 1547-1555.

81. Eurocrete-EV1065 (Eureka): (1997) *The Development of Non-Ferrous Reinforcement for Concrete Structures,* IL 12/2/120 (UK DTI LINK).

82. Anon: (1997) 'Shöck ComBAR - Betonbewehrugselemente aus glasfaserverstarktem Kunststoff', Shöck Bauteile GmbH, Baden-Baden-Steinbach.

83. Anon: (1989) 'Fibreglass Reinforced Plastic Rebar Data Sheet', KODIAK International Gratings Inc., Houston.

84. Chamis, C.C.: (1987) 'Simplified composite micromechanical equations for mechanics, thermal, and moisture related properties', *Engineering Guide to Composite Materials* (Eds. J.W. Weeton; D.M. Peters and K.L. Thomas), American Society for Metals, Ohio, pp 8-24

BIBLIOGRAPHY

Allen, H.G. and Bulson, P.S.: (1980) *Background to Buckling*, McGraw-Hill, London.

Basham, K.D.: (1994) *Infrastructure: New Materials and Methods of Repair – Proc. 3rd Materials Engineering Conference,* San Diego, ASCE.

Bazant, Z.P. and Cedolin, L.: (1991) *Stability of Structures: Elastic, Inelastic, Fracture and Damage Theories,* Oxford University Press, New York.

Elwi, A.A. and Murray, D.W.: (1979) 'A 3D hypoelastic concrete constitutive relationship', *Journal of the Engineering Mechanics Division, Proc. ASCE,* Vol. 105, No. EM4, pp 623-641.

Gardner, N.J.: (1969) 'Triaxial behaviour of concrete', *Journal of the American Concrete Institute*, Vol. 66, No. 2, pp 136-146.

Herakovich, C.T.: (1998) *Mechanics of Fibrous Composites,* John Wiley & Sons, New York.

Hognestad, E.: (1951) 'A study of combined bending and axial load in reinforced concrete members', *Engineering Experiment Station Bulletin No. 399*, University of Illinois, pp 128.

Kurt, C.E.: (1978) 'Concrete filled structural plastic columns', *Journal of the Structural Division, Proc. ASCE,* Vol. 104, No. ST1, pp 55-63.

Madas, P. and Elnashai, A.S.: (1992) 'A new passive confinement model for the analysis of concrete structures subjected to cyclic and transient dynamic loading', *Earthquake Engineering and Structural Dynamics*, Vol. 21, No. 5, pp 409-431.

Moy, S.S.J.: (1981) *Plastic Methods for Steel and Concrete Structures,* Macmillan, London.

Munday, A.J. and Farrar, R.A.: (1979) *An Engineering Data Book*, Macmillan, London.

Nanni, A.: (1993) *Fiber-Reinforced-Plastic (FRP) Reinforcement for Concrete Structures,* Elsevier Science Publishers B.V., Amsterdam.

Nanni, A and Dolan, C.W.: (1993) *Fiber Reinforce Plastic Reinforcement for Concrete Structures – International Symposium,* ACI SP138, Detroit, pp 977

Neale, K.W. and Labossiere, P.: (1992) *Advanced Composite Materials in Bridges and Structures,* Canadian Society for Civil Engineering, Montreal.

Neville, A.M. and Kennedy, J.B.: (1964) *Basic Statistical Methods for Engineers and Scientists*, International Textbook Co, Scranton.

Pantazopoulou, S.J.: (1995) 'Role of expansion on mechanical behaviour of concrete', *Journal of Structural Engineering*, Vol. 12, No. 12, pp 1795-1800.

Taerwe, L.: (1995) *Non-metallic (FRP) Reinforcement for Concrete Structures,* E & FN Spon, London, pp 714.

Timoshenko., S.P. and Goodier, J.N.: (1970) *Theory of Elasticity 3rd Ed.*, McGraw-Hill, New York.

APPENDIX A

THE HOOP STRESS IN A THIN SHELL SUBJECT TO INTERNAL PRESSURE

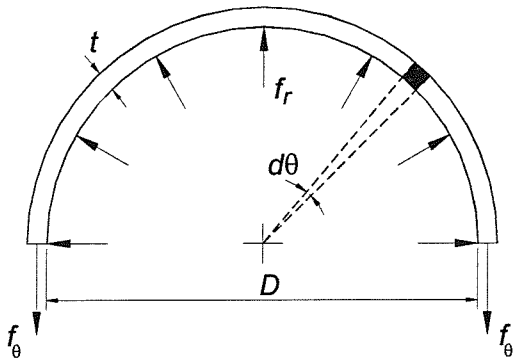

If θ is small arc length $\approx \frac{D}{2} d\theta$

Radial component of force on element $= f_r \frac{D}{2}.d\theta$

Vertical force component acting on element $= f_r \frac{D}{2}.d\theta.\sin\theta$

$$\text{Total vertical force} = \int_0^{\pi} f_r \frac{D}{2} \sin\theta \, d\theta = f_r D$$

Vertical equilibrium $\quad 2f_\theta t = f_r D$

$$f_r = \frac{2t}{D} f_\theta$$

APPENDIX B

EXPERIMENTAL STRESS-STRAIN CURVES FOR CONCRETE-FILLED E-GLASS FRP-COMPOSITE STUB COLUMNS

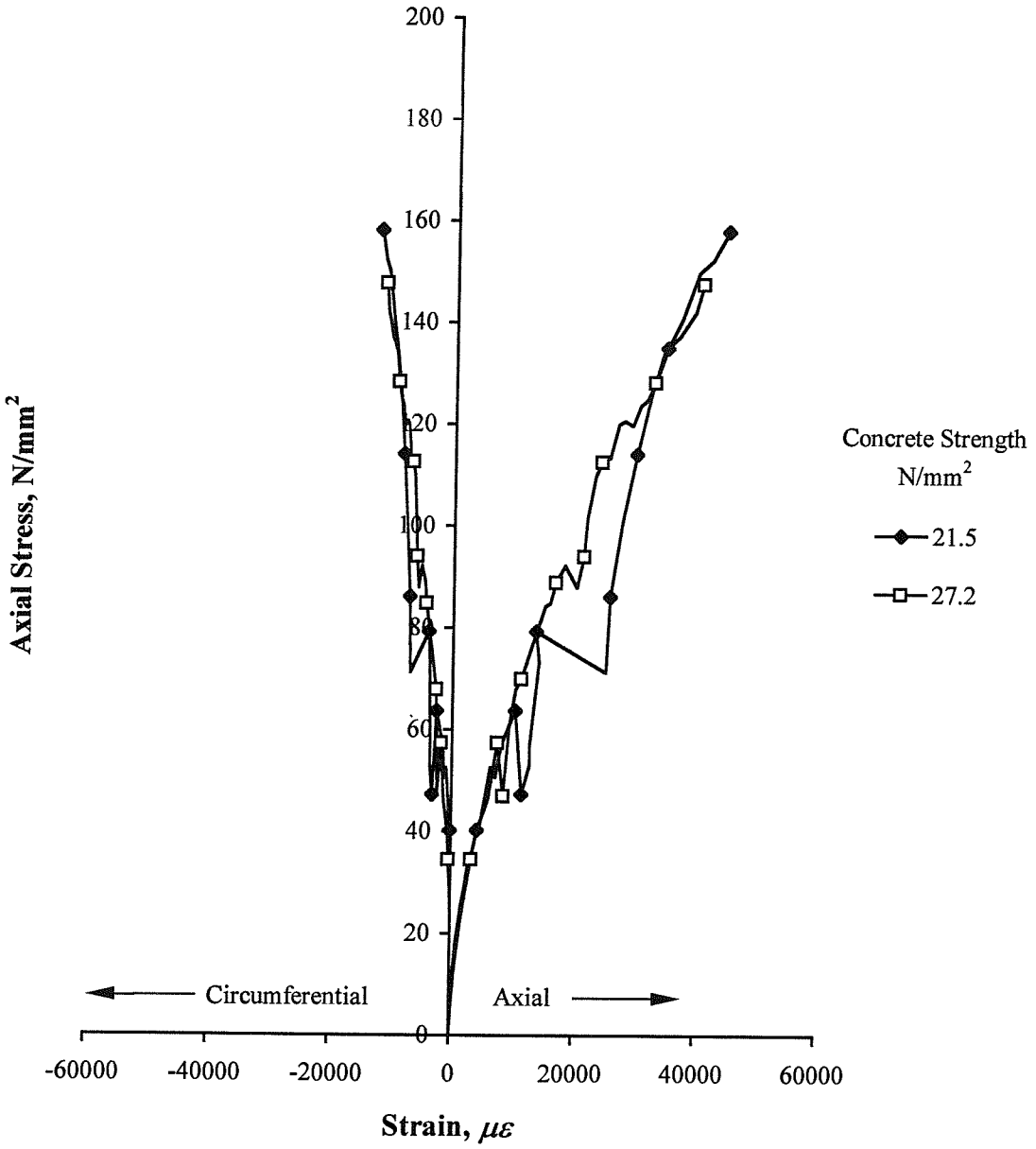

Figure B.1. Stress-strain curves for the 60 mm diameter concrete-filled stub columns confined with E-glass fibres orientated at 75.5 degrees.

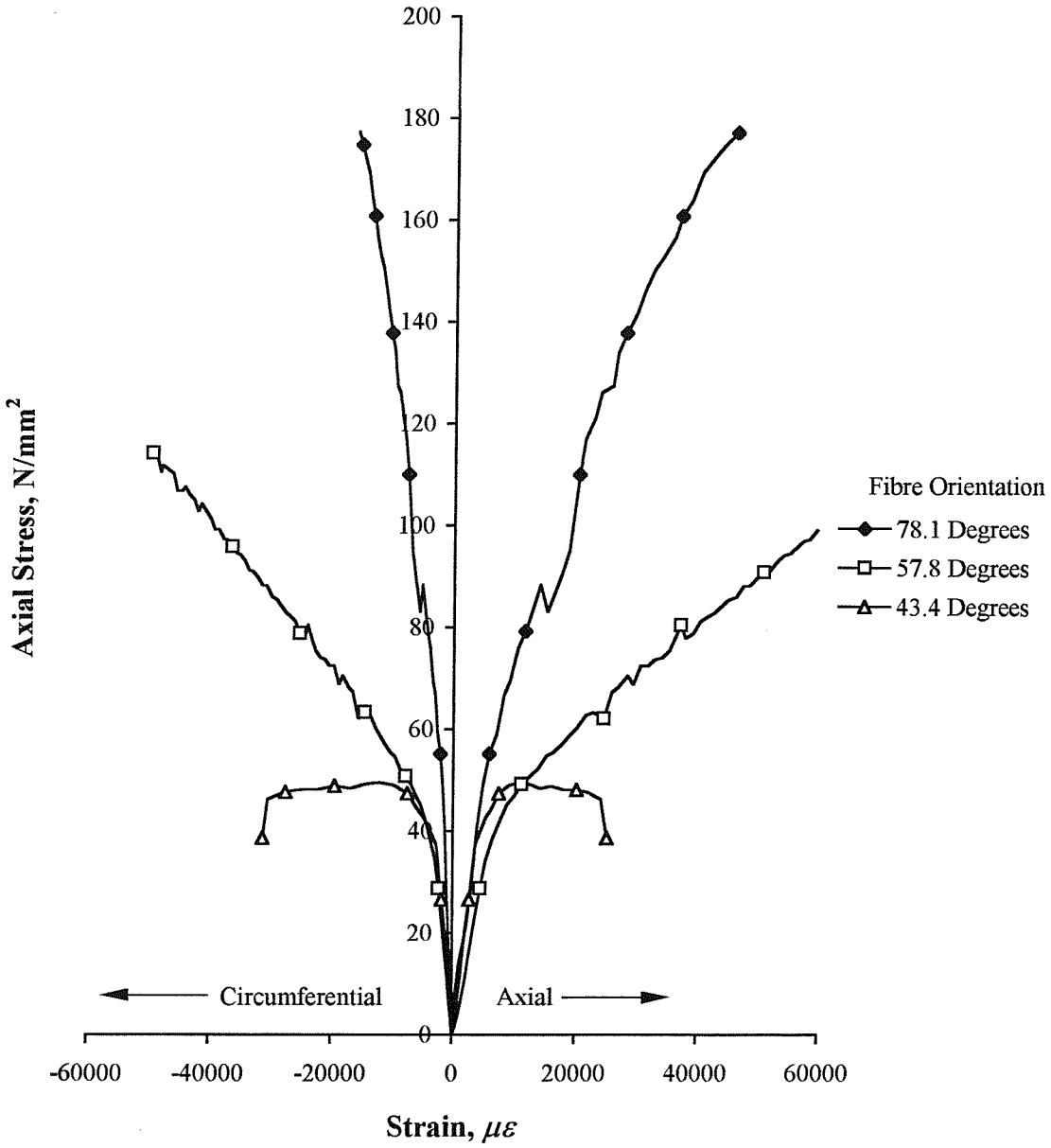

Figure B.2. Stress-strain curves for the 80 mm diameter concrete-filled stub columns confined with E-glass fibres (nominal concrete cube strength = 25 N/mm^2)

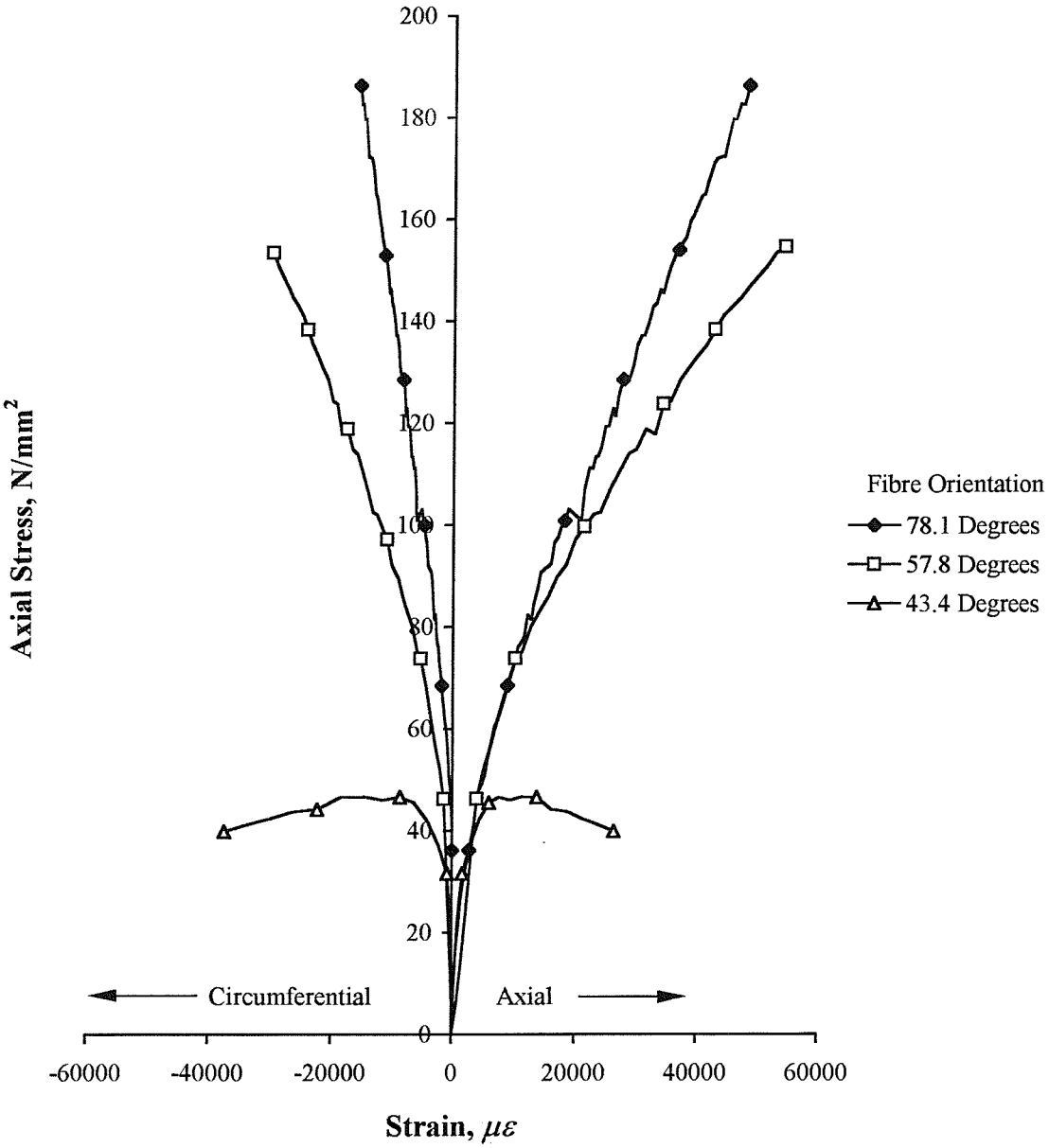

Figure B.3. Stress-strain curves for the 80 mm diameter concrete-filled stub columns confined with E-glass fibres (nominal concrete cube strength = 35 N/mm^2)

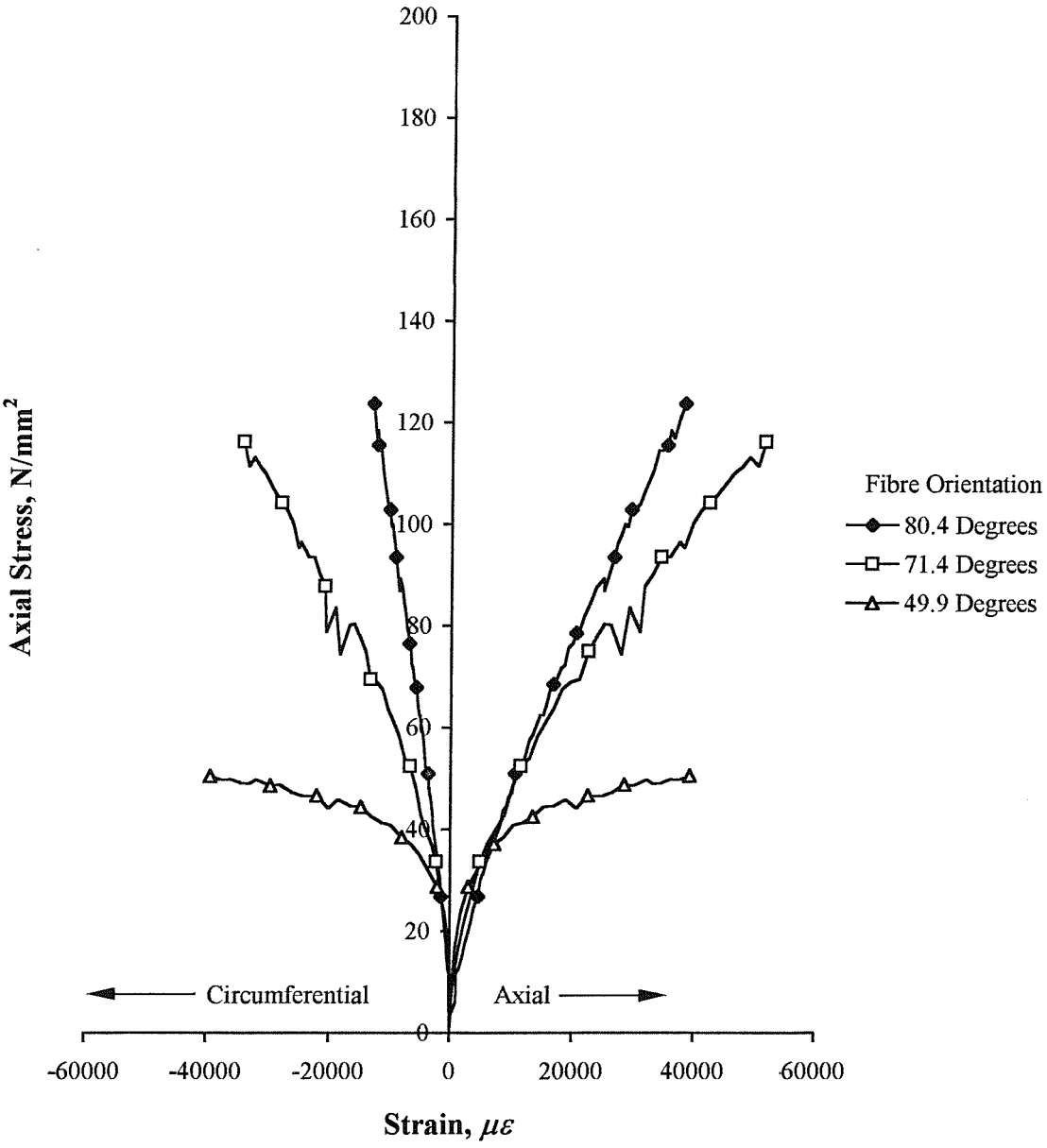

Figure B.4. Stress-strain curves for the 100 mm diameter concrete-filled stub columns confined with E-glass fibres (nominal concrete cube strength = 25 N/mm^2)

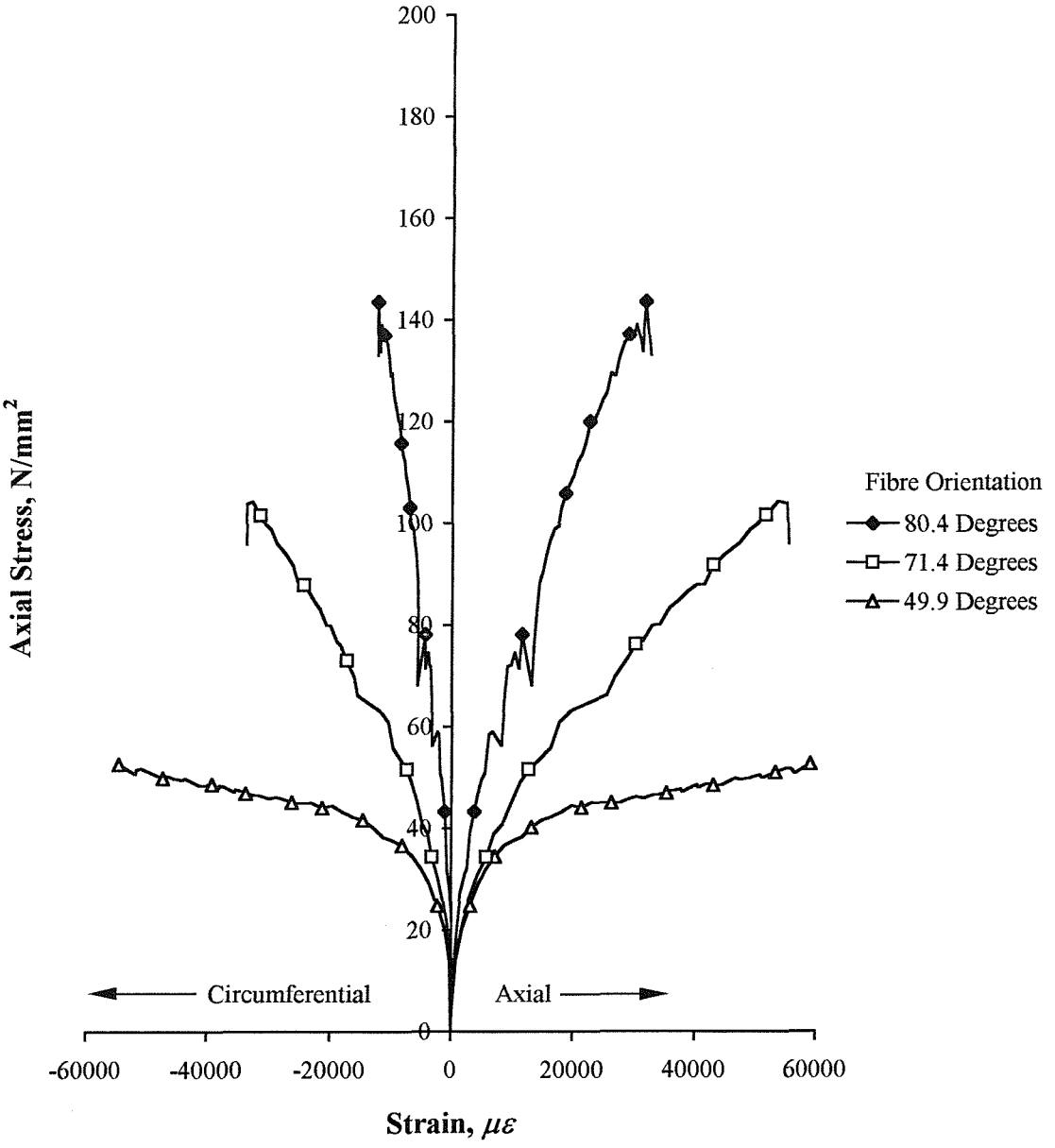

Figure B.5. Stress-strain curves for the 100 mm diameter concrete-filled stub columns confined with E-glass fibres (nominal concrete cube strength = 35 N/mm^2)

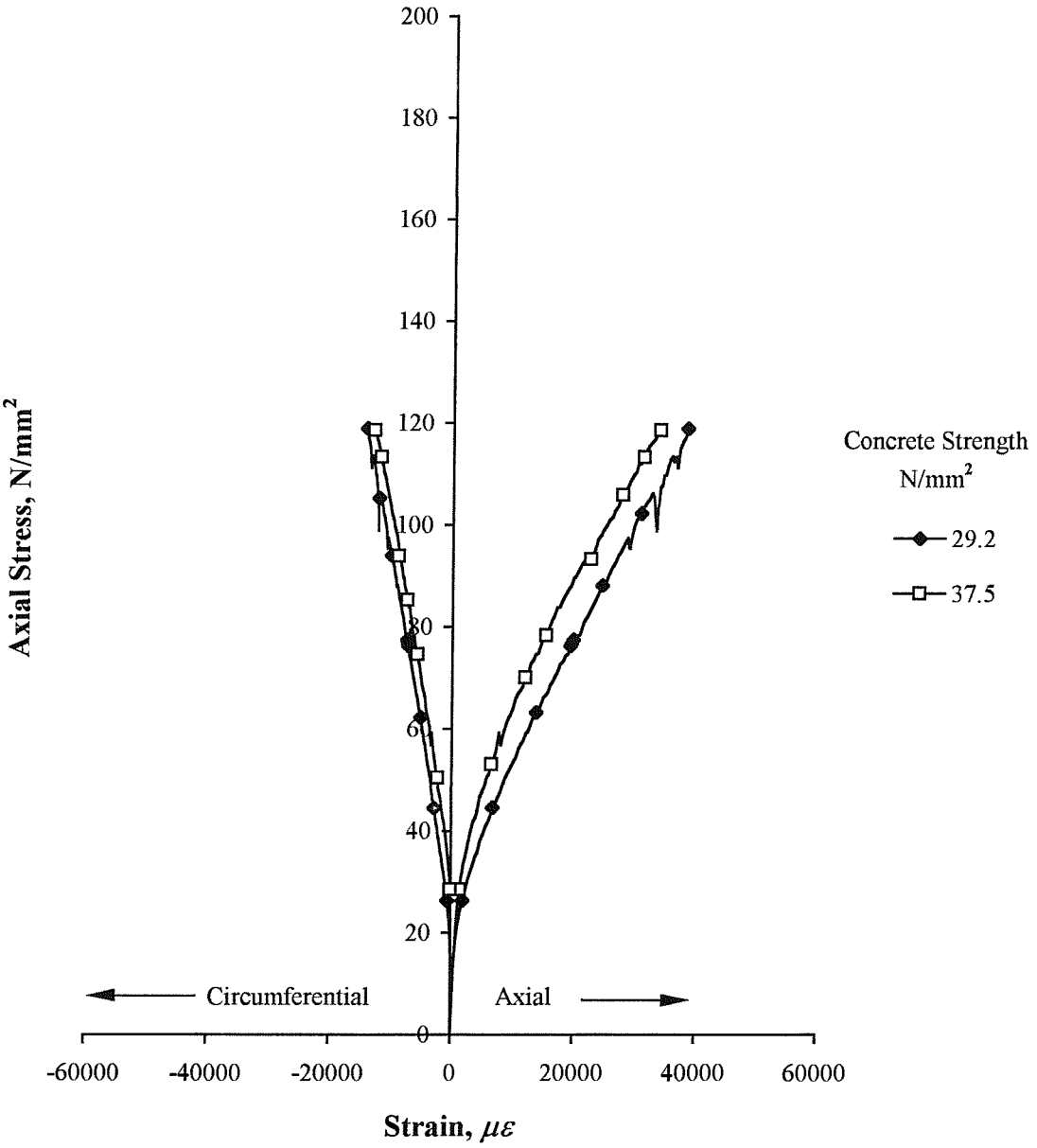

Figure B.6. Stress-strain curves for the 125 mm diameter concrete-filled stub columns confined with E-glass fibres orientated at 82.3 degrees

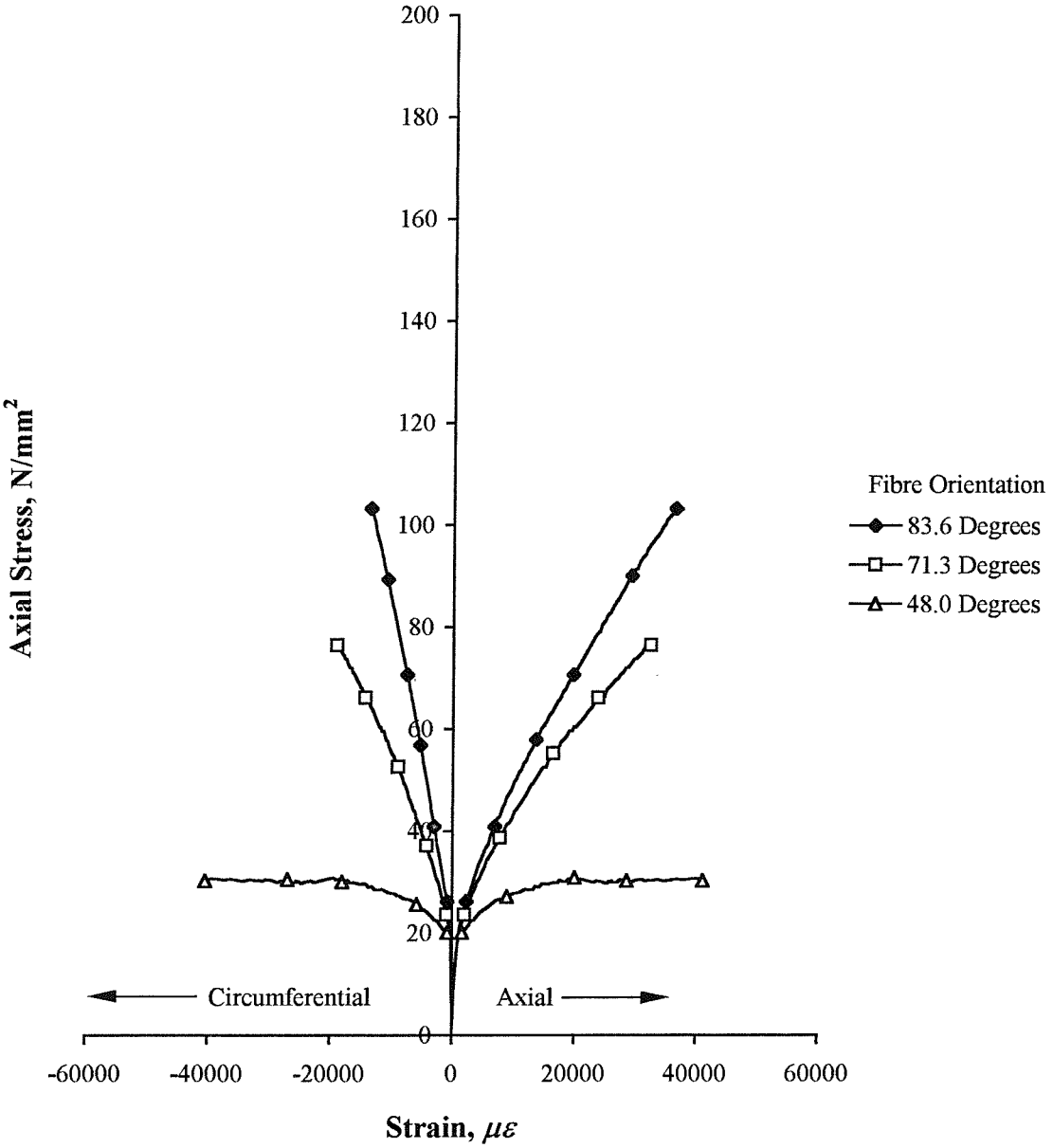

Figure B.7. Stress-strain curves for the 150 mm diameter concrete-filled stub columns confined with E-glass fibres (nominal concrete cube strength = 25 N/mm^2)

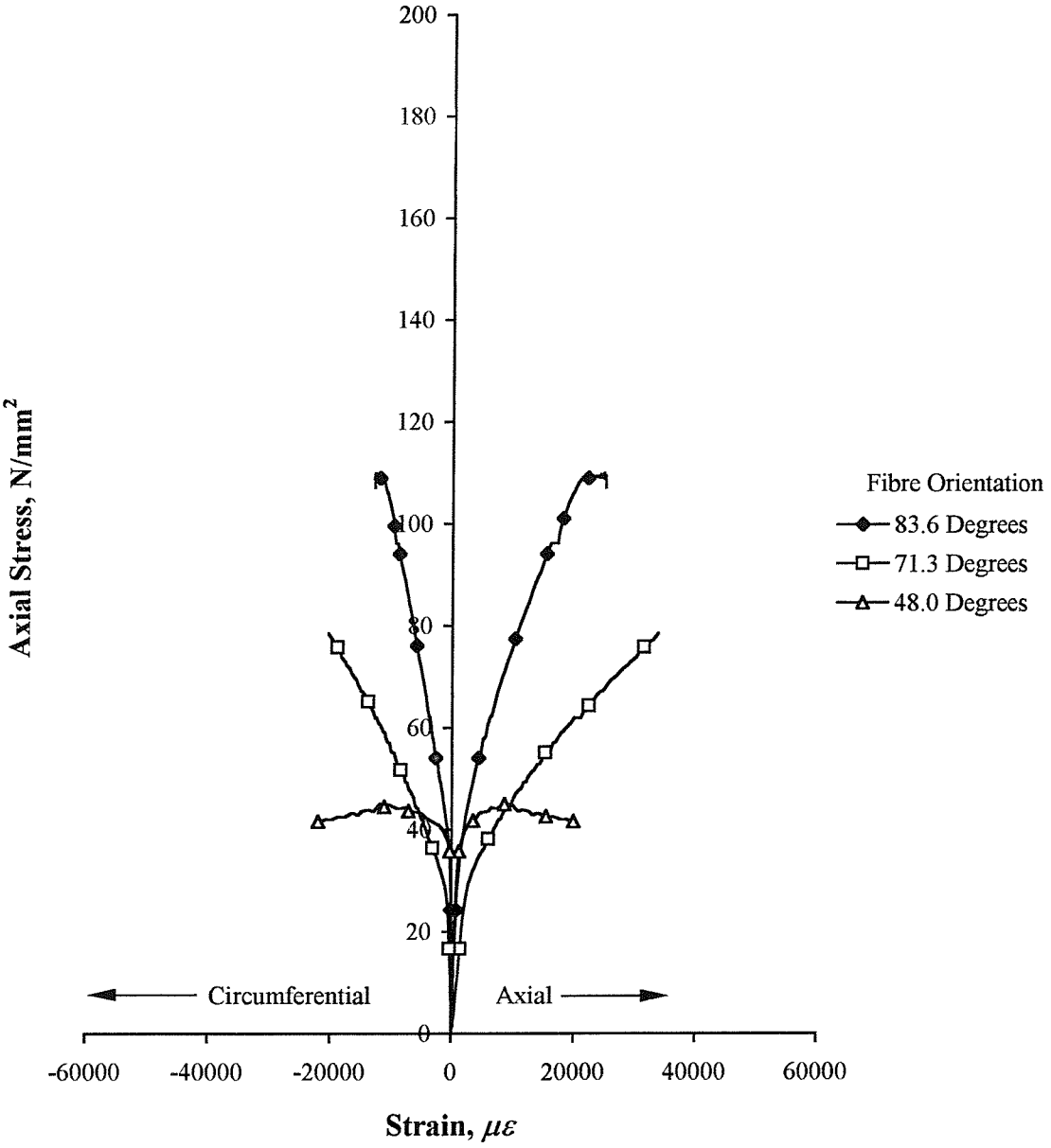

Figure B.8. Stress-strain curves for the 150 mm diameter concrete-filled stub columns confined with E-glass fibres (nominal concrete cube strength = 35 N/mm^2)

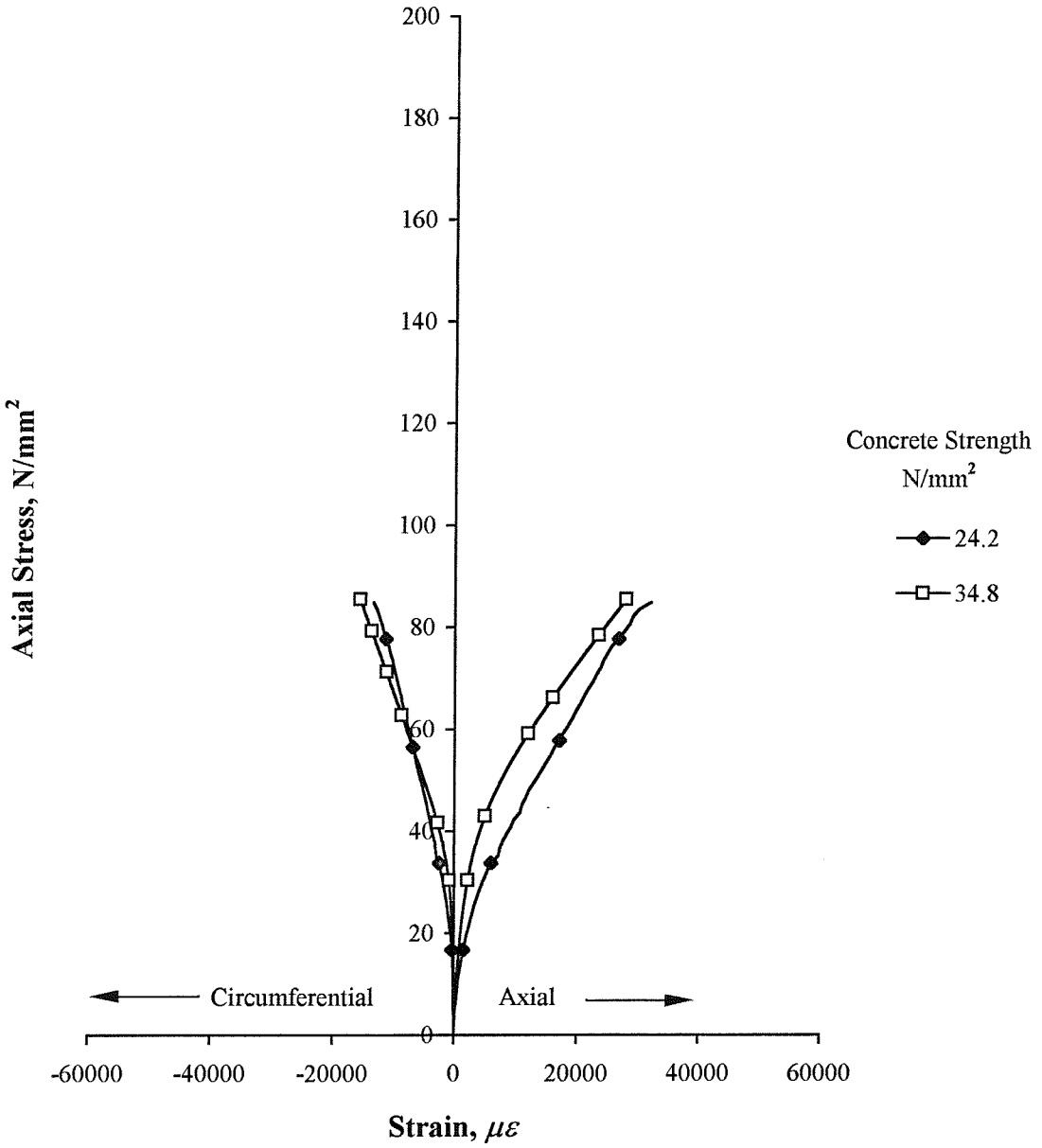

Figure B.9. Stress-strain curves for the 300 mm diameter concrete-filled stub columns confined with E-glass fibres orientated at 86.8 degrees

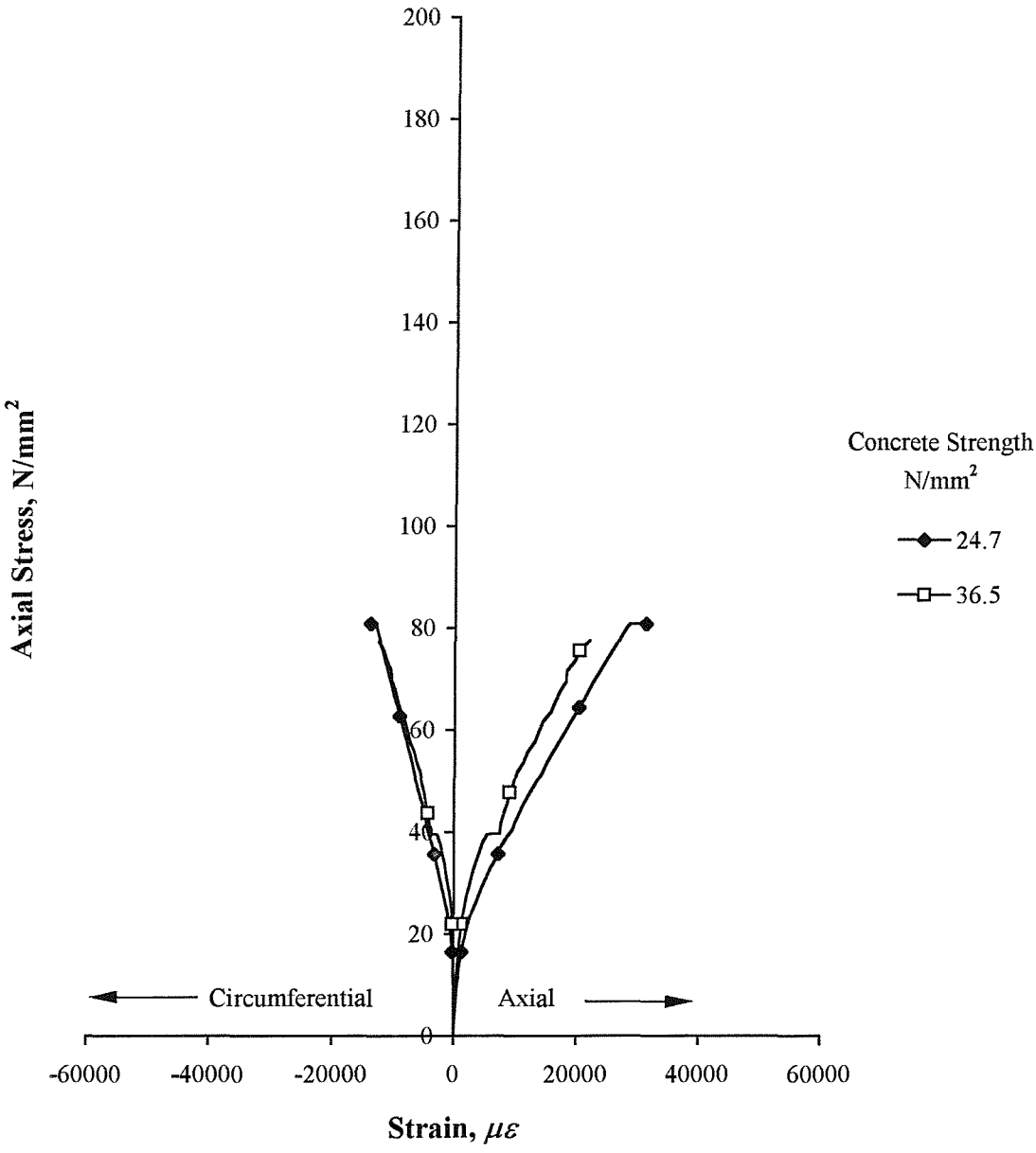

Figure B.10. Stress-strain curves for the 400 mm diameter concrete-filled stub columns confined with E-glass fibres orientated at 87.6 degrees

APPENDIX C

EXPERIMENTAL STRESS-VOLUMETRIC STRAIN CURVES FOR CONCRETE-FILLED E-GLASS FRP-COMPOSITE STUB COLUMNS

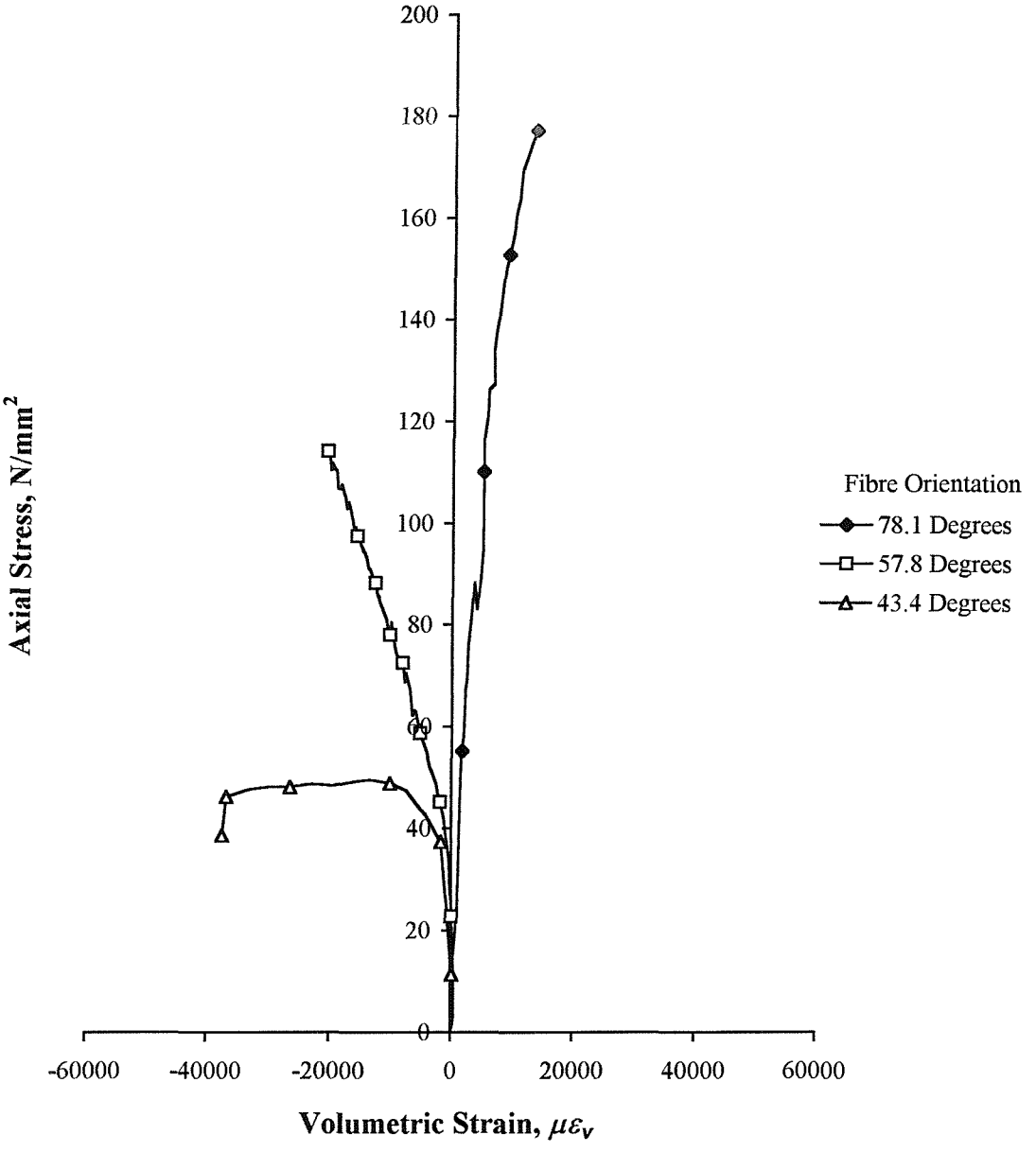

Figure C.1. Stress-volumetric strain curves for the 80 mm diameter concrete-filled stub columns confined with E-glass fibres (nominal concrete cube strength = 25 N/mm^2)

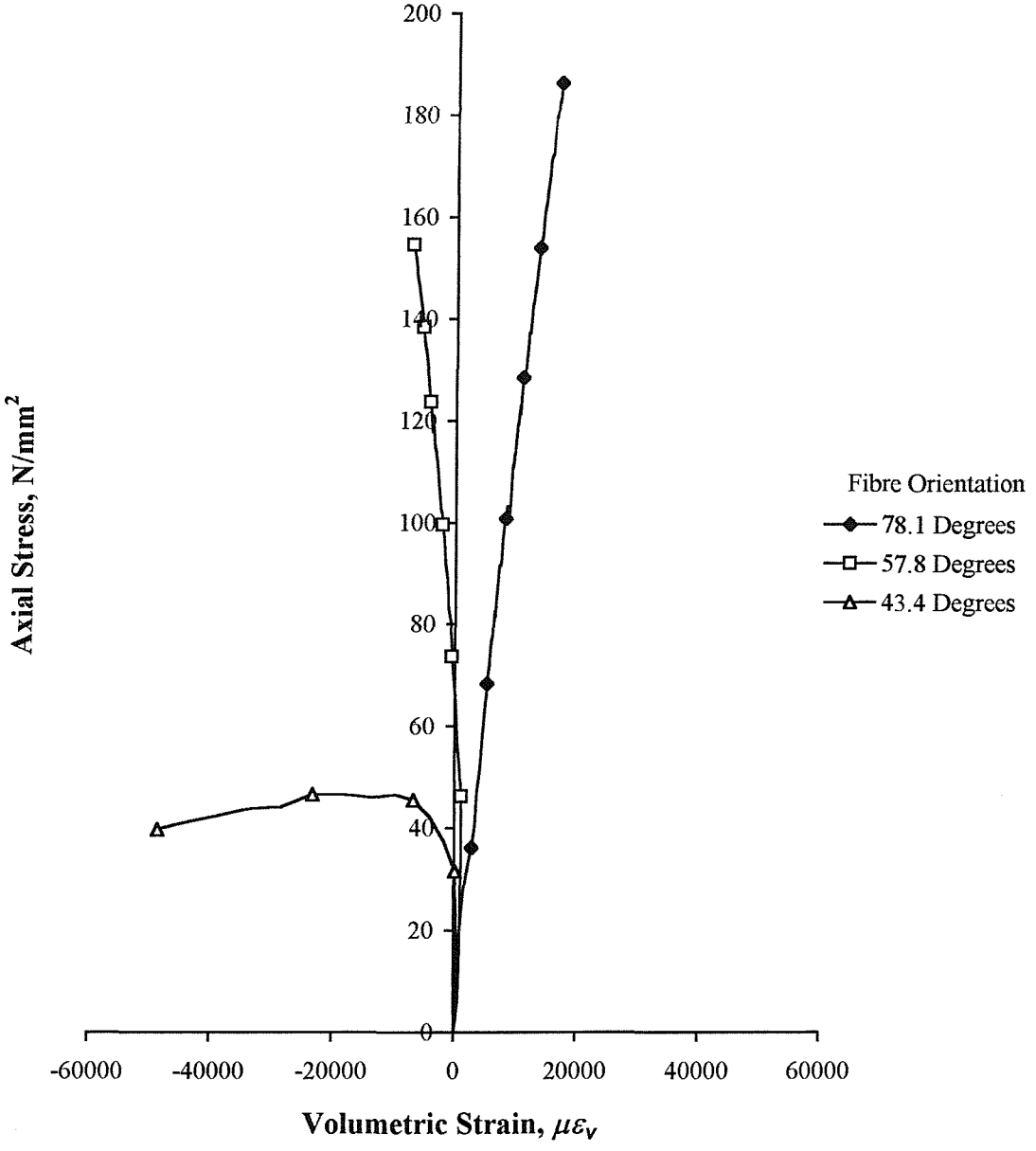

Figure C.2. Stress-volumetric strain curves for the 80 mm diameter concrete-filled stub columns confined with E-glass fibres (nominal concrete cube strength = 35 N/mm^2)

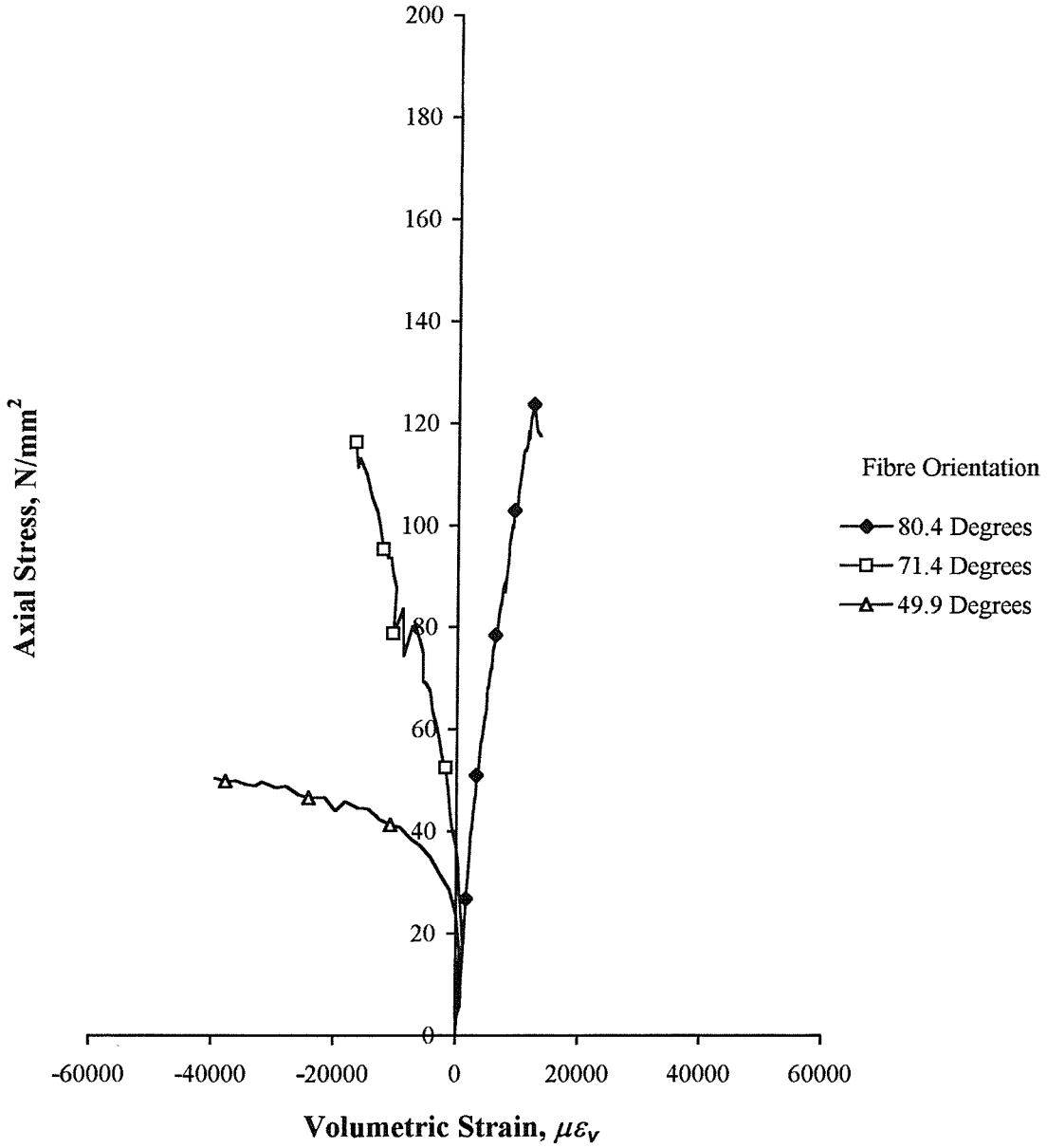

Figure C.3. Stress-volumetric strain curves for the 100 mm diameter concrete-filled stub columns confined with E-glass fibres (nominal concrete cube strength = 25 N/mm^2)

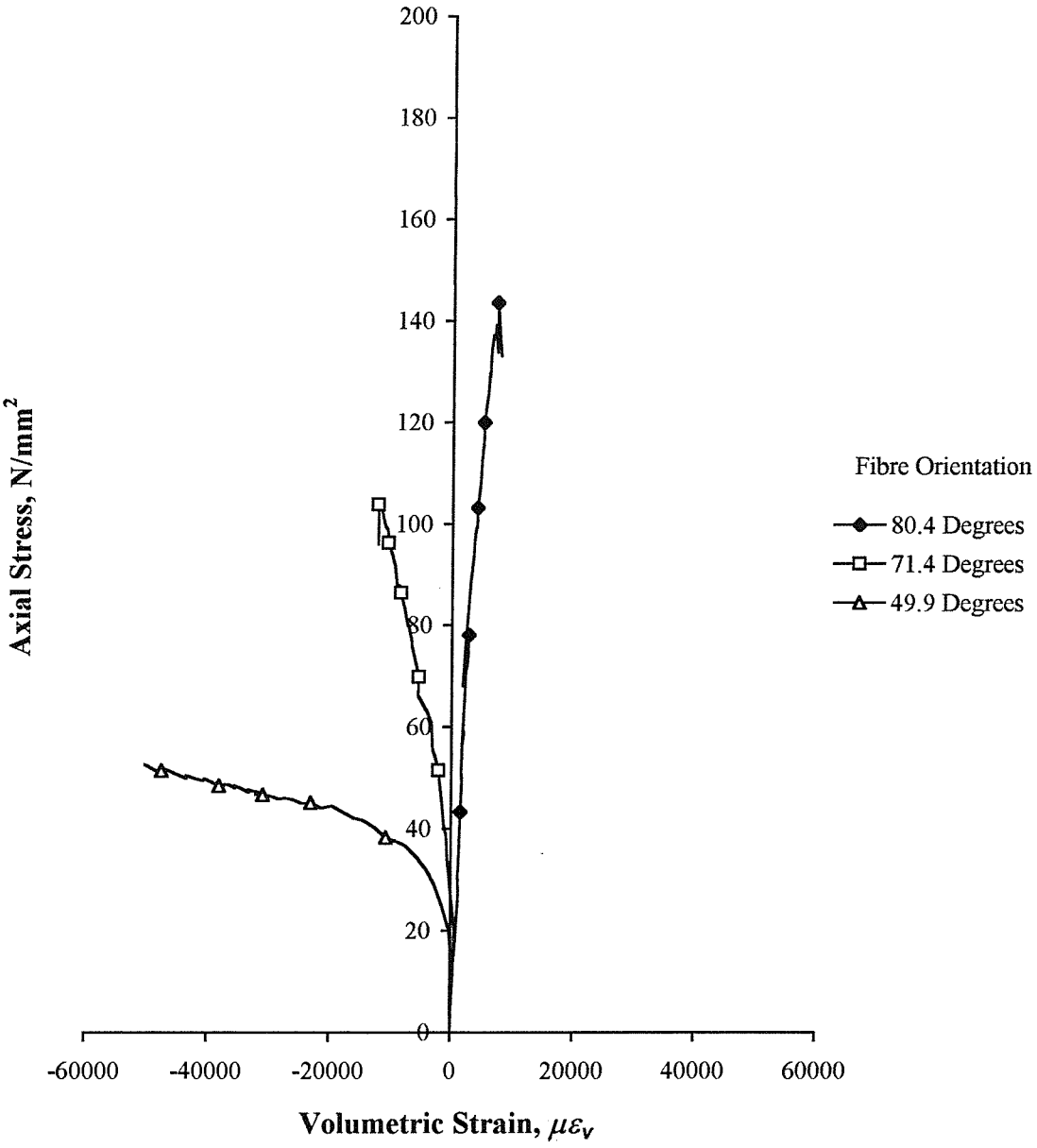

Figure C.4. Stress-volumetric strain curves for the 100 mm diameter concrete-filled stub columns confined with E-glass fibres (nominal concrete cube strength = 35 N/mm^2)

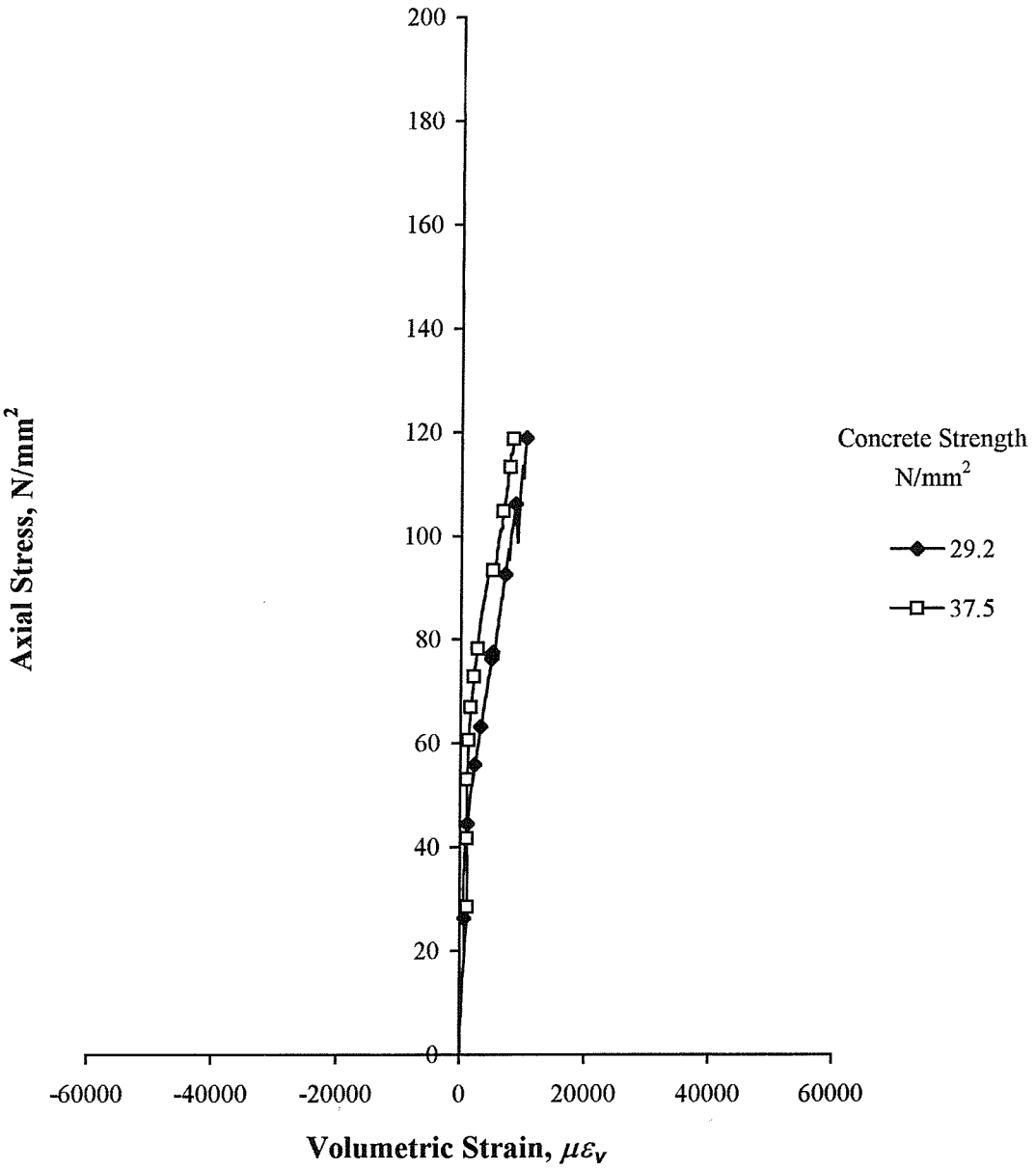

Figure C.5. Stress-volumetric strain curves for the 125 mm diameter concrete-filled stub columns confined with E-glass fibres orientated at 82.3 degrees

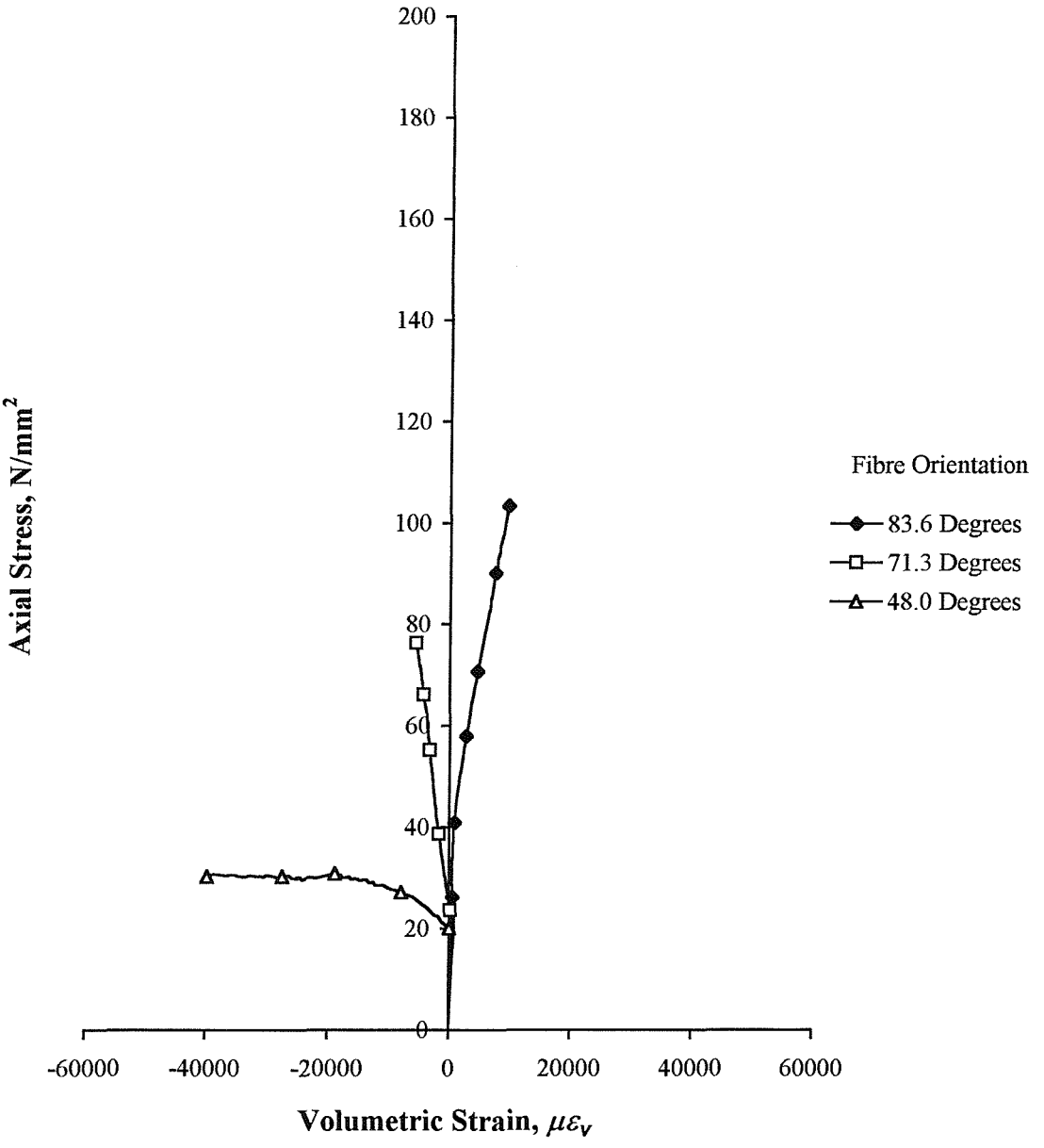

Figure C.6. Stress-volumetric strain curves for the 150 mm diameter concrete-filled stub columns confined with E-glass fibres (nominal concrete cube strength = 25 N/mm^2)

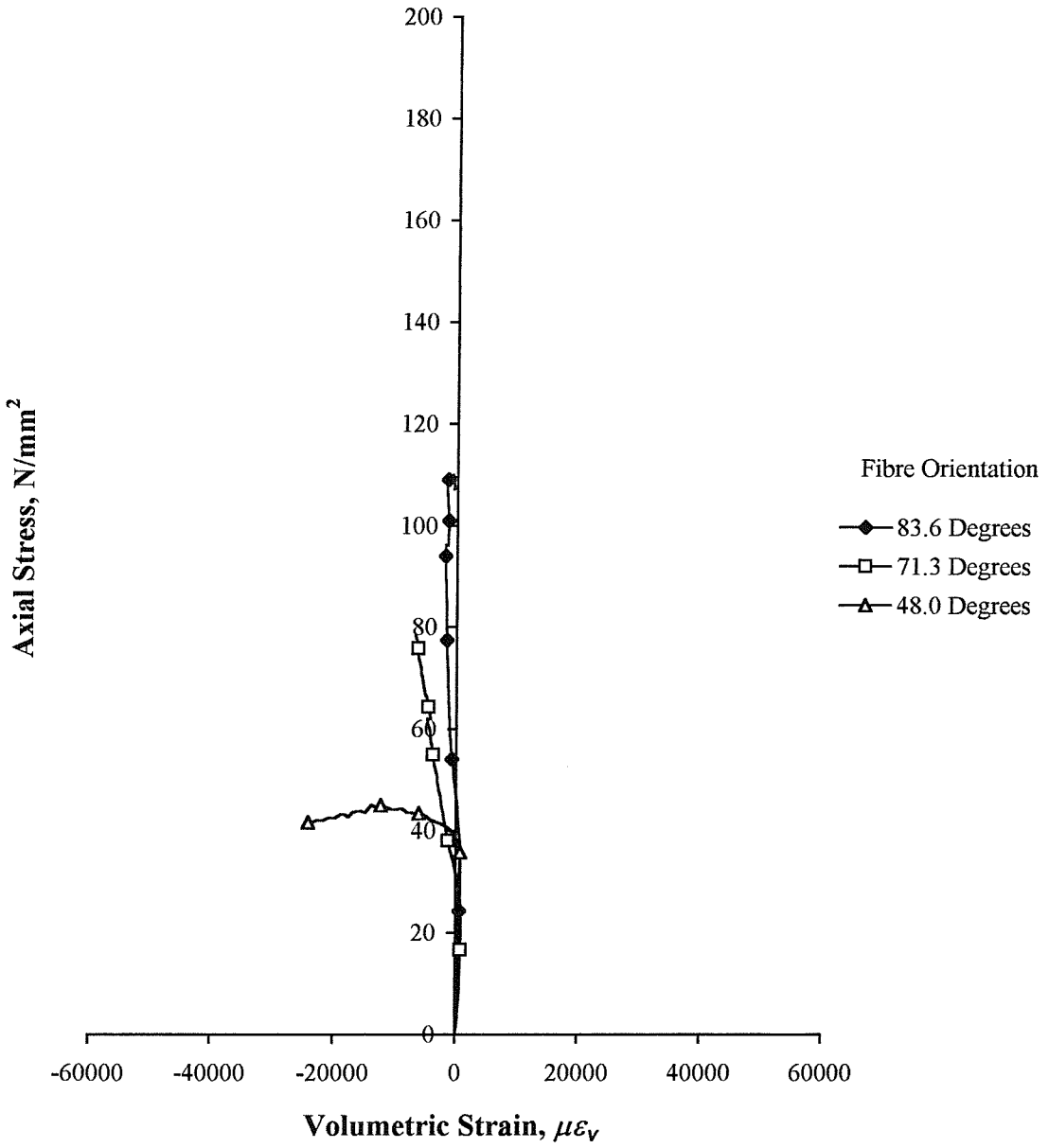

Figure C.7. Stress-volumetric strain curves for the 150 mm diameter concrete-filled stub columns confined with E-glass fibres (nominal concrete cube strength = 35 N/mm^2)

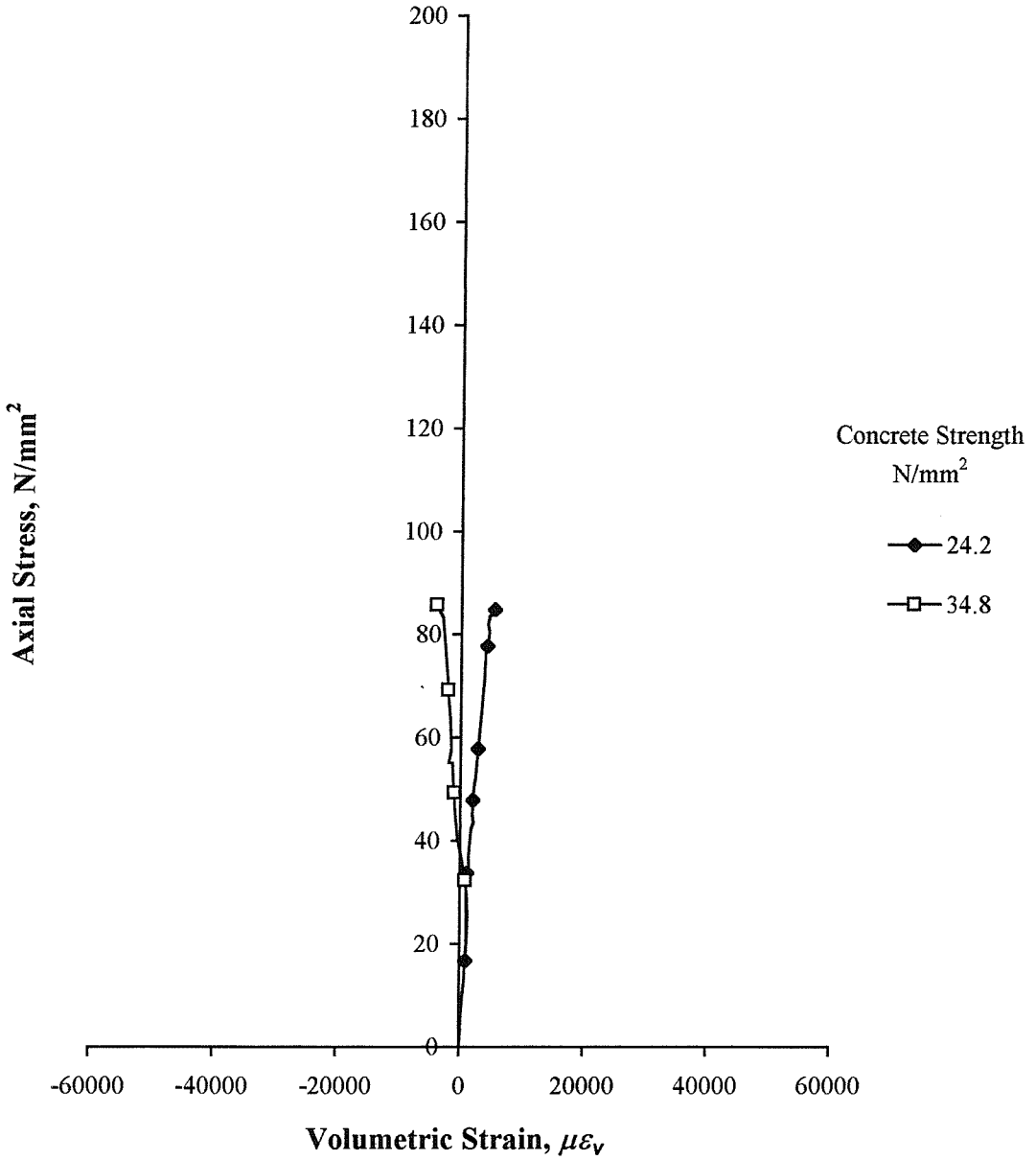

Figure C.8. Stress-volumetric strain curves for the 300 mm diameter concrete-filled stub columns confined with E-glass fibres orientated at 86.8 degrees

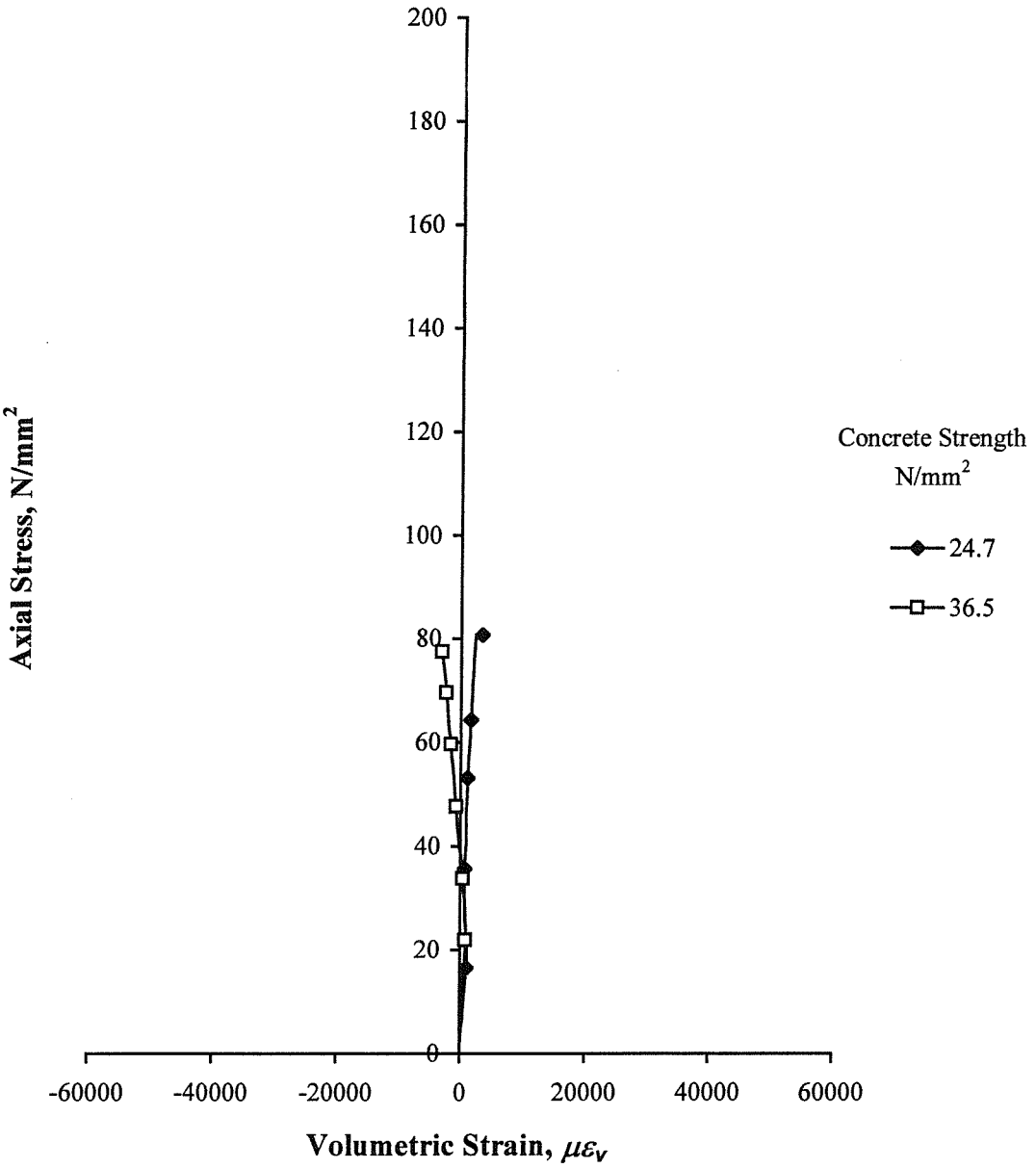

Figure C.9. Stress-volumetric strain curves for the 400 mm diameter concrete-filled stub columns confined with E-glass fibres orientated at 87.6 degrees

APPENDIX D

COMPARISON OF THE THEORETICAL AND EXPERIMENTAL STRESS-STRAIN CURVES FOR CONCRETE-FILLED E-GLASS FRP-COMPOSITE STUB COLUMNS WITH A NOMINAL 90 DEGREE FIBRE ORIENTATION

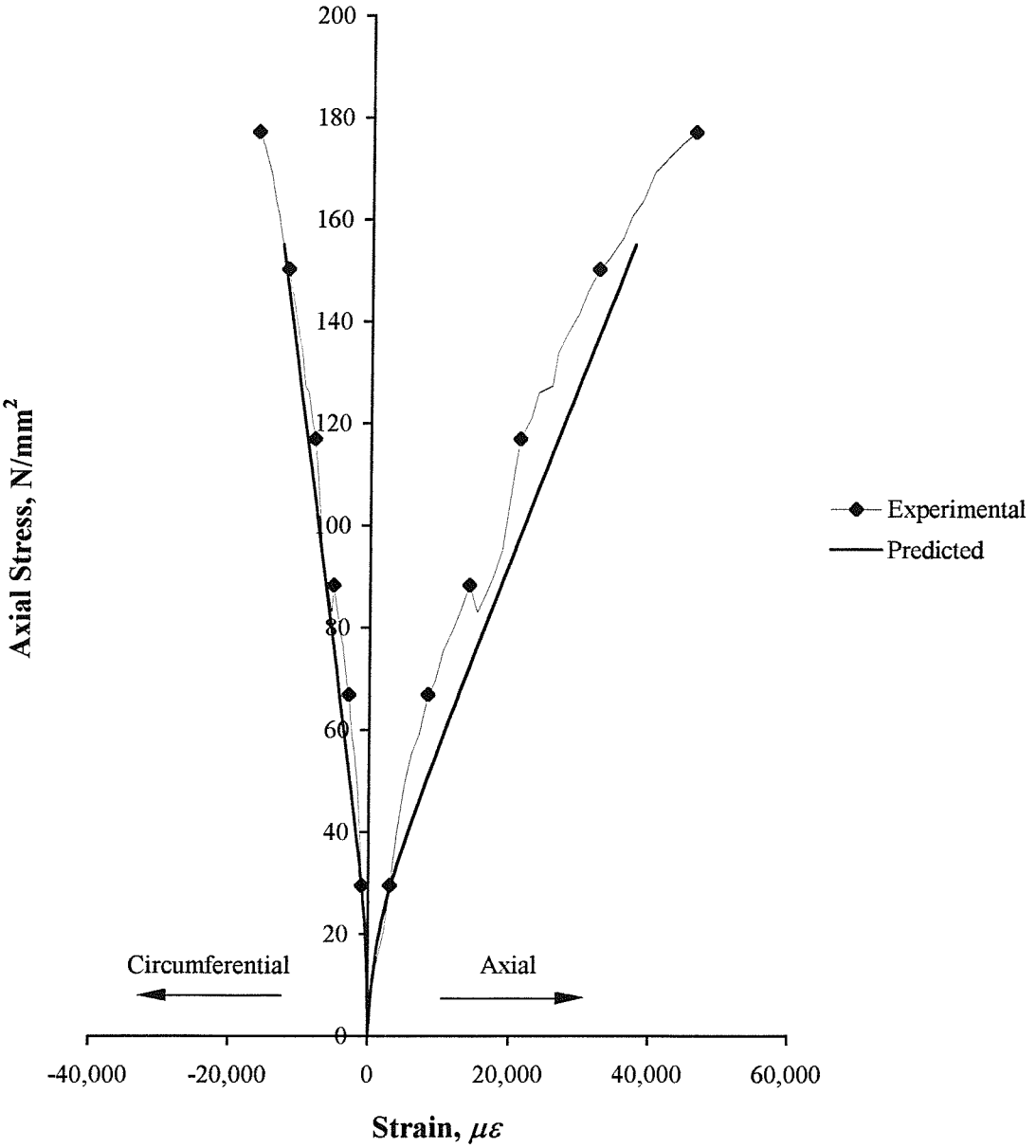

Figure D.1. Comparison of the theoretical and experimental stress-strain curves for the 80 mm diameter concrete-filled stub column confined with E-glass fibres orientated at 78.1 degrees (concrete cube strength = 23.4 N/mm^2)

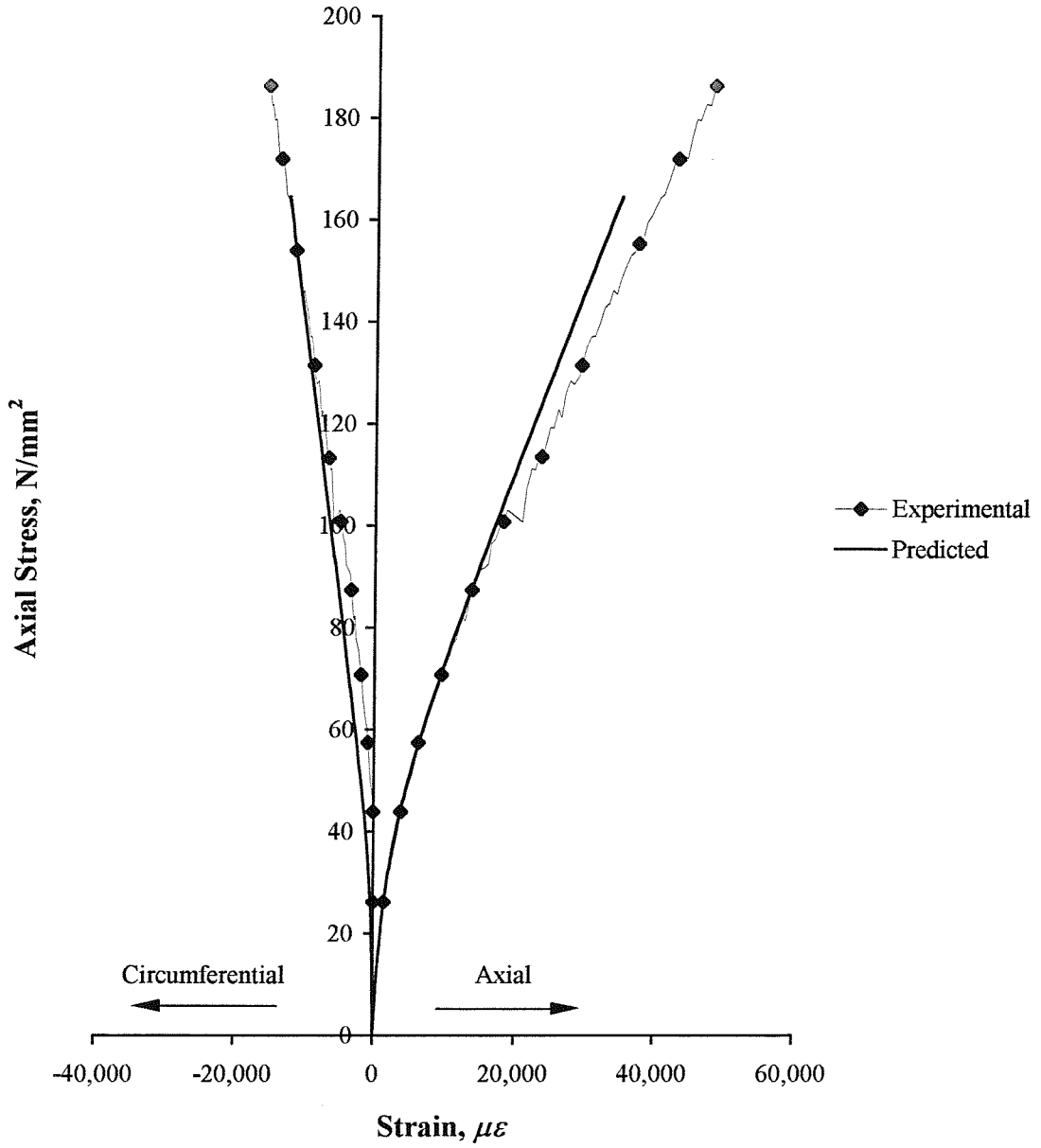

Figure D.2. Comparison of the theoretical and experimental stress-strain curves for the 80 mm diameter concrete-filled stub column confined with E-glass fibres orientated at 78.1 degrees (concrete cube strength = 35.2 N/mm^2)

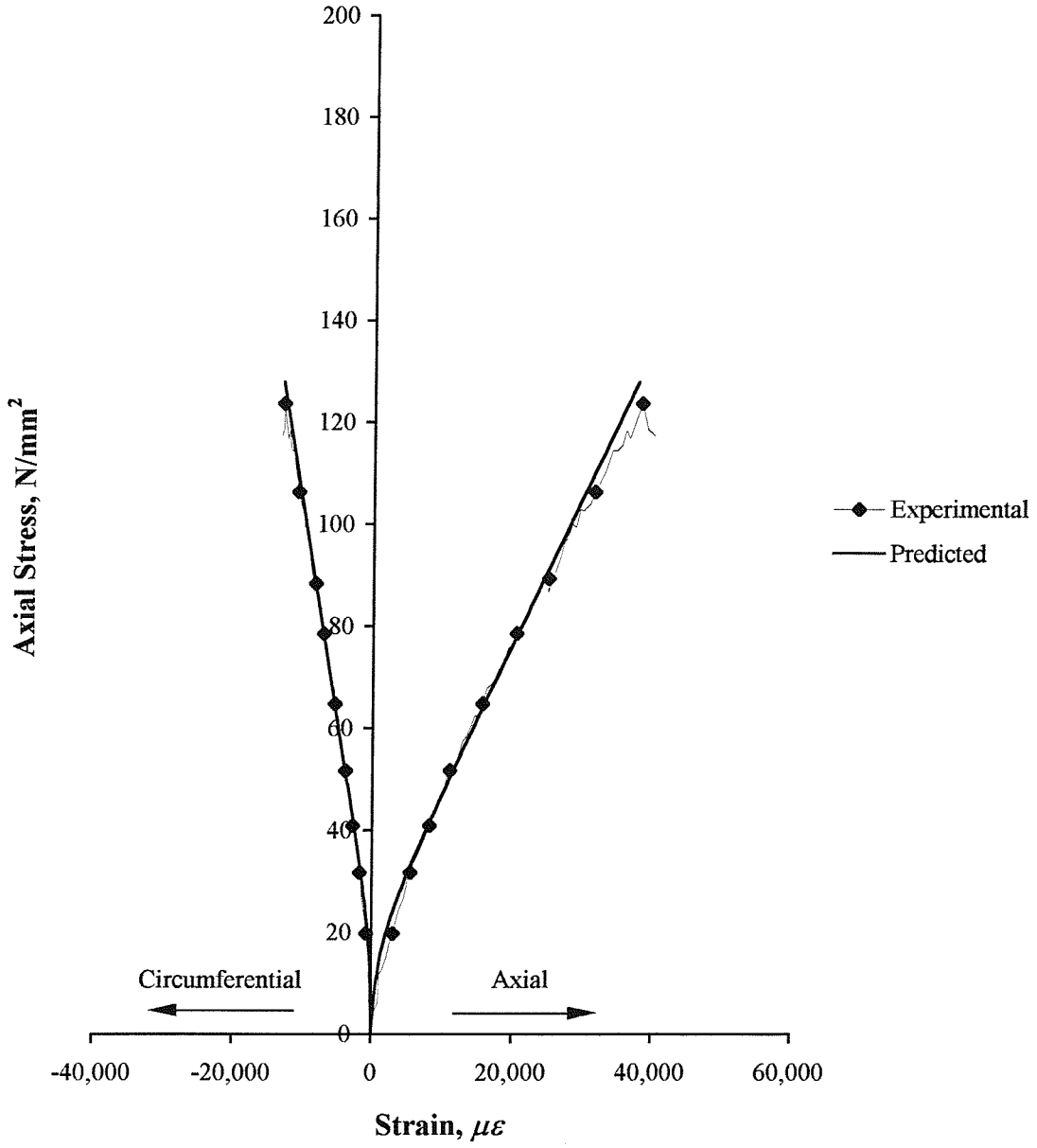

Figure D.3. Comparison of the theoretical and experimental stress-strain curves for the 100 mm diameter concrete-filled stub column confined with E-glass fibres orientated at 80.4 degrees (concrete cube strength = 19.7 N/mm^2)

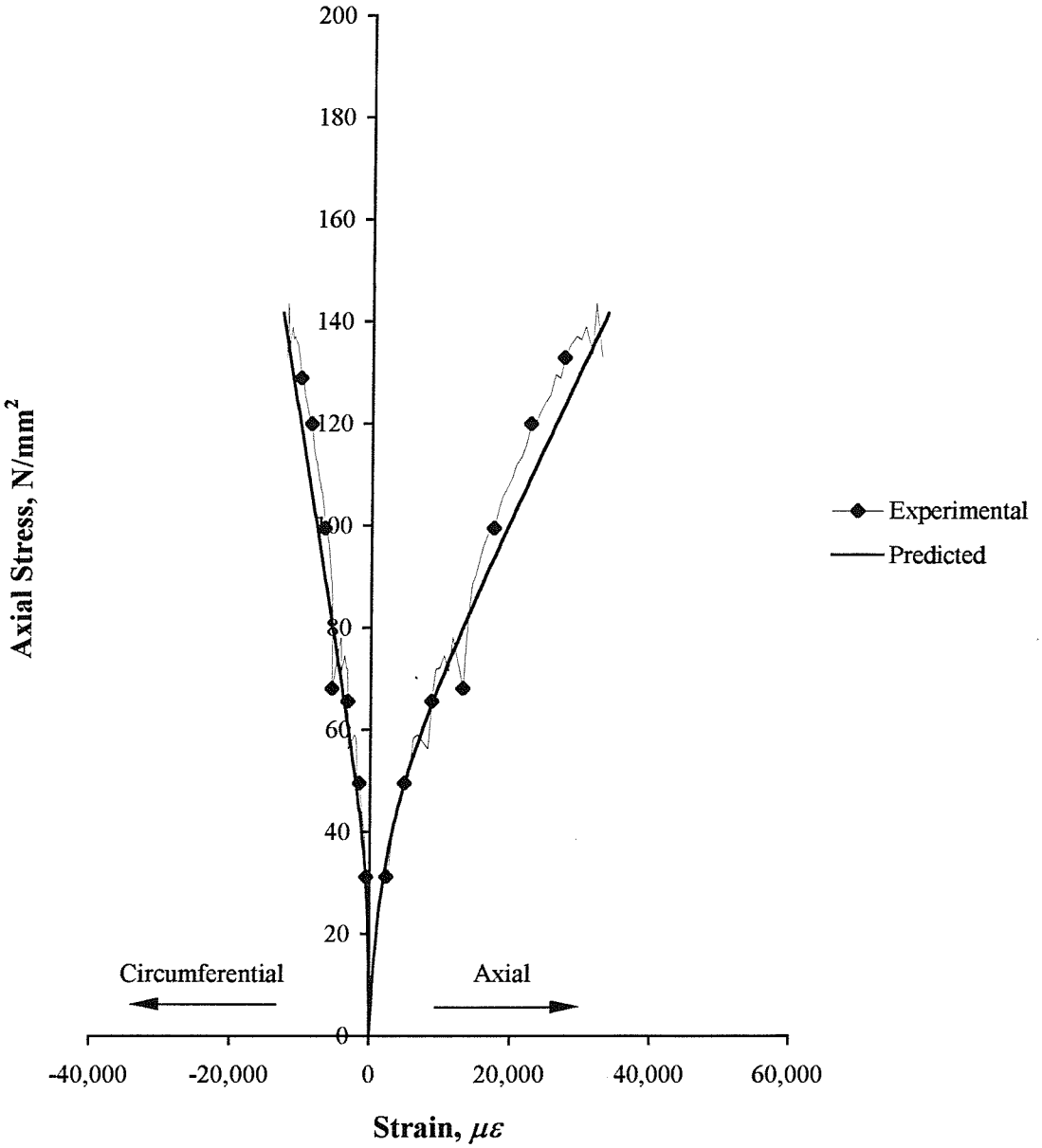

Figure D.4. Comparison of the theoretical and experimental stress-strain curves for the 100 mm diameter concrete-filled stub column confined with E-glass fibres orientated at 80.4 degrees (concrete cube strength = 36.2 N/mm^2)

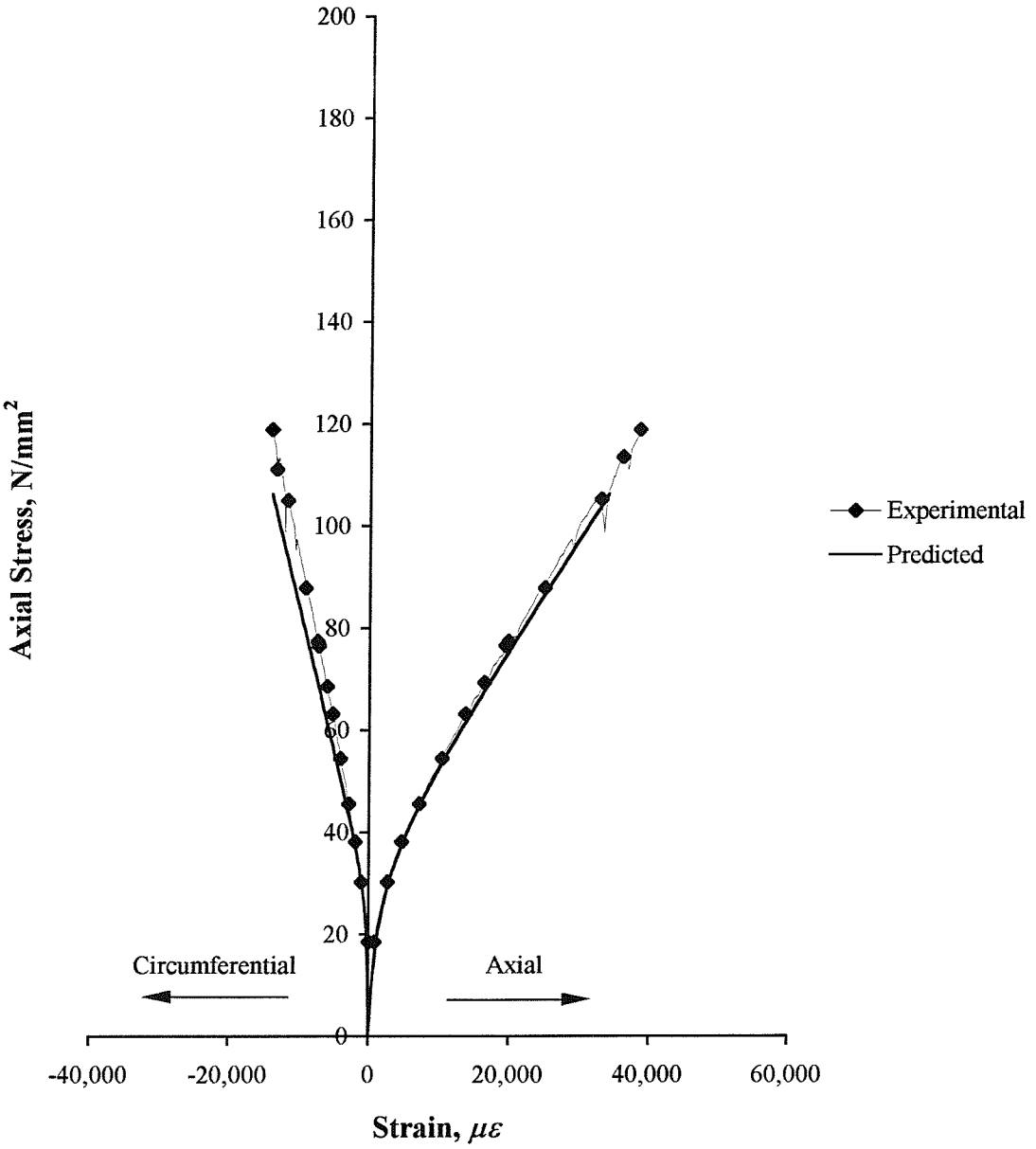

Figure D.5. Comparison of the theoretical and experimental stress-strain curves for the 125 mm diameter concrete-filled stub column confined with E-glass fibres orientated at 82.3 degrees (concrete cube strength = 29.2 N/mm^2)

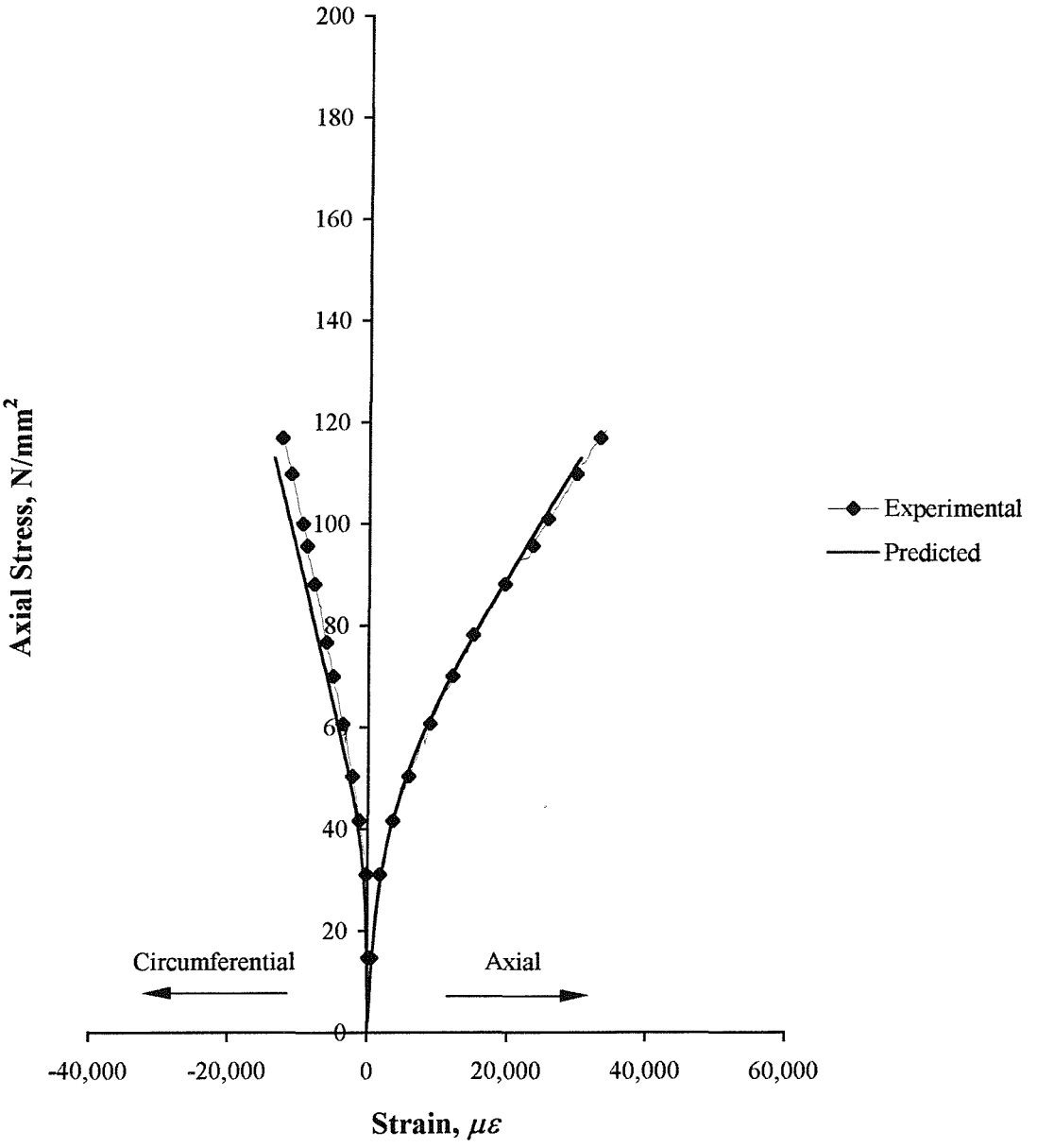

Figure D.6. Comparison of the theoretical and experimental stress-strain curves for the 125 mm diameter concrete-filled stub column confined with E-glass fibres orientated at 82.3 degrees (concrete cube strength = 37.5 N/mm^2)

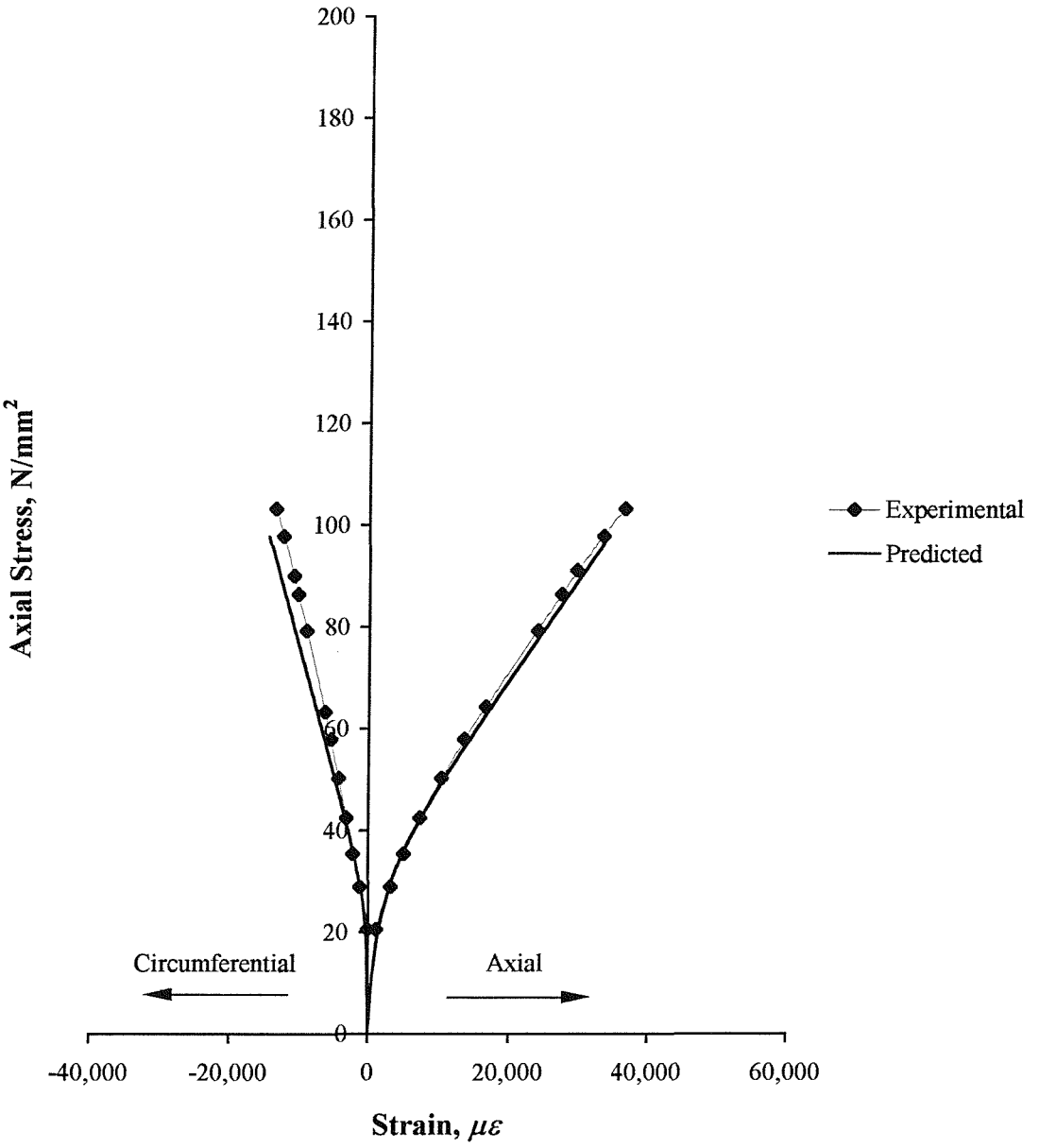

Figure D.7. Comparison of the theoretical and experimental stress-strain curves for the 150 mm diameter concrete-filled stub column confined with E-glass fibres orientated at 83.6 degrees (concrete cube strength = 27.4 N/mm^2)

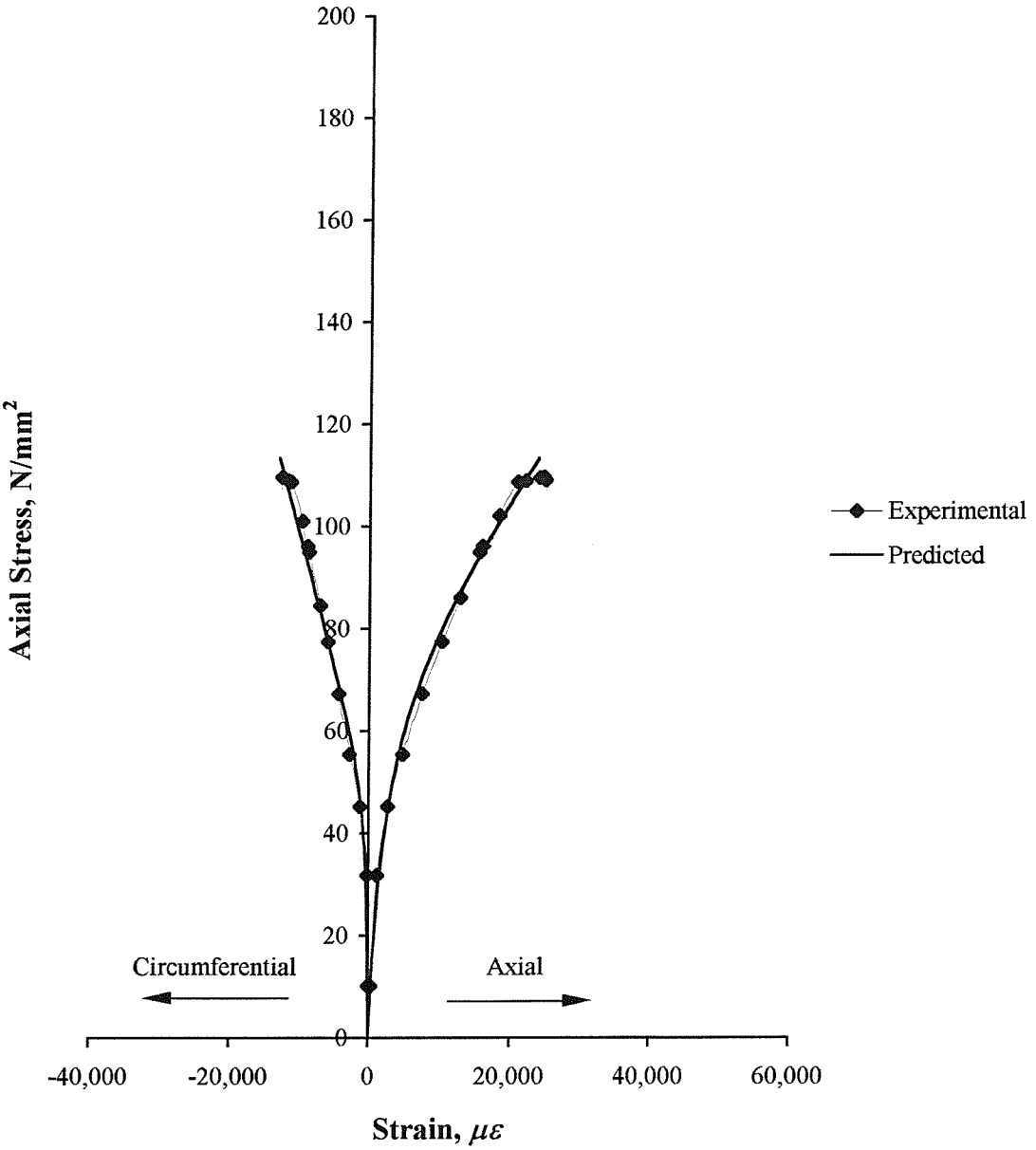

Figure D.8. Comparison of the theoretical and experimental stress-strain curves for the 150 mm diameter concrete-filled stub column confined with E-glass fibres orientated at 83.6 degrees (concrete cube strength = 46.3 N/mm^2)

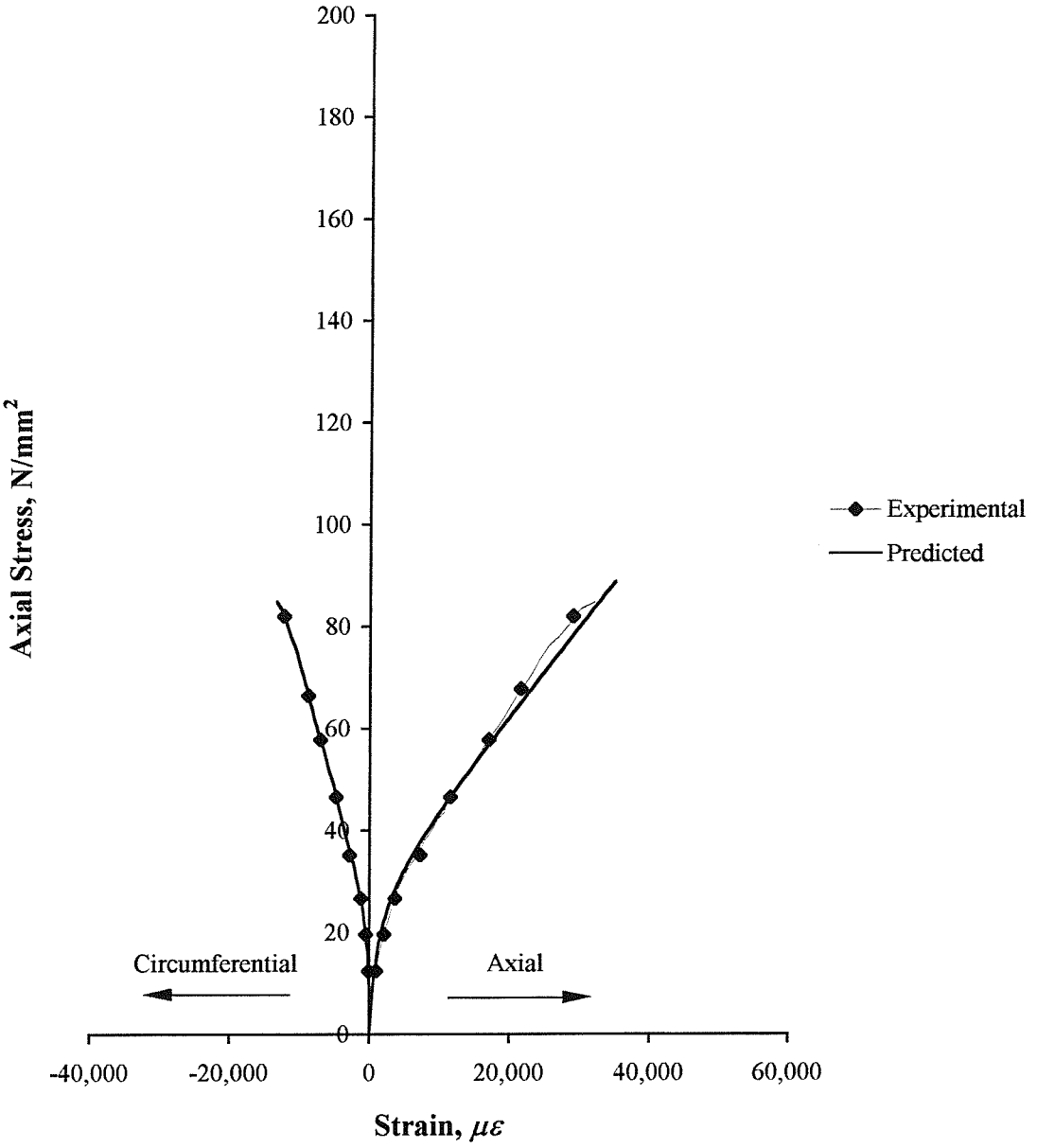

Figure D.9. Comparison of the theoretical and experimental stress-strain curves for the 300 mm diameter concrete-filled stub column confined with E-glass fibres orientated at 86.8 degrees (concrete cube strength = 34.0 N/mm^2)

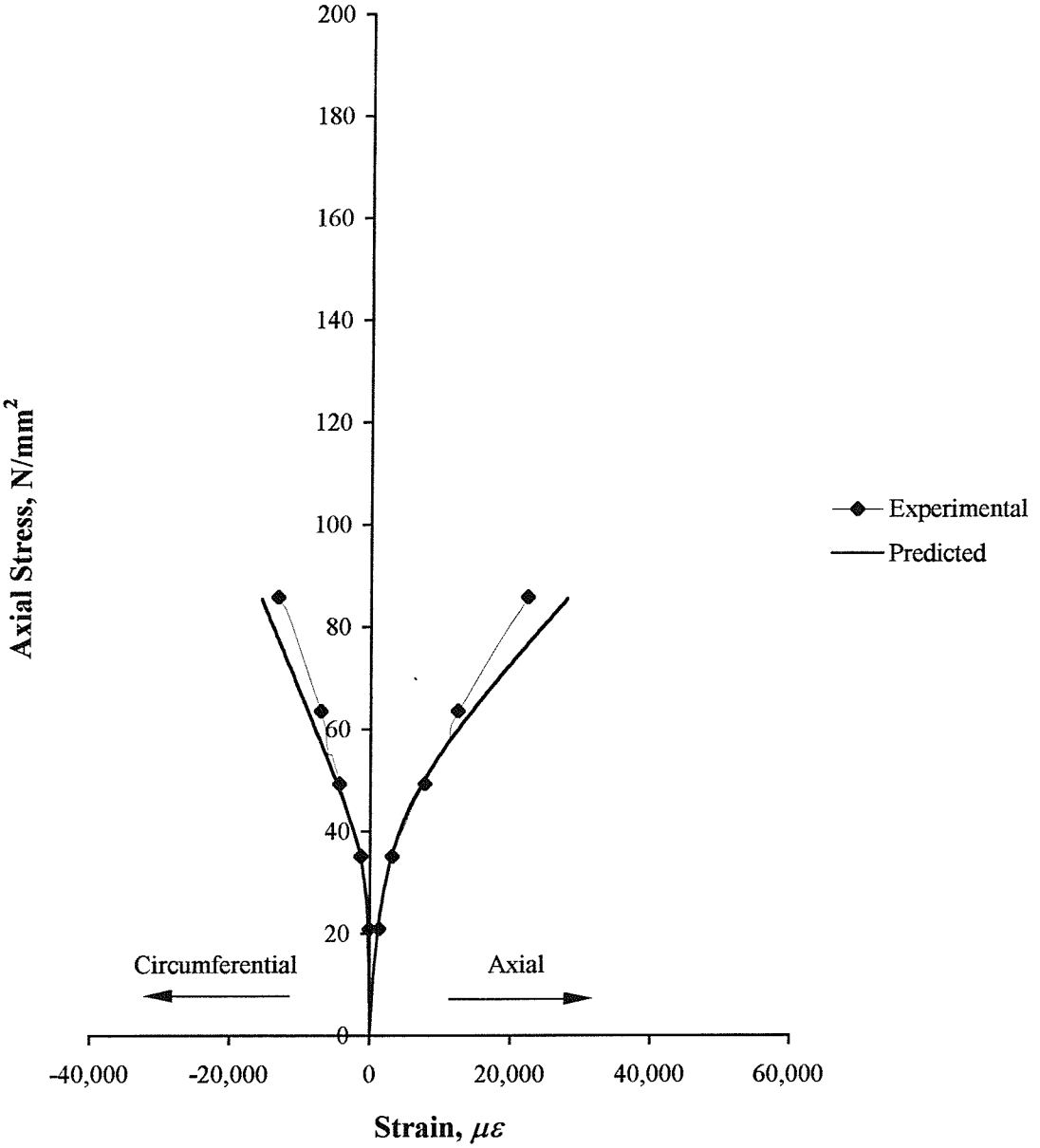

Figure D.10. Comparison of the theoretical and experimental stress-strain curves for the 300 mm diameter concrete-filled stub column confined with E-glass fibres orientated at 86.8 degrees (concrete cube strength = 38.6 N/mm^2)

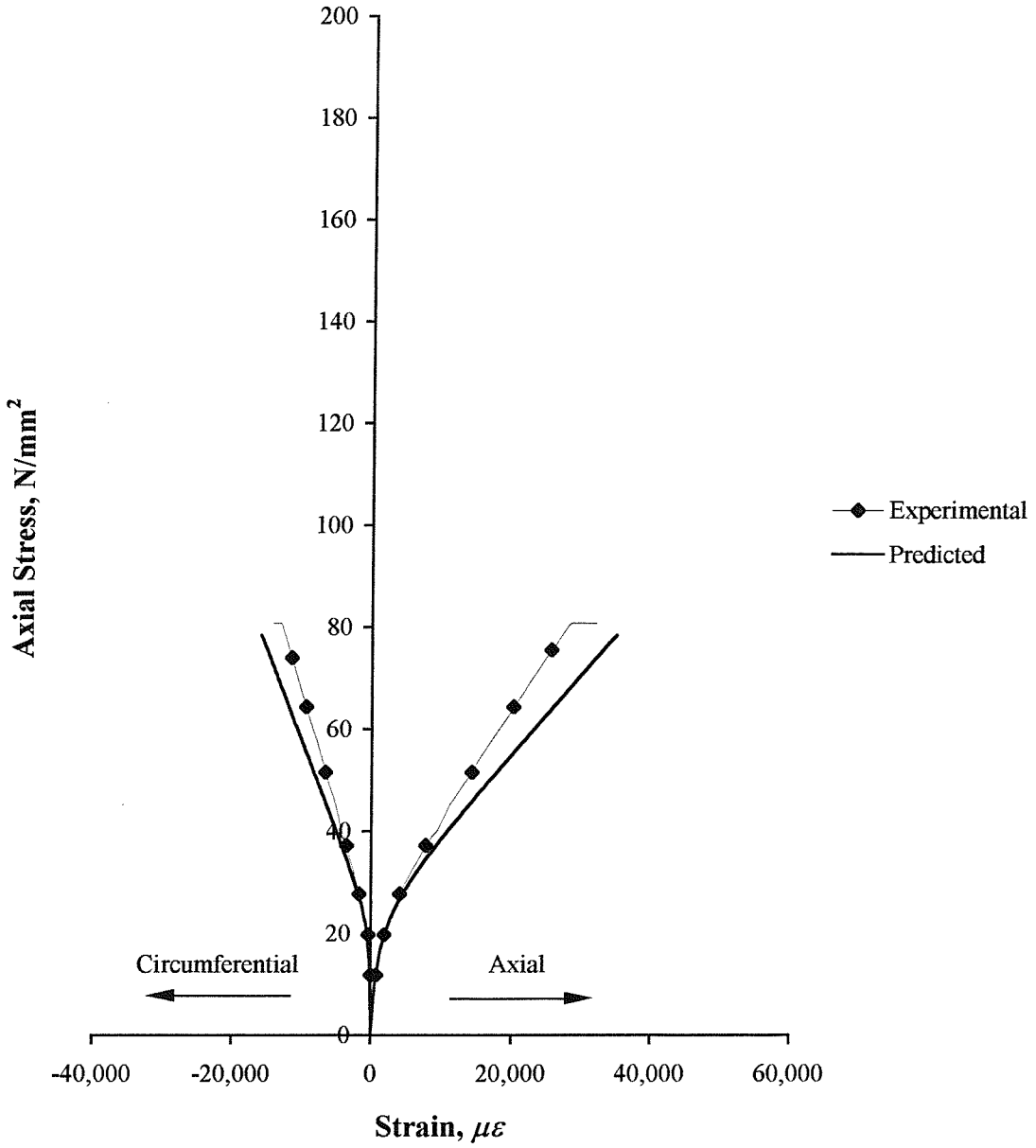

Figure D.11. Comparison of the theoretical and experimental stress-strain curves for the 400 mm diameter concrete-filled stub column confined with E-glass fibres orientated at 87.6 degrees (concrete cube strength = 32.3 N/mm^2)

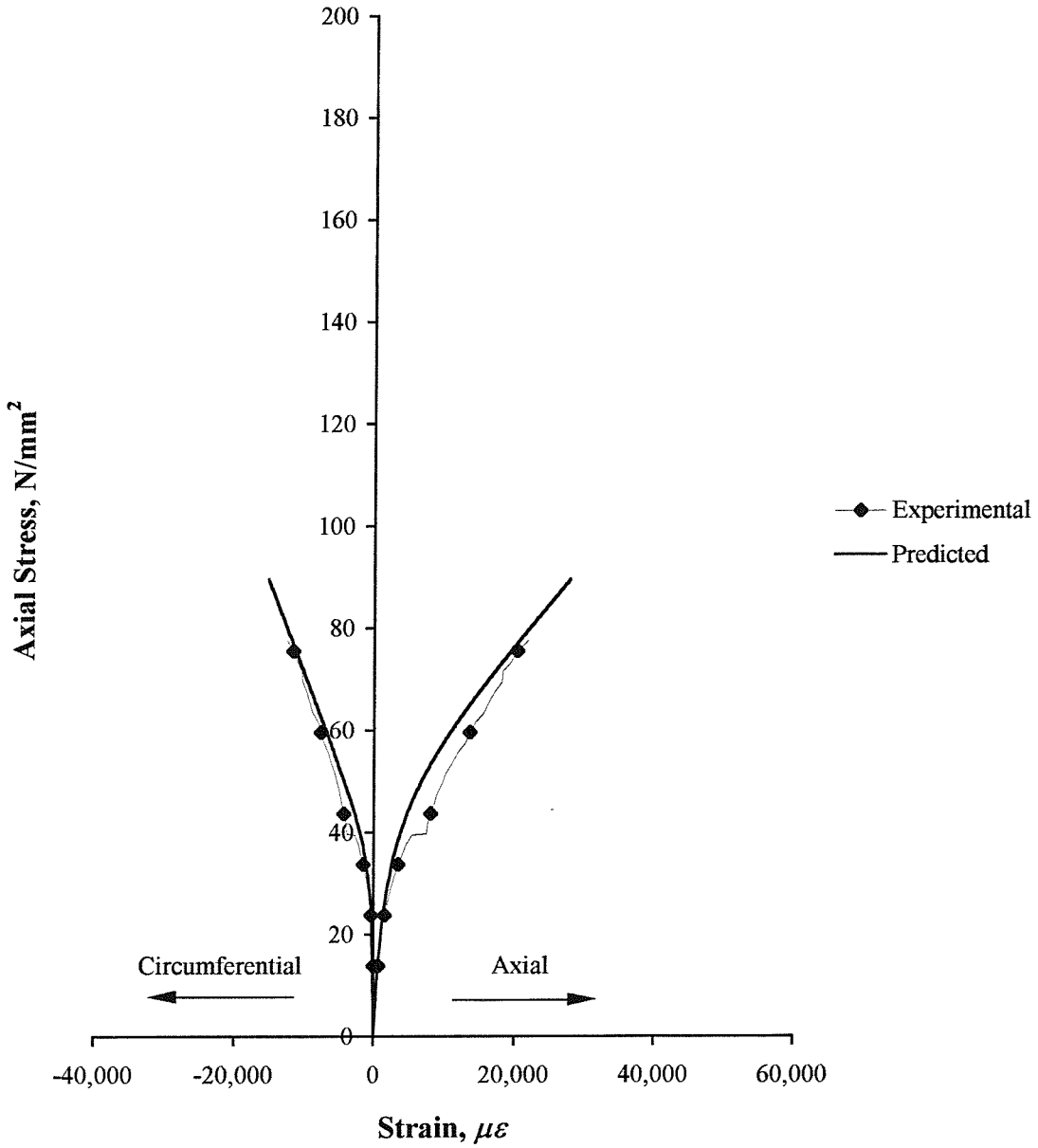

Figure D.12. Comparison of the theoretical and experimental stress-strain curves for the 400 mm diameter concrete-filled stub column confined with E-glass fibres orientated at 87.6 degrees (concrete cube strength = 40.8 N/mm^2)

APPENDIX E

COMPARISON OF THE THEORETICAL AND EXPERIMENTAL STRESS-VOLUMETRIC STRAIN CURVES FOR CONCRETE-FILLED E-GLASS FRP-COMPOSITE STUB COLUMNS WITH A NOMINAL 90 DEGREE FIBRE ORIENTATION

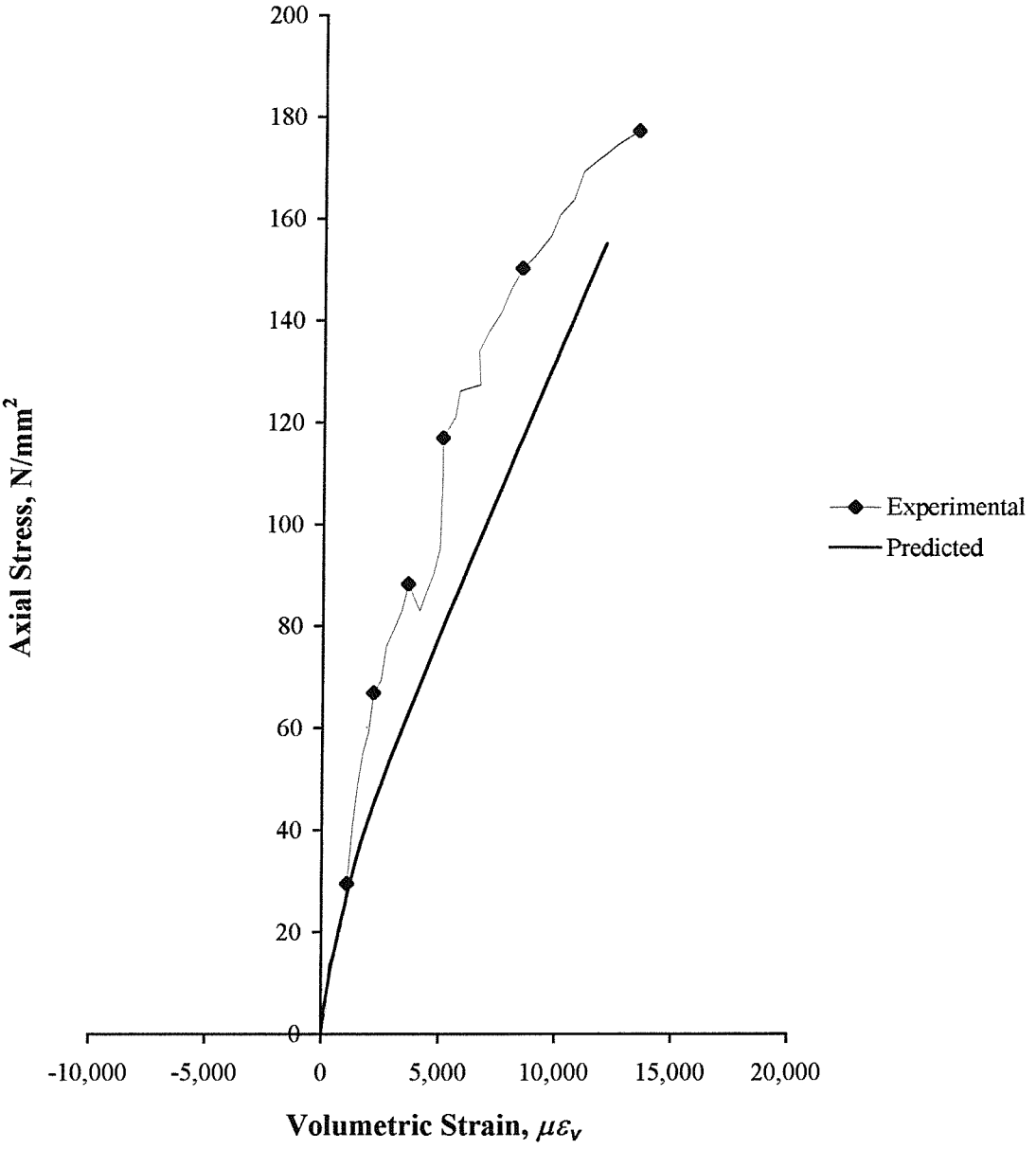

Figure E.1. Comparison of the theoretical and experimental stress-volumetric strain curves for the 80 mm diameter concrete-filled stub column confined with E-glass fibres orientated at 78.1 degrees (concrete cube strength = 23.4 N/mm^2)

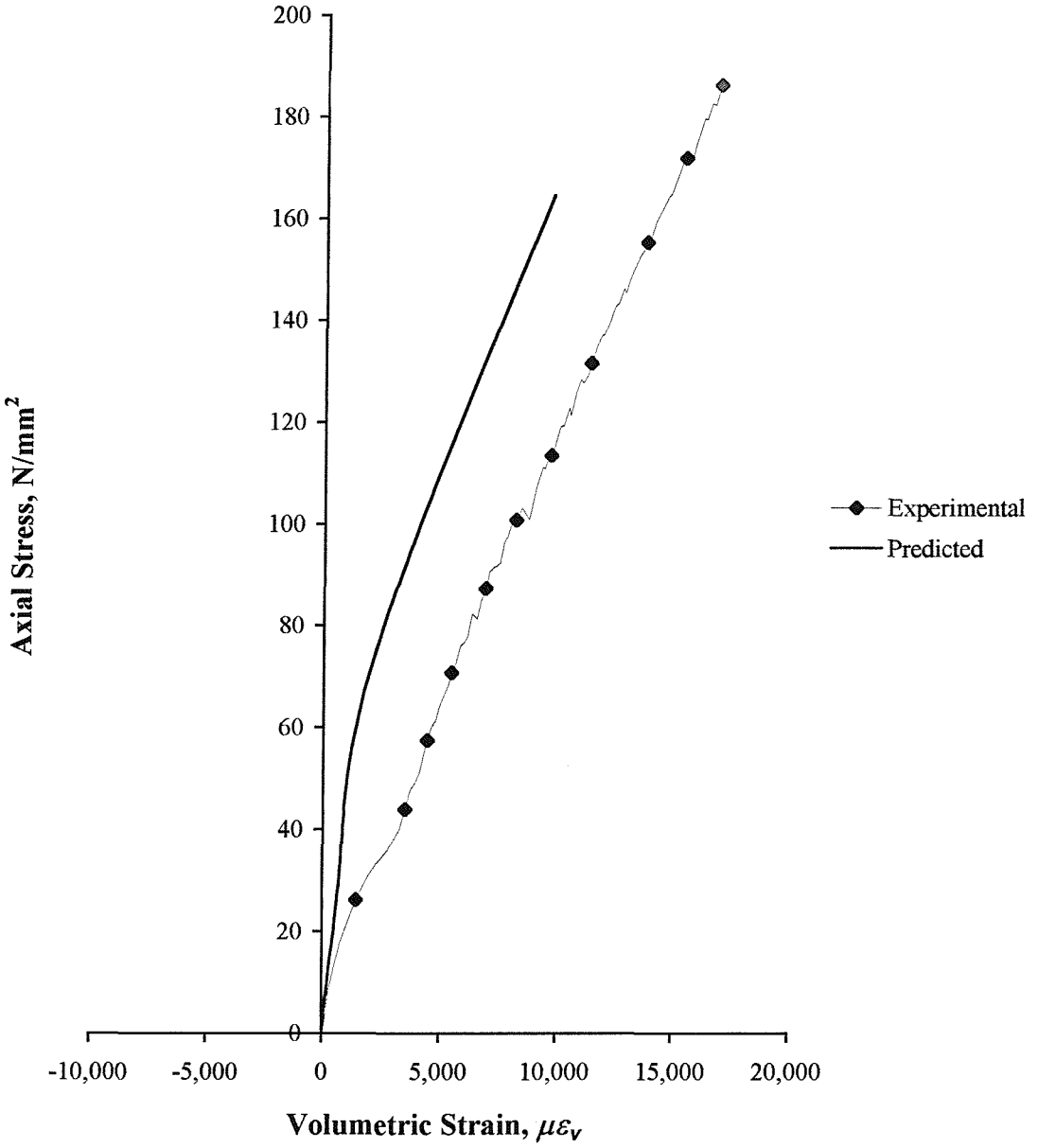

Figure E.2. Comparison of the theoretical and experimental stress-volumetric strain curves for the 80 mm diameter concrete-filled stub column confined with E-glass fibres orientated at 78.1 degrees (concrete cube strength = 35.2 N/mm^2)

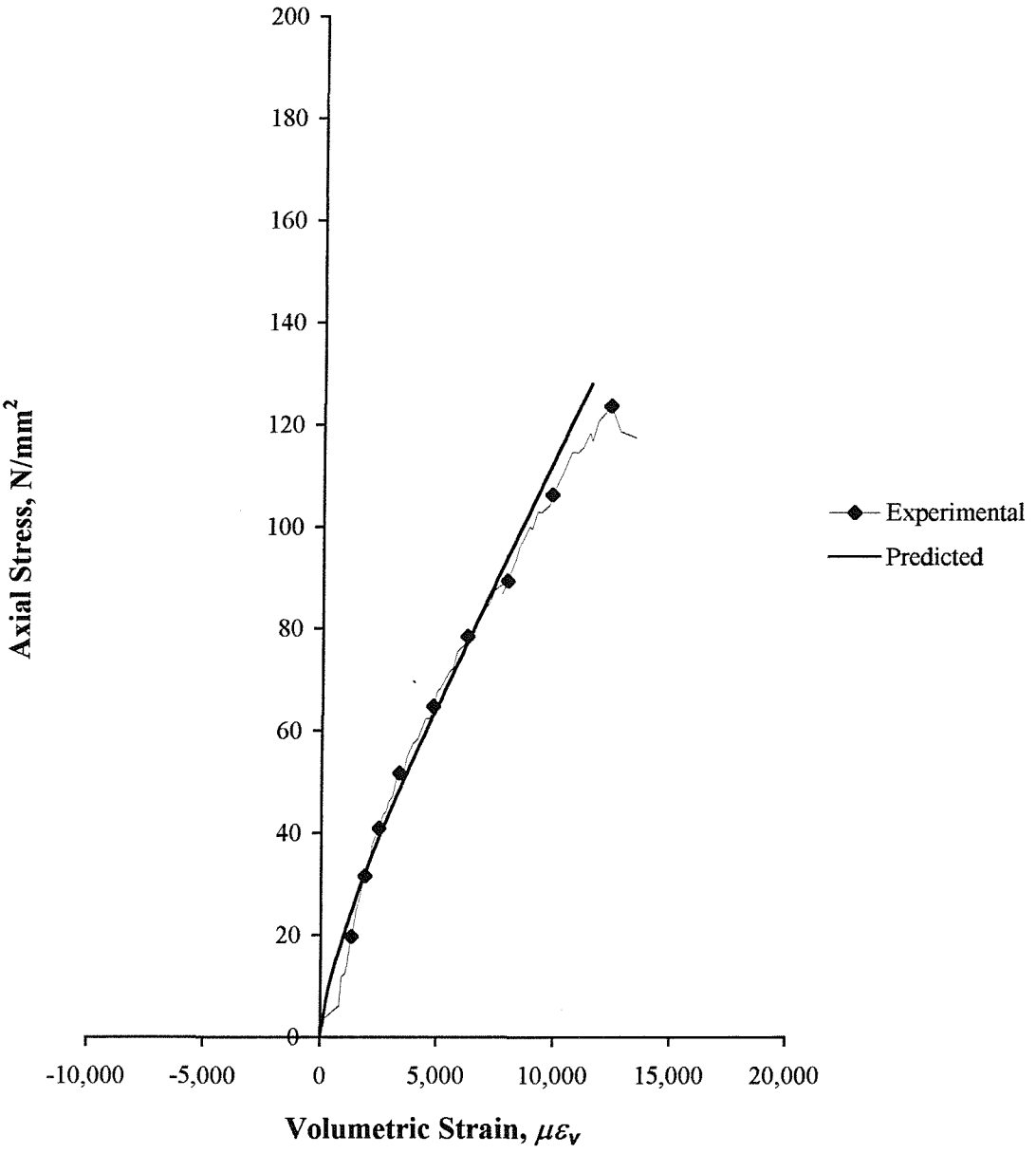

Figure E.3. Comparison of the theoretical and experimental stress-volumetric strain curves for the 100 mm diameter concrete-filled stub column confined with E-glass fibres orientated at 80.4 degrees (concrete cube strength = 19.7 N/mm^2)

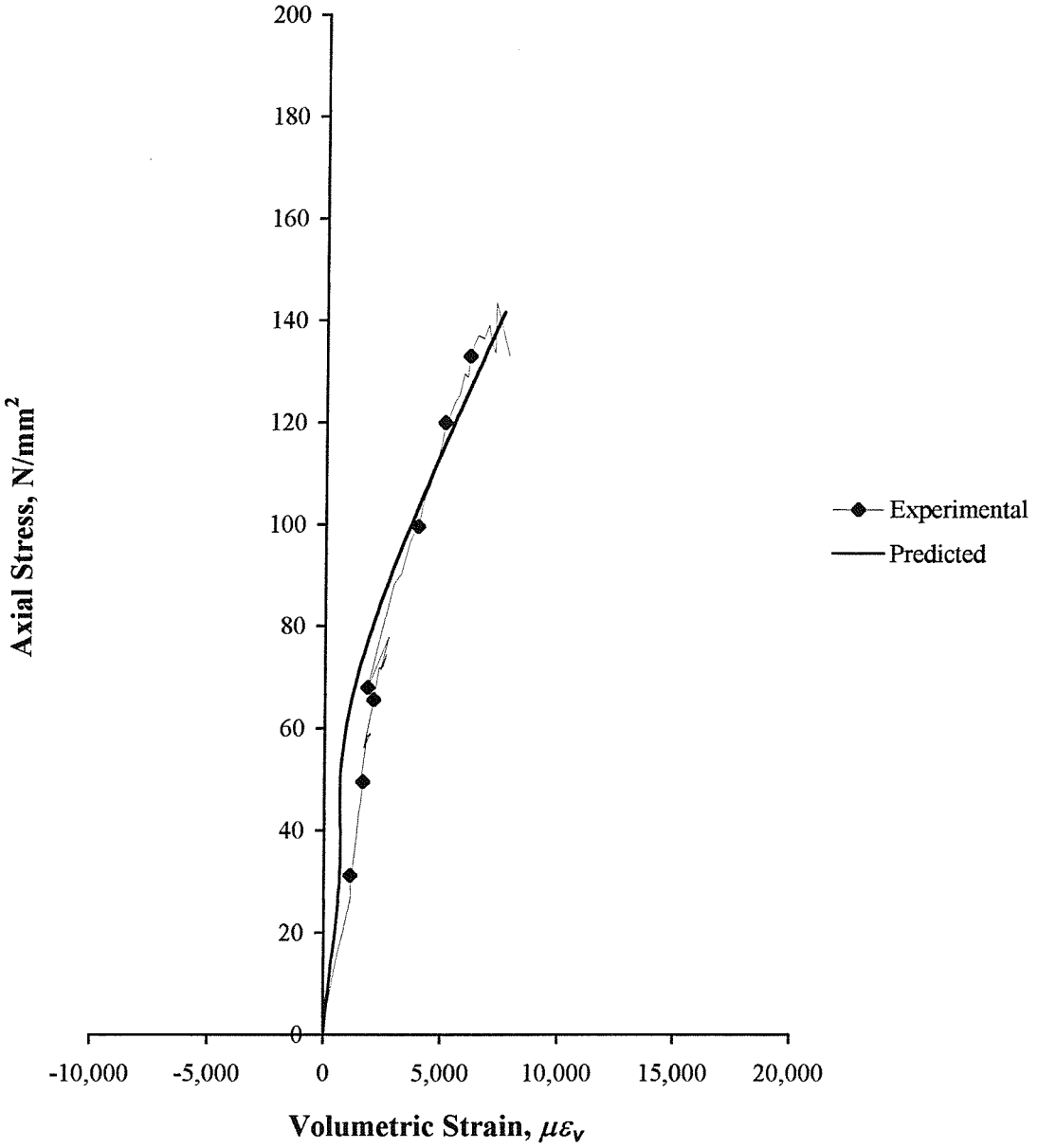

Figure E.4. Comparison of the theoretical and experimental stress-volumetric strain curves for the 100 mm diameter concrete-filled stub column confined with E-glass fibres orientated at 80.4 degrees (concrete cube strength = 36.2 N/mm^2)

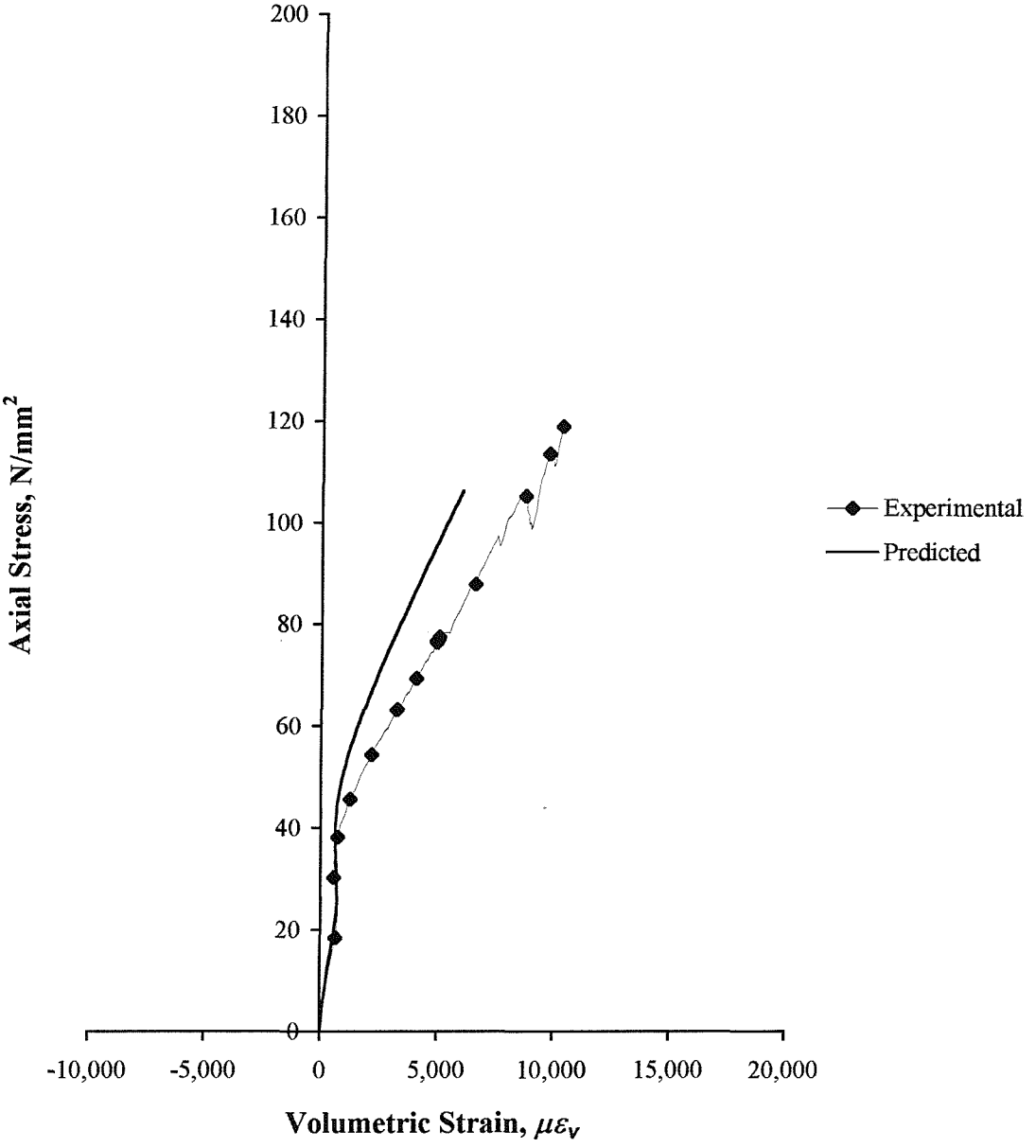

Figure E.5. Comparison of the theoretical and experimental stress-volumetric strain curves for the 125 mm diameter concrete-filled stub column confined with E-glass fibres orientated at 82.3 degrees (concrete cube strength = 29.2 N/mm^2)

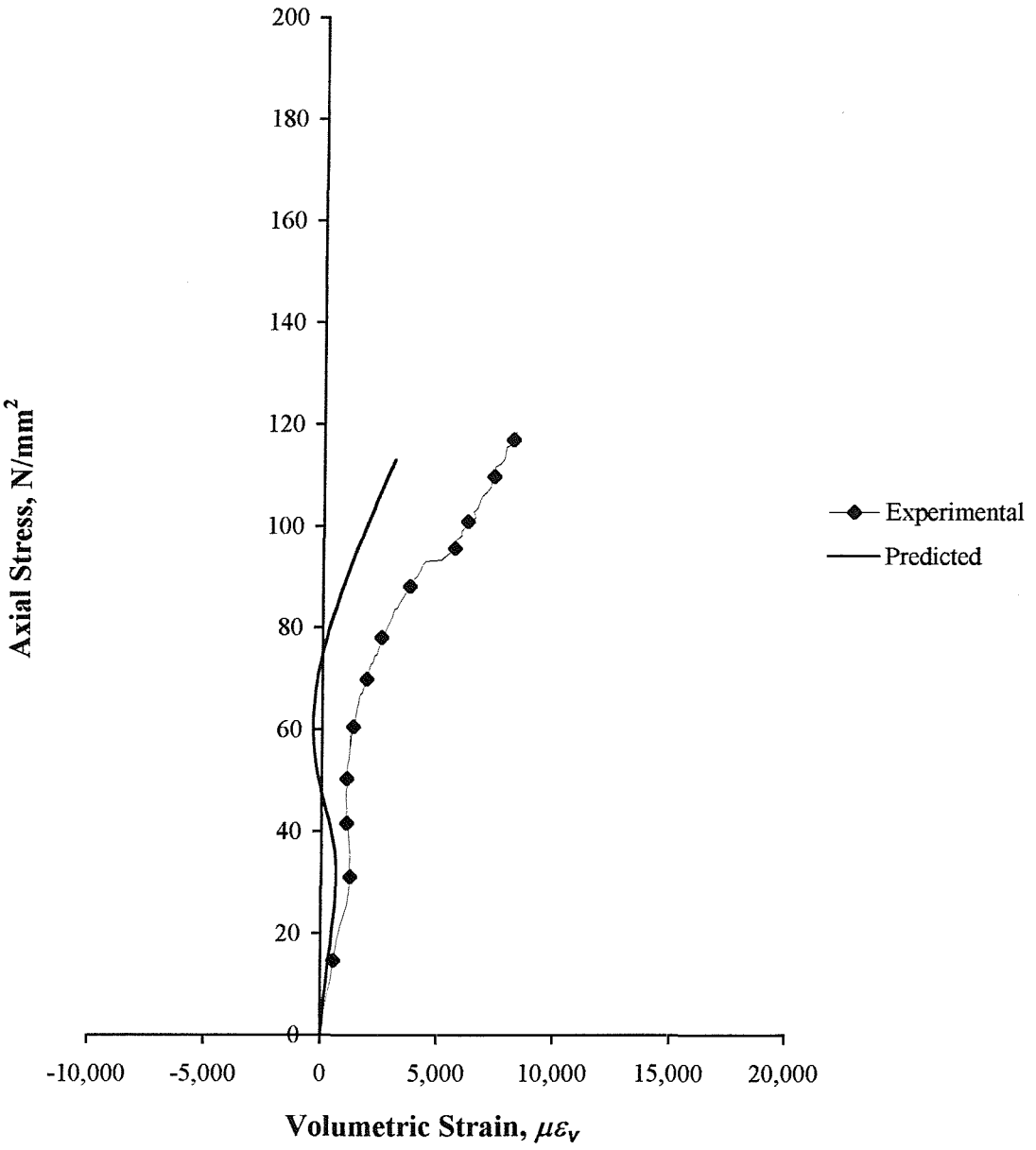

Figure E.6. Comparison of the theoretical and experimental stress-volumetric strain curves for the 125 mm diameter concrete-filled stub column confined with E-glass fibres orientated at 82.3 degrees (concrete cube strength = 37.5 N/mm^2)

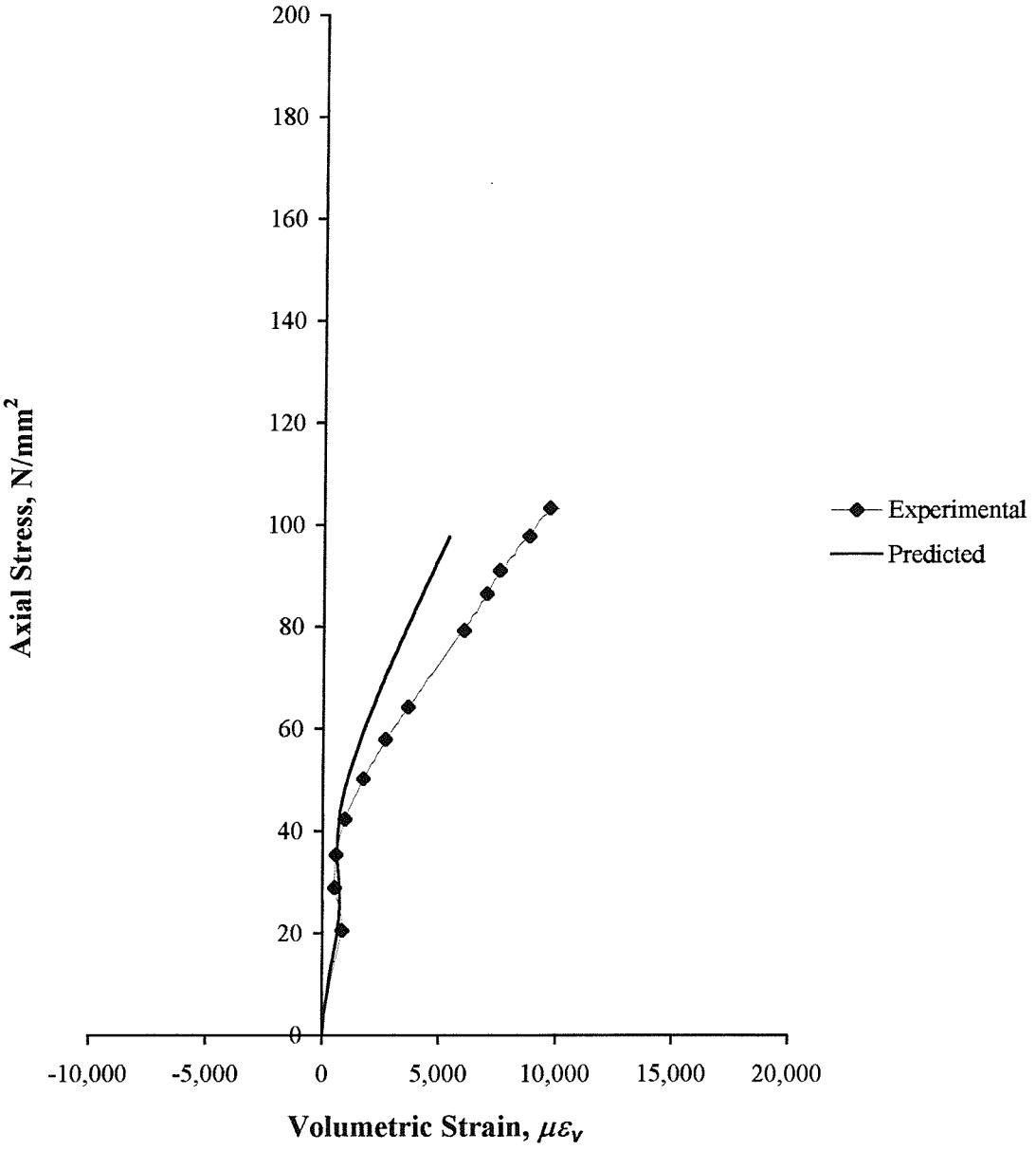

Figure E.7. Comparison of the theoretical and experimental stress-volumetric strain curves for the 150 mm diameter concrete-filled stub column confined with E-glass fibres orientated at 83.6 degrees (concrete cube strength = 27.4 N/mm^2)

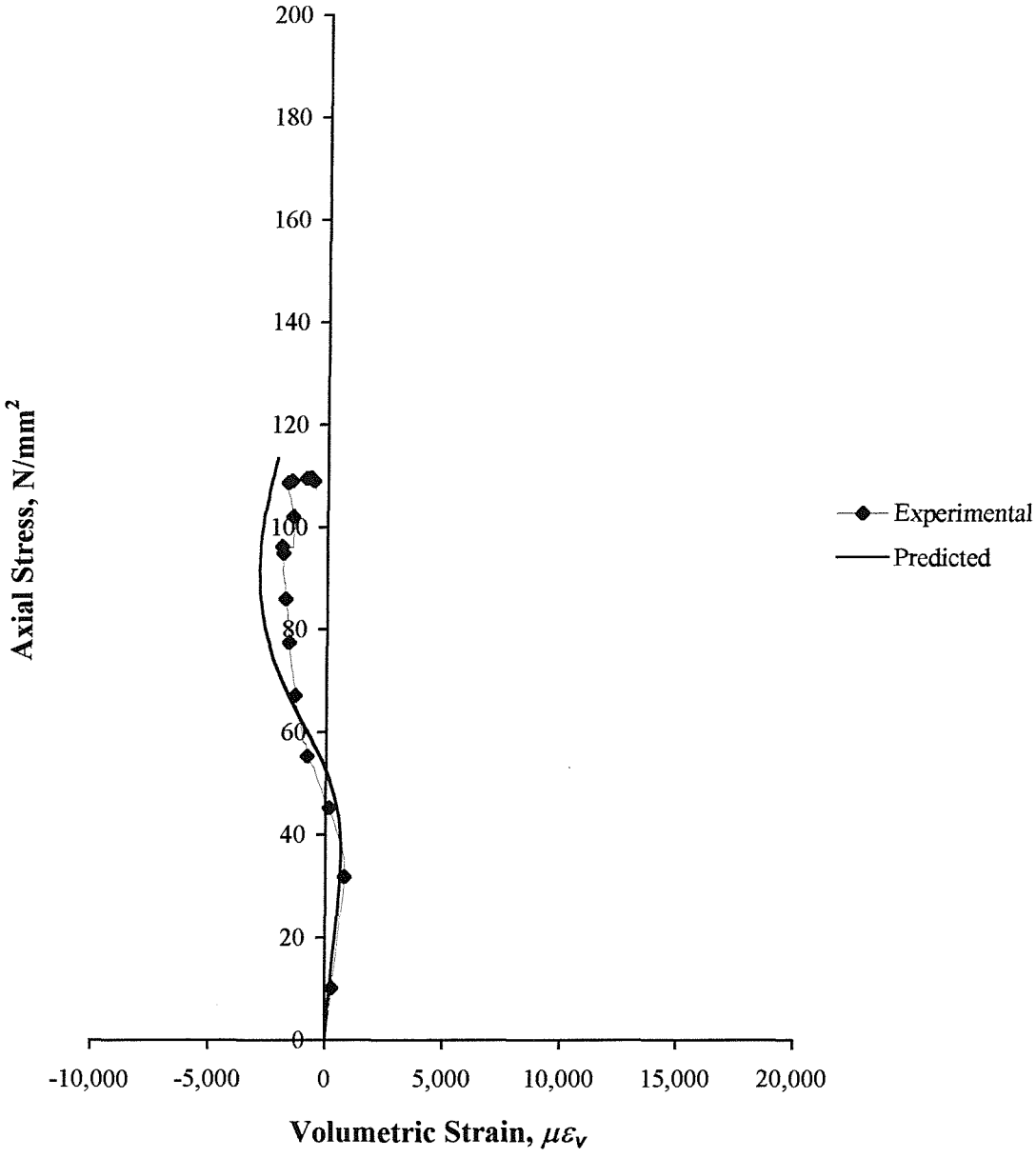

Figure E.8. Comparison of the theoretical and experimental stress-volumetric strain curves for the 150 mm diameter concrete-filled stub column confined with E-glass fibres orientated at 83.6 degrees (concrete cube strength = 46.3 N/mm^2)

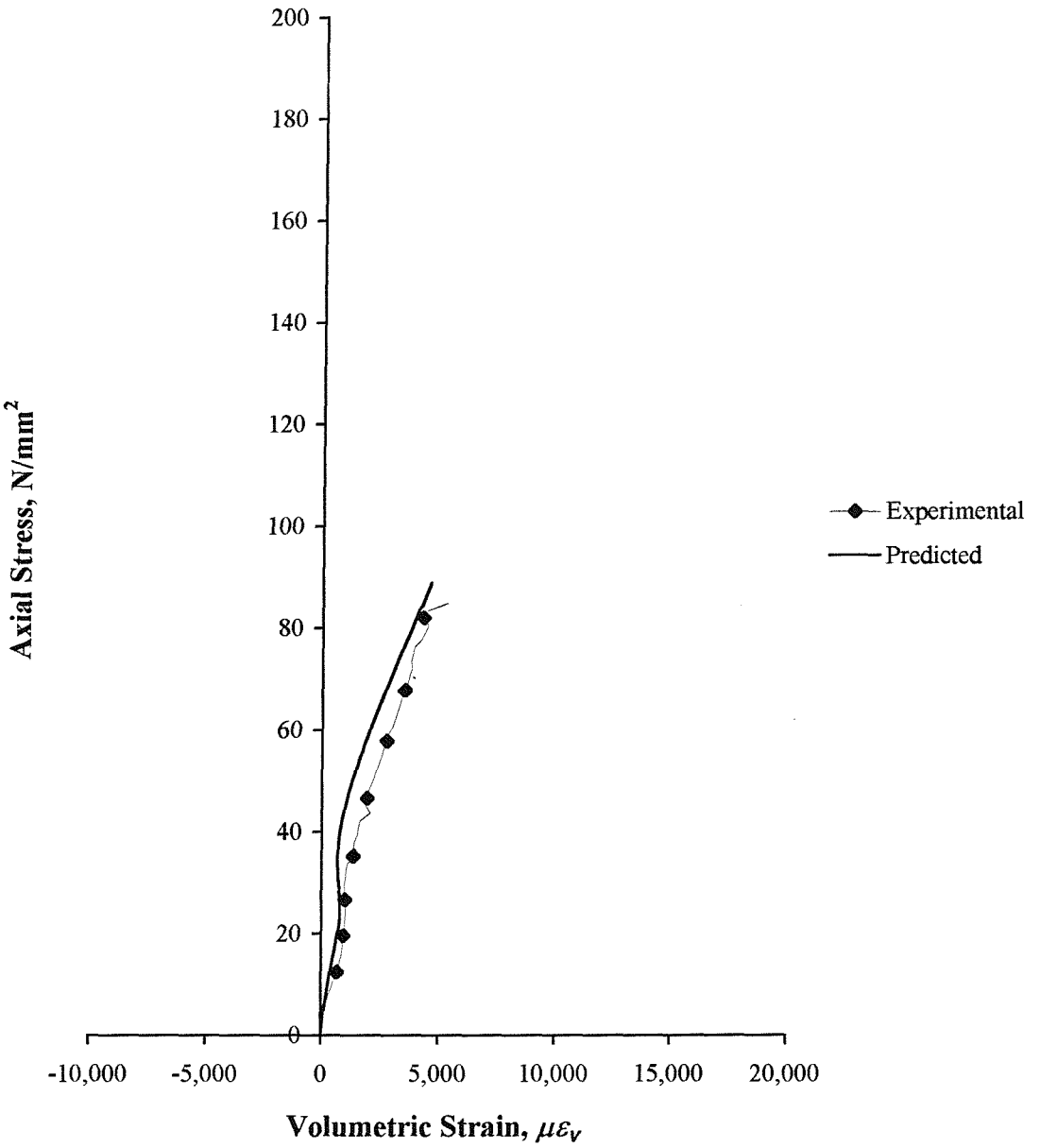

Figure E.9. Comparison of the theoretical and experimental stress-volumetric strain curves for the 300 mm diameter concrete-filled stub column confined with E-glass fibres orientated at 86.8 degrees (concrete cube strength = 34.0 N/mm^2)

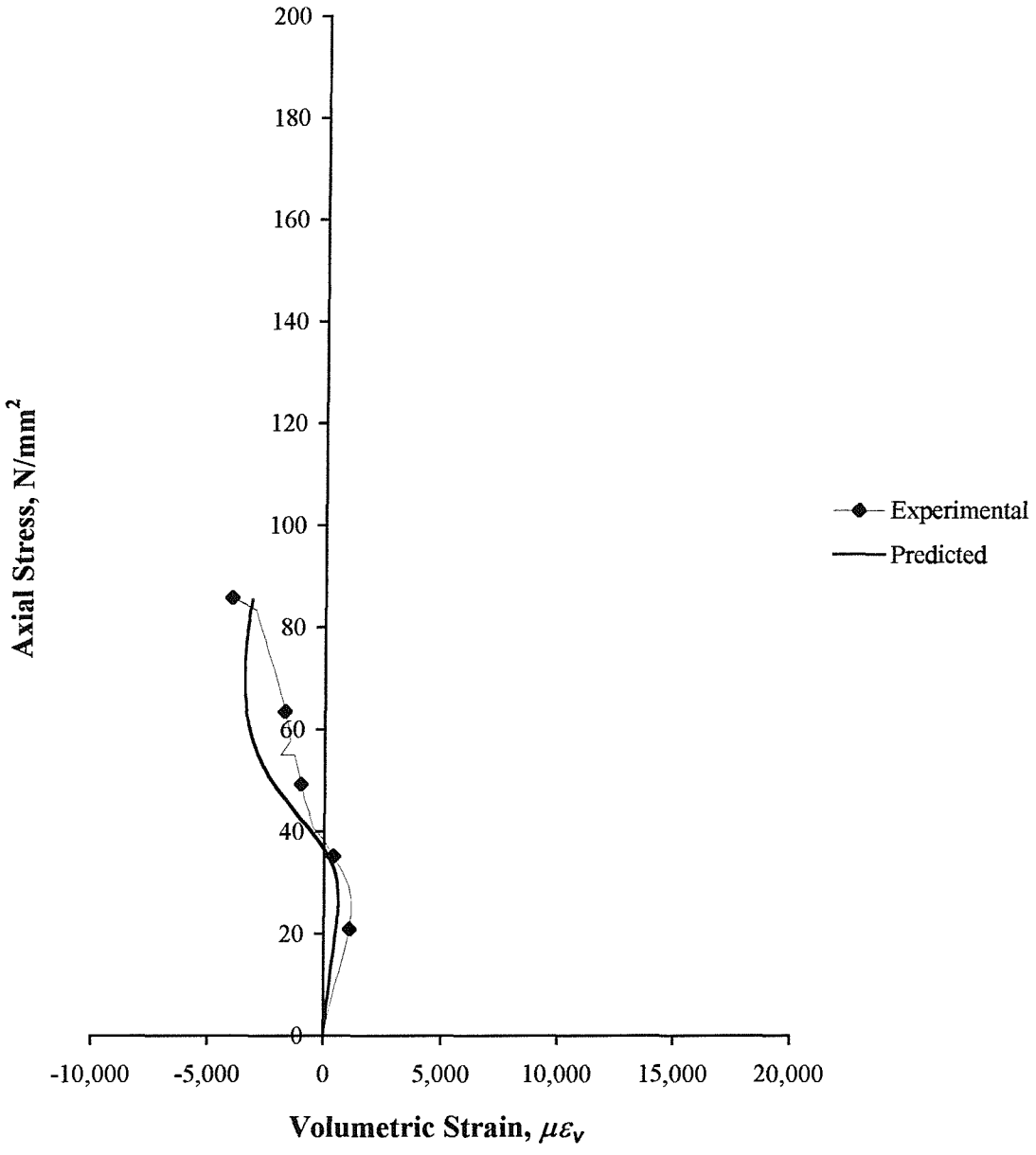

Figure E.10. Comparison of the theoretical and experimental stress-volumetric strain curves for the 300 mm diameter concrete-filled stub column confined with E-glass fibres orientated at 86.8 degrees (concrete cube strength = 38.6 N/mm^2)

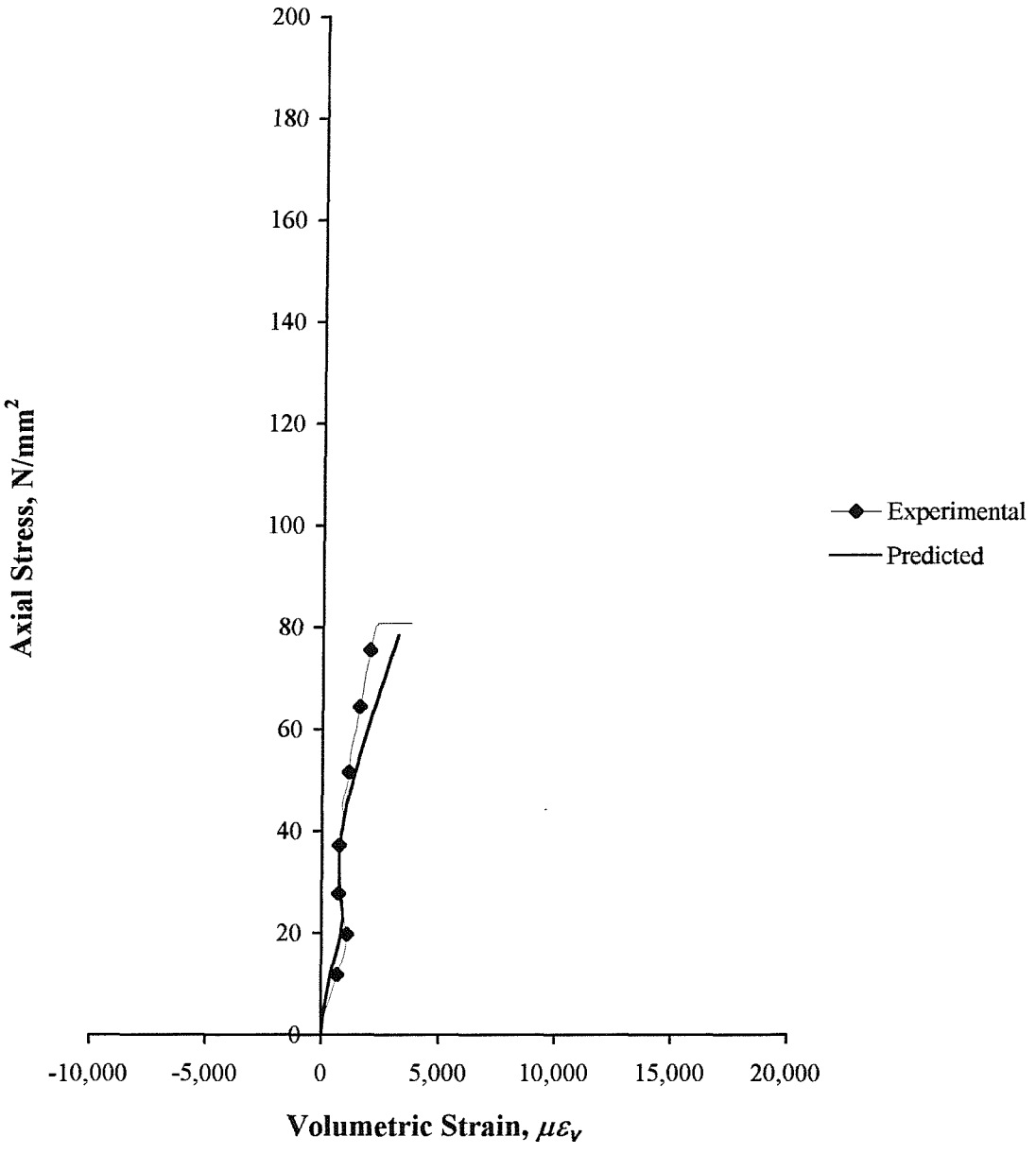

Figure E.11. Comparison of the theoretical and experimental stress-volumetric strain curves for the 400 mm diameter concrete-filled stub column confined with E-glass fibres orientated at 87.6 degrees (concrete cube strength = 32.3 N/mm^2)

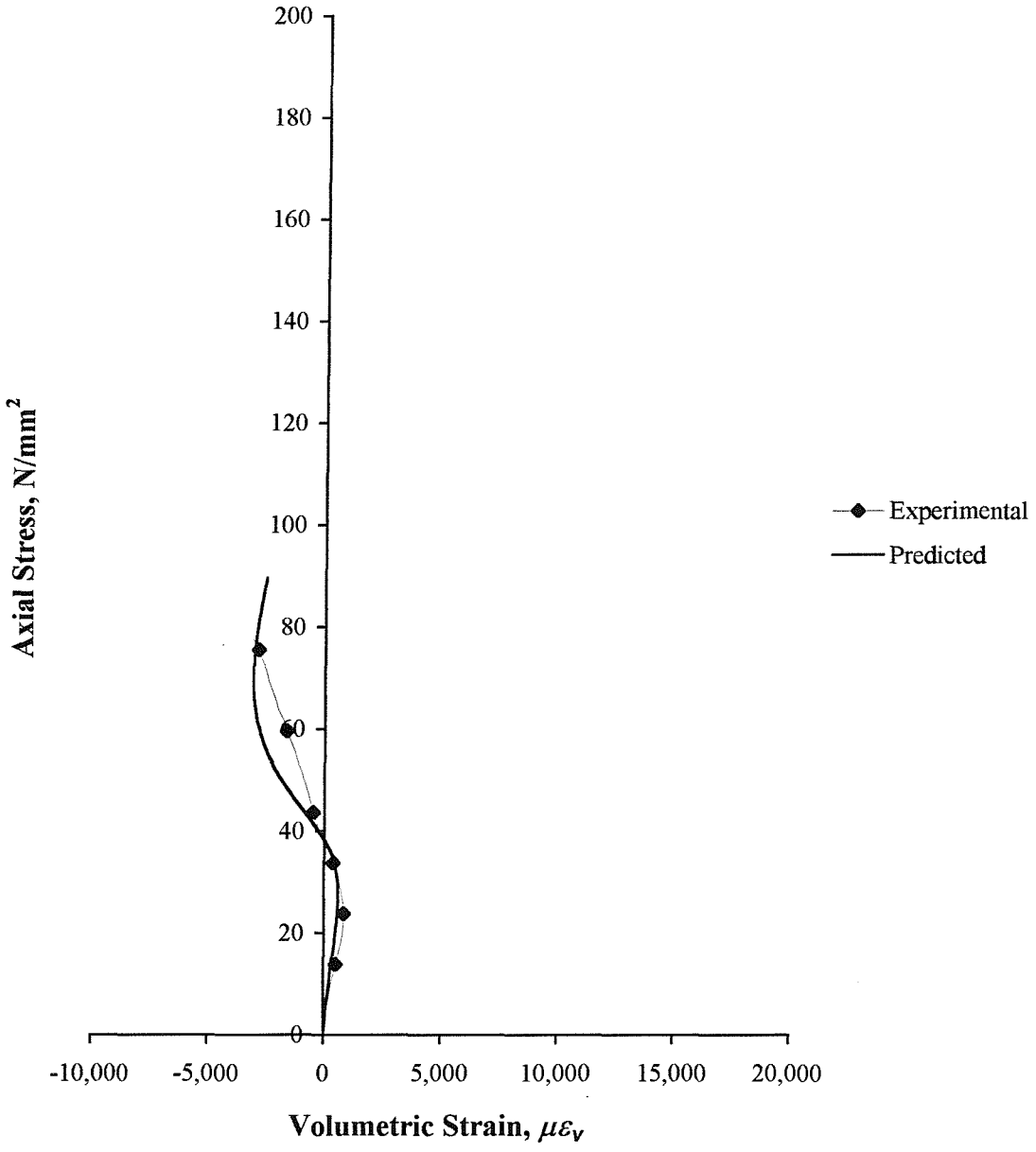

Figure E.12. Comparison of the theoretical and experimental stress-volumetric strain curves for the 400 mm diameter concrete-filled stub column confined with E-glass fibres orientated at 87.6 degrees (concrete cube strength = 40.8 N/mm^2)

APPENDIX F

COMPARISON OF THE THEORETICAL AND EXPERIMENTAL STRESS-VOLUMETRIC STRAIN CURVES FOR CONCRETE-FILLED E-GLASS FRP-COMPOSITE STUB COLUMNS WITH A NOMINAL 67½ DEGREE FIBRE ORIENTATION

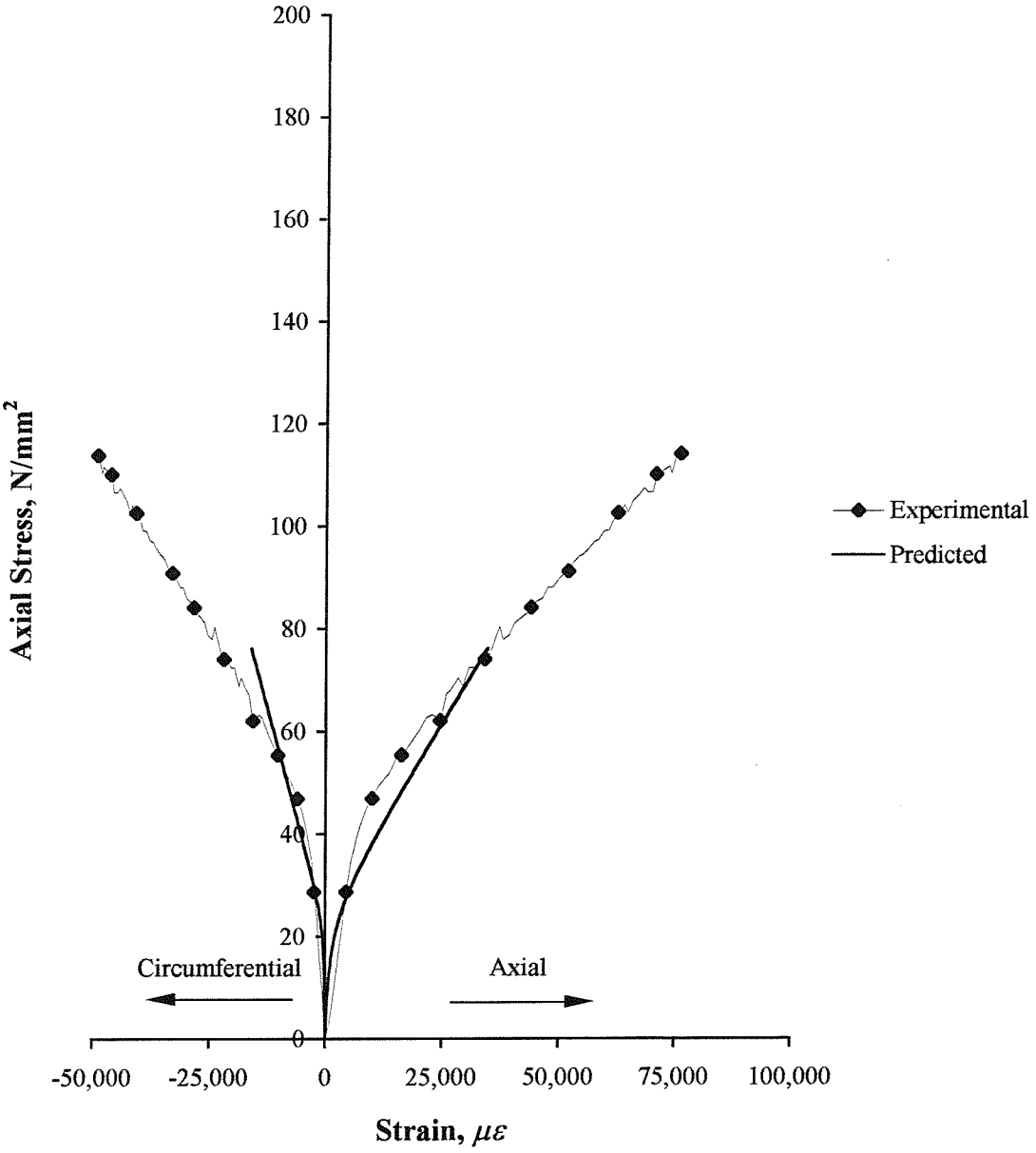

Figure F.1. Comparison of the theoretical and experimental stress-strain curves for the 80 mm diameter concrete-filled stub column confined with E-glass fibres orientated at 57.8 degrees (concrete cube strength = 22.6 N/mm^2)

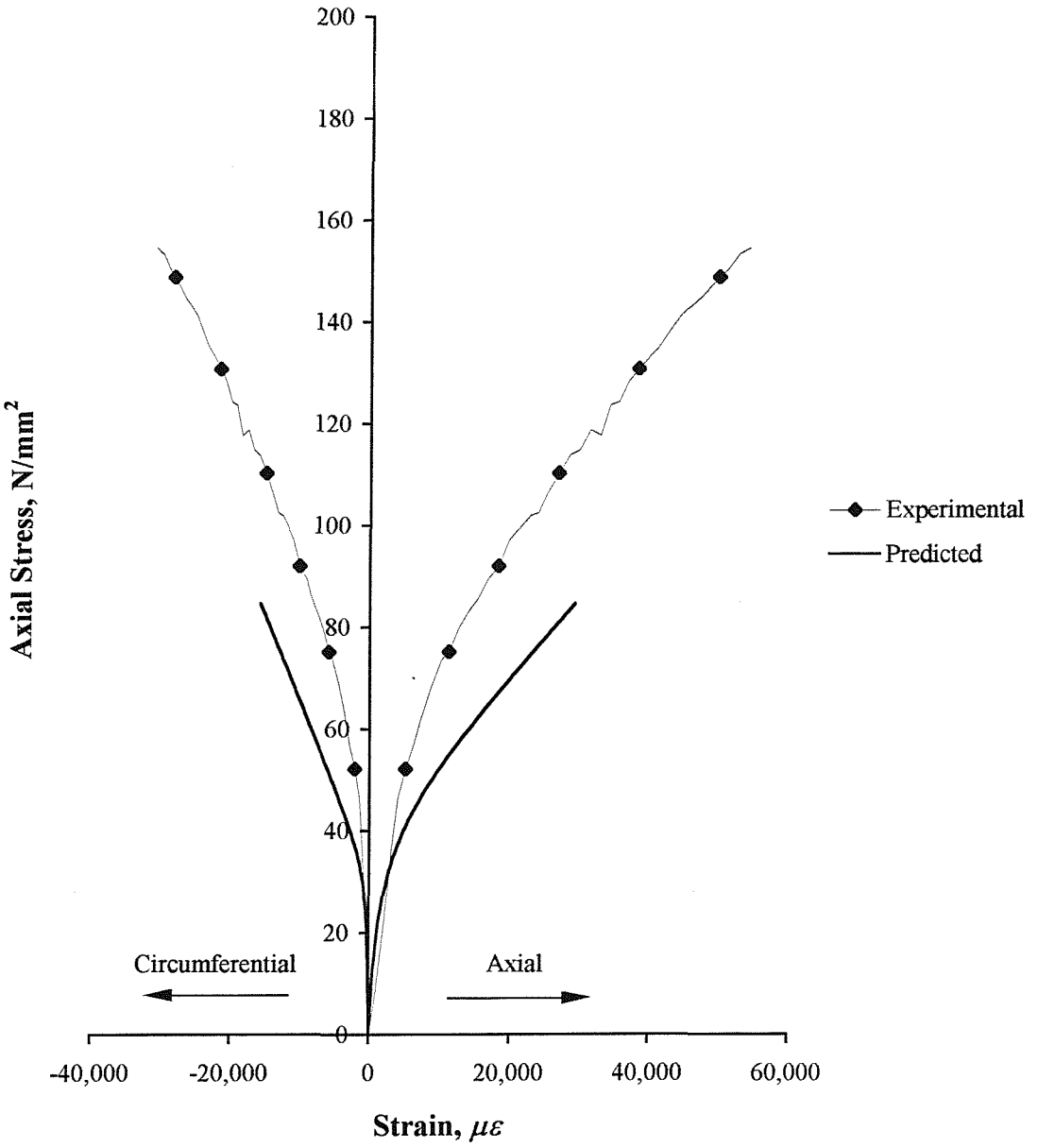

Figure F.2. Comparison of the theoretical and experimental stress-strain curves for the 80 mm diameter concrete-filled stub column confined with E-glass fibres orientated at 57.8 degrees (concrete cube strength = 32.8 N/mm^2)

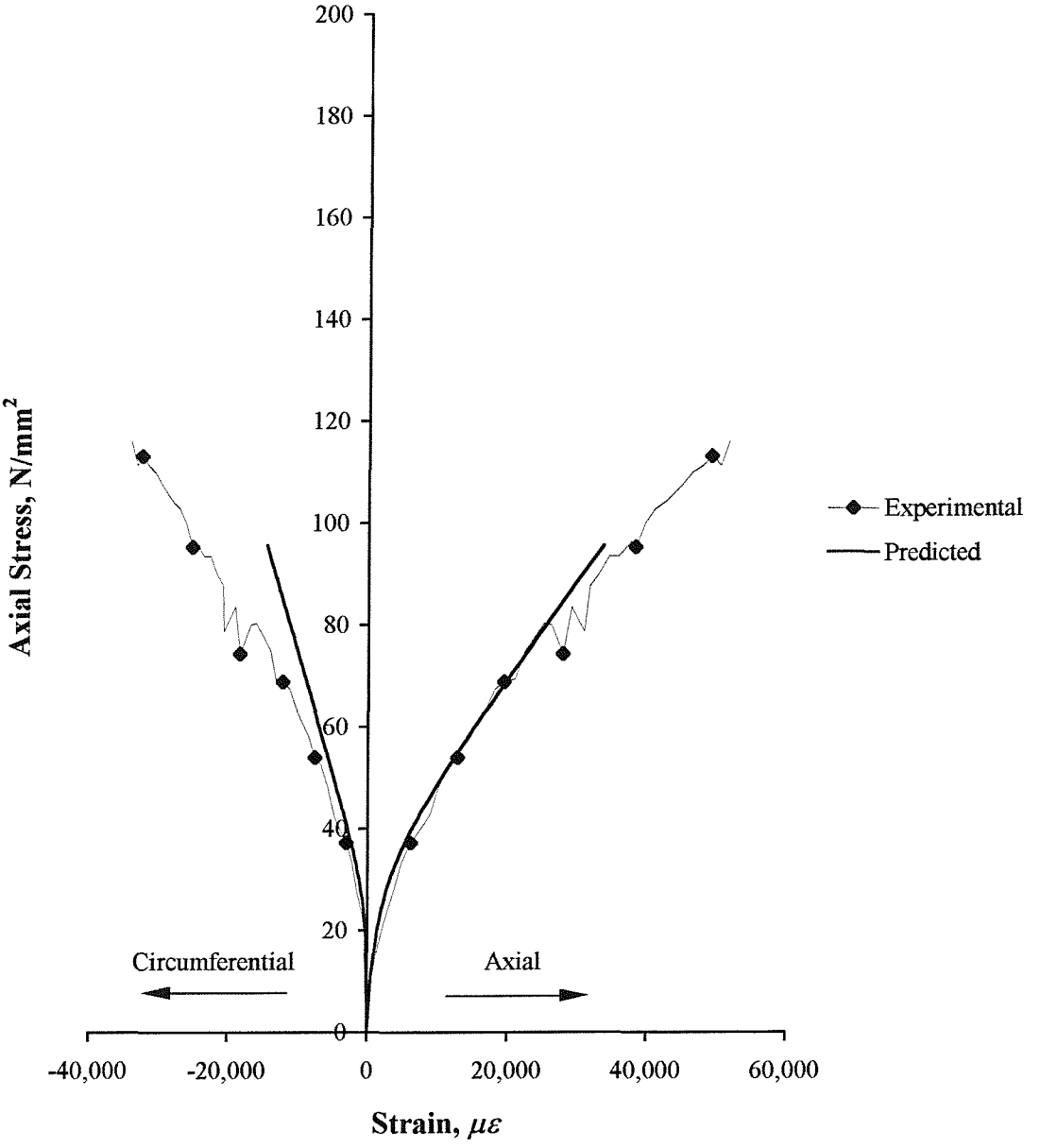

Figure F.3. Comparison of the theoretical and experimental stress-strain curves for the 100 mm diameter concrete-filled stub column confined with E-glass fibres orientated at 71.4 degrees (concrete cube strength = 28.2 N/mm^2)

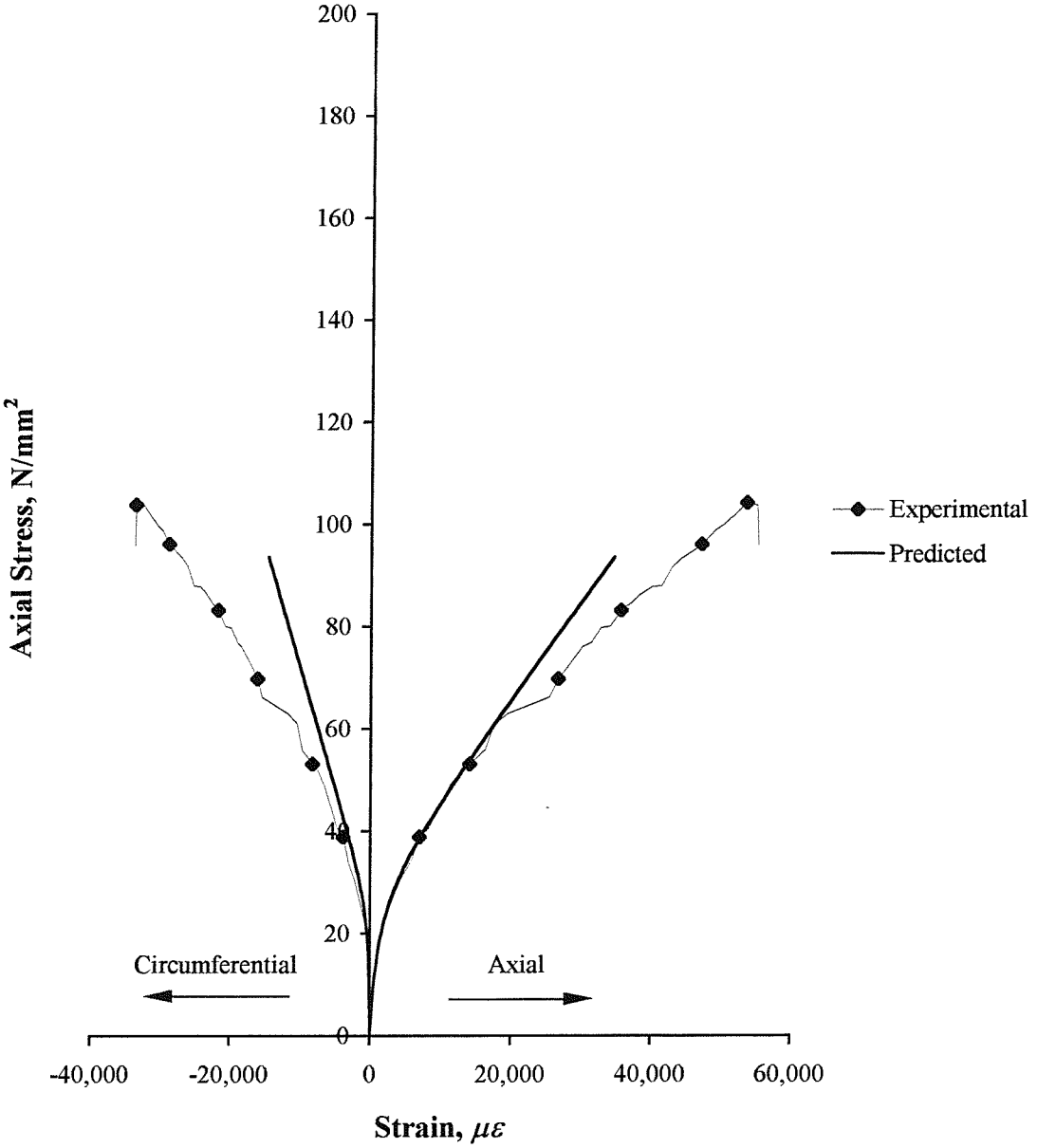

Figure F.4. Comparison of the theoretical and experimental stress-strain curves for the 100 mm diameter concrete-filled stub column confined with E-glass fibres orientated at 71.4 degrees (concrete cube strength = 25.6 N/mm^2)

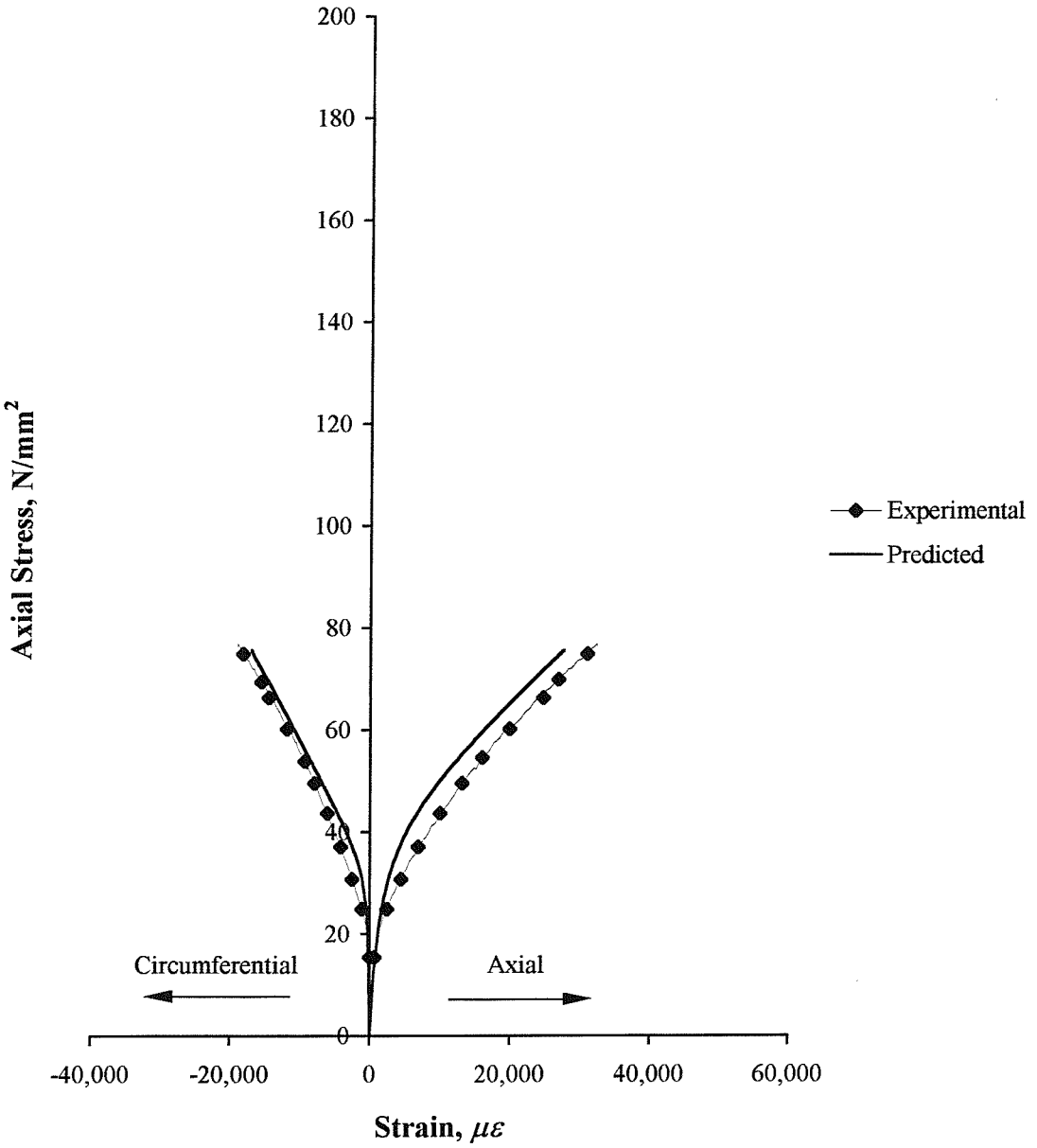

Figure F.5. Comparison of the theoretical and experimental stress-strain curves for the 150 mm diameter concrete-filled stub column confined with E-glass fibres orientated at 71.3 degrees (concrete cube strength = 32.7 N/mm^2)

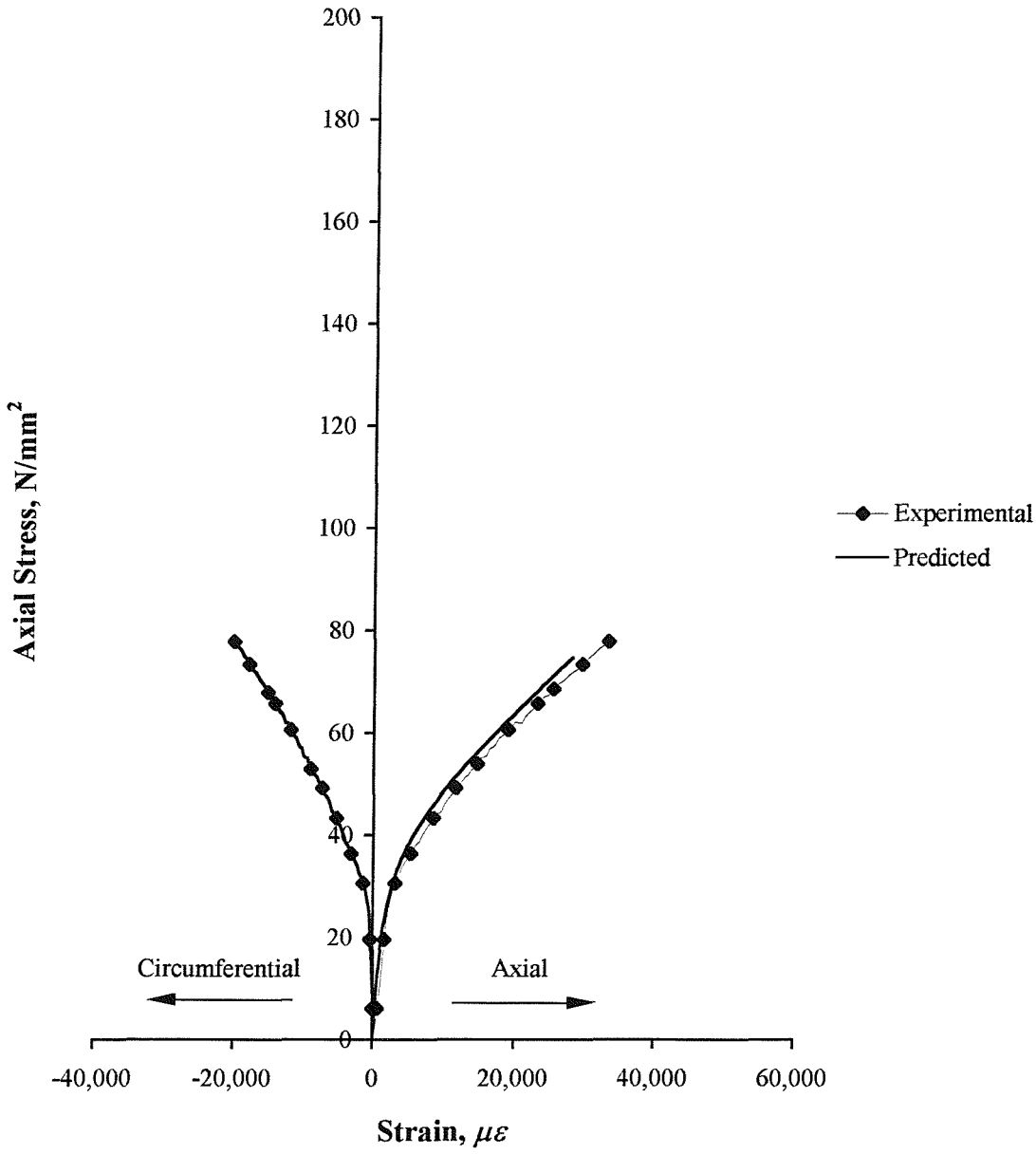

Figure F.6. Comparison of the theoretical and experimental stress-strain curves for the 150 mm diameter concrete-filled stub column confined with E-glass fibres orientated at 71.3 degrees (concrete cube strength = 31.7 N/mm^2)

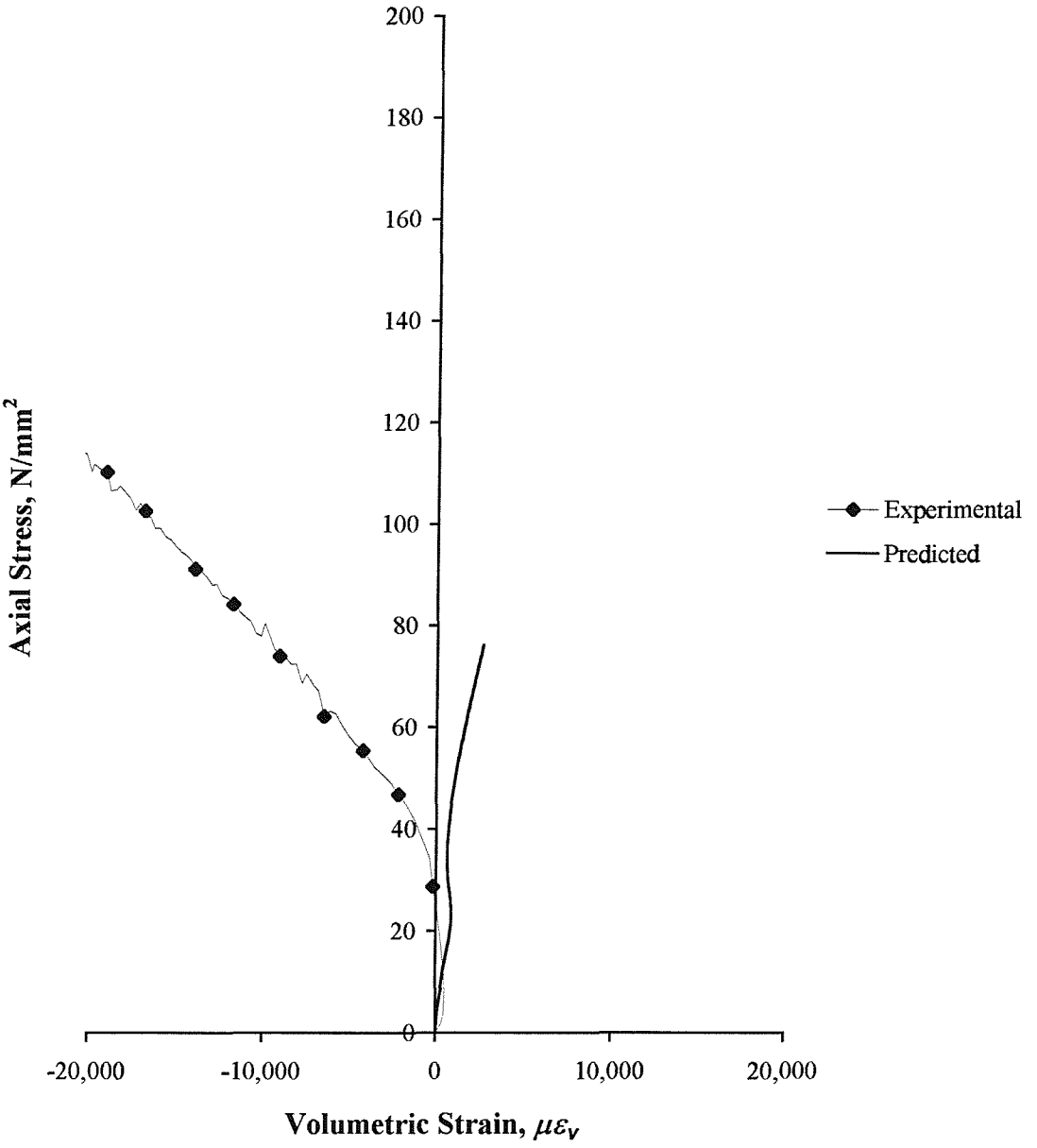

Figure F.7. Comparison of the theoretical and experimental stress-volumetric strain curves for the 80 mm diameter concrete-filled stub column confined with E-glass fibres orientated at 57.8 degrees (concrete cube strength = 22.6 N/mm^2)

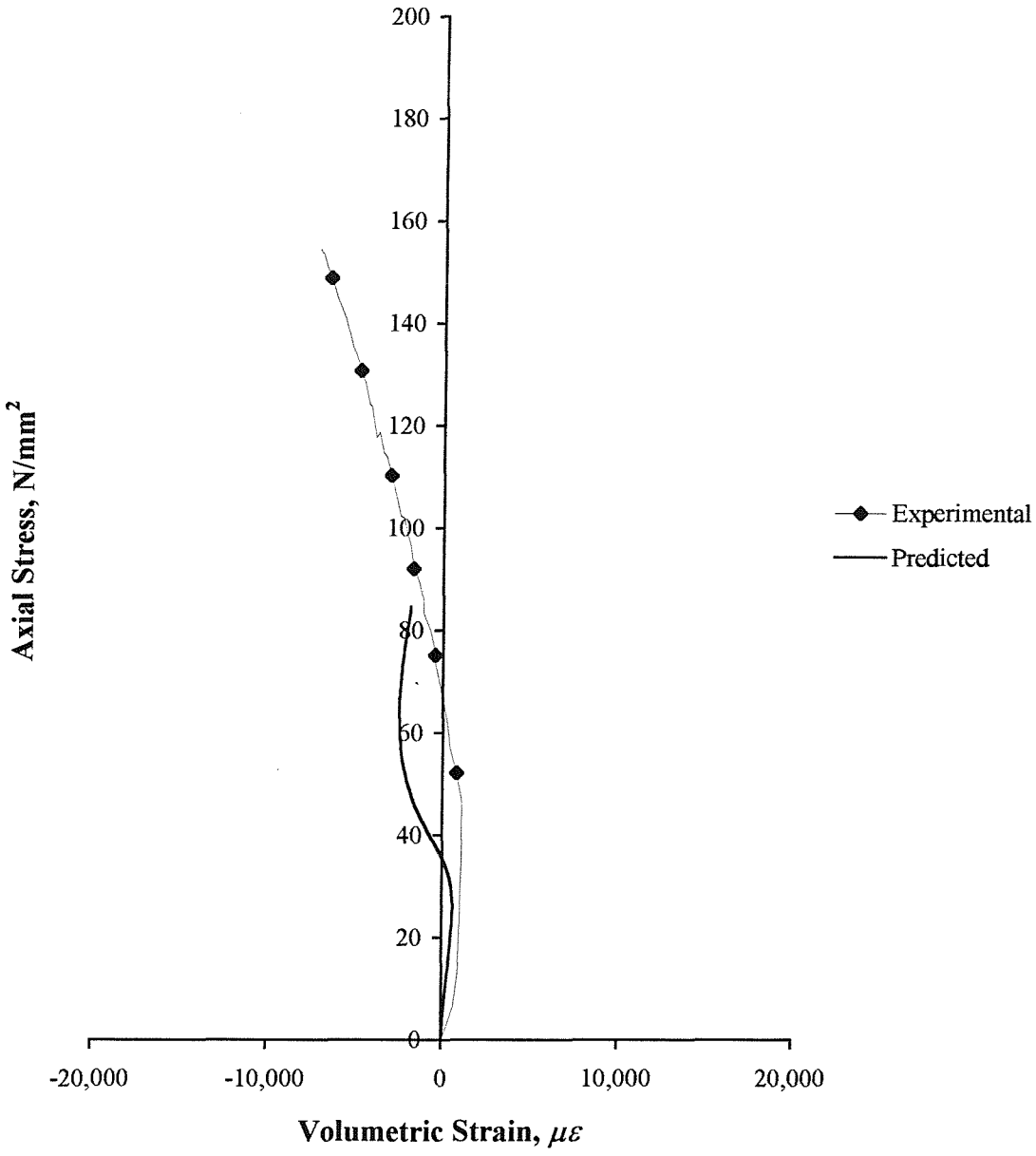

Figure F.8. Comparison of the theoretical and experimental stress-volumetric strain curves for the 80 mm diameter concrete-filled stub column confined with E-glass fibres orientated at 57.8 degrees (concrete cube strength = 32.8 N/mm^2)

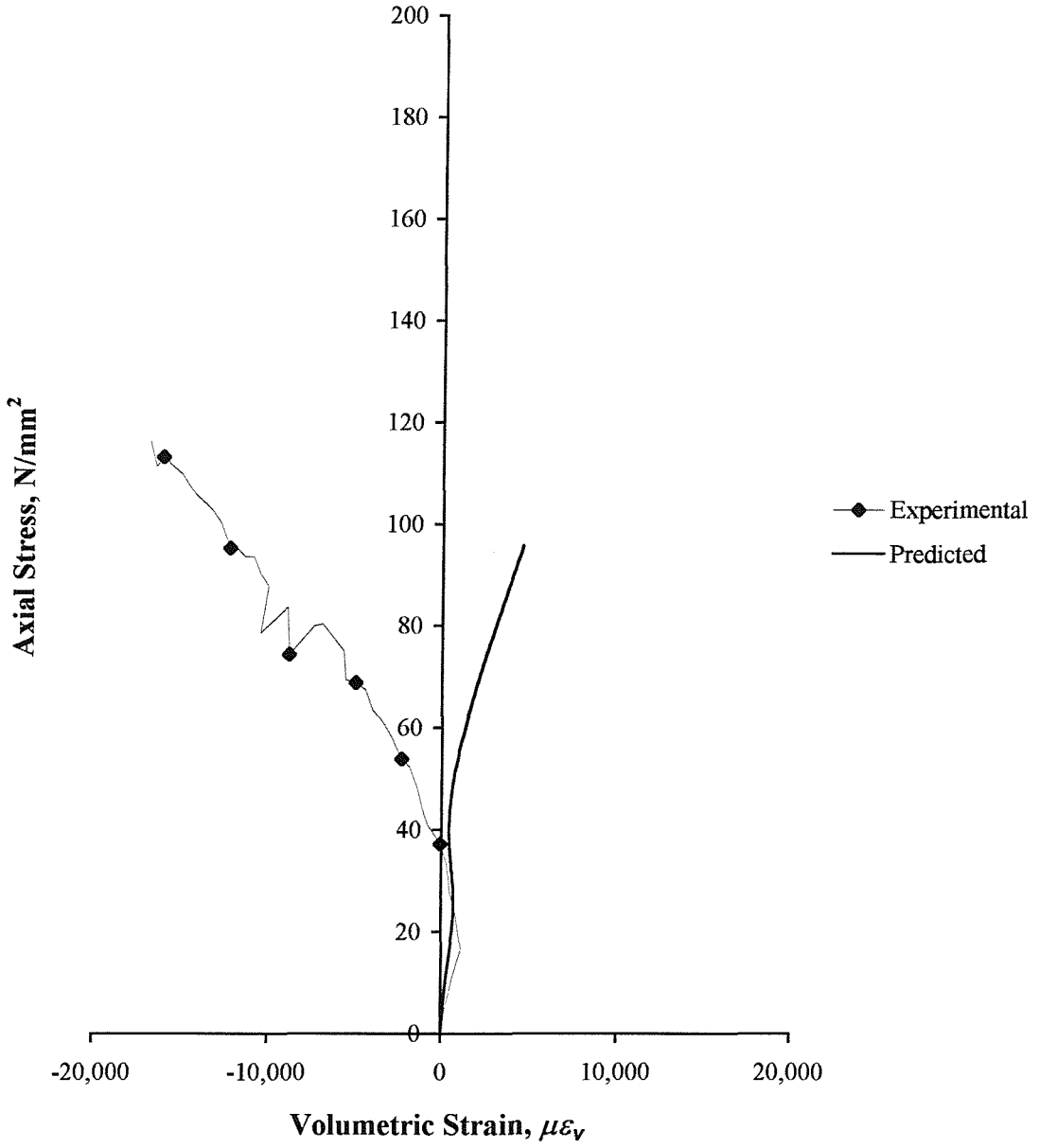

Figure F.9. Comparison of the theoretical and experimental stress-volumetric strain curves for the 100 mm diameter concrete-filled stub column confined with E-glass fibres orientated at 71.4 degrees (concrete cube strength = 28.2 N/mm^2)

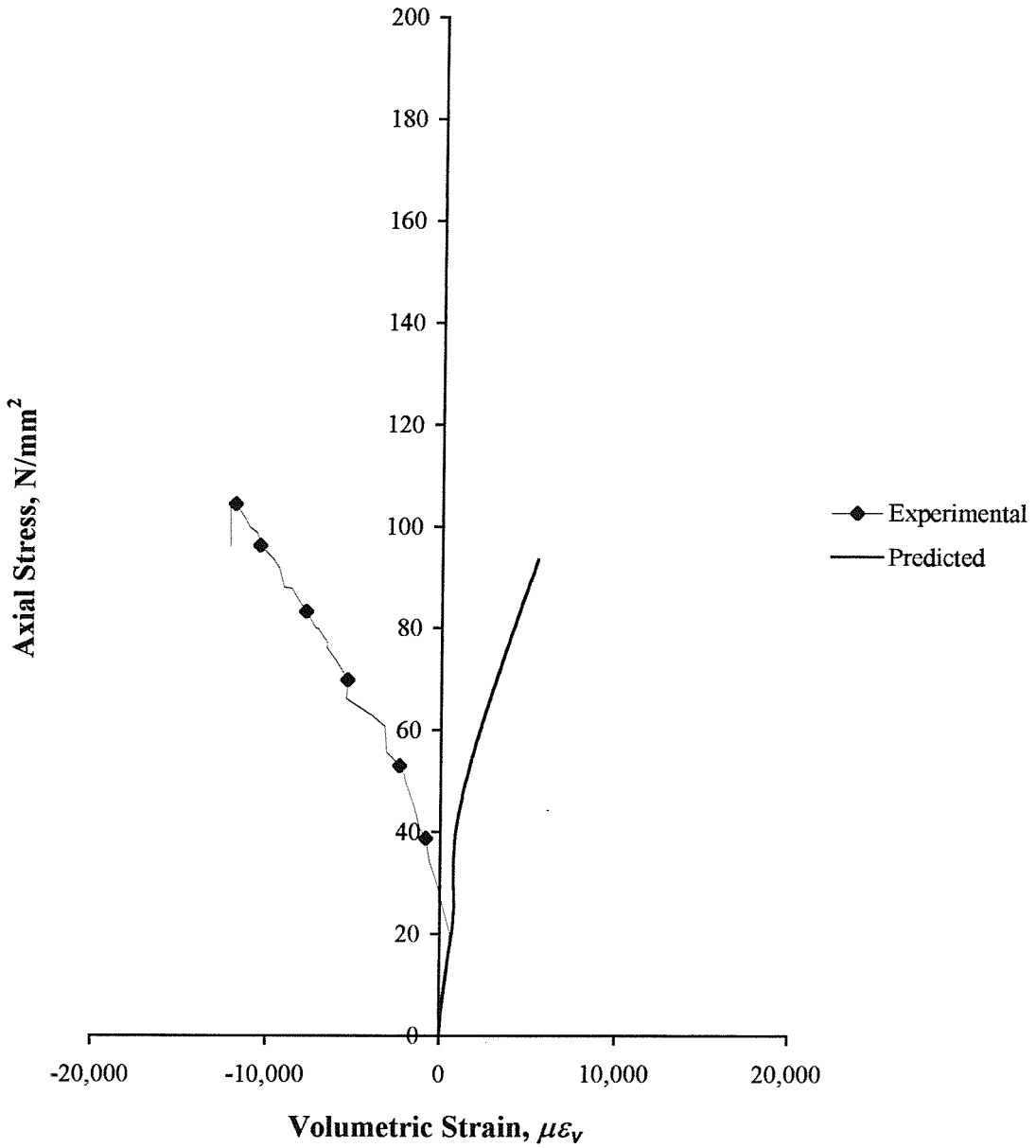

Figure F.10. Comparison of the theoretical and experimental stress-volumetric strain curves for the 100 mm diameter concrete-filled stub column confined with E-glass fibres orientated at 71.4 degrees (concrete cube strength = 25.6 N/mm^2)

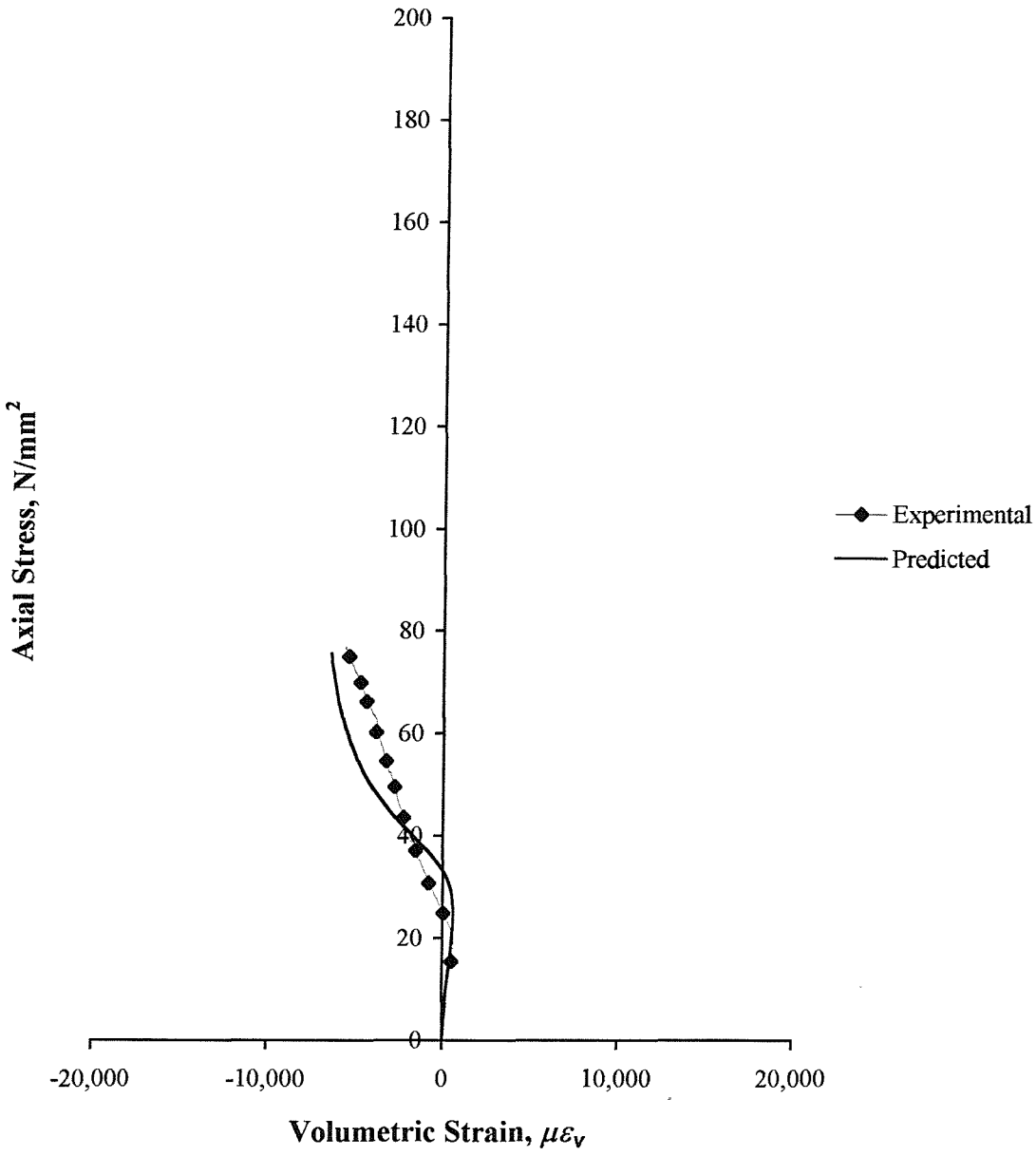

Figure F.11. Comparison of the theoretical and experimental stress-volumetric strain curves for the 150 mm diameter concrete-filled stub column confined with E-glass fibres orientated at 71.3 degrees (concrete cube strength = 32.7 N/mm^2)

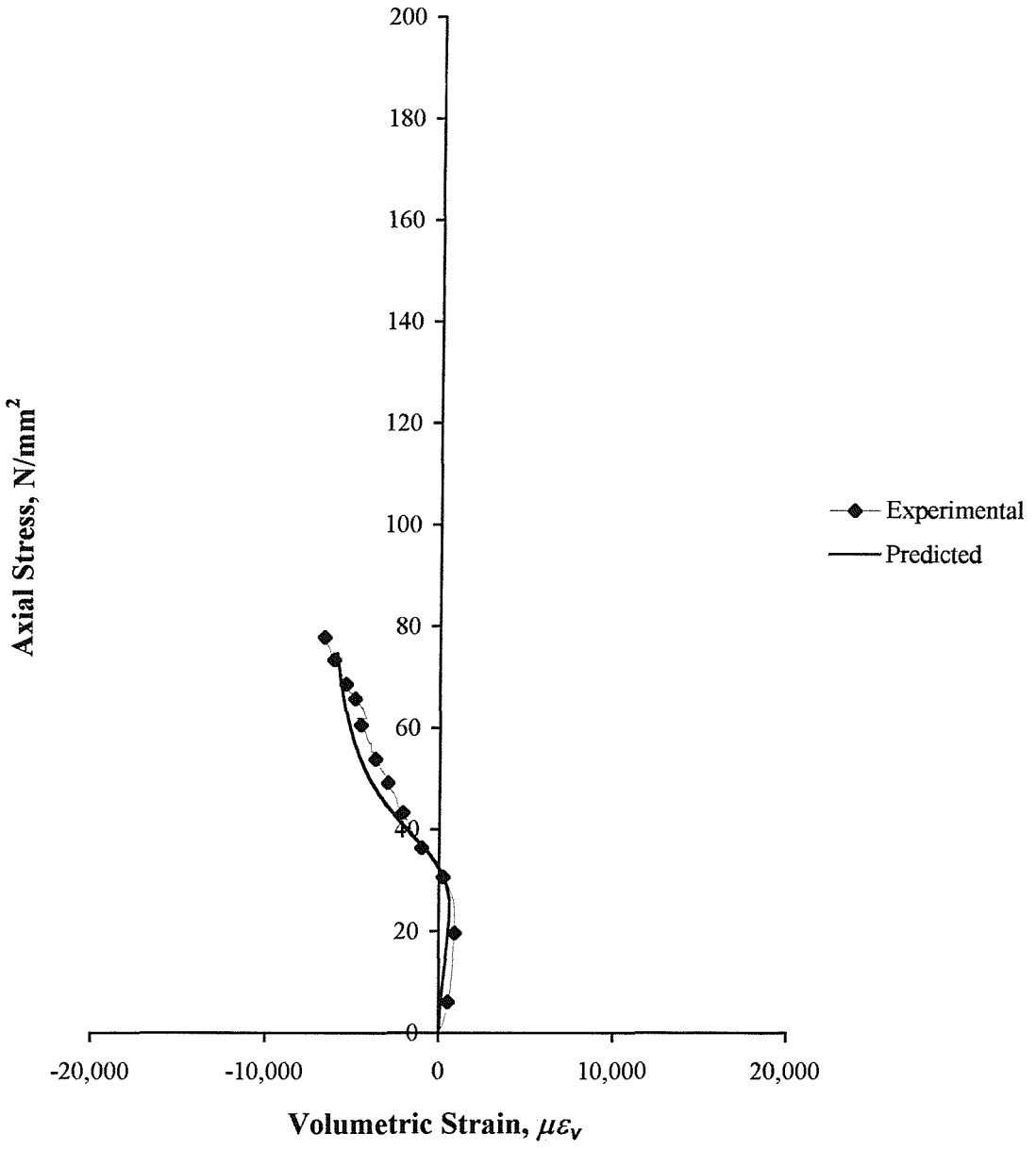

Figure F.12. Comparison of the theoretical and experimental stress-volumetric strain curves for the 150 mm diameter concrete-filled stub column confined with E-glass fibres orientated at 71.3 degrees (concrete cube strength = 31.7 N/mm^2)

APPENDIX G

EXPERIMENTAL LOAD-DEFLECTION CURVES FOR CONCRETE-FILLED E-GLASS FRP-COMPOSITE COLUMNS

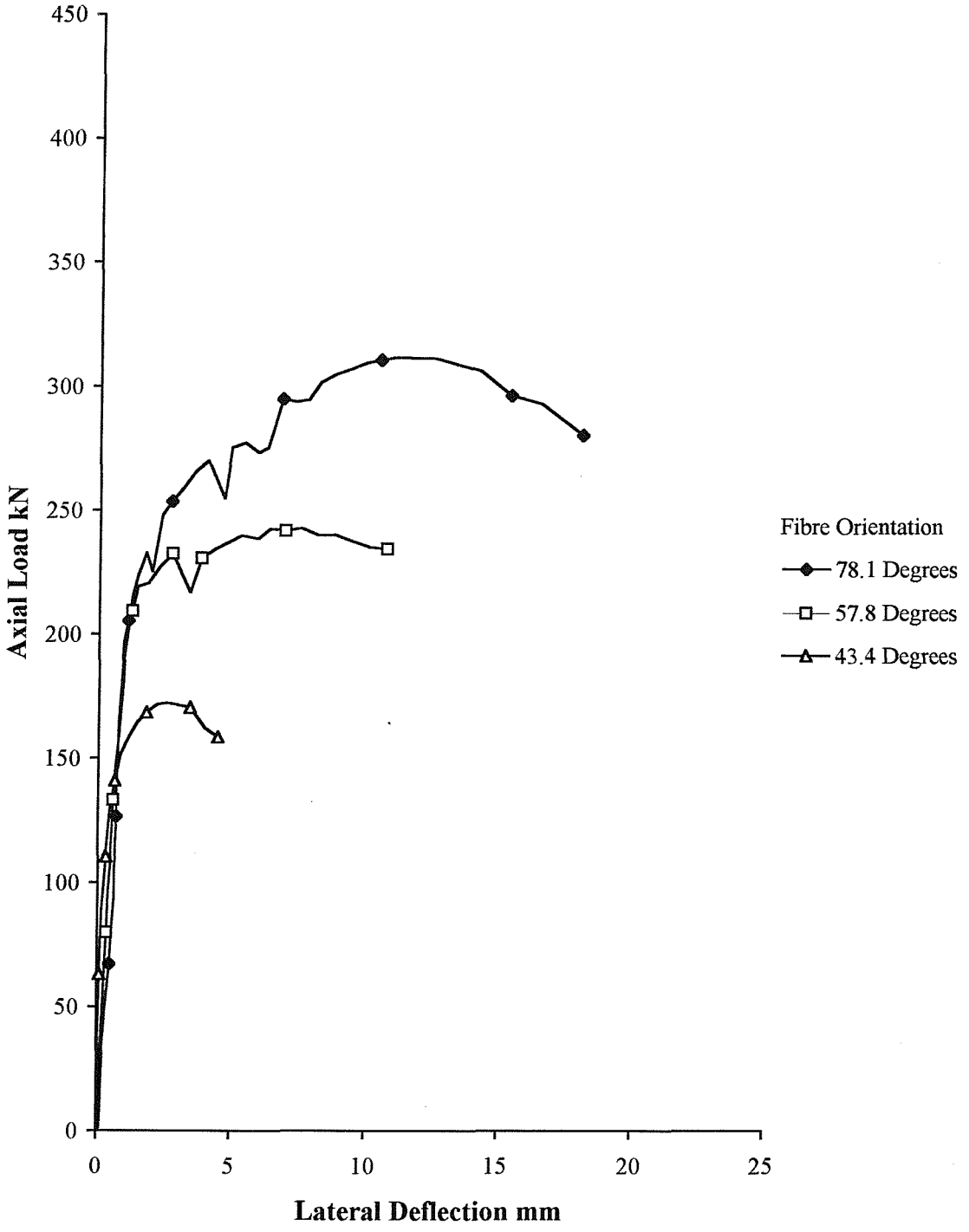

Figure G.1. Load-deflection curves for the 80 mm diameter concrete-filled FRP-composite columns with a slenderness ratio of 5 (nominal concrete cube strength = 25 N/mm^2)

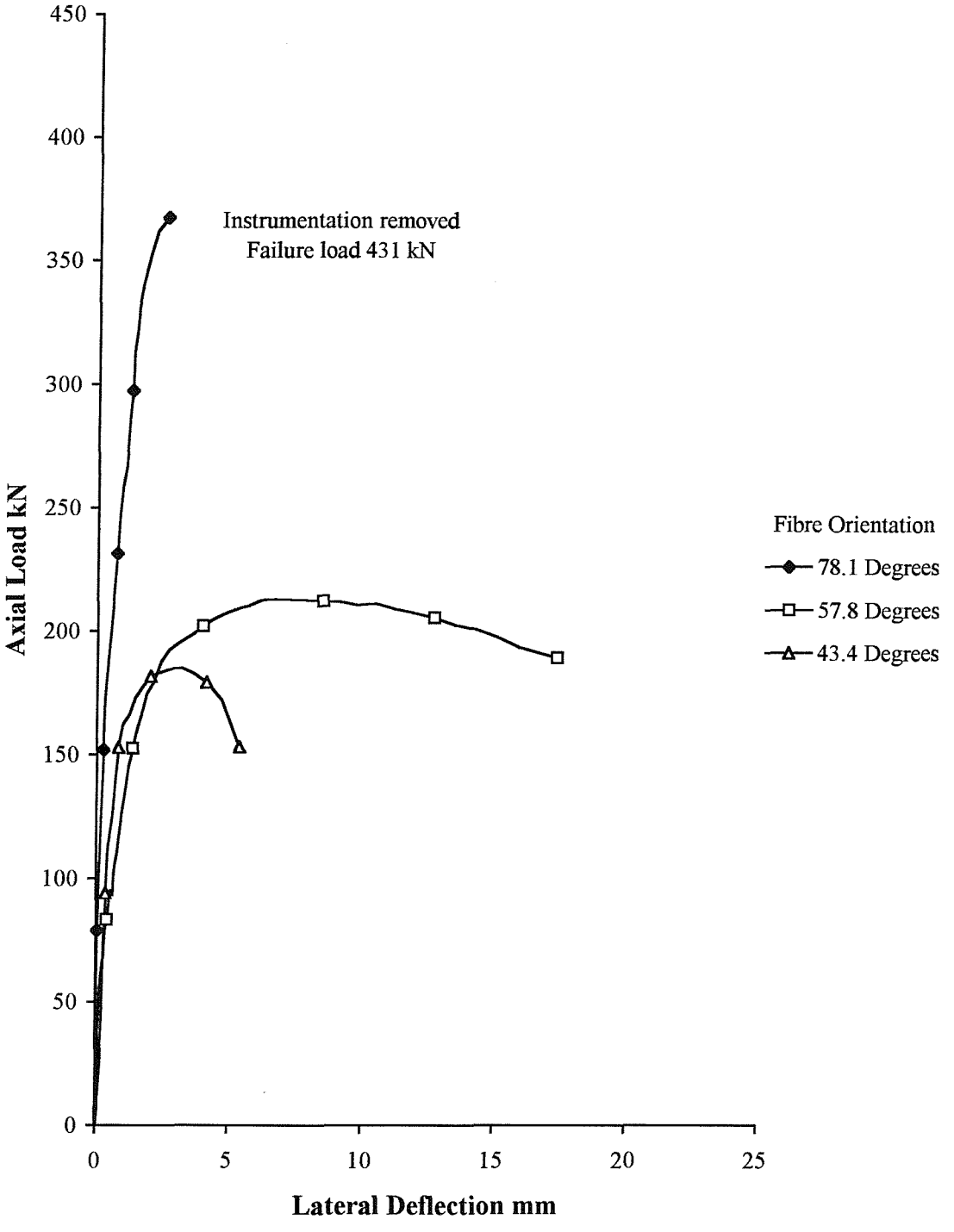

Figure G.2. Load-deflection curves for the 80 mm diameter concrete-filled FRP-composite columns with a slenderness ratio of 5 (nominal concrete cube strength = 35 N/mm^2)

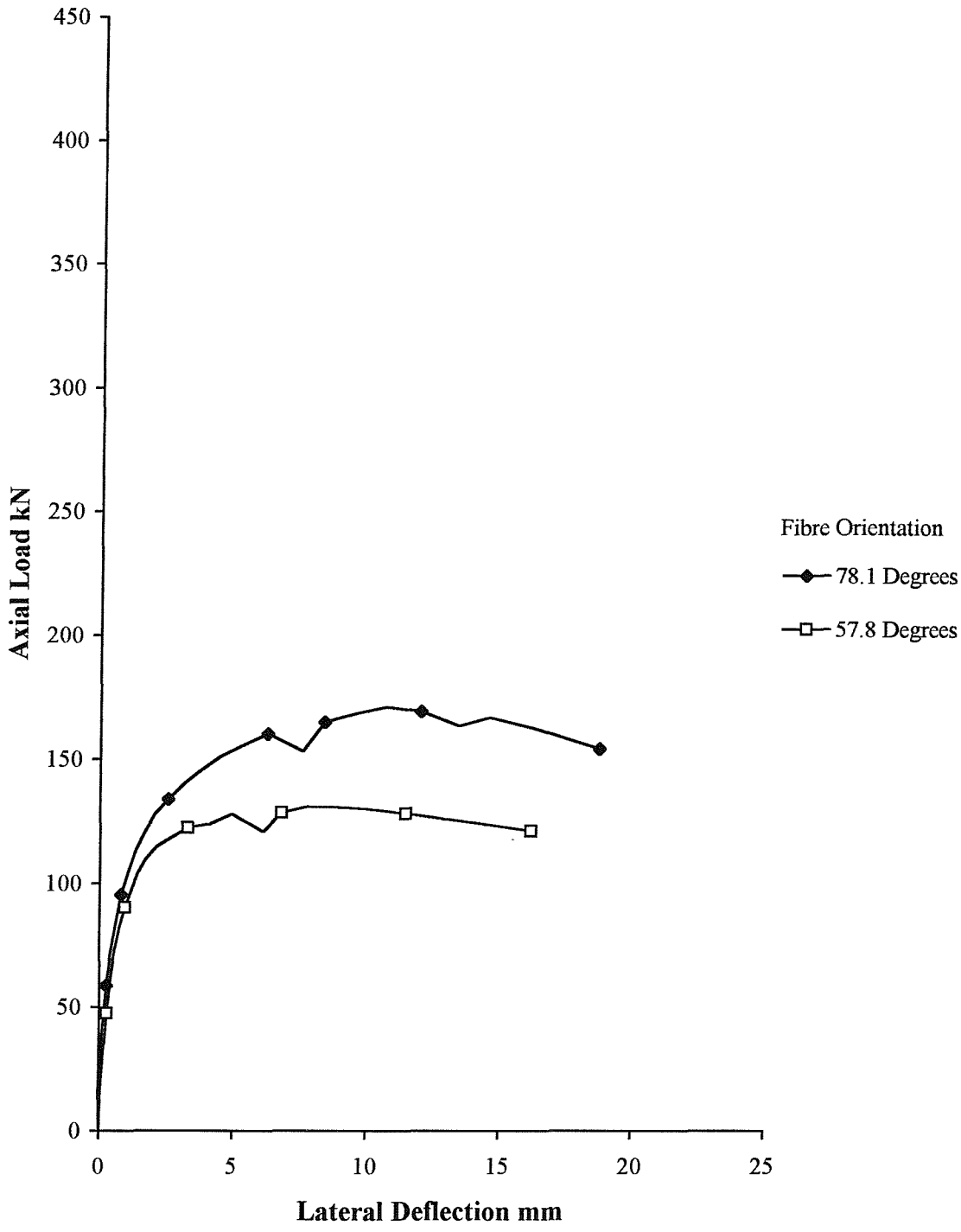

Figure G.3. Load-deflection curves for the 80 mm diameter concrete-filled FRP-composite columns with a slenderness ratio of 10 (nominal concrete cube strength = 25 N/mm^2)

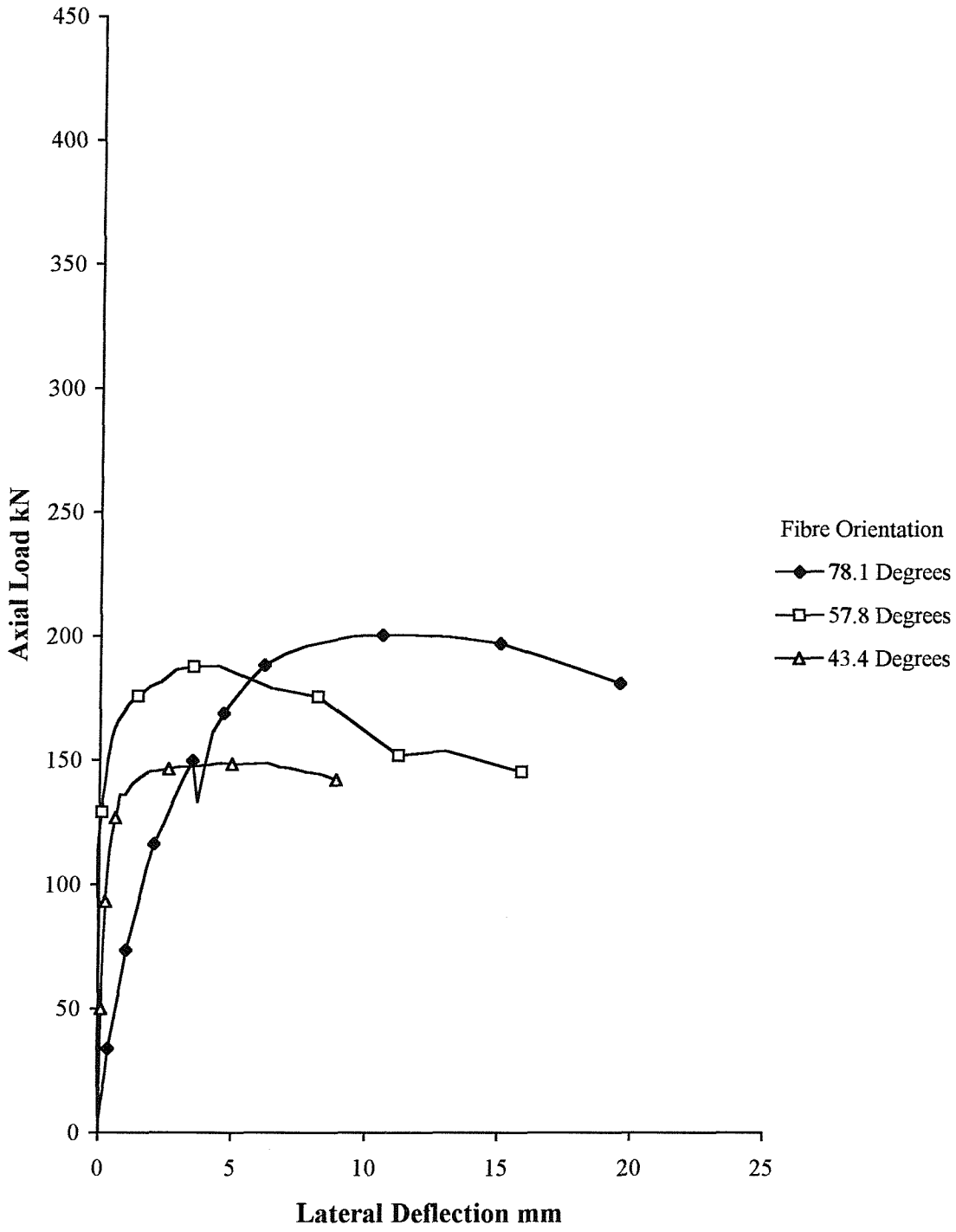

Figure G.4. Load-deflection curves for the 80 mm diameter concrete-filled FRP-composite columns with a slenderness ratio of 10 (nominal concrete cube strength = 35 N/mm^2)

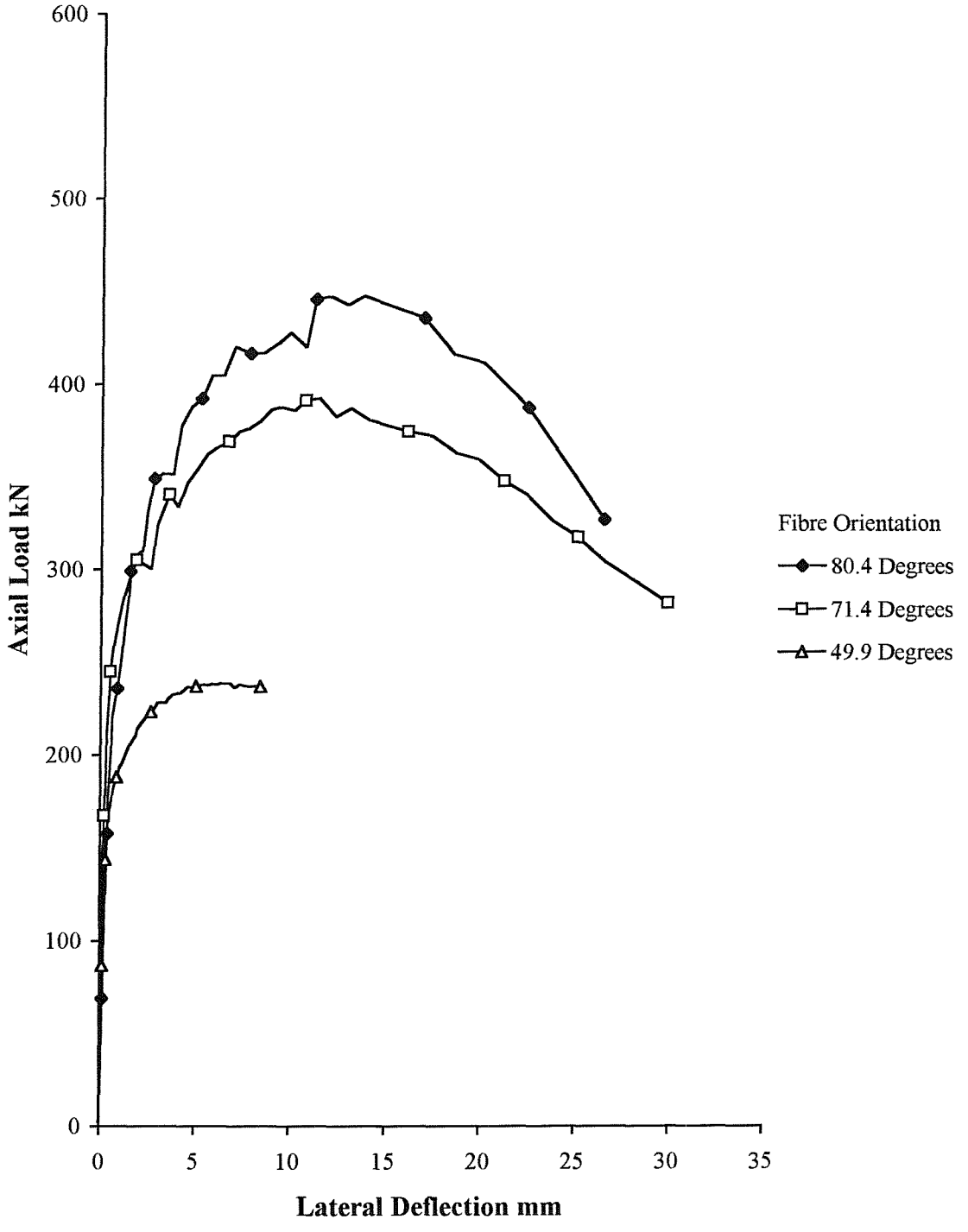

Figure G.5. Load-deflection curves for the 100 mm diameter concrete-filled FRP-composite columns with a slenderness ratio of 5 (nominal concrete cube strength = 25 N/mm^2)

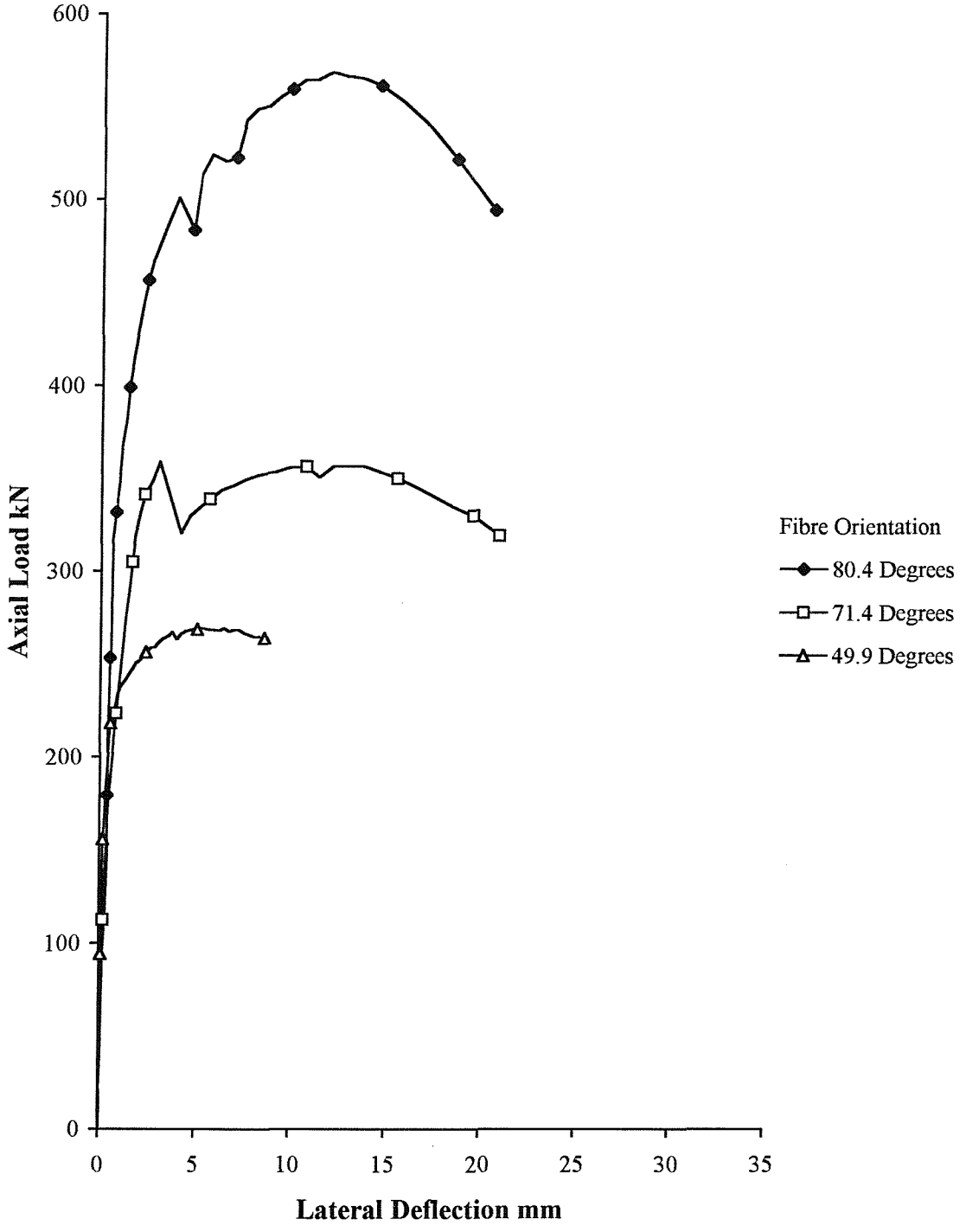

Figure G.6. Load-deflection curves for the 100 mm diameter concrete-filled FRP-composite columns with a slenderness ratio of 5 (nominal concrete cube strength = 35 N/mm^2)

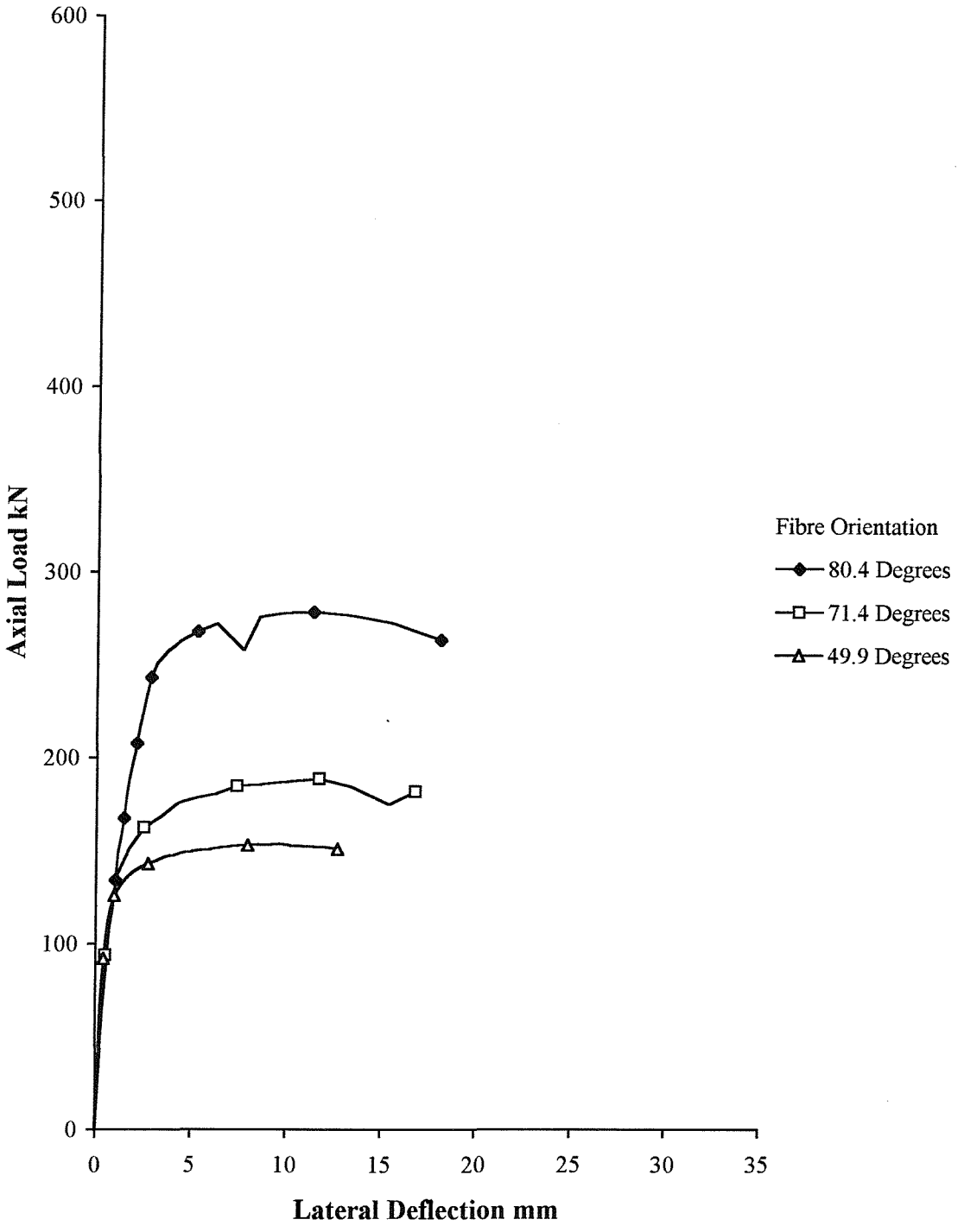

Figure G.7. Load-deflection curves for the 100 mm diameter concrete-filled FRP-composite columns with a slenderness ratio of 10 (nominal concrete cube strength = 25 N/mm^2)

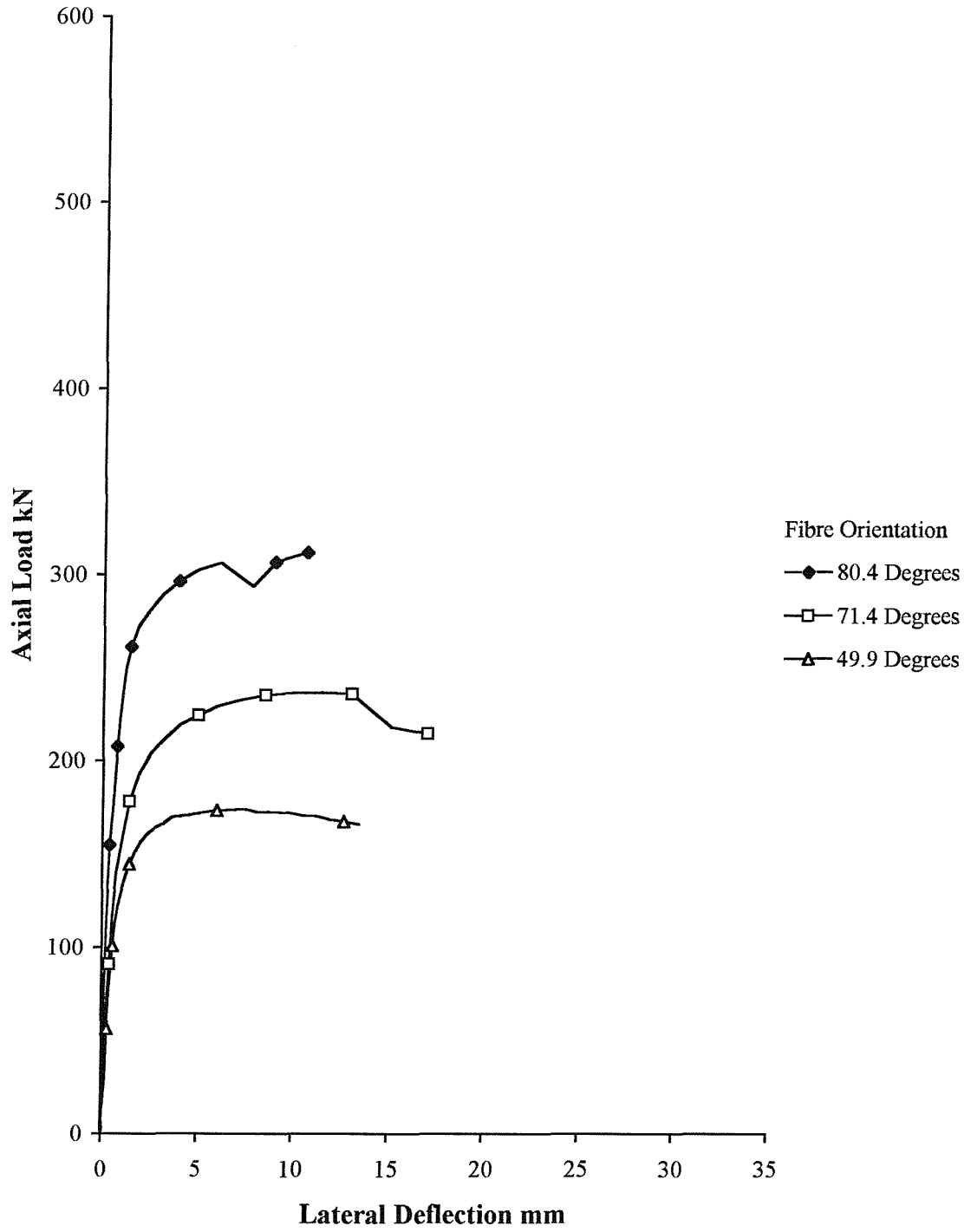

Figure G.8. Load-deflection curves for the 100 mm diameter concrete-filled FRP-composite columns with a slenderness ratio of 10 (nominal concrete cube strength = 35 N/mm^2)

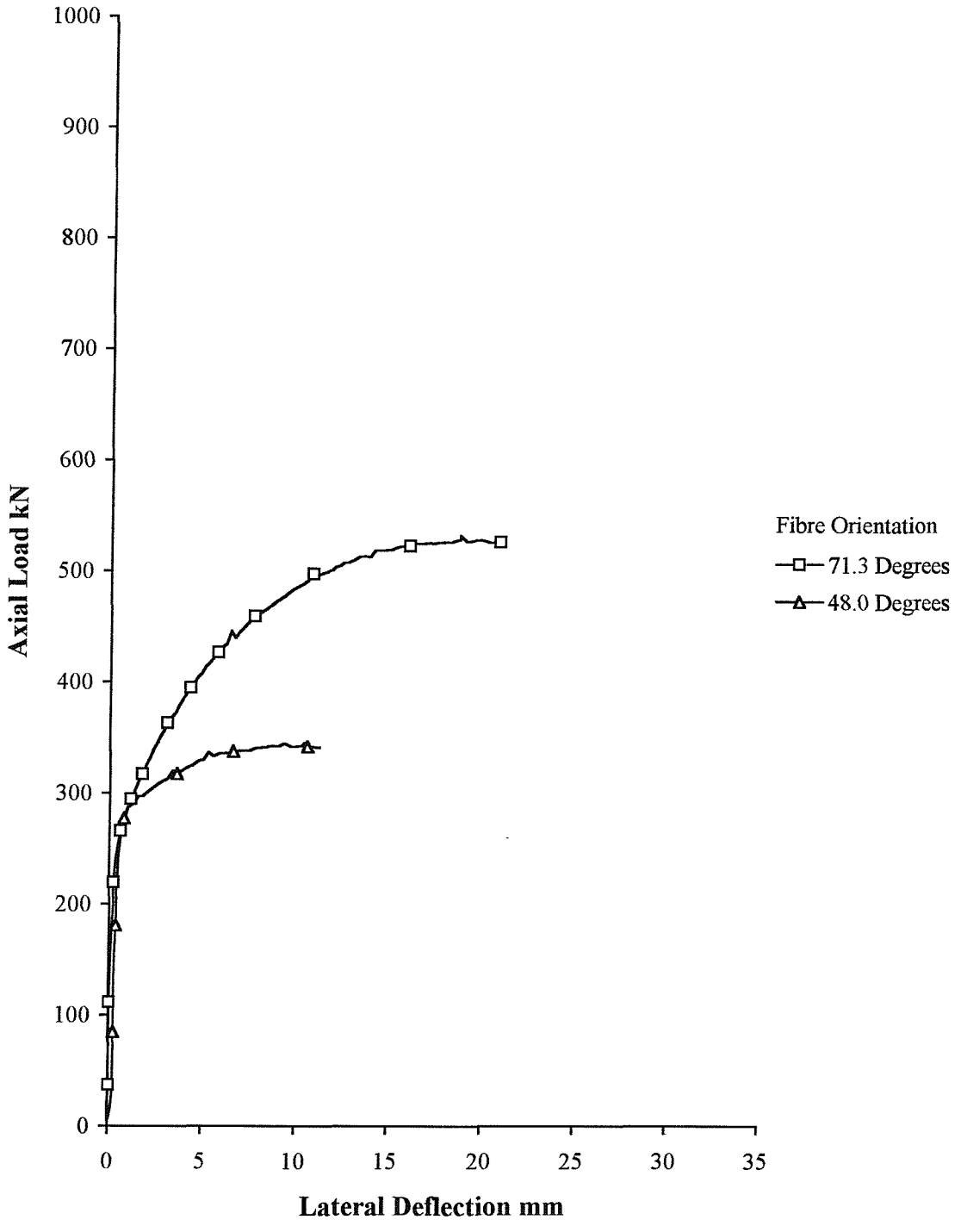

Figure G.9. Load-deflection curves for the 150 mm diameter concrete-filled FRP-composite columns with a slenderness ratio of 5 (nominal concrete cube strength = 25 N/mm^2)

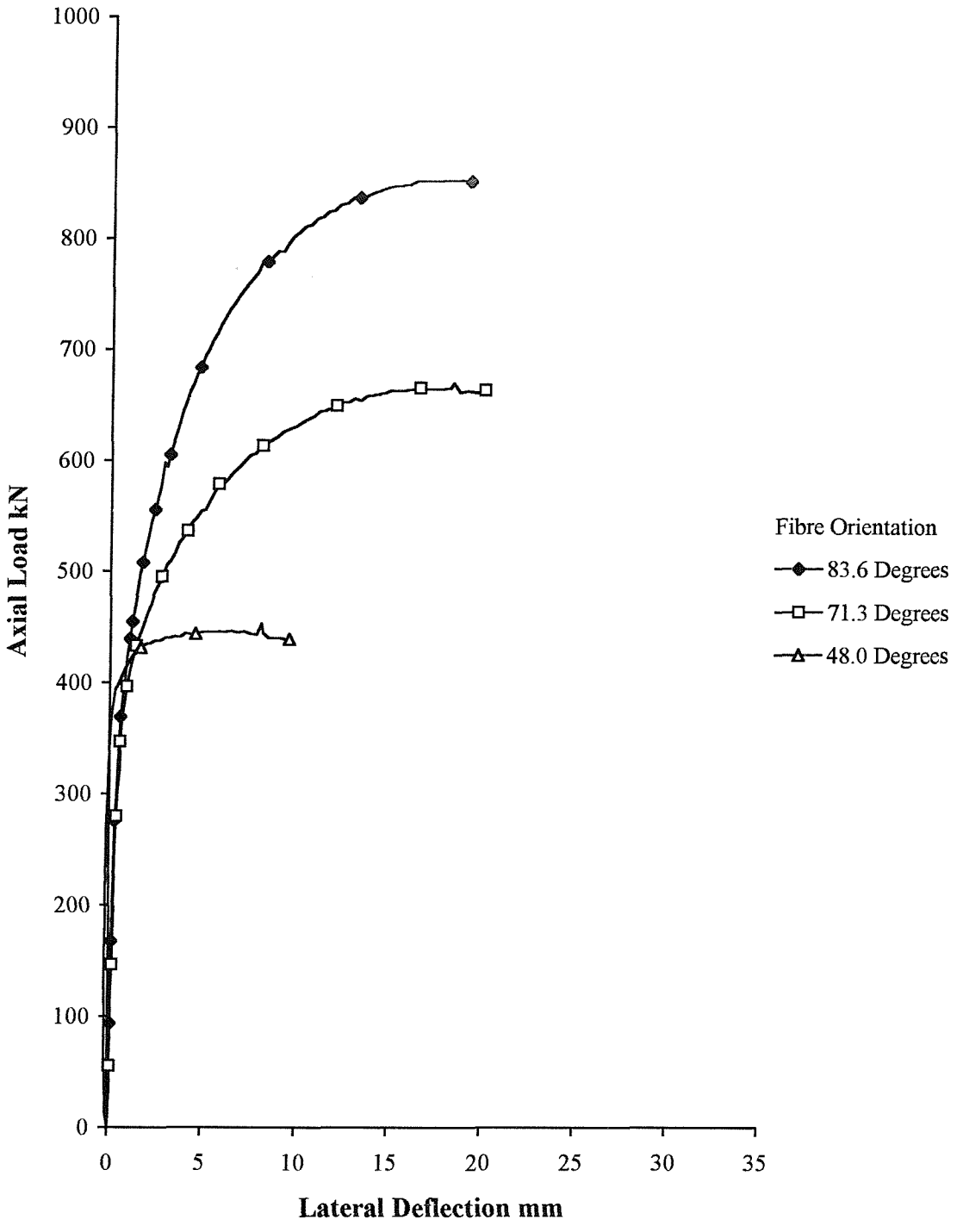

Figure G.10. Load-deflection curves for the 150 mm diameter concrete-filled FRP-composite columns with a slenderness ratio of 5 (nominal concrete cube strength = 35 N/mm^2)

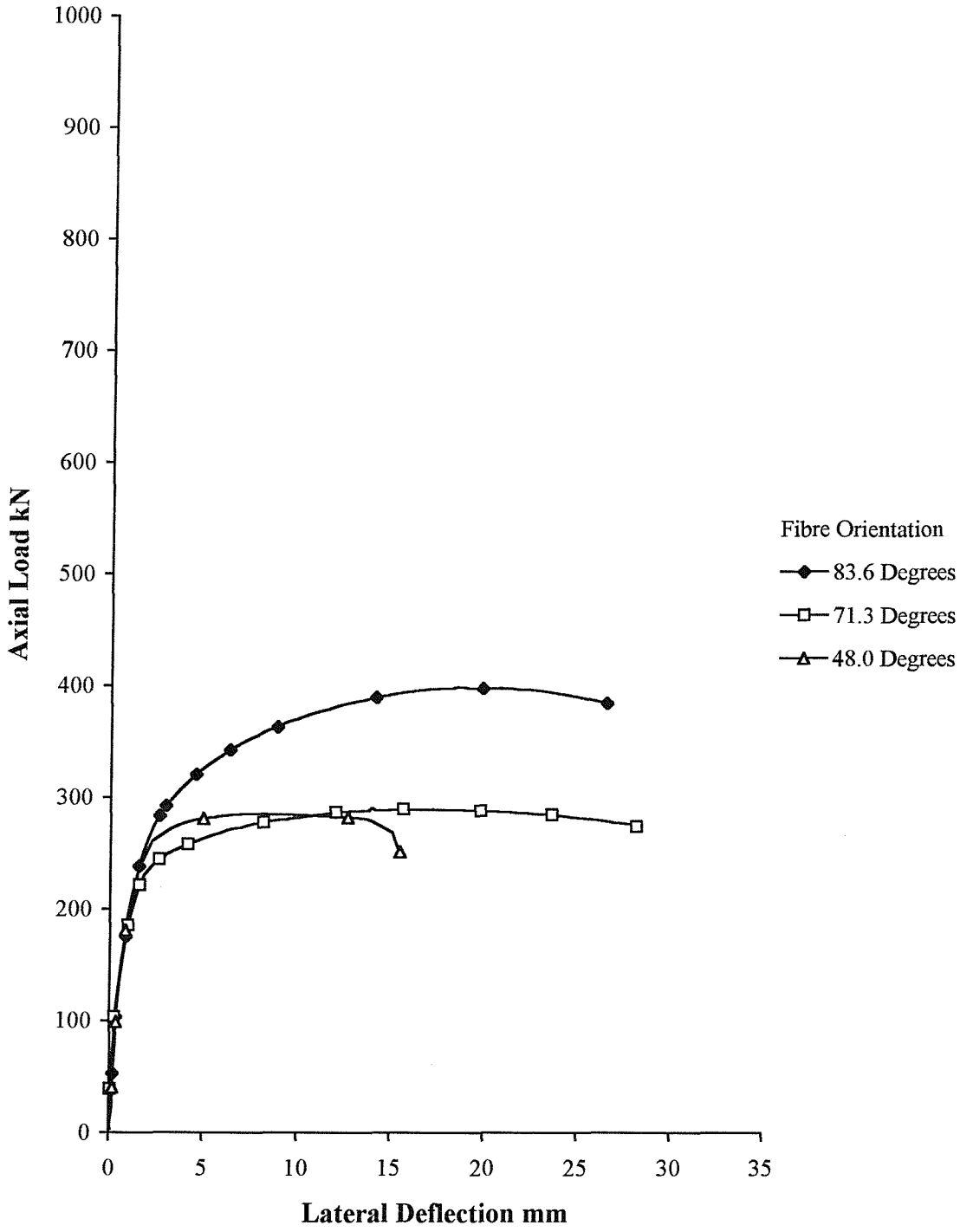

Figure G.11. Load-deflection curves for the 150 mm diameter concrete-filled FRP-composite columns with a slenderness ratio of 10 (nominal concrete cube strength = 25 N/mm^2)

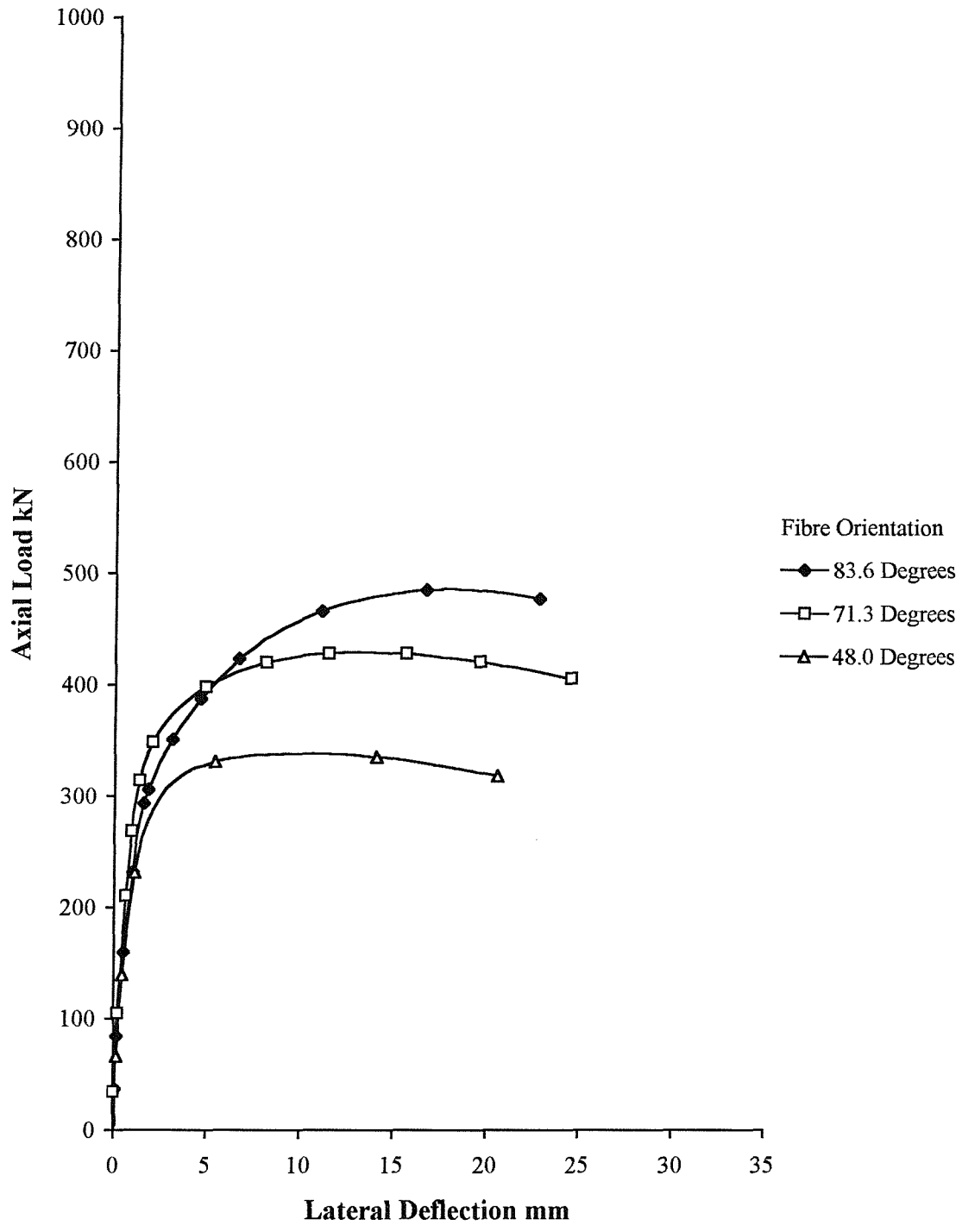

Figure G.12. Load-deflection curves for the 150 mm diameter concrete-filled FRP-composite columns with a slenderness ratio of 10 (nominal concrete cube strength = 35 N/mm^2)

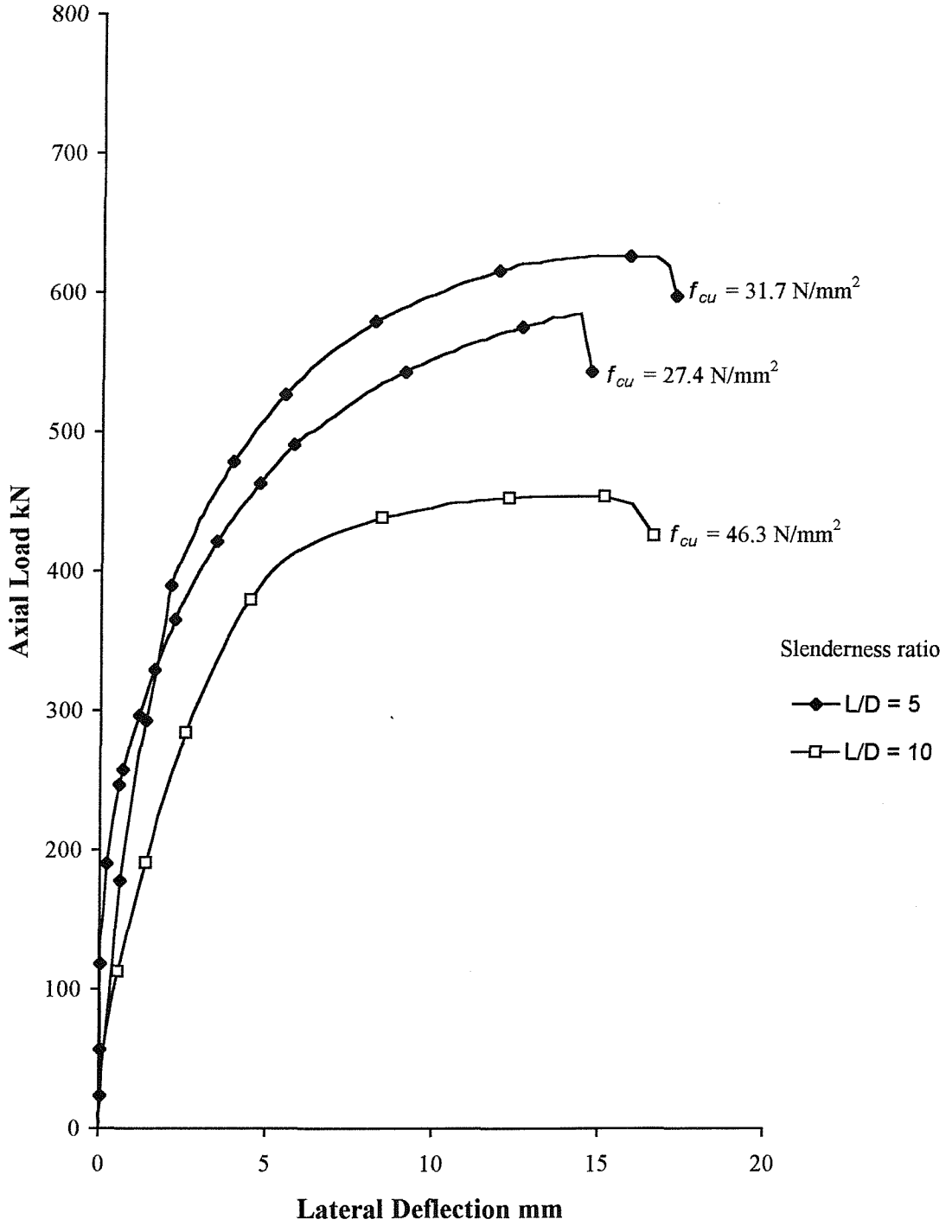

Figure G.13. Load-deflection curves for the 125 mm diameter concrete-filled FRP-composite columns confined with E-glass fibres orientated at 82.3 degrees

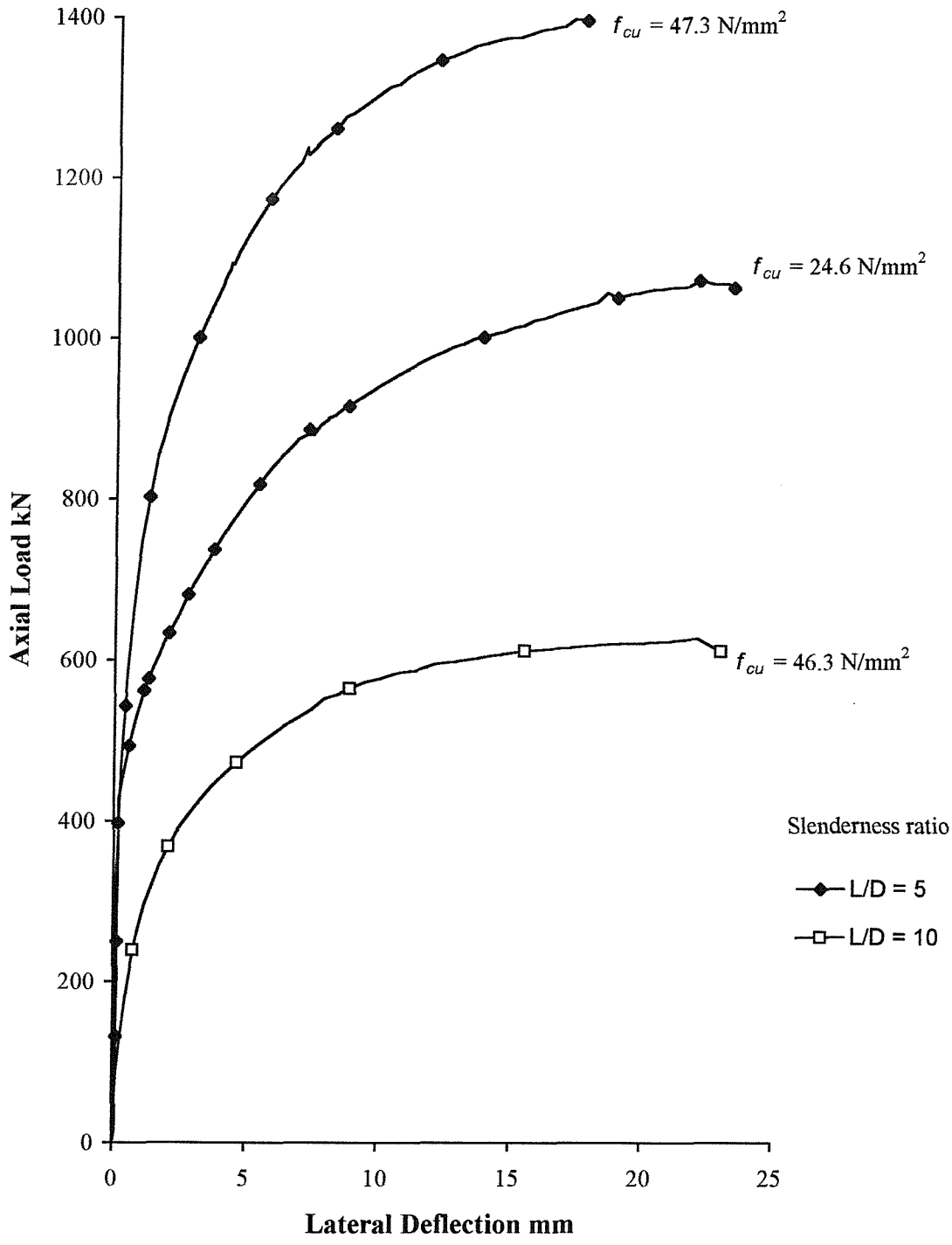

Figure G.14. Load-deflection curves for the 200 mm diameter concrete-filled FRP-composite columns confined with E-glass fibres orientated at 85.2 degrees

APPENDIX H

EXPERIMENTAL LOAD-STRAIN CURVES FOR CONCRETE-FILLED E-GLASS FRP-COMPOSITE COLUMNS

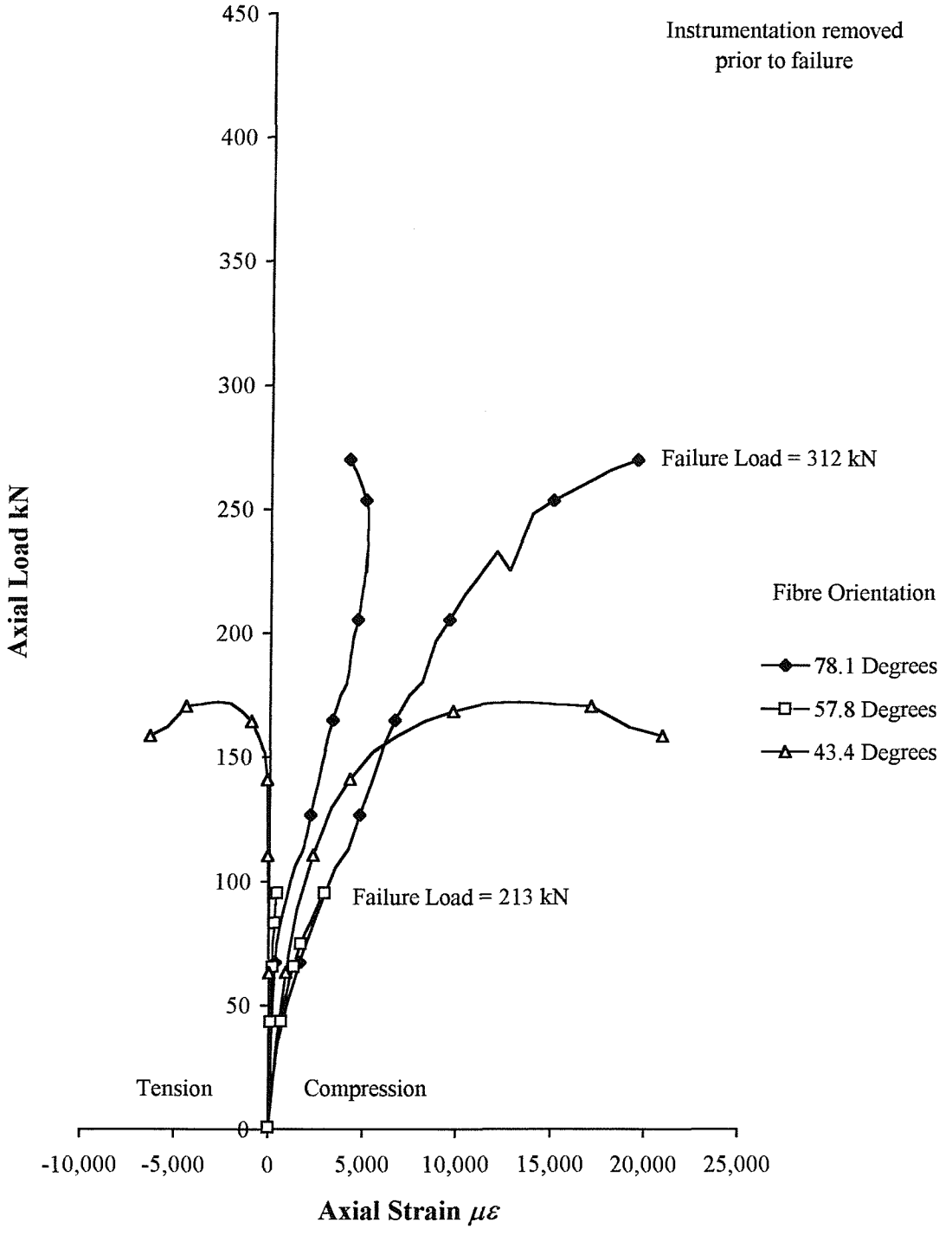

Figure H.1. Load-strain curves for the 80 mm diameter concrete-filled FRP-composite columns with a slenderness ratio of 5 (nominal concrete cube strength = 25 N/mm^2)

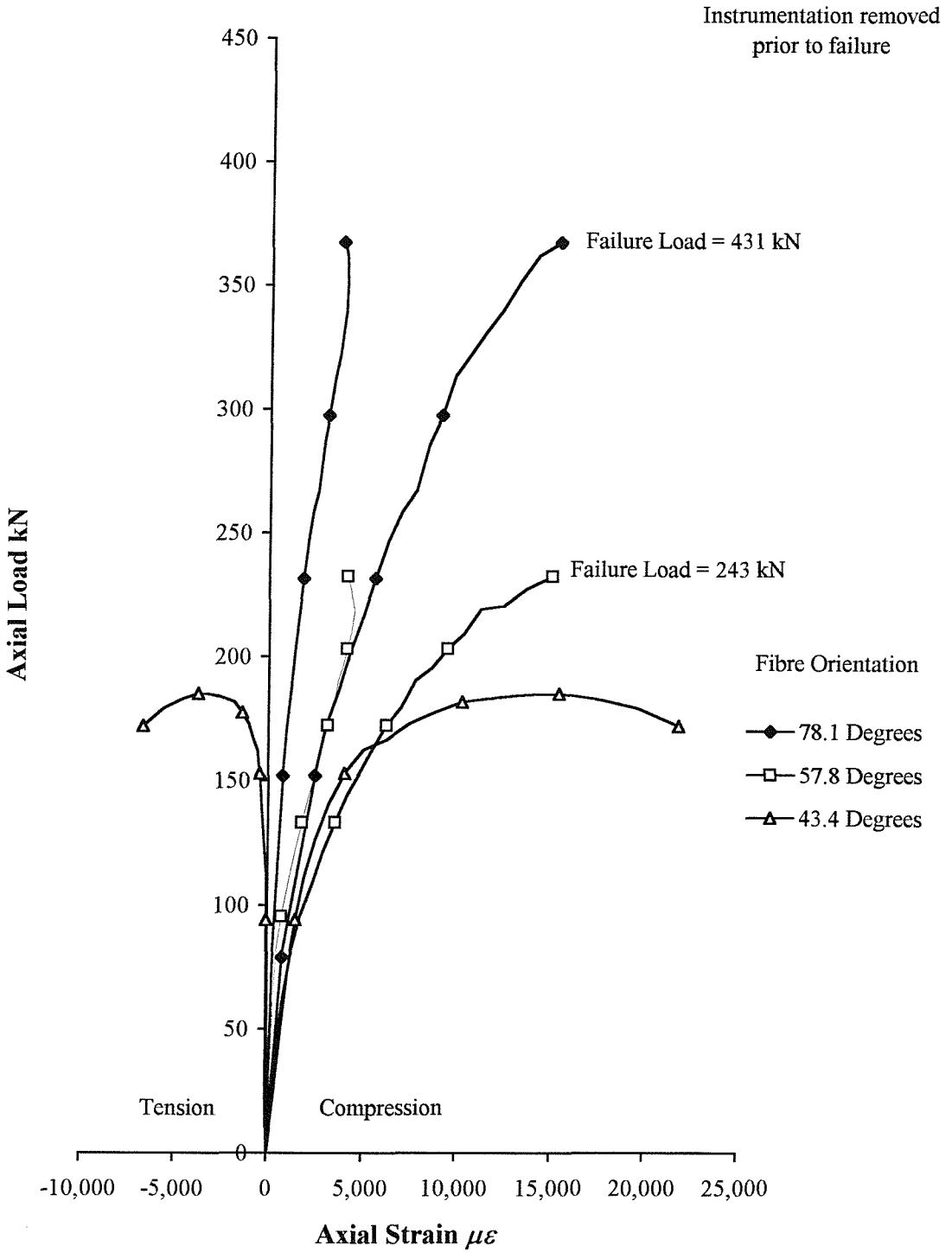

Figure H.2. Load-strain curves for the 80 mm diameter concrete-filled FRP-composite columns with a slenderness ratio of 5 (nominal concrete cube strength = 35 N/mm^2)

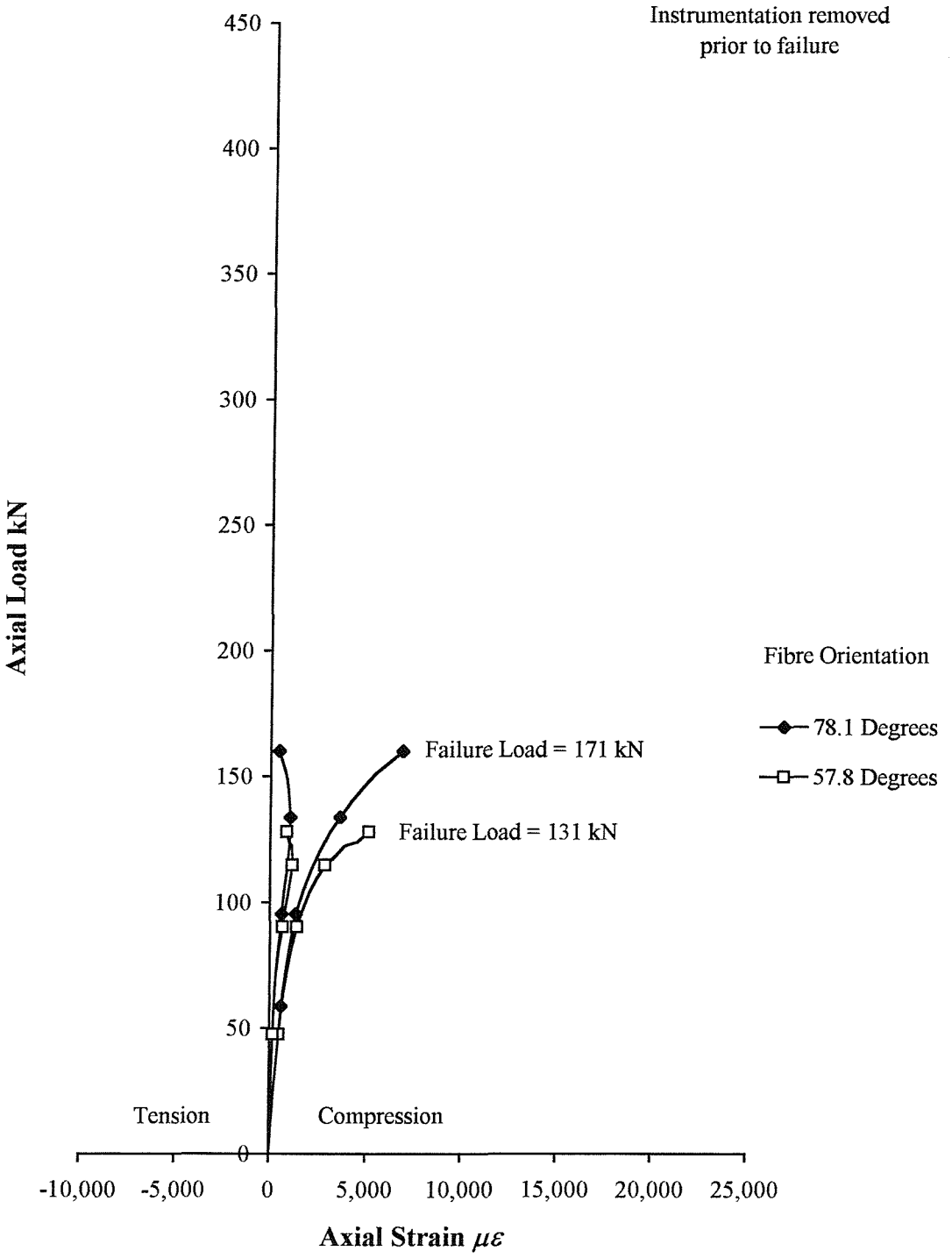

Figure H.3. Load-strain curves for the 80 mm diameter concrete-filled FRP-composite columns with a slenderness ratio of 10 (nominal concrete cube strength = 25 N/mm^2)

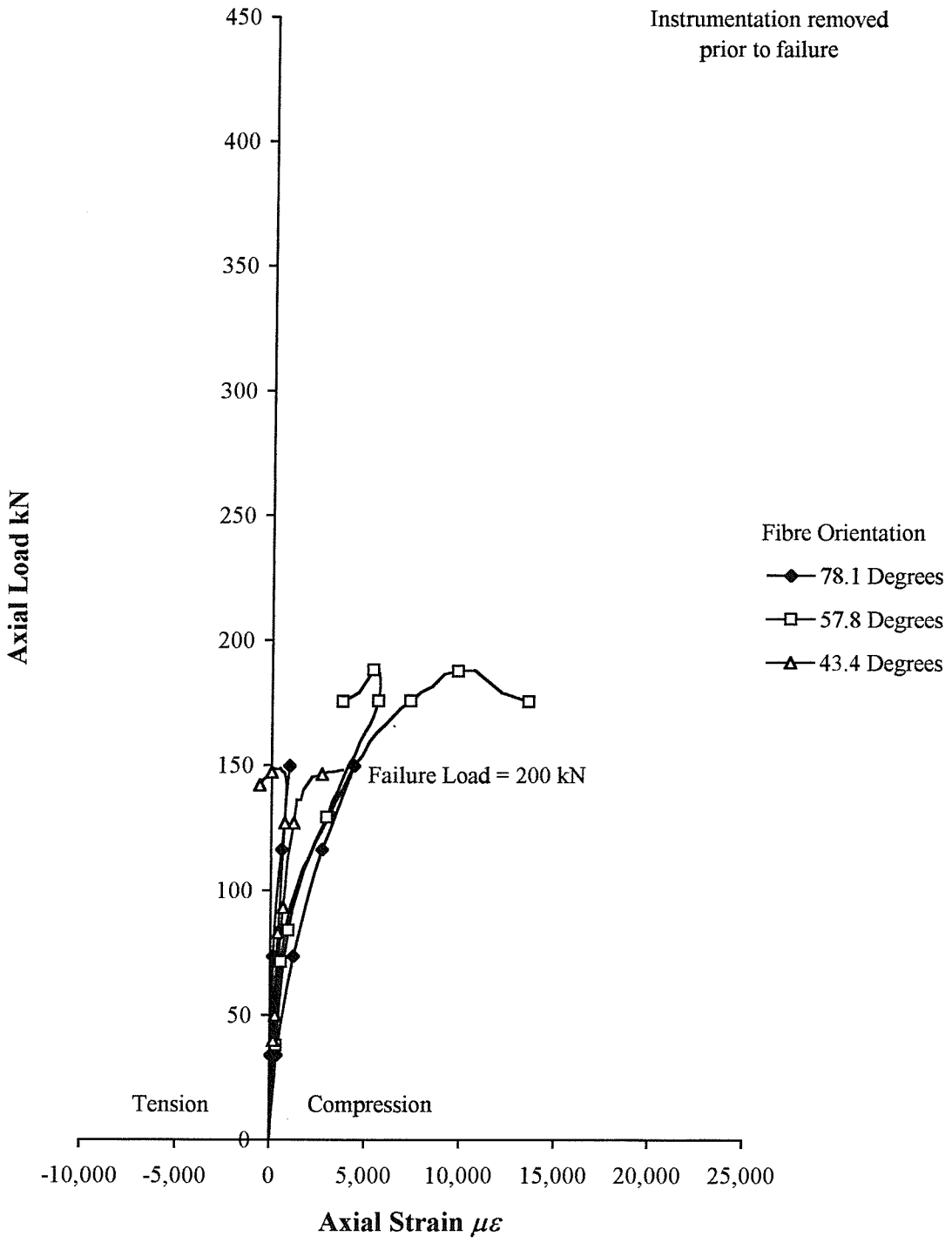

Figure H.4 Load-strain curves for the 80 mm diameter concrete-filled FRP-composite columns with a slenderness ratio of 10 (nominal concrete cube strength = 35 N/mm^2)

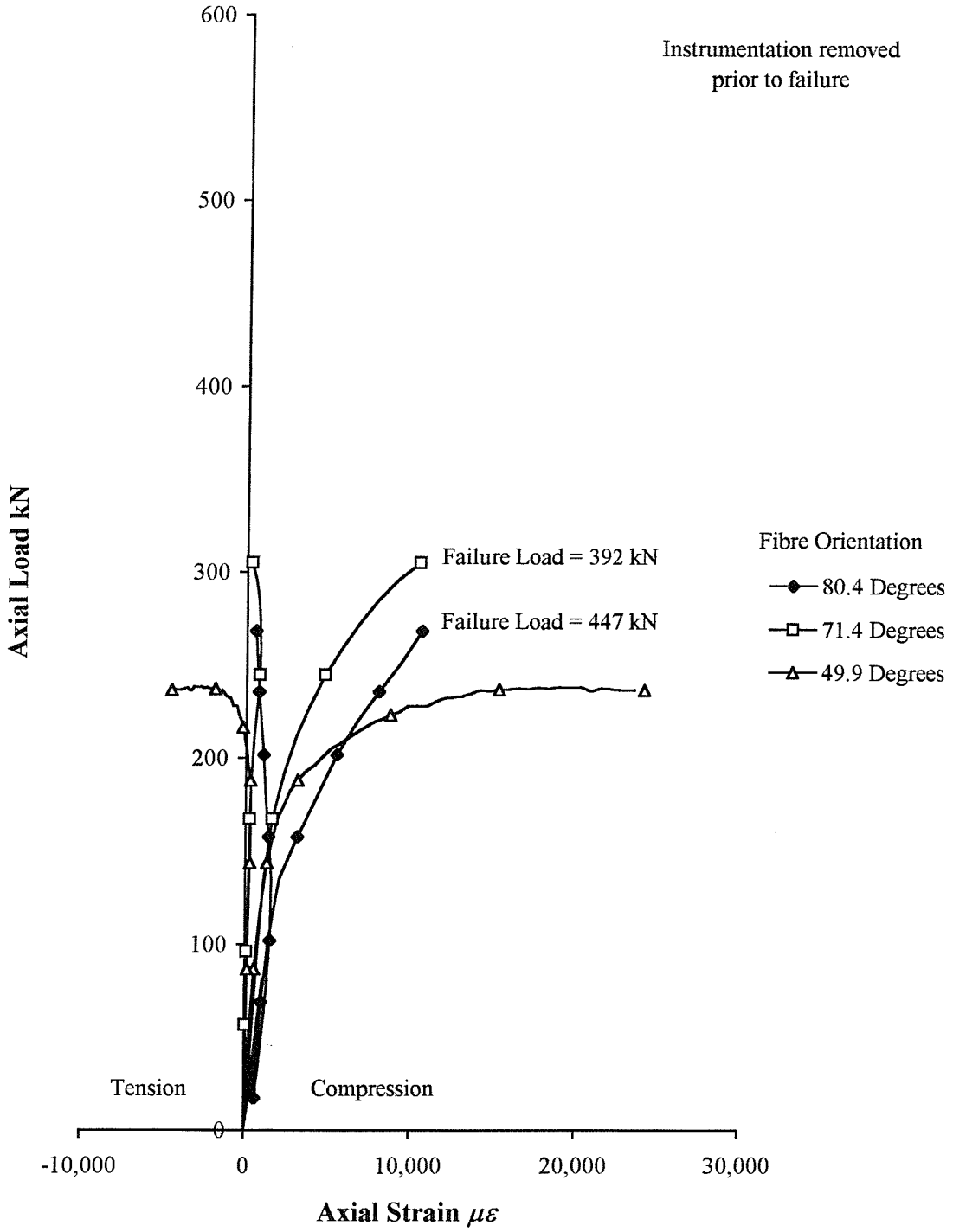

Figure H.5. Load-strain curves for the 100 mm diameter concrete-filled FRP-composite columns with a slenderness ratio of 5 (nominal concrete cube strength = 25 N/mm^2)

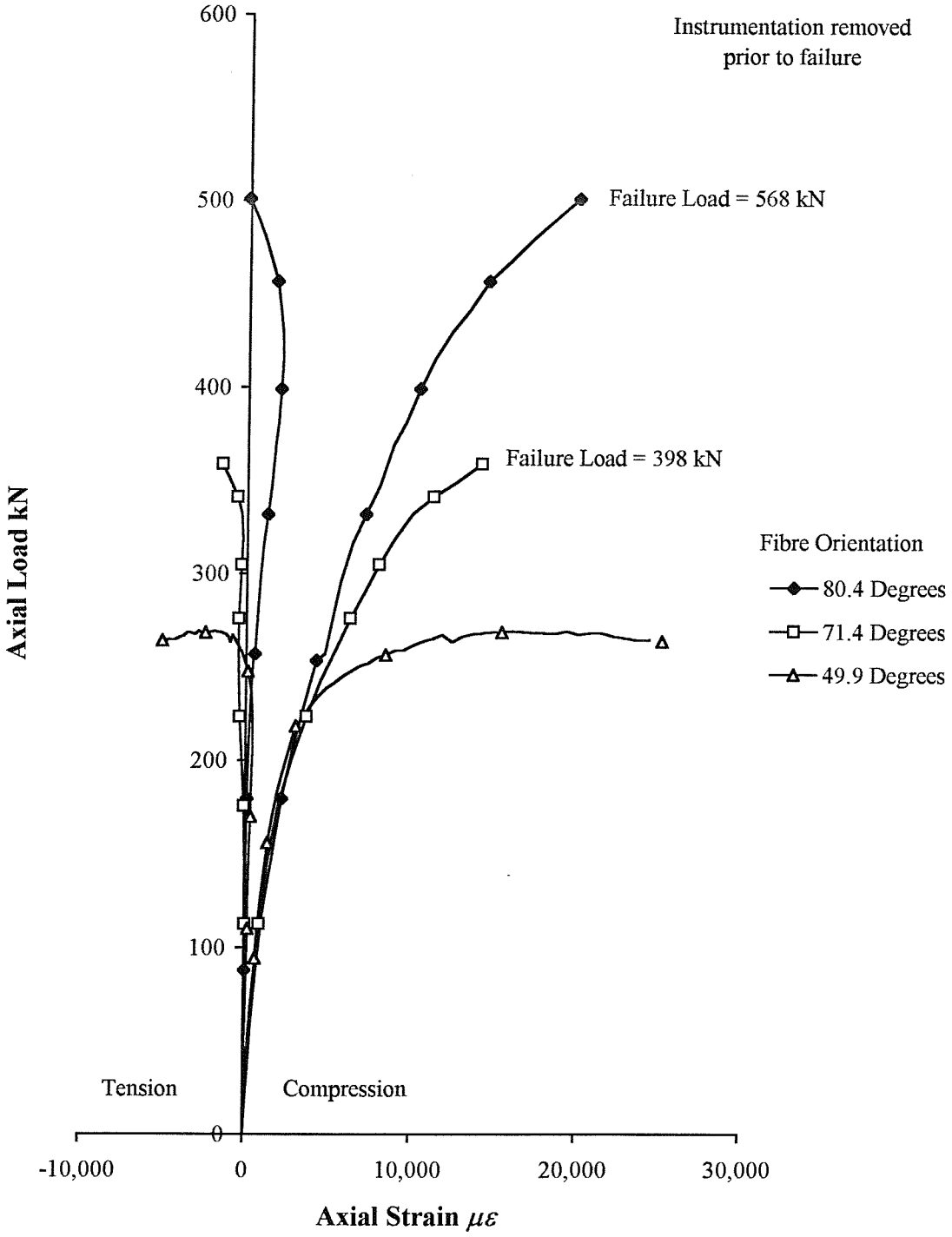

Figure H.6. Load-strain curves for the 100 mm diameter concrete-filled FRP-composite columns with a slenderness ratio of 5 (nominal concrete cube strength = 35 N/mm^2)

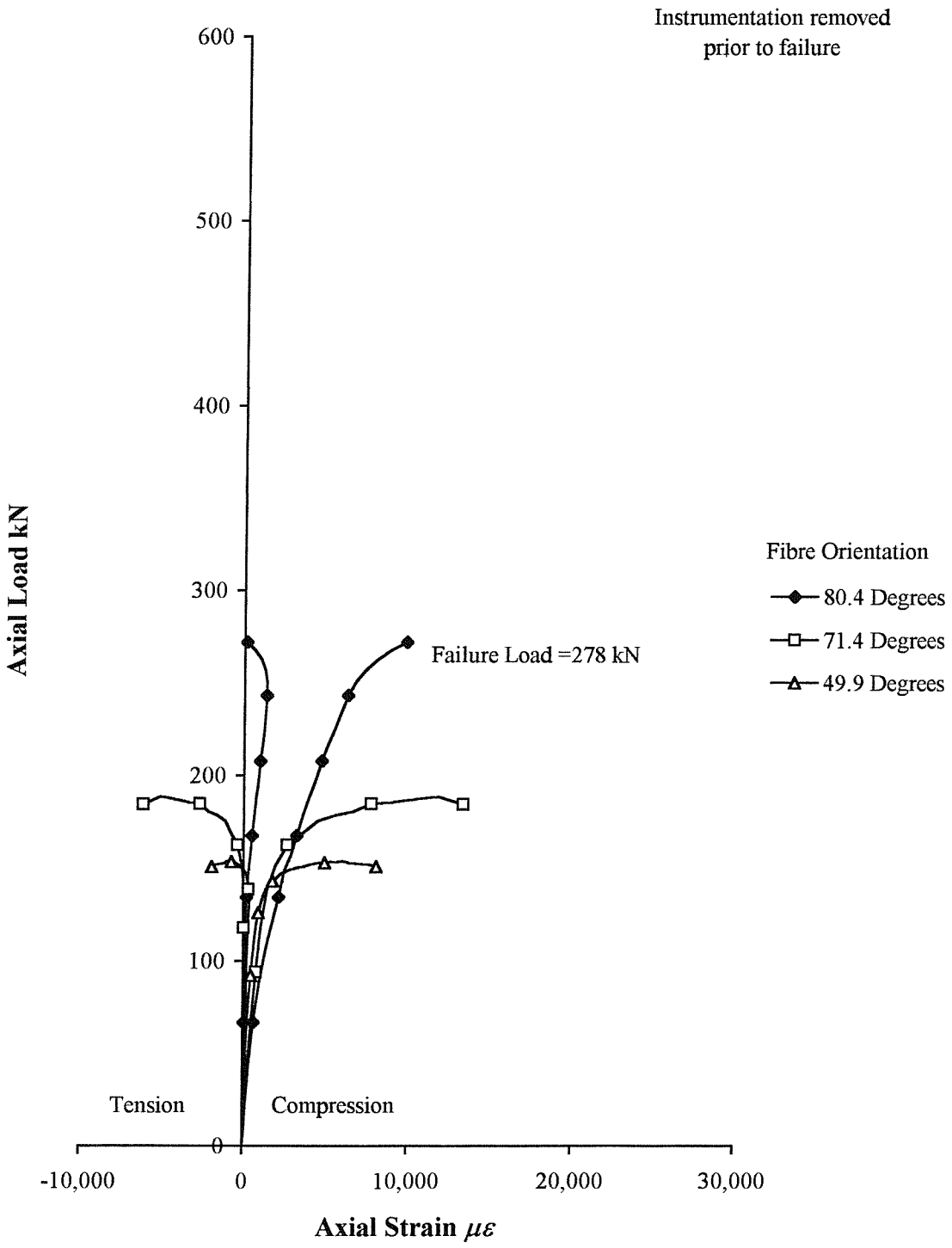

Figure H.7. Load-strain curves for the 100 mm diameter concrete-filled FRP-composite columns with a slenderness ratio of 10 (nominal concrete cube strength = 25 N/mm^2)

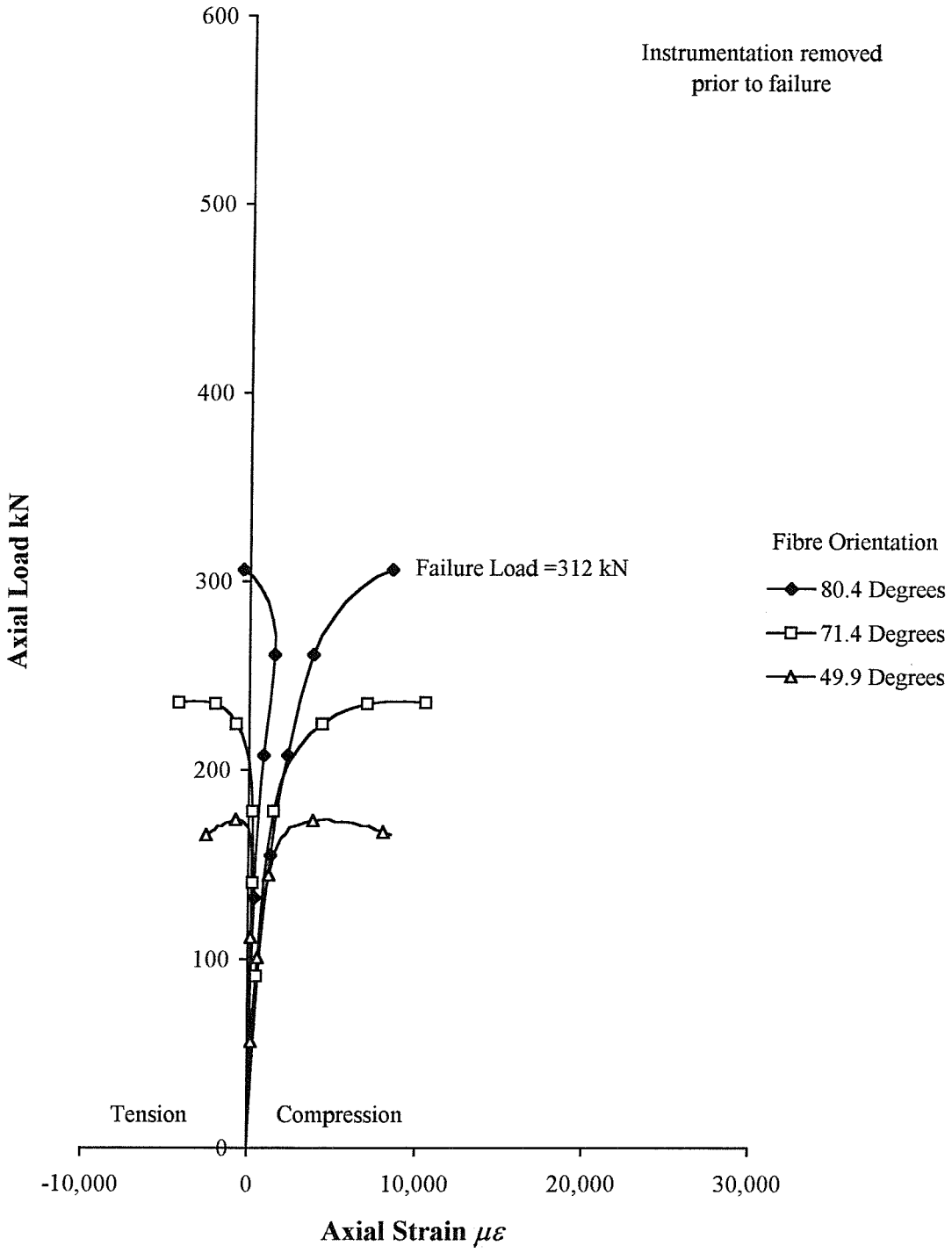

Figure H.8. Load-strain curves for the 100 mm diameter concrete-filled FRP-composite columns with a slenderness ratio of 10 (nominal concrete cube strength = 35 N/mm^2)

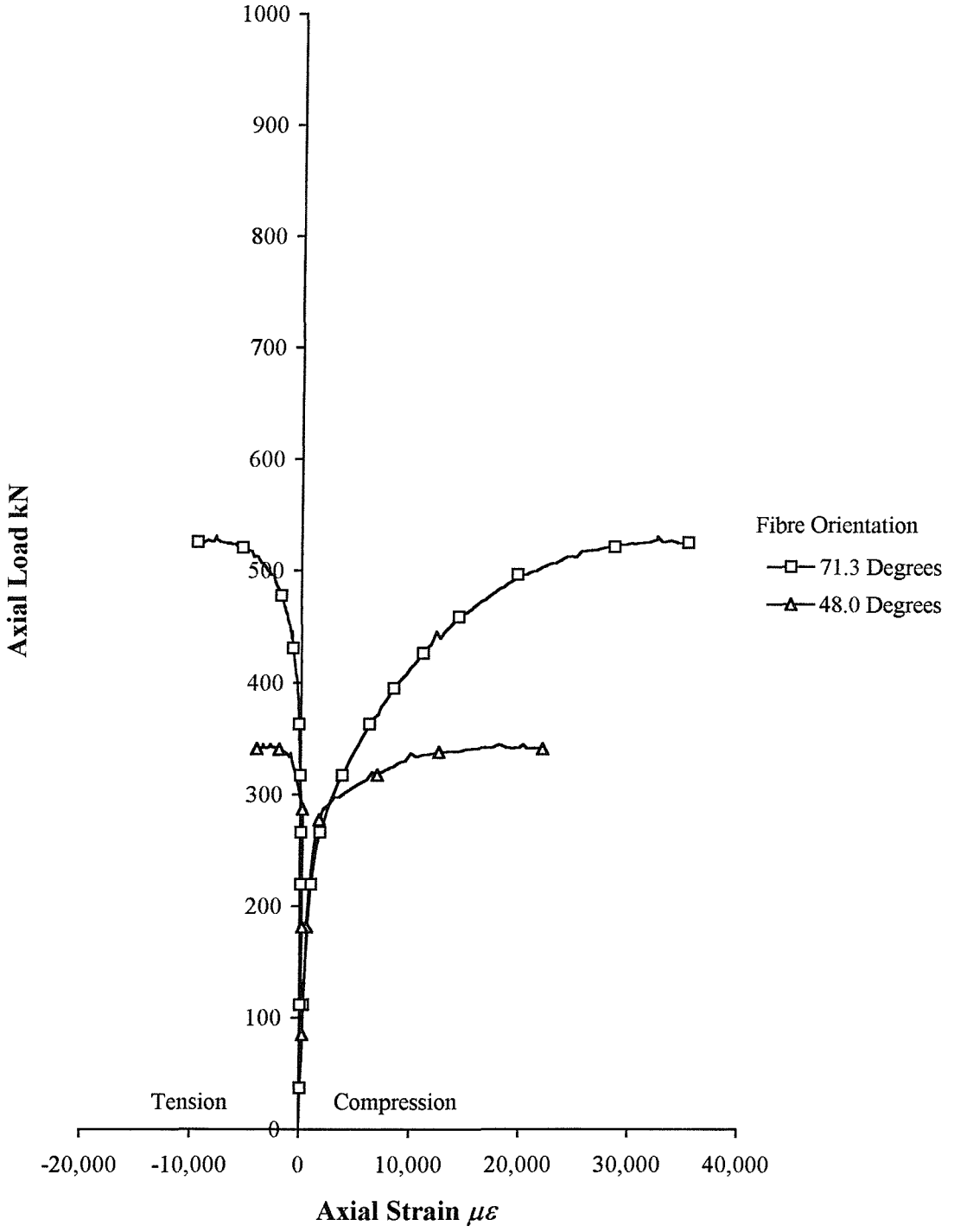

Figure H.9. Load-strain curves for the 150 mm diameter concrete-filled FRP-composite columns with a slenderness ratio of 5 (nominal concrete cube strength = 25 N/mm^2)

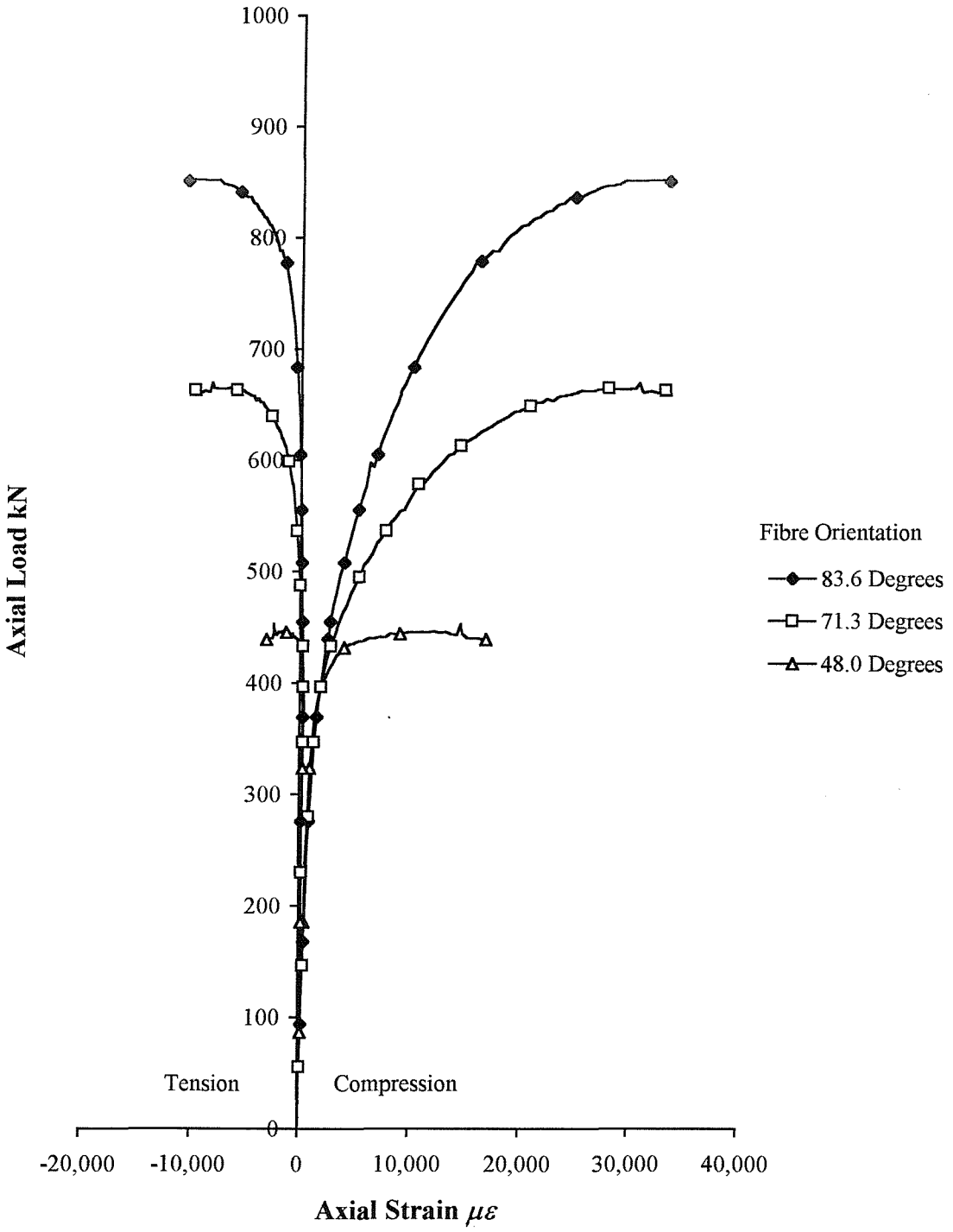

Figure H.10. Load-strain curves for the 150 mm diameter concrete-filled FRP-composite columns with a slenderness ratio of 5 (nominal concrete cube strength = 35 N/mm^2)

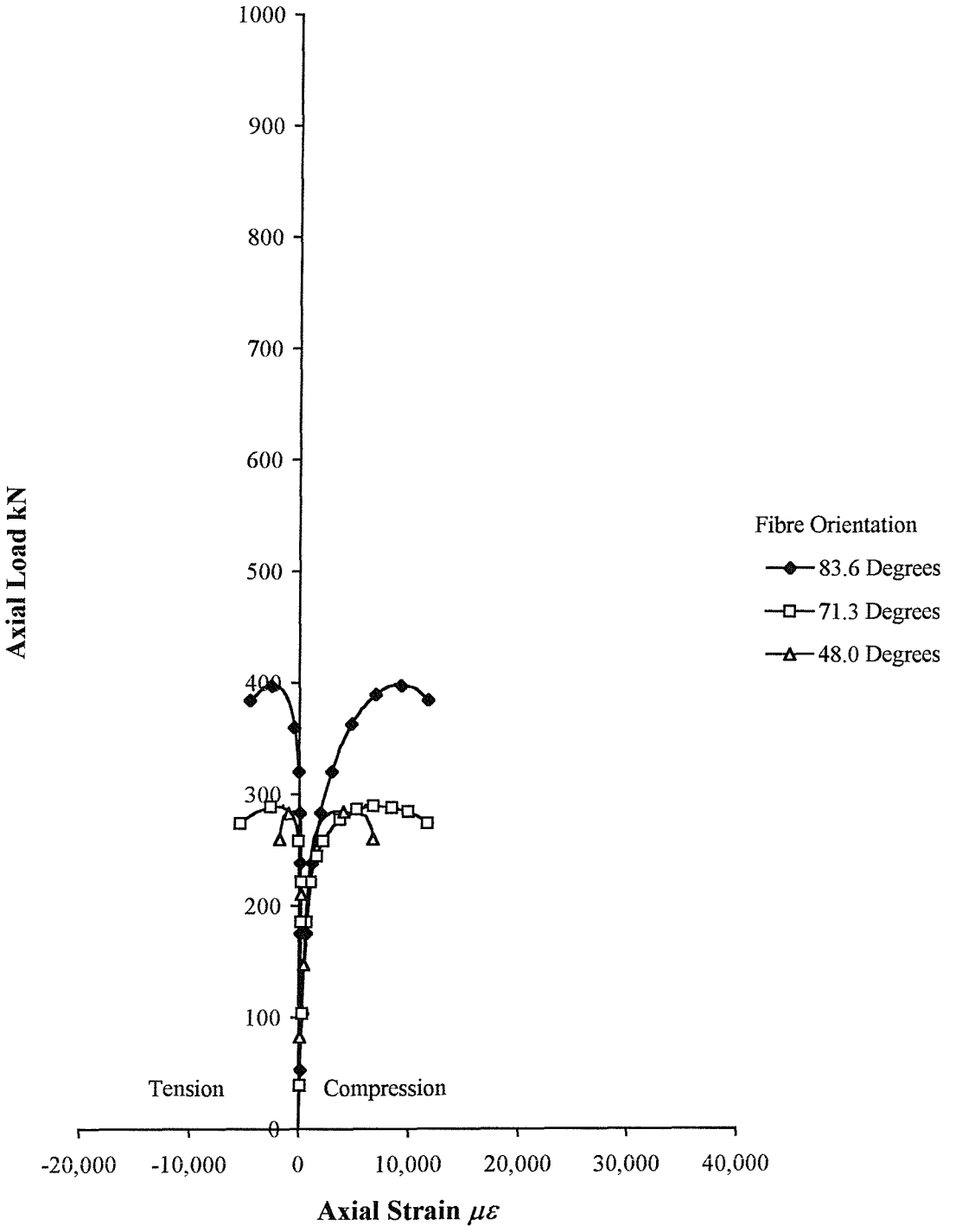

Figure H.11. Load-strain curves for the 150 mm diameter concrete-filled FRP-composite columns with a slenderness ratio of 10 (nominal concrete cube strength = 25 N/mm^2)

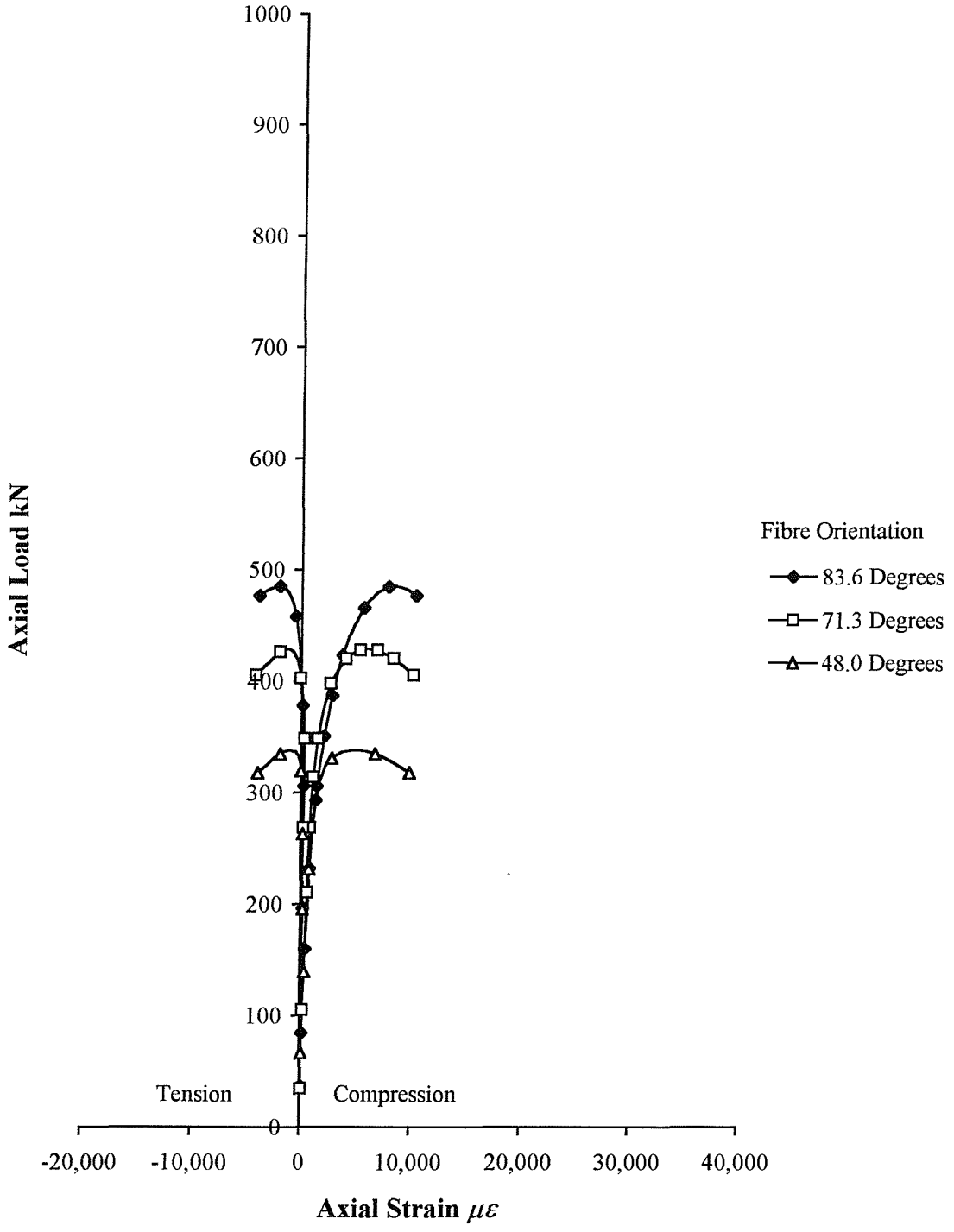

Figure H.12. Load-strain curves for the 150 mm diameter concrete-filled FRP-composite columns with a slenderness ratio of 10 (nominal concrete cube strength = 35 N/mm^2)

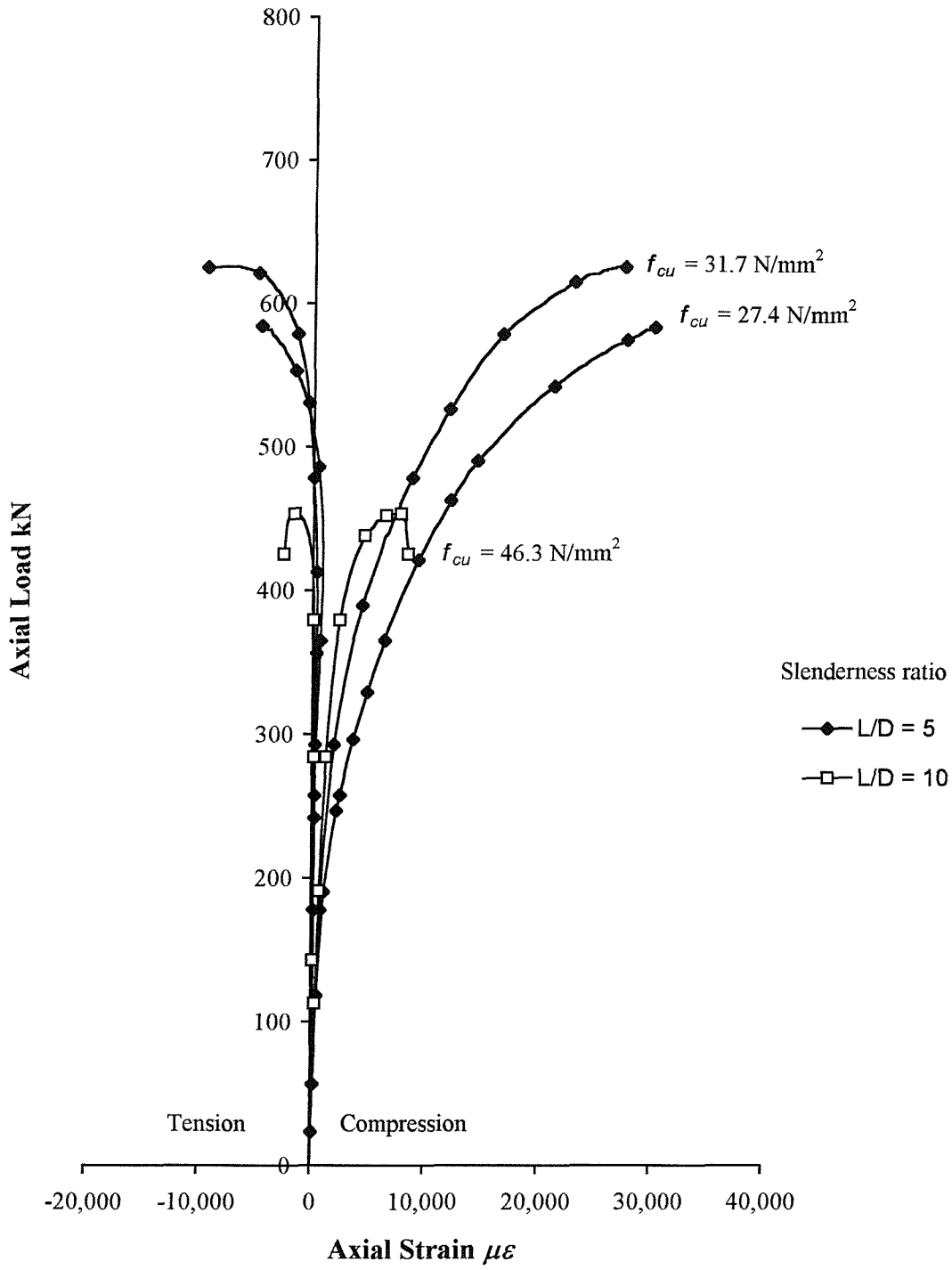

Figure H.13. Load-strain curves for the 125 mm diameter concrete-filled FRP-composite columns confined with E-glass fibres orientated at 82.3 degrees

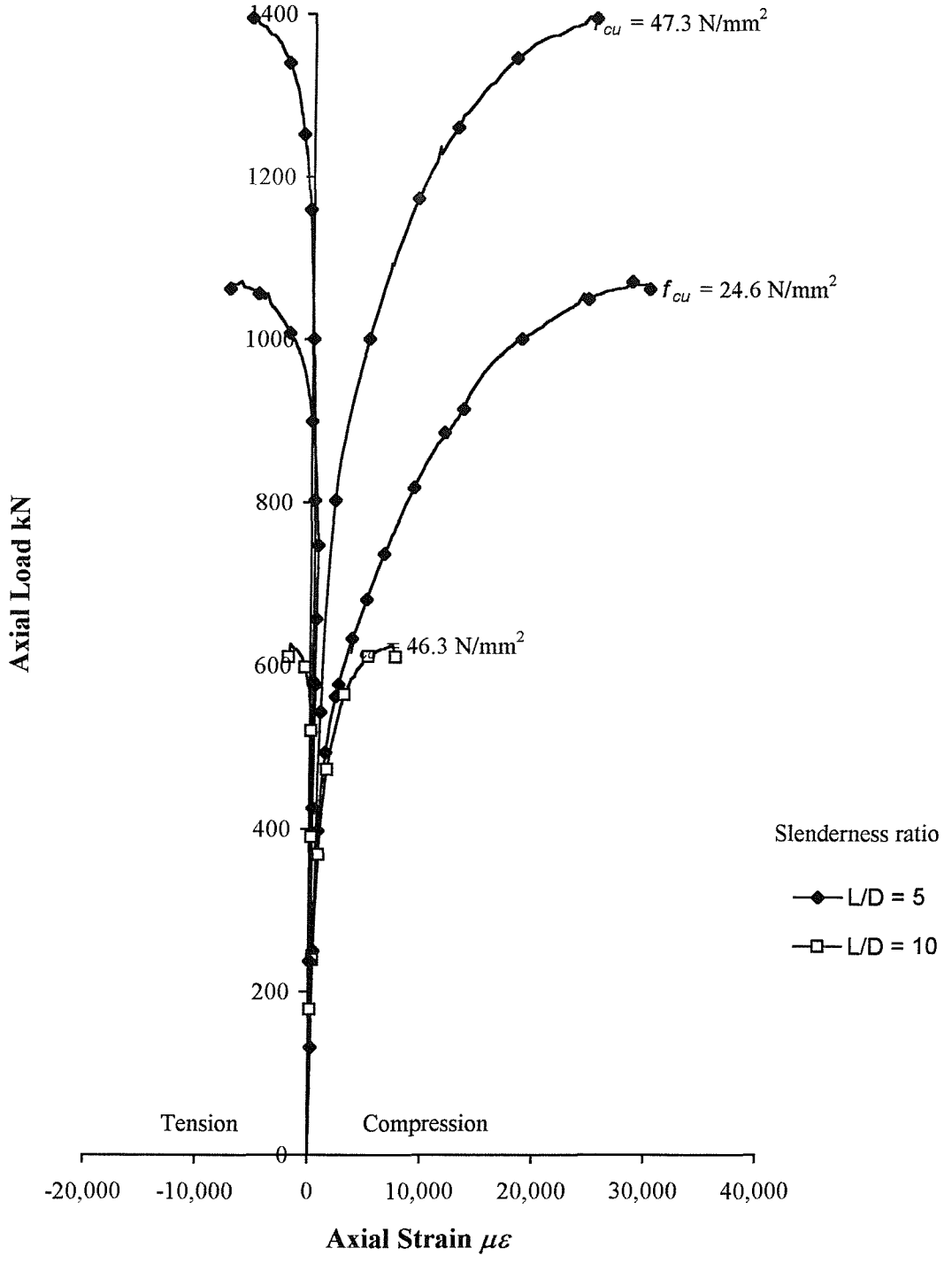

Figure H.14. Load-strain curves for the 200 mm diameter concrete-filled FRP-composite columns confined with E-glass fibres orientated at 85.2 degrees

APPENDIX I

EXPERIMENTAL MOMENT-CURVATURE RELATIONSHIPS FOR CONCRETE-FILLED E-GLASS FRP-COMPOSITE COLUMNS

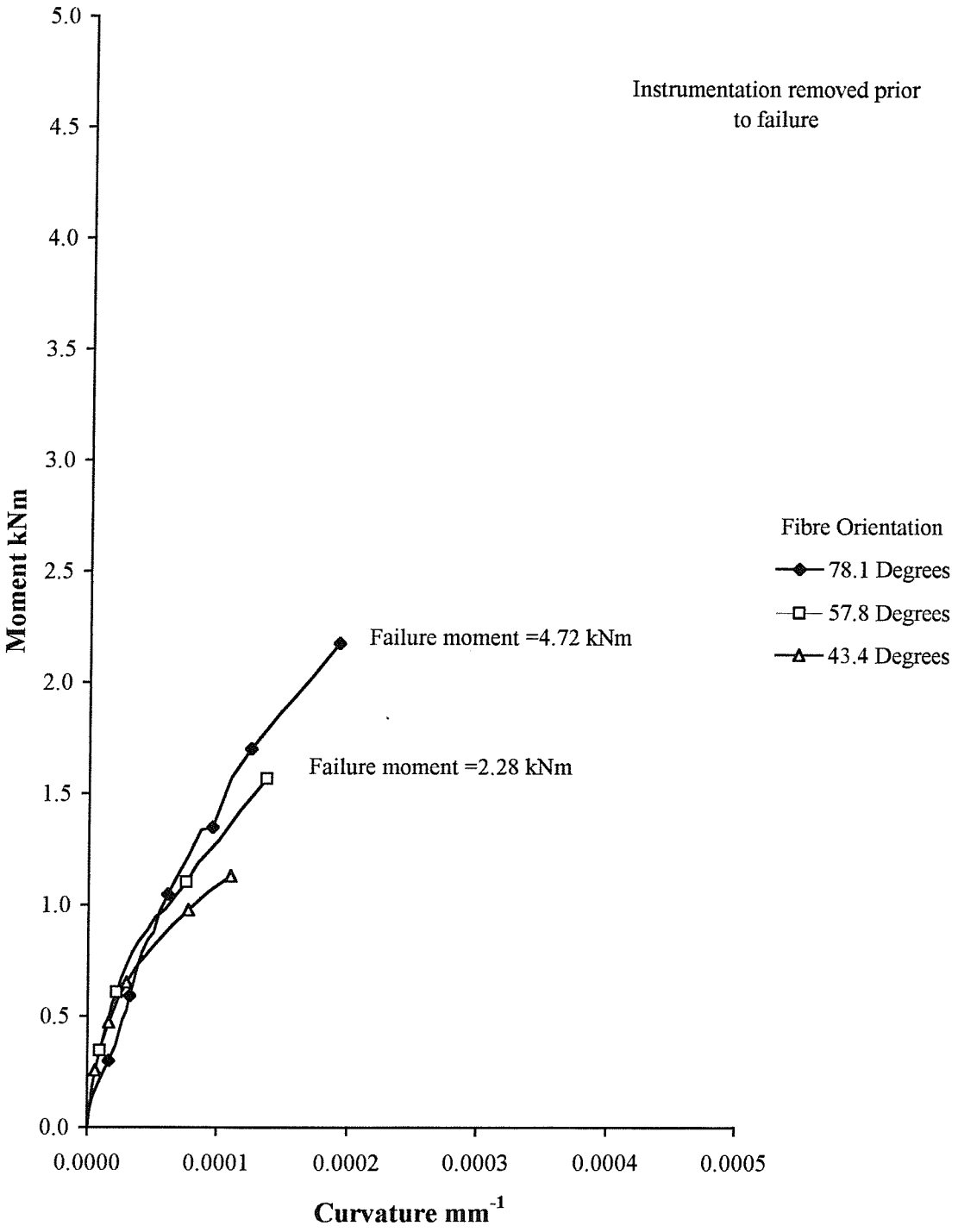

Figure I.1. Moment-curvature relationships for the 80 mm diameter concrete-filled FRP-composite columns with a slenderness ratio of 5 (nominal concrete cube strength = 25 N/mm^2)

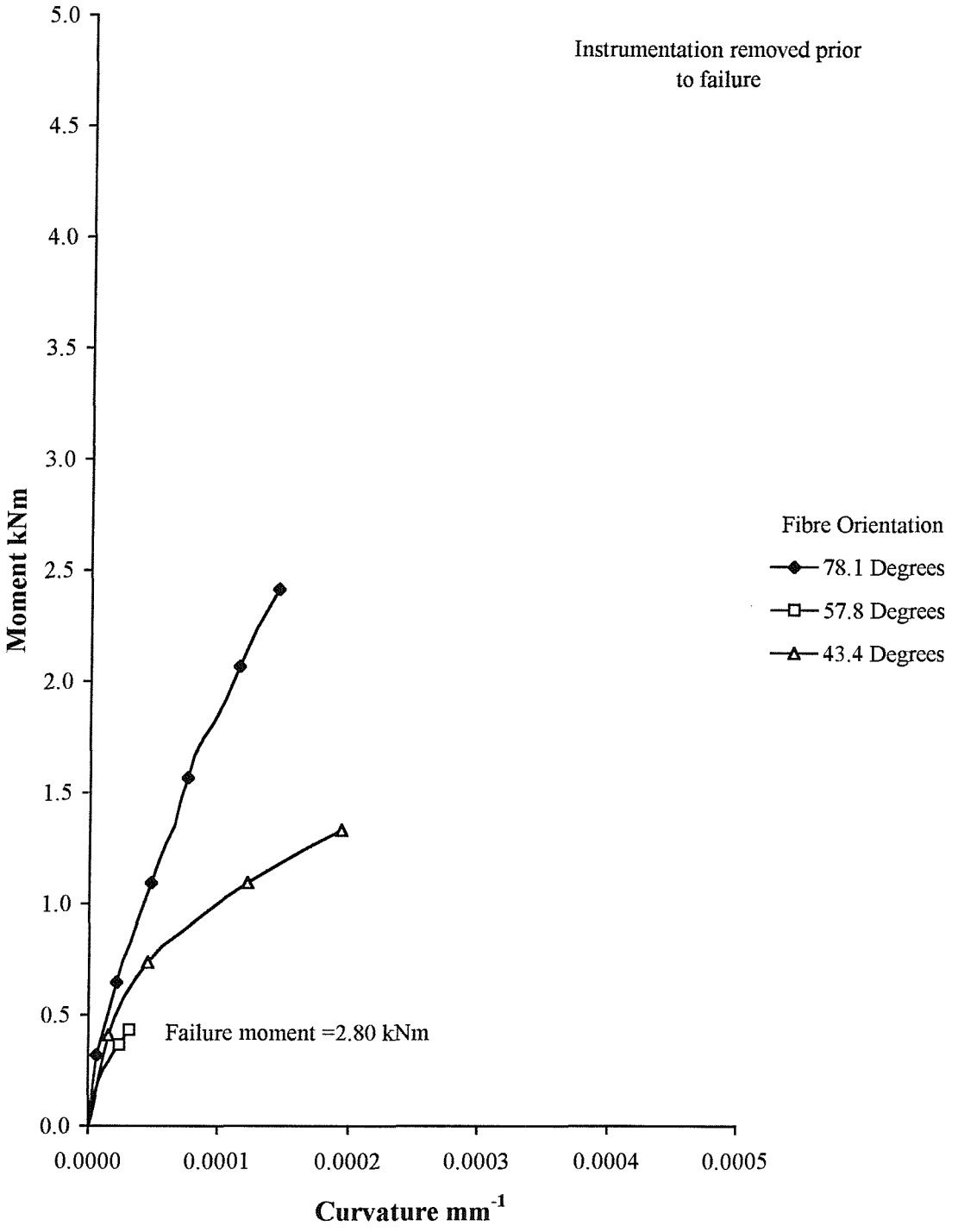

Figure I.2. Moment-curvature relationships for the 80 mm diameter concrete-filled FRP-composite columns with a slenderness ratio of 5 (nominal concrete cube strength = 35 N/mm^2)

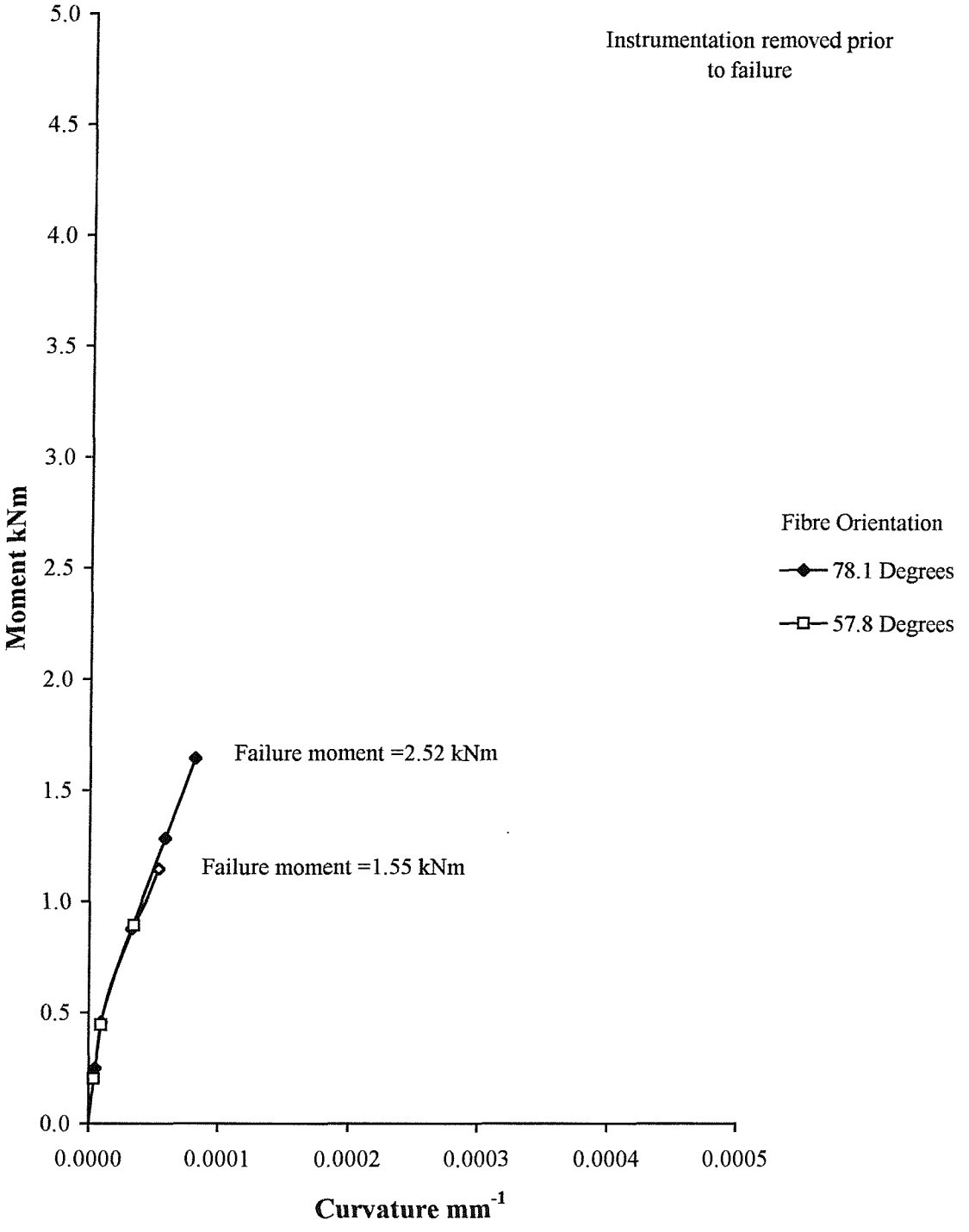

Figure I.3. Moment-curvature relationships for the 80 mm diameter concrete-filled FRP-composite columns with a slenderness ratio of 10 (nominal concrete cube strength = 25 N/mm^2)

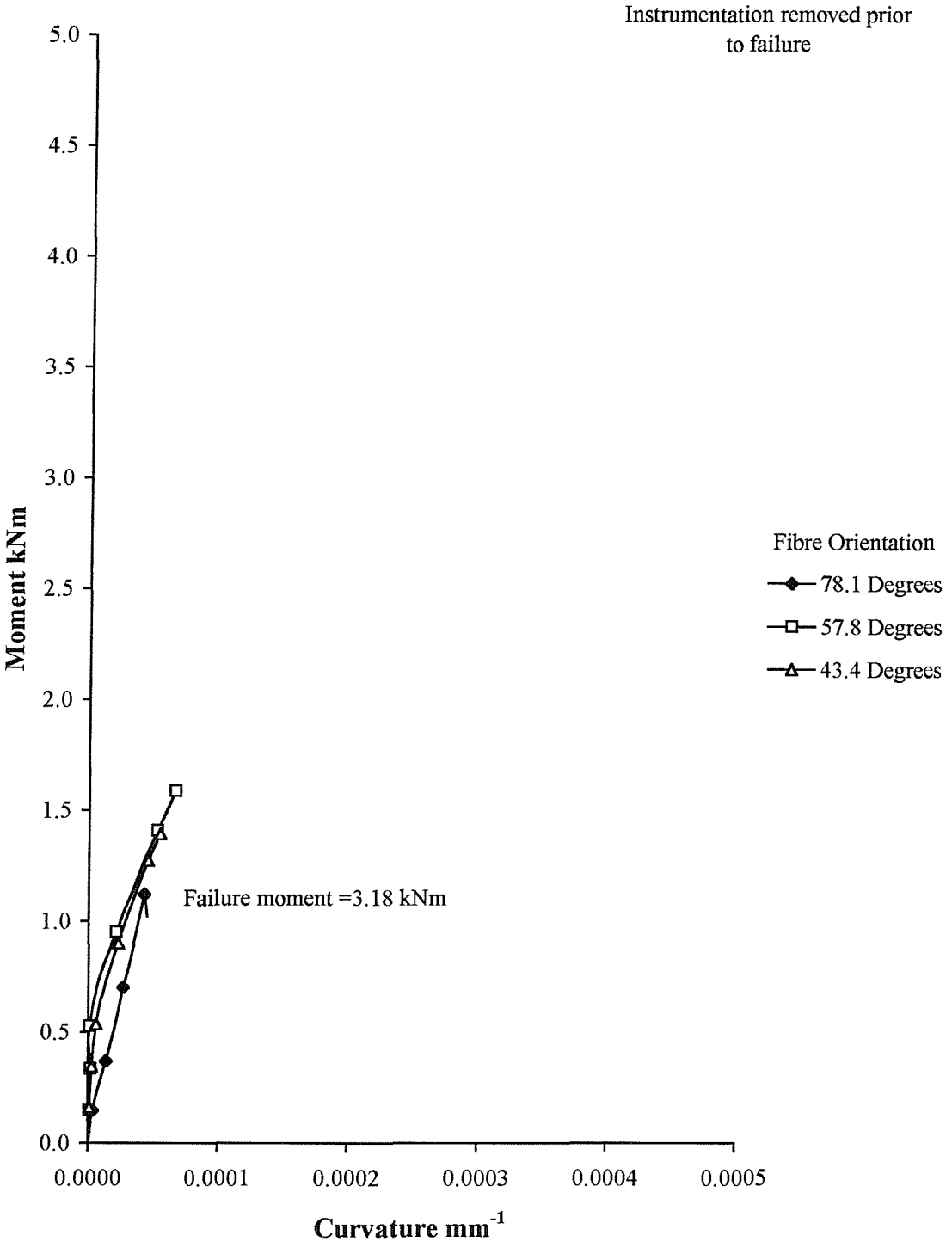

Figure I.4. Moment-curvature relationships for the 80 mm diameter concrete-filled FRP-composite columns with a slenderness ratio of 10 (nominal concrete cube strength = 35 N/mm^2)

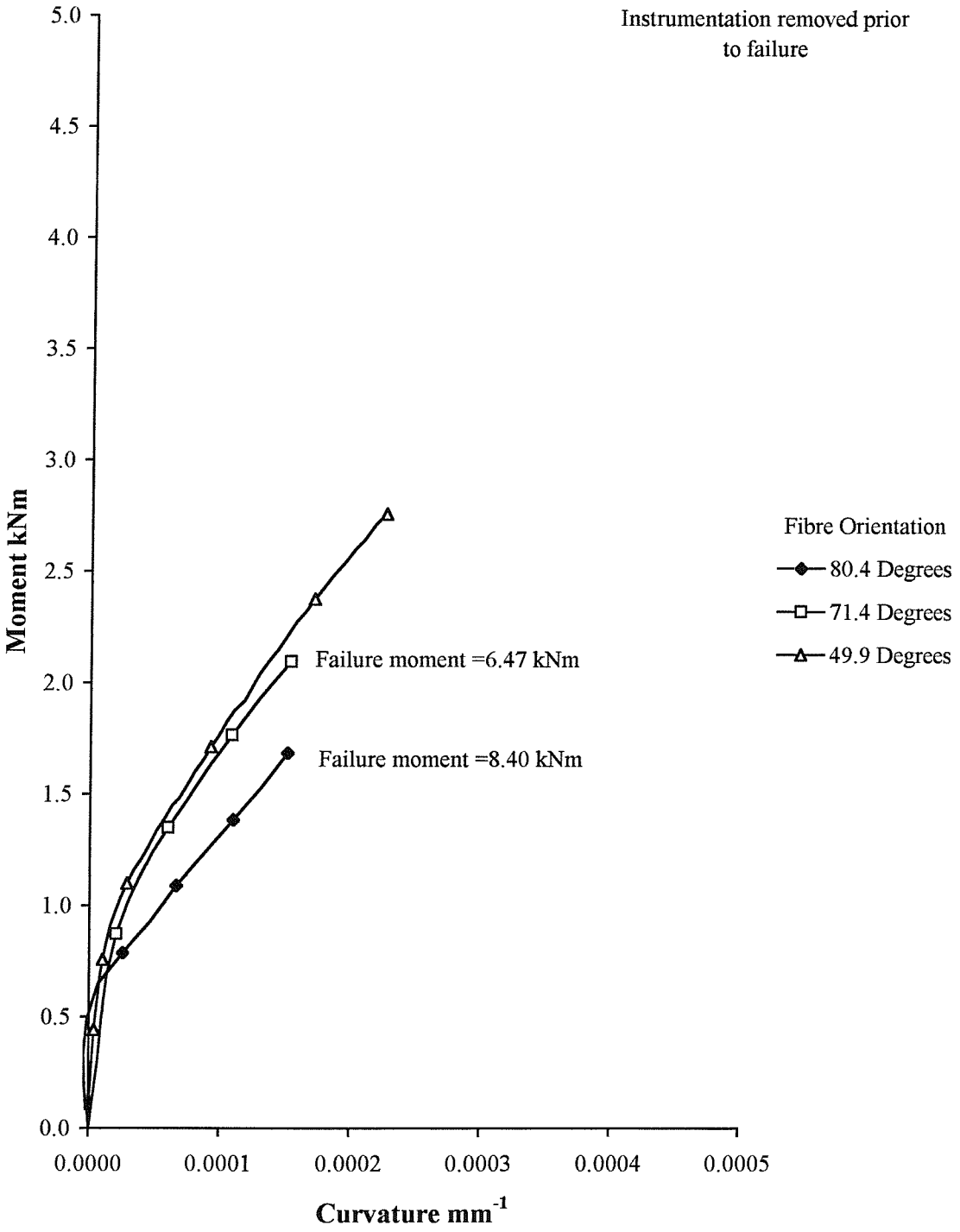

Figure I.5. Moment-curvature relationships for the 100 mm diameter concrete-filled FRP-composite columns with a slenderness ratio of 5 (nominal concrete cube strength = 25 N/mm^2)

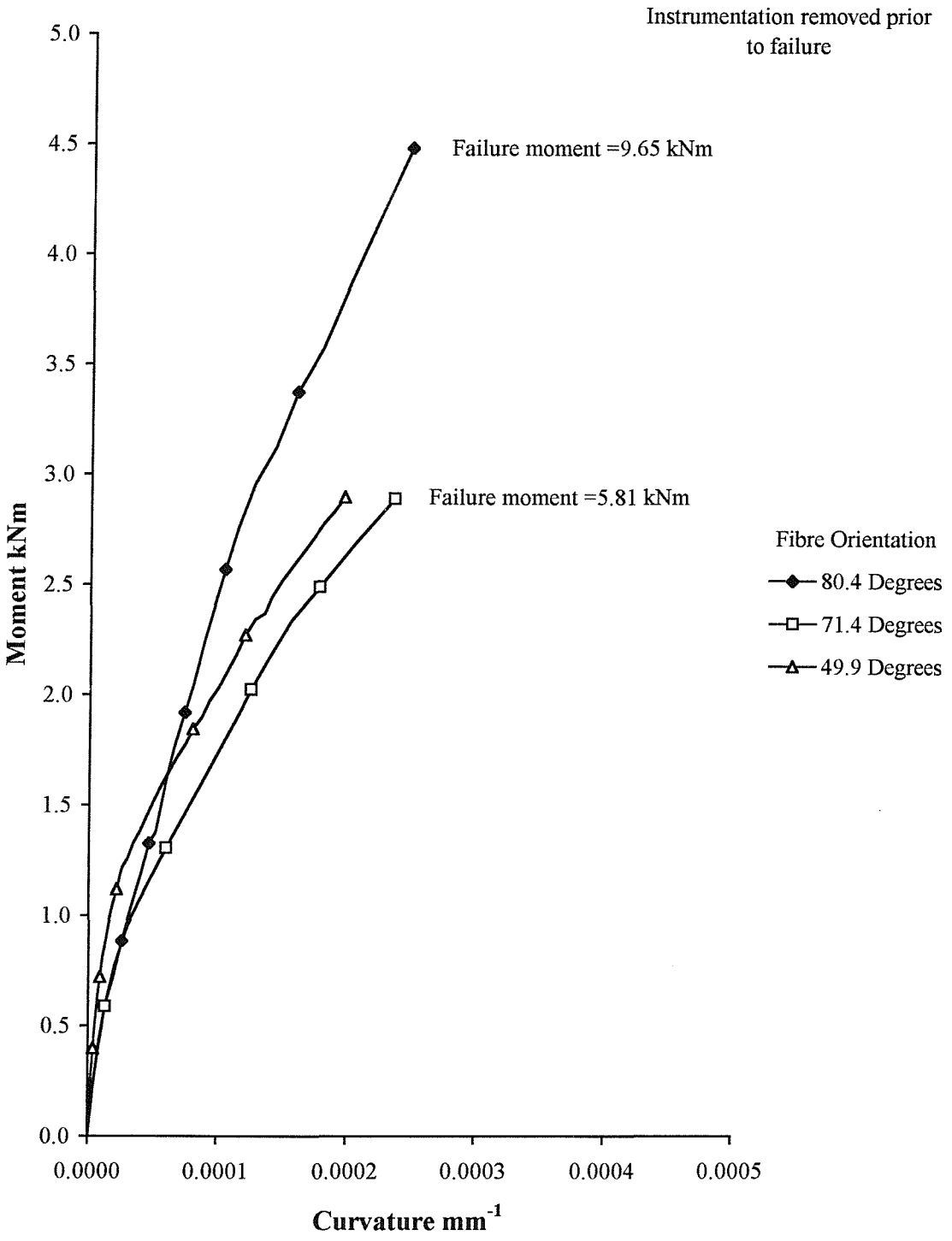

Figure I.6. Moment-curvature relationships for the 100 mm diameter concrete-filled FRP-composite columns with a slenderness ratio of 5 (nominal concrete cube strength = 35 N/mm^2)

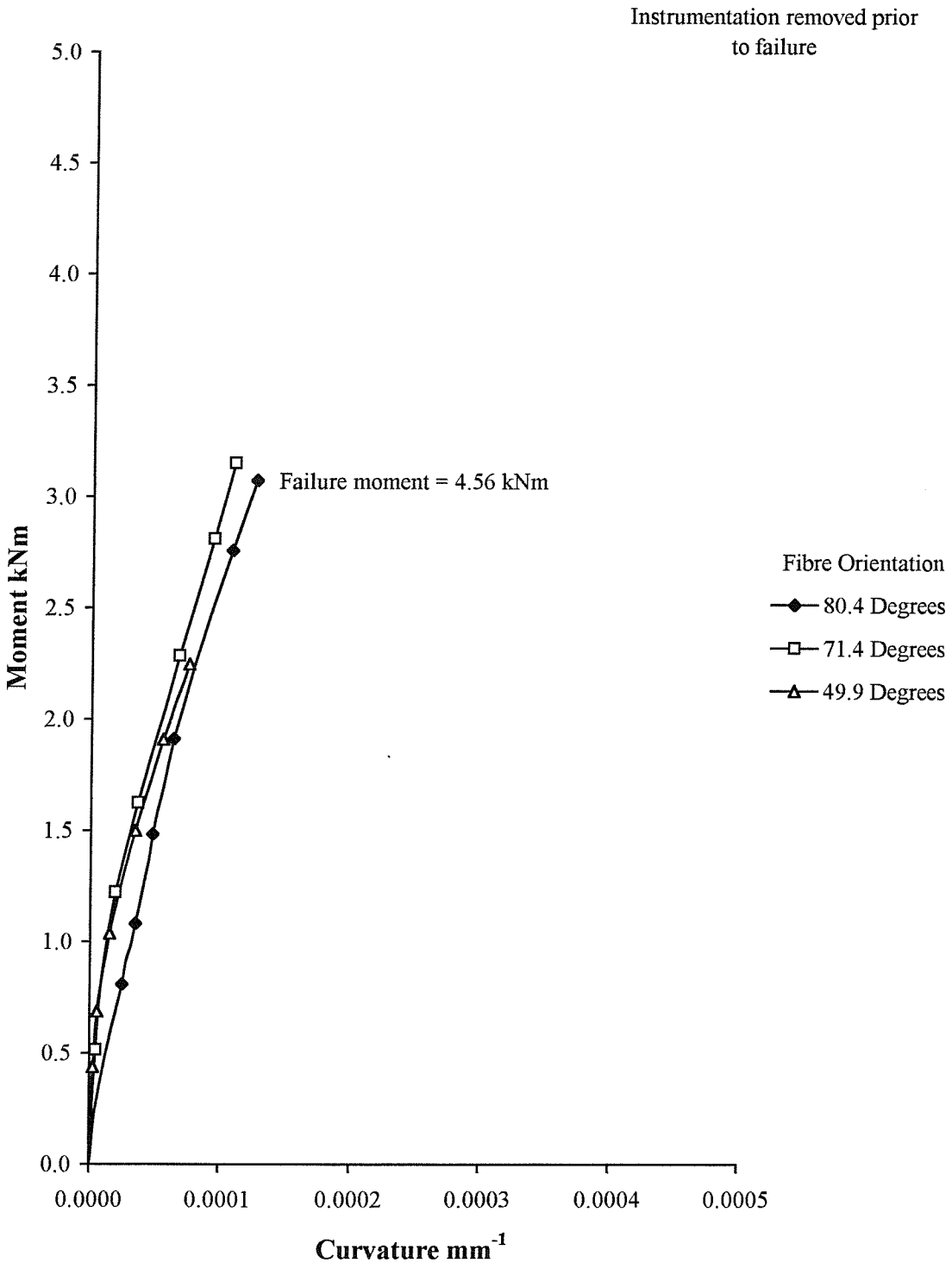

Figure I.7. Moment-curvature relationships for the 100 mm diameter concrete-filled FRP-composite columns with a slenderness ratio of 10 (nominal concrete cube strength = 25 N/mm^2)

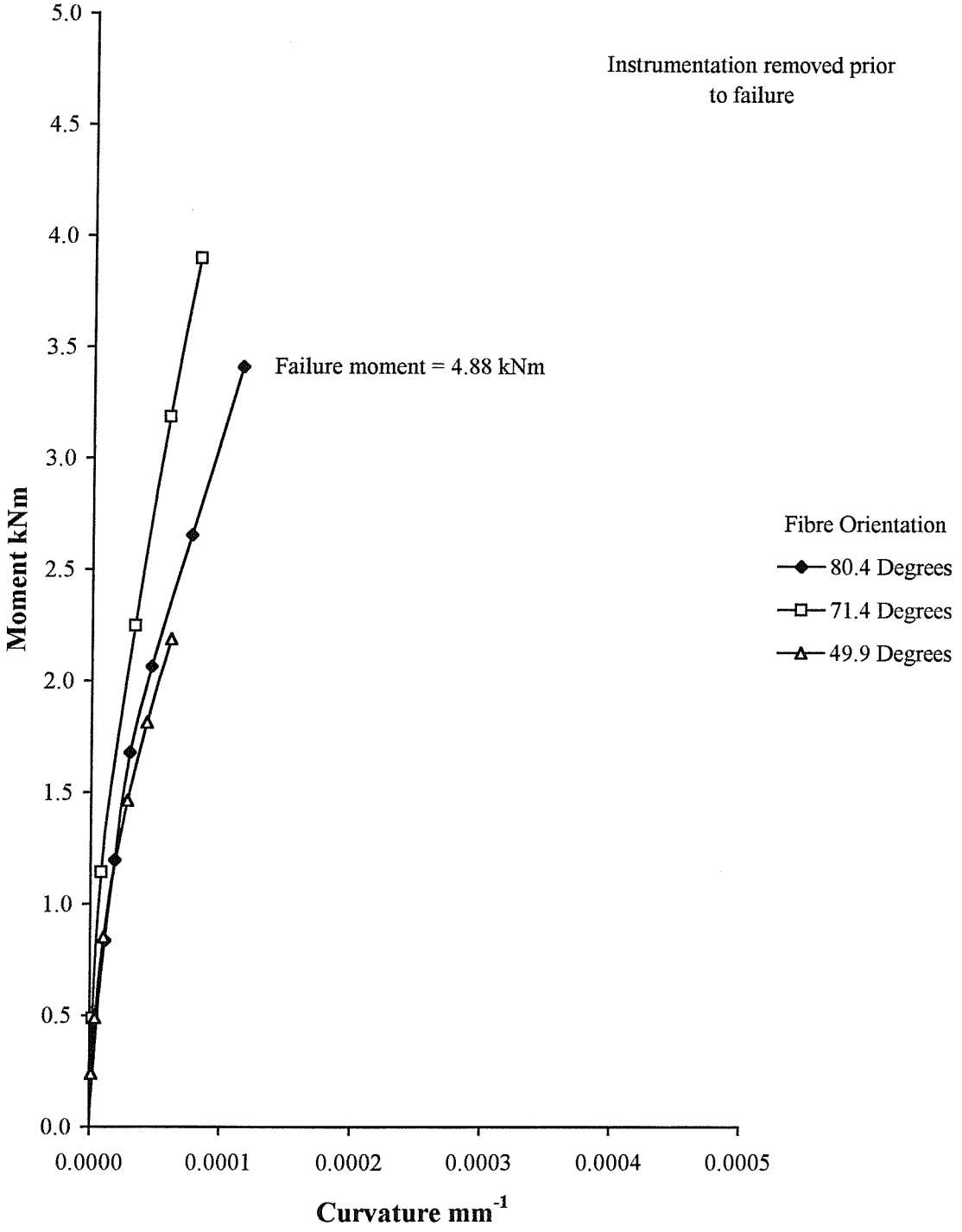

Figure I.8. Moment-curvature relationships for the 100 mm diameter concrete-filled FRP-composite columns with a slenderness ratio of 10 (nominal concrete cube strength = 35 N/mm^2)

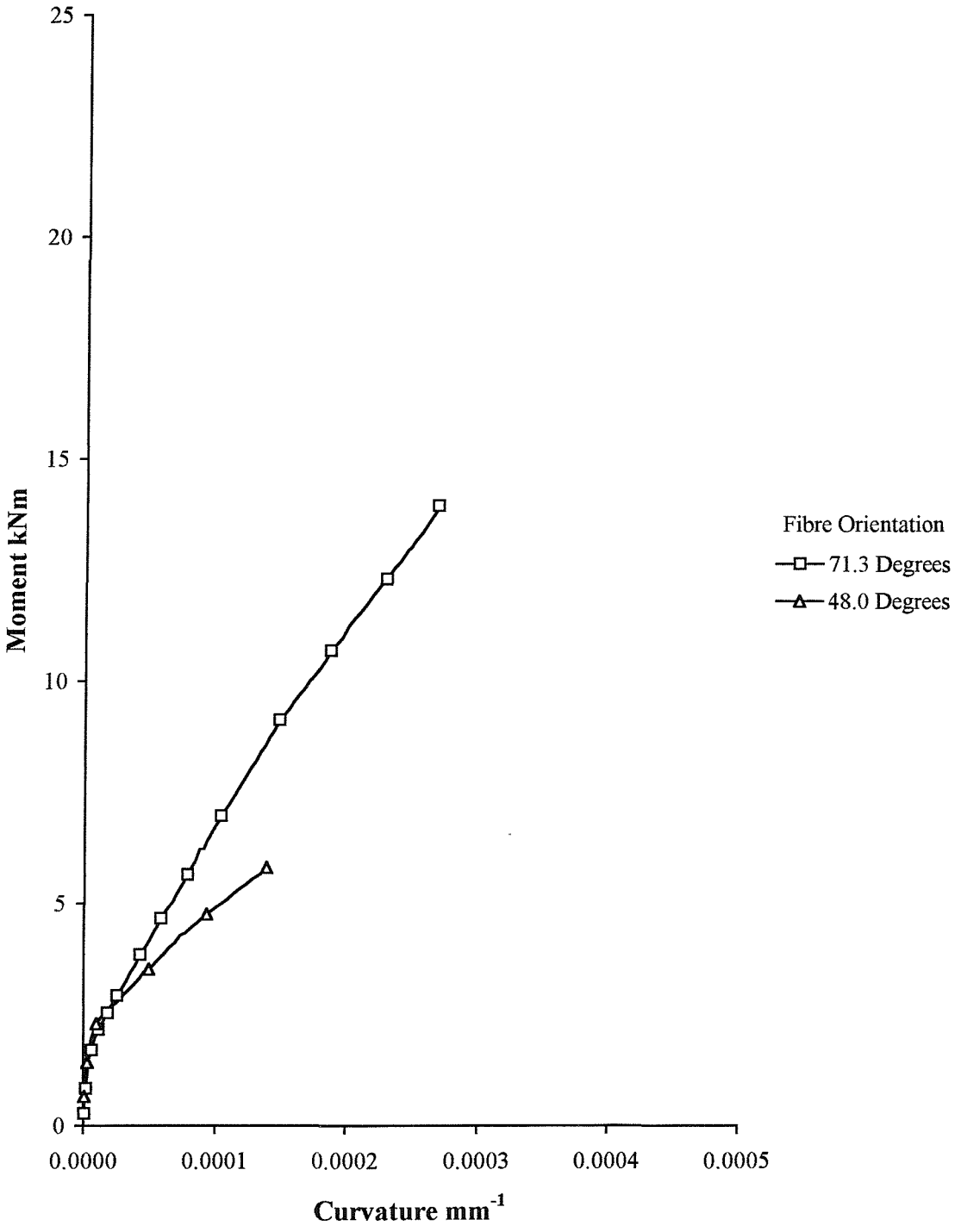

Figure I.9. Moment-curvature relationships for the 150 mm diameter concrete-filled FRP-composite columns with a slenderness ratio of 5 (nominal concrete cube strength = 25 N/mm^2)

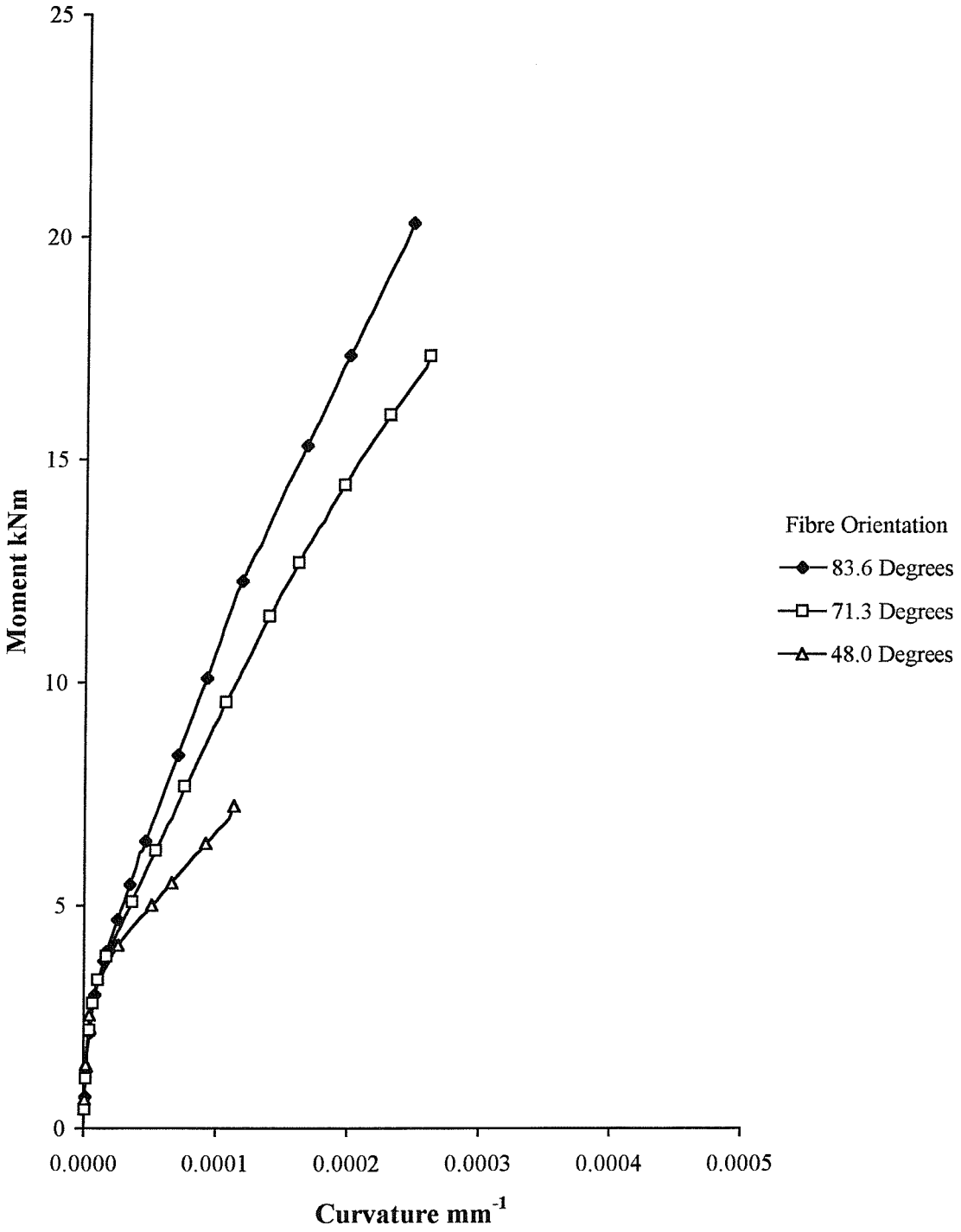

Figure I.10. Moment-curvature relationships for the 150 mm diameter concrete-filled FRP-composite columns with a slenderness ratio of 5 (nominal concrete cube strength = 35 N/mm^2)

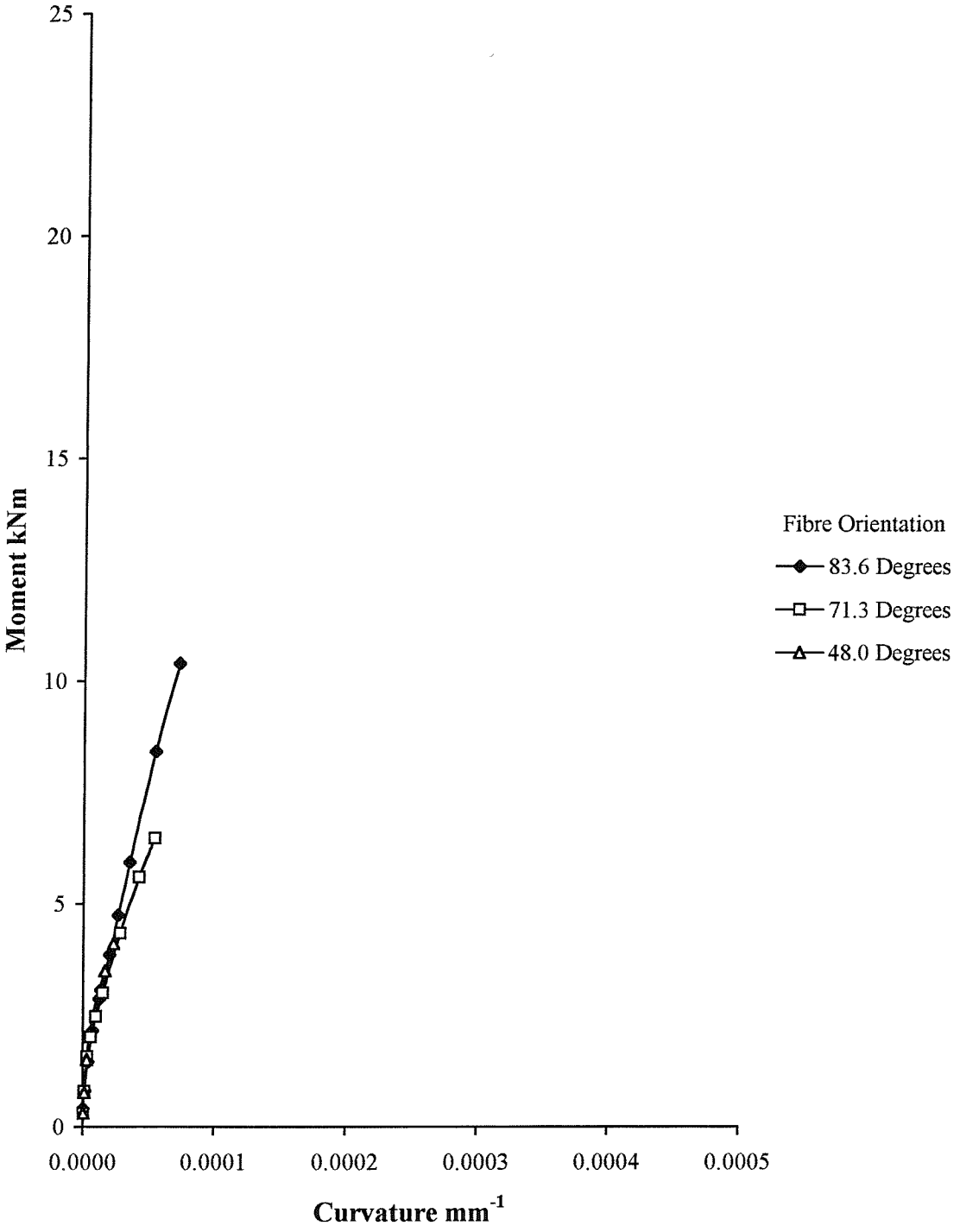

Figure I.11. Moment-curvature relationships for the 150 mm diameter concrete-filled FRP-composite columns with a slenderness ratio of 10 (nominal concrete cube strength = 25 N/mm^2)

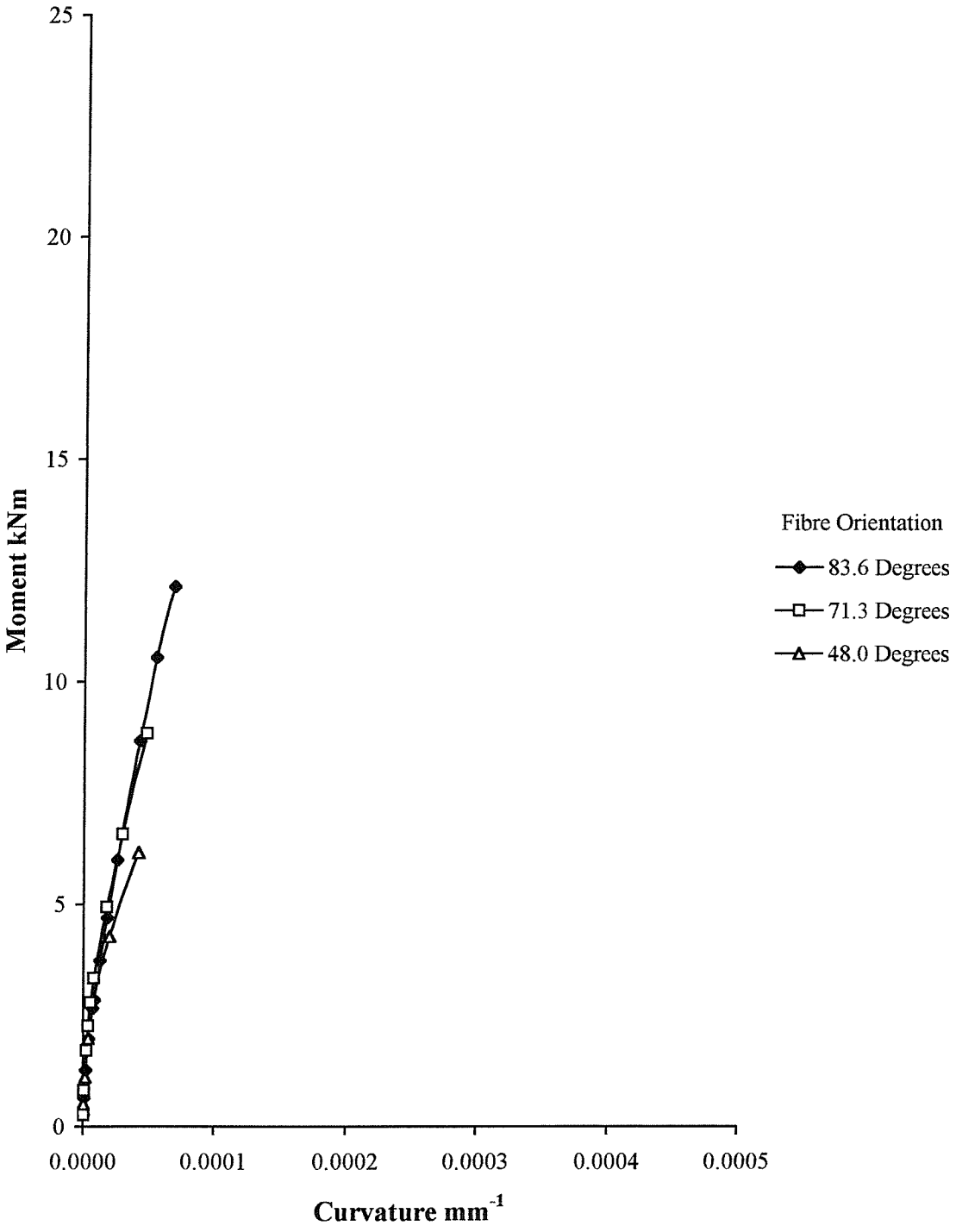

Figure I.12. Moment-curvature relationships for the 150 mm diameter concrete-filled FRP-composite columns with a slenderness ratio of 10 (nominal concrete cube strength = 35 N/mm^2)

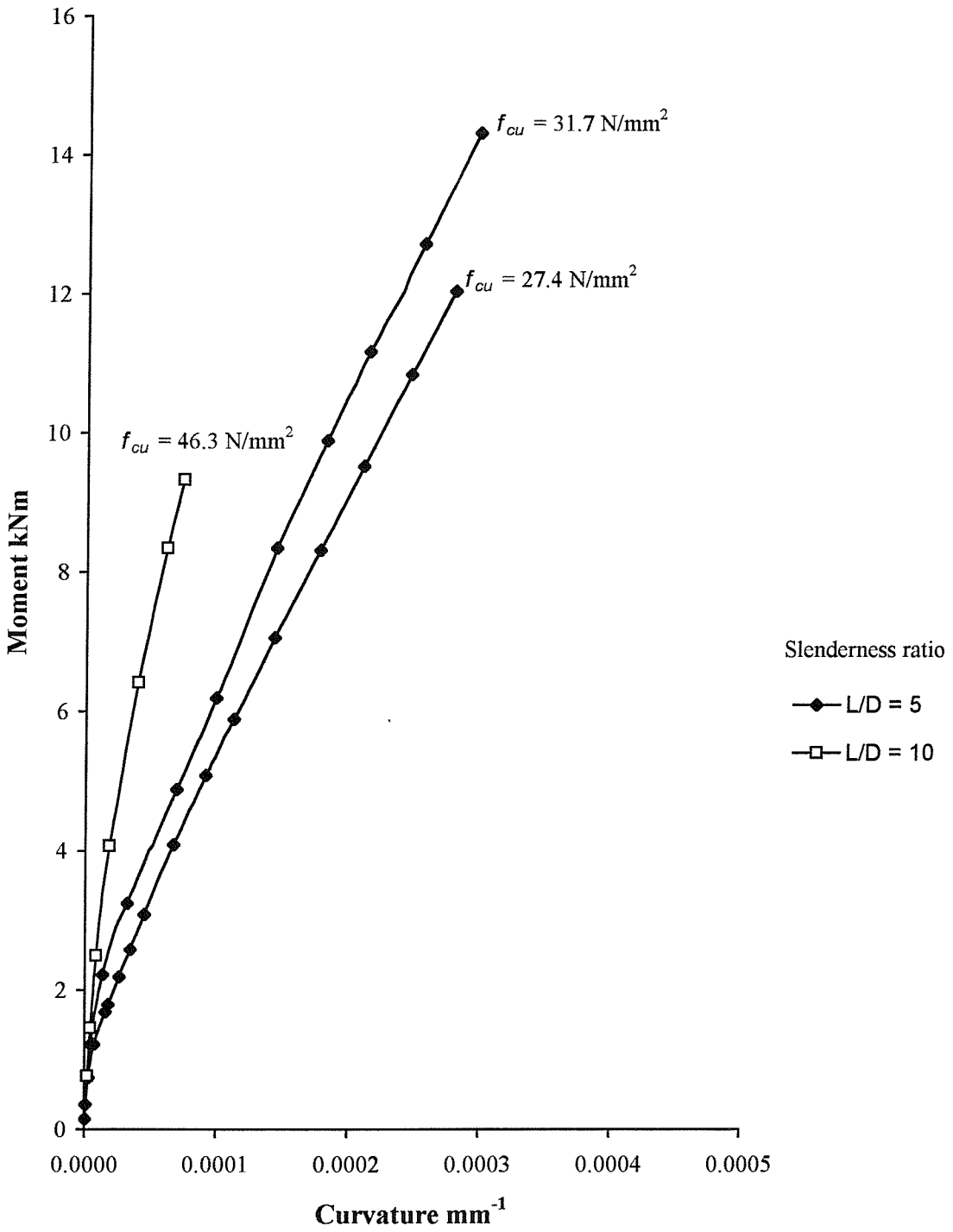

Figure I.13. Moment-curvature relationships for the 125 mm diameter concrete-filled FRP-composite columns confined with E-glass fibres orientated at 82.3 degrees

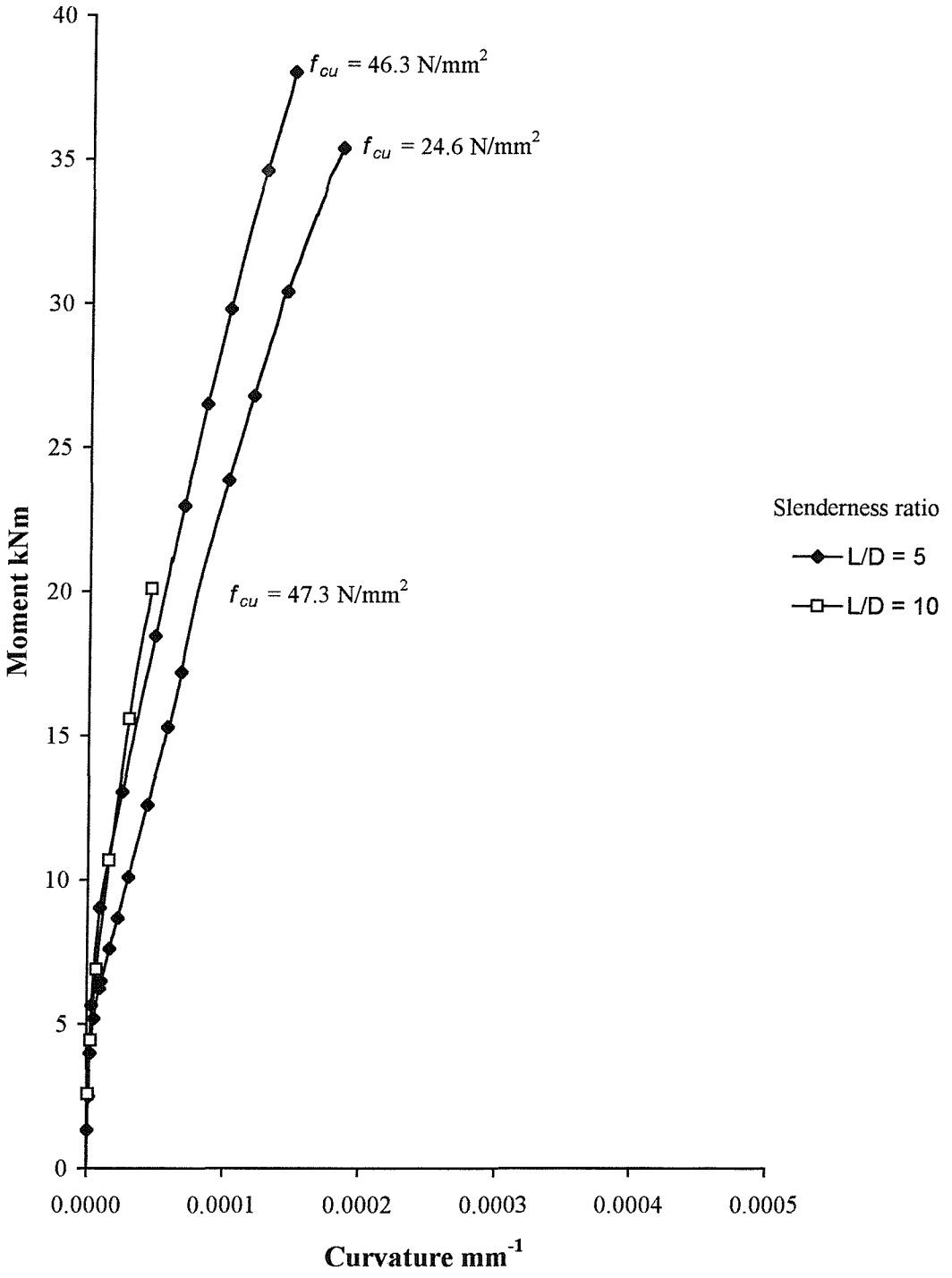

Figure I.14. Moment-curvature relationships for the 200 mm diameter concrete-filled FRP-composite columns confined with E-glass fibres orientated at 85.2 degrees

APPENDIX J

EXPERIMENTAL LOAD-DEFECTION CURVES FOR CONCRETE-FILLED E-GLASS FRP-COMPOSITE COLUMNS REINFORCED LONGITUDINALLY WITH CARBON FRP-COMPOSITE BARS

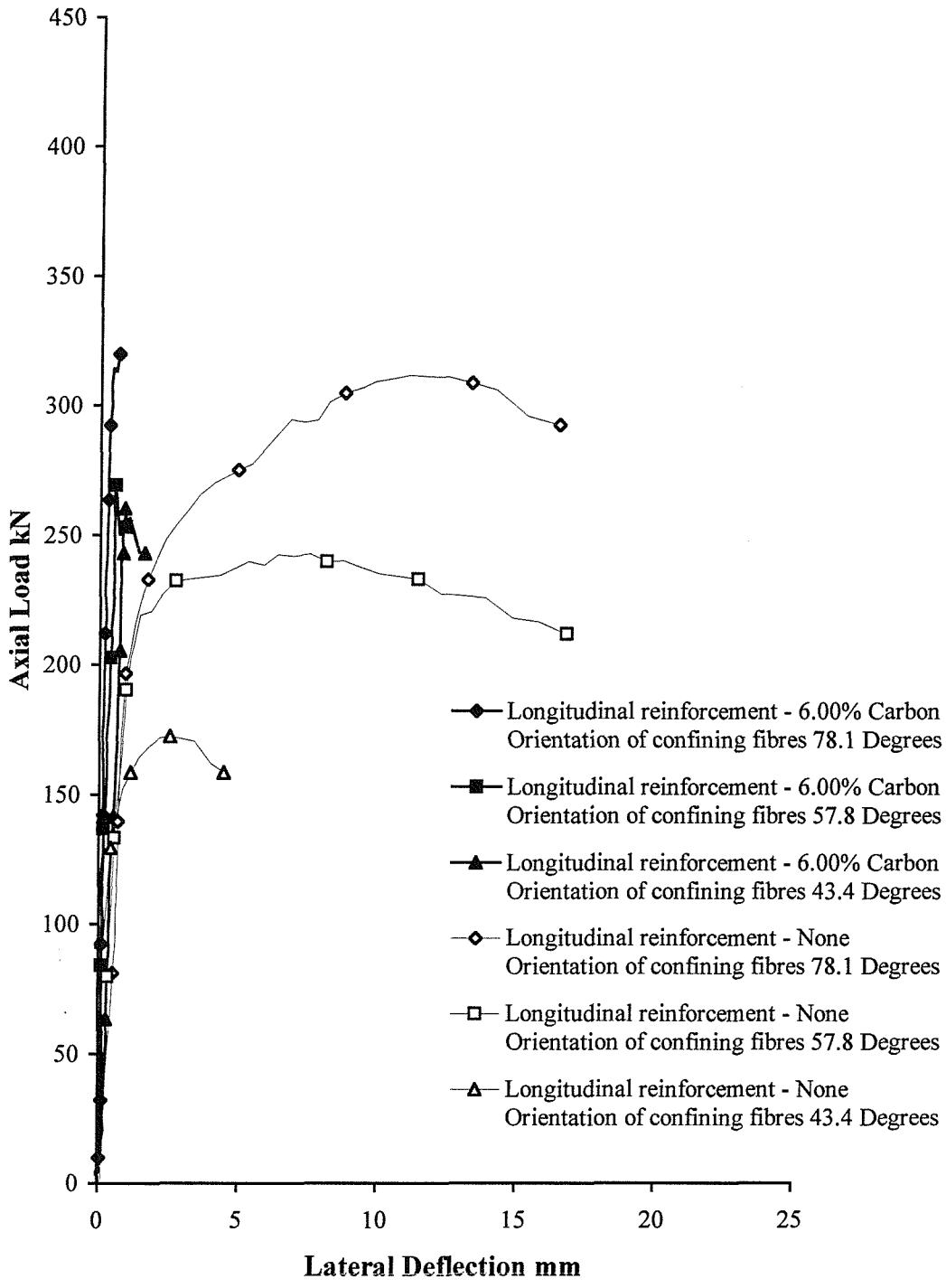

Figure J.1. Load-deflection curves for the 80 mm diameter concrete-filled E-glass FRP-composite columns with longitudinal carbon FRP-composite bars (slenderness ratio = 5)

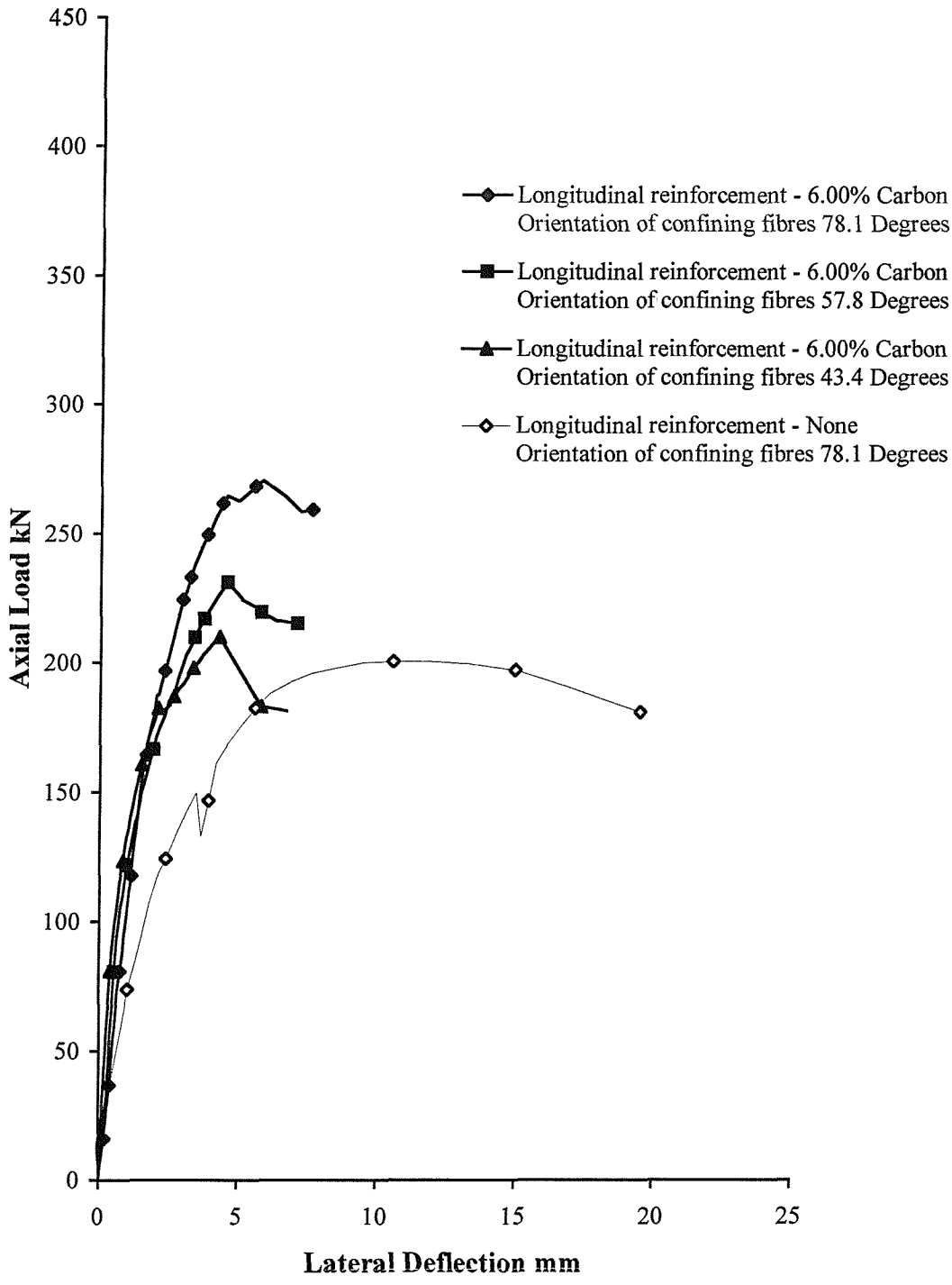

Figure J.2. Load-deflection curves for the 80 mm diameter concrete-filled E-glass FRP-composite columns with longitudinal carbon FRP-composite bars (slenderness ratio = 10)

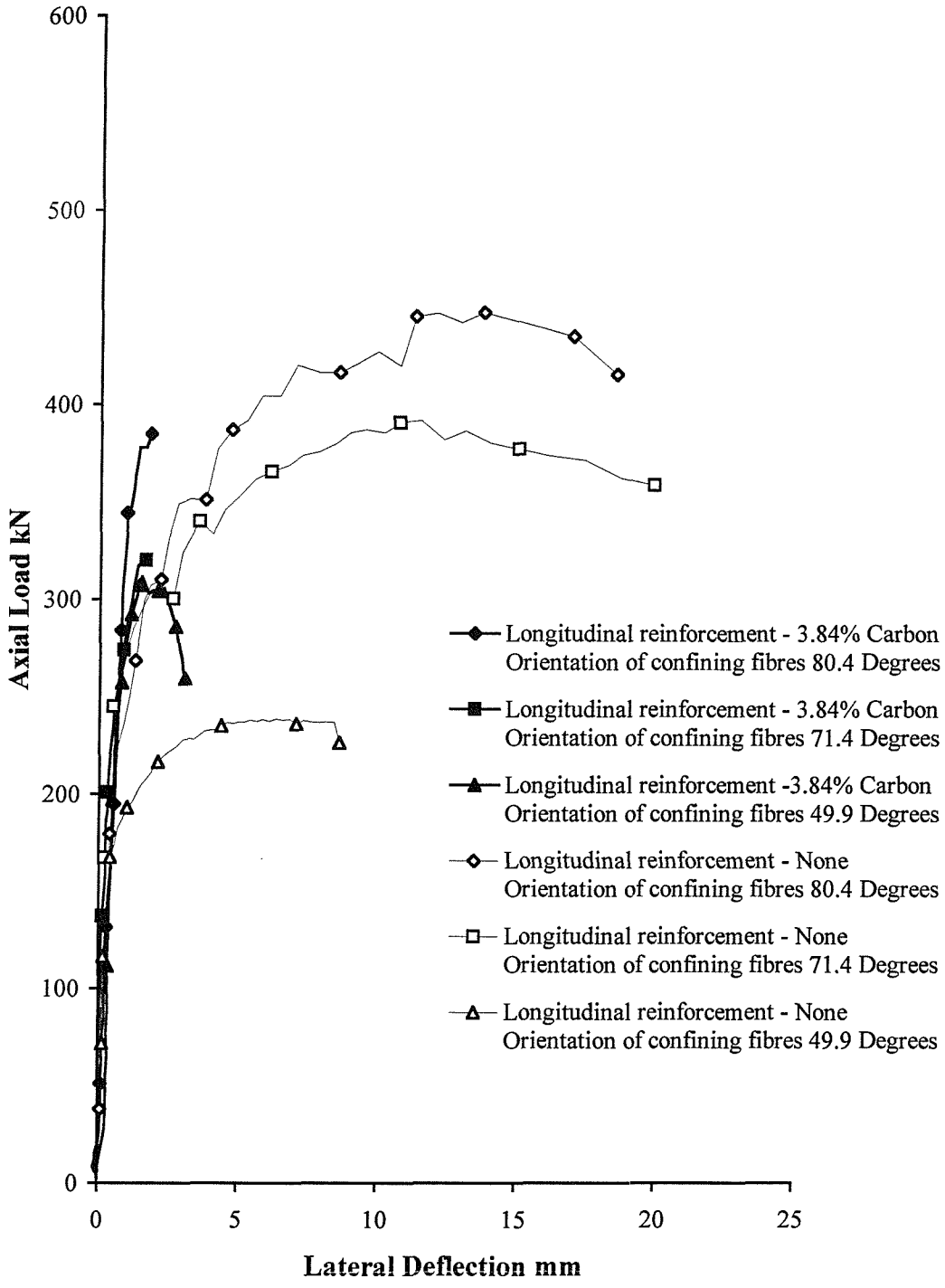

Figure J.3. Load-deflection curves for the 100 mm diameter concrete-filled E-glass FRP-composite columns with longitudinal carbon FRP-composite bars (slenderness ratio = 5)

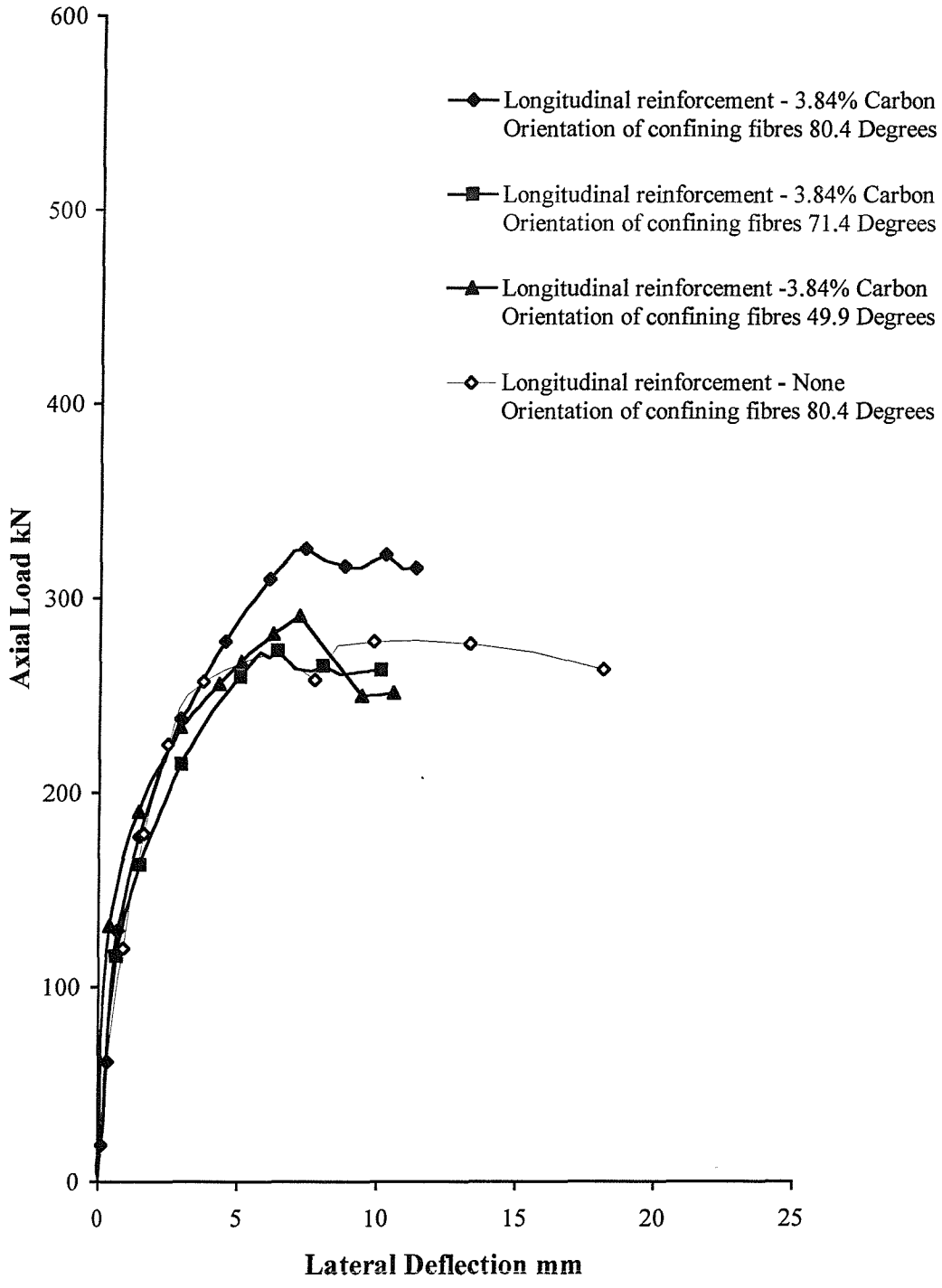

Figure J.4. Load-deflection curves for the 100 mm diameter concrete-filled E-glass FRP-composite columns with longitudinal carbon FRP-composite bars (slenderness ratio = 10)

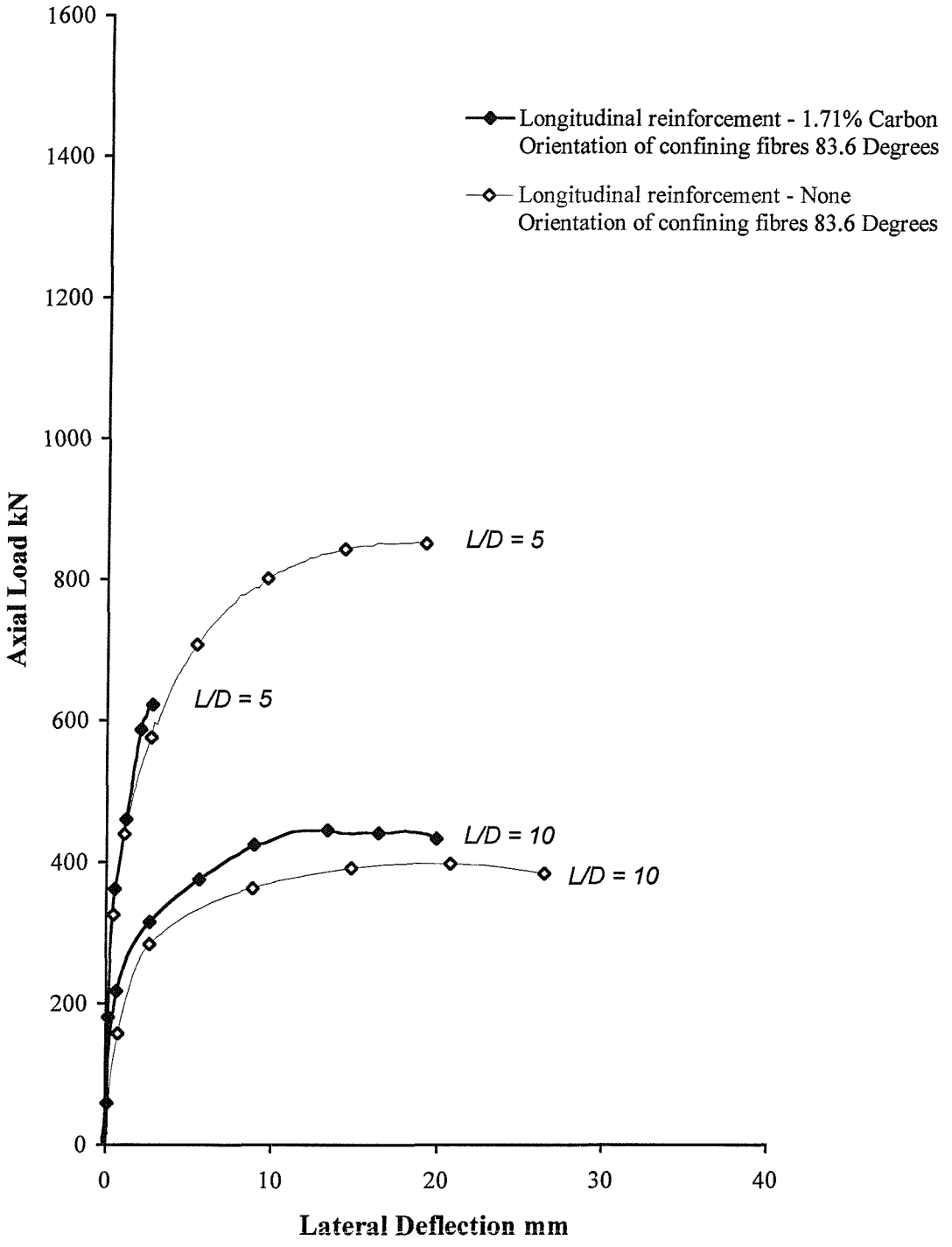

Figure J.5. Load-deflection curves for the 150 mm diameter concrete-filled E-glass FRP-composite columns with longitudinal carbon FRP-composite bars

APPENDIX K

EXPERIMENTAL LOAD-DEFECTION CURVES FOR CONCRETE-FILLED E-GLASS FRP-COMPOSITE COLUMNS REINFORCED LONGITUDINALLY WITH E-GLASS FRP-COMPOSITE BARS

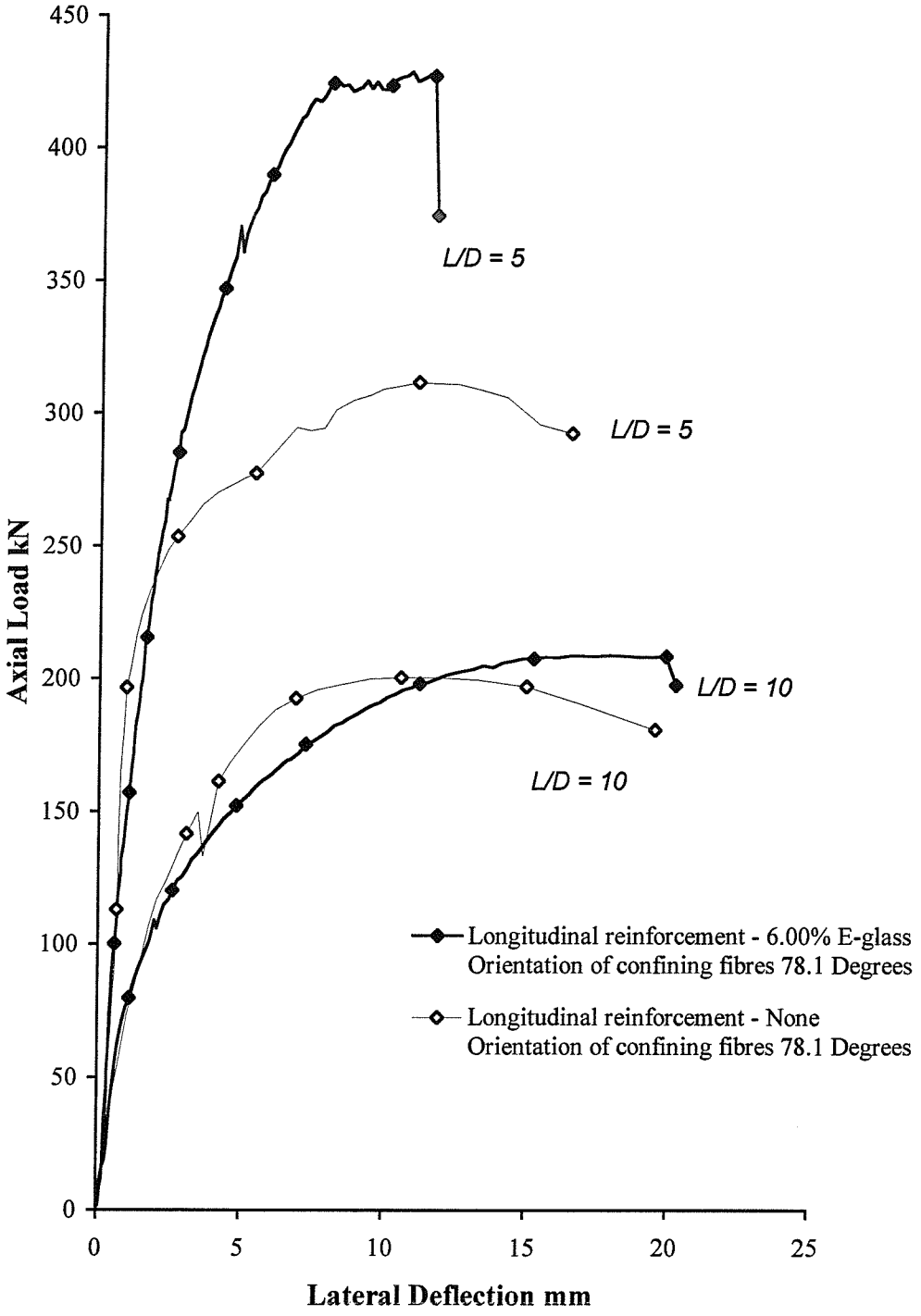

Figure K.1. Load-deflection curves for the 80 mm diameter concrete-filled E-glass FRP-composite columns with longitudinal E-glass FRP-composite bars

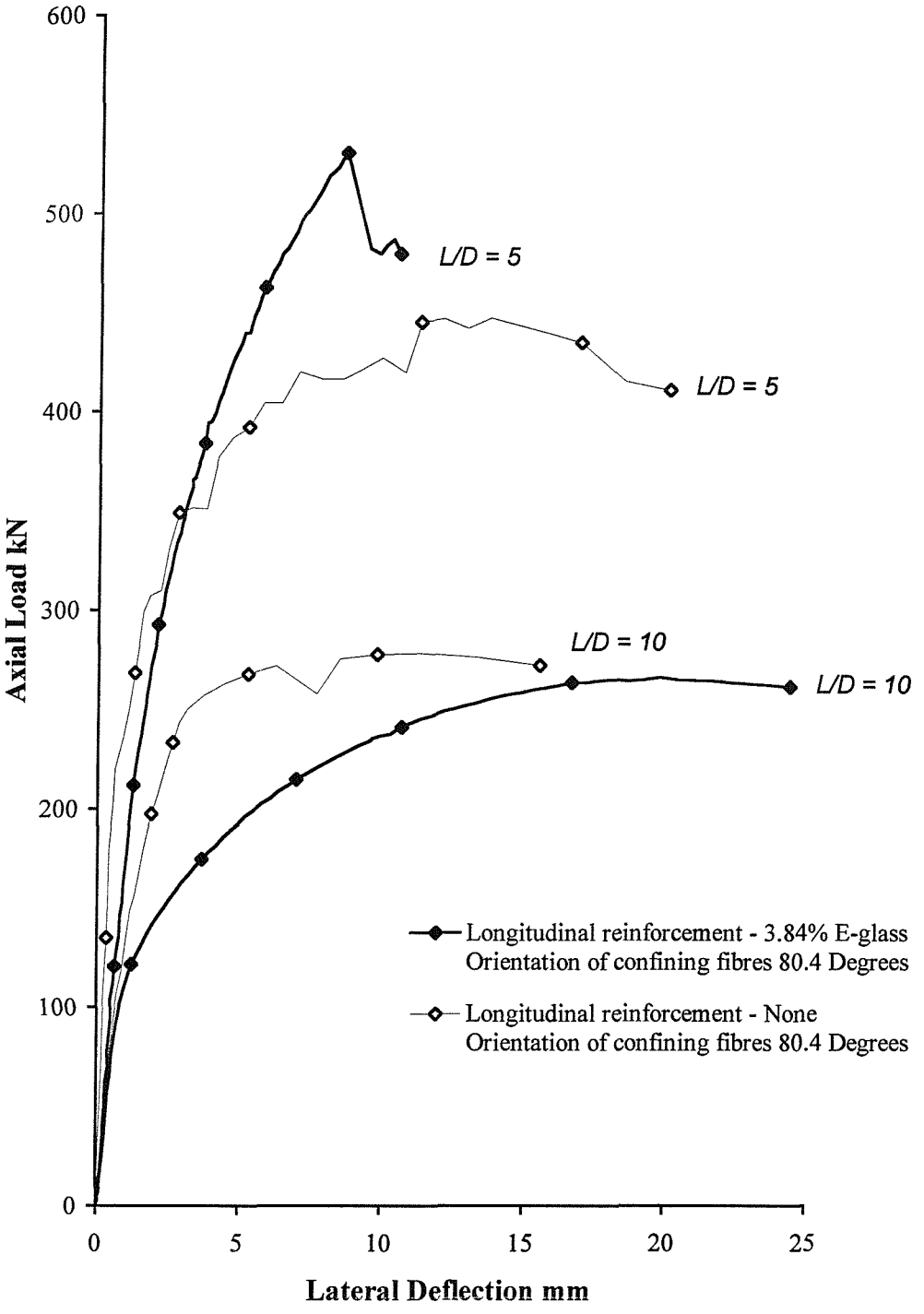

Figure K.2. Load-deflection curves for the 100 mm diameter concrete-filled E-glass FRP-composite columns with longitudinal E-glass FRP-composite bars

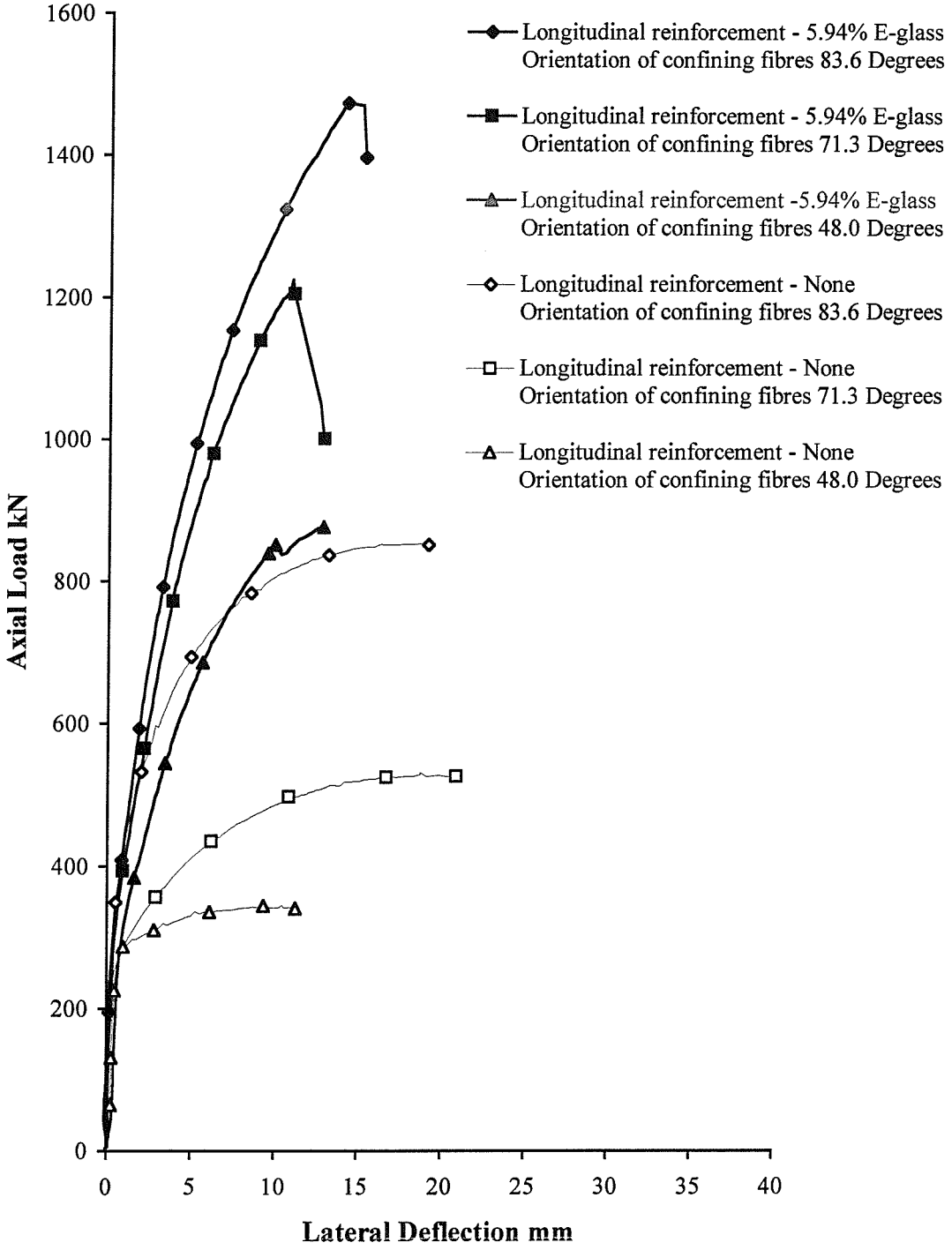

Figure K.3. Load-deflection curves for the 150 mm diameter concrete-filled E-glass FRP-composite columns with longitudinal E-glass FRP-composite bars and a slenderness ratio of 5 (nominal concrete cube strength = 25 N/mm^2)

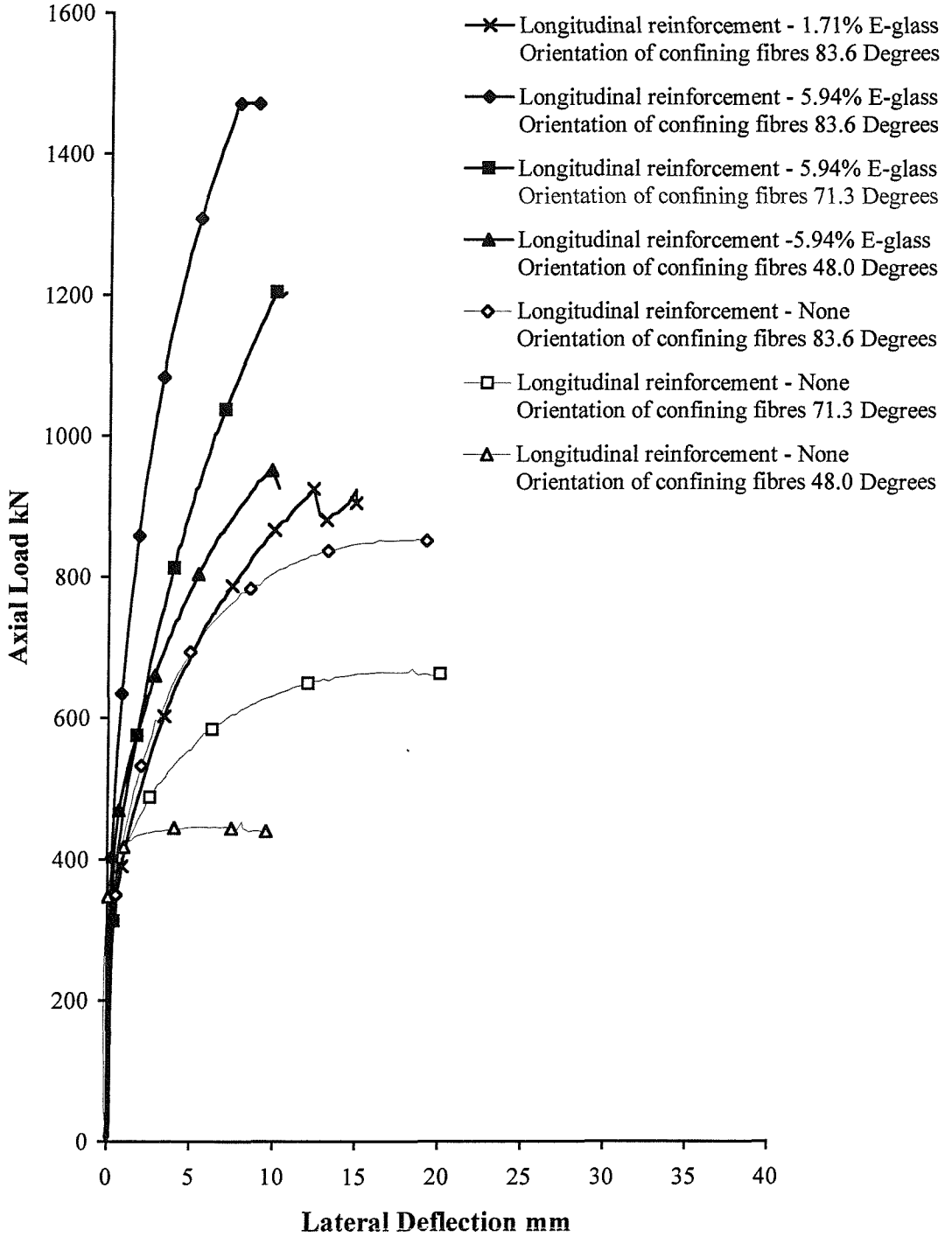

Figure K.4. Load-deflection curves for the 150 mm diameter concrete-filled E-glass FRP-composite columns with longitudinal E-glass FRP-composite bars and a slenderness ratio of 5 (nominal concrete cube strength = 35 N/mm^2)

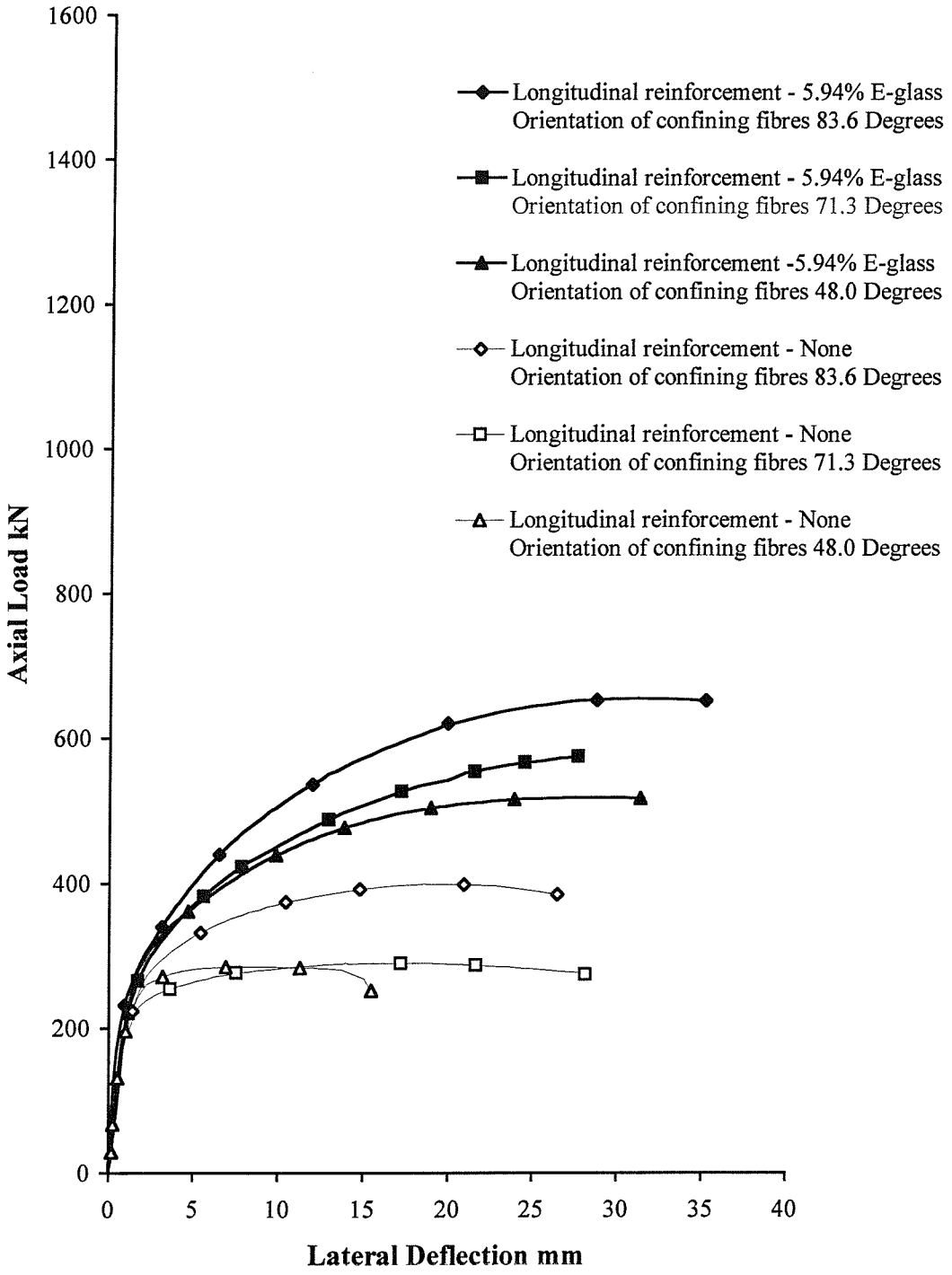

Figure K.5. Load-deflection curves for the 150 mm diameter concrete-filled E-glass FRP-composite columns with longitudinal E-glass FRP-composite bars and a slenderness ratio of 10 (nominal concrete cube strength = 25 N/mm^2)

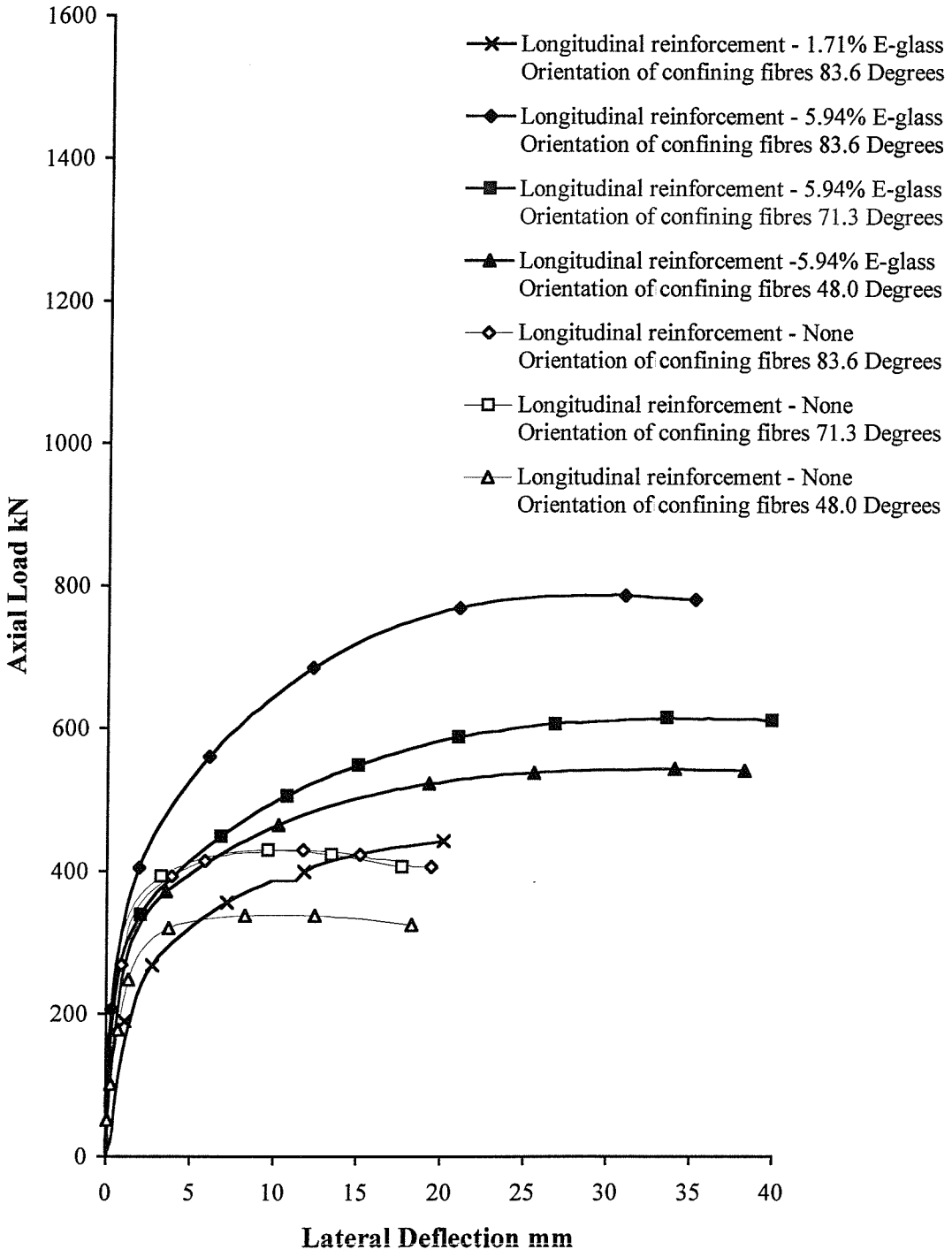

Figure K.6. Load-deflection curves for the 150 mm diameter concrete-filled E-glass FRP-composite columns with longitudinal E-glass FRP-composite bars and a slenderness ratio of 10 (nominal concrete cube strength = 35 N/mm^2)

APPENDIX L

EXPERIMENTAL MOMENT-CURVATURE RELATIONSHIPS FOR CONCRETE-FILLED E-GLASS FRP-COMPOSITE COLUMNS REINFORCED LONGITUDINALLY WITH FRP-COMPOSITE BARS

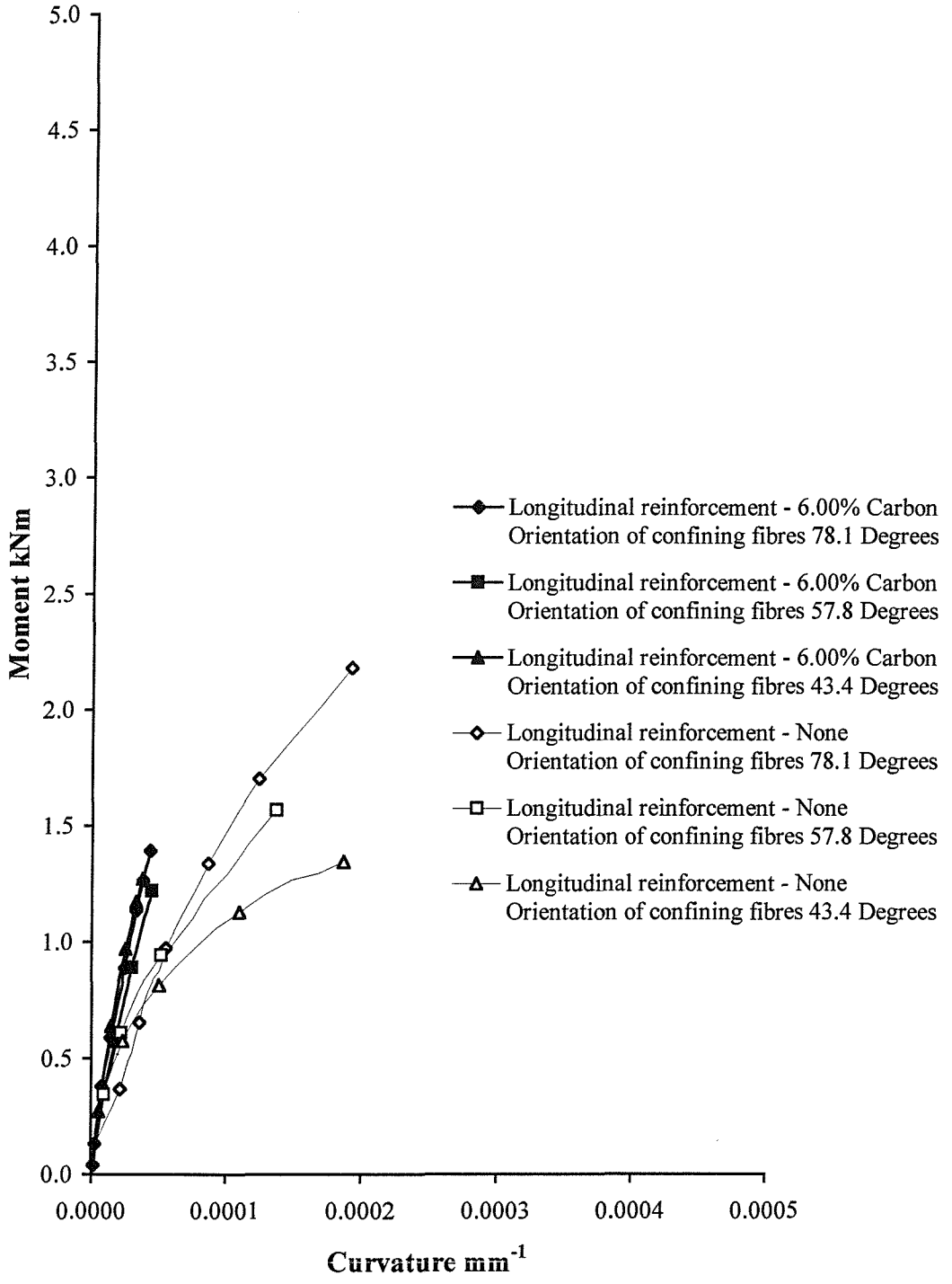

Figure L.1. Moment-curvature relationships for the 80 mm diameter concrete-filled E-glass FRP-composite columns, reinforced longitudinally with carbon FRP-composite bars (slenderness ratio = 5)

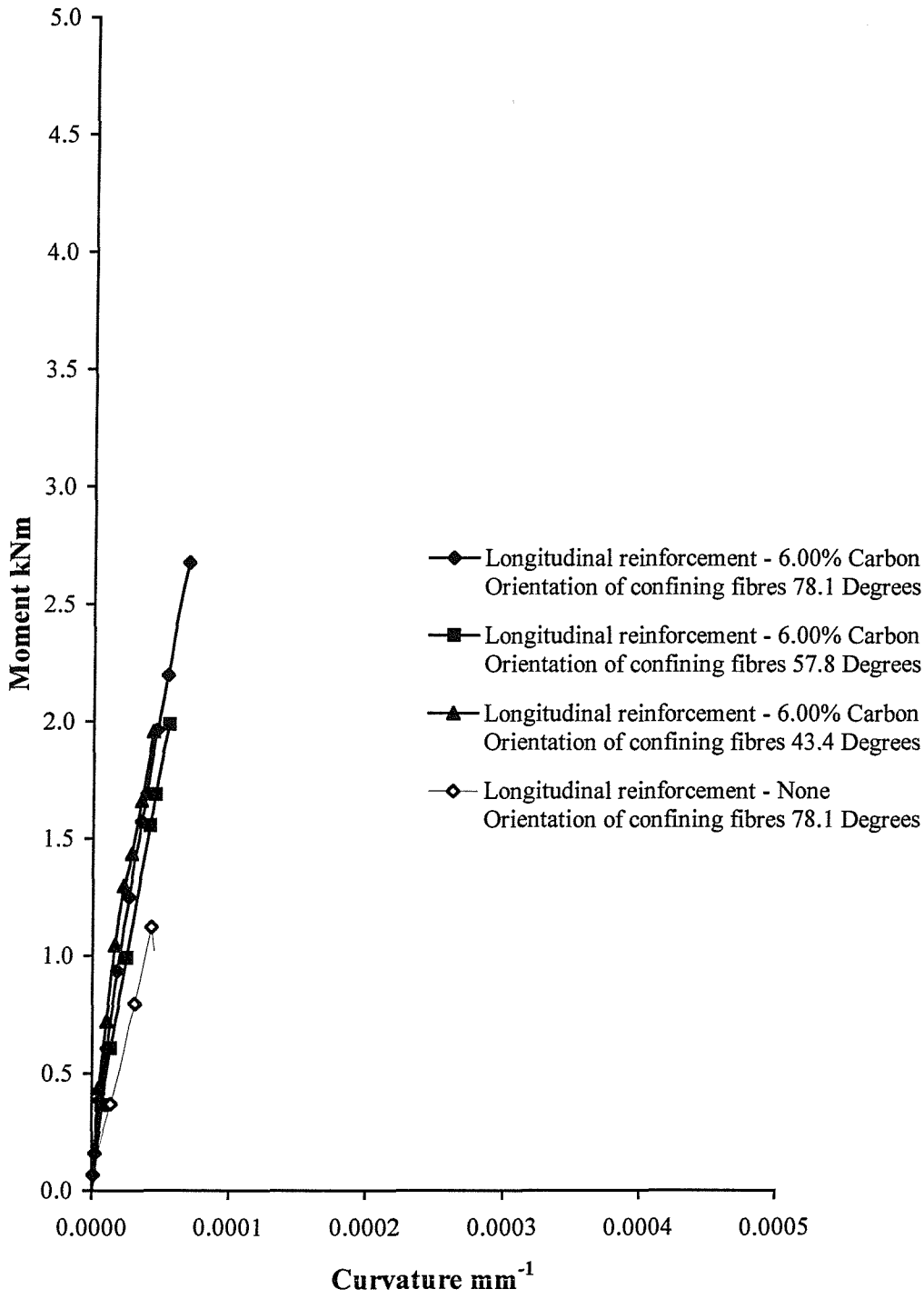

Figure L.2. Moment-curvature relationships for the 80 mm diameter concrete-filled E-glass FRP-composite columns, reinforced longitudinally with carbon FRP-composite bars (slenderness ratio = 10)

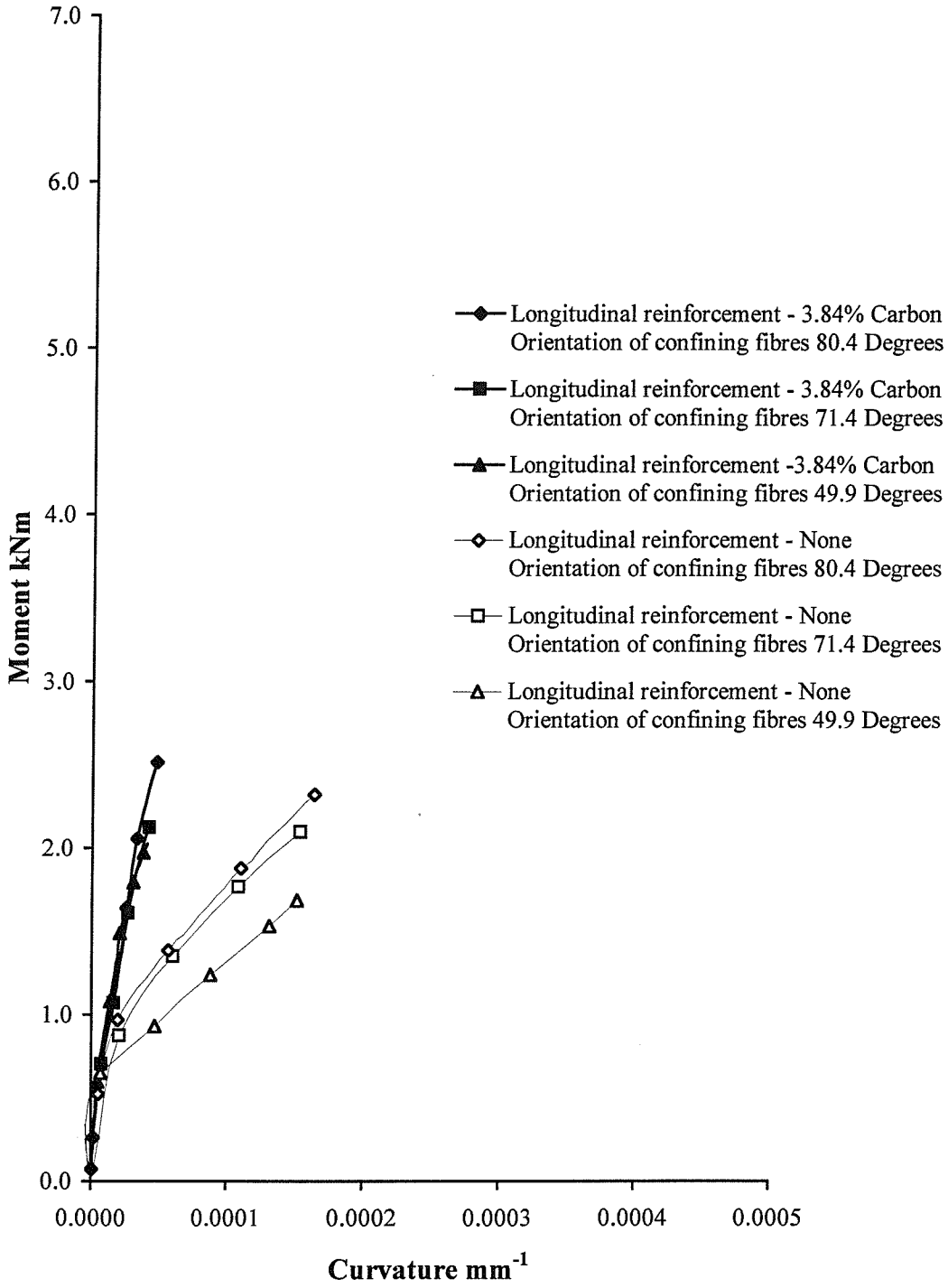

Figure L.3. Moment-curvature relationships for the 100 mm diameter concrete-filled E-glass FRP-composite columns, reinforced longitudinally with carbon FRP-composite bars (slenderness ratio = 5)

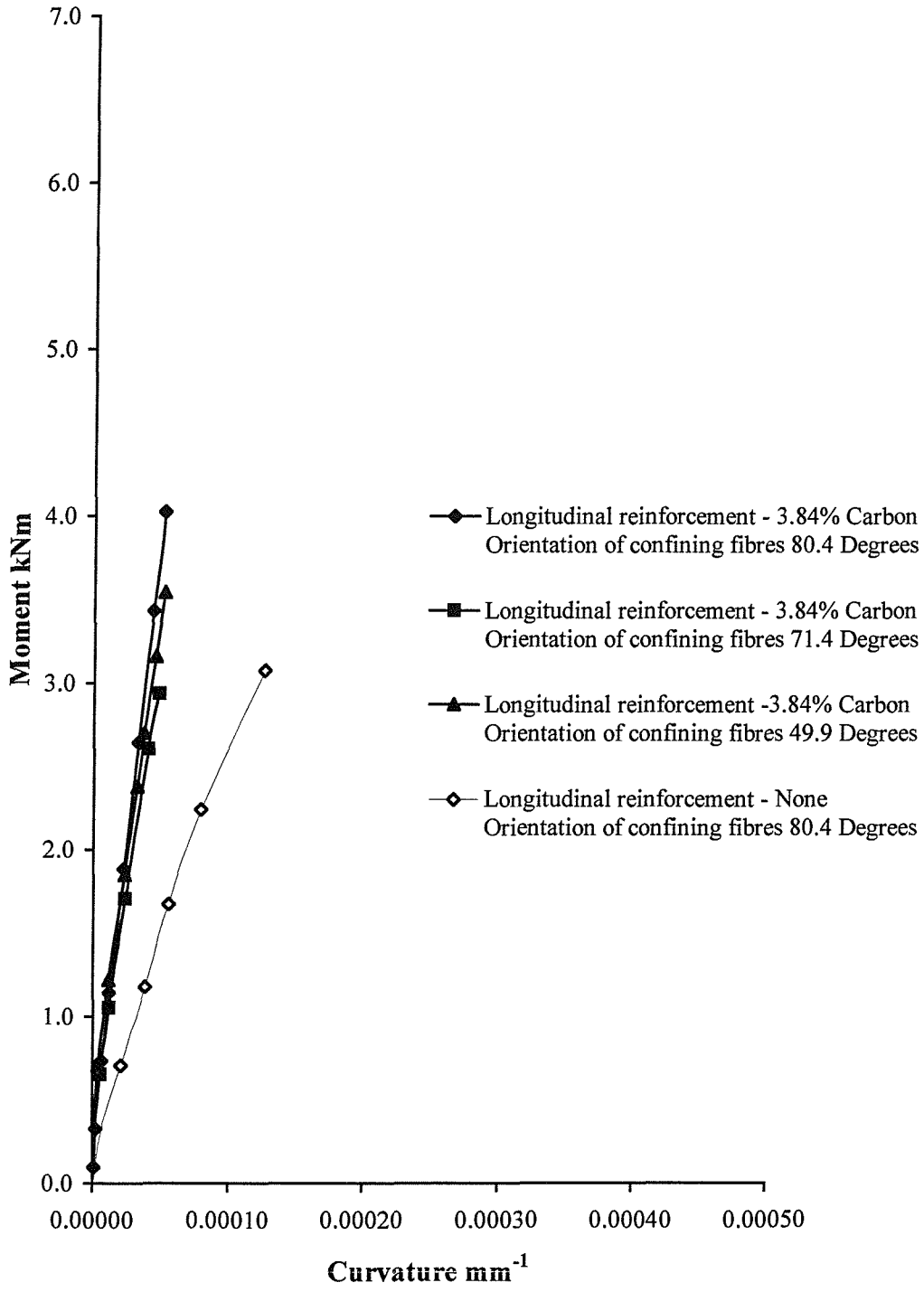

Figure L.4. Moment-curvature relationships for the 100 mm diameter concrete-filled E-glass FRP-composite columns, reinforced longitudinally with carbon FRP-composite bars (slenderness ratio = 10)

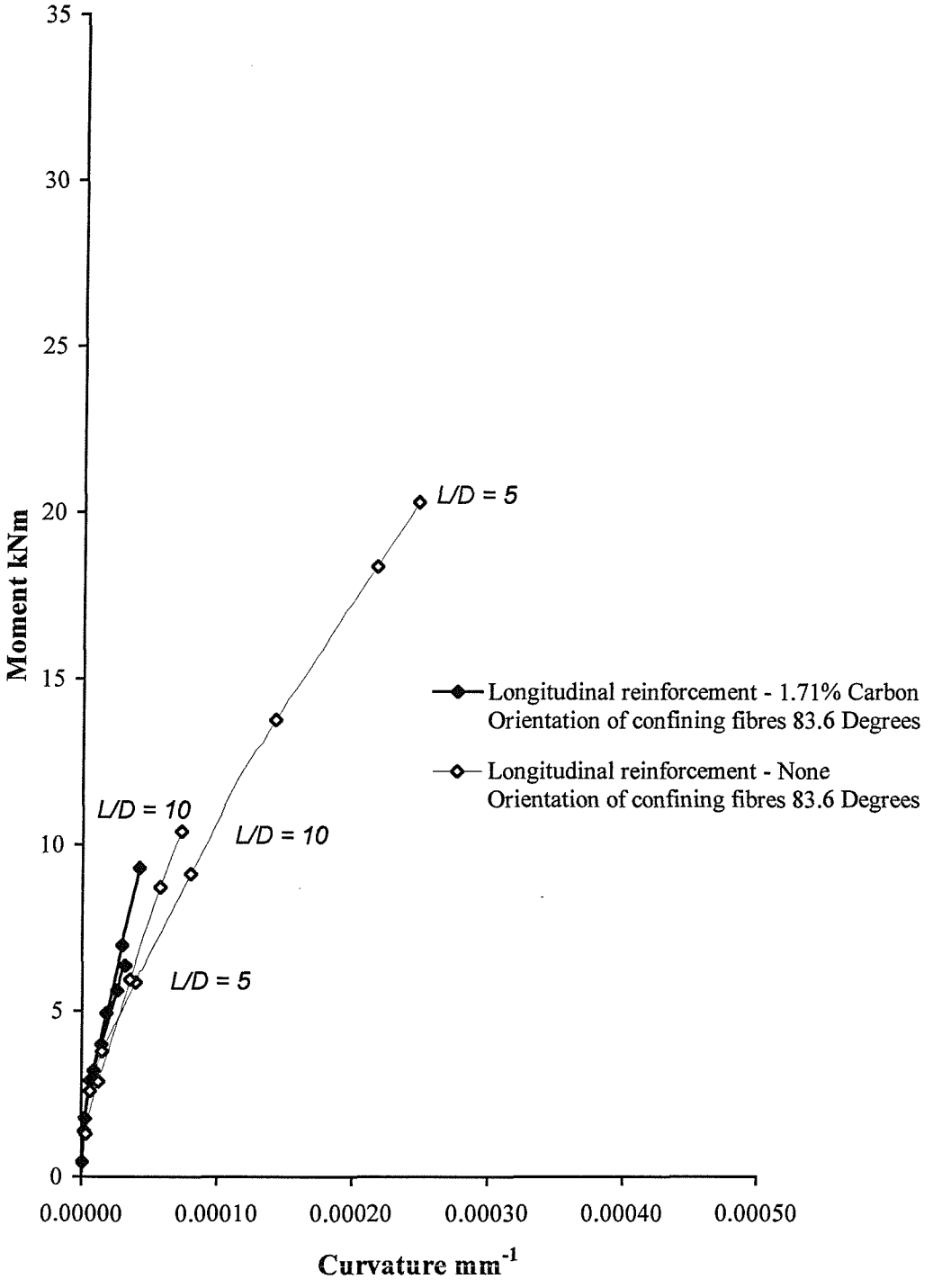

Figure L.5. Moment-curvature relationships for the 150 mm diameter concrete-filled E-glass FRP-composite columns, reinforced longitudinally with carbon FRP-composite bars

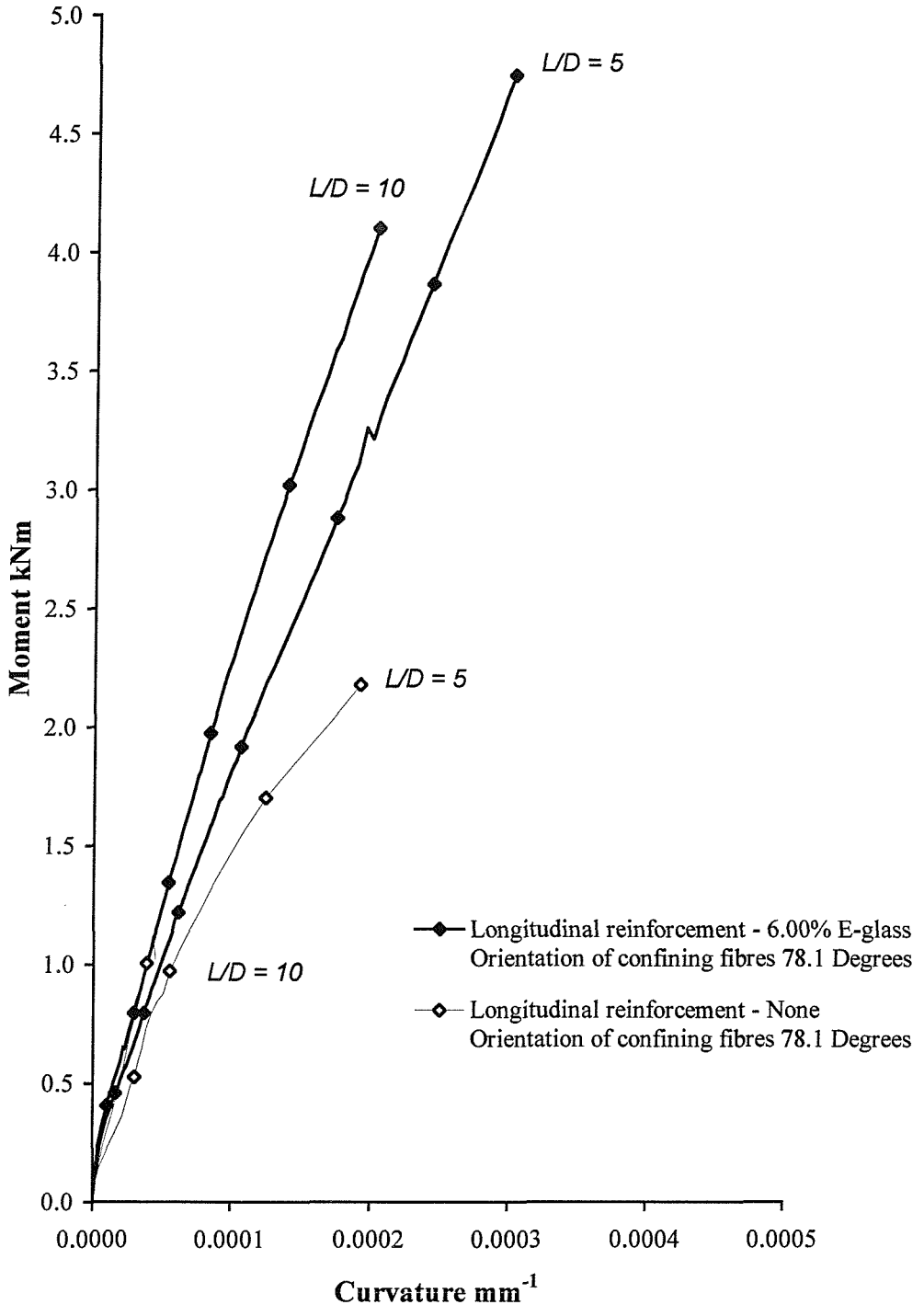

Figure L.6. Moment-curvature relationships for the 80 mm diameter concrete-filled E-glass FRP-composite columns, reinforced longitudinally with E-glass FRP-composite bars

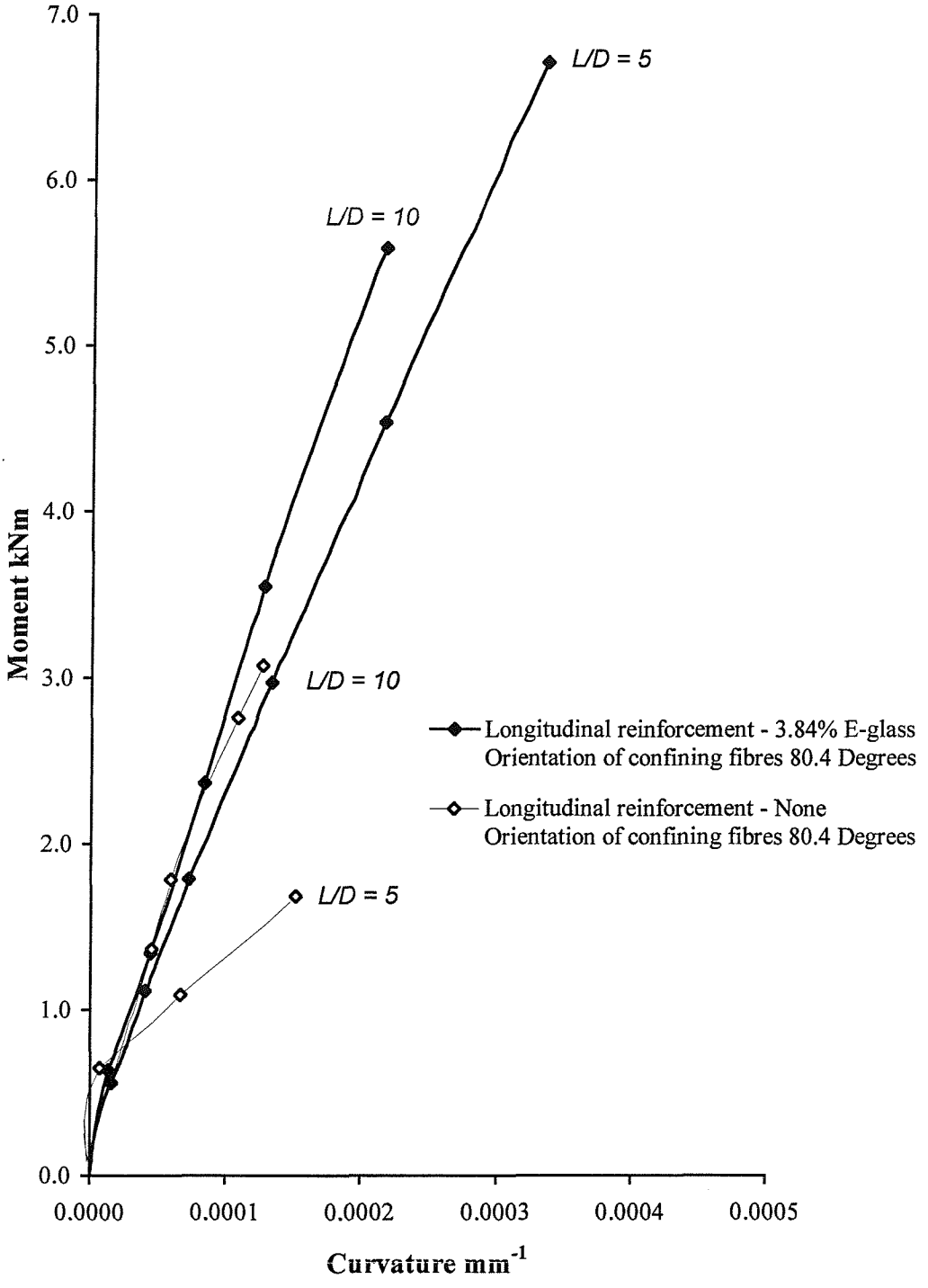

Figure L.7. Moment-curvature relationships for the 100 mm diameter concrete-filled E-glass FRP-composite columns, reinforced longitudinally with E-glass FRP-composite bars

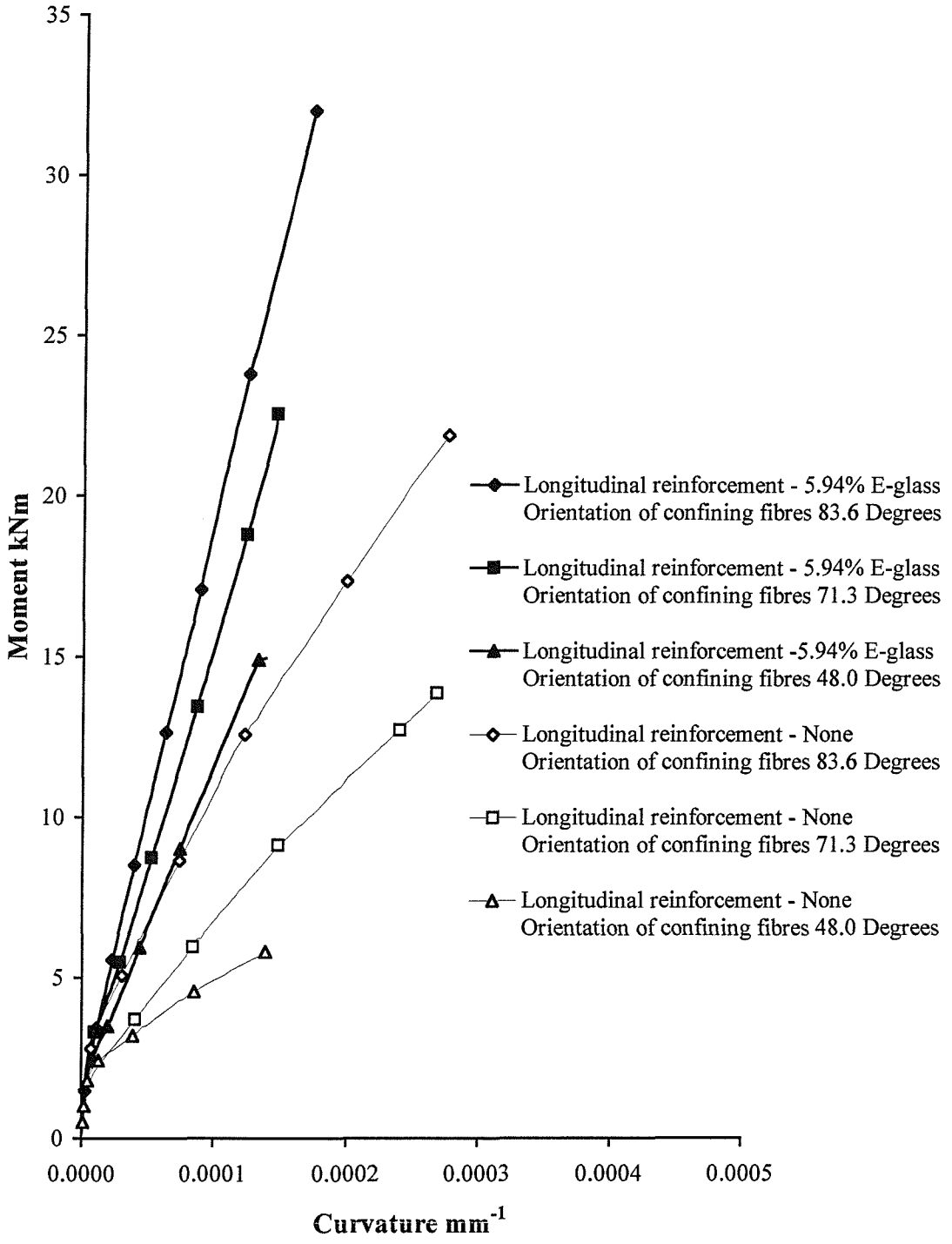

Figure L.8. Moment-curvature relationships for the 150 mm diameter concrete-filled E-glass FRP-composite columns, reinforced longitudinally with E-glass FRP-composite bars and a slenderness ratio of 5 (nominal concrete cube strength = 25 N/mm^2)

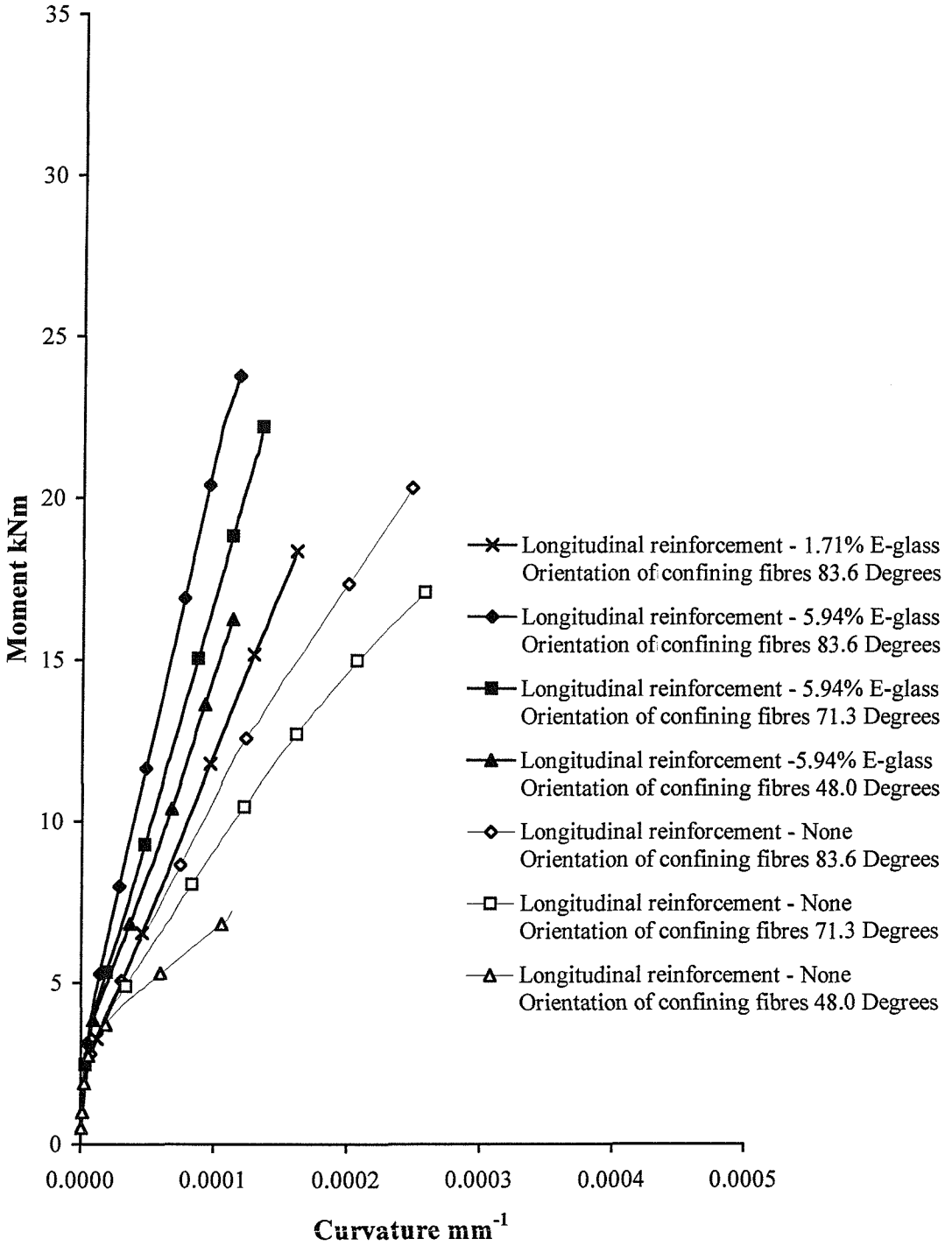

Figure L.9. Moment-curvature relationships for the 150 mm diameter concrete-filled E-glass FRP-composite columns, reinforced longitudinally with E-glass FRP-composite bars and a slenderness ratio of 5 (nominal concrete cube strength = 35 N/mm^2)

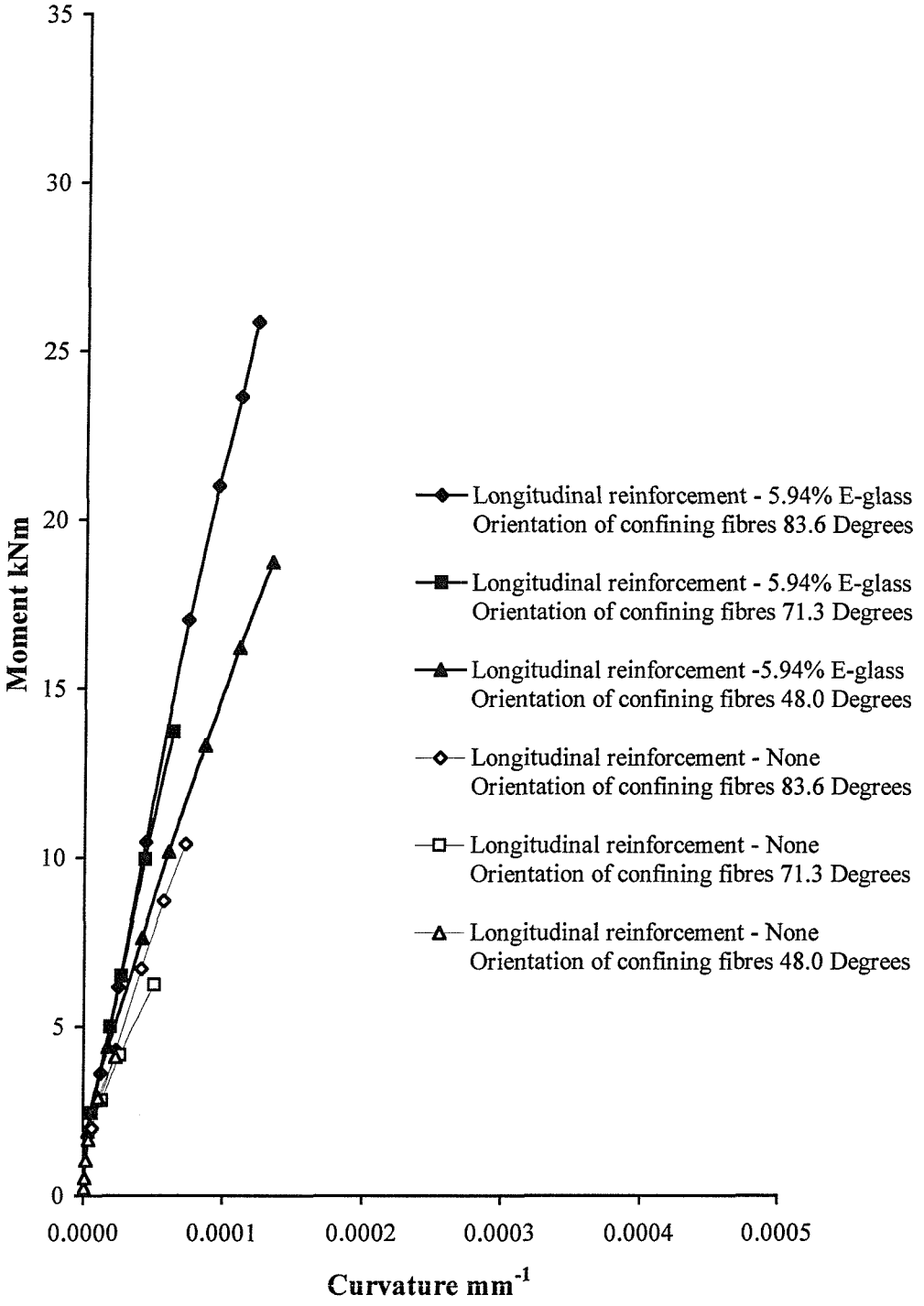

Figure L.10. Moment-curvature relationships for the 150 mm diameter concrete-filled E-glass FRP-composite columns, reinforced longitudinally with E-glass FRP-composite bars and a slenderness ratio of 10 (nominal concrete cube strength = 25 N/mm^2)

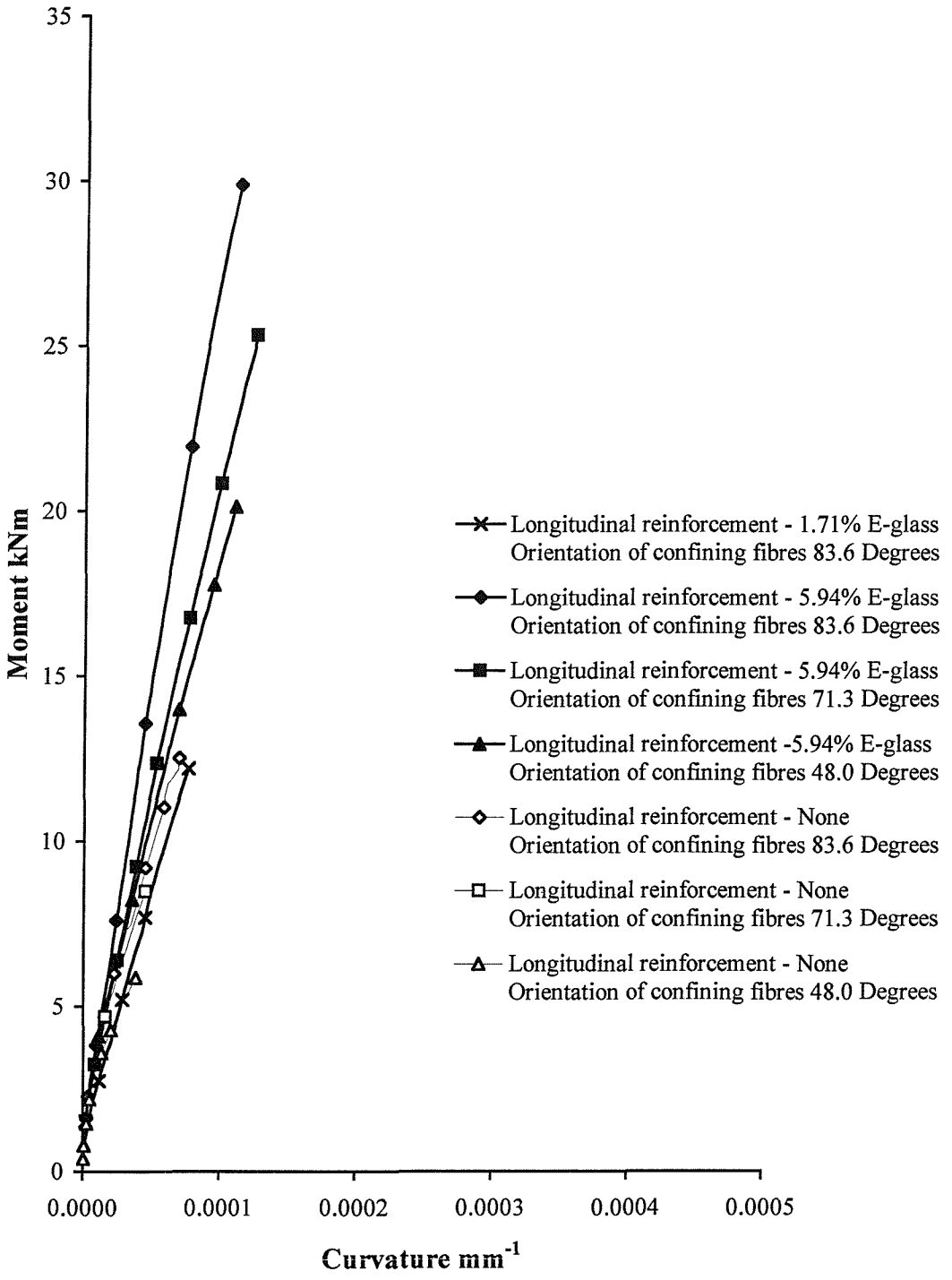

Figure L.11. Moment-curvature relationships for the 150 mm diameter concrete-filled E-glass FRP-composite columns, reinforced longitudinally with E-glass FRP-composite bars and a slenderness ratio of 10 (nominal concrete cube strength = 35 N/mm^2)

APPENDIX M

EXPERIMENTAL LOAD-STRAIN CURVES FOR CONCRETE-FILLED E-GLASS FRP-COMPOSITE COLUMNS REINFORCED LONGITUDINALLY WITH FRP-COMPOSITE BARS

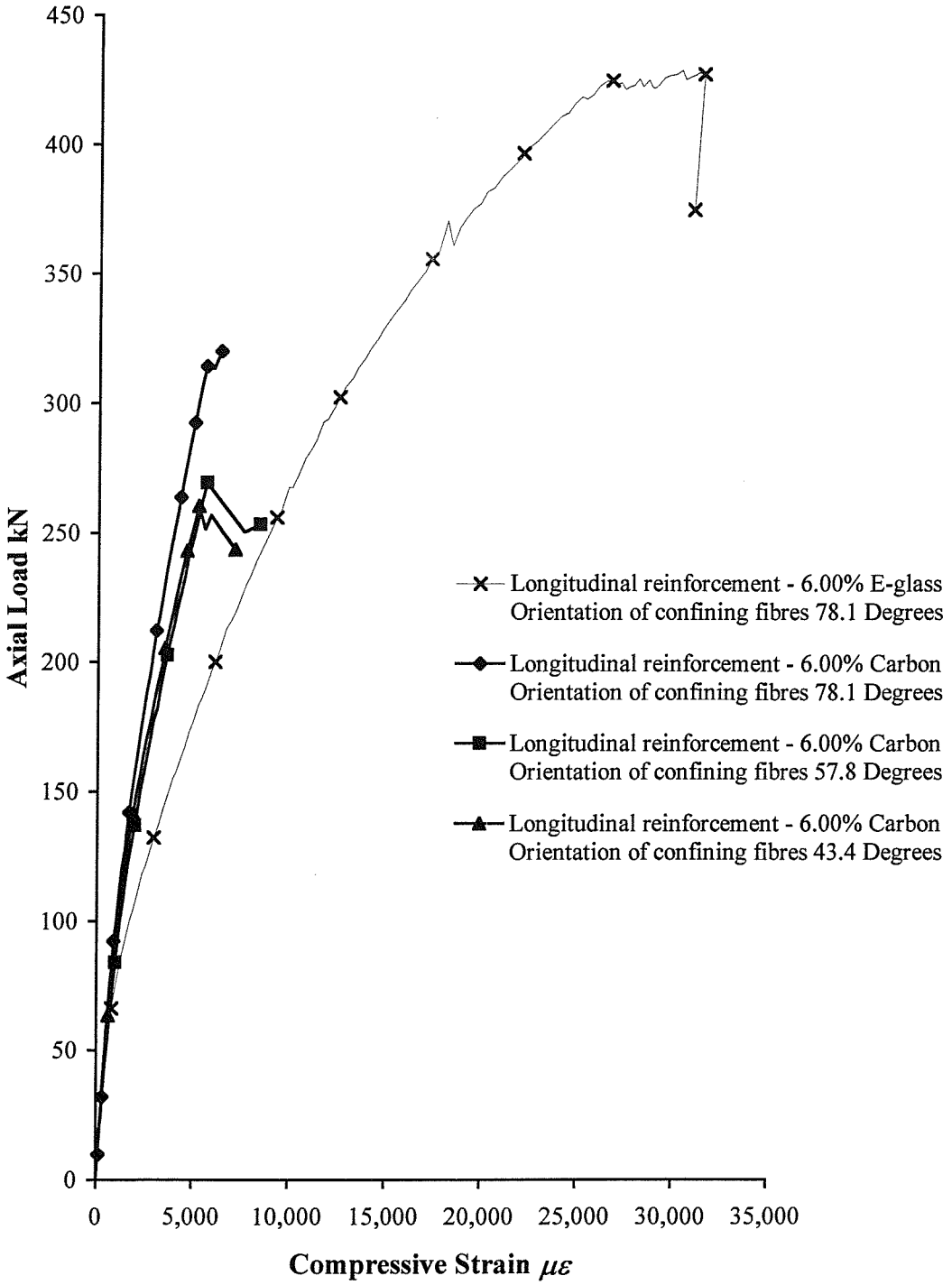

Figure M.1. Load-strain curves for the 80 mm diameter concrete-filled E-glass FRP-composite columns, reinforced longitudinally with FRP-composite bars (slenderness ratio = 5)

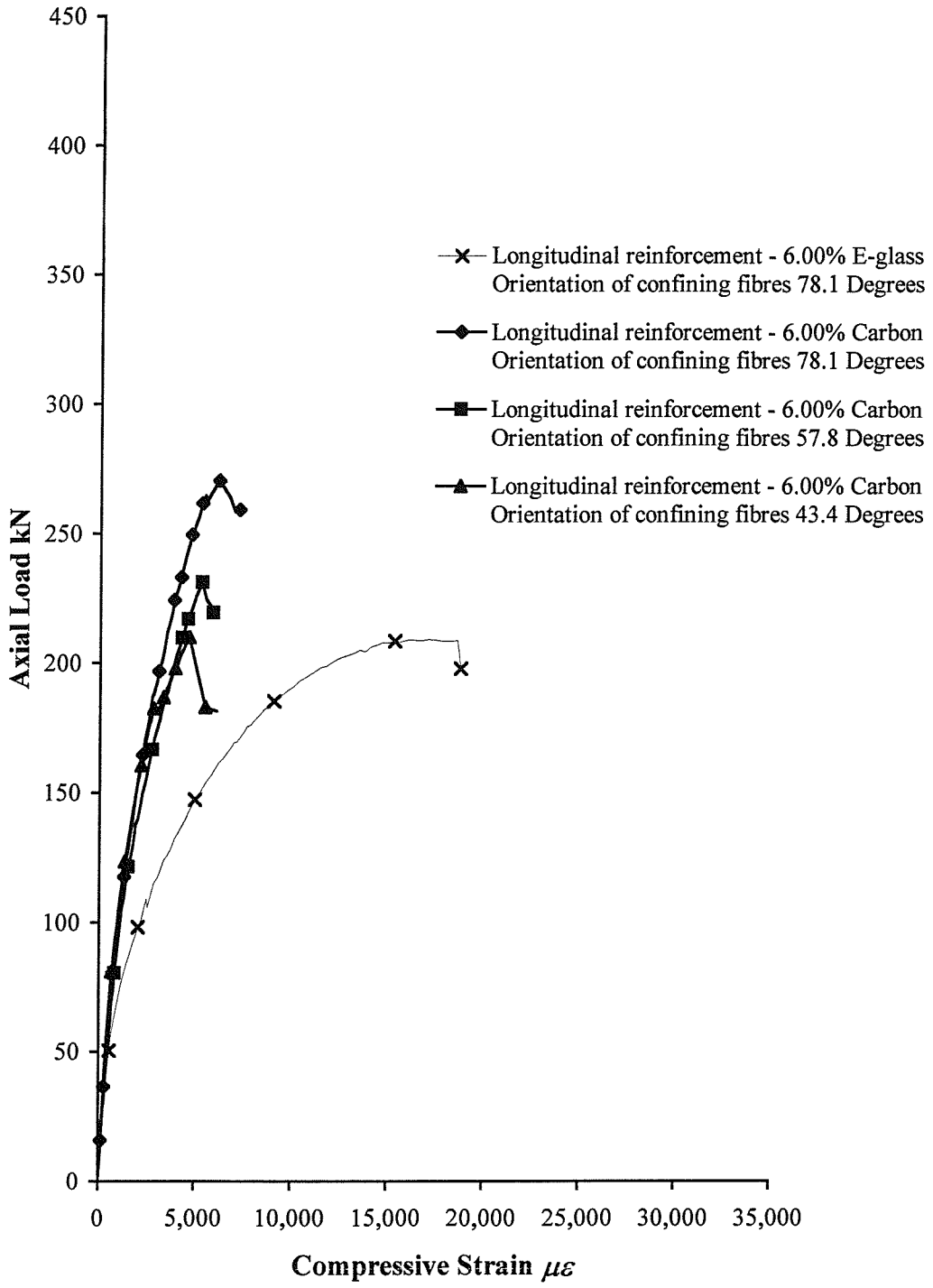

Figure M.2. Load-strain curves for the 80 mm diameter concrete-filled E-glass FRP-composite columns, reinforced longitudinally with FRP-composite bars (slenderness ratio = 10)

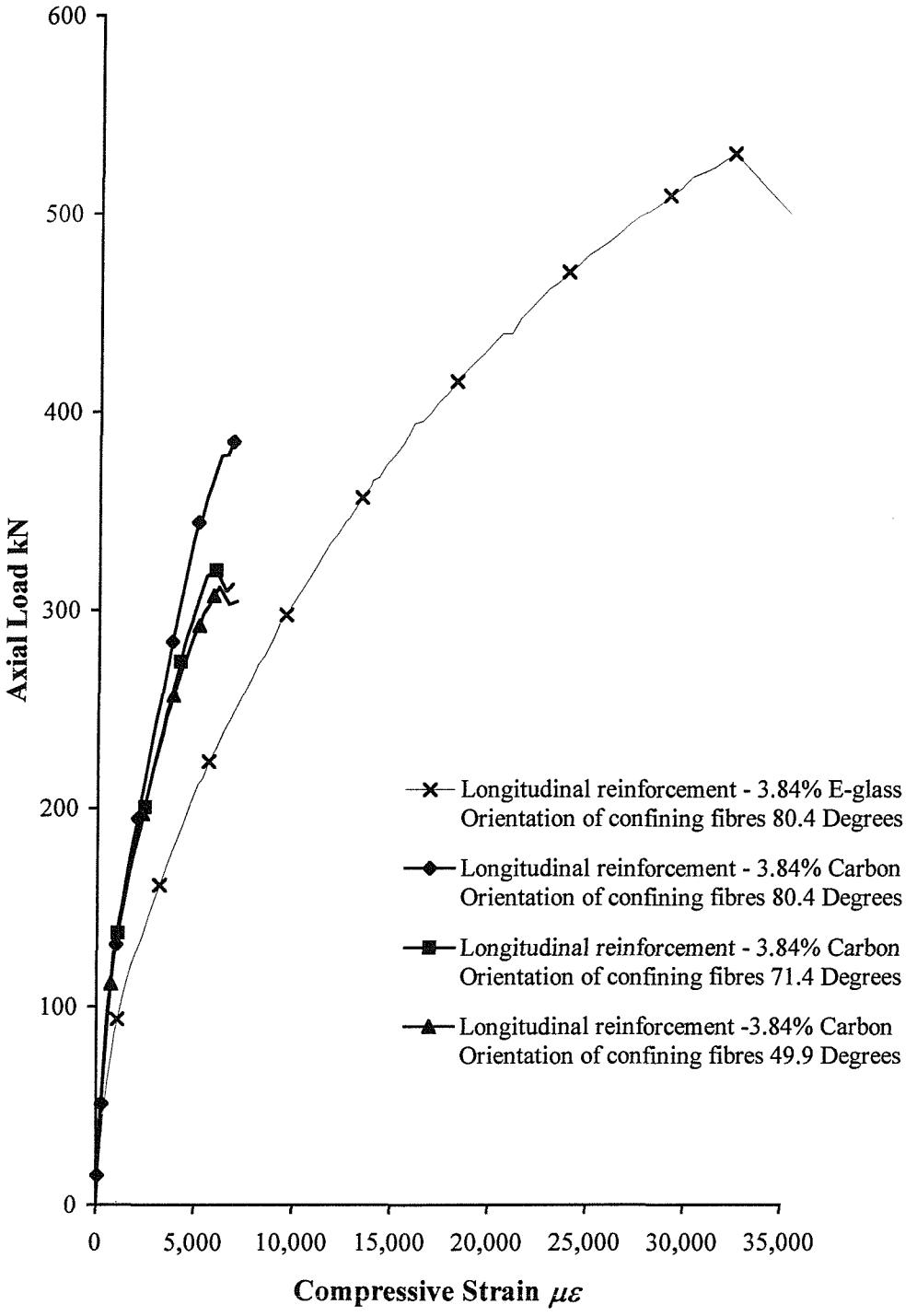

Figure M.3. Load-strain curves for the 100 mm diameter concrete-filled E-glass FRP-composite columns, reinforced longitudinally with FRP-composite bars (slenderness ratio = 5)

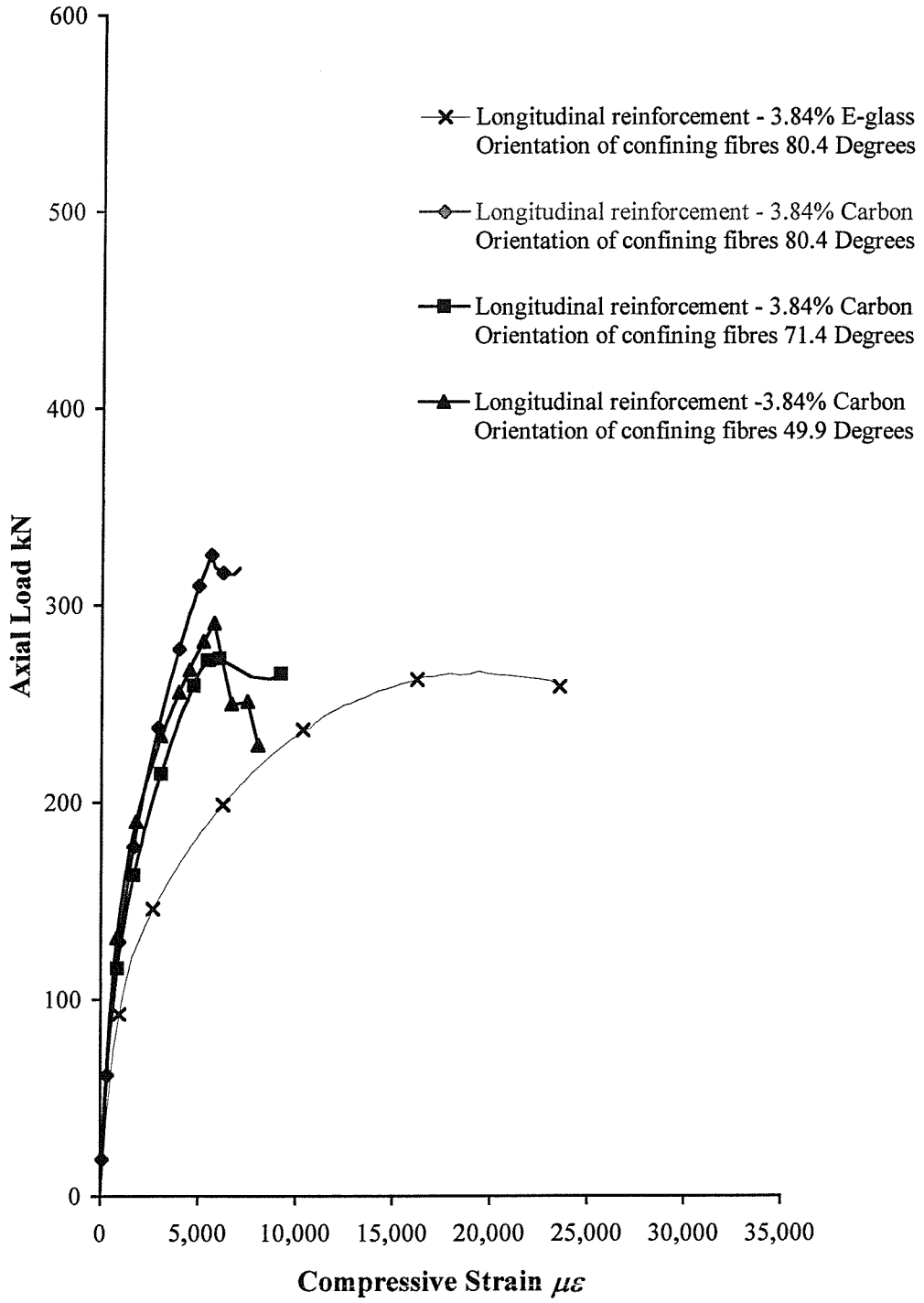

Figure M.4. Load-strain curves for the 100 mm diameter concrete-filled E-glass FRP-composite columns, reinforced longitudinally with FRP-composite bars (slenderness ratio = 10)

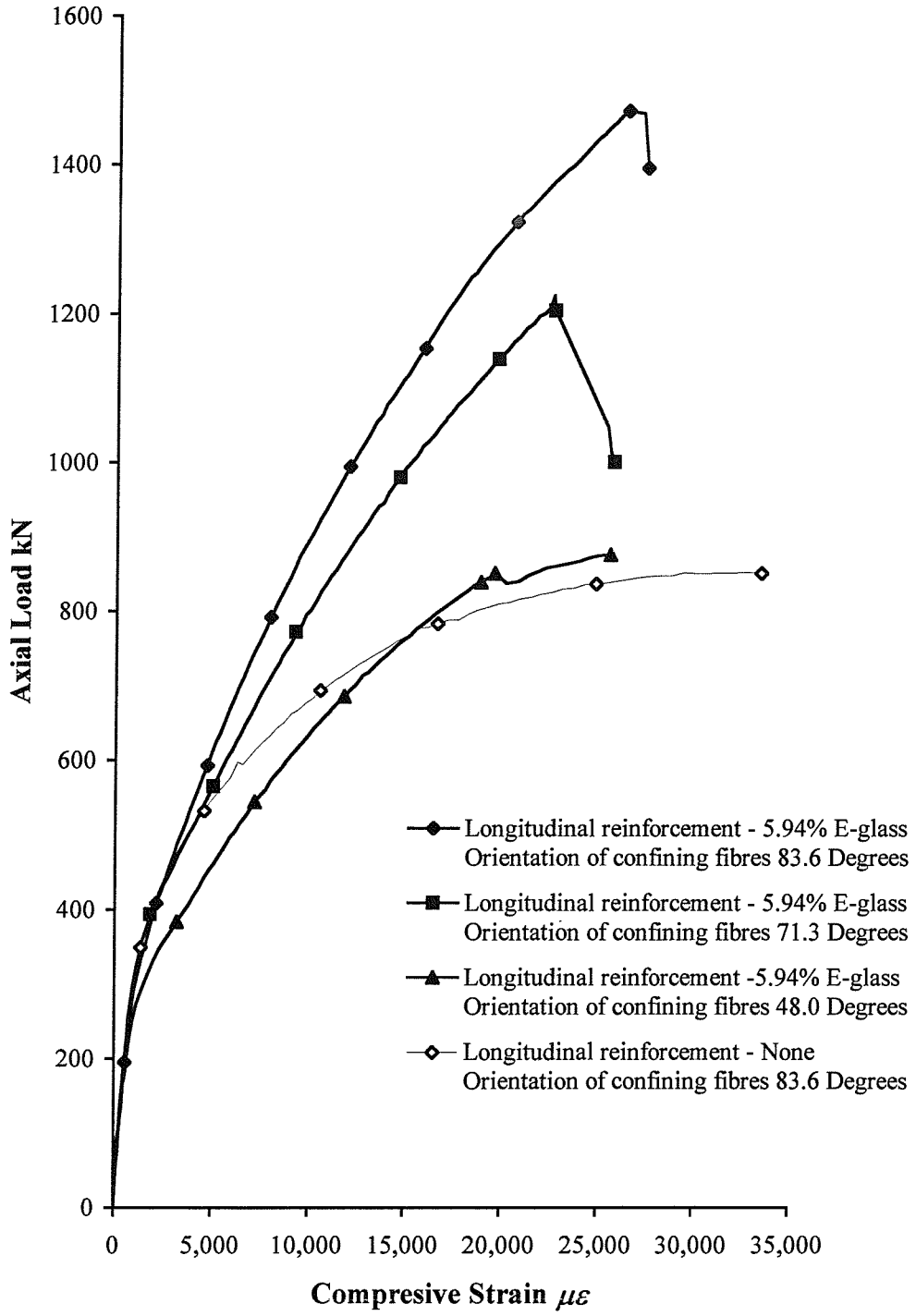

Figure M.5. Load-strain curves for the 150 mm diameter concrete-filled E-glass FRP-composite columns, reinforced longitudinally with FRP-composite bars and a slenderness ratio of 5 (nominal concrete cube strength = 25 N/mm^2)

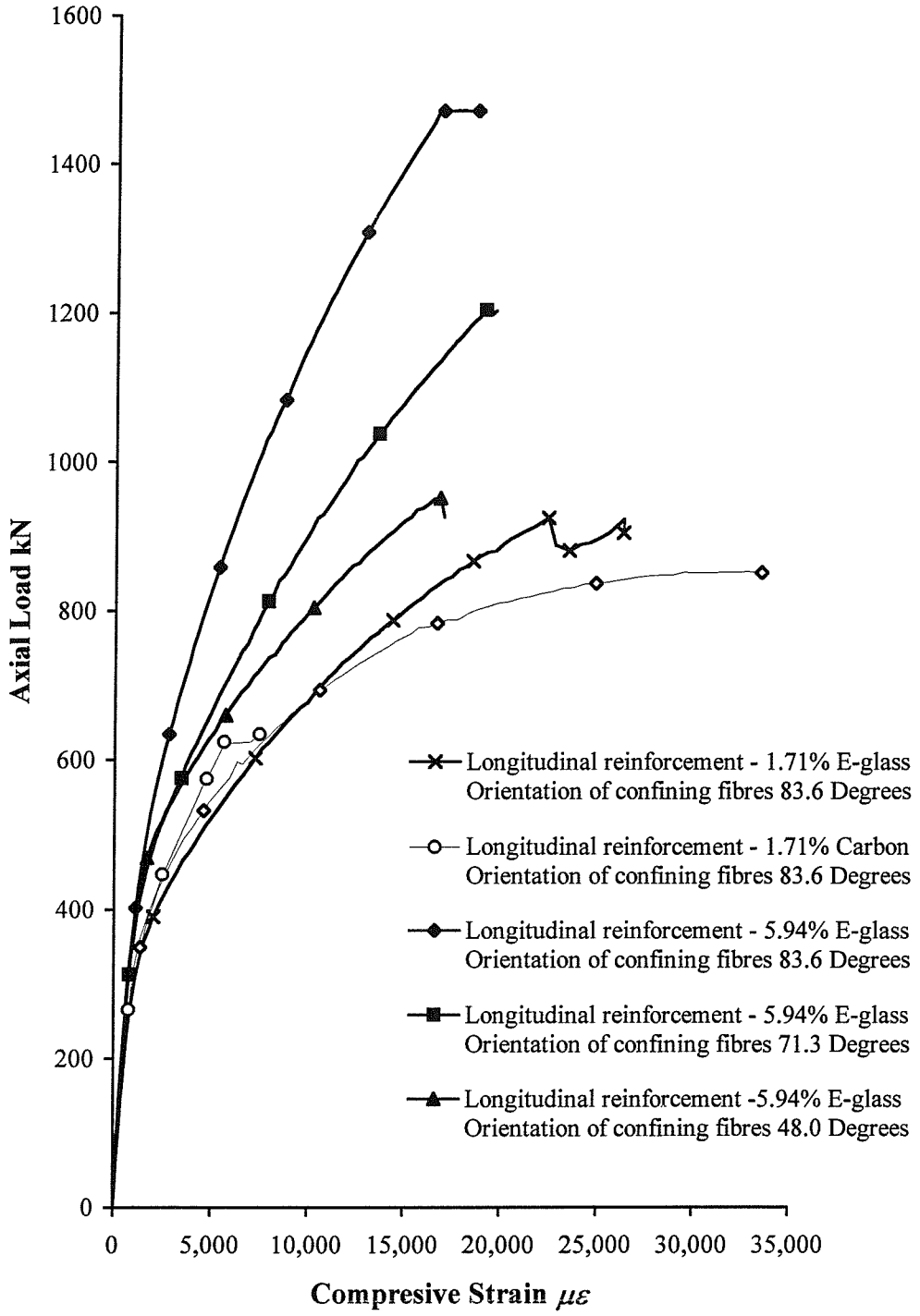

Figure M.6. Load-strain curves for the 150 mm diameter concrete-filled E-glass FRP-composite columns, reinforced longitudinally with FRP-composite bars and a slenderness ratio of 5 (nominal concrete cube strength = 35 N/mm^2)

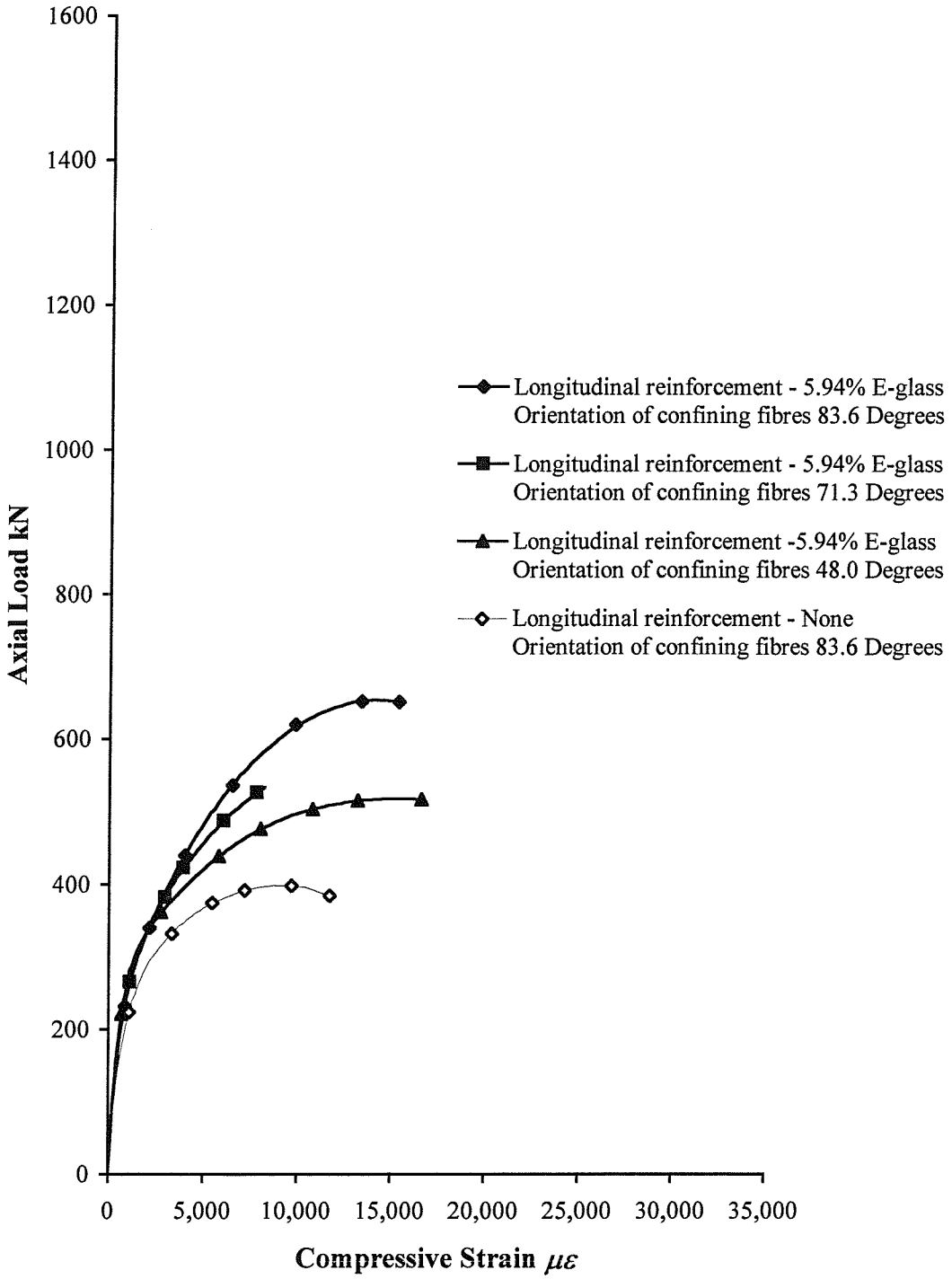

Figure M.7. Load-strain curves for the 150 mm diameter concrete-filled E-glass FRP-composite columns, reinforced longitudinally with FRP-composite bars and a slenderness ratio of 10 (nominal concrete cube strength = 25 N/mm^2)

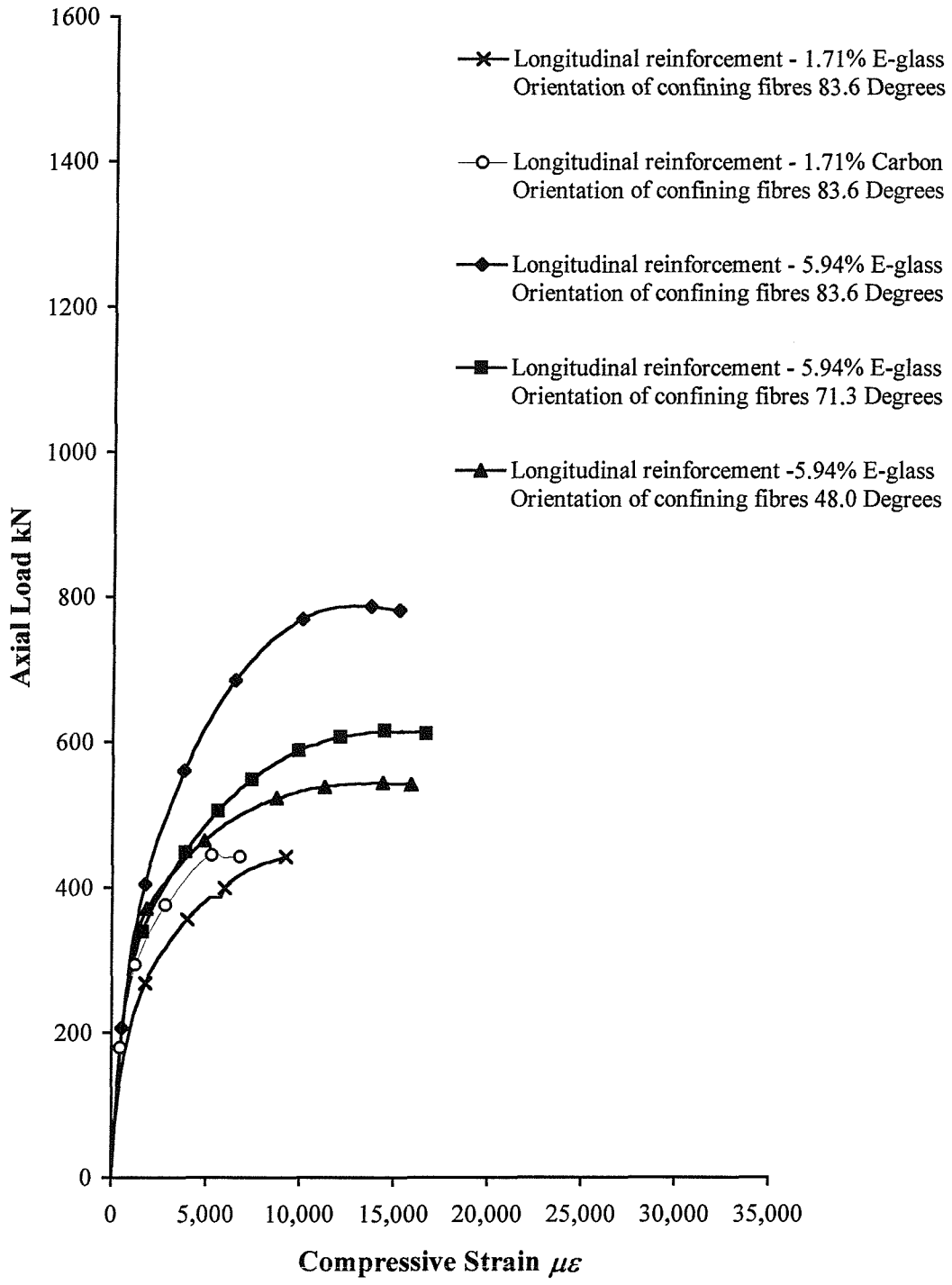

Figure M.8. Load-strain curves for the 150 mm diameter concrete-filled E-glass FRP-composite columns, reinforced longitudinally with FRP-composite bars and a slenderness ratio of 10 (nominal concrete cube strength = 35 N/mm^2)